UNITED STATES PATENT AND TRADEMARK OFFICE

BEFORE THE PATENT TRIAL AND APPEAL BOARD

LG INNOTEK CO. LTD.,

Petitioner,

v.

SEOUL SEMICONDUCTOR CO., LTD.,

Patent Owner.

Case IPR2019-01154
Patent 9,293,664

DECLARATION OF DR. WILLIAM ALAN DOOLITTLE IN SUPPORT OF PATENT OWNER'S PRELIMINARY RESPONSE TO PETITION FOR *INTER PARTES* REVIEW

TABLE OF CONTENTS

I. Legal Standards 5

A. Claim Construction 5

B. Anticipation 6

C. Obviousness.....7

II. The ’664 Patent.....9

A. Claim Construction 19

III. Petitioner Has Not Demonstrated Invalidity 29

A. Illek does not anticipate claims 1–6, 8, 9, 11, or 12 or render obvious claims 1–6 or 8–18 29

B. Donofrio does not teach the protective insulation layer 37

C. A POSITA would not have been motivated to combine Donofrio and Sano.....40

D. None of Sano or Donofrio’s Insulating Layers Cover Sidewalls 41

LIST OF APPENDICES

Appendix A	Curriculum Vitae of William Alan Doolittle
Appendix B	S. W. Ing, Jr., et al., "Gas Permeation Study and Imperfection Detection of Thermally Grown and Deposited Thin Silicon Dioxide Films", J. Electrochemical Soc'y, 109 (3), 221-226 (March 1962).
Appendix C	A. Ortiz, et al., "Plasma Enhanced Chemical Vapor Deposition of SiO_2 Films at Low Temperatures Using $SiCl_4$ and O_2", J. Elec. Materials, 19 (12), 1411-1415 (1990).
Appendix D	A. Barranco, et al., "Room temperature synthesis of porous SiO_2 thin films by plasma enhanced chemical vapor deposition", J. Vacuum Sci. Tech., 22 (4), 1275-1284 (Jul/Aug 2004).
Appendix E	E. Hammarberg, et al., "Antireflection treatment of low-emitting glazings for energy efficient windows with high visible transmittance", Thin Solid Films, 442, 222-226 (2003).
Appendix F	C. H. Chiu, et al., "Enhancement of InGaN/GaN Flip-Chip ITO LEDs with Incline Sidewalls Coated with TiO_2/SiO_2 Omnidirectional Reflector", J. Electrochemical Soc'y, 154 (11), H944-H947 (Sept 2007).
Appendix G	C. Cho, et al., "Enhanced light extraction in light-emitting diodes with photonic crystal structure selectively grown on p-GaN", Appl. Phys. Lett., 96, 181110 (2010).
Appendix H	K. Kusakabe, et al., "Fabrication and optical properties of blue LEDs with silica microsphere coating", Phys. Stat. Sol., 4 (1), 25-28 (2007).
Appendix I	K. Barla, et al., "Stress in oxidized porous silicon layers", J. Appl. Phys., 59 (2), 439-441 (1986).

Appendix J	G. Xu, et al., "Optical investigation of silicon nitride thin films deposited by r.f. magnetron sputtering", Thin Solid Films, 425, 196-202 (2003).
Appendix K	Z. Yin, et al., "Optical dielectric function and infrared absorption of hydrogenated amorphous silicon nitride films: Experimental results and effective-medium-approximation analysis", Physical Review B, 42 (6), 196-202 (Aug 1990).
Appendix L	G. Abromavicius, et al., "The microstructure and LIDT of Nb_2O_5 and Ta_2O_5 optical coatings", Prog. Photovolt: Res. Appl., 7, 245-260 (1999).
Appendix M	H. Nagel, et al., "Optimised Antireflection Coatings for Planar Silicon Solar Cells using Remote PECVD Silicon Nitride and Porous Silicon Dioxide", Proc. of SPIE, 6403, 640315 (Jan 2007).
Appendix N	J. Dupuis, et al., "Optical and structural properties of silicon oxynitride deposited by plasma enhanced chemical vapor deposition", Thin Solid Films, 519, 1325-1333 (2010).
Appendix O	U. Chakrabarti, et al., "A new process of oxide growth on silicon", Indian Inst. Sci., 28-36 (1975).
Appendix P	A. Ikeda, et al., "Effect of nitrogen plasma conditions on electrical properties of silicon oxynitrided thin films for flash memory applications", Thin Solid Films, 386, 111-116 (2001).
Appendix Q	U.S. Patent No. 6,797,650 "Flash memory devices with oxynitride dielectric as the charge storage media" issued to Wang et al.
Appendix R	A. Tricoli, et al., "Highly porous TiO_2", J. Mater. Chem., 28 (2012).

Appendix S	Producer® Black Diamond® PECVD, Applied Materials, http://www.appliedmaterials.com/products/producer-black-diamond-pecvd

I Dr. William Alan Doolittle, declare as follows:

1. I have been retained by Patent Owner Seoul Semiconductor Co., Ltd. as an expert witness in the above-captioned proceeding. I am being compensated for the time I spend on this proceeding on an hourly basis. This declaration is based upon my knowledge, skill, experience, training, and education in my field of expertise, and upon information reviewed in connection with my retention as an expert witness in this matter. My compensation does not depend on any outcome or order in this proceeding.

2. I am the Joseph M. Pettit Professor in the School of Electrical and Computer Engineering at Georgia Institute of Technology ("Georgia Tech"). A complete history of my employment history, honors and awards, and scholarship can be found in my curriculum vitae, attached as Appendix A.

3. I received a Bachelor's degree in Electrical Engineering from Georgia Tech in 1989. I then received a Doctorate (Ph.D.) in Electrical Engineering from Georgia Tech in 1996.

4. Since obtaining my Ph.D., I have held numerous roles at Georgia Tech, including as a professor, associate professor, and research engineer. I have won numerous awards for my teaching and research, including the 2004 National Science Foundation CAREER Award, three Multidisciplinary University Research Initiative awards for Epitaxial Multifunctional Materials and Applications,

Laboratory Instrumentation Design Research for Scalable Next Generation Epitaxy, and Cross Disciplinary Electronic-ionic Research Enabling Biologically Realistic Autonomous Learning, and numerous research and teaching awards.

5. I have published over 150 refereed journal and conference papers and conference proceedings in the subject matter areas of compound semiconductor materials and devices. These works have been published in journals including Scientific Reports, Journal of Applied Physics, Applied Physics Letters, Journal of Crystal Growth, IEEE Journal of Photovoltaics, Electronic Materials Letters, and Current Topics in Solid State Physics, among many others. I am a named inventor on eight issued patents and four pending applications. I am the founder of two companies, Innovative Advanced Materials Inc. and Innovative Advanced Technologies. Both of these companies focus on commercialization of state of the art epitaxial growth systems that bridge the benefits of the two most popular growth methodologies, MOCVD and MBE. I have been awarded numerous grants totaling about $38 million dollars and have published numerous papers that examine III-Nitride LEDs , solar cells, photodetectors and various transistors including HEMTs and HBTs as well as the fundamental physics of III-Nitride epitaxial growth. I pioneered hyper-doping of III-Nitrides and have led the field in the new emerging area of tunnel junctions in the nitride semiconductor family.

6. I have given over 150 talks and seminars in the U.S. and abroad,

including over 35 invited and keynote addresses. I am also a Senior Member of the Institute of Electrical Electronic Engineering (IEEE). I have twice (2016 and 2019) been selected by a diverse international advisory committee made up of some of the most prominent scientists in the III-Nitride semiconductor community to lead (Chair) the two largest conferences in the field: the International Workshop on Nitride Semiconductors (IWN - 2016) and the International Conference on Nitride Semiconductors (ICNS 2019). Additionally, I have served as a program chair selecting the best contributions and organizing lectures for each of these meetings in 2010 (IWN) and 2013/2017 (ICNS). In these capacities, I have not only been recognized as an international leader in the field but also as an expert in what the entire III-Nitride community is doing. This breadth of experience and knowledge of what is ongoing in the field sets me apart from Dr. Bretschneider in this specific technical area since most of his experience has been narrower in lighting systems and very targeted/specific LED designs and applications. I am aware of Dr. Bretschneider's background and accomplishments and respect him as a colleague. Thus, my opinions are not meant to disparage him, but to point out the technical deficiencies in his report, some of which are fairly obvious to a person skilled in the art.

7. I do not have any financial or other interest in the outcome of this matter or in any of the parties to these actions. My hourly rate is $400/hour plus

expenses, and my compensation does not depend in any way upon the contents of this report, the outcome of this proceeding, or the results of my service as an expert.

8. Based on the above education and experience, I believe that I have a detailed understanding of the state of the art during the relevant period, as well as a sound basis for opining how persons of skill in the art at that time would understand the technical issues in this case.

9. I have reviewed the specification and file history of U.S. Pat. No. 9,293,664 (the "'664 Patent), and exhibits filed with LG Innotek Co. Ltd.'s ("Petitioner") Petition.

10. Petitioner's grounds from the Petition are excerpted below:

Ground	'664 Patent Claims	Basis for Rejection
Ground 1A	1-6, 8, 9, 11, 12	§102 over Illek
Ground 1B	1-6, 8-18	§103 over Illek
Ground 1C	7, 19	§103 over Illek and Begemann
Ground 2A	1-19	§103 over Donofrio and Sano
Ground 2B	19	§103 over Donofrio, Sano, and Begemann

11. For the reasons described herein, I conclude that petitioner has not demonstrated that the challenged claims of the '664 Patent are anticipated or rendered obvious.

12. This declaration is based on the information currently available to me.

To the extent that additional information becomes available, I reserve the right to continue my investigation and study.

I. Legal Standards

13. I have been informed by counsel that the following legal standards apply. I have applied them in my analysis.

A. Claim Construction

14. I understand that claim terms are generally given their ordinary and customary meaning as understood by a person of ordinary skill in the art at the time of the invention when read in the context of the specification and prosecution history unless a patentee sets out a different definition or clearly disavows claim scope. I further understand that extrinsic evidence such as expert or inventor testimony, dictionaries, and learned treatises can help determine the meaning of claim terms, although that evidence is less significant than the claims, specification, and prosecution history.

15. I understand that claims are to be interpreted from the perspective of a person of ordinary skill in the relevant art at the time of invention. I understand that, to assess the level of ordinary skill in the art, that one may consider factors such as the education level of the inventor, the type of problems encountered in the art, prior art solutions to those problems, rapidity with which innovations are made, sophistication of the technology, and educational level of those in the field.

16. For the purposes of my analysis herein, I have applied the standard set forth in Petitioner's Petition, *i.e.*, that a person of ordinary skill in the art has "Bachelor of Science degree (or equivalent) in electrical engineering, physics, or a comparable field… Additionally, a POSITA would have had two or more (e.g., 2-5 years of experience in design and/or manufacturing of LED devices." I reserve the right to challenge this formulation at a later date.

B. Anticipation

17. It is my understanding that if each and every element of a claim is disclosed in a single prior art reference, then the claimed invention is anticipated. In order for an invention in a claim to be anticipated, all of the elements and limitations of the claim must be disclosed in a single prior reference, arranged as in the claim. A claim is anticipated only if each and every element as set forth in the claim is found, either expressly or inherently described, in a single prior art reference. To anticipate, there must be no difference between the claimed invention and the reference disclosure, as viewed by a person of ordinary skill in the art.

18. It is my understanding that in order for a reference to inherently disclose a claim limitation, that claim limitation must necessarily be present in the reference. Inherency may not be established by probabilities or possibilities.

19. I understand that, for anticipation, that the prior art references must be

viewed from the perspective of a person of ordinary skill in the relevant art, at the time the invention was made.

C. Obviousness

20. It is my understanding that obviousness is a basis for invalidity. I understand that where a prior art reference does not disclose all of the limitations of a given patent claim, that patent claim is invalid if the differences between the claimed subject matter and the prior art reference are such that the claimed subject matter as a whole would have been obvious at the time the invention was made to a person having ordinary skill in the relevant art. I understand that obviousness can be based on a single prior art reference or a combination of references that either expressly or inherently disclose all limitations of the claimed invention. In an obviousness analysis, it is not necessary to find precise teachings in the prior art directed to the specific subject matter claimed because inferences and creative steps that a person of ordinary skill in the art would employ can be taken into account.

21. I understand that obviousness must be analyzed from the perspective of a person of ordinary skill in the relevant art, at the time the invention was made. In analyzing obviousness, I understand that it is important to understand the scope of the claims, the level of skill in the relevant art, the scope and content of the prior art, the differences between the prior art and the claims, and any secondary

considerations.

22. I understand that assessing which prior art references to combine and how they may be combined to match the asserted claim may not be based on hindsight reconstruction or ex-post reasoning. Hindsight reconstruction is using the patent itself as a road map for recreating the invention. In assessing obviousness, only what was known before the invention was made can be considered.

23. I understand that one important guard against such hindsight reconstruction is a determination whether a person having ordinary skill in the art would have been motivated, taught, or suggested to combine the relevant teachings of the prior art to duplicate the patent claims at the time of the patented invention.

24. I understand that determining the scope and content of the prior art requires consideration of whether the prior art was reasonably relevant to the particular problem the inventors faced in making the invention covered by the patent claims.

25. I understand that determining whether there are any material differences between the scope and content of the prior art and each challenged claim of the patent under review requires consideration of the claimed invention as a whole to determine whether or not it would have been obvious in light of the prior art. If the prior art discloses all the steps or elements in separate references,

consideration should be given to whether it would have been obvious to combine those references. I understand that a claim is not obvious merely because all of the steps or elements of that claim already existed.

26. I also understand that when prior art teaches away from combining prior art references, the discovery of a successful way to combine them is less likely to be obvious. Prior art teaches away from an invention when a person or ordinary skill would be discouraged or diverted from following the path leading to the invention because of the prior art.

27. I understand that in order to rely on inherency in an obviousness analysis for establishing the existence of a claim limitation in the prior art, the missing descriptive material must necessarily be present in the prior art and not merely probably or possibly present.

II. THE ’664 PATENT

28. The ’664 Patent is directed towards reducing deterioration to the semiconductor stack during the wafer-level fabrication process, before any single LED device is separated. *See, e.g.*, ’664 Patent at 1:23–26; 2:47–49; 7:28–29; 13:49–50. The protection is demonstrated in Fig. 12. Discussion of the steps demonstrating how the claimed LED is created can be found in Figs. 4 through 12. *See, e.g., id.* at 4:26–38; 8:15-18; and FIGS. 4 through 12.

29. Shown below in Fig. 1 is an illustration of the improved LED, with

relevant features annotated. *See* '664 Patent at 4:26–28. The LED package includes a semiconductor stack 30 (green) that comprises two conductive semiconductor layers and an active layer while, surrounding the semiconductor stack 30 is a protective insulation layer that includes a first protective insulation layer 33 and/or a second protective insulation layer 37. *Id.* at 5:22–26 and 7:19–21. The protective insulation layer with one or both of the protective insulation layers 33 and 37, in addition to being protective and being insulating, can be implemented as a combination of protective insulation layers 33 and 37 of different indices of refraction surrounding the semiconductor stack 30 to further provide an optical function: being as an optical reflector to improve the optical output efficiency of the final LED device. The protective insulation layer prevents deterioration of the light-emitting semiconductor stack 30 (green) due to moisture. *See id.* at 7:17–42; 13:38–58 and 10:43–44. This protective nature is the key innovation of '664 and seems to be ignored in the petition.

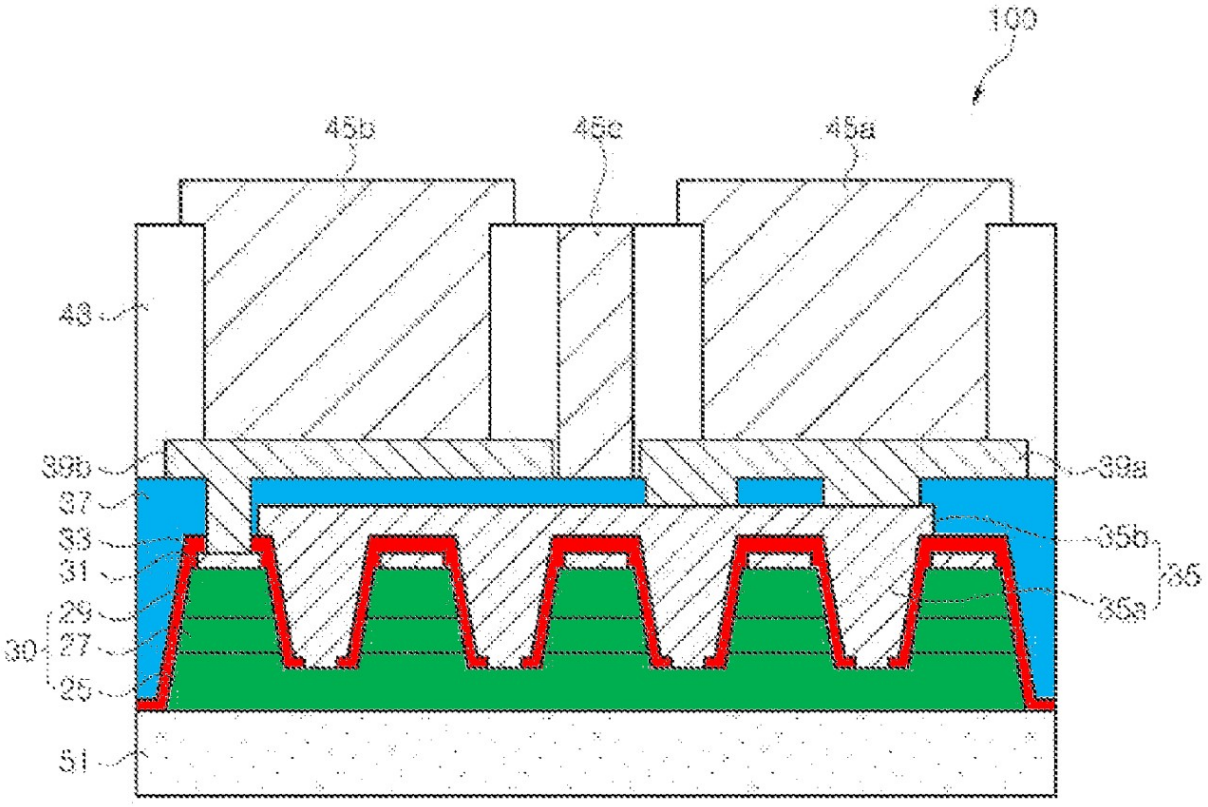

FIG. 12 of the ’664 Patent (Annotated)

30. The device is formed by the follow steps, which are summarized. he semiconductor structure 30 (green) is first formed on a growth substrate 21 (aqua). *See* ’664 Patent at 8:15–18; Fig. 4.

FIG. 4 of the ’664 Patent (Annotated)

31. Then, holes 30a (circled) are formed. *See, e.g.,* '664 Patent at 8:40–46. A second contact layer 31 (orange) is then formed to provide an electrical contact to the semiconductor layer 29. *See id.* at 8:61–65.

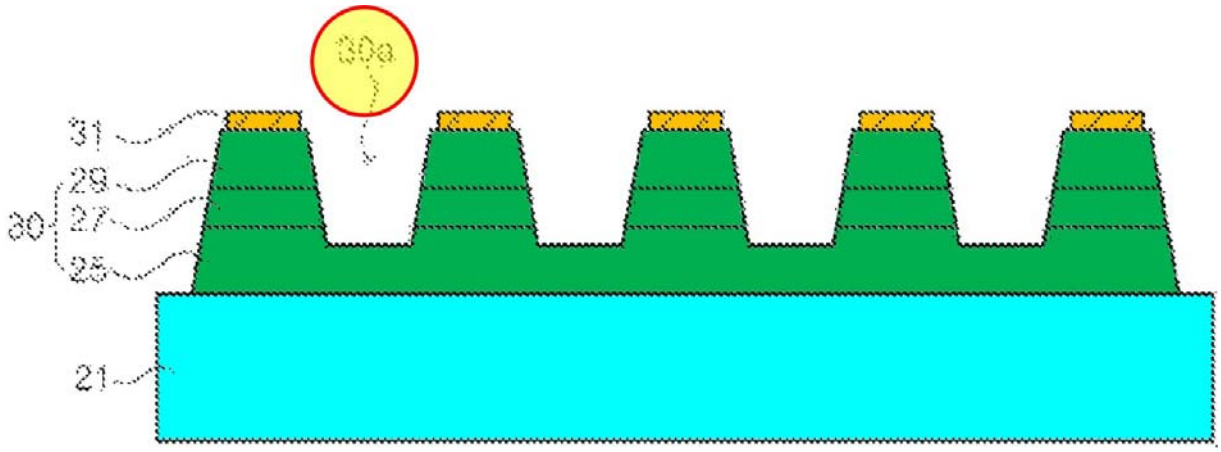

FIG. 6(b) of the '664 Patent (Annotated)

32. Thereafter, the first protective insulation layer 33 (red) is formed to cover the second contact layer 31 (orange). '664 Patent at 9:8–15.

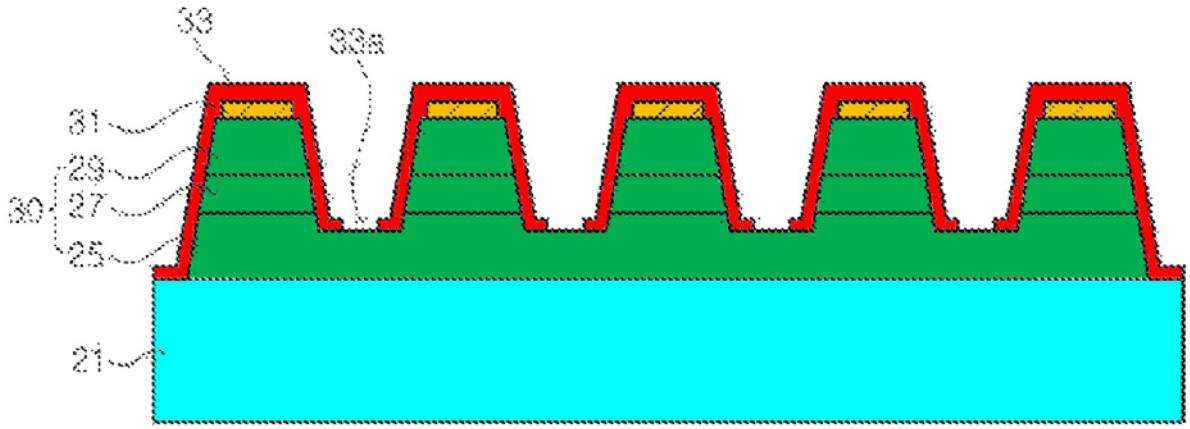

FIG. 7(b) of the '664 Patent (Annotated)

33. Following the above, a first contact layer 35 (also annotated orange) is

formed in the holes 30a to provide an electrical contact to the semiconductor layer 25. As can be seen from the below, the contacts 35 and 31 are electrically connected through the semiconductor layers, so that when current is applied, the active layer emits light. *Id.* at 9:27-34 and 6:8-18

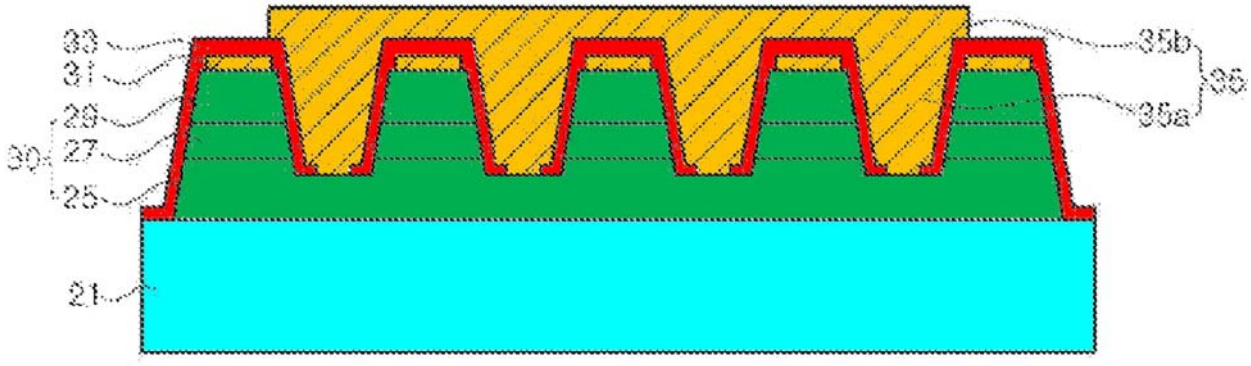

FIG. 8(b) of the '664 Patent (Annotated)

34. Then the protective insulation layer 37 (blue) is formed onto the first contact layer 35 (orange). '664 Patent at 9:39–59. The second insulation layer is formed with holes 37a and b to expose the contact layers. *See id.* The first and second protective insulation layers 33 and 37 protect the semiconductor structure (green) from deterioration due to moisture. *See id.* at 7:17–29. Other elements (*e.g.*, the insulation layer 43 and bumps 45, not annotated) are thereafter formed. *See, e.g., id.* at Figs. 10–12; 9:54–59; 9:65–67.

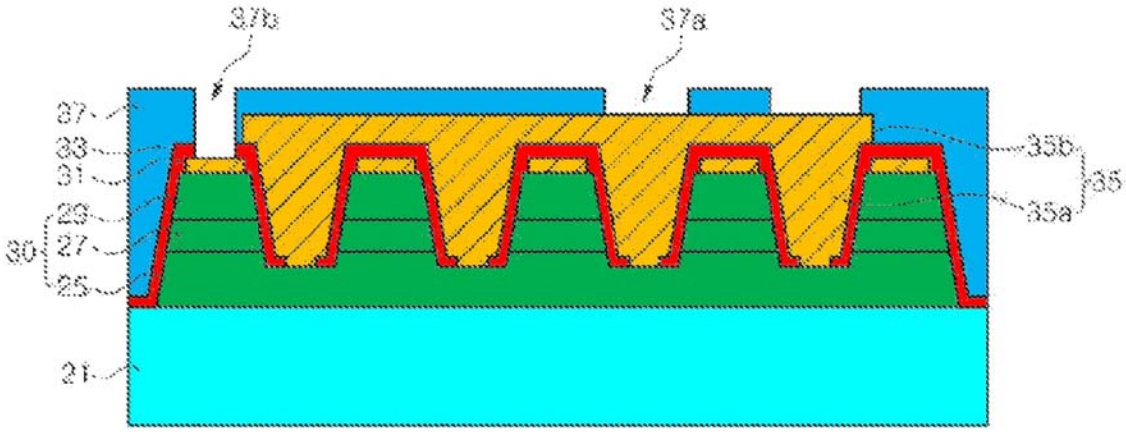

FIG. 9(b) of the '664 Patent (Annotated)

35. The "LED package structure [is then] divided into individual packages along the chip separating region." '664 Patent at 10:43–44. The figures have illustrated a single section of the wafer, but a POSITA would understand that a whole wafer would be fabricated. The chip separating regions (annotated in purple dashes, below) are locations in the wafer where the individual LEDs would be cut.

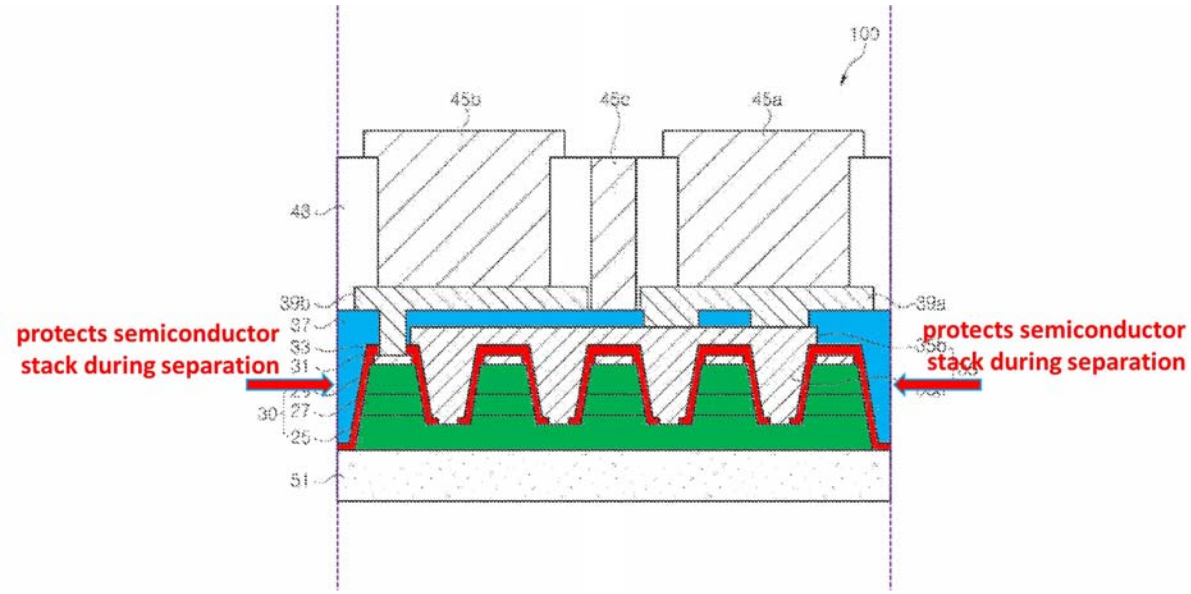

FIG. 12 of the ’664 Patent (Annotated)

36. The protective insulation layer (annotated red and blue, above) protects the semiconductor stack 30 (green) during the chip separation process and subsequently throughout the life of the chip. *See, e.g.*, ’664 Patent at 7:30–42 and 13:38–58. The protective insulation layer prevents against contaminants such as moisture from entering the semiconductor stack and causing deterioration. *See, e.g., id.* at 7:27–28 and 13:49–50.

37. The layers protect the semiconductor stack from deterioration from environmental factors from moisture. There are two types of chip separation processes typically used for LEDs, both of which could expose the chips to moisture if the claimed protective layers were not present. When separating chips from a wafer, a low cost wafer saw might be used which would typically create a highly contaminated slurry of water, metal, semiconductor, dielectric materials, diamond (from the saw blade) and epoxy (from the diamond impregnated saw blade) particles. And a POSITA would expect that the slurry would introduce many contaminants. By including the protective insulation layers during the semiconductor wafer separation process, the active layer is protected. A second method of chip separation that might be utilized is a more expensive laser scribing system wherein a high thermal flux from a laser ablates (vaporizes) materials along the cutting path. While this method of dicing is certainly “less messy” than the

wafer sawing method absent its slurry, it unfortunately elevates the local temperature of the chip along the scribe mark to extremely high temperatures, allowing any ambient moisture or undesirable gas to be highly reactive to the laser exposed region, often forming very stable, undesirable contaminating byproducts. A person of skill in the art would recognize many processes such as post wafer cleaning and gaseous ambient control that could help minimize contamination but he/she would also recognize that in production, things go wrong and contamination is best avoided not corrected. Furthermore, the ’664 protective layers act to protect the semiconductor stack during subsequent use. This protection prevents deterioration and increases LED efficiency. It also increases production yield. If protection were added after wafer separation, the semiconductor would still suffer from deterioration during the separation process.

38. The independent claims of the ’664 Patent have been excerpted below.

> **Claim 1.** A light emitting diode (LED) package, comprising:
> a semiconductor stack comprising a first conductive type semiconductor layer, an active layer, and a second conductive type semiconductor layer;
> a plurality of contact holes arranged in the second conductive type semiconductor layer and the active layer,

the contact holes exposing the first conductive type semiconductor layer;

a first electrode pad arranged over a first side of the semiconductor stack, the first electrode pad being electrically connected to the first conductive type semiconductor layer via some of the plurality of contact holes;

a second electrode pad arranged over the first side of the semiconductor stack, the second electrode pad being electrically connected to the second conductive type semiconductor layer; and

a protective insulation layer covering a sidewall of the first conductive type semiconductor layer and the second conductive type semiconductor layer,

wherein the protective insulation layer includes insulation layers having different indices of refraction from each other.

Claim 6: A light emitting diode (LED) module, comprising:

a circuit board; a LED package arranged over the circuit board without bonding wires, wherein the LED package includes:

a semiconductor stack comprising a first conductive type semiconductor layer, an active layer, and a second conductive type semiconductor layer;

a plurality of contact holes arranged in the second conductive type semiconductor layer and the active layer, the contact holes exposing the first conductive type semiconductor layer;

a first electrode pad arranged over a first side of the semiconductor stack, the first electrode pad being electrically connected to the first conductive type semiconductor layer via some of the plurality of contact holes;

a second electrode pad arranged over the first side of the semiconductor stack, the second electrode pad being electrically connected to the second conductive type semiconductor layer; and

a protective insulation layer covering a sidewall of the first conductive type semiconductor layer and the second conductive type semiconductor layer,

wherein the protective insulation layer includes insulation layers having different indices of refraction from each other; and

a lens to adjust an orientation angle of light emitted from the LED package.

Claim 8: A light emitting diode (LED) module, comprising:

a circuit board;

a LED package bonded on the circuit board without bonding wires;

wherein the LED package comprising

a semiconductor stack comprising a first conductive type semiconductor layer, an active layer, and a second conductive type semiconductor layer;

a plurality of contact holes arranged in the second conductive type semiconductor layer and the active layer, the contact holes exposing the first conductive type semiconductor layer;

a first electrode pad arranged over a first side of the semiconductor stack, the first electrode pad being electrically connected to the first conductive type semiconductor layer via some of the plurality of contact holes;

a second electrode pad arranged over the first side of the semiconductor stack, the second electrode pad being electrically connected to the second conductive type semiconductor layer; and

a protective insulation layer covering a sidewall of the first conductive type semiconductor layer.

A. Claim Construction

"protective insulation layer" (all challenged claims)

39. Petitioner's application of this term in the petition neglects to describe

the protective functions of the claim. The petition focuses on the electrical isolation, but ignores that the protective function substantially prevents the deterioration of the semiconductor stack. The claim has two different words, protective, and insulation, and a POSITA would not have read one of them out, but would have instead given meaning to both. In my opinion, a POSITA would have understood the ordinary and customary meaning of "protective insulation layer" to be "a layer that is structured to be both protective by substantially preventing the deterioration of the semiconductor stack and insulating by substantially preventing the flow of an electrical current."

40. The '664 Patent describes both the electrical insulation, and the protective qualities of the layer. As a POSITA recognizes in the insulator art, one of the functions of an insulator is to prevent the flow of current across the layer, so that the flow of current can be appropriately controlled. This is done so that current can flow from electrode to electrode, and active the active layer to emit light.

41. The specification of the '664 Patent makes-clear that "insulation" refers to electrical isolation—to substantially prevent the flow of an electrical current. One of the main functions of the insulator is to electrically insulate two conductive layers, so that the flow of an electrical current can be controlled. Insulation layers are commonly used terms in the art to describe electrical

isolation. And this can be seen from the references provided by Petitioner. *See, e.g.*, EX1005 at Fig. 1B, element 10; EX1007 at ¶ 5; EX1008 at ¶ 10; EX1009 at ¶ 41; EX1011 at ¶ 6; EX1012 at 4:65; EX1013 at 7:49–64. A POSITA would have recognized that an "insulation layer" to be one that performs electrical isolation—it substantially prevents the flow of an electrical current. This can be seen from the figures of the '664 Patent, where the protective insulator 33 (red) electrically isolates the first contact layer 35 (brown) from the second contact layer 31 (orange) so that electrical current can run through the stack to power the active layer. *See, e.g.*, '664 Patent at 9:8–15; 5:27–45; 5:63-6:1. Isolation is important so that current flow can be managed so that it flows through the holes (red arrows).

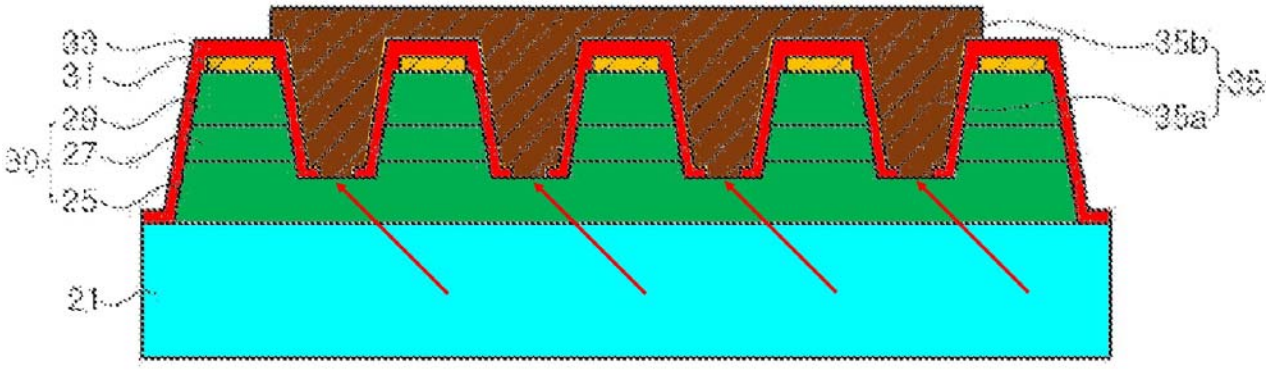

FIG. 8(b) of the '664 Patent (Annotated)

42. But the '664 Patent describes more than merely electrical isolation—it describes protection and this feature is not present in any of the petitions prior art. The protective insulating layer must protect. It must substantially prevent the deterioration of the semiconductor stack in addition to performing electrical

isolation. The "protective insulation layer" is described in two portions of the specification and both of these sections describe preventing deterioration of the semiconductor stack due to moisture. *See* '664 Patent at 7:17–43 and 13:38–58. When the LED is separated at the wafer-level, the protective insulating layer (annotated red and blue below) protects the semiconductor stack in each LED. *See id.* at 3:23–25; 7:17–42; 13:38–58; 10:43–44.

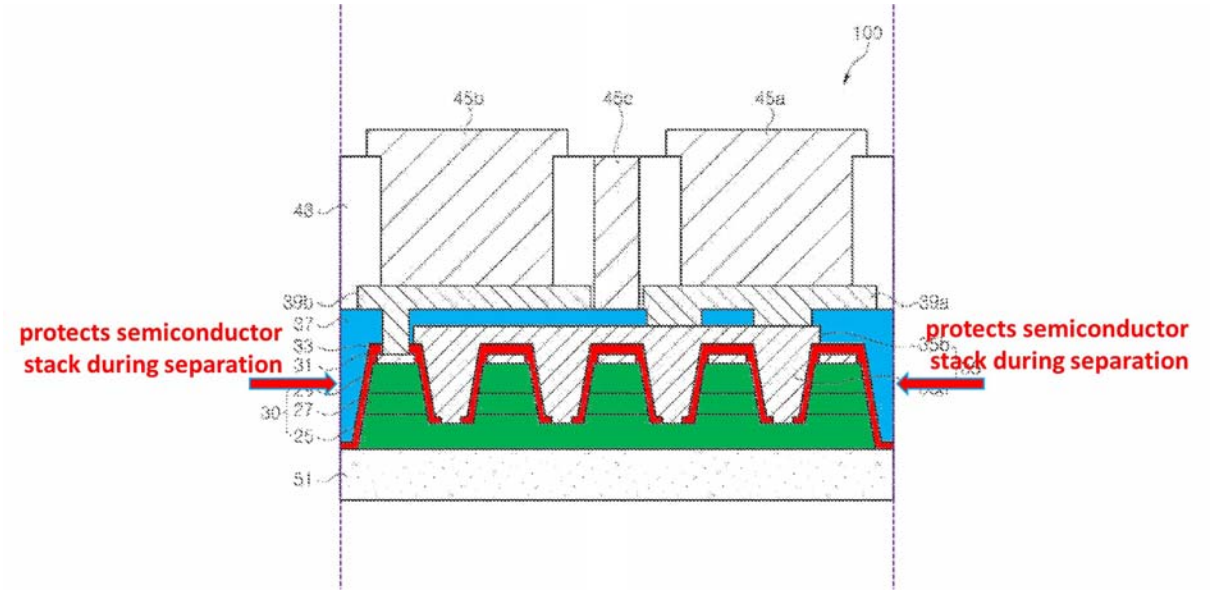

FIG. 12 of the '664 Patent (Annotated)

43. A POSITA would give meaning to the term "protective," because an insulator that electrically isolates does not also necessarily protect. Certain materials will electrically isolate, but will not prevent the migration of moisture. For even the most common insulator materials like SiO_2, for example, preventing moisture migration depends on how porous the material is. It has been known since at least 1962 that SiO_2 films have a tendency to be permeable to gases and

moisture especially through various pores in the films ["Gas permeation study and imperfection detection of thermally grown and deposited thin silicon dioxide films", S. W. Ing et al, J. Elect. Chem. Society, Vol 109, No. 3, March 1962, pp. 211-223], attached as appendix B. Often this is due to micro (or even macro) porosity allowing gas permeation. Ing et. Al. concludes "from the data collected it is shown that pores and microchannels (orders of magnitude smaller than pores) are formed in these films, and permeation through them is the main diffusion mechanism involved" [abstract of Ing et al]. Moisture and gas permeation can thus come from pores or even smaller molecular sized pathways throughout the amorphous SiO_2 films. LEDs cannot benefit from the same high quality thermally "grown" oxides that are available to other semiconductors like Si or SiC. But even an undergraduate who has taken a semiconductor processing class would recognize that SiO_2 even in these highly idealized semiconductors comes in a dense form (called dry oxides) and a slightly less dense form (called a wet oxide with less molecular bridging bonds than dry oxides) [See text books like "The science and engineering of microelectronic fabrication" by Stephen Campbell for example]. The use of less dense wet oxides to form lower capacitance insulating layers is fundamental to traditional silicon semiconductor processing and modern day dielectrics amplify this approach by adding impurities that lower the film density and thus introduce some added degree of porosity [see for example the industry

standard marketed as "Black Diamond" (it is actually Silicon based not "diamond based") dielectric from Applied Materials Inc., http://www.appliedmaterials.com/products/producer-black-diamond-pecvd, attached as Appendix S]. But LEDs cannot take advantage of these thermally grown oxides and must rely on low temperature deposited oxides where the porosity concern is even more pertinent. This is shown in the reference attached to my declaration, which shows that the most common form of deposited oxide, PECVD at lower temperatures typically resulted in porous materials. *See* Ortiz et al. in "Plasma Enhanced Chemical Vapor Deposition of SiO_2 Films at Low Temperatures Using $SiCl_4$ and O_2" in Journal of Electronic Materials, Vol. 19, No. 12, 1411-1415 (1990) (demonstrating that a SiO_2 layer that is porous absorbs moisture), attached as Appendix C. Often times, it is desirable to lower the index of refraction of a dielectric layer so as to obtain an optical advantage in the form of increased transmission, reflection or reduced UV absorption as demonstrated in [see for example, see "Room temperature synthesis of porous thin films by plasma enhanced chemical vapor deposition", A. Barranco et al, J. Vac Sci. & Tech. A, Vol 22 (2004), attached as Appendix D, who claims in their abstract, "A preliminary ultraviolet-visible characterization of the optically transparent thin films reveals that transmission of light through glass increases by 7%–8% when the porous silica is deposited on this substrate"; or "Antireflection treatment of

low-emitting glazings for energy efficient windows with high visible transmittance", Elin Hammarberg et al Thin Solid Films, V 442 (2003), attached as Appendix E, who claim a 9.8% visible transmittance improvement with a highly porous SiO_2 film [see abstract]. Indeed far before the '664 patent, it was known to use dielectric layers such as SiO_2 and TiO_2 for optical reflectance enhancement and light extraction improvement but the concept of "protection from moisture" was not considered part of this process [see for example "Enhancement of InGaN/GaN Flip-Chip ITO LEDs with Incline Sidewalls Coated with TiO_2/SiO_2 Omnidirectional Reflector", C. H. Chiu et al, J. Electrochemical Soc., V 154 No 11, H944-H947, (2007), attached as Appendix F. Indeed, in some cases for LEDs, intentionally produced pores in the forms of holes drilled in or spaces between spheres formed into the SiO_2 for optical advantage [see for example "Enhanced light extraction in light-emitting diodes with photonic crystal structure selectively grown on –GaN", Chu-Young Cho et al, Appl. Phys. Lett. 96, 181110 (2010), attached as Appendix G; and "Fabrication and optical properties of blue LEDs with silica microsphere coating", K. Kusakabe et al, phys. stat. sol. (c) 4, No. 1, 25– 28 (2007), attached as Appendix H].

44. Porous SiO_2 layers will typically electrically isolate, but will not protect against moisture and won't prevent against deterioration. Porous layers will, however, have the benefit of reducing stress of the layer [see for example,

"Stress in oxidized porous silicon layers", K. Barla, et al, J. of Applied Physics 59, 439 (1986), attached as Appendix I, which claim that for porous SiO_2 (formed in this case from oxidized porous Si) show "when porosity increases, the oxide stiffness decreases", an amazingly obvious conclusion extendable to all porous films and easily understood by laymen as well. Simply put, a material with hole in it is more pliable than a solid material. Thus, porosity has been used to tune mechanical properties reducing the potential for cracking or delamination of underlying layers. Porous layers are common in the art.

45. While the above points are made based in regards to the most common dielectric SiO_2, other dielectrics cited in '664 and the prior art share similar issues regarding porosity. Specifically, Silicon Nitride (Si_3N_{4-x}, SiN_x or SiN) is particularly prone to porosity and stress variations, even more so than SiO_2. See for example Xu et al among many who conclude [see abstract] "Several different deposition routines showed that sputtering pressure played the most dominant role in film oxygen incorporation, film packing density [i.e. porosity] and resistance to oxidation. ["Optical investigation of silicon nitride thin films deposited by r.f. magnetron sputtering", Xu et al, Thin Solid Films 425 (2003) 196–202], attached as Appendix J. Similarly, Yin et al have showed that film densities that are ~17% lower than fully densified films having a lower index of refraction weighted by the voids in the porous materials can be obtained via a wide

range of deposition parameters [See table 1"Optical dielectric function and infrared absorption of hydrogenated amorphous silicon nitride films: Experimental results and effective-medium-approximation analysis", Z. Yin et al, Physical Review B, Vol 42, No 6, 15 August (1990)], attached as Appendix K. SiN_x is particularly susceptible to porosity because its deposition can contain enormous amounts of hydrogen 30-40% according to Yin et al) which can easily break away and leave the film leaving a substantial volume of dead space. Similar arguments are given for the porosity of other films such as TiO_2 which is produced in a wide range of porosity for use in LEDs, solar cells and catalysis [see among many "Highly porous TiO_2 films for dye sensitized solar cells", Antonio Tricoli et al, Journal of Materials Chemistry Issue 28, (2012), attached as Appendix and countless references therein] and Nb_2O_5 ["The microstructure and LIDT of Nb_2O_5 and Ta_2O_5 optical coatings", Abromavicius et al, Proc. of SPIE Vol. 6403, 640315, (2007), attached as Appendix L, which concludes "Fast deposition on unheated substrates leads to formation of porous layer structure, which exhibits smaller refractive index." and "… porous dielectric coatings are more resistant to intense laser radiation, however they have smaller environmental stability than denser coatings…". Here, again we see a common theme. We see the trade off in optical properties (index of refraction tunability and laser damage thresholds) versus loss of environmental stability. This theme is carried over for all optical coatings and

can again be exemplified in for example "Optimised [spelling error repeated] Antireflection Coatings for Planar Silicon Solar Cells using Remote PECVD Silicon Nitride and Porous Silicon Dioxide", Nagel et al, Progress in Photovoltaics Research and Applications, V 7, pp. 245-260 (1999), attached as Appendix M. This reference not only declares the wide spread optoelectronics utility of porous SiO_2, stating "A very promising alternative to MgF_2 is porous SiO_2 , which might be deposited cost-effectively onto large areas and which features a very low refractive index that can be varied between 1.10 and 1.46 via the porosity of the films" but goes on to describe the value of double layer SiN_x/SiO_2 films for low cost reflection control in optoelectronic devices. For the sake of completeness, this trend of trade offs in optical properties at the expense of protection properties continues in SiON (i.e. mixtures of SiO_2 and SiN_x)as shown for example in Dupuis et al ["Optical and structural properties of silicon oxynitride deposited by plasma enhanced chemical vapor deposition", J. Dupuis et al, Thin Solid Films 519 (2010) pp. 1325–1333, attached as Appendix N] where refractive index tunability is described saying "it exhibits low absorbance and an adjustable refractive index below 1.5 and up to 3.0" and conclude "The trend before and after a rapid thermal annealing showed opposite results which could be explained by the high porosity of the layers and the formation of Si–O bonds."

46. In general, given the plethora of functions a dielectric layer can

implement, insulating, optically reflective/transmissive, mechanical stress management a POSITA could not read the prior art presented in the petition as inherently inferring protective. As will be shown, there are actually reasons including statements that protection is not needed that lead a POSITA to conclude that the petitioner's prior art taught away from the invention of '664 and that they would have prioritized other properties, such as optical advantages, over any protective quality. Regardless, no protective property is claimed in the prior art.

III. Petitioner Has Not Demonstrated Invalidity

47. Petitioner's grounds are reproduced below.

Ground	'664 Patent Claims	Basis for Rejection
Ground 1A	1-6, 8, 9, 11, 12	§102 over Illek
Ground 1B	1-6, 8-18	§103 over Illek
Ground 1C	7, 19	§103 over Illek and Begemann
Ground 2A	1-19	§103 over Donofrio and Sano
Ground 2B	19	§103 over Donofrio, Sano, and Begemann

48. In my opinion, Petitioner's grounds do not demonstrate invalidity of the '664 Patent claims.

A. Illek does not anticipate claims 1–6, 8, 9, 11, or 12 or render obvious claims 1–6 or 8–18

49. Illek does not teach the claimed "protective insulation layer." Illek's semiconductor stack would suffer from deterioration due to moisture. Illek does

not add moisture protection during the wafer fabrication. This means that when the LEDs are cut, typically with a slurry or high temperature reactive environment, that moisture contaminants would be introduced. The '664 Patent, in contrast, because it uses a protective insulation layer, would not suffer from the same deterioration. *See* '664 Patent at 7:17–29.

50. Illek's disclosure demonstrates that none of the first insulation layer 10, second insulation layer 13, and dielectric mirror layer 14 provide protective functions. And this can be seen from Illek's disclosure, which states that these layers need protection. Illek teaches that an encapsulant is necessary in order to protect the layers from deterioration due to environmental conditions such as from moisture. *See* EX1005 at ¶¶ 147 and 150. And the encapsulant is added after the chips have been cut from the wafers. The encapsulant is not a layer in the chip fabrication sequence but is an optional addition after the chip is completed.

51. When a POSITA reads that an encapsulant is needed after chip separation, a POSITA would understand that there is no moisture protection prior to chip separation. Adding moisture protection, when moisture protection already exists does not make sense. Moisture protection requires a dense film with additional rigidity, because the materials cannot be porous. This introduces stress, and makes the layer itself and the underlying layers more prone to breakage and/or delamination. So, a POSITA does not see protection as something that is

necessarily always a good thing. It is a trade-off. Sometimes protection against moisture is good, and sometimes it is not. When a moisture protective encapsulant is being added on top of a layer, a POSITA would have seen that designing the layer to be moisture protective to be redundant, and would have seen it as undesirable. In my opinion, a POSITA would not have read any of Illek's layers 10/13/14 to have protective qualities.

52. And this lack of protective properties for layers 10/13/14 is emphasized by the disclosure of Illek. Illek teaches away from the semiconductor stack being vulnerable to moisture and instead describes the mirror/metal stacks as being vulnerable to water. Illek states when one would want moisture protection, that they would use a BCB encapsulant. EX1005 at ¶ 149. Illek is specific when it tells a POSITA to design something towards protection, and a POSITA would not infer a lack of description of moisture protection to mean that moisture protection should be added to, e.g., the layers 10/13/14. Furthermore, Illek instructs a POSITA that it is "advantageous[]" to use Al in the mirror layer 14 (EX1005 at ¶ 132), which Illek recognizes as being susceptible to water damage (*i.e.*, its underlying layer stack would be susceptible to deterioration) (*id.* at ¶ 151). Illek also describes using other types of metals, such as silver, which are susceptible to water damage. And Illek states that, when moisture protection is unnecessary, that no moisture protection would be used. *Id.* at ¶ 150. Illek teaches away from '664

and states that certain compounds such as nitrides may not need moisture protection, because there is little risk of damage. Thus, Illek is at a difference of opinion as to the need for protection of the semiconductor stack than the opinions of the inventors of '664. Illek specifically says "Nitride compound semiconductors are particularly resistant to external influences, which means that encapsulation of a nitride-based component can be dispensed with comparatively little risk." *Id.* But low risk of damage to one semiconductor layer, does not necessarily mean that it is protective. For instance, a porous or hydrophilic dielectric layer may electrically insulate, may optically reflect and may not be damaged by water. But it does not mean that this dielectric layer protects the underlying semiconductor stack (it does not, it is a very poor protector as it is permeable to moisture and gases). Contrarily, the inventors of '664 Patent felt the semiconductor stack could be harmed by moisture, particularly before, during and after the separation of the chips. The inventors of '664 Patent thus identified a problem and offered a solution to that problem that Illek directly opposed having specifically discounted the problem '664 claims to solve.

53. The encapsulation and the layers 10/13/14 are entirely different structures, with different functions. Layers are added during the wafer fabrication step. The encapsulant is added after. The layers, and the encapsulant, are made from entirely different materials at completely different times in the process

sequence. It would be a mistake to conflate them, and to read a function of the encapsulant, such as its protective qualities, onto any of the layers. In my opinion, Petitioner appears to not pay any attention to the different structure, and imparts the encapsulant's functions onto the layers (*See* Petition at 19). This is a mistake, and not what Illek teaches. The Petition, and Petitioner's expert declaration, only demonstrate that the encapsulant provides moisture protection. It says nothing about the layers 10/13/14. Petitioner does not explain why Illek's protective teachings of the encapsulation (a separate structure) would lead to the conclusion that layers 10, 13, and 14 would also necessarily provide protection. This is a mistake in analysis in my opinion.

54. None of the materials that Illek describes as using for the first insulation layer 10, second insulation layer 13, and dielectric mirror layer 14 necessarily demonstrate protection. Illek only describes the first insulation layer 10 and second insulation layer 13 as potentially being "a silicon nitride such as SiN, a silicon oxide such as SiO_2, or a silicon oxynitride such as SiON." EX1005 at ¶¶ 112 and 120. And the dielectric mirror layer 14 can be a silicon dioxide, dielectric materials, or various metalizations with Au, Ag, or Al. *See id.* at ¶¶ 130–132.

55. Silicon nitrides are used in the art to provide layers that are not protective. Given the wide range of deposition parameters for SiNx that lead

toward porosity, a POSITA would be wise to assume that generically stated SiNx, as appearing in Illek, is not inherently protective against moisture absent of any other disclaimer. Furthermore, Illek did not care to protect his semiconductor stack, saying it was not needed. The '664 Patent identified the need for protection, and invented a solution. Unlike the generic name "SiN_x" of Illek, a "protective insulating layer" from the '664 Patent would be deposited under conditions that led to high density films that were protective.

56. Silicon oxides are used in the art to provide insulating layers that are not protective. As discussed above, it is very common to intentionally use porous, low density, or even geometrically patterned SiO_2 for reasons of optical improvements [see Barranco, Hammarberg, Cho, and Kusakabe] and/or stress management [example Barla]. SiO_2 is used in layers that are insulating but aren't protective. Chakrabarti et al states what is obvious to anyone skilled in the art that porous films allow moisture to penetrate stating "The films of SiO_2 have also been produced by decomposition of ethyl silanes such as tetraethoxy silane [2] or the oxidation of silane [3] but these films suffer from the disadvantages of high porosity…and less stability towards moisture." [See "A new Process of Oxide Growth on Silicon", Chakrabarti et al., Journal of the Indian Institute of Science, v 58, n 1, p 28-35, Jan. 1976, attached as Appendix O]. Tetraethoxy silane, also known as TEOS, is a standard CVD precursor (gaseous source) of SiO_2 widely

used in the silicon industry and included in some plasma processes as well. For a material like SiO_2, for example, moisture migration depends on how porous the material is [Chakrabarti]. *See also* Ortiz et al. in "Plasma Enhanced Chemical Vapor Deposition of SiO_2 Films at Low Temperatures Using $SiCl_4$ and O_2" in Journal of Electronic Materials, Vol. 19, No. 12, 1411-1415 (1990) (demonstrating that a SiO_2 layer that is porous absorbs moisture); *see also* U.S. Pat. No. 7,262,142 at 1:37–49 and 10:19–22 (demonstrating that a SiO_2 layer that is porous absorbs moisture).

57. Silicon oxynitrides are used in the art to provide insulating layers that are not inherently protective. SiON layers are used to tune an optical index of refraction to obtain a desired optical reflectance/transmission property [see for example Dupuis et al] but is also used as a FLASH memory gate in older flash technology ["Effect of nitrogen plasma conditions on electrical properties of silicon oxynitrided thin films for flash memory applications", Iked et al, Thin Solid Films Vol 386 (2001), pp. 111-116, attached as Appendix P, and patent US6797650, attached as Appendix O]. It is noted that in Flash memory applications, the electrical insulation property is intentionally compromised so that a small programming current can deposit charge inside the oxide (or in later technology on a floating gate buried inside the dielectric). Thus, simply stating that SiON is used does not even explicitly describe a fully insulating property

much less a protective insulating property. SiON is used in layers that aren't protective. For example Dupuis describes the use of SiON for its optical properties irrespective of any insulating property. Dupuis specifically says "it [SiON] exhibits low absorbance and an adjustable refractive index below 1.5 and up to 3.0" and conclude "The trend before and after a rapid thermal annealing showed opposite results which could be explained by the high porosity of the layers and the formation of Si–O bonds." Dupuis demonstrates that porous SiON is used in the art, and that SiON is not inherently protective.

58. Deposited dielectric materials such as SiO_2, Si_3N_{4-x}, SiON, TiO_2 and Nb_2O_5 are used in the art to provide insulating, optically functional and stress management layers but in general, all these deposited oxide layers are not inherently protective. Indeed in many cases presented here, the desirable property of the films renders them porous or more broadly permeable, making them not inherently protective.

59. Metalizations, like Au, Ag, or Al, are well-known to be susceptible to moisture and thus need protection. Metalizations are well-known to be susceptible to water damage. *See, e.g.,* EX1005 at ¶ 151,

60. As an example of a suitable protective material, Illek teaches that the encapsulation 40 is made of a molding compound BCB (benzo-cyclo-butene). *Id.* at ¶ 149. No such moisture-protective materials are described as being used by

layers 10/13/14.

61. A POSITA would not have understood any of the first insulation layer 10, second insulation layer 13, or the dielectric mirror layer 14 to teach protection. In my opinion, Illek does not teach a "protective insulating layer" and in fact teaches away from a protective insulating layer such that none of claims 1–6, 8, 9, 11, and 12 are anticipated.

62. In my opinion, Petitioner does not describe how a POSITA would have found the "protective insulating layer" obvious. As I have noted, Illek teaches using a separate, latter applied encapsulant if moisture protection is wanted. But this encapsulant would not offer protection during the chip separation process. Petitioner's rationale does not address that, at all. In my opinion, Illek does not render claims 1–19 obvious.

B. Donofrio does not teach the protective insulation layer

63. Petitioner relies on Donofrio and Sano to render obvious claims 1–19. In my opinion, Donofrio and Sano do not render claims 1–19 obvious for the reasons below. I have presented several reasons why I believe that the claims are not rendered obvious, including:

- Donofrio does not teach a "protective insulating layer"
- A POSITA would not have combined Donofrio and Sano
- Neither Donofrio or Sano provide sidewall coverage, as required by

the claims

Ground	'664 Patent Claims	Basis for Rejection
Ground 1A	1-6, 8, 9, 11, 12	§102 over Illek
Ground 1B	1-6, 8-18	§103 over Illek
Ground 1C	7, 19	§103 over Illek and Begemann
Ground 2A	1-19	§103 over Donofrio and Sano
Ground 2B	19	§103 over Donofrio, Sano, and Begemann

64. Petitioner states that Donofrio teaches a "protective insulation layer," but this is not the case. Petitioner only states that the "protective insulation layer" provides protection against shorts. *See* Petition at 55. But, as I have mentioned, protective means that the semiconductor stack needs to be protected from deterioration.

65. Petitioner's reference to its expert support echoes the shorting commentary. (EX1002 at ¶ 160). Petitioner's expert vaguely throws in the word "chemical reactivity" but that does not mention any actual teachings of Donofrio's layer, or describe any protective qualities a layer exhibits. For instance, a porous layer may not be chemically reactive, and even could be a good insulator but would be a very poor protector.

66. Petitioner only references Donofrio's materials for the insulating later. Such as oxide and nitride. But, as I have described above in the preceding section, these materials do not necessarily mean that the layer is protective. The material

could be porous, and the semiconductor stack would be damaged by water. Given the focus of Donofrio is on optical extraction, it is a good conclusion, albeit conjecture since Donofrio is silent on the matter, that Donofrio's "oxide and nitride" insulating layers are deposited in a manner selected for optical properties not protection. This is mere speculation as Donofrio says nothing about these layers and teaches nothing in regard to the need for or solution to protection.

67. Inferring any protection from Donofrio would be a far stretch from its actual teachings. Donofrio's sidewalls are completely exposed to the environment, without anything. Based on this exposure, a POSITA would not have thought that Donofrio even considered protecting against the environment, such as against water. The semiconductor stack of Donofrio would deteriorate when the LED chip was cut at the wafer level, and it would deteriorate after when it was being used. Donofrio represents the type of prior art problem expressed by the '664 Patent, and does not teach a protective insulating layer. This is shown below in the below figure.

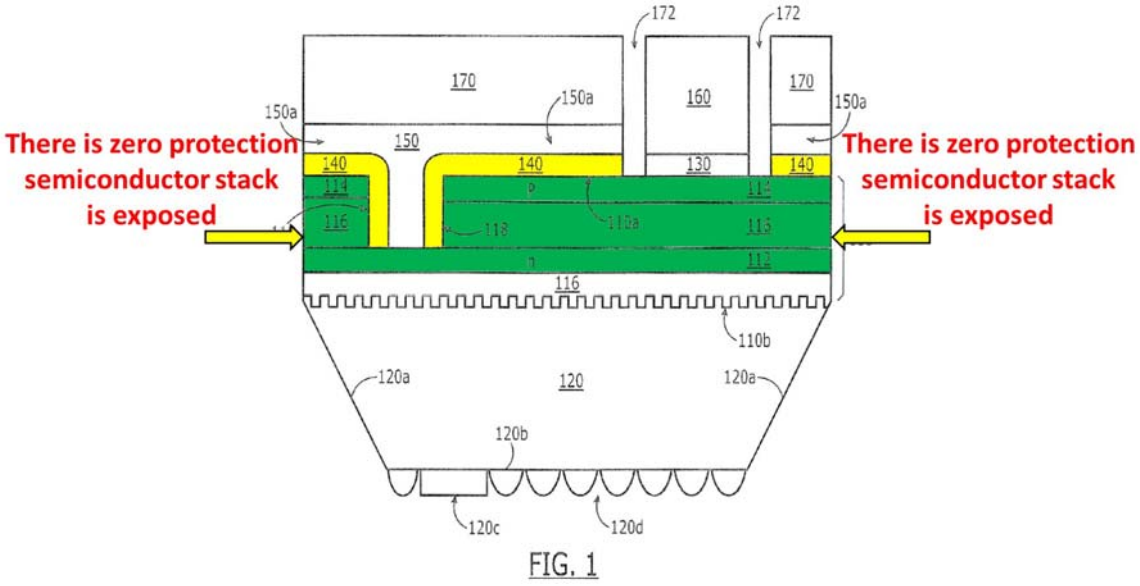

FIG. 1 of Donofrio (Annotated)

68. For the above reason, Donofrio does not teach the "protective insulating layer." Petitioner has not argued that Sano teaches a protective insulating layer.

C. A POSITA would not have been motivated to combine Donofrio and Sano

69. In my opinion, a POSITA would not have been motivated to combine Donofrio and Sano. Petitioner's rationale does not make sense. Petitioner equates the concept of a slight over-etch to the entirety of Sano. Sano does not teach a slight over-etch, but instead teaches a particular semiconductor structure that differs from Donofrio. Because a slight over-etch may occur in one instance, does not mean that any semiconductor structure, whether or not it is compatible, would have been looked at for solutions.

70. And Petitioner's rationale that a POSITA would look to Sano to improve electrical contact is not supported. Donofrio addresses this issue, because it states that its n-type layer is completely exposed and, to improve ohmic contact, a contact layer is added. EX1009 at ¶ 42 and ¶ 62. Petitioner does not actually point to anything in Sano that provides an improved electrical contact, beyond what Donofrio already teaches. A POSITA would not have found Sano's electric contact to provide any benefit to Donofrio's exposed n-type layer with an ohmic contact. Donofrio is already optimized, and Petitioner's rational does not make sense.

71. For this reason, I do not believe that a POSITA would have combined Donofrio and Sano.

72. For at least this reason, it is my opinion that Donofrio and Sano do not render claims 1–19 obvious.

D. None of Sano or Donofrio's Insulating Layers Cover Sidewalls

73. Furthermore, both Donofrio and Sano's sidewalls are exposed—they do not even describe an insulating layer that covers the side walls. As can be seen from the Sano excerpt below, its sidewalls are entirely exposed.

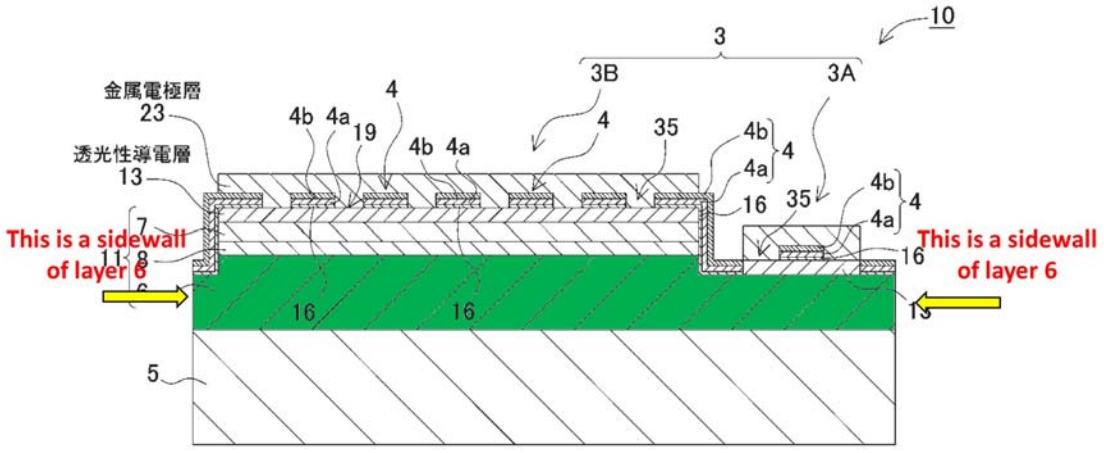

FIG. 3 of Sano (Annotated)

74. Donofrio's sidewalls are also entirely exposed. As can be seen from the below, n-type layer has zero coverage.

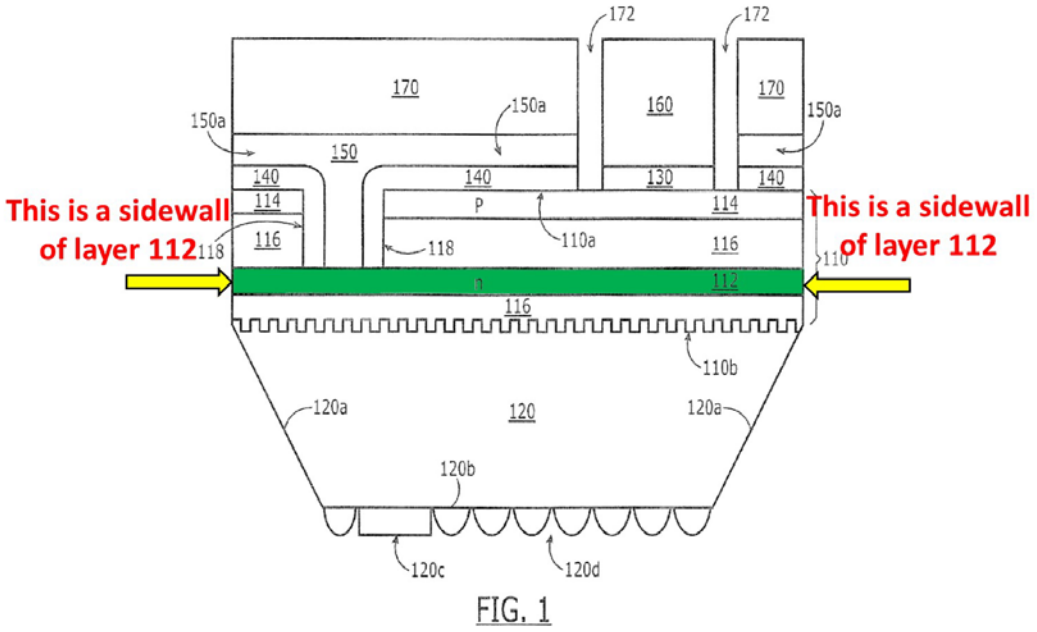

FIG. 1

FIG. 1 of Donofrio (Annotated)

75. A partial over-etch into the n-type layer of interior regions is not a sidewall. A POSITA looking at the figures of Donofrio, they would recognize that the sidewalls exist on the sides, where the chip is cut. This is where the '664

Patent seeks to protect during chip separation. And Donofrio and Sano have semiconductor stacks that are clearly exposed and susceptible to damage.

76. For at least this reason, it is my opinion that none of claims 1–19 are rendered obvious by Sano and Donofrio.

77. I have personally downloaded and obtained the documents in Appendices B through R. Appendix S was downloaded to PDF at my request. These documents are what they purport to be on their face.

I hereby declare under penalty of perjury under the laws of the United States of America that all statements made herein of my own knowledge are true and that all statements made on information and belief are believed to be true; and further that these statements were made with the knowledge that willful false statements and the like so made are punishable by fine or imprisonment, or both, under Section 1001 of Title 18 of the United States Code.

Date: 09/18/2019

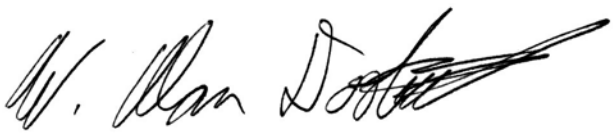

_____

Dr. William Alan Doolittle

APPENDIX A

GEORGIA INSTITUTE OF TECHNOLOGY

CURRICULUM VITAE FOR WILLIAM ALAN DOOLITTLE

Last Updated June 24, 2019

CURRICULUM VITAE FOR WILLIAM ALAN DOOLITTLE

PROFESSOR

SCHOOL OF ELECTRICAL AND COMPUTER ENGINEERING

DECEMBER 2016

TABLE OF CONTENTS

I. Earned Degrees 3
II. Employment History 3
III. Honors and Awards 3
A. International or National Awards 3
B. Institute or School Awards 3
IV. Research, Scholarship, and Creative Activities 4
A. Published Books, Book Chapters, and Edited Volumes 4
A1. Books 4
A2. Refereed Book Chapters 4
A3. Edited Volumes 4
B1. Published and Accepted Journal Articles 4
B2. Conference Presentation with Proceedings (Refereed) 13
B3. Other Refereed Material 17
B4. Submitted Journal Articles (with date of submission) 17
B5. Submitted Conference Papers (with date of submission) 17
C. Other Publications and Creative Products 17
C1. Non-refereed Conference Presentations with Proceedings 17
C2. Patents 17
D. Presentations 19
D1. Keynote Addresses and Plenary Lectures 19
D2. Invited Conference and Workshop Presentations 19
D3. Conference and Workshop Presentations 23
E. Grants and Contracts 33
E1. As Principal Investigator 33
E2. As Co-Principal Investigator 38
E3. As Senior Personnel or Contributor 38
E4. Pending Proposals 39
E5. Proposals Submitted But Not Funded (last two years): 39
F. Other Scholarly and Creative Accomplishments 41
F1 Startup Companies 41
F2 Inventions Disclosures Filed (all filed with Georgia Tech Research Corp.) 41
G. Societal and Policy Impacts 42
H. Other Professional Activities 42
V. Teaching 43
B1. Ph.D. Students 45
B2. M.S. Students 48
B3. Undergraduate Students 49
B4. Service on thesis or dissertation committees 52
B5. Mentorship of postdoctoral fellows or visiting scholars 52
C. Other Teaching Activities 52
C1. Course Development 52

Seoul Semiconductor, Exhibit 2001
LGI v. SSC, IPR2019-01154

C2. Course Improvement 52
C3. Professional Development/Continuing Education 52
C4. Other Teaching Activities 52
Vi. Service 53
A. Professional Contributions 53
A1. Editorial Board Memberships 53
A2. Society Offices, Activities, and Membership 53
A3. Organization and Chairmanship of Technical Sessions, Workshops and Conferences 53
A4. Technical Journal or Conference Referee Activities 54
A5. Proposal Panels and Reviews 55
B. Public and Community Service 55
C. Institute Contributions 55
C1. Institute Committee Service 55
C2. College Committee Service 55
C3. School Committee Service 55
C4. Program Development: Research 56
C5. Program Development: Academic 56
C6. Other Institute Service Contributions 56

Seoul Semiconductor, Exhibit 2001
LGI v. SSC, IPR2019-01154

CURRICULUM VITAE FOR WILLIAM ALAN DOOLITTLE
PROFESSOR
SCHOOL OF ELECTRICAL AND COMPUTER ENGINEERING
DECEMBER 2016

I. EARNED DEGREES

a. BEE 1989 Georgia Institute of Technology School of Electrical and Computer Engineering
b. Ph.D. 1996 Georgia Institute of Technology School of Electrical and Computer Engineering

II. EMPLOYMENT HISTORY

a. Professor, Georgia Institute of Technology, School of Electrical and Computer Engineering, 2012-present
b. Associate Professor, Georgia Institute of Technology, School of Electrical and Computer Engineering, 2006-2012
c. Assistant Professor, Georgia Institute of Technology, School of Electrical and Computer Engineering, 2001-2006
d. Research Engineer II, Georgia Institute of Technology, School of Electrical and Computer Engineering, 1996-2000

III. HONORS AND AWARDS

A. INTERNATIONAL OR NATIONAL AWARDS

a. National Science Foundation CAREER Award, 2004
b. MURI: Cross-disciplinary Electronic-ionic Research Enabling Biologically Realistic Autonomous Learning (CEREBRAL)
c. MURI: Epitaxial Multifunctional Materials and Applications (EMMA) - Revolutionary Epitaxial Solutions Creating a Platform for a New Generation of Military Applications, 2004
d. MURI: Laboratory Instrumentation Design Research for Scaleable Next Generation Epitaxy: Non-Equilibrium Wide Application Epitaxial Patterning by Intelligent Control – (NEW -EPIC), 2003
e. With student Michael Moseley, Won the North American Molecular Beam Epitaxy Conference Best Student Presentation Award in 2009 and again in 2010
f. With student Brendan Gunning, Won the best Contribution at the by invitation only, longest continually running compound semiconductor meeting, the Workshop on Compound Semiconductor Materials and Devices 2015

B. Institute or School Awards

a. Awarded the 2002-2003 Student Government Faculty of the Year Award
b. Awarded the Richard M. Bass, Eta Kappa Nu Outstanding Teacher Award by ECE senior class, 2003

Seoul Semiconductor, Exhibit 2001
LGI v. SSC, IPR2019-01154

c. Awarded the 2005 ECE Outstanding Junior Faculty Member Award
d. Awarded the Lockheed Martin Aeronautics Company's Dean's Award for Teaching Excellence, March 2005
e. Awarded the 2006 Georgia Institute of Technology Class of 1940 Teaching Award
f. 2008 Georgia Institute of Technology Outstanding Achievement in Research Program Development Award
g. Awarded the Richard M. Bass, Eta Kappa Nu Outstanding Teacher Award by ECE senior class, 2011
h. Undergraduate student advisement of Hitesh Upadhyay resulted in a President's Undergraduate Research Award (PURA) for the topic "Implementation of a variable magnetic field hall measurement system using Labview", Fall 2002 / Spring 2003

IV. RESEARCH, SCHOLARSHIP, AND CREATIVE ACTIVITIES

An asterisk marks those that resulted from work done at Georgia Tech and put the names of advisees (i.e., post-docs, graduate or undergraduate students) in boldface.

A. PUBLISHED BOOKS, BOOK CHAPTERS, AND EDITED VOLUMES

A1. BOOKS

No Data

A2. REFEREED BOOK CHAPTERS

Molecular Beam Epitaxy of III-Nitrides (In process).

A3. EDITED VOLUMES

No Data

B. REFEREED PUBLICATIONS AND SUBMITTED ARTICLES

B1. PUBLISHED AND ACCEPTED JOURNAL ARTICLES

B1A. INVITED JOURNAL PUBLICATIONS (REFEREED)

1) * **Invited:** W. A. Doolittle, **A. G. Carver, and W. Henderson**, "MBE of Complex Metal-oxides: Where have we come, where are we going and how are we going to get there?", **J. of Vac. Sci. and Tech. B**, Vol. 23, No. 3, May/Jun (2005).
2) * **Invited: A. G. Carver**, W. A. Doolittle, **W. Henderson, W. L. Calley**, "Molecular Beam Epitaxy of Lithium Niobate Multifunctional Materials Using a Chloride Refractory Metal Chemistry", ECS Transactions, 2 (5) 103-114 (2006)
3) * **Invited: J. D. Greenlee, W. L. Calley, W. Henderson**, and W. A. Doolittle, "Halide based MBE of Crystalline Metals and Oxides," Phys. Status Solidi C, vol. 9, no. 2, pp. 155-160, (2011).

Seoul Semiconductor, Exhibit 2001
LGI v. SSC, IPR2019-01154

B1B. JOURNAL PUBLICATIONS (REFEREED)

1) * W. A. Doolittle and A. Rohatgi, "A novel computer based pseudo-logarithmic capacitance/conductance DLTS system specifically designed for transient analysis," **Rev. Sci. Instrum.**, Vol. 63, No. 12, pp. 5733-5741, (1992).
2) * Z. Chen, K. Yastuke, W. A. Doolittle, and A. Rohatgi, "Record low SiO_2 / Si interface state density for low temperature oxides prepared by direct plasma-enhanced chemical vapor deposition," **Appl. Phys. Lett.**, Vol. 63, No. 15, pp. 2117-2119, 11 Oct. (1993).
3) * W. A. Doolittle, and A. Rohatgi, "A new figure of merit and methodology for quantitatively determining defect resolution capabilities in deep level transient spectroscopy analysis," **J. Appl. Phys**., Vol. 75, No. 9, pp. 4570-4575, 1 May (1994).
4) * W. A. Doolittle and A. Rohatgi, "Comparison of Covariance Linear Predictive Modeling to the Modulation Function Method for Use in Deep Level Transient Spectroscopy," **J. Appl. Phys**., Vol. 75, No. 9, pp. 4560-4569, 1 May (1994).
5) * F. Fournier, R. A. Metzger, W. A. Doolittle, A. Brown, C. Carter-Coman, N. M. Jokerst, and R. Bicknell-Tassius, "Growth Dynamics of InGaAs/GaAs by MBE," **J. Cryst. Growth**, Vol. 175-176, pt. 1, p. 203, May (1997).
6) * T. J. Kropewnicki, W. A. Doolittle, C. Carter-Coman, S. Kang, P. A. Kohl, N. M. Jokerst, and A. S. Brown, "Selective Wet Etching of Lithium Gallate," **J. Electrochem. Soc. Lett**., Vol. 145, No. 5, L88-L90, May (1998).
7) * W. A. Doolittle, T. Kropenwicki, C. Carter-Coman, S. Stock, P. Kohl, N. M. Jokerst, R. A. Metzger, S. Kang, K. Lee, G. May, and A. S. Brown, "Growth of GaN on Lithium Gallate Substrates for Development of a GaN Thin Compliant Substrate," **J. Vac. Sci. & Tech. B**, Vol. 16, No. 3, pp. 1300-1304, May/June, (1998).
8) * W. A. Doolittle, S. Kang, T. J. Kropewnicki, S. Stock, P. A. Kohl, and A. S. Brown, "MBE Growth of High Quality GaN on $LiGaO_2$," **J. Electron. Mat**., Vol. 27, pp. L58-L60, No. 8, (1998).
9) * R. J. Matyi, W. A. Doolittle, and A. S. Brown, "High resolution X-ray diffraction analysis of GaN/$LiGaO_2$," **J. Phys. D: Appl. Phys.**, Vol. 32, No. 10A, pp. A61-A64, (1999).
10) * S. Kang, W. A. Doolittle, A. S. Brown, and S. R. Stock, "Electrical and structural characterization of $Al_xGa_{1-x}N$/GaN heterostructures grown on $LiGaO_2$ substrates," **Appl. Phys. Lett.**, Vol. 74, No. 22, pp. 3380-3382, 31 May (1999).
11) * W. A. Doolittle, S. Kang, and A. S. Brown, "MBE growth of high quality GaN on $LiGaO_2$ for high frequency, high power electronic applications," **Solid St. Electronics**, Vol. 44, No. #2, pp. 229-238, Feb. (2000).
12) * K. Lee, W. A. Doolittle, T. Kim, A. S. Brown, G. S. May, and S. Stock, "Using statistical experimental design to investigate the role of the initial growth conditions on GaN epitaxial films grown by molecular beam epitaxy," **J. Vac. Sci. & Tech. B**, 18(3), pp. 1448-1452, May/June (2000).
13) * A. S. Brown, W. A. Doolittle, S. Kang, J.J. Shen, Z. L. Wang, and Z. Dai, "The growth of GaN on lithium gallate ($LiGaO_2$) substrates," **J. Elect. Mat**., Vol. 29, No. 7, pp. 894-896, July (2000).
14) * A. S. Brown and W. A. Doolittle, "The Status and Promise of Compliant Substrate Technology," **Appl. Surface Science**, Vol. 166, pp. 392-398, 9 Oct. (2000).

Seoul Semiconductor, Exhibit 2001
LGI v. SSC, IPR2019-01154

15) * **G. Namkoong**, W. A. Doolittle, S. R. Stock, and A. S. Brown, "Incorporation of Mg in GaN grown by plasma-assisted molecular beam epitaxy," **Appl. Phys. Lett.**, Vol. 77, No. 26, pp. 4386-4388, 25 Dec. (2000).
16) * **G. Namkoong**, W. A. Doolittle, S. Huang, S. R. Stock, and A. S. Brown, "Low Temperature Nitridation Combined With High Temperature Buffer Annealing for High Quality GaN Grown by Plasma-Assisted MBE," **Materials Research Society Internet J. of Nitride Semiconductor Research,** Vol. 5, Art. # 10, (2000).
17) * K. Lee, W. A. Doolittle, A. S. Brown, G. S. May, and S. Stock, "A comparative study on surface reconstruction of wurzite GaN on (0001) sapphire by RF plasma-assisted molecular beam epitaxy," **J. of Cryst. Growth**, Vol. 231, No. 1-2, pp. 8-16, (2001).
18) * S. Kang, W. A. Doolittle, S. R. Stock, A. S. Brown, Z. R. Dai, and Z. L. Wang, "Characterization of AlGaN/GaN Heterojunctions Grown by Radio Frequency-plasma Assisted Molecular Beam Epitaxy," **J. Electron. Materials**, Vol. 30, No. 3, pp. 156-161, (2001).
19) * S.W. Seo, K.K. Lee, S. Kang, S. Huang, W. A. Doolittle, N. M. Jokerst, and A. S. Brown, "GaN metal-semiconductor-metal photodetectors grown on lithium gallate substrates by molecular-beam epitaxy," **Appl. Phys. Lett.**, Vol. 79, No. 9, pp.1372-1374, 27 Aug. (2001).
20) * W. A. Doolittle, A. S. Brown, S. Kang, S. W. Seo, S. Huang, and N. M. Jokerst, "Recent advances in III-nitride devices grown on lithium gallate," **Phys. Stat. Sol. A**, Vol. 188, No. 2, pp. 491-495, 23 Nov. (2001).
21) * M. Losurdo, P. Capezzuto, G. Bruno, **G. Namkoong**, W. A. Doolittle, and A. S. Brown, "The Chemistry of Sapphire Nitridation in Relation to the GaN Structural Quality: Why Low Temperature 200 °C Nitridation?", **Phys. Stat. Sol. A**, Vol. 188, No. 2, pp. 561-565, Nov. (2001).
22) * S. Seo, K.K. Lee, S. Kang, S. Huang, W. A. Doolittle, N. M. Jokerst, A. S. Brown, and M. A. Brooke, "The Heterogenous Integration of GaN Thin Film Metal-Semiconductor-Metal Photodetectors onto Silicon," **Photon. Technol. Lett.**, Vol. 14, No. 2, pp. 185-187, Feb. (2002).
23) * **G. Namkoong**, W. A. Doolittle, A. S. Brown, M. Losurdo, P. Capezzuto, and G. Bruno, "Role of sapphire nitridation temperature on GaN growth by plasma assisted molecular beam epitaxy: Part I. Impact of the nitridation chemistry on material characteristics," **J. Appl. Phys.,** Vol. 91, No. 4, pp. 2499-2507, 15 Feb. (2002).
24) * M. Losurdo, P. Capezzuto, G. Bruno, **G. Namkoong**, W. A. Doolittle, and A. S. Brown, "Role of sapphire nitridation temperature on GaN growth by plasma assisted molecular beam epitaxy: Part II. Interplay between chemistry and structure of layers," **J. Appl. Phys.**, Vol. 91, No. 4, pp. 2508-2518, 15 Feb. (2002).
25) * M. Losurdo, P. Capezzuto, G. Bruno, **G. Namkoong**, W. A. Doolittle, and A. S. Brown, "Plasmas for The Low-Temperature Growth Of High-Quality GaN Films By Molecular Beam Epitaxy and Remote Plasma MOCVD," **Phys. Stat. Sol. A**, Vol. 190, No. 1, pp. 43-51, 15 Feb. (2002).
26) * **G. Namkoong**, W. A. Doolittle, A. S. Brown, M. Losurdo, P. Capezzuto, and G. Bruno, "The Role of Low Temperature (200 °C) Nitridation in the Growth of GaN by Plasma-Assisted Molecular Beam Epitaxy," **J. Vac. Sci. Technol. B**, Vol. 20, No. 3, pp. 1221-1228, May/June (2002).

Seoul Semiconductor, Exhibit 2001
LGI v. SSC, IPR2019-01154

27) * W. A. Doolittle, **A. Carver, G. Namkoong**, and A. S. Brown, "Challenges and Potential Payoff for Crystalline Oxides in Wide Bandgap Semiconductor Technology," **Solid-State Electronics,** Vol. 47, No. 12, pp. 2143-2147, Dec. (2003).
28) ***** **G. Namkoong**, W. A. Doolittle, A. S. Brown, M. Losurdo, M. M. Giangregorio, and G. Bruno, "The impact of substrate nitridation temperature and buffer design and synthesis on the polarity of GaN epitaxial films," **J. of Cryst. Growth**, Vol. 252, No. 1-3, p. 159, May (2003).
29) * M. Losurdo, M. M. Giangregorio, P. Capezzuto, G. Bruno, **G. Namkoong**, W. A. Doolittle, and A. S. Brown, "Interplay Between GaN Polarity and Surface Reactivity Towards Atomic Hydrogen," **J. Appl. Phys.**, Vol. 95, No. 12, pp. 8408-8418, 15 June (2004).
30) * M. Losurdo, M. M. Giangregorio, P. Capezzuto, G. Bruno, **G. Namkoong**, W. A. Doolittle, and A. S. Brown, "Interaction of GaN epitaxial layers with atomic hydrogen," **Appl. Surf. Sci.**, Vol. 235, No. 3, pp. 267–273 (2004).
31) * S. E. Ralph and W. A. Doolittle, "Epitaxial integration of III-Nitride devices with Lithium Niobate Optical Waveguides," **IEEE LEOS Hot Topics**, Vol. 18, No. 3, pp. 1, June 2004.
32) * G. Bu, D. Ciplys, M. S. Shur, **G. Namkoong**, W. A. Doolittle, and W. D. Hunt, "Leaky surface acoustic waves in Z-$LiNbO_3$ substrates with epitaxial AIN overlays," **Appl. Phys. Lett.**, Vol. 85, No. 15, pp. 3313-3315, 11 Oct. (2004).
33) ***** **E. Trybus, G. Namkoong**, W. Henderson, W. A. Doolittle, R. Liu, J. Mei, F. Ponce, M. Cheung, F. Chen, M. Furis, and A. Cartwright, "Growth of InN on Germanium by Molecular Beam Epitaxy," **J. of Cryst. Growth**, Vol. 279, No. 3/4, pp. 311–315, 2005.
34) ***** **S. D. Burnham**, W. A. Doolittle, **G. Namkoong**, and W. Henderson, "Mg Doped GaN Using a Valved, Thermally Energetic Source: Enhanced Incorporation, and Control," **J. of Cryst. Growth**, Vol. 279, No. 1/2, pp. 26–30, 2005.
35) * M.C. Cheung, **G. Namkoong**, F. Chen, M. Furis, H. E. Pudavar, A. N. Cartwright, and W. A. Doolittle, "Photoluminescence Study of MBE Grown InGaN with Intentional Indium Segregation," **Phys. Stat. Sol. (c)** Vol. 2, No. 7 , pp. 2779-2782, 2005.
36) ***** **G. Namkoong**, W. A. Doolittle, M. Losurdo, P. Capezzuto, G. Bruno, B. Nemeth and J. Nause, "III-nitrides on O and Zn face ZnO substrates," **Appl. Phys. Lett**., Vol. 87, 184104, 2005.
37) ***** **G. Namkoong, K. K. Lee, S. M. Madison**, W. Henderson, W. A. Doolittle, and S. E. Ralph, "III-Nitride Integration on Ferroelectric Materials of Lithium Niobate by Molecular Beam Epitaxy," **Appl. Phys. Lett.**, Vol. 87, 171107, Oct. 2005
38) * E. Trybus, G. Namkoong, W. Henderson, S. Burnham, W. A. Doolittle, M. Cheung and A. Cartwright "InN: A material with Photovoltaic Promise and Challenges," **J. of Cryst. Growth**, Vol 288, pp. 218, 2005.
39) * N. Takeuchi, A. Selloni, T. H. Myers, and W. A. Doolittle, "Adsorption and diffusion of Ga and N adatoms on GaN surfaces: comparing the effects of Ga-coverage and electronic excitation", **Phys. Rev. B**, Vol. 72, 115307, 2005.
40) ***** **G. Namkoong**, **S. D. Burnham, K.-K. Lee, E. Trybus**, W. A. Doolittle, M. Losurdo, P. Capezzuto, G. Bruno, B. Nemeth, and J. Nause, "III-nitrides on oxygen- and zinc-face ZnO substrates," **Appl. Phys. Lett.**, Vol. 87, pp. 184104-3, 2005.

Seoul Semiconductor, Exhibit 2001
LGI v. SSC, IPR2019-01154

41) * **E. Trybus, G. Namkoong**, W. Henderson, **S. Burnham**, W. A. Doolittle, M. Cheung, and A. Cartwright, "InN: A material with Photovoltaic Promise and Challenges", **Journal of Crystal Growth, V**ol. 288, pp 218, (2006).
42) * **D. Pritchett**, W. Henderson, **S. D. Burnham**, W. A. Doolittle, "Influence of growth conditions and surface reaction byproducts on GaN grown via metal organic molecular beam epitaxy: toward an understanding of surface reaction chemistry", **Journal of Electronic Materials**, Vol. 35, No. 4, p 562-7, April 2006
43) * Q. Sun, A. Selloni, T. H. Myers, W. Alan Doolittle, "Energetics of Mg incorporation at GaN(0001) and GaN(000$1^{-}$) surfaces", **Physical Review B** (Condensed Matter and Materials Physics), Vol. 73, No. 15, p 155337-1-9, 15 April 2006
44) * **K.-K. Lee, G. Namkoong**, W. A. Doolittle, M. Losurdo, G. Bruno, and D. Jundit, "III-nitride growth and characteristics on ferroelectric materials using plasma-assisted MBE," **Journal of Vacuum Science Technology B**, Vol. 24, no. 4, pp. 2093-9, July 2006.
45) * T. Chen, A. K. Sutton, B. M. Haugerud, **W. Henderson**, A.P.G. Prakash, J. D. Cressler, W. A. Doolittle, X.Liu; A. Joseph, P. W. Marshall "An investigation of the effects of radiation exposure on stability constraints in epitaxial SiGe strained layers", **Solid-State Electronics**, Vol. 50, No. 7-8, p 1194-200, July-Aug. 2006
46) * **S. D. Burnham**, E. W. Thomas, W. A. Doolittle, "Resistivity analysis of epitaxially grown, doped semiconductors using energy dependent secondary ion mass spectroscopy", **Journal of Applied Physics**, Vol. 100, No. 11, p 113719-1-6 , 1 Dec. 2006
47) * **S. D. Burnham** and W. A. Doolittle, " In situ growth regime characterization of AlN using reflection high energy electron diffraction", **Journal of Vacuum Science & Technology B**, Vol 24, pp 2100-2104, 2006.
48) * **S. D. Burnham, G. Namkoong, K.-K. Lee**, and W. A. Doolittle, "Reproducible RHEED signatures for improvement of AlN using *in situ* growth regime characterization," **Journal of Vacuum Science and Technology B**, Vol. 25, no. 3, pp. 1009-13, May/June 2007.
49) * **K.-K. Lee, G. Namkoong, S. M. Madison**, S. E. Ralph, W. A. Doolittle, M. Losurdo, G. Bruno, and H. K. Choi, "III-nitride growth and AlGaN/GaN heterostructures on ferroelectric materials," **Material Science Engineering B**, Vol. 140, pp.203, June 2007.
50) * **G. Namkoong, E. Trybus, K. K. Lee, M. Moseley**, W. A. Doolittle, D. C. Look, "Metal modulation epitaxy growth for extremely high hole concentrations above 10^{19} cm^{-3}in GaN", **Appl. Phys. Lett.**, Vol. 93, No. 17, p 172112 (3 pp.), 27 Oct. 2008
51) * **D. Pritchett**, W. Henderson, **D. Billingsley**, W. A. Doolittle, "Mixed alkyl exchange and exploitable surface interactions in InGaN by NH_3-based metal organic molecular beam epitaxy", **J. Crys. Growth**, Vol. 310, No. 24, p 5297-5302, 1 Dec. 2008
52) * **A. G. Carver**, W. Henderson, W. A. Doolittle, "Reclamation of a molecular beam epitaxy system and conversion for oxide epitaxy", **J. Vac. Sci. & Tech. A**, Vol. 26, No. 6, pp. 1501-6, Nov.-Dec. 2008
53) * **S. D. Burnham, G. Namkoong**, D. C. Look, B. Clafin, W. A. Doolittle,, "Reproducible increased Mg incorporation and large hole concentration in GaN using metal modulated epitaxy", **J. Appl. Phys.**, Vol. 104, No. 2, pp. 024902-7, 15 July 2008

Seoul Semiconductor, Exhibit 2001
LGI v. SSC, IPR2019-01154

54) * **E. Trybus**, O. Jani, **S. D. Burnham**, I. Ferguson, C. Honsberg, M. Steiner, and W. A. Doolittle, "Characteristics of InGaN Designed for Photovoltaic Applications", **Phys. Stat. Sol. C**, Vol. 5, No. 6, p 1843-5, May 2008.
55) * **S. D. Burnham**, **W. Henderson**, W. A. Doolittle, "Closed-loop MBE growth of droplet-free GaN with very metal rich conditions using metal modulated epitaxy with Mg and In", **Phys. Stat. Sol. C**, Vol. 5, No. 6, pp. 1855-8, May 2008
56) * **D. Pritchett**, **W. Henderson**, **D. Billingsley**, W.A. Doolittle, "InGaN compositional patterning by ultraviolet photoexcitation during NH_3-based MOMBE: a pathway to 3D epitaxy", **Phys. Stat. Sol. C**, Vol. 5, No. 6, pp. 1726-9, May 2008
57) * **D. Billingsley**, **D. Pritchett**, **W. Henderson**, **A. G. Carver, S. D. Burnham**, W. A. Doolittle, "Investigation into the use of molecular hydrogen on the growth of gallium nitride via metal-organic molecular beam epitaxy", **Phys. Stat. Sol. C**, Vol. 5, No. 6, pp. 1723-5, May 2008
58) * A. Barnett, A. D. Kirkpatrick, C. Honsberg, D. Moore, M. Wanlass, K. Emery, R. Schwartz, D. Carlson, S. Bowden, D. Aiken, A. Gray, S. Kurtz, L. Kazmerski, M. Steiner, J. Gray, T. Davenport, R. Buelow, L. Takacs, N. Shatz, J. Bortz, O. Jani, K. Goossen, F. Kiamilev, A. Doolittle, I. Ferguson, B. Unger, G. Schmidt, E. Christensen, D. Salzman, "Very high efficiency solar cell modules", **Progress in Photovoltaics: Research and Applications**, Vol. 17, No. 1, p 75-83, Jan. 2009.
59) * **D. Billingsley**, **W. Henderson**, **D. Pritchett**,W. A. Doolittle, "Growth and characterization of $Al_xGa_{1-x}N$ via NH_3-based metal-organic molecular beam epitaxy", **J. Cryst. Growth**, Vol. 311, No. 5, pp. 1328-32, 15 Feb. 2009
60) * **M. Moseley, D. Billingsley**, **W. Henderson**, **E. Trybus**, W. A. Doolittle, "Transient atomic behavior and surface kinetics of GaN", **J. Appl. Phys.**, Vol. 106, No. 1, pp. 014905-12, 1 July 2009
61) * **G. Namkoong, S. Huang, M. Moseley**, and W. A. Doolittle, "In-plane anisotropic strain of elastically and plastically deformed III-nitrides on lithium gallate", **Thin Solid Films**, Vol. 517, p. 6508 (2009).
62) * J. F. Ihlefeld, T. Wei; L. Z.-Kui; W. A. Doolittle, M. Bernhagen, P. Reiche, R. Uecker, R. Ramesh, D. G. Schlom, "Adsorption-controlled growth of $BiFeO_3$ by MBE and integration with wide band gap semiconductors", **IEEE Trans. Ultrasonics, Ferroelectrics and Frequency Control**, Vol. 56, No. 8, p 1528-33, Aug. 2009
63) * **K. K. Lee**, Z. Cai, K. Ziemer, W. A. Doolittle, "The origin of the residual conductivity of GaN films on ferroelectric materials", **J. Cryst. Growth**, Vol. 311, No. 16, p. 4001-6, 1 Aug. 2009
64) * **E. Trybus**, W. A. Doolittle, **M. Moseley**, W. Henderson, **D. Billingsley, G. Namkoong**, and D. C. Look, "Extremely High Hole Concentrations in c-Plane GaN", **Phys. Stat. Sol. C**, Vol. 6, p. S788, (2009).
65) * **M. Moseley, D. Billingsley**, W. Henderson, **E. Trybus**, and W. A. Doolittle, "Transient Atomic Behavior and Surface Kinetics of GaN," J. Appl. Phys. 106, 014905 (2009).
66) * **G. Namkoong**, S. Huang, **M. Moseley**, and W. A. Doolittle, "In-plane anisotropic strain of elastically and plastically deformed III-nitrides on lithium gallate," Thin Solid Films, 517, 6508 (2009).
67) * **E. Trybus**, W. A. Doolittle, **M. Moseley**, **W. Henderson**, **D. Billingsley**, G. Namkoong, and D. C. Look, "Extremely High Hole Concentrations in c-Plane GaN," Phys. Status Solidi C, 6, S788 (2009).

Seoul Semiconductor, Exhibit 2001
LGI v. SSC, IPR2019-01154

68) * **D. Billingsley**, **W. Henderson**, **D. Pritchett**, and W. A. Doolittle, "Growth Kinetics of $Al_xGa_{1-x}N$ Grown via Ammonia-Based Metal-Organic Molecular Beam Epitaxy," **J. Cryst. Growth,** Vol. 312, p. 209, (2010).
69) * **D. Billingsley**, **W. Henderson**, and W. A. Doolittle, "High-temperature Growth of GaN and $Al_xGa_{1-x}N$ via Ammonia-Based Metal-Organic Molecular Beam Epitaxy," **J. Electron. Mater**., V. 39, No 5, pp. 473-7, 2010
70) * **G. Namkoong, E. Trybus**.; M.C. Cheung, W. A. Doolittle, A. N. Cartwright, I. Ferguson, T. Y. Seong, J. Nause, "Dual-Color Emission in Hybrid III-Nitride/ZnO Light Emitting Diodes", **Appl. Phys. Express**, V. 3, No 2, p 022101-4, Feb. 2010
71) * **M. Moseley, J. Lowder, D. Billingsley**, W. A. Doolittle, "Control of surface adatom kinetics for the growth of high-indium content InGaN throughout the miscibility gap", **Appl. Phys. Lett.**, Vol. 97, No 19, p 191902-5, 8 Nov. 2010
72) * **W. E. Henderson**, **W. L. Calley**, **A. G. Carver**, **H. Chen**, and W. A. Doolittle, "A versatile metal-halide vapor chemistry for the epitaxial growth of metallic, insulating and semiconducting films", **J. Cryst. Growth**, Vol. 324, Issue 1, pp134-141, 1 June, (2011)
73) * M. E. Zvanut, Y. Uprety, J. Dashdorj, **M. Moseley**, and W. Alan Doolittle, "Passivation and Activation of Mg acceptors in heavily doped GaN," **J. Appl. Phys.**, 110, 044508 (2011).
74) * **G. Namkoong**, P. Boland, Si-Young Bae, Jae-Phil Shim, Dong-Seon Lee, Seong-Ran Jeon, K. Foe, K. Latimer, W. A. Doolittle, "Effect of III-nitride polarization on VOC in p-i-n and MQW solar cells", **Physica Status Solidi (RRL) - Rapid Research Letters**, V5, n 2, p 86-8, Feb. 2011
75) * **J. D. Greenlee**, **W. L. Calley, W. Henderson**, and W. A. Doolittle, "Halide based MBE of Crystalline Metals and Oxides," **Phys. Status Solidi C**, vol. 9, no. 2, pp. 155-160, 2011.
76) * **J. Greenlee**, **W. Calley**, **M. Moseley**, W. A. Doolittle, "Comparison of Interfacial and Bulk Ionic Motion in Analog Memristors," **IEEE Trans. Electron Dev.**, 60, 427 (2012).
77) * **B. Gunning**, **J. Lowder**, **M. Moseley**, W. A. Doolittle, "Negligible carrier freeze-out facilitated by impurity band conduction in highly p-type GaN," **Appl. Phys. Lett.**, 101, 082106 (2012).
78) * **J. D. Greenlee**, C. F. Petersburg, **W. L. Calley**, C. Jaye, D. A. Fischer, F. M. Alamgir, and W. A. Doolittle, "In-situ oxygen x-ray absorption spectroscopy investigation of the resistance modulation mechanism in $LiNbO_2$ memristors," **Appl. Phys. Lett.**, vol. 100, no. 18, pp. 182106 - 182106-4, (2012).
79) * **M. Moseley, B. Gunning, J. Greenlee, J. Lowder**, **G. Namkoong**, W. A. Doolittle, "Observation and Control of the Surface Kinetics of InGaN for the Elimination of Phase Separation," **J. Appl. Phys.**, V112, 014909 (2012).
80) * **J. Greenlee, W. Calley, M. Moseley**, W. A. Doolittle, "Comparison of Interfacial and Bulk Ionic Motion in Analog Memristors," **IEEE Trans. Electron Dev.**, Vol. 60, p. 427 (2012).
81) * **M. Moseley, B. Gunning, J. Lowder**, W. A. Doolittle, **G. Namkoong** "Structural and electrical characterization of InN, InGaN, and p-InGaN grown by metal-modulated epitaxy**", J. Vac. Sci. & Tech. B**, V31, no 3, p 03C104 (6 pp.), May 2013
82) * **W. Laws Calley, J. D. Greenlee, W. E. Henderson**, **J. Lowder, M. W. Moseley**, W. A. Doolittle, P. G. Staib, "In situ Auger probe enabling epitaxy composition

Seoul Semiconductor, Exhibit 2001
LGI v. SSC, IPR2019-01154

control of alloys by elemental surface analysis", **J. Vac. Sci. & Tech. B**, V31, n 3, p 03C126 (5 pp.), May 2013

83) * **J. D. Greenlee** , C. F. Petersburg , **W. G. Daly** , F. M. Alamgir, W. A. Doolittle, " In-situ investigation of the channel conductance of a $Li_{1-x}CoO_2$ ($0 < x < 0.5$) ionic-electronic transistor," **Appl. Phys. Lett.**, V102, No 21, p 213502 (4 pp.), 27 May (2013)

84) * A. M. Fischer, Y. O. Wei, F. A. Ponce, **M. Moseley, B. Gunning** and W. A. Doolittle, "Highly luminescent, high-indium-content InGaN film with uniform composition and full misfit-strain relaxation", **Appl. Phys. Lett.**, 103, 131101 (2013).

85) * **M. Moseley, B. Gunning, J. Lowder**, W. A. Doolittle and **G. Namkoong**, "Structural and electrical characterization of InN, InGaN, and p-InGaN grown by metal-modulated epitaxy**", J. Vac. Sci. Technol. B**, 31, 01C104-1 (2013).

86) * **C. A. M. Fabien**, **M. Moseley, B. Gunning**, W. A. Doolittle, "Simulations, Practical Limitations, and Novel Growth Technologies for InGaN-based Solar Cells," ***IEEE J. Photovoltaics***, vol. PP, no. 99, pp.1-6, 2013.

87) * **J. D. Greenlee, J. C. Shank, M. B. Tellekamp**, and W. A. Doolittle, "Spatiotemporal drift-diffusion simulations of analog ionic memristors," **J. Appl. Phys.**, vol. 114, p. 034504, 2013.

88) * **Jordan D. Greenlee, Joshua C. Shank, M. Brooks Tellekamp**, Enxia Zhang, Jinshun Bi, Daniel M. Fleetwood, Michael L. Alles, Ronald D. Schrimpf, and W. Alan Doolittle, "Radiation Effects on $LiNbO_2$ Memristors for Neuromorphic Computing Applications", **IEEE Transactions on Nuclear Science**, v 60, n 6, pt.1, p 4555-62, Dec. 2013

89) * **C. A. M. Fabien**, W. A. Doolittle, "Guidelines and limitations for the design of high-efficiency InGaN single-junction solar cells", **Solar Energy Materials and Solar Cells**, v 130, p 354-63, Nov. 2014

90) * **C.A.M. Fabien, M. Moseley, B. Gunning**, W. A. Doolittle, A. M. Fischer, Y. O. Wei, F. A. Ponce, "Simulations, Practical Limitations, and Novel Growth Technology for InGaN-Based Solar Cells", **IEEE J. of Photovoltaics**, v 4, n 2, p 601-6, March 2014

91) * **J. D. Greenlee, J. C. Shank, M. B. Tellekamp, B. Gunning, C. A. Fabien**, and W. A. Doolittle, "Liquid Phase Electro-Epitaxy of Memristive $LiNbO_2$ Crystals," **Crystal Growth & Design**, vol. 14, pp. 2218-2222, 2014.

92) * **B. P. Gunning, C.A.M. Fabien, J. J. Merola, E. A. Clinton**, W. A. Doolittle, S. Wang; A. M. Fischer, and F. A. Ponce, "Comprehensive study of the electronic and optical behavior of highly degenerate p-type Mg-doped GaN and AlGaN", **J. Appl. Phys.**, v 117, n 4, p 045710 (11 pp.), 28 Jan. 2015

93) * **J. C. Shank, M. B. Tellekamp**, and W. A. Doolittle, "Evidence of ion intercalation mediated band structure modification and opto-ionic coupling in lithium niobite", **J. Appl. Phys.**, v 117, n 3, p 035704 (6 pp.), 21 Jan. 2015

94) * **J. C. Shank, M. B. Tellekamp**, E. X. Zhang, W. G. Bennett, M. W. McCurdy, D. M. Fleetwood, M. L. Alles, R. D. Schrimpf, and W. A. Doolittle, "Self-Healing of Proton Damage in Lithium Niobite ($LiNbO_2$)," ***IEEE Trans. Nucl. Sci.,*** 2015.

95) * **M.B. Tellekamp, J.D. Greenlee, J.C. Shank**, W.A. Doolittle, "Molecular beam epitaxy growth of niobium oxides by solid/liquid state oxygen source and lithium assisted metal-halide chemistry", **Journal of Crystal Growth**, v 425, p 225-9, 1 Sept. 2015

Seoul Semiconductor, Exhibit 2001
LGI v. SSC, IPR2019-01154

96) * **C.A.M. Fabien, B. P. Gunning**, W. A. Doolittle, A. M. Fischer, Y.O. Wei, X. Hongen, F. A. Ponce, "Low-temperature growth of InGaN films over the entire composition range by MBE", **Journal of Crystal Growth**, v 425, p 115-18, 1 Sept. 2015

97) * **B. P. Gunning, E. A. Clinton, J. J. Merola**, W. A. Doolittle, R. C. Bresnahan, "Control of ion content and nitrogen species using a mixed chemistry plasma for GaN grown at extremely high growth rates >9 μm/h by plasma-assisted molecular beam epitaxy", **J. Appl. Phys.**, v 118, n 15, p 155302 (8 pp.), 21 Oct. 2015

98) * **Jordan D. Greenlee, Brendan Gunning**, Boris N. Feigelson, Travis J. Anderson, Andrew D. Koehler, Karl D. Hobart, Francis J. Kub, and W. Alan Doolittle, "Defect Reduction in MBE-Grown AlN by Multicycle Rapid Thermal Annealing", **Electronic Materials Letters**, V12, Issue 1, pp133-138, Jan 2016

99) * **C.A.M. Fabien**, A. Maros, C. B. Honsberg, W. A. Doolittle, "III-Nitride Double-Heterojunction Solar Cells With High In-Content InGaN Absorbing Layers: Comparison of Large-Area and Small-Area Devices", **IEEE Journal of Photovoltaics**, v 6, n 2, p 460-4, March 2016

100) * **J. C. Shank, M. B. Tellekamp**, and W. A. Doolittle, "The Crystallization and Properties of Sputter Deposited Lithium Niobite", Thin Solid Films, Volume 609, 30 June 2016, Pages 6-11

101) J. D. Greenlee, **B. P. Gunning**, B. N. Feigelson, T. J. Anderson, A. D. Koehler, K. D. Hobart, F. J. Kub, W. A. Doolittle, "Defect reduction in MBE-grown AlN by multicycle rapid thermal annealing", Source: Electronic Materials Letters, v 12, n 1, p 133-8, Jan. 2016

102) ***M. B. Tellekamp**, **J. C. Shank**, M. S. Goorsky, W. A. Doolittle, "Molecular Beam Epitaxy Growth of High Crystalline Quality $LiNbO_3$", Journal of Electronic Materials, v 45, n 12, p 6292-9, Dec. 2016

103) ***M. B. Tellekamp**, **J. C. Shank**, W. A. Doolittle, "Molecular beam epitaxy of lithium niobium oxide multifunctional materials", Journal of Crystal Growth, v 463, p 156-61, 1 April 2017

104) * A.M.Fischer, S. Wang, F. A. Ponce, **B. P. Gunning**, **C. A. M. Fabien**, W. A. Doolittle," Origin of high hole concentrations in Mg-doped GaN films", Physica Status Solidi B - Basic Solid State Physics, v 254, n 8, p 1600668 (6 pp.), Aug. 2017

105) ***E. A. Clinton**, **E. Vadiee**, **C. A. M. Fabien**, **M. W. Moseley**, **B. P. Gunning**, W. A. Doolittle, A. M. Fischer, Y. O. Wei, Xie Hongen, F. A. Ponce, "A review of the synthesis of reduced defect density $In_xGa_{1-x}N$ for all indium compositions", Solid-State Electronics, v 136, p 3-11, Oct. 2017

106) *Rong Jiang, En Xia Zhang, S. E. Zhao, D. M. Fleetwood, R. D. Schrimpf, R. A. Reed, M. L. Alles, **J. C. Shank**, **M. B. Tellekamp**, W. A. Doolittle, "Total-Ionizing-Dose Response of Nb_2O_5-Based MIM Diodes for Neuromorphic Computing Applications", IEEE Transactions on Nuclear Science, v 65, n 1, pt.1, p 78-83, Jan. 2018

107) ***J. C. Shank**, **M. B. Tellekamp**, M. J. Wahila, S. Howard, **A. S. Weidenbach**, **B. Zivasatienraj**, L. F. J. Piper, W. A. Doolittle, "Scalable Memdiodes Exhibiting Rectification and Hysteresis for Neuromorphic Computing", Scientific reports, Vol 8, Article number: 12935, August 8, 2018

108) ***E. A. Clinton**, **E. Vadiee**, Shyh-Chiang Shen; K. Mehta, P. D. Yoder, W. A. Doolittle, "Negative differential resistance in GaN homojunction tunnel diodes and low voltage loss tunnel contacts", Applied Physics Letters, v 112, n 25, p 252103 (5 pp.), 18 June 2018

Seoul Semiconductor, Exhibit 2001
LGI v. SSC, IPR2019-01154

109) ***E. Vadiee**, **E. A. Clinton**, H. McFavilen, **A. S. Weidenbach**, **Z. Engel**, **C. Matthews**, Chaomin Zhang, C. Arena, R. R. King, C. B. Honsberg, W. A. Doolittle, "InGaN solar cells with regrown GaN homojunction tunnel contacts", Applied Physics Express, v 11, n 8, p 082304 (5 pp.), Aug. 2018

110) Zhe Cheng, A. S. Weidenbach, Tianli Feng, M. B. Tellekamp, S. Howard, M. J. Wahila, B. Zivasatienraj, B. Foley, S. T. Pantelides, L. F. J. Piper, W. A. Doolittle, S. Graham, "Diffuson-driven ultralow thermal conductivity in amorphous Nb_2O_5 thin films", Physical Review Materials, v 3, n 2, p 025002 (7 pp.), arXiv:1807.05483 [cond-mat.mes-hall] , Feb. 2019

111) **E. A. Clinton**, **E. Vadiee**, **M. B. Tellekamp**, and W. A. Doolittle, "Observation and mitigation of RF-plasma-induced damage to III-nitrides grown by molecular beam epitaxy", J. Applied Physics, Accepted- Expected Publication June 2019 Issue 22

112) **E. A. Clinton**, **Z. Engel**, **E. Vadiee**, J. V. Carpenter, Z. C. Holman, and W. A. Doolittle, "Ultra-Wide-Bandgap AlGaN Homojunction Tunnel Diodes with Negative Differential Resistance", Appl. Phys. Lett., Submitted June 2019

B2. CONFERENCE PRESENTATION WITH PROCEEDINGS (REFEREED)

No Data

B2A INVITED CONFERENCE PROCEEDINGS (REFEREED)

1) * **Invited**: W. A. Doolittle and A. S. Brown, "Compliant Substrate Processes," Proceedings of Materials Research Society, Epitaxial Growth-Principles and Applications Symposium, San Francisco, CA, April 5-8, (1999).

B2B CONFERENCE PROCEEDINGS (REFEREED)

2) * A. Rohatgi, W. A. Doolittle, A. W. Smith, F. V. Wald, R. O. Bell, and C. E. Dube, "Doping and Oxygen Dependence of Efficiency of EFG Silicon Solar Cells," Proceedings of the 21st Photovoltaic Specialists Conference, Kissimmee, FL, , p. 581, May 21-25 (1990).

3) * W. A. Doolittle, A. Rohatgi, and R. Brenneman, "Correlation between Impurities, Defects, and Cell Performance in Semicrystalline Silicon," Proceedings of the 21st Photovoltaic Specialists Conference, Kissimmee, FL, p. 681, May 21-25 (1990).

4) * B. L. Sopori, K.M. Jones, X.R. Matson, M. Al-Jassim, S. Tsuo, W. A. Doolittle, and A. Rohatgi, "Hydrogen in Silicon: Diffusion and Defect Passivation," Proceedings of the 22nd Photovoltaic Specialists Conference, Las Vegas, NV, Vol. 2, pp. 833-841, Oct., (1991).

5) * A. Rohatgi, Z. Chen, P. Sana, N. Evers, R. Ramanachalam, and W. A. Doolittle, "Gettering and Passivation Techniques for Quality Enhancement of Multicrystalline Silicon," American Institute of Physics Conference Proceedings, Proceedings of 1994 12th NREL Photovoltaic Review, Denver, CO, Vol. 303, pp. 505-518. Oct. 13-15 (1993).

6) * A. Rohatgi, P. Doshi, M. Ropp, L. Cai, W. A. Doolittle, S. Narashima, T. Krygowski, J. Rand, D. Ruby, and D.L. Meier, "Improved understanding and optimization of RTP and PECVD processes for high efficiency silicon solar cells," Proc. 13th European Photovoltaic Solar Energy Conference and Exhibition, Oct. (1995).

Seoul Semiconductor, Exhibit 2001
LGI v. SSC, IPR2019-01154

7) * A. Rohatgi, P. Sana, L. Cai, W. A. Doolittle, S. Kamra, P. Doshi, T. Krygowski, and G. Crotty, "Fabrication and analysis of high efficiency multicrystalline silicon solar cells," American Institute of Physics Conference Proceedings, 1996, Proceedings of 13th NREL Photovoltaics Review, Lakewood, CO, Vol. 353, pp. 126-34, , May 16-19 (1995).
8) * J. Cowles, R.A. Metzger, A. Gutierrez-Aitken, A. S. Brown, D. Streit, A. Oki, T. Kim, and W. A. Doolittle, "Double heterojunction bipolar transistors with InP epitaxial layers grown by solid-source MBE," 1997 International Conference on Indium Phosphide and Related Materials, Cape Cod, MA, pp. 548-50, , May 11-15 (1997).
9) * T. Ciszek, T. Wang, W. A. Doolittle, and A. Rohatgi, "Minority Carrier Lifetime Degradation in Silicon Co-Doped with Iron and Gallium," Proceedings of the 26th Photovoltaic Specialists Conference, Anaheim, CA, pp. 59-62, Sept. 29-Oct. 3 (1997).
10) * W. A. Doolittle, T. Kropewnicki, C. Carter-Coman, S. Stock, P. Kohl, N. M. Jokerst, R. A. Metzger, S. Kang, K. Lee, G. May, and A. S. Brown, "Growth of GaN on lithium gallate substrates for development of a GaN thin compliant substrate," Proceedings of the Materials Research Society, Nitride Semiconductors Symposium, Boston, MA, pp. 283-288, Fall (1997).
11) * G. Augustine, H. McD. Hobgood, V. Balakrishna, G. T. Dunne, R. H. Hopkins, R. N. Thomas, W. A. Doolittle, and A. Rohatgi, "High purity and semi-insulating 4H-SiC crystals grown by physical vapor transport," Proceedings of the Silicon Carbide, III-Nitrides and Related Materials. 7th International Conference, Stockholm, Sweden, Materials Science Forum, Vol. 264-268, pt.1, pp. 9-12, Aug. 31-Sept. 5, (1997) .
12) * W. A. Doolittle, A. Rohatgi, R. Ahrenkiel, D. Levi, G. Augustine, and R. H. Hopkins, "Understanding the Role of Defects in Limiting the Minority Carrier Lifetime in SiC," Proceedings of the Materials Research Society, Power Semiconductor Materials and Devices Symposium, Boston, MA, pp. 197-202, Fall (1997).
13) * T. F. Ciszek, T. H. Wang, W. A. Doolittle, A. Rohatgi, C. L. Claeys, P. Rai-Choudhury, M. Watanbabe, P. Stallhofer, and H. J. Dawson, "Iron-gallium pair defects in float-zoned silicon," Proceedings of the Fifth International Symposium on High Purity Silicon V, Boston, MA, pp. 230-237, Nov. 2-6 (1998).
14) * K. Lee, S. Seo, S. Huang, Y. Joo, W. A. Doolittle, S. Fike, N. Jokerst, M. Brooke, and A. S. Brown, "Design of a smart pixel multispectral imaging array using 3D stacked thin film detectors on Si CMOS circuits," 2000 Digest of the IEEE Lasers and Electro-Optic Society (LEOS) Summer Topical Meetings, Cat. No.00TH8497, pp. I57-8, Nov. (2000).
15) * S. Seo, K. Lee, S. Huang, Y. Joo, W. A. Doolittle, N. Jokerst, A. S. Brown, and M. Brooke, "GaN Thin Film Material Bonded to Host Substrates Using Selective Chemical Etching," 2000 Digest of the IEEE Lasers and Electro-Optic Society (LEOS) Summer Topical Meetings, Cat. No.00CH37080, Vol. 2, pp. 559-560, Nov. (2000).
16) * S. Kang, W. A. Doolittle, A. S. Brown, and S. R. Stock, "Comparison of AlGaN and GaN grown on various substrates; step flow growth on LiGaO2 at low growth temperature," Proceedings of the International Conference on Silicon Carbide and Related Materials, Raleigh, NC, Materials Science Forum, Vol. 338-342, part 2, pp. 1499-1502, Oct. 10-15, (2000).
17) * **G. Namkoong**, W. A. Doolittle, S. Kang, S. Huang, A. S. Brown, and S. R. Stock, "Low temperature nitridation combined with high temperature buffer annealing

Seoul Semiconductor, Exhibit 2001
LGI v. SSC, IPR2019-01154

for high quality GaN grown by plasma-assisted MBE," MRS Internet Journal of Nitride Semiconductor Research, Vol. 5S1, 2000.

18) * M. Losurdo, M. Giangregorio, P. Capezzuto, G. Bruno, **G. Namkoong**, W. A. Doolittle, and A. S. Brown, "A Chemical Perspective of GaN Polarity: The Use of Hydrogen Plasma Dry Etching Versus NaOH Wet Etching to Determine Polarity," Materials and Devices for Optoelectronics and Microphotonics Symposia (Materials Research Society Symposium Proceedings, Vol. 722, pp. 103-108 (2002)
19) * M. Cheung, F. Chan, M. Furis, A. Cartwright, **G. Namkoong**, and W. A. Doolittle, "Time-Resolved Optical Studies of InGaN Layers Grown on LGO substrates," GaN and Related Alloys - 2002 Symposium (Mater. Res. Soc. Symposium Proceedings), Boston, MA, Vol. 743, L11.6, pp. 659-664, Dec. 2-6, (2002).
20) * W. A. Doolittle, **G. Namkoong, A. Carver, W. Henderson**, and A. S. Brown, "III-Nitride Growth on Lithium Niobate: A new substrate material for Polarity Engineering in III-Nitride Heteroepitaxy," GaN and Related Alloys - 2002 Symposium (Mater. Res. Soc. Symposium Proceedings), Boston, MA, Vol. 743, L1.4, pp. 9-14, Dec. 2-6, (2002).
21) * H. Wu, W. J. Schaff, M. Furis, A. Cartwright, **W. Henderson**, W. A. Doolittle, and A. V. Osinsky, "Molecular Beam Epitaxial Growth of AlN/GaN Multiple Quantum Wells", GaN and Related Alloys - 2002 Symposium (Mater. Res. Soc. Symposium Proceedings), Boston, MA, Vol. 743, L6.2, pp. 375-380, Dec. 2-6, (2002).
22) * W. A. Doolittle, **G. Namkoong, A. G. Carver, and W. Henderson**, "Crystalline Functional Oxides Integrated with Wide Bandgap Semiconductors via Epitaxy: A Novel Platform for Multifunctional Materials Integration and Devices", Advanced Research Workshop: Future Trends in Microelectronics-4: The Nano, the Giga, the Ultra, and the Bio, Corsica, France, June 23-27 (2003).
23) * **G. Namkoong**, W. A. Doolittle, **A. G. Carver, W. Henderson**, D. Jundt, and A.S. Brown, "III-Nitride Growth on a Ferro/Pyro/Piezoelectric/Nonlinear Optical Substrate for Advanced Functionality", Workshop on Compound Semiconductor Materials and Devices (WOCSEMMAD), Atlanta, GA., Feb. (2003).
24) * **S. Burnham, G. Namkoong**, and W. A. Doolittle, "Mg Doped GaN using a thermally energetic source: Enhanced incorporation, control and quantitative optimization," GaN and Related Alloys - 2003 Symposium (Mater. Res. Soc. Symposium Proceedings, Vol. 798), 2004, pp. 479-484, Dec. (2003).
25) * S. E. Ralph, M. King, **G. Namkoong**, and W. A. Doolittle, "Monolithic Integration of GaN Electronic Amplifiers with $LiNbO_3$ Optical Modulators," 2003 IEEE LEOS Annual Meeting Conference Proceedings, (IEEE Cat. No.03CH37460), pt. 2, pp. 652-653, Vol. 2, (2003).
26) * **A. G. Carver, W. Henderson**, W. A. Doolittle, "Novel chlorine based chemistry for growth of ferroelectric materials by molecular beam epitaxy", Materials Research Society Fall 2003 Meeting, December (2003).
27) * **S. D. Burnham**, W. A. Doolittle, **G. Namkoong, W. Henderson**, "Mg doped GaN using a valved, thermally energetic source: enhanced incorporation, control and quantitative optimization," Mater. Res. Soc. 2003 Symposium Proceedings – GaN and Related Alloys, Vol. 798, pp. 479-484, (2004).
28) * S. Madison, **W. Henderson, G. Namkoong**, K. M. Patel, W. A. Doolittle, S. Ralph, "Monolithic integration of AlGaN/GaN-$LiNbO_3$ optical-electronic-structures," 2004 IEEE LEOS Annual Meeting Conference Proceedings, Vol. 1, pp. 232-233, (2004).

Seoul Semiconductor, Exhibit 2001
LGI v. SSC, IPR2019-01154

29) * M. Losurdo, M. Giangregorio, G. Bruno, A. Brown, W. A. Doolittle, **G. Namkoong**, and T. Meyers, "Surface potential measurements of doping and defects of p-GaN," GaN and Related Alloys - 2003 Symposium (Mater. Res. Soc. Symposium Proceedings), Boston, MA, Dec. 1-5, 2003, Vol. 798, pp. 805-810, (2004).
30) * **G. Namkoong**, W. A. Doolittle, A. S. Brown, M. Losurdo, M. M. Giangregorio, and G. Bruno, "Effect of buffer design on AlGaN/AlN/GaN heterostructures by MBE," GaN and Related Alloys - 2003 Symposium (Mater. Res. Soc. Symposium Proceedings), Boston, MA, Dec. 1-5, 2003, Vol. 798, pp. 359-364, (2004).
31) * M. Losurdo, M. M. Giangregorio, G. Bruno, A. S. Brown, W. A. Doolittle, A. J. Ptak, T. H. Myers, "Surface potential measurements of doping and defects in p-GaN", GaN and Related Alloys - 2003 Symposium (Mater. Res. Soc. Symposium Proceedings Vol.798), p 805-10, (2004).
32) * S. M. Madison, **W. Henderson, G. Namkoong, K. K. Lee**, K. M. Patel, W. A. Doolittle, and S. E. Ralph, "Monolithic Integration of Electronic and Electro-Optical Devices Exploiting the AlGaN/GaN-LiNbO3 Material System," 2004 IEEE LEOS Annual Meeting Conference Proceedings (IEEE Cat. No.04CH37581), pt. 1, pp. 232-3, Vol. 1, (2004).
33) * C. Honsberg, O. Jani, W. A. Doolittle, **E. Trybus, G. Namkoong**, I. Ferguson, D. Nicole, and A. Payne, "InGaN– A New Solar Cell Material," Proceedings of the 19th European Photovoltaic Solar Energy Conference, Paris, 2004.
34) * O. Jani, C. Honsberg, A. Asghar, D. Nicol, I. Ferguson, W. A. Doolittle, and S. Kurtz, "Characterization and analysis of InGaN photovoltaic devices", Conference Record of the Thirty-First IEEE Photovoltaic Specialist Conference, (IEEE Cat. No. 05CH37608), 3-7 Jan. 2005, Lake Buena Vista, FL, pp. 37-42, (2005).
35) * **S. M. Madison**, **W. Henderson, G. Namkoong, K. K. Lee**, K. M. Patel, W. A. Doolittle, S. E. Ralph, S. E., "Monolithic integration of electronic and electro-optical devices exploiting the AlGaN/GaN-LiNbO3 material system," 2005 Conference on Lasers and Electro-Optics, Vol. 3, part 3, pp. 1605-1607, 2005.
36) * O. Jani, C. Honsberg, S. Y. Huang, I. Ferguson**, G. Namkoong, E. Trybus**, W. A. Doolittle, S. Kurtz, "Design, growth, fabrication and characterization of high-band gap InGaN/GaN solar cells", Conference Record of the 2006 IEEE 4th World Conference on Photovoltaic Energy Conversion (IEEE Cat. No. 06CH37747), p. 6, 2006.
37) * O. Jani, H. Yu**, E. Trybus**, B. Jampana, I. Ferguson, W. A. Doolittle, and C. Honsberg, " Effect of Phase Separation on Performance of III-V Nitride Solar Cells", Conference Proceedings of the 22nd European Photovoltaic Solar Energy Conference, Milan, Italy, September, 2007.
38) * **C.A.M. Fabien, B. P. Gunning, J. J. Merola, E. A. Clinton**, W. A. Doolittle, "Large-area III-nitride double-heterojunction solar cells with record-high in-content InGaN absorbing layers", 2015 IEEE 42nd Photovoltaic Specialist Conference (PVSC) Proceedings, p 1-3, 2015
39) * **J. C. Shank, M. B. Tellekamp**, W. A. Doolittle, "A scalable non-electroformed memdiode for neuromorphic circuitry", 2016 74th Annual Device Research Conference (DRC), p 1-2, 2016
40) * **E. Vadiee, E. A. Clinton**, H. McFavilen, A. M. Fischer, Yi Fang, J. J. Williams, C. B. Honsberg, W. A. Doolittle, S. M. Goodnick, "Progress towards double-junction

Seoul Semiconductor, Exhibit 2001
LGI v. SSC, IPR2019-01154

InGaN solar cell ", 2017 IEEE 44th Photovoltaic Specialist Conference (PVSC), p 0305-8, 2017 (appeared in print in 2018).

41) * **E. Vadiee, E.A. Clinton**, A.M. Fischer, H. McFavilen, C. Arena, C.B. Honsberg, S.M. Goodnick, and W.A. Doolittle, "DC and Small Signal AC Performance Analysis of InGaN/GaN Multi-Quantum-Well Solar Cells Operated at Elevated Temperatures", in 2018 IEEE 7th World Conf. Photovolt. Energy Convers (IEEE, 2018), pp. 3861–3864.

42) * **E. Vadiee, E.A. Clinton**, H. McFavilen, Z. Engel, C. Matthews, C. Arena, C.B. Honsberg, S.M. Goodnick, and W.A. Doolittle, "InGaN based solar cells with GaN tunnel junction contacts", in 2018 IEEE 7th World Conf. Photovolt. Energy Convers. (IEEE, 2018), pp. 0965–0968.

B3. OTHER REFEREED MATERIAL

No Data

B4. SUBMITTED JOURNAL ARTICLES (WITH DATE OF SUBMISSION)

No Data

B5. SUBMITTED CONFERENCE PAPERS (WITH DATE OF SUBMISSION)

No Data

C. OTHER PUBLICATIONS AND CREATIVE PRODUCTS

C1. NON-REFEREED CONFERENCE PRESENTATIONS WITH PROCEEDINGS

1) *P. Gunning and W. A. Doolittle, "Improving p-type nitrides", Compound Semiconductor Magazine, 11th May 2015

C2. PATENTS

C2A. US PATENTS

a. *US Patent #5,521,839 for a Deep Level Transient Spectroscopy System and Method, May 28, 1996.
b. *US Patent #7,173,286 for Semiconductor devices formed of III-nitride compounds, lithium-niobate-tantalate, and silicon carbide, February 6, 2007.
c. *US Patent Applied for, High Efficiency Solar Cell, application number 60/833-994 filed July 28, 2006
d. *US Patent #7,888,669 B2, "Nitride/Zinc Oxide Based Light-Emitting Diodes" , February 15, 2011
e. *U.S. Patent No. 8,261,690 B2 "In-Situ Flux Measurement Devices, Methods, And Systems" W. Alan Doolittle and Alexander G. Carver, September 11, 2012
f. *U.S. Patent No. 8,360,002 B2 "In-Situ Flux Measurement Devices, Methods, And Systems" W. Alan Doolittle and Alexander G Carver, January 29, 2013
g. *U.S. Patent No. 8,377,518 "In-Situ Flux Measurement Devices, Methods, And Systems", W. Alan Doolittle and Alexander G Carver, February 19, 2013

Seoul Semiconductor, Exhibit 2001
LGI v. SSC, IPR2019-01154

h. *International Patent Applied for, PCT/US10/40108, Metal Oxide Structures, Devices and Fabrication Methods
i. *U. S. Patent No. 9,142,413, “Methods for growing a non-phase separated group-III nitride semiconductor alloy”, M. Moseley and W. A. Doolittle, September 22, 2015

C2B. PROVISIONAL PATENTS

j. *Integrated Transistors and Circuitry with Lithium Niobate Optical Modulator. Filed with Dr. Stephen Ralph on Oct. 11, 2002. (GT Disclosure 2776) Provisional Patent Application #60/512,157.
k. *Lithium Niobate Based Optical Modulators and Waveguides on SiC and III-Nitrides. Filed with Dr. Stephen Ralph on Oct. 11, 2002. (GT Disclosure 2777) Provisional Patent Application #60/512,156.
l. *Low-Cost Nitride Power Electronics with Integrated Active Cooling. Filed with Samuel Graham (ME), Ari Glezer (ME), Ian Ferguson (ECE) on Jan. 12, 2005 (GT Disclosure 3358).
m. *Dynamically Tunable Terahertz Radiation Emission Through Standing Wave Acoustical Poling of Ferroelectric Thin Films. Filed with W. Hunt (ECE), and David Citrin (ECE) on Feb. 21, 2005. (GT Disclosure 3396).
n. *W. A. Doolittle, D. Pritchett, W. Henderson, "Maskless and Dynamic AlInGaN Compositional and Doping Patterning for Three Dimensional Epitaxy," U. S. Patent Pending, February 19, 2007 (GT Disclosure 4122). Refiled as GTRC ID No. 4122
o. *W. A. Doolittle, "Novel Epitaxial Metal Interconnects to the III-Nitride Material System for Advanced Photovoltaic Devices", US Patent Pending filed on (GT Disclosure 3890).
p. *W. A. Doolittle, “Lithium Metal Oxide Memristor and Related Constrictive Current Flow Device” , US Patent Pending filed on June 25, 2009, (GT Disclosure 4910), serial number 61/220,366
q. *W. A. Doolittle, “Photo-electrolytic Water Splitting for Hydrogen Generation” US Patent Pending filed on June 16, 2009 (GTRC ID No. 4900).
r. *W. A. Doolittle, “Integrated Solar Cell and Battery” US Patent Pending filed on June 16, 2009 (GTRC ID No. 4901)
s. *W. A. Doolittle and M. Moseley, “Non-Phase Separated InGaN for use in Light-Emitting Diodes, LASERs, and Solar Cells” (GTRC ID 5459).
t. *J. D. Greenlee, W. A. Doolittle, M. B. Tellekamp, J. C. Shank, B. P. Gunning, and C. A. M. Fabien. Method of $LiNbO_2$ synthesis. Georgia Tech Research Corporation, assignee. Provisional 61/946,998. US Patent Pending filed on 17 February 2014
u. “Systems and methods for growing a non-phase separated group-III nitride semiconductor alloy”, Michael William Moseley, William Alan Doolittle, Publication date, 2018/6/19, Patent office, US, Application number10000381
v. “System and Method for Increasing III-Nitride Semiconductor Growth Rate and Reducing Damaging Ion Flux”, William Alan Doolittle, Evan A Clinton, Chloe AM Fabien, Brendan Patrick Gunning, Joseph J Merola, Publication date 2018/5/17, Patent office US, Application number, 15738458

Seoul Semiconductor, Exhibit 2001
LGI v. SSC, IPR2019-01154

D. Presentations

D1. Keynote Addresses and Plenary Lectures

1) * **Invited Plenary:** W. A. Doolittle and A. S. Brown, "GaN Growth on Sapphire and Lithium Gallate," Seventeenth Conference on Crystal Growth, June 4-7, 2000, (AACG/WEST), Fallen Leaf Lake, CA.

D2. Invited Conference and Workshop Presentations

2) * **Invited**: W. A. Doolittle and A. S. Brown, "Growth of GaN on LGO for Compliant Substrates," TMS Workshop on Bonding and Compliant Substrates, Feb. 1998, San Juan, Puerto Rico.
3) * **Invited**: W. A. Doolittle, A. S. Brown, and A. Rohatgi, "Characterization of SiC and GaN for Minority Carrier Devices," TMS Workshop on Minority Carrier Wide Bandgap Devices, Feb. 1999, Panama City, FL.
4) * **Invited**: W. A. Doolittle and A. S. Brown, "High Quality Gallium Nitride on Lithium Gallate for High Frequency Power Devices," TMS Workshop on Minority Carrier Wide Bandgap Devices, Feb. 1999, Panama City, FL.
5) * **Invited**: W. A. Doolittle and A. S. Brown, "Compliant Substrate Processes," Materials Research Society Meeting, Epitaxial Growth-Principles and Applications Symposium, April 5-8, 1999, San Francisco, CA.
6) * **Invited**: A. S. Brown and W. A. Doolittle, "Compliant Substrates," International Conference on Compliant and Bonded Substrates, Sept. 1999, Orlando, FL.
7) * **Invited**: A. S. Brown and W. A. Doolittle, "Status and Promise of Compliant Substrate Technology," International Conference of Semiconductor Interface Science and Technology, June 1999, Gothenberg, Sweden.
8) *__Invited__: W. A. Doolittle, **G. Namkoong**, S.S. Stock, and A. S. Brown, "Workshop on Polarization Effects on Semiconductors," Aug. 27-31, 2000, Glacier National Park, Montana.
9) * **Invited**: W. A. Doolittle, A. S. Brown, **G. Namkoong**, S. Huang, and C. Wood, "How much can we get in and where can we put it?" Doping, Dopants, and Carrier Dynamics on Wide Gap Semiconductors Workshop, April 2-6, 2000, Copper Mountain Resort, Copper Mountain, CO.
10) * Invited: A. S. Brown and W. A. Doolittle, "Molecular Beam Epitaxial GaN," Frontiers in Science Meeting, April 4, 2000, La Jolla, CA.
11) * **Invited**: W. A. Doolittle, "The Role of Innovative Materials Research in the Wide Bandgap Electronics and Optoelectronics," University of Buffalo-The Institute for Lasers, Photonics, and Biophotonics Colloquium, Oct. 26, 2001.
12) * **Invited**: W. A. Doolittle, A. S. Brown, and S. Kang, "The Critical Role of Surface Finish and Crystallinity on the Performance of AlGaN/GaN 2DEGs and UV Metal Semiconductor Metal Photodetectors Grown on LiGaO2," Office of Naval Research Workshop on Near-surface effects in semiconductor substrates, Aug. 5-10, 2001, Kodiak Island, Alaska.
13) * **Invited**: W. A. Doolittle, "The Role of Innovative Materials Research in the Wide Bandgap Electronics and Optoelectronics," Ohio State University Electronic Nanostructures Seminar, May 28, 2002.

Seoul Semiconductor, Exhibit 2001
LGI v. SSC, IPR2019-01154

14) * **Invited**: W. A. Doolittle, "The Role of Innovative Materials Research in the Wide Bandgap Electronics and Optoelectronics," North Carolina State University, School of Materials Science and Engineering Colloquium, Aug. 30, 2002.
15) * **Invited**: W. A. Doolittle, "The Role of Innovative Materials Research in the Wide Bandgap Electronics and Optoelectronics," Auburn University, School of Physics Colloquium, Sept. 6, 2002.
16) * **Invited**: W. A. Doolittle and **A. G. Carver**, "Crystalline Oxides on Wide Bandgap Semiconductors: A Novel Platform for Multifunctional Materials Integration and Devices," Office of Naval Research Workshop on Multifunctional Materials, Oct. 27-31, Pucon, Chile (2002).
17) * **Invited**: W. A. Doolittle, **G. Namkoong, A. Carver**, S. Huang, S. Kang, **W. Henderson** and A. S. Brown, "Lithium –(Niobate, Gallate and Aluminate) Alternative Substrates for III-Nitride Epitaxy: New Technology and Devices," International Conference on Alternative Substrate Technologies, Sept. 15-19, 2002, Cancun, Mexico.
18) * **Invited**: W. A. Doolittle and **G. Namkoong**, "III-Nitride epitaxy on oxide substrates: new understanding and novel device alternatives," 50th anniversary meeting of the American Vacuum Society, Nov. 3, 2003, Baltimore, MD.
19) * **Invited:** W. A. Doolittle, **G. Namkoong, A. Carver, W. Henderson**, and A. S. Brown, "III-Nitride Alternative Substrates SiC, ZnO and ???: Filling in the ??? with Lithium Oxides: Lithium Gallate, Lithium Aluminate, Lithium Niobate and Lithium Tantalate as Substrates for III-Nitrides," Workshop on Compound Semiconductor Materials and Devices (WOCSEMMAD), 2002, Austin, Texas.
20) * **Invited: G. Namkoong**, W. A. Doolittle, **A. Carver, W. Henderson**, D. Jundt, and A. S. Brown, "III-Nitride Growth on a Ferro/Pyro/Piezoelectric/Nonlinear Optical Substrate for Advanced Functionality," Workshop on Compound Semiconductor Materials and Devices (WOCSEMMAD), 2003, Atlanta, GA.
21) * **Invited:** S. Huang, W. A. Doolittle, and A. S. Brown, "Asymmetric Strain in III-N Resulting from the Substrate with Direction-Dependent Thermal Expansion Coefficient," Workshop on Compound Semiconductor Materials and Devices (WOCSEMMAD), 2003, Atlanta, GA.
22) * **Invited**: W. A. Doolittle, **G. Namkoong, A. Carver, and W. Henderson**, "Crystalline Functional Oxides Integrated with Wide Bandgap Semiconductors via Epitaxy: A Novel Platform for Multifunctional Materials Integration and Devices," Advanced Research Workshop: Future Trends in Microelectronics-4: The Nano, the Giga, the Ultra, and the Bio, June 23-27, 2003, Corsica, France.
23) * **Invited**: W. A. Doolittle, "Electrostatic Boundary Conditions in Epitaxy: New strength for an old problem," ONR Workshop on Epitaxial Heterogeneous Interfaces – Formation and Stability, May 4-8, 2003, Yosemite, CA.
24) * **Invited**: W. A. Doolittle, "Process-induced changes in and elimination/creation of SiC surface and bulk defects for $LiNbO_3$ and III-V Nitride Epitaxy," Tri-Services/DARPA Workshop on Process Induced Defects in Wide Gap Semiconductors, Aug. 17-21, 2003, Grants Pass, OR.
25) * **Invited**: W. A. Doolittle, **E. Trybus, and G. Namkoong**, "Alternative Substrates For InN Epitaxy: Choices to Enable Novel Device Opportunities," International Indium Nitride Workshop, Nov. 16-20, 2003, Freemantle, Australia.

Seoul Semiconductor, Exhibit 2001
LGI v. SSC, IPR2019-01154

26) * **Invited**: W. A. Doolittle, "The Role of Innovative Materials Research in the Wide Bandgap Electronics and Optoelectronics," University of Alabama Birmingham, School of Physics Colloquium, Sept. 10, 2004.
27) * **Invited**: W. A. Doolittle, **A. G. Carver, and W. Henderson**, "MBE of Complex Metal-Oxides: Where have we come, where are we going and how are we going to get there?" North American MBE Conference, Oct. 11-14, 2004, Banff, Alberta, Canada.
28) * **Invited**: W. A. Doolittle, "Heteroepitaxy in the Lithium Oxide (niobate, tantalate, aluminate and gallate)/III-Nitride/SiC Wide Bandgap Family," ONR Workshop on Frontiers of Epitaxial Engineering, May 2-6, 2004, Sorrel River Ranch, Moab, Utah.
29) * **Invited**: W. A. Doolittle, "Lithium Niobate and Tantalate - a naturally multifunctional material," ONR Workshop on International Workshop on Multifunctional Materials II, Oct. 17-21, 2004, Huatulco, Mexico.
30) * **Invited**: W. A. Doolittle, "Lithium Niobate/Tantalate Epitaxial Integration With Wide Bandgap Semiconductors: Could This Be The Next "Great" Platform For Advanced Optoelectronic Devices?" WOFE-04 (Workshop on Future Electronics), Dec. 18-22, 2004, Aruba.
31) * **Invited:** W. A. Doolittle, **S. D. Burnham, G. Namkoong, and W. Henderson**, "Mg Doped GaN Using A Valved, Thermally Energetic Source: Enhanced Incorporation, Control and Quantitative Optimization," Workshop on Compound Semiconductor Materials and Devices (WOCSEMMAD), Jan. 2004, Pasadena, CA.
32) * **Invited**: W. A. Doolittle**, E. Trybus, W. Henderson, G. Namkoong, S. Burnham, K. K. Lee**, I. Ferguson, and C. Honsberg, "InN: A Material with Photovoltaic Promise and Challenges," AFOSR Indium Nitride Workshop 2, Jan. 9-13, 2005, Kailua-Kona, Hawaii.
33) * **Invited**: **W. Henderson, A. Carver**, W. A. Doolittle, and D. Citrin, "New Device Possibilities for Tunable THz Emitters and Detectors," Workshop on Compound Semiconductor Materials and Devices (WOCSEMMAD) , Miami, FL., Jan. 2005
34) * **Invited**: **A. G. Carver, W. Henderson**, and W. A. Doolittle, "Lithium Niobate and Related Oxides Using Chlorine Based Chemistries," Workshop on Compound Semiconductor Materials and Devices (WOCSEMMAD), Miami FL., Jan. 2005.
35) * **Invited**: S. M. Madison, **W. Henderson**, K. M. Patel, **G. Namkoong, K.-K. Lee**, S. E. Ralph, and W. A. Doolittle, "III-Nitride HEMTs on LiNbO3 for Integrated Electro-Optic Applications," Workshop on Compound Semiconductor Materials and Devices (WOCSEMMAD), Miami FL., Jan. 2005.
36) * **Invited**: **E. Trybus**, W. A. Doolittle, **W. Henderson, G. Namkoong, S. Burnham, K. Lee**, I. Ferguson, and C. Honsberg "InN: Revolutionary Photovoltaic Material or Just a Revolting Material," Workshop on Compound Semiconductor Materials and Devices (WOCSEMMAD), Miami FL., Jan. 2005.
37) * **Invited**: **S. D. Burnham, G. Namkoong**, and W. A. Doolittle, "New Physical Understanding of the Nature of Sublimed Mg and Mg Doped GaN," Workshop on Compound Semiconductor Materials and Devices (WOCSEMMAD), Miami FL., Jan. 2005.
38) * **Invited:** W. A. Doolittle, **A. Carver, W. Henderson, G. Namkoong**, S. Madison, K. Lee, and S. E. Ralph, "MBE of Complex Metal-Oxides: What is in the toolbox and how can we use these tools to construct devices?", University of Iowa's Workshop on Materials and Devices Incorporating Functional Interfaces, April 11-14, 2005, Palm Springs, CA.

Seoul Semiconductor, Exhibit 2001
LGI v. SSC, IPR2019-01154

39) * **Invited:** W. A. Doolittle, **A. Carver, W. Henderson, and W. L. Calley**, "In-situ Flux Measurement of Individual Effusion Cells for Stoichiometry Control of Multifunctional Oxides," West Virginia University Workshop on Multifunctional Material Stoichiometry, Jackson Hole, WY, July 17-21, (2005).
40) * **Invited:** W. A. Doolittle, **A. G. Carver, W. Henderson**, "Molecular Beam Epitaxy of complex metal-oxides: where have we come, where are we going, and how are we going to get there?," 22nd North American Conference on Molecular Beam Epitaxy (2004).
41) * **Invited: E. Trybus, G.Namkoong, W. Henderson**, W. A. Doolittle, "Interesting Anomaly in InGaN Growth by Molecular Beam Epitaxy," Workshop on Compound Semiconductor Materials and Devices (WOCSEMADD), Savannah, GA, February, 2007.
42) * **Invited: D. Pritchett, D. Billingsley, W. Henderson**, and W. A. Doolittle, "Influence of Ultraviolet Photoexcitation on the Growth of InGaN via NH3-based MOMBE", 2007 Workshop on Compound Semiconductor Materials and Devices, February 19, 2007.
43) * **Invited:** W. A. Doolittle, **M. Moseley, E. Trybus**, "Deeply degenerate p-type GaN grown by metal modulated epitaxy", 2009 International Semiconductor Device Research Symposium (ISDRS 2009), December (2009)
44) * **Invited:** Christiana Honsberg, **M. Moseley**, and W. A. Doolittle, "Progress and Future Prospects for InGaN Solar Cells", 6th International Workshop on Nitride Semiconductors, Tampa, Florida, USA, September 2010.
45) * **Invited: W. L. Calley, W. Henderson, A. Carver**, and W. A. Doolittle "New Complementary (n & p-type) Oxide Memristor Technology For Potential Neuromorphic Computing Applications", 2010 Workshop on Compound Semiconductor Materials and Devices, Newport Beach, CA, February 16, 2010.
46) * **Invited: W. Laws Calley, Jordan Greenlee**, and W. Alan Doolittle, "Halide Based MBE of Epitaxial Metals and Epitaxial Oxides", International Symposium on Compound Semiconductors, Berlin, May 22 to 27, (2011)
47) * **Invited:** W. Alan Doolittle , **Chloe A. Fabien, Michael Moseley, Brendan Gunning**, Alec M. Fisher, Yong Wei, Fernando A. Ponce, "New Advances in III-Nitride Optoelectronic Materials", Symposium on Compound Semiconductors, 2013 Materials Research Society Fall Meeting, December 1-6, 2013, Boston, Massachusetts
48) * **Invited: J. D. Greenlee, J. C. Shank, J. L. Compagnoni, B. Tellekamp**, and W. A. Doolittle. "New Ways to Make a Synthetic Brain: Material Synthesis Pathways Toward Neuromorphic Computing," Workshop on Compound Semiconductor Materials and Devices, New Orleans, LA 2013.
49) * **Invited:** W. A. Doolittle, **B. Gunning, C. Fabien**, A. Fischer, Y. Wei, and F. Ponce, "New advances in III-Nitride epitaxy", Workshop on Compound Semiconductor Materials and Devices, San Antonio, Texas, USA, Feb. 2014.
50) * **Invited: B. Gunning, C. Fabien, and W. A. Doolittle**, "Breaching the perceived upper bounds of p-type doping in GaN and InGaN", Workshop on Compound Semiconductor Materials and Devices, San Antonio, Texas, USA, Feb. 2014.
51) * **Invited:** W. A. Doolittle, **B. Gunning, C. Fabien**, A. Fischer, S. Wang, Y. Wei, and F. Ponce, "Extremely high hole concentrations in III-Nitrides", International Workshop on Nitride Semiconductors, Wrocław, Poland, August 2014

Seoul Semiconductor, Exhibit 2001
LGI v. SSC, IPR2019-01154

52) * **Invited:** W. A. Doolittle, "Brains For All: How to compute with new devices", Workshop on Compound Semiconductor Materials and Devices (WOCSEMMAD) 2015, Isle of Palms, South Carolina, February 2015
53) * **Invited: B. Gunning, C. Fabien, J. Merola, E. Clinton**, W. A. Doolittle, A. Fischer, S. Wang, Y. Wei, and F. Ponce, "Electronic and Optical Behavior of Highly p-type GaN and AlGaN, and High Growth Rate GaN by MBE", Workshop on Compound Semiconductor Materials and Devices, Isle of Palms, South Carolina, USA, February 2015.
54) * **Invited:** W. A. Doolittle, **J. Shank, M. B. Tellekamp, E. Clinton, J. Merola, B. Gunning, C. A. M. Fabien**, A. Fischer and F. Ponce, "An Overview of Materials Innovation Research at Georgia Tech Enabling Oxide Memristors, Neuromorphic Circuitry, and III-Nitride Devices", Workshop on Compound Semiconductor Materials and Devices (WOCSEMMAD), San Diego, February 3, 2016
55) * **Invited:** W. A. Doolittle, **E. Clinton, E. Vadiee**, "High Temperature III-Nitride Solar Cells", Workshop on Compound Semiconductor Materials and Devices (WOCSEMMAD) 2017, Clearwater FL Feb 20 2017
56) * **Invited:** W. A. Doolittle, **E. Clinton, E. Vadiee, B. Gunning, C. A. M. Fabien**, A. Fischer and F. Ponce, "The Beauty and New Utility of and Dirty Secrets Behind Plasma Assisted MBE of III-Nitrides", Workshop on Compound Semiconductor Materials and Devices (WOCSEMMAD) 2018, Feb 21, 2018
57) * **Invited:** W. A. Doolittle, **E. Clinton, E. Vadiee, Z. Engle, and C. Matthews**, "MBE of III-Nitrides in an Era Dominated by CVD: Opportunities and Challenges", International Conference on Molecular Beam Epitaxy, Shanghai China, Sept 3 2018
58) * **Invited: E. Clinton, Z. Engel, E. Vadiee**, W. A. Doolittle, "Synthesis and Performance of AlGaN Tunnel Diodes", Workshop on Compound Semiconductor Materials and Devices (WOCSEMMAD) 2019, Jacksonville Beach FL, February, 2019

D3. CONFERENCE AND WORKSHOP PRESENTATIONS

1) * W. A. Doolittle, S. Kang, T. Kropewnicki, K. Lee, S. Stock, P. Kohl, G. May, and A. S. Brown, "High Quality GaN on $LiGaO_2$," 40th Electronic Materials Conference, 1998, Charlottesville, VA.
2) * A. S. Brown and W. A. Doolittle, "Status of Compliant Substrates," Advanced Heterostructures Workshop 98, Dec. 1998, Hawaii.
3) * W. A. Doolittle and A. S. Brown, "Comparison of AlGaN and GaN Grown on Various Substrates: Benefits and Limitations of Growth on LGO at Low Substrate Temperature," First GaN Electronic Device Workshop, Aug. 1999, Cornell University, Ithaca, NY.
4) * S. Kang, W. A. Doolittle, S. R. Stock, A. S. Brown, Z. R. Dai, and Z. L. Wang, "Characterization of AlGaN/GaN Heterojunctions Grown by MBE," 42nd Electronic Materials Conference, 2000, Denver, CO.
5) * **G. Namkoong**, W. A. Doolittle, S.R. Stock, and A. S. Brown, "Growth, Characterization and Optimization of Magnesium Doped GaN," 42nd Electronic Materials Conference, 2000, Denver, CO.
6) * M. Losurdo, P. Capezzuto, G. Bruno, **G. Namkoong**, W. A. Doolittle, and A. S. Brown, "The Chemistry of Sapphire Nitridation in Relation to the GaN Structural Quality- Why Low Temperature 200°C Nitridation," The Fourth International Conference on III-Nitride Semiconductors, July 16-20, 2001, Denver, CO.

Seoul Semiconductor, Exhibit 2001
LGI v. SSC, IPR2019-01154

7) * W. A. Doolittle, A. S. Brown, S. Kang, S. W. Seo, S. Huang, and N. M. Jokerst, "Recent Advances in III-Nitride Devices Grown on Lithium Gallate," The Fourth International Conference on III-Nitride Semiconductors, July 16-20, 2001, Denver, CO.
8) * M. Losurdo, P. Capezzuto, G. Bruno, **G. Namkoong**, W. A. Doolittle, and A. S. Brown, "Plasma for the low-temperature growth of high-quality GaN films by MBE and remote plasma MOCVD," International Workshop on the Physics of Light-Matter Coupling in Nitrides (PLMCN-1), Sept. 2001, Rome, Italy.
9) * **G. Namkoong**, W. A. Doolittle, and A. S. Brown, "InN nanowires grown by Molecular Beam Epitaxy," The Second Georgia Tech Conference on Nanoscience and Nanotechnology, Sept. 2001, Georgia Tech, Atlanta, GA.
10) * A. S. Brown, N. M. Jokerst, W. A. Doolittle, M. Brooke, T. F. Kuech, S.W. Seo, S. Kang, S. Huang, and J.J. Shen, "Heterogeneous Integration: From Substrate Technology to Active Packaging," International Electron Device Meeting, Dec. 2001, Washington, DC.
11) **G. Namkoong**, W. A. Doolittle, A. S. Brown, M. Losurdo, P. Capezzuto, and G. Bruno, "The Role of Low Temperature (200 °C) Nitridation in the Growth of GaN by Plasma-Assisted Molecular Beam Epitaxy," 20th North American Conference on Molecular Beam Epitaxy, Oct. 2001, Providence, RI.
12) * W. A. Doolittle, **A. Carver, G. Namkoong**, and A. S. Brown, "Challenges and Potential Payoff for Crystalline Oxides in Wide Bandgap Semiconductor Technology," International Workshop on Oxide Electronics, Oct. 20-23, 2002, St. Petersburg, FL.
13) * W. A. Doolittle, **G. Namkoong, A. Carver, W. Henderson**, and A. S. Brown, "III-Nitride Growth on Lithium Niobate: A new substrate material for Polarity Engineering in III-Nitride Heteroepitaxy," Materials Research Society Fall Meeting, Dec. 2-6 2002, Boston, MA.
14) * **G. Namkoong**, W. A. Doolittle, A. S. Brown, M. Losurdo, M. M. Giangregorio, and G. Bruno, "Characteristics of GaN Epitaxial Layers Grown on GaN and AlN Buffers by RF Molecular Beam Epitaxy," 44th Electronic Materials Conference, June 2002, Santa Barbara, CA.
15) * M. Losurdo, M. M. Giangregorio, P. Capezzuto, and G. Bruno, **G. Namkoong**, W. A. Doolittle, and A. S. Brown, "Determination of GaN polarity by interaction with H2 remote plasmas," 44th Electronic Materials Conference, June 2002, Santa Barbara, CA.
16) * **G. Namkoong**, W. A. Doolittle, **A. Carver, W. Henderson**, D. Jundt, and A. S. Brown, "III-Nitride Growth on Lithium Niobate: Polarity Control by Electrostatic Boundary Condition," 45th Electronic Materials Conference, June 2003, Salt Lake, UT.
17) * M. Losurdo, G. Bruno, A. S. Brown, S. Kang, T. Kim, and W. A. Doolittle, "The Chemistry and Kinetics of $LiGaO_2$ Substrate Nitridation for the Optimization of GaN Epitaxial Growth," 45th Electronic Materials Conference, June 2003, Salt Lake, UT.
18) * S. Huang, S. Kang, W. A. Doolittle, A. S. Brown, "Asymmetric Strain in III-N Resulting from the Substrate with Direction-Dependent Thermal Expansion Coefficients," 45th Electronic Materials Conference, June 2003, Salt Lake, UT.
19) * M.C. Cheung, **G. Namkoong**, F. Chen, M. Furis, H. E. Pudavar, A. N. Cartwright, and W. A. Doolittle, "Photoluminescence Study of MBE Grown InGaN with

Seoul Semiconductor, Exhibit 2001
LGI v. SSC, IPR2019-01154

Intentional Indium Segregation," International Workshop on Nitride Semiconductors, Pittsburgh, PA, July 19-23 2004.

20) * **S. Burnham, G. Namkoong**, and W. A. Doolittle, "Mg Doped GaN using a thermally energetic source: Enhanced incorporation, control and quantitative optimization," Materials Research Society Fall Meeting, Dec. 1-5, 2003, Y8.11, Boston, MA.
21) * **A. Carver, W. Henderson**, and W. A. Doolittle, "Novel chlorine based chemistry for growth of ferroelectric materials by molecular beam epitaxy," Materials Research Society Fall Meeting, Boston, MA, C3.28, Dec. 1-5 (2003).
22) * **K.-K. Lee, G. Namkoong**, S. M. Madison, **W. Henderson**, S. E. Ralph, and W. A. Doolittle, "Prospects for, problems with and practical implementation strategies for heteroepitaxy integrated electronics-optoelectronics utilizing the III-nitride /lithium niobate material system," IEEE Lester Eastman Conference on High-Performance Devices, Troy, NY, Aug. 4-6, 2004.
23) * **K.-K. Lee, G. Namkoong, W. Henderson**, and W. A. Doolittle, "III-Nitrides on Ferroelectric Lithium Niobate: Impact of the Electrostatic Boundary Condition," American Physical Society (APS) Meeting, Los Angeles, CA, March 2005.
24) * **D. C. Pritchett, S. Burnham, W. Henderson**, and W. A. Doolittle, "Metalorganic Molecular Beam Epitaxy (MOMBE) of GaN: Towards an Understanding of Surface Reaction Chemistry" 47th Electronic Materials Conference, June 22-24, 2005, Santa Barbara, CA.
25) * S. M. Madison, **W. Henderson, G. Namkoong, K.-K. Lee**, K. M. Patel, W. A. Doolittle, and S. E. Ralph, "Monolithic Integration of Electronic and Electro-Optical Devices Exploiting the AlGaN/GaN-$LiNbO_3$ Material System," Presented at CLEO/QELS Annual Meeting, May 2005.
26) * **G. Namkoong, K.-K. Lee**, S. M. Madison, S. E. Ralph, W. A. Doolittle, M. Losurdo, G. Bruno, and D. Jundit, "Crystalline stability of congruent and Li-rich lithium niobate for III-nitride optoelectronic-acoustic-electronic applications," presented at 23rd North American Conference on Molecular Beam Epitaxy, Santa Barbara, CA, Sept. 11th-14th, 2005.
27) * **D. Pritchett, W. Henderson, S. D. Burnham**, W. A. Doolittle, "Influence of Intense Ultraviolet Photoexcitation on Surface Reactions during Gallium Nitride Growth via Metal Organic Molecular Beam Epitaxy," 33rd Physics and Chemistry of Semiconductor Interfaces Conference, January 17, 2006.
28) * **E. Trybus, G. Namkoong, W. Henderson, A. Carver**, W. A. Doolittle, and H. J. Lee, "High-Energy Electron Beam Interactions with Indium Nitride During Growth via MBE," 33rd Conference on the Physics and Chemistry of Semiconductor Interfaces, Cocoa Beach, FL, February, 2006.
29) * **K.-K. Lee, G. Namkoong**, W. A. Doolittle, M. Losurdo, and G. Bruno, "III-nitride growth and characteristics on ferroelectric materials using plasma-assisted MBE, presented at 33rd Conference on the Physics and Chemistry of Semiconductor Interfaces, Cocoa Beach, FL, 2006.
30) * **D. Billingsley, D. Pritchett, W. Henderson, E. Trybus, K.K. Lee**, and W. A. Doolittle, "Influence of Surface Nitridation on Gallium Nitride Grown via Ammonia based Metal Organic Molecular Beam Epitaxy," 2006 North American Molecular Beam Epitaxy Conference, October 9, 2006.
31) * **D. Billingsley, D. Pritchett, W. Henderson, E. Trybus, K. K. Lee**, W. A. Doolittle, "Influence of Surface Nitridation on Gallium Nitride Grown via Ammonia based

Seoul Semiconductor, Exhibit 2001
LGI v. SSC, IPR2019-01154

Metal Organic Molecular Beam Epitaxy, " 24th North American Conference on Molecular Beam Epitaxy, Durham, NC, October, 2006.

32) * **S. D. Burnham, G. Namkoong, K.-K. Lee**, and W. A. Doolittle, "Reproducible RHEED signatures for in situ growth regime characterization of AlN," presented at 24th North American Conference on Molecular Beam Epitaxy, Durham, NC, 2006.
33) * **E. Trybus**, O. Jani, **S. Burnham**, J. Bai, D. Citrin, I. Ferguson, C. Honsberg, M. Steiner, and W. A. Doolittle, "Characteristics of InGaN Designed for Photovoltaic Applications", 7th International Conference of Nitride Semiconductors, Las Vegas, NV, September, 2007.
34) * **D. Pritchett, W. Henderson, D. Billingsley**, W. A. Doolittle, "InGaN Compositional Control by Ultraviolet Photoexcitation during NH3-based MOMBE - A Pathway to 3D Epitaxy", 7th International Conference of Nitride Semiconductors, September 18, 2007.
35) * **D. Billingsley, D. Pritchett, S. D. Burnham, W. Henderson**, W. A. Doolittle, "Investigation into the Use of Molecular Hydrogen on the Growth of Gallium Nitride via Metal-Organic Molecular Beam Epitaxy", 7th International Conference of Nitride Semiconductors, September 18, 2007.
36) * **K.-K. Lee, G. Namkoong**, W. A. Doolittle, M. Losurdo, G. Bruno, and H. K. Choi, "Interface Property Study of III-Nitrides on Lithium-Niobate to Improve the Device Performance of Optoelectronic-Acoustic-Electronic Applications", 7th International Conference of Nitride Semiconductor, Las Vegas, NV, 2007.
37) * **E. Trybus, S. Burnham, G. Namkoong**, D. C. Look, **D. Billingsley, M. Moseley, W. Henderson,** and W. A. Doolittle, "Systematic Study of High Hole Concentration, Low Temperature Grown GaN Approaching the Compensated Region," 50th Electronic Materials Conference, Santa Barbara, CA, June 2008.
38) * **E. Trybus**, W. A. Doolittle, **M. Moseley, W. Henderson, D. Billingsley, G. Namkoong**, and D. C. Look, "Extremely High Hole Concentrations in c-Plane GaN," 7th International Workshop on Nitride Semiconductors, Montreux Switzerland, October 6-10, 2008.
39) * **D. Billingsley, W. Henderson**, and W. A. Doolittle, "Study of Growth Kinetics and Characterization of AlxGa1-xN Grown by Ammonia-Based Metal-Organic Molecular Beam Epitaxy", 51st Electronic Materials Conference, June 24-26, 2009.
40) * **E. Trybus, W. Henderson, M. Moseley, G. Namkoong**, D. Look, J. Freitas, and W. A. Doolittle, "Analysis of Degenerate p-type GaN by Metal-Modulated Epitaxy", 51st Electronic Materials Conference, University Park, PA, June 2009.
41) * **E. Trybus, W. Henderson, M.l Moseley, G. Namkoong**, David Look, Jaime Freitas, and W. Alan Doolittle, "Analysis of Degenerate p-type GaN by Metal-Modulated Epitaxy," 51st Electronic Materials Conference, University Park, PA, June 2009.
42) * **M. Moseley, E. Trybus, D. Billingsley, W. Henderson, G. Namkoong**, D. Look, and W. A. Doolittle, "Deeply Degenerate p-GaN Grown by Metal-Modulated Epitaxy", 26th North American Molecular Beam Epitaxy Conference, Princeton, VA, August 2009. – Won Best student Presentation Award
43) * W. Alan Doolittle, **M. Moseley, E. Trybus, D. Billingsley, W. Henderson**, David Look, M. E. Zvanut, and J. Dashdorj, "Deeply Degenerate p-GaN Grown by Metal-Modulated Epitaxy," 8th International Conference on Nitride Semiconductors, Jeju, Korea, October 2009.

Seoul Semiconductor, Exhibit 2001
LGI v. SSC, IPR2019-01154

44) * J. A. Freitas Jr., D. Look, P. Klein, **M. Moseley, E. Trybus, W. Henderson**, and W. A. Doolittle, "Compensation and Activation Mechanism in Metal Modulated Epitaxy p-GaN," 8th International Conference on Nitride Semiconductors, Jeju, Korea, October 2009.
45) * J. A. Freitas Jr., D. Look, P. Klein, **M. Moseley, E. Trybus, W. Henderson**, and W. A. Doolittle, "Compensation and Activation Mechanism in Metal Modulated Epitaxy p-GaN," 8th International Conference on Nitride Semiconductors, Jeju, Korea, October 2009.
46) * W. A. Doolittle, **M. Moseley, E. Trybus, D. Billingsley, W. Henderson**, David Look, M. E. Zvanut, and J. Dashdorj, "Deeply Degenerate p-GaN Grown by Metal-Modulated Epitaxy," 8th International Conference on Nitride Semiconductors, Jeju, Korea, October 2009.
47) * W. A. Doolittle, **W. L. Calley, W. Henderson**, "Complementary oxide memristor technology facilitating both inhibitory and excitatory synapses for potential neuromorphic computing applications", 2009 International Semiconductor Device Research Symposium (ISDRS 2009), University of Maryland, December 2009.
48) * W. A. Doolittle, **M. Moseley, and E. Trybus**, "Deeply-degenerate p-type GaN grown by metal modulated epitaxy," International Semiconductor Device Research Symposium 2009, College Park, Maryland, USA, December 2009.
49) *** J. Lowder, M. Moseley, E. Trybus, D. Billingsley, W. Henderson, G. Namkoong**, D. Look, and W. A. Doolittle, "Deeply Degenerate p-GaN with Hole Concentrations Exceeding 7×10^{19} cm^{-3} Grown by Metal-Modulated Epitaxy", 6th International Workshop on Nitride Semiconductors, Tampa, Florida USA, September 19-24, 2010
50) *** M. Moseley, J. Lowder, D. Billingsley, G. Namkoong** and W. A. Doolittle, "Control of Adlayer Kinetics for the Growth of High Quality InGaN Throughout the Miscibility Gap", 6th International Workshop on Nitride Semiconductors, Tampa, Florida USA, September 19-24, 2010
51) * M. E. Zvanut, J. Dashdorj, **M. Moseley**, and W. A. Doolittle, "The Local Environment of the Mg Impurity in High Hole Density p-type GaN:Mg", 6th International Workshop on Nitride Semiconductors, Tampa, Florida, USA, September 2010.
52) *** M. Moseley, J. Lowder, D. Billingsley, G. Namkoong** and W. A. Doolittle, "Control of Adlayer Kinetics for the Growth of High Quality InGaN Throughout the Miscibility Gap", 27th North American Molecular Beam Epitaxy Conference, Breckenridge Colorado, Sept. 26-29th 2010 - Won Best student Presentation Award
53) *** W. L. Calley**, P. Staib, **J. Lowder, W. Henderson**, and W. A. Doolittle, "An Auger Electron Analyzer System for In Situ MBE Stoichiometry Control", 27th North American Molecular Beam Epitaxy Conference, Breckenridge Colorado, Sept. 26-29th 2010
54) *** W. L. Calley, J. Greenlee, W. Henderson**, W. A. Doolittle, "Advances in Metal-Halide MBE Thin Film Growth", 27th North American Molecular Beam Epitaxy Conference, Breckenridge Colorado, Sept. 26-29th 2010
55) *** J. Greenlee, W. L. Calley**, and W. A. Doolittle, "MBE Growth of Metal Oxides for Complementary Memristive Applications", 27th North American Molecular Beam Epitaxy Conference, Breckenridge Colorado, Sept. 26-29th 2010 – Won Best Student Abstract Award

Seoul Semiconductor, Exhibit 2001
LGI v. SSC, IPR2019-01154

56) * W. A. Doolittle, "InGaN Solar – Role for MBE in Photovoltaics?", 27th North American Molecular Beam Epitaxy Conference, Breckenridge Colorado, Sept. 26-29th 2010
57) * C. Honsberg, **M. Moseley**, and W. A. Doolittle, "Progress and Future Prospects for InGaN Solar Cells," 6th International Workshop on Nitride Semiconductors, Tampa, Florida, USA, September 2010.
58) * **W. L. Calley**, P. Staib**, J. D. Greenlee, W. Henderson**, and W. A. Doolittle. "An Auger Electron Analyzer System for In-situ MBE Stoichiometry Control," 27th North American Molecular Beam Epitaxy Conference, Breckenridge, CO 2010.
59) * **M. Moseley, J. Lowder, B. Gunning, E. Trybus, D. Billingsley, W. Henderson, G. Namkoong**, W. A. Doolittle, "Deeply Degenerate p-type Doping in III-Nitrides: Critical Milestones Achieved for High Power Electronics," Poster presented at Air Force Office of Scientific Research Joint Electronics Program Review, Arlington, VA, USA, May 2011.
60) * **M. Moseley, J. Lowder, B. Gunning, D. Billingsley, G. Namkoong**, W. A. Doolittle, "Observation and Elimination of Indium Surface Segregation," Presented at Electronic Materials Conference 2011, Santa Barbara, CA, USA, June 2011.
61) * **B. Gunning, M. Moseley, J. Lowder**, W. A. Doolittle, J. Wierer, S. Lee, D. Koleske, and Q. Li, "InGaN/GaN p-i-n solar cells grown by metal-modulated epitaxy," Poster presented at 9th International Conference on Nitride Semiconductors, Glasgow, Scotland, UK, July 2011.
62) * **M. Moseley, B. Gunning, J. Lowder**, W. A. Doolittle, "Elimination of Indium Surface Segregation in InGaN Grown Throughout the Miscibility Gap," Presented at 9th International Conference on Nitride Semiconductors, Glasgow, Scotland, UK, July 2011.
63) * **J. Lowder, M. Moseley, B. Gunning**, W. A. Doolittle, M. E. Zvanut, J. Dashdorj, "Characterization of Mg Acceptors in GaN:Mg grown by Metal Modulated Epitaxy and MOCVD," Presented at 9th International Conference on Nitride Semiconductors, Glasgow, Scotland, UK, July 2011.
64) * **B. Gunning, M. Moseley, J. Lowder**, W. A. Doolittle, J. Wierer, S. Lee, D. Koleske, and Q. Li, "Metal-modulated epitaxy growth of InGaN/GaN p-i-n solar cells," Presented at American Vacuum Society 58th International Symposium & Exhibition, Nashville, TN, USA, October 2011.
65) * **M. Moseley, J. Lowder, B. Gunning**, M. E. Zvanut, J. Dashdorj, W. A. Doolittle, "Characterization of Mg Acceptors in GaN:Mg Grown by Metal Modulated Epitaxy and MOCVD," Presented at American Vacuum Society 58th International Symposium and Exhibition, Nashville, TN, USA, October 2011.
66) * **M. Moseley, B. Gunning, J. Lowder, G. Namkoong**, W. A. Doolittle, "Elimination of Indium Surface Segregation in InGaN Grown Throughout the Miscibility Gap," Presented at American Vacuum Society 58th International Symposium and Exhibition, Nashville, TN, USA, October 2011.
67) * **W. Laws Calley**, P. G. Staib, Jonathan Lowder, **Jordan Greenlee, Michael Moseley, Walter Henderson**, W. Alan Doolittle, "An Auger Electron Analyzer System for In Situ MBE Growth Monitoring" American Vacuum Society 58th International Symposium and Exhibition, Nashville, Tennessee, USA, October 2011.
68) * F. Zaman, M. Rubio-Roy, **M. Moseley, J. Lowder**, W. A. Doolittle, C. Berger, R. Dong, J. Meindl, W. de Heer, "Selective Epitaxial Graphene Growth on SiC via AlN Capping," APS March Meeting 2011, Dallas, Texas, USA, March 2011.

Seoul Semiconductor, Exhibit 2001
LGI v. SSC, IPR2019-01154

69) * M. E. Zvanut, Y. Uprety, J. Dashdorj, **M. Moseley**, W. A. Doolittle, "Hydrogen incorporation in high hole density GaN:Mg," APS March Meeting 2011, Dallas, Texas, USA, March 2011.
70) * **J. D. Greenlee, W. L. Calley**, C. F. Petersburg, C. Jaye, D. A. Fischer, F. M. Alamgir, and W. A. Doolittle. "Advances in the Growth of Metal Oxides for Neuromorphic Computing Applications," AVS 58th International Symposium and Exhibition, Nashville, TN 2011.
71) * **W. L. Calley, J. D. Greenlee, W. Henderson**, W. A. Doolittle. "Halide Based MBE of Epitaxial Metals and Epitaxial Oxides," 38th International Symposium on Compound Semiconductors, Berlin, Germany 2011.
72) * **W. L. Calley**, P. Staib, **W. Henderson, J. Greenlee**, and W. A. Doolittle. "An In situ Auger Electron Analyzer System for Harsh Environment MBE," 29th North American Molecular Beam Epitaxy Conference, Atlanta, GA 2012.
73) * **J.C. Shank, J.D. Greenlee, J.L. Compagnoni**, and W.A. Doolittle. "Neuromorphic Computing Applications of $LiNbO_2$ Grown by Molecular Beam Epitaxy," 29th North American Molecular Beam Epitaxy Conference, Atlanta, GA 2012.
74) * **J. L. Compagnoni, W. Laws Calley, J.D. Greenlee, J.C. Shank**, and W.A. Doolittle. "Molecular Beam Epitaxy of Complex Transition-Metal Oxides by a Versatile Metal-Chloride Growth Chemistry," 29th North American Molecular Beam Epitaxy Conference, Atlanta, GA 2012.
75) * **C. A. M. Fabien, M. Moseley, B. Gunning**, W. A. Doolittle, A. M. Fisher, Y. Wei, F. A. Ponce, "Characterization of MBE-Grown, Low Threading-Dislocation Density, High-Indium InGaN without Phase Separation," 29th North American Molecular Beam Epitaxy Conference, Stone Mountain Park, GA, USA, Oct. 2012.
76) * **J. D. Greenlee, W. L. Calley, J. L. Compagnoni, J. C. Shank**, and W. A. Doolittle. "MBE-Grown Analog Memristor Characterization by Electrochemical Impedance Spectroscopy," 29th North American Molecular Beam Epitaxy Conference, Atlanta, GA 2012.
77) * **B. Gunning, M. Moseley**, and W. A. Doolittle, "Impurity Band Conduction in Highly p-type GaN and InGaN", 29th North American Molecular Beam Epitaxy Conference, Atlanta, Georgia, USA, October 2012.
78) * **J. D. Greenlee, J. C. Shank, J. L. Compagnoni, B. Tellekamp**, E. Zhang, J. Bi, M. L. Alles, R. D. Schrimpf, and W. A. Doolittle. "Radiation Effects on Lithium Metal Oxide Analog Memristors for Neuromorphic Computing," GOMACTech 13, Las Vegas, NV 2013.
79) * **J. D. Greenlee, J. C. Shank, M. B. Tellekamp**, E. Zhang, J. Bi, D. M. Fleetwood, M. L. Alles, R. D. Schrimpf, and W. A. Doolittle, "Radiation Effects on LiNbO2 Memristors for Neuromorphic Computing Applications," NSREC 2013, San Francisco, CA 2013.
80) * **C. A. M. Fabien, B. Gunning, M. Moseley**, W. A. Doolittle, A. M. Fischer, Y. Wei and F. A. Ponce, "Advances in Nitride Growth Technology for InGaN-Based Solar Cells," 10th International Conference on Nitride Semiconductors, Washington, D.C., USA, Aug. 2013.
81) * **B. Gunning, J. Lowder, M. Moseley, C. Fabien, G. Namkoong**, W. A. Doolittle, "Optimization of Growth and Electrical Transport Properties of Highly p-type GaN and InGaN", 10th International Conference on Nitride Semiconductors, Washington, D.C., USA, Aug. 2013.

Seoul Semiconductor, Exhibit 2001
LGI v. SSC, IPR2019-01154

82) * F. A. Ponce, A. M. Fischer, Y. Wei, **M. Moseley, B. Gunning** and W. A. Doolittle, "High-Indium-Content InGaN Layers with Uniform Composition, Full Misfit-Strain Relaxation, and High Light-Emission Efficiency," 10th International Conference on Nitride Semiconductors, Washington, D.C., USA, Aug. 2013.
83) * W. A. Doolittle, **B. Gunning, C. A. M. Fabien, M. Moseley**, "Growth methodologies for overcoming the perceived limitations of phase separation and p-type doping in InGaN," 17th International Conference on Crystal Growth and Epitaxy, Warsaw, Poland, Aug. 2013.
84) ***** **C. A. M. Fabien, M. Moseley, B. Gunning**, W. A. Doolittle, "Simulations, Practical Limitations, and Novel Growth Technologies for InGaN-based Solar Cells," 39th IEEE Photovoltaic Specialists Conference, Tampa, FL, USA, June 2013.
85) * W. A. Doolittle, **B. Gunning, C. A. M. Fabien, M. Moseley**, "Growth Methodologies for Overcoming the Challenges of Phase Separation and p-type Doping in InGaN," Collaborative Conference on Crystal Growth, Cancun, Mexico, June 2013.
86) * W. Alan Doolittle , **Chloe A. Fabien, Michael Moseley, Brendan Gunning**, Alec M. Fisher, Yong Wei, Fernando A. Ponce, "MBE Growth Methodologies for Overcoming the Perceived Limitations of Phase Separation and p-type Doping in InGaN," 30th North American Molecular Beam Epitaxy Conference, Banff, CA, Oct. 2013.
87) ***** **J. C. Shank, J. D. Greenlee, M. B. Tellekamp**, W. A. Doolittle, "Building a Brain without Transistors", WOCSEMMAD 2014, San Antonio, TX Feb. 2014.
88) ***** **C. Fabien, B. Gunning, M. Moseley**, W. A. Doolittle, A. Fischer, Y. Wei, and F. Ponce, "Prospects of InGaN-Based Solar Cells by Metal-Modulated Epitaxy", 5th International Symposium on Growth of III-Nitrides, Atlanta, Georgia, USA, May 2014.
89) ***** **B. Gunning, C. Fabien, J. Merola, E. Clinton**, and W. A. Doolittle, "Highly Conductive P-Type GaN and AlGaN Using Both Bulk and 2-Dimensional Heavily Mg-Doped Layers", 5th International Symposium on Growth of III-Nitrides, Atlanta, Georgia, USA, May 2014.
90) ***** **C. Fabien, B. Gunning, M. Moseley**, W. A. Doolittle, A. Fischer, Y. Wei, and F. Ponce, "Comparison of N-rich and MME-grown InGaN Throughout the Miscibility Gap", 18th International Conference on Molecular Beam Epitaxy, Flagstaff, Arizona, USA, September 2014.
91) ***** **B. Gunning, C. Fabien, J. Merola, E. Clinton**, W. A. Doolittle, A. Fischer, S. Wang, Y. Wei, and F. Ponce, "Highly Conductive P-type III-Nitrides Using Both Bulk and 2-Dimensional Heavily Mg-doped Layers", 18th International Conference on Molecular Beam Epitaxy, Flagstaff, Arizona, USA, September 2014.
92) ***** **M. B. Tellekamp, J. D. Greenlee, J. C. Shank**, W. Alan Doolittle, "New Equipment for Oxide Epitaxy: A Solid State Oxygen Source and Stable Two Zone Effusion Cell," ICMBE 2014, Flagstaff, AZ 2014.
93) ***** **M. B. Tellekamp, J. D. Greenlee, J. C. Shank**, W. A. Doolittle, "MBE Oxide Growth Rate Limitations Quantified by in situ Auger Electron Spectroscopy," ICMBE 2014, Flagstaff, AZ 2014.
94) ***** **B. Gunning, C. Fabien, J. Merola, E. Clinton**, and W. A. Doolittle, "III-Nitride Optoelectronic Devices Using Highly Mg-doped p-type Layers Grown by Metal-Modulated Epitaxy", 18th International Conference on Molecular Beam Epitaxy, Flagstaff, Arizona, USA, September 2014.

Seoul Semiconductor, Exhibit 2001
LGI v. SSC, IPR2019-01154

95) * **J. C. Shank, M. B. Tellekamp, J. D. Greenlee**, W. A. Doolittle, "Evidence of Optically-Induced Band Structure Modifications in Lithium Niobite", EMC 2014, Santa Barbara, CA 2014.

96) * **J. C. Shank, M. B. Tellekamp**, W. A. Doolittle, "New Pathways to Multi-functionality: Ionic Intercalation into Metal Oxides", International Workshop on Oxide Electronics 2014, Bolton Landing, New York 2014.

97) * T. Smyth, H. Xia, Y. Feng, M. Dvorak, M. Tayebjee, S. Shrestha, S. Bremner, S. Huang, G.J. Conibeer, S. Yagi, **C. A. M. Fabien, B. Gunning**, W.A. Doolittle, C. Tessarek, M. Latzel, T.W. Schmidt, and M. Sugiyama, "Hot Carrier Relaxation and Phonon Dispersion in III-V Alloys," 29th European Photovoltaic Solar Energy Conference and Exhibition, Amsterdam, the Netherlands, Sept. 2014.

98) * **C. M. Matthews, E. Clinton**, W. A. Doolittle, "Conduction in GaN-Si Heterojunctions", Jacksonville Beach FL, February, 2019

99) ***B. Zivasatienraj**, **A. S. Weidenbach**, and W. A. Doolittle, "Understanding Intercalation Enabling Device Structures Resulting in Non-Volatile Behavior of Lithium Niobite Memristors", The 60th Electronic Materials Conference 2018 (EMC 2018), Santa Barbara, CA, June 27-29, 2018

100) ***J. C. Shank**, **M. B. Tellekamp**, M. J. Wahila, S. Howard, **A. S. Weidenbach**, **B. Zivasatienraj**, L. F. J. Piper, and W. A. Doolittle, "Correlation of Oxygen Vacancies to Niobium Pentoxide Memdiode Electrical Responses", The 60th Electronic Materials Conference 2018 (EMC 2018), Santa Barbara, CA, June 27-29, 2018

101) ***B. Zivasatienraj**, **A. S. Weidenbach**, **A. Ghosh**, **T. McCrone**, and W. A. Doolittle, "Scalability of Non-Volatile Lithium Niobite Memristors: Potential for millivolt Operation of Neuromorphic Devices", The 61st Electronic Materials Conference 2019 (EMC 2019), Ann Arbor, MI, June 26-28, 2019

102) ***A. Ghosh**, **B. Zivasatienraj**, **A. Weidenbach**, **T. McCrone**, W. A. Doolittle; "Impact of Alloying Contact Metal on Non-Volatile performance of Lithium Niobite Memristors for Neuromorphic Computing", The 61st Electronics Materials Conference (EMC 2019), Ann Arbor Michigan, June 26-28, 2019.

103) * **Z. Engel, E. Clinton, C. Matthews**, W. Alan Doolittle, "Demonstration of High Quality Aluminum Indium Nitride with High Indium Content Grown via Metal Modulated Epitaxy", The 61st Electronics Materials Conference (EMC 2019), Ann Arbor Michigan, June 26-28, 2019.

104) * **Z. Engel, E. Clinton, C. Matthews**, W. Alan Doolittle, "Demonstration of High-Quality Aluminum Indium Nitride Grown Via Metal Modulated Epitaxy and Application Towards Polar/Non-Polar Optical Devices", The International Conference on Nitride Semiconductors 2019, Bellevue Washington, July 7-13 2019

105) * **Z. Engel, E. Clinton, C. Matthews**, W. Alan Doolittle, "Advancements in High Indium Content AlInN Grown Via Metal Modulated Epitaxy and Application Towards Polar/Non-Polar Optical Devices", The North American Molecular Beam Epitaxy Conference (NAMBE) 2019, Ketchum Idaho, September 22-25, 2019

106) * **H. Ahmad , E. A Clinton , C. M. Matthews , Z. Engel**, W. A. Doolittle, "Dramatic Improvement in the Surface Quality of High Temperature Annealed c-plane (0001) Sapphire Substrates and its Impact on the Quality of AlN Films from 1 nm to 2 µm,"

Seoul Semiconductor, Exhibit 2001
LGI v. SSC, IPR2019-01154

The International Conference on Nitride Semiconductors 2019, Bellevue Washington, July 7-13 2019

107) Yee Rui Koh, J. T. Gaskins, J. L. Braun, **H. Ahmad**, J. Tomko, W. A. Doolittle, and Patrick E. Hopkins, "Size effects of the AlN on the Thermal Transport across Metal/semiconductor Interface," The International Conference on Nitride Semiconductors 2019, Bellevue Washington, July 7-13 2019

108) * **C. M. Matthews, E. Clinton, Z. Engel, H. Ahmad, K. Motoki**, W. Alan Doolittle, "Rectification in Vertically Conducting Power GaN-on-Si Heterojunctions", The 61st Electronics Materials Conference (EMC 2019), Ann Arbor Michigan, June 26-28, 2019.

109) * **T. McCrone, A. Ghosh, B. Zivasatienraj, A. Weidenbach**, W. A. Doolittle "High Quality Lithium Niobite grown by Liquid Phase Electroepitaxy for use as a Memristor." The 61st Electronics Materials Conference (EMC 2019), Ann Arbor Michigan, June 26-28, 2019.

110) * **C. M. Matthews, E. Clinton, Z. Engel, H. Ahmad, K. Motoki**, "Electrical Characterization of Vertically Conducting GaN-on-Si Heterojunctions", The International Conference on Nitride Semiconductors 2019, Bellevue Washington, July 7-13 2019

Seoul Semiconductor, Exhibit 2001
LGI v. SSC, IPR2019-01154

E. Grants and Contracts

E1. As Principal Investigator

Doolittle share of Total Funding=$16,778,057 of $37,523,401 Total Awarded

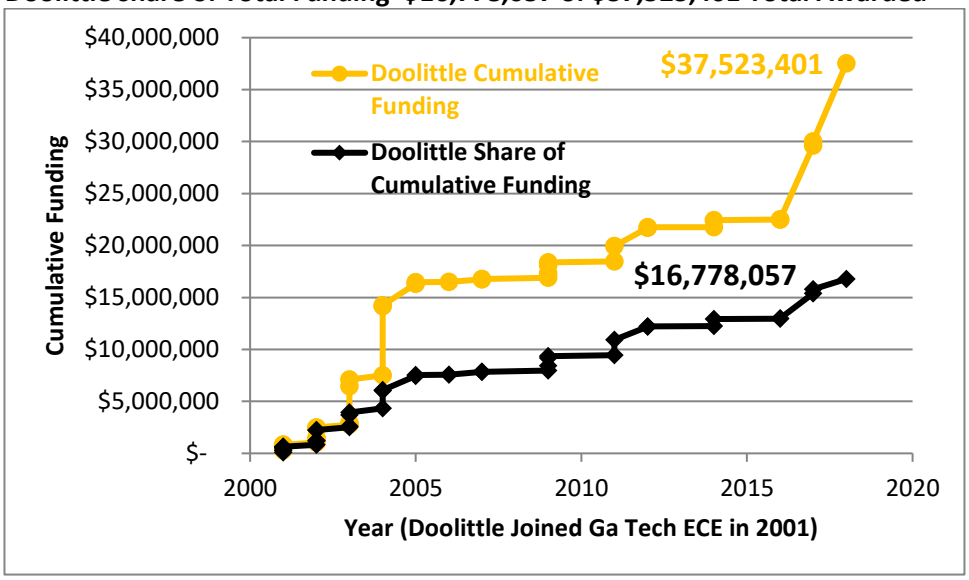

1. Title: ADVANCES IN THE EXPLOITATION OF GAN HETEROSTRUCTURES ON LITHIUM GALLATE
   Sponsor: NAVY
   Role: PI
   Collaborators: DOOLITTLE, WILLIAM ALAN;BRENNAN, KEVIN
   Period of the Contract: 01/01/1998 - 09/30/2003
   Doolittle Share: 30% = $91,000 of $300,000 total awarded
2. Title: DEVELOPMENT OF A RAPID THERMAL MOLECULAR BEAM EPITAXY SYSTEM
   Sponsor: NAVY
   Role: PI
   Collaborators: None
   Period of the Contract: 03/02/1998 - 12/12/1999
   Doolittle Share: 100% = $174,298 of $174,298 total awarded
3. Title: FERMI-ENERGY CONTROL DURING SEMICONDUCTOR GROWTH FOR ENHANCED DOPANT ACTIVATION I
   Sponsor: NAVY
   Role: PI
   Collaborators: None
   Period of the Contract: 03/15/1999 - 09/30/2003
   Doolittle Share: 100% = $150,000 of $150,000 total awarded
4. Title: FERMI-ENERGY CONTROL DURING SEMICONDUCTOR GROWTH FOR ENHANCED DOPANT ACTIVATION II
   Sponsor: NAVY
   Role: PI
   Collaborators: None
   Period of the Contract: 03/15/1999 - 09/30/2003

Seoul Semiconductor, Exhibit 2001
LGI v. SSC, IPR2019-01154

Doolittle Share: 100% = $300,000 of $300,000 total awarded

5. Title: ACQUISITION OF EQUIPMENT TO FACILITATE ENERGY MODIFIED SEMICONDUCTOR EPITAXY
   Sponsor: NAVY
   Role: PI
   Collaborators: None
   Period of the Contract: 04/01/2001 - 03/31/2002
   Doolittle Share: 100% = $172,740 of $172,740 total awarded
6. Title: DEVELOPMENT OF AN AUTOMATICALLY TUNABLE RF IMPEDANCE MATCHING SYSTEM
   Sponsor: APPLIED EPI INC
   Role: PI
   Collaborators: None
   Period of the Contract: 05/01/2001 - 03/31/2004
   Doolittle Share: 100% = $11,290 of $11,290 total awarded
7. Title: DEVELOPMENT OF A TRULY LATTICE-MATCHED III-NITRIDE TECHNOLOGY FOR "NEAR-DISLOCATION FREE" OPTOELECTRONIC AND HIGH FREQUENCY ELECTRONIC APPLICATIONS
   Sponsor: CERMET INC
   Role: PI
   Collaborators: None
   Period of the Contract: 09/05/2001 - 03/04/2002
   Doolittle Share: 100% = $30,000 of $30,000 total awarded
8. Title: MBE GROWTH OF SINGLE CRYSTAL LITHIUM OXIDES FOR ELECTRONIC AND OPTOELECTRONIC APPLICATIONS I
   Sponsor: NAVY
   Role: PI
   Collaborators: None
   Period of the Contract: 02/15/2002 - 09/30/2005
   Doolittle Share: 100% = $193,907 of $193,907 total awarded
9. Title: FERRO-ELECTRICALLY SWITCHED HIGH POWER ELECRONICS
   Sponsor: NAVY/DARPA
   Role: PI
   Collaborators: None
   Period of the Contract: 05/15/2002 - 05/14/2004
   Doolittle Share: 100% = $371,236 of $371,236 total awarded
10. Title: OPTICAL MATERIALS
    Sponsor: GEORGIA TECH BROADBAND INSTITUTE
    Role: PI
    Collaborators: Ralph, Steven
    Period of the Contract: 8/6/02 - 8/5/04
    Doolittle Share: 50% = $40,000 of $80,000 total awarded
11. Title: MBE GROWTH OF SINGLE CRYSTAL LITHIUM OXIDES FOR ELECTRONIC AND OPTOELECTRONIC APPLICATIONS II
    Sponsor: NAVY
    Role: PI
    Collaborators: None
    Period of the Contract: 10/01/2002 - 12/31/2008

Seoul Semiconductor, Exhibit 2001
LGI v. SSC, IPR2019-01154

Doolittle Share: 100% = $960,000 of $960,000 total awarded

12. Title: DEVELOPMENT OF A LATTICE-MATCHED AIINN OFR UV EMITTERS
    Sponsor: CERMET INC
    Role: PI
    Collaborators: None
    Period of the Contract: 10/11/2002 - 04/11/2003
    Doolittle Share: 100% = $30,600 of $30,600 total awarded
13. Title: DURIP - ACQUISITION OF EQUIPMENT TO FACILITATE NEXT GENERATION INTEGRATED OPTICS: MATERIALS DEVELOPMENT AND PERFORMANCE CHARACTERIZATION EQUIPMENT
    Sponsor: NAVY
    Role: PI
    Collaborators: RALPH, STEPHEN
    Period of the Contract: 05/01/2003 - 07/31/2004
    Doolittle Share: 73% = $95,000 of $130,000 total awarded
14. Title: MURI: LABORATORY INSTRUMENTATION DESIGN RESEARCH FOR SCALEABLE NEXT GENERATION EPITAXY: NON-EQUILIBRIUM WIDE APPLICATION EPITAXIAL PATTERNING BY INTELLIGENT CONTROL
    Sponsor: AIR FORCE
    Role: PI
    Collaborators: FRAZIER, ALBERT + other universities.
    Period of the Contract: 05/15/2003 - 02/14/2009
    Doolittle Share: 30% = $1,065,068 of $3,558,100 total awarded
15. Title: CAREER: NEW DEVICE OPPORTUNITIES ENABLED BY POLAR DIELECTRIC AND SEMICONDUCTOR HETEROEPITAXY
    Sponsor: NATIONAL SCIENCE FOUNDATION
    Role: PI
    Collaborators: None
    Period of the Contract: 04/01/2004 - 03/31/2009
    Doolittle Share: 100% = $398,344 of $398,344 total awarded
16. Title: MURI: EPITAXIAL MULTIFUNCTIONAL MATERIALS AND APPLIATIONS: REVOLUNTIONARY EPITAXIAL SOLUTIONS CREATING A PLATFORM FOR A NEW GENERATION OF MILITARY APPLICATIONS
    Sponsor: NAVY
    Role: PI
    Collaborators: Hunt, Bill; Citrin, David + other universities
    Period of the Contract: 05/01/2004 - 02/28/2010
    Doolittle Share: 25% = $1,696,160 of $6,657,550 total awarded
17. Title: NOVEL HIGH EFFICIENCY PHOTOVOLTAIC DEVICES BASED ON THE III-N MATERIAL SYSTEM
    Sponsor: UNIVERSITY OF DELAWARE
    Role: PI
    Collaborators: DOOLITTLE, WILLIAM ALAN
    Period of the Contract: 06/08/2004 - 01/08/2005
    Doolittle Share: 100% = $73,322 of $73,322 total awarded
18. Title: VERY-HIGH EFFICIENCY SOLAR CELL (VHESC)
    Sponsor: UNIVERSITY OF DELAWARE
    Role: PI

Seoul Semiconductor, Exhibit 2001
LGI v. SSC, IPR2019-01154

Collaborators: FERGUSON, IAN;CITRIN, DAVID
Period of the Contract: 10/01/2005 - 06/30/2007
Doolittle Share: 65% = $1,347,413 of $2,067,413 total awarded

19. Title: HIGH EFFICIENCY III NITRIDE SOLAR CELLS
    Sponsor: UNIVERSITY OF DELAWARE
    Role: PI
    Collaborators: FERGUSON, IAN
    Period of the Contract: 12/07/2005 - 12/06/2007
    Doolittle Share: 55% = $79,854 of $146,048 total awarded
20. Title: X-RAY DETECTION FOR RAPID DEVELOPMENT OF MOLECULAR BEAM EPITAXY OF LITHIUM.
    Sponsor: NAVY
    Role: PI
    Collaborators: None
    Period of the Contract: 05/26/2006 - 08/25/2007
    Doolittle Share: 100% = $29,300 of $29,300 total awarded
21. Title: WHITE LIGHT EMITTER USING A SELF-LUMINESCENT, LATTICE MATCHED SUBSTRATE
    Sponsor: NATIONAL SCIENCE FOUNDATION
    Role: PI
    Collaborators: None
    Period of the Contract: 05/01/2007 - 04/30/2011
    Doolittle Share: 100% = $270,000 of $270,000 total awarded
22. Title: BME EQUIPMENT REPAIR AT GEORGIA TECH
    Sponsor: NAVY
    Role: PI
    Collaborators: None
    Period of the Contract: 07/17/2007 - 09/30/2008
    Doolittle Share: 100% = $10,760 of $10,760 total awarded
23. Title: DURIP: ULTRA HIGH VACUUM SCANNING PROBE SYSTEM FOR INVESTIGATION OF NOVEL EPITAXIAL MATERIALS
    Sponsor: ARMY
    Role: PI
    Collaborators: None
    Period of the Contract: 05/01/2009 - 10/30/2010
    Doolittle Share: 100% = $125,900 of $125,900 total awarded
24. Title: LITHIUM-SEMICONDUCTOR BASED MIXED IONIC-ELECTRONICS FOR COMPLEMENTARY TWO TERMINAL NEUROMORPHIC BRAIN SIMULANT
    Sponsor: NAVY
    Role: PI
    Collaborators: None
    Period of the Contract: 10/01/2009 - 09/30/2013
    Doolittle Share: 100% = $449,765 of $449,765 total awarded
25. Title: SYSTEMATIC STUDY OF P-TYPE DOPING AND RELATED DEFECTS IN III-NITRIDES: PATHWAY TOWARD A NITRIDE HBT
    Sponsor: AIR FORCE
    Role: PI
    Collaborators: None

Seoul Semiconductor, Exhibit 2001
LGI v. SSC, IPR2019-01154

Period of the Contract: 10/01/2009 - 09/30/2012
Doolittle Share: 100% = $747,446 of $747,446 total awarded

26. Title: METAL ORGANIC MOLECULAR BEAM EPITAXY CONVERSION FOR FREQUENCY AGILE WAVEGUIDE
    Sponsor: NAVY
    Role: PI
    Collaborators: None
    Period of the Contract: 07/01/2011 - 11/30/2011
    Doolittle Share: 100% = $90,000 of $90,000 total awarded
27. Title: QESST: ERC FOR QUANTUM ENERGY AND SUSTAINABLE SOLAR TECHNOLOGIES
    Sponsor: ARIZONA STATE UNIVERSITY/ NSF/DOE
    Role: PI
    Collaborators: None
    Period of the Contract: 08/15/2011 - 10/31/2016
    Doolittle Share: 100% = $916,249 of $916,249 total awarded
28. Title: RADIATION TOLERANCE OF NEW SELF-HEALING CRYSTALLINE MEMRISTORS FOR NEUROMORPHIC APPLICATIONS
    Sponsor: US DEPT OF DEFENSE
    Role: PI
    Collaborators: University of Vanderbilt
    Period of the Contract: 07/09/2012 - 07/08/2017
    Doolittle Share: 71% = $1,245,721 of $1,745,721 total awarded
29. Title: III-NITRIDE QD SOLAR CELLS
    Sponsor: ADDVENTURE SUPPORT ENTERPRISES INC (ASE INC)
    Role: PI
    Collaborators: None
    Period of the Contract: 12/12/2012 - 12/31/2014
    Doolittle Share: 100% = $50,000 of $50,000 total awarded
30. Title: WORKSHOP ON COMPOUND SEMICONDUCTOR MATERIALS & DEVICES (WOCSEMMAD) 2014
    Sponsor: NATIONAL SCIENCE FOUNDATION
    Role: PI
    Collaborators: None
    Period of the Contract: 02/15/2014 - 07/31/2014
    Doolittle Share: 100% = $15,300 of $15,300 total awarded
31. Title: HIGH TEMPERATURE INGAN THERMIONIC TOPPING CELLS
    Sponsor: ARIZONA STATE UNIVERSITY / ARPA-E
    Role: PI
    Collaborators: None
    Period of the Contract: 06/04/2014 - 06/03/2017
    Doolittle Share: 100% = $677,100 of $677,100 total awarded
32. Title: STIR: BIOLOGICALLY REALISTIC IONIC RETINA (BiRIR)
    Sponsor: ARMY
    Role: PI
    Collaborators: None
    Period of the Contract: 05/01/2016 - 01/31/2017
    Doolittle Share: 100% = $50,000 of $50,000 total awarded

Seoul Semiconductor, Exhibit 2001
LGI v. SSC, IPR2019-01154

33. Title: I-CORPS TEAMS: NOVEL ENGINEERED SUBSTRATE TECHNOLOGY FOR LOW-DEFECT, HIGH QUALITY III-NITRIDE OPTOELECTRONICS
    Sponsor: NATIONAL SCIENCE FOUNDATION
    Role: PI
    Collaborators: None
    Period of the Contract: 06/15/2016 - 07/31/2016
    Doolittle Share: 100% = $9,562 of $9,562 total awarded
34. Title: CROSS-DISCIPLINARY ELECTRONIC-IONIC RESEARCH ENABLING BIOLOGICALLY REALISTIC AUTONOMOUS LEARNING (CEREBRAL)
    Sponsor: Department of Defense
    Role: PI
    Collaborators: Doolittle, William Alan; Graham, Samual; Vogel, Eric; Raychowdhury, Arijit; Piper, Louis; and Lee, Wei-Cheng
    Period of the Contract: 11/1/2017 – 10/31/2022
    Doolittle Share: 34% = $2,401,722 of $7,124,304 Total Award
35. Title: TOWARDS UNDERSTANDING ALINGAN/SILICON INTERFACE KINETICS
    Sponsor: National Science Foundation
    Role: PI
    Collaborators: None
    Period of the Contract: 8/1/2017 – 7/30/2020
    Doolittle Share: 100% = $400,000

E2. AS CO-PRINCIPAL INVESTIGATOR

36. Title: LATTICE MATCHED , HIGH EFFICIENCY SOLID STATE EMITTERS ON ZnO SUBSTRATES
    Sponsor: CERMET INC / DEPARTMENT OF ENERGY
    Role: Co-PI
    Collaborators: FERGUSON, IAN
    Period of the Contract: 09/01/2003 - 08/30/2006
    Doolittle Share: 38% = $250,000 of $650,000 total awarded
37. Title: MULTIFERROIC MATERIALS FOR MICROWAVE PARAMETRIC POWER AMPLIFIERS
    Sponsor: AIR FORCE
    Role: Co-PI
    Collaborators: Steven Kenney, William Alan Doolittle, Ioannis Papapolymerou
    Period of the Contract: 09/30/2009 - 05/15/2011
    Doolittle Share: 67% = $200,000 of $298,146 total awarded
38. Title: MURI-Leveraging a New Theoretical Paradigm to Enhance Interfacial Thermal Transport in Wide Bandgap Power Electronics
    Sponsor: Office of Naval Research
    Role: Co-PI
    Collaborators: Samuel Graham (PI), W. Alan Doolittle
    Period of Contract: 8/01/18- 7/30/23
    Doolittle Share: 14% = $1,050,00 of $7,500,000 Total Awarded

E3. AS SENIOR PERSONNEL OR CONTRIBUTOR

No Data

Seoul Semiconductor, Exhibit 2001
LGI v. SSC, IPR2019-01154

E4. PENDING PROPOSALS

Total Pending Funding=$750,755

1) Pending Proposal: Title: High Temperature Reactive Parallel Sputtering System for Intelligent and Multi-functional Systems, AFOSR, Proposed Award Amount : $360,685, Total Award Period Covered : 6/2/20- 3/14/21 , PI Salary: 0 month per year
2) Pending Proposal: Title: Time-Resolved Spectroscopy of Hot-Carrier Dynamics, AFOSR, Proposed Award Amount : $390,070, Total Award Period Covered : 6/15/19-3/14/20 , PI Salary: 0 month per year

E5. PROPOSALS SUBMITTED BUT NOT FUNDED (LAST TWO YEARS):

Total Declined Funding in the Last 3 Years: $ 5,587,268

1. Title: III-NITRIDE P-TYPE CONTACTS, TUNNEL JUNCTION PERFORMANCE AND STABILITY FOR
   Sponsor: NATIONAL SCIENCE FOUNDATION
   Role: PI
   Collaborators: None
   Proposal Due Date: 11/01/2016
   Proposal Amount: $450,000
2. Title: HIGH THERMAL CONDUCTIVITY SEMICONDUTOR ALLOYS
   Sponsor: NATIONAL SCIENCE FOUNDATION
   Role: Co-PI
   Collaborators: GRAHAM, SAMUEL;DOOLITTLE, WILLIAM ALAN
   Proposal Due Date: 01/19/2016
   Proposal Amount: $1,337,654
3. Title: EAGER: TDM SOLAR CELLS: A PROCESS INTEGRATED APPROACH TO TANDEM SOLAR CELLS
   Sponsor: NATIONAL SCIENCE FOUNDATION
   Role: PI
   Collaborators: None
   Proposal Due Date: 09/30/2016
   Proposal Amount: $300,000
4. Title: III-Nitride p-type Contacts, Tunnel Junction Performance and Stability for Improved Efficiency in Deep and Near UV Light Emitters
   Sponsor: NATIONAL SCIENCE FOUNDATION
   Role: PI
   Collaborators: None
   Proposal Due Date: 11/01/2017
   Proposal Amount: $450,000
5. Title: VLF Generation Using Electret Materials for High Charge Density and Lifetime
   Sponsor: DARPA
   Role: PI
   Collaborators: Morris Cohen (Co-PI), Samuel Graham (Co-PI)

Seoul Semiconductor, Exhibit 2001
LGI v. SSC, IPR2019-01154

Proposal Due Date: 11/01/2017
Proposal Amount: $2,588,929

6. Title: High Temperature Reactive Parallel Sputtering System for Intelligent and Multi-functional Systems
   Sponsor: AFOSR
   Role: PI
   Collaborators: None
   Proposal Due Date: 7/1/2018
   Proposal Amount: $360,685
7. Title: MRSEC Seed Funding: Development of New Crystalline Ionic-Electronic Heterostructure Materials for a New Computational Element – Memristors
   Sponsor: NATIONAL SCIENCE FOUNDATION
   Role: PI
   Collaborators: None
   Proposal Due Date: 11/01/2017
   Proposal Amount: $100,000

.

Seoul Semiconductor, Exhibit 2001
LGI v. SSC, IPR2019-01154

F. Other Scholarly and Creative Accomplishments

F1 Startup Companies

In 2015/16 Dr. Doolittle started two companies that are not related to any Ga Tech Research but for completeness are listed herein:

1) Innovative Advanced Materials Inc. is commercializing Epitaxy Tools and Semiconductor Components for research scale applications.
2) Innovative Advanced Technologies Inc. is commercializing Epitaxy Tools and Semiconductor Components for production scale applications.

F2 Inventions Disclosures Filed (all filed with Georgia Tech Research Corp.)

Int Ref #	Title	Date Submitted
1249	Pseudo-logarithmic Transient Capacitance/Conductance	3/13/1992
2497	Automatically Tunable RF Impedance Matching System for the Applied EPI Unibulb Plasma Source	5/21/2001
2582	Increased Acceptor Doping in Aluminum-Gallium-Indium Nitride Alloys by Be Doping	11/26/2001
2583	Doping of III-Nitride Substrate Materials to Facilitate Broad Wavelength Range Luminescence	11/26/2001
2584	Increased Acceptor Doping by Pre-cracking and Exciting Dopants	11/26/2001
2585	Novel Approach to Design and Fabrication of Power Field Effect Transistors Using Metal-Oxide Ferroelectric Materials to Enhance their Performance	11/26/2001
2586	Novel Approach to Growth of Lithium Metal Oxides Using Metal Chloride Salts	11/26/2001
2587	Deposition of Lithium Salts on Wide Bandgap Semiconductors Including but not limited to Alloys of Aluminum Nitride, Gallium Nitride, Indium Nitride and Polytypes of Silicon Carbide 4H and 6H	11/26/2001
2624	Silicon Carbide and III-Nitride Substrate Technology Based on Lithium Niobate and Lithium Tantalate	2/13/2002
2776	Integrated Transistors and Circuitry with Lithium Niobate Optical Modulator	10/14/2002
2777	Lithium Niobate Based Optical Modulators and Waveguides on SiC and III-Nitrides	10/14/2002
3133	III-Nitride Phase Modulators	3/16/2004
3358	Low-Cost Nitride Power Electronics with Integrated Active Cooling	1/7/2005
3396	Tunable Terahertz Emitters Through Standing Wave Acoustical Poling of Ferroelectric Thin Films	2/22/2005
3556	In-Situ Molecular Flux Measurement Device and Method	7/18/2005
3797	Phosphor-Free White LED using Self-Fluorescent Substrates	3/29/2006
3890	Novel Epitaxial Metal Interconnects to the III-Nitride Material System for Advanced Photovoltaic Devices	6/5/2006

Seoul Semiconductor, Exhibit 2001
LGI v. SSC, IPR2019-01154

4122	3D Epitaxy	2/19/2007
4811	High Efficiency Solar Cell	4/3/2009
4900	Photo-Electrolytic Water Splitting for Hydrogen Generation	6/9/2009
4901	Integrated Solar Cell & Battery	6/9/2009
4910	Metal Oxide Structures, Devices, and Fabrication Methods	6/25/2009
5459	Non-Phase Separated InGaN for use in Light-Emitting Diodes, Lasers, and Solar Cells	11/8/2010
6083	Improved Ohmic Contact to p-type InAlGaN Devices	5/31/2012
6617	Method of LiNbO2 synthesis	2/17/2014
7009	Method of Increasing III-Nitride Semiconductor Growth Rate and Reduced Damaging Ion Flux Content	5/29/2015
7200	A Scalable Memdiode - Rectification and Hysteresis in Metal - Nb2O5 - Metal Diodes Without Electroforming	2/2/2016

G. Societal and Policy Impacts

The work published on high p-type doping of III-Nitride semiconductors was so revolutionary, initially it was not widely accepted. After years of effort and others now having duplicated the results, the industry is just now realizing new devices utilizing these features including tunnel junctions useful for improved energy efficiency, both consumed and produced. It is anticipated that new solar cells, power diodes and transistors will be forthcoming.

The work published on neuromorphic computational devices has a much further horizon of impact. As such, future low power computational alternatives are expected but have only just begun to be realized. I anticipate that a seminal paper on low voltage memristive computation will be submitted in 2019/2020. We currently have data showing operation as low as 150 mV (not a lower limit).

H. Other Professional Activities

Dr. Doolittle has consulted with numerous law, government and industrial organizations including, Orrick, Herrington & Sutcliffe, Baker Botts, Latham & Watkins, Allwood and Associates, Ryan Owens and Associates LLC, The USA securities and exchange commission, and Brilliant Light Inc.

Seoul Semiconductor, Exhibit 2001
LGI v. SSC, IPR2019-01154

V. TEACHING

A. COURSES TAUGHT

List course taught at Georgia Tech. (Most recent first and include the last six years. Do not include CIOS scores here.)

Undergraduate Courses:

Term/Year	Course Number/Name	Mean Score		
		# of Students	# of Responses	Teaching Effectiveness
Fall/2001*	**ECE 3040 / Microelectronic Circuits/ 3 sections**	**51**	**29**	**4.65**
Spr./2002	**ECE 3040 / Microelectronic Circuits**	**57**	**23**	**4.40**
Sum./2002	**ECE 3040 / Microelectronic Circuits**	**25**	**5**	**5.00**
Spr./2003	**ECE 3040 / Microelectronic Circuits**	**39**	**14**	**4.80**
Fall/2003**	**ECE 4000 / Proj. Eng. & Prof. Practice/2 sections**	**35**	**14**	**4.45**
Spr./2004	**ECE 3040 / Microelectronic Circuits**	**29**	**14**	**4.90**
Spr./2004	**ECE 3040 / Microelectronic Circuits**	**30**	**12**	**4.50**
Fall/2004	**ECE 3080 / Semiconductor Devices**	**16**	**7**	**4.60**
Spr./2006**	**ECE 3040 / Microelectronic Circuits**	**78**	**31**	**4.04**
Spr./2007**	**ECE 3040 / Microelectronic Circuits**	**61**	**26**	**4.80**
Spring/2008	**ECE3080 / Semiconductor Devices**	**18**	**0**	**n/a**
Spring/2008	**ECE 3040 / Microelectronic Circuits**	**30**	**11**	**4.80**
Fall/2009**	**ECE 3040 / Microelectronic Circuits**	**45**	**20**	**4.50**
Spring 2010	**ECE 4833/ Renewable Energy Devices**	**12**	**5**	**4.90**
Spring /2011	**ECE 3040 / Microelectronic Circuits**	**36**	**9**	**4.90**
Spring /2012	**ECE 3080 / Semiconductor Devices**	**20**	**12**	**4.60**
Spring /2012	**ECE 3040 / Microelectronic Circuits**	**42**	**14**	**4.00**
Spring /2013	**ECE 3040 / Microelectronic Circuits**	**51**	**16**	**4.77**
Spring /2013	**ECE 4833 / Materials and Device Characterization**	**7**	**3**	**4.75**
Spring /2014	**ECE 3040 / Microelectronic Circuits**	**56**	**20**	**4.79**
Spring /2015	**ECE 4803 A/ Renewable Energy Devices**	**10**	**7**	**4.80**
Fall /2015	**ECE 3040 / Microelectronic Circuits**	**41**	**16**	**4.70**
Fall /2015	**ECE 4803 B/ Renewable Energy Devices**	**26**	**5**	**4.00**
Spring /2015	**ECE 3450 A / Semiconductor Devices**	**8**	**4**	**4.80**
Spring /2015	**ECE 4803 A/ Renewable Energy Devices**	**27**	**15**	**4.70**
Spring /2017	**ECE 3040 / Microelectronic Circuits**	**34**	**11**	**4.95**
Spring /2017	**ECE 4803 B/ Renewable Energy Devices**	**15**	**1**	**5.00**
Spring /2018	**ECE 3040 / Microelectronic Circuits**	**38**	**18**	**4.80**
Spring /2019	**ECE 3040 / Microelectronic Circuits**	**32**	**12**	**4.80**
Spring /2019	**ECE 4823 A/ Renewable Energy Devices**	**21**	**10**	**4.90**
Totals (Students/Responses) and Averages (Means)		**990**	**384**	**4.68**

Seoul Semiconductor, Exhibit 2001
LGI v. SSC, IPR2019-01154

Graduate Courses:

Term/Year	Course Number/Name	Mean Score # of Students	# of Responses	Teaching Effectiveness
Fall/2002	**ECE6450A / Introduction to Microelectronic Device Fabrication**	**47**	**21**	**4.80**
Fall/2004	**ECE6450A / Introduction to Microelectronic Device Fabrication**	**43**	**26**	**4.50**
Fall/2005	**ECE6451A / Microelectronic Theory**	**13**	**5**	**4.90**
Fall/2008	**ECE6450A / Introduction to Microelectronic Device Fabrication**	**36**	**19**	**4.60**
Fall/2017	**ECE6450A / Introduction to Microelectronic Device Fabrication**	**39**	**17**	**4.90**
Totals (Students/Responses) and Averages (Medians)		**35.60**	**17.60**	**4.74**

Seoul Semiconductor, Exhibit 2001
LGI v. SSC, IPR2019-01154

B. INDIVIDUAL STUDENT GUIDANCE

B1. PH.D. STUDENTS

B.1.A. GRADUATED PH.D. STUDENTS

1) Gon Namkoong (co-advised with April S. Brown), Ph.D.
   Began advising Spring 2001
   Graduation date: Summer 2003
   Ph.D Thesis Title: Molecular Beam Epitaxy Grown III-Nitride Materials for High-Power and High-Temperature Applications: Impact of Nucleation Kinetics on Material and Device Structure Quality
   Currently Employed at: Old Dominion University – Professor
2) Shawn Burnham, Ph.D.
   Began advising Fall 2001
   Graduation date: Summer 2007
   Ph.D Thesis Title: Improved Understanding and Control of Magnesium-Doped Gallium Nitride By Plasma Assisted Molecular Beam Epitaxy
   Currently Employed at: HRL Laboratories, Malibu, CA
3) Alexander Carver, Ph.D.
   Began advising Fall 2001
   Graduation date: Spring 2009
   Project Title: Single Crystal Ferroelectric Oxides for Power Electronic and Optoelectronic Applications
   Currently Employed at: Jet Propulsion Laboratory, Pasadena, CA
4) Elaissa Trybus, Ph.D.
   Began advising: Summer 2003
   Graduation date: Spring 2009
   Project Title: InN Low Bandgap Semiconductors for Photovoltaic Applications
   Currently Employed at: Johns Hopkins University, Assistant Professor
5) David C. Pritchett, Ph.D.
   Began advising: Fall 2003
   Graduation date: Spring 2009
   Project Title: Epitaxial Patterning by Intelligent Real Time Control
   Currently Employed at: Northrop Grumman Inc., Los Angeles, CA
6) Kyoung-Keon Lee, Ph.D.
   Began advising Spring 2004
   Graduation date: Spring 2009
   Project Title: Integrated Optoelectronics using III-Nitride Epitaxy on LiNbO3 – Epitaxy and Device Fabrication
   Currently Employed at: Texas State University
7) Daniel Billingsley
   Began advising Fall 2005
   Graduation date: Spring 2010
   Project Title: Photo-assisted Epitaxy for In-Situ Epitaxial Patterning
   Currently Employed at: Sensor Electronic Technology, Columbia, SC
8) Michael Moseley
   Began Advising: Spring 2008
   Graduation Date: Spring 2013
   Project Title: Novel LED Using a Self-Luminescent, Lattice Matched Substrate

Seoul Semiconductor, Exhibit 2001
LGI v. SSC, IPR2019-01154

Won the North American Molecular Beam Epitaxy Conference Best Student Presentation Award in 2009 and again in 2010
Currently Employed at: Sandia National Laboratory, Albuquerque, NM

9) Jordan Greenlee
Date Began Advising: Spring 2010
Graduation Date: Spring 2014
Project Title: Cation Based Complimentary Memristors for Neuromorphic Applications
Won the Oscar P. Cleaver Award for making highest preliminary exam score
Won the North American Molecular Beam Epitaxy Conference Best Student Abstract Award in 2010
Currently Employed at the Micron Inc., Boise Idaho

10) Brendan Gunning
Date Began Advising: Fall 2010
Graduation Date: Spring 2016
Won the best Contribution at the Workshop on Compound Semiconductor Materials and Devices
Exams Passed and dates: Preliminary Exam, Fall 2010.
Project Title: III-Nitride Heterojunction Diodes and Bipolar Transistors
Currently Employed at: Sandia National Laboratory, Albuquerque, NM

11) Chloe Fabien
Date Began Advising: Fall 2011
Graduation Date: Spring 2016
Exams Passed and dates: Fall 2011.
Project Title: "InGaN Photovoltaics"
Currently Employed at: Oculus Inc., WA

12) Joshua Shank
Date Began Advising: Spring 2012
Graduation Date: Summer 2016
Exams Passed and dates: Spring 2012.
Project Title: "Materials and Devices for Neuromorphic Computing"
Currently Employed at: Sandia National Laboratory, Albuquerque, NM

13) Brooks Tellekamp
Date Began Advising: Fall 2012
Graduation Date: Fall 2018
Exams Passed and dates: Fall 2012.
Project Title: "Devices and Systems for Neuromorphic Computing"
Currently Employed at: National Renewable Energy Laboratory

14) Ehsan Vadiee (Note: Ehsan worked in the Doolittle lab for 2 years but eventually graduated from Arizona State University)
Date Began Advising: Spring 2017
Graduation Date: Spring 2019
Exams Passed and dates: N/A
Project Title: "InGaN Photovoltaics"

B1B. PHD IN PROCESS

Seoul Semiconductor, Exhibit 2001
LGI v. SSC, IPR2019-01154

15) Evan Clinton
    Date Began Advising: Fall 2014
    Expected Graduation Date: Fall 2019
    Exams Passed and dates: Spring 2014.
    Project Title: "AlInGaN Optoelectronic Devices and Tunnel Junctions"

16) Bill Zivasatienraj
    Date Began Advising: Fall 2017
    Expected Graduation Date: Spring 2022
    Exams Passed and dates: N/A
    Project Title: "Scaling of Lithium Metal Oxides for Neuromorphic Computing"
17) Alex Weidenbach
    Date Began Advising: Fall 2017
    Expected Graduation Date: Spring 2022
    Exams Passed and dates: N/A
    Project Title: "Lithium Metal Oxides for Neuromorphic Computing"
18) Chris Matthews
    Date Began Advising: Fall 2017
    Expected Graduation Date: Spring 2022
    Exams Passed and dates: N/A
    NSF Fellowship Winner
    Project Title: "III-Nitride -Silicon Interfaces and Solar Cells"
19) Zachary P. Engel
    Date Began Advising: Fall 2017
    Expected Graduation Date: Spring 2022
    Exams Passed and dates: N/A
    Project Title: "Al based III-Nitrides for Optoelectronics Applications"
20) Habib Ahmad
    Date Began Advising: Fall 2018
    Expected Graduation Date: Spring 2022
    Exams Passed and dates: N/A
    Project Title: "Thermal Interface Design of III-Nitrides for High Power Applications"
21) Aheli Ghosh
    Date Began Advising: Fall 2018
    Expected Graduation Date: Spring 2023
    Exams Passed and dates: N/A
    Project Title: "Three Terminal Devices for Neuromorphic Computing"
22) Timothy M. McCrone
    Date Began Advising: Fall 2018
    Expected Graduation Date: Spring 2023
    Exams Passed and dates: N/A
    Project Title: "Synthesis of Lithium Metal Oxides for Neuromorphic Computing"
23) Keisuke Motoki
    Date Began Advising: Fall 2018
    Expected Graduation Date: Spring 2023
    Exams Passed and dates: N/A
    Project Title: "Structural Characterization of III-Nitrides"

Seoul Semiconductor, Exhibit 2001
LGI v. SSC, IPR2019-01154

B2. M.S. STUDENTS

B2A. GRADUATED WITH M.S. THESIS

24) Jordan Greenlee
Date Began Advising: Spring 2010
Graduation Date: Spring 2014
Project Title: Cation Based Complimentary Memristors for Neuromorphic Applications
Won the Oscar P. Cleaver Award for making highest preliminary exam score
Won the North American Molecular Beam Epitaxy Conference Best Student Abstract Award in 2010
Currently Employed at the Micron Inc., Boise Idaho

25) Joshua Shank
Date Began Advising: Spring 2012
Graduation Date: Summer 2016
Exams Passed and dates: Spring 2012.
Project Title: "Materials and Devices for Neuromorphic Computing"
Currently Employed at: Sandia National Laboratory, Albuquerque, NM

26) James Compagnoni (Materials Science)
Date Began Advising: Fall 2011
Graduation Date: Spring 2013 (Quit Phd Program)
Project Title: MBE of $LiCoO_2$ for RF and Magnetic Applications
Currently Employed at Intel Inc.

B2B. IN PROCESS WITH M.S. THESIS

27) None

B2C. GRADUATED M.S. NON-THESIS

28) Shannon Madison (Co-advised with Stephen Ralph)
Began advising Fall 2004
Graduation date: Fall 2006
Project Title: Integrated Optoelectronics using III-Nitride Epitaxy on LiNbO3 – Device Fabrication and Optical Design

29) Benjamin Small
Began advising Summer 2001
Graduation date: Spring 2002
Project Title: III-Nitride Electronic Device Fabrication

30) Nicholas Brown
Began advising: Spring 2007
Expected Graduation Date: Left Program Early
Exams passed and dates: Preliminary Exam, Spring 2006
Project Title: Modified MBE for In-situ Characterization of LiNbO3

31) Jonathon Lowder
Date Began Advising: Fall 2009

Seoul Semiconductor, Exhibit 2001
LGI v. SSC, IPR2019-01154

Expected Graduation Date: Spring 2014 (Quit Phd Program – did not pass Prelim)
Project Title: III-Nitride Heterojunction Diodes and Bipolar Transistors

32) James Compagnoni (Materials Science)
Date Began Advising: Fall 2011
Graduation Date: Spring 2013 (Quit Phd Program)
Project Title: MBE of LiCoO2 for RF and Magnetic Applications

33) William Laws Calley
Date Began advising: Spring 2005
Graduation date: Spring 2007 (Quit Phd Program)
Project Title: Lithium Niobium Oxide on SiC - Epitaxy and Device Fabrication

34) Joseph Merola
Date Began Advising: Fall 2014
Graduation Date: Spring 2016 (Quit Phd Program)
Exams Passed and dates: Fall 2012.
Project Title: "InGaN Photovoltaics"

Master's Special Problems Students

35) Deepak Janakiraman, Ph.D. Candidate
Began advising Fall 2002, quit Spring 2003
Exams passed: None
Project Title: III-Nitride Technology on Lithium Niobate for Optoelectronic Modulator Applications

36) Changsoo Hong, Ph.D. Candidate
Began advising Spring 2002
Expected Graduation date: Student switched advisors in Fall 2002
Exams passed: None
Project Title: Dual Diamond Damascene III-Nitride Technology for RF Power Electronic Applications

B2D. IN PROCESS M.S. NON-THESIS

None

B3. UNDERGRADUATE STUDENTS

B3A. PAID LABORATORY INTERNSHIP

Starting in 2003, several undergraduate students were integrated into research programs through paid positions. These positions averaged approximately 10 hours per week.

ECE undergraduate students responsible for laboratory equipment development, semiconductor characterization, semiconductor fabrication tool development include:

37) Saurav Sengupta during Fall 2003, Spring 2004 and Fall 2004
38) Brian S. Smith during Spring 2004 and Fall 2004
39) Eshwar Stalin during Summer 2004 and Fall 2004
40) Harris Chen Wang during Summer 2004
41) Abhishek Narula during Fall 2007-Spring 2008
42) Michael Moseley Spring, Summer fall 2007
43) Jack Bell Spring 2011-2012
44) Brooks Tellekamp Summer 2011-2012

Seoul Semiconductor, Exhibit 2001
LGI v. SSC, IPR2019-01154

45) Jacob Yount (ME) Summer, Fall 2015
46) Lauren Murphy (ME) Summer, Fall 2015
47) Mitchell Spears (ECE) Fall 2018

B3B. BUSINESS INTERNSHIPS

Supervised Business Students providing real world management experience for undergraduate students responsible for program administration, financial management, accounting and reporting:

48) Stephanie Pippen Spring, Summer and Fall of 2004
49) Rachel Swafford during Spring 2005
50) Catherine Hammer during Summer 2005
51) Jordan Bush during Fall 2007 to Spring 2008

B3C. UNDERGRADUATE RESEARCH EXPERIENCE ADVISEMENT

52) Brinda K. Ramaiya: Advised on an Undergraduate Research Opportunities Project (UROP) Summer 2001. Topic: "Pyrometer Growth Monitor using Labview"
53) Brian Davis: Advised on a Summer Undergraduate Research in Engineering program Project (SURE) Summer 2001. Topic: "Labview automation of a Hall measurement system"
54) Peter Pappas: Advised on an Undergraduate Research Opportunities Project (UROP) Fall and Spring 2001/2002. Topic: "Microcontroller interface for an auto-tuning RF plasma matching network"
55) Mustayeen Nayeem: Advised on an Undergraduate Research Opportunities Project UROP) Summer 2002. Topic: "Implementation of a differential capacitance circuit in a deep level transient spectroscopy system"
56) Mark Verghese: Advised on an Undergraduate Research Opportunities Project (UROP) Spring and Fall 2002. Topic: "Temperature Control Implementation of a Semiconductor Growth Recipe Reader"
57) Hitesh Upadhyay: Advised on an Undergraduate Research Opportunities Project (UROP) Fall 2002 and Spring 2003. Topic: "Implementation of a variable magnetic field hall measurement system using Labview". ***This project was awarded a President's Undergraduate Research Award (PURA) to pursue this topic in Fall 2002 / Spring 2003.***
58) Dhairya Menta: Advised on an Undergraduate Research Opportunities Project (UROP) Spring 2002 and Fall 2002. Topic: "Implementation of a stepper motor control for a RF plasma source impedance matching network"
59) Reshma Parekh: Advised on an Undergraduate Research Opportunities Project (UROP) Fall 2002 and Spring 2003. Topic: "Development of a pulse interface for a deep level transient spectroscopy system"
60) Vikas J. Parekh: Advised on an Undergraduate Research Opportunities Project (UROP) Fall 2002. Topic: "Development of a MOSFET Characterization System based on source-measurement units"
61) Jinesh Karia: Advised on an Undergraduate Research Opportunities Project (UROP) Fall 2002. Topic: "Implementation of a variable frequency conductance measurement for extraction of the density of interface states"
62) Gautam Khanna: Advised on an Undergraduate Research Opportunities Project (UROP) Fall 2002. Topic: "Study of doping behavior in Lithium Niobate"

Seoul Semiconductor, Exhibit 2001
LGI v. SSC, IPR2019-01154

63) Salil Arora: Advised on an Undergraduate Research Opportunities Project (UROP) Fall 2002. Topic: "Design of a General Electronic Materials Characterization Photomask using AutoCad"
64) Ming Teng Han: Advised on an Undergraduate Research Opportunities Project (UROP) Fall 2002. Topic: "Implementation and Testing of a Mercury for Probe Rapid Characterization of Semiconductor Materials"
65) Ranit Windlass: Advised on an Undergraduate Research Opportunities Project (UROP) Summer 2003. Topic: "Design of a temperature compensated logarithmic voltage amplifier"
66) William Laws Calley III: Advised on an Undergraduate Research Opportunities Project (UROP) Summer 2003 and Fall 2003. Topic: "Sputtering of and Fabrication of LiNbO3 alternative gate dielectrics for SiC power transistors"
67) Brian S. Smith: Advised on an Undergraduate Research Opportunities Project (UROP) Spring 2003 and Summer 2003. Topic: "Implementation of a capacitance voltage measurement system in a Labview environment"
68) Alexis Sanderlin: Advised on an Undergraduate Research Opportunities Project (UROP) Spring 2003. Topic: "Determination of crystal quality by x-ray diffraction"
69) Alan Ngo: Advised on an Undergraduate Research Opportunities Project (UROP) Spring 2003. Topic: "MOSFET parameter extraction using Labview"
70) Arnab Das: Advised on an Undergraduate Research Opportunities Project (UROP) Spring 2004. Topic: "Computer Control of an Antimony valved cracker for molecular beam epitaxy"
71) John Erdelt: Advised on an Undergraduate Research Opportunities Project (UROP) Spring 2004. Topic: "Microcontroller implementation of a fuel injection system"
72) Ephraim Lucas: Advised on a Summer Undergraduate Research in Engineering program Project (SURE) Summer 2004. Topic: "Validation and Calibration of a SiC Chemical Vapor Deposition System"
73) Deborah M. Johnson: Advised on an Undergraduate Research Opportunities Project (UROP) Spring 2004. Topic: "Labview based Current-Voltage Characterization system development"
74) Andera Pinkney-Hawkins: Advised on a Summer Undergraduate Research in Engineering program Project (SURE) Summer 2005. Topic: "Labview Automation of a Photoluminescence Monochromator"
75) Michael Moseley: Advised on a Summer Undergraduate Research in Engineering program Project (SURE) Summer 2007. Topic: "Lapping and Polishing Oxide Substrates"
76) Fletcher Dostie: Advised an Undergraduate Research Opportunities Project (UROP) Fall 2010 and Spring 2011. Topic: Development of a Phase Lock Loop modulator with an analog variable frequency low pass filter.
77) Brookes Tellekamp: Advised a MRCEC Summer Internship Summer 2011. Topic: Metal Organic Molecular Beam Epitaxy of Complex Metal Oxides.
78) Raymond W. Chian: Advised an Undergraduate Research Opportunities Project (UROP) Summer 2012. Topic: Development of a Solar Simulator
79) Theodore Hecker: Advised an Undergraduate Research Opportunities Project (UROP) Spring 2012.Topic: Ultra-Low Current Measuring

Seoul Semiconductor, Exhibit 2001
LGI v. SSC, IPR2019-01154

80) Shukun Yang, Advised an Undergraduate Research Opportunities Project (UROP) Fall 2013. Topic: Development of a Phase Lock Loop modulator with an analog variable frequency low pass filter.
81) Jacob J. Yang, Advised an Undergraduate Research Opportunities Project (UROP) Fall 2014. Topic: Development of a Phase Lock Loop modulator with an analog variable frequency low pass filter.
82) Anand Ramanathan, Advised an Undergraduate Research Opportunities Project (UROP) Fall 2018. Topic: SPICE model of an Analog Memristor

B4. SERVICE ON THESIS OR DISSERTATION COMMITTEES

B4A. INTERNAL

Dates and Numbers not Recorded. Will Do hence forward.

B4B. EXTERNAL

Dates and Numbers not Recorded. Will Do hence forward.

B5. MENTORSHIP OF POSTDOCTORAL FELLOWS OR VISITING SCHOLARS

B5A. SUPPORT/ADVISEMENT OF SUMMER HIGH SCHOOL TEACHERS

1) Michael Lanham (Sprayberry High School) Summer 2003
2) Kaye Sheets (Patrick Henry High School) Summer 2006
3) Jacquelyn Thomas (DeKalb Co High School) Summer 2006
4) Bill Daly (Collins Hill High School) Summer 2011 and Summer 2012

C. OTHER TEACHING ACTIVITIES

C1. COURSE DEVELOPMENT

Developed two senior special topics classes “Semiconductor Materials and Device Characterization” and “Devices for Renewable Energy” both of which have been extremely well received. Prior to these courses, seniors interested in microelectronics only had one senior elective from which to choose.

C2. COURSE IMPROVEMENT

Developed World Wide Web-based course curriculums for ECE 3040, ECE3080, ECE6451, ECE6450 as well as two senior special topics classes “Semiconductor Materials and Device Characterization” and “Devices for Renewable Energy”. These web sites contain animations and computer graphics to aid in the explanation of difficult concepts. They also contain homework assignments, solutions, lecture notes, and exam solutions (present and past) to supply students with adequate resources for the class. Several other professors have used this site as a template for their class development.

C3. PROFESSIONAL DEVELOPMENT/CONTINUING EDUCATION

Taught distance learning section for ECE6450 in Fall 2014 and the GTREP course for ECE 3040 in Fall 2001 and Summer 2002 via distance learning.

C4. OTHER TEACHING ACTIVITIES

No Data

Seoul Semiconductor, Exhibit 2001
LGI v. SSC, IPR2019-01154

VI. SERVICE

A. Professional Contributions

List all national and international contributions of service and positions of leadership in the profession.

A1. EDITORIAL BOARD MEMBERSHIPS

No Data

A2. SOCIETY OFFICES, ACTIVITIES, AND MEMBERSHIP

a. Senior Member of IEEE
b. Member of IEEE Electron Devices Society
c. Member of IEEE Instrumentation and Measurement Society
d. Member of Materials Research Society
e. Member of American Society of Engineering Educators (ASEE)
f. Member of American Physical Society
g. Member of American Vacuum Society

A3. ORGANIZATION AND CHAIRMANSHIP OF TECHNICAL SESSIONS, WORKSHOPS AND CONFERENCES

a. Chair of Office of Naval Research Workshop on Ferroelectronic Semiconductor Interfaces, April 7-11, 2002.
b. Program Committee for 2002 Electronic Materials Conference
c. Program Committee for 2002 IEEE Lester Eastman Conference on High Performance Devices
d. Program Committee for 2004 IEEE Lester Eastman Conference on High Performance Devices
e. Organizing Committee for 2005 International Conference on Silicon Carbide and Related Materials
f. Exhibits Chairman for 2005 International Conference on Silicon Carbide and Related Materials
g. Wide Bandgap Semiconductor Focus Session Chair/Co-organizer for American Physical Society March Meeting 2005
h. Program Committee for 2005 North American Molecular Beam Epitaxy Conference
i. Session Chair for Workshop on the Future of Electronics, Aruba, Dec. 18-22, 2004
j. Session Chair for 1999, 2002 Electronic Materials Conference
k. Program Committee, Workshop on Compound Semiconductor Materials and Devices (WOCSEMMAD), 2005 Miami, FL.
l. Program Chair, Workshop on Compound Semiconductor Materials and Devices (WOCSEMMAD), 2006, Phoenix AZ.
m. Program Chair, Workshop on Compound Semiconductor Materials and Devices (WOCSEMMAD), 2007 Savannah, GA.

Seoul Semiconductor, Exhibit 2001
LGI v. SSC, IPR2019-01154

n. Program Committee, Workshop on Compound Semiconductor Materials and Devices (WOCSEMMAD), 2008 Palm Springs, CA.
o. Program Committee, 2008 Electronic Materials Conference, June 25-27, 2008 Santa Barbara, CA.
p. Program Committee, Workshop on Compound Semiconductor Materials and Devices (WOCSEMMAD), 2009 Fort Myers, FL
q. Program Committee, Workshop on Compound Semiconductor Materials and Devices (WOCSEMMAD), 2010 Newport Beach, CA
r. Program Chair, International Workshop on Nitride Semiconductors 2010, Tampa FL
s. Program Committee for 2010 North American Molecular Beam Epitaxy Conference, Sept 26-29th 2010, Breckenridge, CO
t. Program Committee for 2010 International Molecular Beam Epitaxy Conference, August 22-27th, 2010 Berlin, Germany
u. Organizing and Program Committee, 2010 Electronic Materials Conference, June 22-24, 2011 Santa Barbara, CA.
v. Chair, Workshop on Compound Semiconductor Materials and Devices (WOCSEMMAD), 2011 Savannah, GA
w. Program Chair, International Conference on Nitride Semiconductors 2013, Washington DC
x. Officer (secretary) Organizing Committee, Electronic Materials Conference, 2013-2015.
y. Organizing and Program Committee, Electronic Materials Conference, 2016-2018
z. Organizing Committee, Electronic Materials Conference, 2018-Present
aa. Program Committee, Workshop on Compound Semiconductor Materials and Devices (WOCSEMMAD), 2013 New Orleans, LA
bb. Chair North America Molecular Beam Epitaxy Conference, Atlanta 2012
cc. Organizational Committee, North America Molecular Beam Epitaxy Conference, 2013-present
dd. Program Committee, Workshop on Compound Semiconductor Materials and Devices (WOCSEMMAD), 2014 San Antonio, TX
ee. Program Committee, Workshop on Compound Semiconductor Materials and Devices (WOCSEMMAD), 2015 Tucson, AZ
ff. Chair, International Workshop on Nitride Semiconductors 2016, Orlando FL
gg. Program Committee, International Workshop on Nitride Semiconductors 2018, Kanazawa Japan
hh. Chair, International Conference on Nitride Semiconductors 2019, Bellevue WA

A4. TECHNICAL JOURNAL OR CONFERENCE REFEREE ACTIVITIES

a. Review of Scientific Instruments

Seoul Semiconductor, Exhibit 2001
LGI v. SSC, IPR2019-01154

b. Journal of Electrochemical and Solid State Letters
c. Journal of Electronic Materials
d. Proceedings of the Materials Research Society
e. IEEE Transactions on Electron Devices
f. IEEE Electron Device Letters
g. Applied Physics Letters
h. Journal of Applied Physics
i. Journal of Materials Science
j. Journal of Vacuum Science and Technology
k. Thin Solid Films
l. Solid State Electronics
m. Conference on the Physics of Vacuum Science and Technology

A5. PROPOSAL PANELS AND REVIEWS

a. NSF SBIR panel review, Spring 2001, 2002, 2004, 2008, 2011, 2014
b. NSF CAREER panel review, Fall 2004, 2016
c. United States Army Research Office-proposal, Spring 2004, 2016
d. NSF Division of Materials Research-proposal review, Fall 2004, 2014, 2015, 2016, 2017
e. NSF MRI panel review, Spring 2005, 2007
f. NSF Division of ECCS, Fall 2006, 2014, 2016, 2019

B. PUBLIC AND COMMUNITY SERVICE

No Data

C. INSTITUTE CONTRIBUTIONS

C1. INSTITUTE COMMITTEE SERVICE

ECE Faculty Senate 2018

C2. COLLEGE COMMITTEE SERVICE

No Data

C3. SCHOOL COMMITTEE SERVICE

a. ECE Undergraduate Curriculum Committee, Fall 2001-2009
b. ECE Curriculum Study Committee, Summer 2004, Fall 2004
c. ECE Instrumentation Committee, Spring 2001-Summer 2001
d. EE Curriculum Subcommittee, Fall 2009 and Spring 2010
e. ECE Faculty Recruitment Committee, 2010-2014
f. ECE Statutory Advisement committee, 2009-2013
g. ECE graduate Committee 2014-present
h. ECE Microsystems/Nanotechnology TIG Chair 2015-2019
i. ECE Nanotechnology Faculty Recruitment Committee 2019-Present

Seoul Semiconductor, Exhibit 2001
LGI v. SSC, IPR2019-01154

C4. PROGRAM DEVELOPMENT: RESEARCH
No Data

C5. PROGRAM DEVELOPMENT: ACADEMIC
Co-led through the graduate committee the revision for the School of ECE's preliminary exam improvement.

C6. OTHER INSTITUTE SERVICE CONTRIBUTIONS

1) Hosted a number of laboratory/campus tours for middle school age science and math organizations throughout his academic career.
2) Judged IEEE Undergraduate Student Paper Contest, Spring 2002.
3) Presentation given for the Women of Electrical and Computer Engineering, Women's Undergraduate Research Orientation on April 16, 2005.
4) Hosted three minority students as part of the Summer Undergraduate Research Experience (SURE) program, summer 2001, 2003 and 2005.
5) Advised four high school science teachers summer (GIFT, NRC and MRESEC) internship during summers of 2003, (2) 2006, and 2011
6) Hosted various high school and junior high field trips in 2006-2011.

Seoul Semiconductor, Exhibit 2001
LGI v. SSC, IPR2019-01154

APPENDIX B

age using a series resistor if a proper d-c source and voltage-sensing instrument are used.

Voltages remaining due to the extremely slow charge decay rates of tantalum capacitors can be readily mistaken for internally generated voltages.

Manuscript received May 17, 1961; revised manuscript received Oct. 6, 1961. This paper was prepared for delivery before the Chicago Meeting, May 1-5, 1960.

Any discussion of this paper will appear in a Discussion Section to be published in the December 1962 JOURNAL.

REFERENCES

1. A. Guntherschulze, *Arch. tech. Messen*, **210**, 165 (1953).
2. M. Haissinsley, *Metaux et Corrosion*, **23**, 15 (1948).
3. E. M. Khairy and M. Kamal Hussein, *Chem. Soc. Japan Bull.*, **30**, 944 (1957).
4. W. Ch. van Geel and C. A. Pistorius, *Philips Research Rpts.*, **11**, 471 (1956.)
5. D. A. Vermilyea, *This Journal*, **101**, 388 (1954).
6. W. Ch. van Geel, C. A. Pistorius, and P. Winkel, *Philips Research Rpts.*, **13**, 265 (1956).
7. R. L. Taylor and H. E. Haring, *This Journal*, **103**, 611 (1956).
8. D. A. Vermilyea, *Acta Met.*, **6**, 166 (1958).
9. P. Alley, *Western Electronic News*, **26** (March 1958).
10. L. Young, *Acta Met.*, **5**, 711 (1957).

Gas Permeation Study and Imperfection Detection of Thermally Grown and Deposited Thin Silicon Dioxide Films

S. W. Ing, Jr., R. E. Morrison, and J. E. Sandor[1]

Semiconductor Products Department, General Electric Company, Syracuse, New York

ABSTRACT

Methods have been developed to measure gas permeation through thin thermally grown and deposited silicon dioxide films. From the data collected it is shown that pores and microchannels (orders of magnitude smaller than pores) are formed in these films, and permeation through them is the main diffusion mechanism involved. The existence of imperfections in the oxides is demonstrated by using a chlorine etching technique. An important result from this work is that insufficient surface cleaning is an important factor in the production of relatively large pores in the oxide. Channel size approaching atomic dimensions could be obtained in these films by being extremely careful in the preoxidation or predeposition cleaning of the silicon. Some oxide films show the presence of crystalline structures considered to be caused by a nucleation phenomena due to the presence of foreign particles on the silicon surface.

Measurements of the permeation rate of gases through thin films (10,000-40,000Å) of thermally grown and pyrolytically formed silicon dioxide have been made to determine quantitatively the imperfections existing in these films. Moreover, the procedures and techniques developed may be applied to permeation measurements of thin films of other materials.

A survey of the techniques used for permeation studies of glasses and crystalline material indicates that most classical approaches are not adaptable for studying very thin films, and in particular, most methods require large areas of material. The early permeation studies for silica and glasses, done by Urry (1, 2), Barrer (3), Rayleigh (4, 5) and others (6), utilize a form of double-bulb cell in which the inner bulb is blown from the material being studied. More recent techniques developed for permeation studies of sheet organic polymers (7, 8) satisfy the requirements for this investigation more closely; however, many modifications are still necessary due to the extreme fragility of the silica films and the limited size attainable.

From the existing published permeation studies reviewed, the device and procedures used by Park (7) seemed to satisfy thin film requirements provided gas permeation rate through the film is comparatively high. The device measures the volume of the permeated gas under conditions of constant pressure and temperature while a pressure difference is maintained across the film.

Park obtained ±5% accuracy with this procedure and could measure a flow rate of 2.3×10^{-3} cm³/min (permeation constant of 1×10^{-9} cc-cm/sec-cm²-cm Hg) with excellent reproducibility.

Initial permeability studies were begun by employing this volume change procedure, but as some permeability constants of below 1×10^{-14} cc-cm/sec-cm²-cm Hg were anticipated for these silicon dioxide films, ultimate values were expected to be obtained by using mass spectrometer. However, the semimicro film holder and volume increase measurement procedure proves an excellent method for screening films and collecting information.

Apparatus and Procedure

Semimicro film holder and volume increase measurement procedure.—The film holder, which is a slight modification of Park's device, is shown in Fig. 1. It is constructed of brass with an aluminum tightening ring. The high-pressure side is constructed with a set-screw-ball and socket valve to flush air from the upstream side prior to testing.

[1] Present address: Fairchild Semiconductor Corporation, Palo Alto, California.

Downloaded on 2019-09-16 to IP 143.215.34.165 address. Redistribution subject to ECS terms of use (see ecsdl.org/site/terms_use) unless CC License in place (see abstract).

Seoul Semiconductor, Exhibit 2001
LGI v. SSC, IPR2019-01154

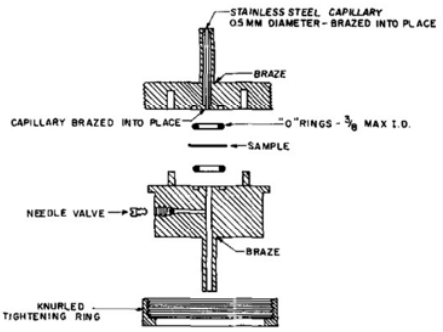

Fig. 1. Cross-sectional view of film holder for permeability measurement.

The volume on the low-pressure half of the device is minimized by brazing a 0.5 mm stainless steel capillary into place. Rubber "O" rings, recessed into the face of the device, provide a gastight seal with the sample when the unit is assembled and the tightening ring is applied. To insure against torsional tearing forces on the sample, three positioning pins are placed on the device halves.

The silicon dioxide films tested range in thickness from 10,000 to 40,000Å. These films are extremely fragile, and it would be impossible, as it is with plastic materials, to simply place the sheet between the device "O" rings and tighten. The film must be mounted or supported on a rigid frame, which will bear all the pressure of the "O" ring contact, and yet the film must lie completely flat on this support surface and adhere tightly about the periphery of the hole drilled into the support.

Many attempts were made to float a stripped silica film onto a polished quartz plate that had a hole of known diameter. Water, alcohol, and acetone were used; however, in most cases the film either wrinkled or would lift around the periphery of the hole creating possible error in the area considered for permeation study. Some success was attained by heat-sealing a sheet of film between two sheets of polyvinyl chloride containing drilled windows. However, this method proved unfeasible as the film cracked readily in most cases due to differences between the thermal properties of the film and the polymer.

Eventually, two satisfactory methods were developed for rigidly mounting the films for testing, the oxide window method and the stripped film sandwich (see Fig. 2).

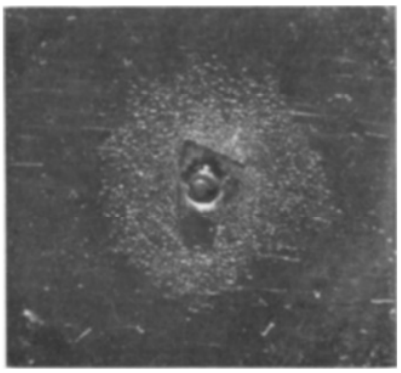

Fig. 2. Stripped film glass-brass sandwich; film 15,000Å

For the oxide window method a silicon wafer (3 cm^2) is completely oxidized on both sides. The surfaces are then completely masked with wax except for a circular area on one side of approximately 1 mm diameter. The silica is removed from this nonmasked area by etching with HF; the surface is washed with distilled water, and all wax removed with solvent. The wafer is then placed-silicon exposed side up–in a dry chlorine gas stream at 900°C for 2 min. In this period a neat vertical channel is cut through the silicon substrate, with very little horizontal undercutting, until the silica film on the opposite side of the wafer is reached. In this method, the silicon itself acts as support for the "O" ring contact, and the permeation area can be measured accurately as the film lies flat over the window area and is, of course, tightly adhered to the silicon substrate.

The stripped-film sandwich method was also used many times with success. Here, a silicon wafer covered with oxide is completely masked on one side with wax. All oxide on the opposite side is etched off with HF leaving the silicon clean and exposed. The wax is removed with solvent, and the wafer is placed silicon side up in a dry chlorine gas stream at 900°C for 10 min. In this period, all the silicon reacts and volatilizes leaving a flat transparent sheet of silicon dioxide.

This film is laid down on a clean, mechanically polished piece of brass which has a drilled hole of known diameter. A very light coating of silicone grease provides a tight seal. Next, a lightly greased glass plate with a matching hole, slightly larger in diameter, is placed on top of the silica-brass making a glass-silica-brass sandwich. "O" ring contact on this assembly gave a tight seal when pressure was applied on the permeation device with the tightening ring. The stripped film sandwich had the advantages of ease of handling and less film breakage; however, if the film does wrinkle or lift from the brass plate, an error is introduced into the assumed area measurement for permeation.

Both methods, however, provide a good film support for insertion into the permeation device.

In operation, the supported silicon dioxide film is placed horizontally on one half of the film holder. The holder is assembled and tightened as hard as possible with hand pressure. The film holder, is then placed between two three-way stopcocks held flush with the holder with Tygon tubing. The test gas is slowly applied until a constant pressure is reached on the manometer. The entrapped air on the upstream side of the film holder is bled off several times through a needle valve.

A glass capillary containing an approximate 2 mm slug of methyl isobutyl ketone is next attached flush to a stopcock with Tygon tubing. A millimeter scale is adjusted to measure accurately the progression of the slug with volume increase.

During a run, the gas pressure is fixed and the rate of displacement of the organic capillary slug

Downloaded on 2019-09-16 to IP 143.215.34.165 address. Redistribution subject to ECS terms of use (see ecsdl.org/site/terms_use) unless CC License in place (see abstract).

Seoul Semiconductor, Exhibit 2001
LGI v. SSC, IPR2019-01154

Table I. Experimental results

Film No.	Gas used	Film mounting method	Film thickness, Å	Means of measurement	P, cm³ cm / sec-cm²-cm Hg
1	Air	PVC* sandwich	16,000	Volume displacement	8.5×10^{-8}
1	Air	PVC sandwich	16,000	Volume displacement	8.9×10^{-8}
2	Hydrogen	Glass-brass sandwich	22,000	Volume displacement	3.7×10^{-7}
2	Argon	Glass-brass sandwich	22,000	Volume displacement	1.98×10^{-7}
2	Air	Glass-brass sandwich	22,000	Volume displacement	2.18×10^{-7}
3	Air	Glass-brass sandwich	22,000	Volume displacement	1.98×10^{-7}
3	Argon	Glass-brass sandwich	22,000	Volume displacement	1.67×10^{-7}
3	Hydrogen	Glass-brass sandwich	22,000	Volume displacement	4.39×10^{-7}
4	Hydrogen	Glass-brass sandwich	22,000	Volume displacement	$<10^{-10}$
4	Air	Glass-brass sandwich	22,000	Volume displacement	$<10^{-10}$
5	Air	Oxide window	21,000	Volume displacement	$<10^{-10}$
6	Helium	Stripped film	38,000	Mass spectrometer	3×10^{-9}
6	Hydrogen	Stripped film	38,000	Mass spectrometer	3.2×10^{-9}
6	Oxygen	Stripped film	38,000	Mass spectrometer	5.6×10^{-10}
6	Xenon	Stripped film	38,000	Mass spectrometer	7.4×10^{-10}
6	Argon	Stripped film	38,000	Mass spectrometer	2.9×10^{-10}
7	Argon	Oxide window	35,000	Mass spectrometer	3×10^{-4}
8	Argon	Oxide window	35,000	Mass spectrometer	6×10^{-5}
9	Argon	Glass-brass sandwich	15,000	Volume displacement	$<10^{-10}$

* Polyvinyl chloride.

is noted over a set 3 cm distance. Repeated determinations on the same piece of film are made by one closing stopcock and gently sucking the slug back to the starting position, again observing the time intervals required to progress the successive sections of the 3 cm distance.

In general, with an exposed film area of approximately 0.01 cm², a range of gas pressure difference across the film can be used without puncturing the film varying from 200 mm Hg for 5000Å thickness to well over 760 mm Hg for 15,000Å.

Since the capillary slug movement is affected by changes in ambient temperature, as much care as possible should be taken to provide a constant ambient temperature.

Mass spectrometer measurement apparatus.— Both oxide window and stripped silicon dioxide films are used. The film is mounted between the polished ends of two capillary glass tubes, 1 mm bore, and is sealed tightly with apiazon wax. The assembly is then incorporated into the mass spectrometer vacuum system. A fraction of a millimeter Hg gas pressure differential is generally applied across the film. The film temperature can be varied by using a heater placed around the film assembly.

Results

For all films investigated, there was no evidence of an initial induction period. In the case of volume change permeation measurements, the rate of displacement of the liquid slug seemed to reach a steady state very readily after the start of each run.

The experimental results of permeation of various gases through different silicon dioxide films are presented in Table I. All films were thermally formed by steam oxidation with the exception of film No. 5, which was formed with oxygen bubbling through a room temperature water supply. *P*, the permeability, is defined as the cc of gas at normal temperature and pressure passing through a film 1 cm thick, per second, per cm² area with 1 cm Hg pressure difference across the film.

Discussion of Permeation Results

As can be seen from the tabulated data, the permeation constants for these thin silicon dioxide films not only vary using the same gas, e.g., air, 2.18×10^{-7} to $< 10^{-10}$ and argon 3×10^{-4} to $< 10^{-10}$, but also the lower values obtained are several orders of magnitude higher than those anticipated (9).

From the spread of permeation results, a proposed spectrum of values is suggested according to the degree of imperfections within the silicon dioxide films. Breaking the values down into permeation ranges, one might categorize the results as follows for a gas like argon or oxygen.

A. 10^{-3} to 10^{-5} — Flow through microcracks, pores, and crystalline portion boundaries.
B. 10^{-7} to 10^{-10} — Flow through micro-channels.
C. $\sim 10^{-15}$ — True diffusion and permeation (9).

If a film contains a crack due to handling or insertion into the film holder, it is readily detected by the rapid progression of the capillary slug. On microscopic examination the crack can usually be observed.

The higher rates of 10^{-4} and 10^{-5} are obtained on films in which many fine crystal-like growths appear. These crystals very closely resemble those described by other authors (10) and are probably also cristobalite. The average diameter of these crystals vary from 4×10^{-4} cm to 3.3×10^{-3} cm (see Fig. 3). It is noted sporadically that this phenomenon occurs independent of the oxidation technique although the standard preoxidation cleaning treatment is used. In advanced stages this "crystallization" can give a milky cast to the oxide, even while still on its silicon substrate, and often after etching away such a film, the silicon surface is noticeably pitted in regions where these "crystals" were observed. This phenomenon seems to be pre-

Downloaded on 2019-09-16 to IP 143.215.34.165 address. Redistribution subject to ECS terms of use (see ecsdl.org/site/terms_use) unless CC License in place (see abstract).

Seoul Semiconductor, Exhibit 2001
LGI v. SSC, IPR2019-01154

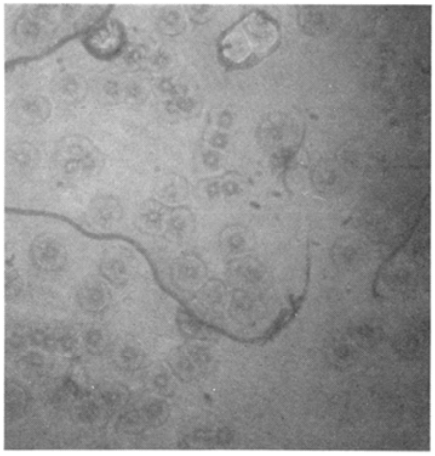

Fig. 3. "Crystalline" growth in stripped thermal oxide film. Magnification 150X.

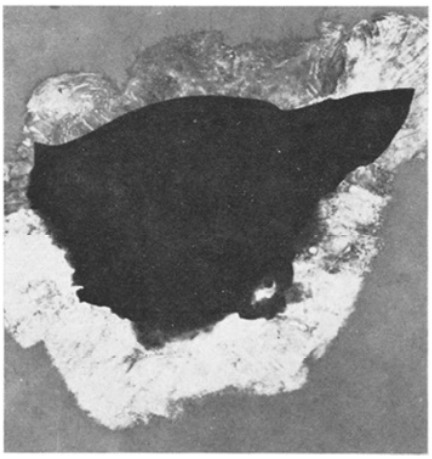

Fig. 4. SiO_2 crystallization around foreign particle; note: produced during electron microscope observation.

dominant in cases in which the amorphous silica can nucleate about a foreign material such as might be found on an insufficiently cleaned silicon surface. Figure 4 illustrates this crystallization phenomenon. This transition occurred while scanning a stripped silica film under the electron microscope. While the photographed area was being observed, some unknown foreign material landed on the silica, and immediately the surrounding silica crystallized.

The bulk of the results fall into the 10^{-7}-10^{-10} permeation range. It is felt that this range indicates permeation through microchannels rather than through the membrane by solubility for several reasons. First, a steady-state flow is immediately observed on starting a run either by mass spectrometer or by volume displacement. Solubility type of permeation should show an initial time lag. Second, mass spectrometer measurement shows H_2 and He are about equal in rate, and H_2 should be approximately 1/10 the rate of that of He for fused silica (9). Third, the temperature dependence is not found to be exponential. Argon was used in the mass spectrometer with a pressure differential of 6 mm Hg. Permeation measurements were made at 29° and 59°C, and the rates were found to be approximately the same with, perhaps, a 3% higher rate for the higher temperature. As a rough approximation with a P of 5×10^{-10} for oxygen it is estimated that using a test area of 3×10^{-2} cm² the total "channel area" would be 3.65×10^{-10} cm². If this entire area is assumed to be one pore, this would correspond to a pinhole of approximately 2×10^{-5} cm in diameter in a test area of 0.2 cm diameter. The electron microscope failed to detect any pores in several films over the limited field observed, even with a resolution down to 50Å, so channels should be numerous and extremely small in size.

The rates obtained with hydrogen and helium (see Table I) approach the values found by other authors using fused silica (11) by one or two orders of magnitude. Leiby and Chen (12) studied the permeation of various gases through Vycor glass, and report permeation constants in the range of 10^{-10} to 10^{-11} cm³-cm/sec-cm²-cm Hg for He at room temperature, which is again one or two orders lower than is found with the least permeable thermally grown oxide. The permeation constant of He in Vycor glass was found to be both a square root and an exponential function of temperature. The square root temperature dependence was considered to indicate the existence of a molecular streaming process through extremely small voids and/or channels of near molecular dimension. If this is the case, then the channels existing in some of these thermally grown oxide films also could not be too much larger than molecular size.

The runs which gave values below 10^{-10} were obtained by the volume displacement method, but this value is certainly the extreme upper limit measurable by this procedure due to time factor and effects of external surroundings such as temperature. For values less than 10^{-9} mass spectrometer is the most accurate and most sensitive method, for with the present system, a permeability for oxygen in the order of 10^{-15} could have been detected if these films were free of imperfections and if permeation occurred through the silica by solubility.

Detection of Film Imperfections

Basically, the films studied for imperfection detection are prepared by either of three methods: (*a*) thermal oxidation of silicon with oxygen, (*b*) thermal oxidation of silicon with steam, and (c) pyrolytic decomposition of an organic-oxy-silane onto a silicon crystal surface. The state of the surface prior to oxidation or deposition appears to affect the quality of the resulting film greatly, as undesirable foreign materials on the silicon surface will produce a poor oxide. In general, few physical differences are noted in the oxides prepared by these three methods. All are amorphous by x-ray and electron diffraction. The films deposited pyrolytically, however, appear to be under considerably more stress than the thermally oxidized films, so an annealing step must be introduced to get them to lie flat and continuous (see Fig. 5). Of course, the reaction kinetics and the preparation tempera-

Downloaded on 2019-09-16 to IP 143.215.34.165 address. Redistribution subject to ECS terms of use (see ecsdl.org/site/terms_use) unless CC License in place (see abstract).

Seoul Semiconductor, Exhibit 2001
LGI v. SSC, IPR2019-01154

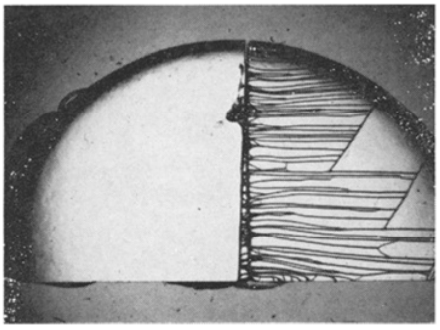

Fig. 5. Effect of annealing on pyrolytic film; left, annealed; right, unannealed; both after 1 min Cl_2 at 900°C.

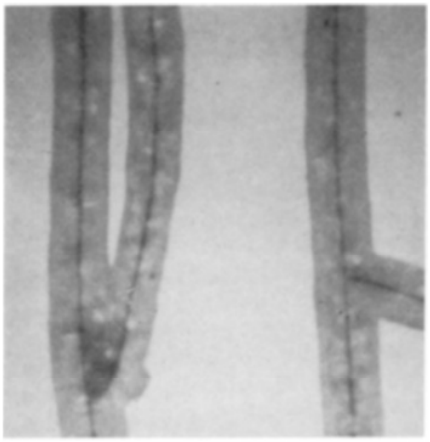

Fig. 6. Unannealed pyrolytic film cracking defined by chlorine etching. Original oxide crack and chlorine channel shown. Magnification 100X.

tures of these three preparation methods are quite different.

A method is developed by which films and silicon preoxidation cleaning processes could be evaluated qualitatively in relation to the imperfections introduced into the silicon dioxide film. Chlorine etching proves to be a very effective method for qualitatively screening films for cracks and pores. A test oxide must still be on its silicon substrate, whether thermally grown or deposited, and the silicon must be completely covered including its edges. Gross film imperfections, even those not visible with the eye, are easily detected after placing the sample in a dry Cl_2 stream at 900°C for 1-2 min. If the sample oxide contains large visible cracks, this time will be almost sufficient to attack the silicon completely, leaving fragments of oxide film.

A 2-min, 900°C Cl_2 etch finely brings out microcracks in oxide films as the chlorine attacks through the discontinuities and slowly undercuts along into the silicon (see Fig. 6). Microscopic examination of the etched areas always discloses the crack in the oxide.

However, to reveal some of the pores previously discussed, at least 30 minutes in Cl_2 at 900°C are required to undercut the silicon sufficiently for observation.

Chlorine etching tends to indicate that there is little difference in the three preparation methods

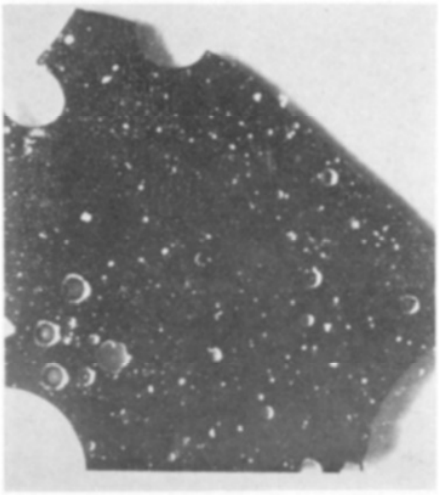

Fig. 7. Effect on oxide by chlorine etching insufficiently cleaned silicon; 10,000Å oxide by dry O_2 at 1200°C.

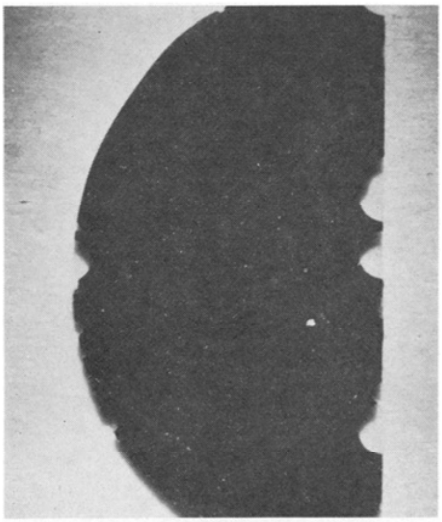

Fig. 8. Effect on oxide by chlorine etching chemically cleaned silicon; 6000Å oxide by steam at 1200°C.

in their relative susceptibility to film imperfections. All are basically equivalent in regard to number of pinholes; however, unannealed pyrolytically deposited oxides do tend to crack more readily in thicknesses over 15,000Å. The factor which appears most critical for imperfection reduction is silicon pretreatment and cleanliness prior to oxidation or deposition (see Fig. 7 and 8).

Conclusions

Methods have been developed to measure gas permeation through thin silicon dioxide films. From the data collected it is shown that pores and microchannels (orders of magnitude smaller than pores) are formed in these films, and permeation through them is the main diffusion mechanism involved.

The existence of imperfections in the oxides is demonstrated by using a chlorine etching technique.

An important result from this work is that surface contamination is an important factor in the production of pores in the oxide. Channel size ap-

Downloaded on 2019-09-16 to IP 143.215.34.165 address. Redistribution subject to ECS terms of use (see ecsdl.org/site/terms_use) unless CC License in place (see abstract).

Seoul Semiconductor, Exhibit 2001
LGI v. SSC, IPR2019-01154

proaching atomic dimensions could be obtained in these films by being extremely careful in the preoxidation cleaning of the silicon.

Some oxide films show the presence of crystalline structures considered to be caused by a nucleation phenomena due to the presence of foreign particles on the silicon surface.

Acknowledgments

The authors wish to express their appreciation to Dr. Frank J. Norton, General Electric Research Laboratory, Schenectady, for making mass spectrometer measurements and also to Dr. William C. Dash, General Electric Research Laboratory, Schenectady, for electron microscope photography.

Manuscript received Sept. 14, 1961.

Any discussion of this paper will appear in a Discussion Section to be published in the December 1962 JOURNAL.

REFERENCES

1. U. Urry, *J. Am. Chem. Soc.*, **54**, 3887 (1932).
2. U. Urry, *ibid.*, **55**, 3242 (1933).
3. R. M. Barrer, *J. Chem. Soc. London*, 378 (1934).
4. Rayleigh, *Proc. Royal Soc. (London)*, **A156**, 350 (1936).
5. Rayleigh, *ibid.*, **A163**, 377 (1937).
6. T. F. Newkirk and F. V. Tooley, *J. Am. Ceramic Soc.*, **32**, 272 (1949).
7. W. R. R. Park, *Anal. Chem.*, **29** [12], 1897 (1957).
8. D. W. Brubaker and K. Kammermeyer, *Anal. Chem.*, **25** [3], 424 (March 1953).
9. F. J. Norton, *J. Am. Ceramic Soc.*, **36** [3] (March 1953).
10. L. A. D'Asaro, Solid-State Electronics, **1** [1], 3 (March 1960).
11. R. M. Barrer, "Diffusion in and through Solids," University Press, Cambridge (1951).
12. C. C. Leiby, Jr. and C. L. Chen, *J. Appl. Phys.*, **31** [2], 268 (1960).

Preparation of Solid Solutions of GaP and GaAs by a Gas Phase Reaction

Frank A. Pizzarello

Chemical Physics Department, Semiconductor Materials Section, Hughes Research Laboratories, Newport Beach, California

ABSTRACT

Homogeneous solid solutions of gallium phosphide and gallium arsenide were synthesized. The synthesis involves the transport of the constituents of the solid solution to a cool substrate by means of a complex reaction with iodine under near-equilibrium conditions. The homogeneity of the samples prepared was demonstrated by x-ray, microscopic, and optical absorption measurements.

Among the first to describe the synthesis of the III-V compounds by a gas phase reaction were Antell and Effer (1). These workers demonstrated that GaAs, GaP, and InP can be successfully synthesized from a mixture of a group III halide and an element of group V. At present, a great deal of work is being devoted to the epitaxial growth of silicon (2) and germanium (3). In these epitaxial growth systems transport of silicon and germanium halides to a substrate occurs either by mixing with a flowing gas or under the influence of a thermal gradient. The substrate temperature is so fixed that deposition takes place by the disproportionation of the silicon and germanium halides.

The technique described in this paper uses the general approach of transport of halides by means of a thermal gradient. The principle advantages of this method of synthesis is that high temperatures, high pressures, and long periods of equilibration are not required to form homogeneous solid solutions.

A mechanical mixture of gallium arsenide and gallium phosphide, together with a measured quantity of iodine, is sealed in a quartz tube that is heated in a furnace of a known temperature gradient. The gallium phosphide-gallium arsenide mixture is placed in the high-temperature zone of the furnace. Material is transported to the cooler zone and deposits on the quartz wall of the reaction vessel as a homogeneous solid solution of gallium phosphide-gallium arsenide. Microscopic examination, x-ray analysis, and optical measurements were made to verify the homogeneous nature of the deposited material.

The net chemical reactions involved in the process can be represented by the following equations:

High-temperature region: Source material

$$4GaP\ (S) + 2I_2\ (g) \rightarrow 4GaI\ (g) + P_4\ (g) \quad [a]$$

$$4GaAs\ (S) + 2I_2\ (g) \rightarrow 4GaI\ (g) + As_4\ (g) \quad [b]$$

Cooler temperature region: substrate

$$4GaI\ (g) + (1-x)P_4\ (g) + (x)As_4\ (g) \rightarrow 4GaAs_xP_{(1-x)}\ (S) + 2I_2\ (g) \quad [c]$$

Reactions [a] and [b] occur at the high source temperature. The gallium iodide, phosphorus, and arsenic formed are transported to the cooler region of the tube by thermal convection. In the cooler region $GaAs_xP_{(1-x)}$ deposits on the walls of the tube as indicated by reaction [c].

Experimental

Mechanical mixtures are prepared by grinding measured quantities of gallium phosphide and gal-

Downloaded on 2019-09-16 to IP 143.215.34.165 address. Redistribution subject to ECS terms of use (see ecsdl.org/site/terms_use) unless CC License in place (see abstract).

Seoul Semiconductor, Exhibit 2001
LGI v. SSC, IPR2019-01154

APPENDIX C

Journal of Electronic Materials, Vol. 19, No. 12, 1990

APPENDIX C

Plasma Enhanced Chemical Vapor Deposition of SiO_2 Films at Low Temperatures Using $SiCl_4$ and O_2

A. ORTIZ and S. LOPEZ

Instituto de Investigaciones en Materiales, UNAM, Apartado Postal 70-360, 04510 Mexico D. F. Mexico

C. FALCONY

Centro de Investigaciones del IPN, Physics Department, Apartado Postal 14-740, 07000 Mexico DF, Mexico

M. FARIAS, L. COTA-ARAIZA, and G. SOTO

Instituto de Fisica, Laboratorio de Ensenada, UNAM, Apartado Postal 2681, Ensenada, CP 22800, BC, Mexico

Silicon dioxide films have been deposited by Plasma-Enhanced Chemical Vapor Deposition (PECVD) technique using $SiCl_4$ and O_2 as reactive materials. Infra-red transmittance, Auger electron spectroscopy analysis, ellipsometry, electrical, and chemical etch measurements have been used to characterize these films. It is possible to obtain good quality oxides at a substrate temperature of 200° C using a low flow of reactant gases. High flow of reactant gases results in highly non-homogeneous porous films. The best oxide films obtained show destructive breakdown at electrical fields above 4 MV/cm and a fixed charge density of the order of 2.6×10^{11} charges/cm^2.

Key words: SiO_2 films, PECVD, Si, insulating films

INTRODUCTION

There is an interest for insulating films deposited at low temperatures with good electronic qualities for applications such as integrated circuits technology and thin film devices based on amorphous materials. The low temperatures are necessary to prevent diffusion of shallow junctions and inter-diffusion of metallic layers in Si based integrated circuits. Also the fabrication of thin film devices on hydrogenated amorphous silicon requires insulating layers deposited at temperatures below those at which hydrogen diffuses out of the α-Si (~300° C). Plasma enhanced chemical vapor deposition (PECVD) is one of the techniques that have been experimented with to deposit insulating films such as SiO_2 and Si_3N_4 films.[1-6] Deposition of SiO_2 films at low temperatures using these technique have resulted in general in a porous, bad electronic quality material with a large concentration of water related impurities.[1-3] In recent work however, it has been reported that good quality oxides can be obtained with PECVD[5,7] or with remote-PECVD[6] by lowering the deposition rate of the oxide using a high flow of inert carrier gas (He). In general, it is likely that some of the byproducts of the chemical reaction remain on the deposited film. In all the cases reported the oxide has been deposited from a mixture of SiH_4 and O_2, N_2O, or CO_2, or deposited from $Si(C_2H_5O)_4$. Therefore it is not surprising to find hydrogen in the films in those cases where no particular care has been taken to minimize the presence of water related species. It has been proposed recently, that the use of silicon halides instead of silane to reduce the amount of hydrogen present during the deposition process by PECVD.[7] $SiCl_4$ and O_2 are an excellent possibility because in this case the only remaining byproduct is Cl. Since one of the major sources of electrical instabilities in oxide films are Na mobile ions this characteristic is advantageous (chlorine is a well known Na passivator used routinely in microelectronics oxidation processes).[8,9] Also, there is a large affinity between hydrogen and chlorine. Thus, chlorine has a hydrogen gettering quality which could result in low O-H content in the films deposited with these materials. In the present work the deposition of SiO_2 films by PECVD using $SiCl_4$ and O_2 is reported. These films have been characterized by infrared (IR) transmission, Auger electron spectroscopy, ellipsometry, electrical, and chemical etch rate measurements.

(Received June 18, 1990; revised August 23, 1990)

EXPERIMENTAL DETAILS

The silicon dioxide films were deposited using a commercial planar system with a 30 kHz power generator. The chamber pressure during deposition was 0.6 Torr (pre-deposition pressure was 10^{-2} Torr) and the power density was 160 mW/cm^2 in all cases reported. The silicon tetrachloride vapors were obtained from a liquid source kept at room temperature for low O_2 flow (sample 5), and at 90° C in the cases of high O_2 flow. The resulting vapors were carried with an oxygen flow of 50 sccm to the deposition chamber (a 3.5 sccm carrier gas flow was used in the case of low O_2 flow). An independent flow of oxygen was fed to the chamber through a

Seoul Semiconductor, Exhibit 2001
LGI v. SSC, IPR2019-01154

flow meter. The oxide films were deposited on crystalline *p*-type Si wafers with a (100) orientation and 25 Ω-cm resistivity. The substrate temperature was kept in the range of 175 to 225° C and the total oxygen flow was varied in the range of 20 to 360 sccm. Table I shows the deposition parameters for the different types of samples tested. The IR transmittance characteristics were obtained with a Nicolet 5-MX Phase Fourier Transform spectrophotometer in the range of 400 to 4600 cm^{-1}. A scanning Auger microprobe (Perkin-Elmer PHI-595) equipped for AES with a single pass cylindrical mirror analyzer and scanning electron microscopy was used for the surface analysis measurements. The background pressure was 2×10^{-10} Torr, and the electron beam energy was 1.5 keV and a 30 nA current. The Auger electrons were collected with the cylindrical mirror analyzer with an energy resolution of 0.5% and were digitally recorded in the E*N(E) mode. The energy increment was 0.5 eV and the signal was averaged over many energy sweeps. The E*N(E) spectra were sequentially smoothed and differentiated with respect to energy by eleven-point and three-point spline routines, respectively. All samples were sputtered with a 1.5 keV Ar beam for 1 to 3 min before the Auger spectra were measured to remove any possible surface contamination. The thickness and refractive index of the films were measured with a Gaertner Mo. L117 ellipsometer using the 630 nm line of a He-Ne laser. The electrical characterization was performed on Metal-Oxide-Semiconductor (MOS) structures fabricated with these oxides deposited on 0.1 Ω-cm *n*-type Si substrate. The metal contacts were aluminum dots 0.14 cm in diameter, thermally evaporated through a metallic mask. After metallization, the devices were given a thermal annealing at 400° C in N_2 for 20 min. The capacitance vs voltage (C-V) measurements of these structures were obtained with a commercial C-V plotter. The current vs voltage (I–V) curves were measured with a log-picoammeter and a ramp voltage generator.

EXPERIMENTAL RESULTS

The deposition rate for oxides obtained with a low O_2 flow was 100 ± 10Å/min and 140 ± 20Å/min for high oxygen flow samples. The thickness of the samples studied were in the range of 400 to 4800Å. Table I shows the deposition parameters as well as the index of refraction (*n*) for the different types of samples tested. The etch rate of low O_2 flow oxides in "P" etch (15 parts of 49% HF, 10 parts of 70% nitric acid, and 300 parts of water)[10] was 8 ± 1Å/sec. For high O_2 flow, it was not possible to determine the etch rate due to the highly non-homogeneous etch of the films. The IR % transmittance spectra, shown in Figs. 1 and 2, present the absorption peaks characteristics of silicon dioxide at ~1075, 800 and 450 cm^{-1}.[11] The spectra for all samples deposited at high oxygen flow (Fig. 1) show also absorption peaks at ~3400 and at 945 cm^{-1} associated with OH and Si-OH and Si-H bonds, respectively.[1,10] The small peak at 1600 cm^{-1} might be associated with water diffused into the oxides after deposition of the films. These peaks are not present

Table I. Deposition parameters and index of refraction for the different types of samples studied. The deposition pressure and the rf frequency were 0.6 Torr and 30 kHz, respectively. The electrode spacing was 1.5 cm.

Sample Type	Ts (°C)	O_2 Flow (cc/min)	*n*
1	175	50	1.5 ± 0.1
2	225	200	2.16 ± 0.3
3	225	360	1.45 ± 0.05
4	175	360	1.3 ± 0.2
5	200	20	1.468 ± 0.005

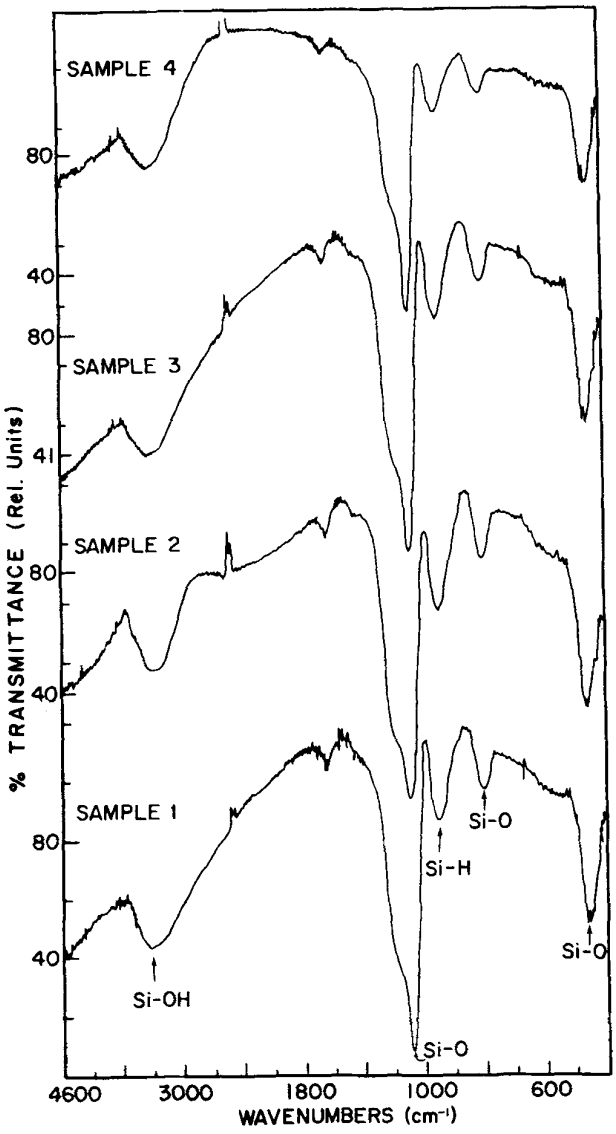

Fig. 1 — IR % transmittance for samples deposited with a high flow of O_2.

Seoul Semiconductor, Exhibit 2001
LGI v. SSC, IPR2019-01154

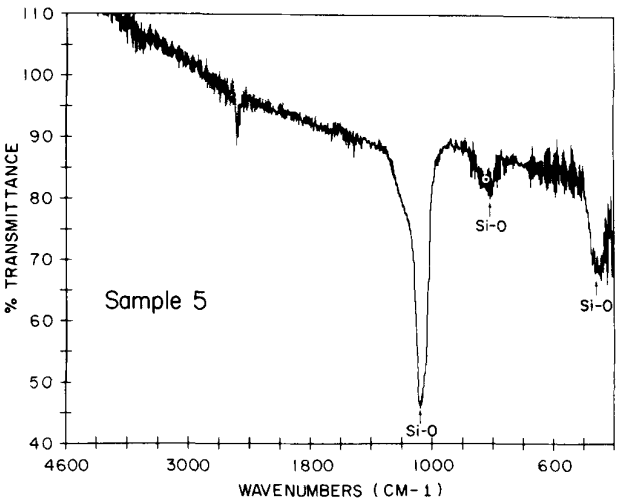

Fig. 2 — IR % transmittance for samples deposited at low O_2 flow.

on the spectra for samples deposited at low O_2 flow, as Fig. 2 shows. Figures 3 and 4 show the Auger spectra of the different types of samples studied. These Auger spectra present the peaks associated with Si (LMM) from SiO at 76 eV and with O (KLL) at 512 eV. The peak associated with Si (LVV) from non-oxydized Si at 92 eV is present only in samples deposited with a high O_2 flow (Fig. 3) indicating that in these samples there is a small quantity of unoxidized Si. Also, the C (KLL) peak at 273 eV is also present in some of these spectra. The presence of this carbon is probably due to post-deposition contamination. No chlorine signal was detected on any of the samples analyzed (minimum amount detectable is 0.1% of a monolayer). Figure 5 shows a typical C-V curve for a MOS structure fabricated with low O_2 flow oxides. These curves did not show any measurable hysteresis effect with the direction of the voltage sweep. If the flat band capacitance for these devices is taken as 0.9 times the oxide capacitance,[12] then an initial flat band voltage shift of 0.5 V can be calculated from Fig. 5. This shift corresponds to a positive fixed charge of 2.6×10^{11} charges/cm^2. Figure 6 shows a characteristic ramp I-V curve for these devices on a semilogarithmic scale. The oxide thickness in this device was 400Å and the ramp rate was 0.75 V/sec. At voltages lower than 15 V there is a displacement current of the order of 10^{-9}A; however, the current at these voltages in point by point measurements was of the order of 10^{-11}A. Above 15 V an electron current across the device is measured, and destructive breakdown was observed to occur at voltages higher than 17 V (electric fields higher than 4 MV/cm).

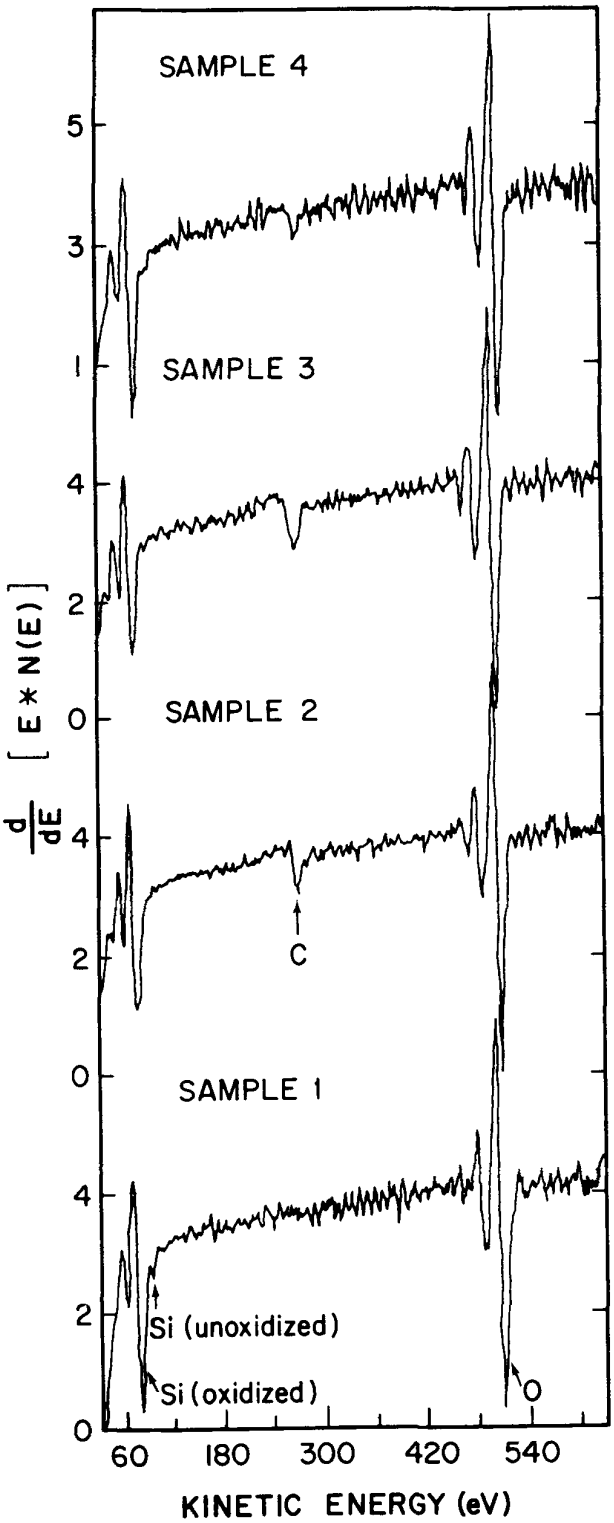

Fig. 3 — Auger spectra for SiO_2 films deposited with a high flow of O_2. The amplitude of each spectrum was scaled to obtain the same magnitude of the oxygen peak for all cases.

DISCUSSION AND CONCLUSIONS

The IR transmittance characteristics of films deposited with a high O_2 flow, indicate the presence of stoichiometric SiO_2. In particular the absorption peak at 1075 cm^{-1} has no substantial shift towards smaller wavelength numbers as expected from SiO_x with $x < 2$.[11] On the other hand, there is a large variation of the index of refraction measured in these

Seoul Semiconductor, Exhibit 2001
LGI v. SSC, IPR2019-01154

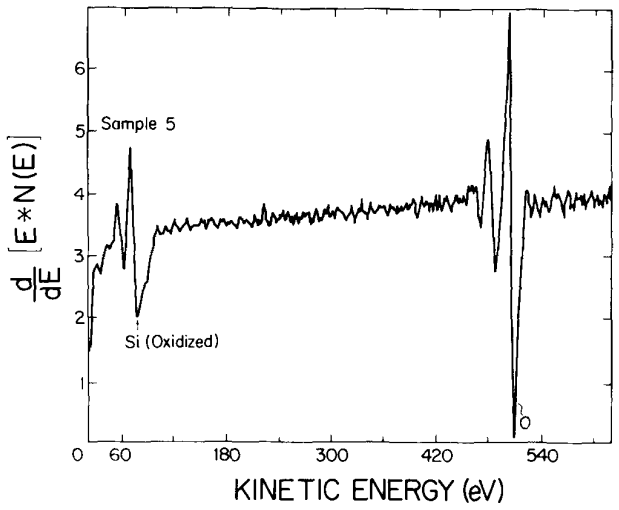

Fig. 4 — Auger spectra for oxides deposited at low O_2 flow.

films and the Auger spectra show a small peak for non-oxidized Si in some cases. These observations together with the highly non-uniform etch rate with the "P" etch indicate that these samples are porous[10] and in some cases, probably composed of two phases (Si aggregates in SiO_2). In the case of oxides deposited at low O_2 flow, the refraction index, the Auger spectra, and the IR % transmittance curves are close to those expected from a stoichiometric SiO_2. Also the etch rate with "P" etch is comparable to that of the best oxides obtained with chemical vapor deposition techniques (CVD) at much higher temperatures (thermal SiO_2 has an etch rate of 2Å/sec, and CVD oxides a rate of 16Å/sec).[5] It appears that by lowering the reactant gases flow and the deposition rate a better overall quality oxide is obtained. Nevertheless, these modifications on the deposition parameters do not explain the fact that no O-H related peaks are observed in the IR % transmittance spectra of these oxides. It is assumed that because of its porosity, the oxides deposited with high O_2 flow did not acquire water related impurities during the deposition process but afterwards when exposed to

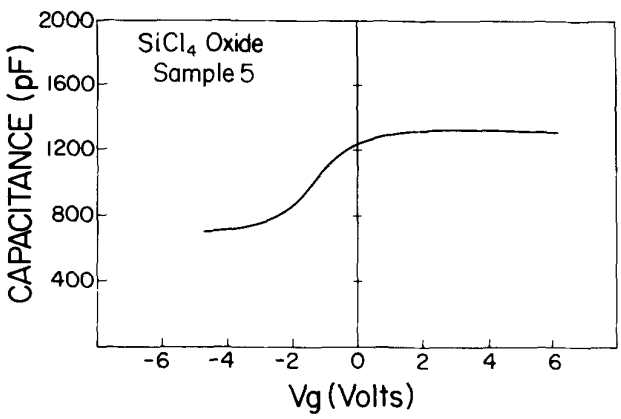

Fig. 5 — Capacitance vs voltage characterisic curve for oxides deposited at low O_2 flow.

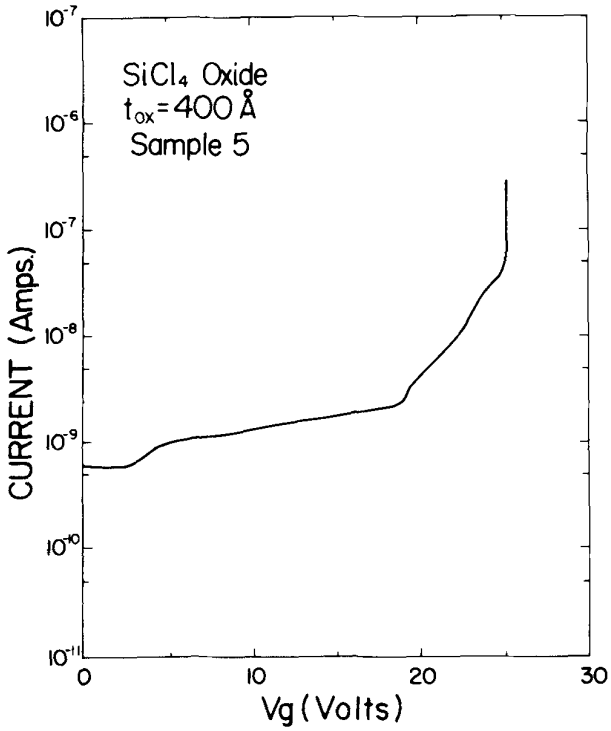

Fig. 6 — Ramp I-V characteristic curve for SiO_2 films deposited with a low flow of O_2.

the ambient humidity. In general, chlorine has a large affinity for hydrogen, thus one would expect the residual gases to act in this process as hydrogen getters, and consequently the deposited oxides to be relatively free of hydrogen impurities; even though no particular care was taken in obtaining good predeposition vacuum conditions. The electrical characteristics of the oxides deposited at low O_2 flow show good insulating qualities at electric fields lower than 4 MV/cm. The C-V curves of these oxides show no measurable hysteresis effects due to interface states or mobile ions. The fixed charge measured (2.6×10^{11} charges/cm^2) is comparable to that obtained with oxides deposited at higher temperatures.

In summary, SiO_2 films have been deposited by plasma enhanced chemical vapor deposition technique at low temperatures using $SiCl_4$ and O_2 as reactant gases. The quality of the oxide films is strongly dependent on the deposition parameters. IR transmittance results show the characteristic absorption peaks associated with stoichiometric SiO_2 for all deposition conditions studied. However, the analysis by Auger spectroscopy, the index of refraction obtained by ellipsometry, and the chemical etch rate of these oxides indicate that high flows of reactant gases result in highly non-uniform and porous films. Low flows of reactant gases resulted in better quality oxides with good electrical characteristics considering the low temperatures at which they were deposited. The use of $SiCl_4$ as reactant gas has the advantage over SiH_4 of having as byproduct of the deposition Cl or Cl containing species which favor the quality of the oxide films by acting as sodium

Seoul Semiconductor, Exhibit 2001
LGI v. SSC, IPR2019-01154

passivator and probably as hydrogen gettering agents.

ACKNOWLEDGEMENTS

The authors would like to acknowledge the technical assistance of M. A. Canseco, E. Martinez, J. Garcia-Coronel and M. Guerrero. This work was partially supported by CONACyT and CONACyT-NSF.

REFERENCES

1. A. C. Adams, Solid State Technol. *26,* 135 (1983).
2. R. H. Vogel, S. R. Butler, and F. J. Feigl, J. Electron. Mater. *14,* 329 (1985).
3. M. E. Zvanut, F. J. Feigl, S. R. Butler and S. L. Titcomb, J. Electron. Mater. *14,* 343 (1985).
4. C. Kaya, T. P. Ma and R. C. Barker, J. Appl. Phys. *64,* 3958 (1988).
5. J. Batey and E. Tierney, J. Appl. Phys. *60,* 3136 (1986).
6. G. Lucovsky, P. D. Richard, D. V. Tsu, S. Y. Lin and R. Markunas, J. Vac. Sci. Technol. *A4,* 681 (1986).
7. C. Falcony, A. Ortiz, S. Lopez, J. C. Alonso and S. Muhl, Thin Solid Films (1990).
8. A. Rohatgi, S. R. Butler, F. J. Feigl, H. W. Kraner and K. W. Jones, Appl. Phys. Lett. *30,* 104 (1977).
9. R. J. Kriegler, Appl. Phys. Lett. *20,* 449 (1971).
10. W. A. Pliskin and H. S. Lehman, J. Electrochem. Soc. *112,* 1013 (1965).
11. P. G. Pai, S. S. Chao, Y. Takagi and G. Lucovski, J. Vac. Sci. Technol. *A4,* 689 (1986).
12. S. M. Sze, "Physics of Semiconductor Devices," 2nd Ed. (J. Wiley & Sons, NY), p. 376 (1981).

Seoul Semiconductor, Exhibit 2001
LGI v. SSC, IPR2019-01154

APPENDIX D

Room temperature synthesis of porous SiO_2 thin films by plasma enhanced chemical vapor deposition

A. Barranco, J. Cotrino, F. Yubero, J. P. Espinós, and A. R. González-Elipe

Citation: Journal of Vacuum Science & Technology A **22**, 1275 (2004); doi: 10.1116/1.1761072
View online: https://doi.org/10.1116/1.1761072
View Table of Contents: https://avs.scitation.org/toc/jva/22/4
Published by the American Vacuum Society

ARTICLES YOU MAY BE INTERESTED IN

Low-temperature plasma enhanced chemical vapor deposition of SiO_2
Applied Physics Letters **65**, 3185 (1994); https://doi.org/10.1063/1.112475

Atomic structure in SiO_2 thin films deposited by remote plasma-enhanced chemical vapor deposition
Journal of Vacuum Science & Technology A **7**, 1136 (1989); https://doi.org/10.1116/1.576242

Review Article: Stress in thin films and coatings: Current status, challenges, and prospects
Journal of Vacuum Science & Technology A **36**, 020801 (2018); https://doi.org/10.1116/1.5011790

Surface chemistry of atomic layer deposition: A case study for the trimethylaluminum/water process
Journal of Applied Physics **97**, 121301 (2005); https://doi.org/10.1063/1.1940727

Plasma deposition of optical films and coatings: A review
Journal of Vacuum Science & Technology A **18**, 2619 (2000); https://doi.org/10.1116/1.1314395

Thermal expansion coefficient of polycrystalline silicon and silicon dioxide thin films at high temperatures
Journal of Applied Physics **87**, 4189 (2000); https://doi.org/10.1063/1.373050

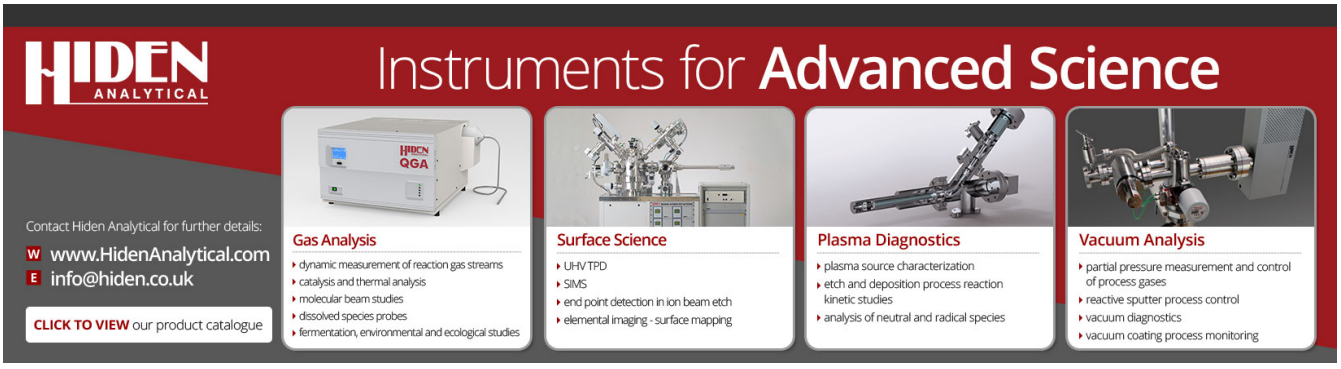

Room temperature synthesis of porous SiO_2 thin films by plasma enhanced chemical vapor deposition

A. Barranco
Instituto de Ciencia de Materiales de Sevilla (CSIC-Universidad de Sevilla) Avda, Américo Vespucio s/n, E-41092 Sevilla, Spain and Dpto. de Química Inorgánica, Facultad de Química, Avda, Reina Mercedes s/n, Sevilla, Spain

J. Cotrino
Instituto de Ciencia de Materiales de Sevilla (CSIC-Universidad de Sevilla) Avda, Américo Vespucio s/n, E-41092 Sevilla, Spain and Dpto. de Física Atómica, Molecular y Nuclear, Facultad de Física, Universidad de Sevilla, Avda, Reina Mercedes s/n, Sevilla, Spain

F. Yubero, J. P. Espinós, and A. R. González-Elipe[a)]
Instituto de Ciencia de Materiales de Sevilla (CSIC-Universidad de Sevilla) Avda, Américo Vespucio s/n, E-41092 Sevilla, Spain and Dpto. de Química Inorgánica, Facultad de Química, Avda, Reina Mercedes s/n, Sevilla, Spain

(Received 10 July 2003; accepted 19 April 2004; published 16 July 2004)

Silicon dioxide thin films with variable and controlled porosity have been prepared at room temperature by plasma enhanced chemical vapor deposition in an electron cyclotron resonance microwave reactor with a downstream configuration. The procedure consists of the deposition of successive cycles consisting of a sacrificial organic-polymeric layer and, afterward, a silicon dioxide layer. Toluene and oxygen are used as precursors of the organic layers and $Si(CH_3)_3Cl$ and oxygen for the SiO_2. During deposition of the latter, the organic layer is simultaneously burned off. In these conditions, the release of gases produced by oxidation of the organic-polymeric layer take place while the oxide layer is being deposited. Thus, modification of the nucleation and growing mechanism of the silicon oxide thin film take place. The porosity of the final porous SiO_2 thin films increases with the thickness of the sacrificial organic layer. The porous SiO_2 films prepared with the aforementioned method are free of carbon and chlorine contamination as confirmed by Fourier-transform infrared spectroscopy, x-ray photoelectron spectroscopy, and Rutherford backscattering spectroscopy. Depending on their porosity, the SiO_2 thin films are either transparent or scattered visible light. The former have refractive index lower than that of thermal silicon dioxide and the latter show membranelike behavior in gas diffusion experiments. All the samples have good adhesion to the substrates used for the deposition, either polished Si wafer, glass plates, or standard porous supports. They have columnar microstructure, as determined by scanning electron microscopy. A preliminary ultraviolet-visible characterization of the optically transparent thin films reveals that transmission of light through glass increases by 7%–8% when the porous silica is deposited on this substrate. These films prove to be very efficient as antireflective coatings and are of interest for photovoltaic and similar applications. It is possible to deposit SiO_2 thin films with densities as low as 0.65 g/cm^3 (corresponding to a porosity of 70%) by adjusting the thickness of the sacrificial and SiO_2 layers. The films with high porosity are promising materials for the fabrication and/or modification of diffusion membranes. The gas adsorption properties and the type of porosity of the SiO_2 thin films are assessed by adsorption isotherms of toluene at room temperature measured with a quartz crystal monitor device. The gas permeation properties of the films (when used as membranes) are analyzed by studying the diffusion rate of different gases through them. © *2004 American Vacuum Society.* [DOI: 10.1116/1.1761072]

I. INTRODUCTION

Fabrication of porous metal oxide thin films with controlled porosity has received much attention during recent years. They are used as antireflective coatings in optics and photovoltaic applications,[1–3] and in electronics as low-*k* materials,[4–6] where relatively thin films are deposited on compact substrates. They are also used as diffusion membranes for separation and purification of fluids.[7–10] In this latter case, thicker films deposited on porous and polycrystalline substrates are required. Furthermore porous layers are used as biosubstrates since the roughness of substrates is a very effective parameter to control the growth and proliferation of cells.[11]

Porous SiO_2 thin films used as membranes or similar applications can be prepared by either wet (sol-gel, etc.) or dry procedures.[3,7–10] Wet routes have been also used for the preparation of many other oxide thin films with controlled microstructure and porosity.[10,12–15] When using sol-gel and other wet or ceramic methods, the synthesis of membrane films involves some heating stages to remove solvents, in-

[a)]Author to whom correspondence should be addressed; electronic mail: agustin@cica.es

Seoul Semiconductor, Exhibit 2001
LGI v. SSC, IPR2019-01154

duce sintering, etc., particularly if the substrate is a ceramic material. However, for other applications or if the membrane is a polymer or any heat-sensitive material, heating steps may have to be avoided and other methods such as evaporation or plasma enhanced chemical vapor deposition (PECVD) are required.

The synthesis of porous thin films can also be achieved by using template procedures. An easily removable material (usually organic) serves to incorporate the inorganic component with a defined morphology, being then removed by combustion or similar methods.[10,16,17] After removing the template, voids are left in the inorganic or ceramic part of the porous film, thus defining a microstructural arrangement that replicates the distribution of the template. Usually, the removal of the template requires a heating stage with the aforementioned inconveniences.

The method described in this article for the deposition of porous thin films resembles the template approach described above. Thus, an organic material that acts as a sacrificial layer is used in the procedure. This organic material is removed simultaneously to the deposition of the silicon dioxide by PECVD.

Preparation of porous SiO_2 coatings in photovoltaic cells by PECVD has recently been reported.[2] The synthesis was carried out in a microwave reactor with SiH_4 as a precursor of Si and N_2O as plasma gas. The control of porosity of these thin films was achieved by adjusting deposition parameters such as the geometry of the reactor, pressure during deposition, etc. However, these variables mainly act by altering the gas phase deposition and agglomeration, so that porosity results from the accumulation of oxide aggregates coming from the gas phase. However, in such a case the obtained layers usually have poor mechanical properties. Also, remote PECVD has been a widely utilized procedure for deposition of SiO_2,[18–20] although the main purpose of these works was not the preparation of thin films with controlled porosity.

In the present article, we propose a PECVD procedure for the room temperature synthesis of porous oxide thin films.[21] The method provides an effective control of film porosity within a large range of values. The procedure consists of the deposition of an organic material that is subsequently removed during the formation of the SiO_2 film. The porosity correlates with the thickness of the organic and oxide layers. The final oxide thin films have good adhesion and mechanical stability, even when the films' porosity is very high. A critical point of this procedure is the requirement that both deposition of the inorganic layer and removal of the organic polymer occur simultaneously. This is accomplished by depositing an organic layer with a high oxygen concentration. Recently, we have reported on the PECVD deposition of such an organic thin film by using oxygen and toluene as precursors.[22]

This article describes the experimental procedure and presents some results of the characterization of porous SiO_2 thin films with different porosities and light scattering properties. These films have been obtained by changing the relative thickness of the organic and inorganic layers. A set of applications of these thin films are also reported to demonstrate the ample variety of porous structures that can be tailored by this method of synthesis. Thus, transparent SiO_2 thin films are examined as antireflective coatings, while SiO_2 thin films with very high porosities and low densities are used for the modification of diffusion properties of commercial membranes. Finally, a phenomenological model is proposed that accounts for the development of porosity during growth based on the characterization of the porous SiO_2 films and their growth rate.

II. EXPERIMENT

A. Preparation of porous SiO_2 thin films

The PECVD procedure to control the porosity of the SiO_2 thin films consists of the deposition of intermediate polymeric oxygenated layers (C_xO_y:H), and subsequently, SiO_2 thin films. The polymeric layer is easily removed by plasma oxidation under the experimental conditions utilized for the deposition of SiO_2. Several deposition cycles are carried out sequentially to control the porosity of the films. In each cycle, an organic film and a SiO_2 thin film are deposited.

Deposition of oxygen-rich organic layers and porous SiO_2 thin films are carried out sequentially in the same reactor. It consists of a remote microwave plasma source (SLAN) supplied with magnets to achieve electron cyclotron resonance (ECR) working conditions. This source is separated from the deposition chamber by a metallic grid preventing the microwave irradiation of the substrates. The distance from the substrates to the grid is ~10 cm. Basically, the SLAN system consists of an annular waveguide (ring resonator) with axial slot antennas positioned azimuthally at regular intervals of the waveguide's inner side. The ring resonator surrounds the plasma chamber that consists of a quartz bell jar with a diameter of 16 cm and a height of 20 cm. An ion concentration of 10^{11} cm^{-3} is achieved at the SLAN center. The concentration decays downstream and the average electron density and energy shows the same behavior. An estimation of ion concentration and average electron energy close to the substrate position gives values of 10^9 cm^{-3} and 1 eV, respectively. Typical ion energies range from 5 to 10 eV. Under these working conditions, a sheath potential results in the substrate where it is expected that a very low energy ion bombardment induces minimum damage. A more detailed description of the source and experimental setup has been published previously.[22–25] The source is fitted to a deposition chamber, where a base pressure lower than 10^{-6} Torr can be obtained with a turbomolecular pump. The toluene and $Si(CH_3)_3Cl$ flows were dosed over the sample holder with a shower-type annular dispenser placed 6 cm from the substrate to ensure its homogeneous spatial distribution. Oxygen was dosed directly into the plasma source. Oxygen, toluene, and $Si(CH_3)_3Cl$ flows were controlled with mass flow controllers. The organic and the SiO_2 layers were prepared under completely different working conditions of the source, although in both cases a plasma of oxygen was used to induce the deposition. SiO_2 thin films were deposited at 2

Seoul Semiconductor, Exhibit 2001
LGI v. SSC, IPR2019-01154

$\times 10^{-2}$ Torr using 5 sccm of the organosilicon precursor, 20 sccm of oxygen, and 200 W of microwave power.[24]

Deposition of the organic sacrificial layer was possible only when the working parameters were adjusted around the following values: microwave power 600 W, oxygen/toluene flow ratio 4:1, and total pressure ~1 Torr. To get these conditions, a very precise adjustment was required of the mass flow controllers and the pumping capacity of the system, this latter with a throttle valve placed prior to a primary pump. At lower pressures, the organic layer was always burned out by the oxygen plasma and no deposition of the organic polymer was detected. The material of the organic layer was a highly oxygenated polymer with a high concentration of COO-, C═O, and C–OH groups. An important characteristic of this polymeric-like thin film is that it is easily removed by the plasma of oxygen used for SiO_2 deposition. Under these conditions, an etching rate of about 200 nm/min was determined for the polymer. This value is lower than rates selected for the deposition of the silicon oxide (~16 nm/min).[24] It seems critical that this sacrificial layer has a very high O/C ratio and, consequently, that the PECVD protocol of preparation of this polymeric layer utilizes an oxygen rich plasma. More details about the synthesis, characterization and properties of these highly oxygenated polymeric thin films, including their etching properties under oxidizing plasma treatments, have been published recently.[22]

B. Chemical and microstructural characterization

Chemical and microstructural characterization of the thin films was studied using several techniques. Chemical analysis was carried out by Rutherford backscattering spectroscopy (RBS), electron recoil detection analysis (ERDA), and x-ray photoelectron spectroscopy (XPS). Fourier-transform infrared spectroscopy (FTIR) was also used to verify the removal of organic functional groups after deposition of the inorganic silicon dioxide. Meanwhile, assessment of microstructure was done by observation of samples by scanning electron microscopy (SEM), atomic force microscopy (AFM), and the measurement of gas adsorption isotherms with a quartz crystal microbalance (QCM).

RBS and ERDA measurements of porous SiO_2 thin films deposited on polished Si(100) wafers were performed at the Ion Accelerator ARAMIS (Orsay, France) by using 1.5 and 3.0 MeV α^{++} particles, respectively. The RBS spectra were recorded in channeling conditions. The quantification of the measured ion spectra was performed by means of the RUMP code.

XPS spectra were acquired in a VG-ESCALAB 210 spectrometer working in the constant pass energy mode with a value of 20 eV. Unmonochromatized Mg Kα radiation ($h\nu = 1253.6$ eV) was used as excitation source.

FTIR spectra in the 400–4000 cm^{-1} energy range were collected in transmission mode at normal incidence in a Nicolet 510 spectrometer for samples deposited on intrinsic Si wafers.

Images of the surface of the porous SiO_2 thin films deposited on Si(100) wafers were taken with a JEOL-JSM5400 SEM microscope after metallization of the surface of the samples. Cross-section SEM images were also obtained for SiO_2 thin films deposited on either aluminum foil or Si(100) wafers properly cut for examination. The thicknesses of the films were obtained from either these cross-sectional SEM images and also by using a DekTak profilometer. AFM surface images were also obtained in air by using a Topometrix Explorer microscope working in the noncontact mode. Both topographic (constant force) and direct signal (constant height) images were acquired. The cantilever, with a spring constant of 42.6 $N\,m^{-1}$, was oscillated at 130 kHz. Amplitude reduction was monitored while the surface was scanned at a typical rate of one line per second. The scanner was calibrated in X, Y, and Z directions with gratings provided with the equipment.

Adsorption isotherms were measured by means of a QCM in a temperature controlled vacuum chamber. In this case, porous SiO_2 thin films were deposited on the quartz oscillators used in the QCM. Thus, toluene adsorption isotherms were measured at 292 ± 0.8 K. This procedure has been previously applied for the characterization of thin films and provides a qualitative assessment of their porous structure.[26,27]

C. Optical and gas diffusion properties

Porous SiO_2 thin films can find applications as optical coatings and gas diffusion membranes.

Ultraviolet-visible (UV-vis) transmission spectra at normal incidence of samples deposited on glass plates were obtained with a Shimadzu UV-2101PC spectrometer.

Measurements of gas diffusion through porous SiO_2 thin films acting as membranes were carried out in a homemade apparatus consisting of two chambers (chambers 1 and 2) separated by the membrane. The experimental procedure to get the permeability of a membrane to a gas A (Π_A) was the following. Chamber 2 was set initially under vacuum and chamber 1 under a certain pressure of a gas (P_1). Then, the variation of the pressure with time in chamber 2 ($\Delta P_2/\Delta t$) was monitored. In these conditions, Π_A can be determined using the equation[12,28]

$$\Pi_A = \frac{d}{A(P_1 - P_2)} \frac{V_2}{RT} \frac{\Delta P_2}{\Delta t},$$

where d is the thickness of the membrane, V_2 is the volume of chamber 2, A the membrane area, T is the temperature, and R the ideal gas constant. The ideal separation factor of a membrane for two gases A and B, α_B^A, can be determined as $\alpha_B^A = \Pi_A/\Pi_B$. To carry out this analysis, the porous silicon dioxide thin films were deposited on commercial alumina porous substrates Anodisc 47 from Anopore with nominal pore sizes of 100 and 20 nm (in the following Anodisc-100 and Anodisc-20, respectively).

III. RESULTS AND DISCUSSION

A. Composition of the porous silicon oxide thin films

The method of preparation of porous SiO_2 thin films consists of depositing the silicon oxide by PECVD using ECR

Seoul Semiconductor, Exhibit 2001
LGI v. SSC, IPR2019-01154

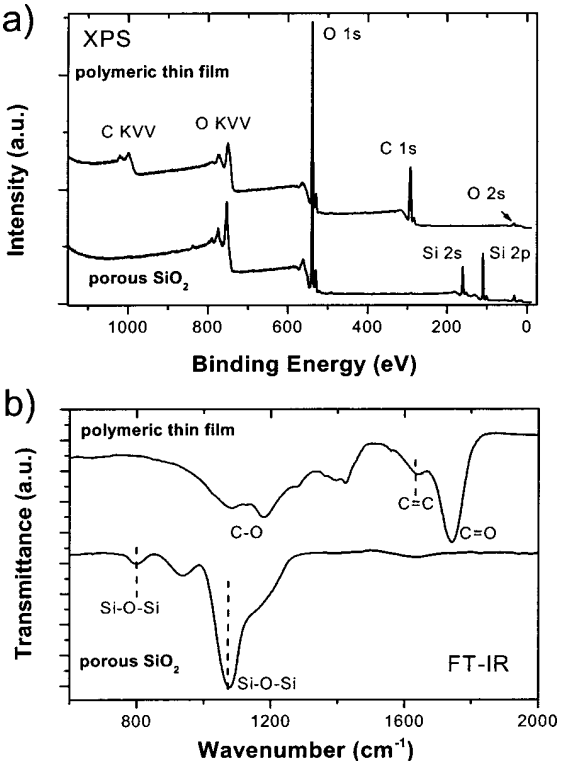

FIG. 1. (a) XPS spectra of a sacrificial organic layer of ~45 nm thick and the film resulting from the deposition of a ~220 nm SiO_2 thin film on top it. (b) FTIR spectra for the same samples.

conditions that are very effective for the complete removal of a previously deposited organic sacrificial layer. It is critical that during this process, total removal of the organic layer is accomplished and that, therefore, the final SiO_2 thin film is free from any organic contaminant. Survey XPS spectra of the sacrificial organic layer and after deposition of a SiO_2 layer on this sacrificial layer are shown in Fig. 1(a). Note that the sacrificial layer shows only peaks due to C and O atoms that evidences the presence of a highly oxygenated organic layer. After deposition of the SiO_2 film, the C1*s* peak disappears from the spectrum, indicating that no carbon contamination remains in the sample. Moreover, only peaks attributed to silicon (in particular Si^{4+} species) and oxygen atoms can be seen in this spectrum.

Since XPS is a surface sensitive probe, we have also used channeling RBS to prove the absence of carbon in the SiO_2 layers. Thus, we found that the bulk compositions of the films are stoichiometric silicon dioxide and that their carbon content is below the detection limit of this technique.

Figure 1(b) shows the FTIR spectra corresponding to the sacrificial layer (top) and a SiO_2 deposit on this sacrificial layer (bottom). In the FTIR spectrum of the sacrificial layer there are signals due to C and O groups[22,29] (i.e., C—O, C═O, C═C, etc.) typical of a highly oxygenated organic polymeric layer. After silicon oxide deposition, the signals of carbon-oxygen groups completely vanish, indicating that no carbon remains in the sample after this treatment. Note also

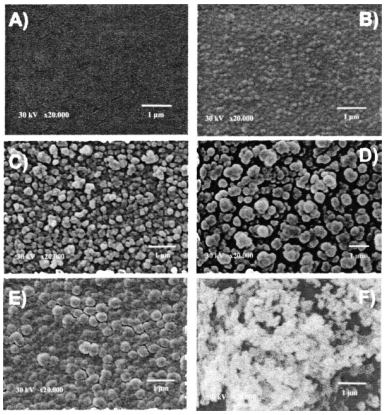

FIG. 2. SEM micrographs of SiO_2 thin films with increasing porosities. The preparation protocols of samples A–F are reported in Table I.

that, the FTIR spectrum after removal of the organic groups depicts the typical bands of SiO_2.[24,30,31]

B. Microstructure of the SiO_2 thin films

Control of the porosity of the SiO_2 thin films is achieved by adjusting the thicknesses of the polymeric C_xO_y:H and SiO_2 layers. As an example of the possibilities of the method, Figs. 2(a)–2(d) shows a series of SEM micrographs of SiO_2 thin films with a similar total thickness of ~600 nm but increasing porosity. These samples have been prepared by different preparation protocols consisting of two cycles of deposition. In each cycle, an organic thin film (i.e., the polymeric C_xO_y:H described below) and a SiO_2 thin film are deposited. The preparation protocols of these samples are shown in Table I. Deposition is carried out in two steps and the thickness of the organic and inorganic materials has been adjusted to achieve the desired porosities. It is apparent in this set of micrographs that, for a constant thickness of the final SiO_2, the porosity increases as the thickness of the organic phase increases.

However, for the same thickness of the sacrificial organic layer, the final microstructure of the films also depends on the final thickness of the oxide film. An example of the effect of the thickness of the intermediate oxide films in the final microstructure of the porous films is evidenced by the comparison of Figs. 2(d) and 2(e). The corresponding films are obtained by two cycles with similar polymeric films, but different thickness of the final oxide films (cf. Table I). It is possible to see that as the thickness of the oxide layers increases, the percolation degree of the individual aggregates (i.e., the degrade of interconnection among them) of the layer increases and the final structure at the surface becomes more compact.

It can be also seen in this figure that the percolation degree of the SiO_2 aggregates is relatively high, and the pore size small, when the oxide is deposited on top of an organic layer of ~25 nm [i.e., Fig. 5(b)]. For an organic layer thinner than approximately 25 nm, the final SiO_2 thin films, although still having much porosity, are transparent and do not present any observable light scattering. However, SiO_2 films pre-

Seoul Semiconductor, Exhibit 2001
LGI v. SSC, IPR2019-01154

TABLE I. Preparation protocols of selected porous SiO_2 samples.

Sample	Step 1	Step 2	Substrate	Density (g/cm^3)	Porosity (%)
A	600 nm SiO_2	–	Si(100)	1.98	10.0
B	25 nm C_xO_y:H+ 150 nm SiO_2	25 nm C_xO_y:H+ 450 nm SiO_2	Si(100)	1.66	24.6
C	40 nm C_xO_y:H+ 150 nm SiO_2	40 nm C_xO_y:H+ 450 nm SiO_2	Si(100)	1.25	43.2
D	60 nm C_xO_y:H+ 150 nm SiO_2	60 nm C_xO_y:H +450 nm SiO_2	Si(100)	1.10	55.4
E	60 nm C_xO_y:H+ 475 nm SiO_2	60 nm C_xO_y:H+ 475 nm SiO_2	Si(100)	1.56	29.4
F	250 nm C_xO_y:H+ 150 nm SiO_2	250 nm C_xO_y:H+ 375 nm SiO_2	Si(100)	0.78	64.5
G	40 nm C_xO_y:H+ 275 nm SiO_2	40 nm C_xO_y:H+ 275 nm SiO_2	Al sheet	–	–
H	7 cycles (50 nm C_xO_y:H+275 nm SiO_2)		Al sheet	–	–

pared after deposition of thicker organic films had a milky appearance due to light dispersion in the individual aggregates or columns of SiO_2.

The micrographs in Fig. 2 also show that by controlling the thickness of the oxide and polymeric layers, it is possible to achieve precise control of the final pore size and concentration of the films. With our procedure, successive deposition of different oxide layers with specific and tailored porosity would permit the fabrication of thin films with variable in-depth porosity and optical properties. This type of thin film with gradient porosity is of interest for certain type of optical filters, the so-called rugate filters.[32,33]

The microstructure of the SiO_2 samples was of the columnar type in all cases, except when deposited on top of a very thick organic film (i.e., 250 nm). In this case, Fig. 2(f) shows that the film has a granular microstructure. This sample is the result of the aggregation of small powdered particles and, therefore, this film's mechanical stability was very poor. To illustrate the columnar growth of the porous thin films, Fig. 3 shows two cross-sectional views of SiO_2 samples deposited on an aluminum foil. Both views depict a well-defined columnar microstructure. Sample G in this figure corresponds to a film deposited by two cycles C_xO_y:H polymer/SiO_2, while sample H corresponds to a thick film obtained after seven cycles of deposition of organic and inorganic layers (cf. Table I). The micrograph of this latter sample clearly shows that a common columnar microstructure develops independently of the final thickness of the films (i.e., ~500 and ~2850 nm for the films shown in Figs. 3(g) and 3(h), respectively) and of the number of cycles used for deposition of the film. No boundary interfaces between the intermediate individual SiO_2 layers can be detected in sample G. This proves that the final porous thin films are homogeneous in thickness, even for several deposition-removal steps of the sacrificial organic layers.

A similar microstructure to that reported in Fig. 3, with vertical pores and columns, was found for all the samples, although the pore size and type of columns depend on the actual preparation conditions used in each case. Such a columnar microstructure does not develop in the SiO_2 films deposited at 2×10^{-2} Torr without deposition of the intermediate polymeric films (i.e., sample A in Table I). The development of columns in the porous thin films is justified by a phenomenological model described below.

AFM images were taken to study the surface morphology and growing mechanisms of the porous SiO_2 thin films. Figure 4(a) shows the surface of a dense SiO_2 thin film (i.e., prepared without mediation of the intermediate organic layer) of ~110 nm thickness and Fig. 4(b) that of an porous oxide film of a similar thickness grown onto a previously deposited organic layer of ~25 nm. At first glance, the

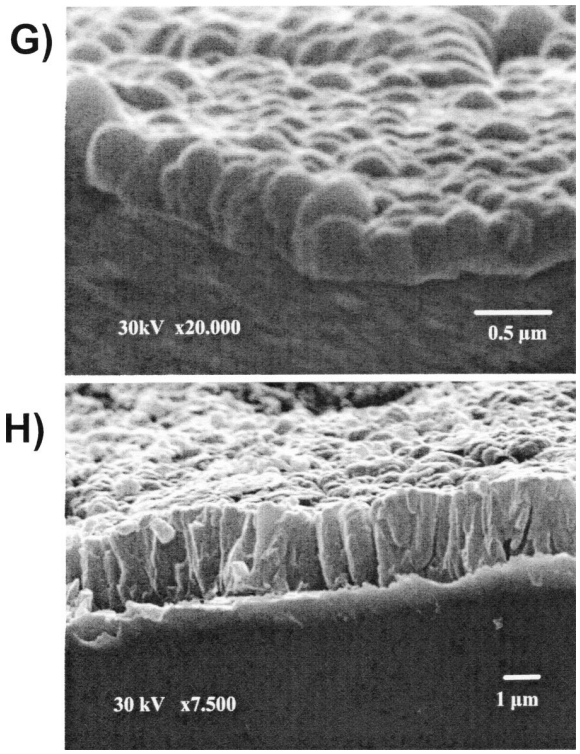

FIG. 3. Cross-sectional SEM micrograph corresponding to samples G and H in Table I.

Seoul Semiconductor, Exhibit 2001
LGI v. SSC, IPR2019-01154

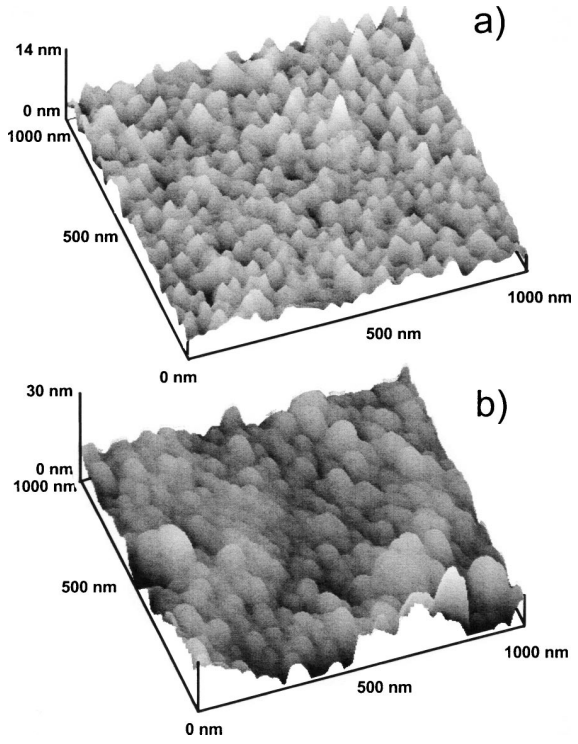

FIG. 4. AFM images of dense (a) and porous (b) SiO_2 thin films prepared by PECVD. The films have a thickness of ~100 nm. The porous layer has been prepared according to the protocol 20 nm C_xO_y:H+100 nm SiO_2.

latter depicts a more corrugated aspect than the former. The statistical analysis of the particle size distributions, depicted in Fig. 5 in the form of bearing plots, shows that the mean size of the aggregates in the porous sample is higher by 11.5 nm than that in the compact thin film, although the size dispersion profiles are similar in both cases. A rather homogeneous size distribution points to a growth mechanism controlled by the aggregation of material to a given number of initially formed nuclei and not to a complex process involving both growth of particles and formation of new nuclei.

The density ρ of the films was determined from the Si, O, and H atomic surface concentration (by means of channeling-RBS and ERDA measurements) and the film

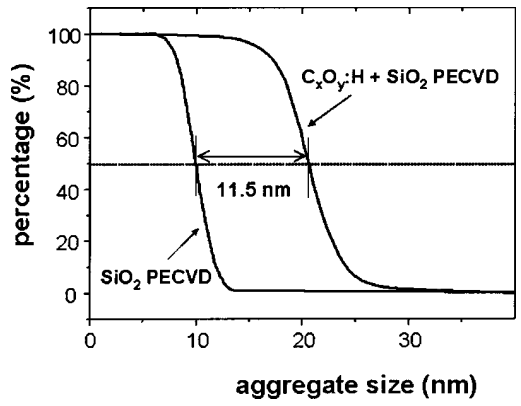

FIG. 5. Bearing plots of samples whose AFM images are reported in Fig. 4.

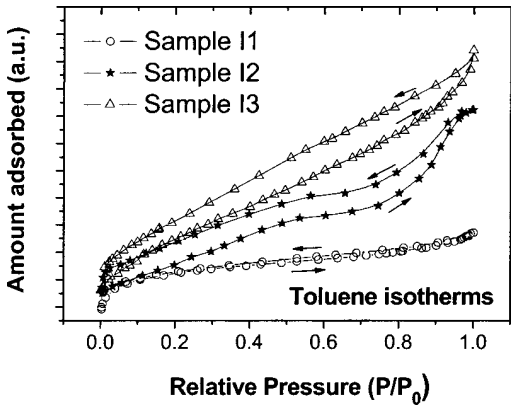

FIG. 6. Selected adsorption/desorption isotherms of toluene vapor on porous thin films I1, I2, and I3 (see text).

thickness obtained by cross-sectional SEM images and/or profilometry. The porosity Γ of each film was calculated using the relationship $\Gamma = 100 \times (1 - \rho/\rho_s)$, where ρ_s corresponds to the density of compact bulk silica[34] ($\rho_s = 2.20\ \mathrm{cm}^3/\mathrm{g}$). Our results show that it is possible to control the density of the SiO_2 films in the range 1.98–0.65 g/cm^3, i.e., a set of values which corresponds to porosities from 10% to 65%. Table I lists the density and porosity of the films whose SEM micrographs have been shown in Fig. 2. The reported values clearly prove that for a fixed thickness of the intermediate oxide film used in the cycles, the thicker the organic sacrificial layer, the larger the porosity, and the smaller the density of the porous silicon oxide thin films.

The analysis of the adsorption–desorption isotherms of a gas or vapor in a material provides information about its porous microstructure.[35] In the present work, we have used a QCM to measure gas adsorption isotherms in our thin films according to the procedure described in the experimental section. A similar procedure has been used for the analysis of porosity of silica thin films using nonpolar adsorbates.[26,27] Figure 6 shows three selected adsorption/desorption isotherms of toluene carried out on three thin films with well differentiated adsorption properties. The isotherms correspond to samples I1 (3 cycles of 8 nm C_xO_y:H+300 nm SiO_2), I2 (4 cycles of 30 nm C_xO_y:H+150 nm SiO_2), and I3 (4 cycles of 70 nm C_xO_y:H+100 nm SiO_2). The shapes of the isotherms of samples I1, I2, and I3 in Fig. 6 are close to types I, IV and II of The International Union of Pure and Applied Chemistry (IUPAC) classification,[35] respectively. According to this classification, the pores are characterized by their average width w, i.e., the diameter of a cylindrical pore, or the distance between the sides of a slit-shaped pore. Type II and IV isotherms are indicative of macroporosity ($w \geqslant 50$ nm) and mesoporosity ($2 \leqslant w \leqslant 50$ nm), respectively. Both isotherms have hysteresis loops that approach to the type H_3 of the IUPAC classification for isotherms with hysteresis loops. This type of hysteresis is characteristic of the adsorption in slit-shaped pores.[35] It is therefore likely that the pores between the columns that define the microstructure of the films

Seoul Semiconductor, Exhibit 2001
LGI v. SSC, IPR2019-01154

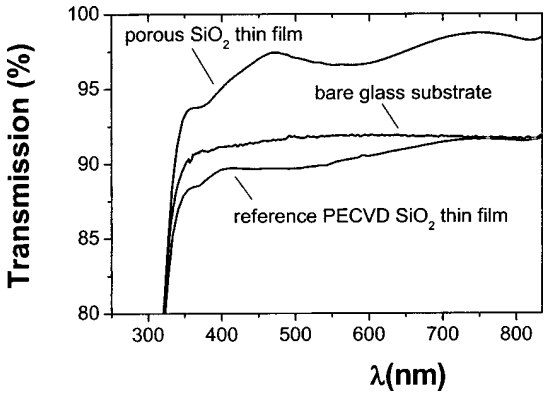

FIG. 7. UV-Vis spectra of a bare glass substrate and this substrate covered by a compact and a porous SiO_2 thin films.

I2 and I3 are responsible for the shape of the hysteresis loops found for the isotherms of these two samples. By contrast, sample I1 presents a smaller porosity with practically no hysteresis loop between the adsorption and desorption branches of the isotherm. This isotherm is close to type I of the IUPAC classification and the pore size falls within the range of micropores ($w<2$ nm). Therefore, from this analysis of isotherms, it is concluded that the present PECVD method provides an effective control of the porosity of thin films in the range of macro-, meso-, or micro-pores.

C. Potential applications

1. Porous SiO_2 thin films as antireflective coatings

The incorporation of porous SiO_2 thin films as antireflective coatings has been claimed as a possible way to increase the light transmission through glass or polymer covers used in photovoltaic modules and other applications in optics.[2,3] An increase in the light transmission coefficient is expected when a layer with a low refractive index is deposited on these substrates. With our method, transparent porous SiO_2 thin films with negligible light dispersion are prepared when using sacrificial organic layers thinner than ~25 nm.

To demonstrate the antireflective character of the SiO_2 thin films prepared with our method, we have measured the UV-vis spectra of a glass plate covered with such a thin film. Figure 7 shows three UV-vis absorption spectra corresponding to a bare glass plate, to one-side of this plate covered by a dense 500 nm SiO_2 thin film prepared directly by PECVD, and to a porous SiO_2 thin film deposited by two cycles C_xO_y:H/SiO_2 (i.e., 5 nm C_xO_y:H, 150 nm SiO_2 + 5 nm C_xO_y:H, 375 nm SiO_2). In this latter case, an enhancement of about 7%–8% transmission occurs for the whole range of visible wavelengths. Such an effect is not observed when a compact SiO_2 layer is deposited without intermediate polymeric films [cf., Fig. 2(a)], for which the transmission is lower than that of the bare glass plate.

Although similar results have been reported recently for SiO_2 thin films prepared by PECVD in a rf setup,[2] the advantage of the method reported here relies on the fact that the porosity is controlled in a reproducible way within a very large set of values.

2. Porous SiO_2 thin films as gas-diffusion membranes

Another possible application of porous thin films is as membranes for separation of fluids. Here we present a preliminary characterization of the gas-diffusion behavior of some SiO_2 thin films. The purpose is to show that by adjusting the porosity of the films, it is possible to prepare membranes with different gas-diffusion rates.

Table II summarizes the results of gas-diffusion experiments with selected samples deposited on commercial alumina Anodisc 47 porous substrates. The table also reports the values corresponding to the bare alumina porous substrates without SiO_2 covering layer. Sample M1 in the table corresponds to a SiO_2 sample of ~800 nm thickness prepared by PECVD at 2×10^{-2} Torr without any intermediate sacrificial layer [i.e., similar to the sample whose SEM micrograph is shown in Fig. 2(a)]. The low gas permeability found for this sample indicates that the film is compact and grows without cracks and voids onto the porous alumina substrates. This compact SiO_2 film acts as a barrier against diffusion of gases.

Similar experiments were carried out with samples of controlled porosity (cf. Table II). Thin films M2 and M3, with a thickness of ~500 nm, were deposited on the Anodisc-100 substrates. The preparation protocols of these two samples differ in the thickness of the organic layer, with 100 nm for sample M2 and 65 nm for sample M3. Both samples have been prepared with two cycles of ~200 and ~300 nm of SiO_2, respectively. As expected, the permeability of sample M2 is about 10%–20% higher than that of

TABLE II. Permeability Π (mol m^{-1} s^{-1} Pa^{-1}) to several gases of selected SiO_2 membranes deposited on Anodisc 47 substrates. The ideal separation factor of the membranes for CH_4 and CO_2, $\alpha_{CO_2}^{CH_4}$ is also included.

Film/substrate	H_2	CH_4	C_3H_6	Kr	$\alpha_{CO_2}^{CH_4}$
M1/Anodisc-20	$1.4\,10^{-13}$	$3.1\,10^{-14}$	$2.2\,10^{-14}$	–	–
M2/Anodisc-100	$7.6\,10^{-10}$	$3.3\,10^{-10}$	$2.4\,10^{-10}$	$1.5\,10^{-10}$	1.60
M3/Anodisc-100	$6.3\,10^{-10}$	$2.6\,10^{-10}$	$1.8\,10^{-10}$	$1.4\,10^{-10}$	1.62
M4/Anodisc-20	$4.4\,10^{-10}$	$1.8\,10^{-10}$	$1.3\,10^{-10}$	$7.7\,10^{-11}$	1.58
M5/Anodisc-20	$8.6\,10^{-13}$	–	$1.6\,10^{-13}$	$1.0\,10^{-13}$	–
Anodisc-20	$9.0\,10^{-10}$	–	$2.2\,10^{-10}$	$1.7\,10^{-10}$	–
Anodisc-100	–	–	–	$>3\,10^{-9}$	–

Seoul Semiconductor, Exhibit 2001
LGI v. SSC, IPR2019-01154

sample M3, although the permeability of both samples is much smaller than that of the Anodisc-100 substrate (cf. Table II). The permeabilities of samples M2 and M3 are even lower than those found for the Anodisc-20 substrate. These results evidence the possibility of adjusting the transport properties of commercial bulk membranes by depositing thin porous layers on their surface.

Samples M4 and M5 in Table II have a thickness of ~750 nm and were deposited on Anodisc-20 substrates. They were prepared using two intermediate organic layers 60 and 4.5 nm thick, respectively. In the first case, the decrease in gas permeability was higher than for samples M2 and M3, reaching a percentage of 40%–55%. In the case of sample M5, it is possible to observe in the table a dramatic decrease in the gas permeability of several orders of magnitude. Many procedures have been reported in the literature to restrict the flow of gases through bulk porous membranes. For example, methods have been reported that consist of depositing different oxide thin films by thermal chemical vapor deposition (CVD) or the impregnation with colloidal SiO_2 particles.[36–40] The deposition of either compact or porous SiO_2 thin films by PECVD according to the present procedure may be an interesting alternative to these methods, particularly when no heating step during preparation is required. In this sense, it could also be expected that our method, furnishing an arrangement of pores perpendicular to the surface, could be an alternative to the anodic oxidation used commercially for the synthesis of supports with controlled permeability.[7,40]

Table II also reports the separation coefficients for CO_2 and CH_4 through the different films. The obtained values are rather similar for the four samples M2, M3, and M4, indicating that within the degree of porosity studied here, the selectivity for these two gases is practically the same. This behavior is expected when diffusion of gases occurs through membrane thin films whose porous size falls within the range of mesopores.[8,12,40]

D. Growth mechanism of porous SiO_2 thin films

Porosity in SiO_2 or other metal oxide thin films prepared by plasma CVD procedures is usually controlled by adjusting the pressure during deposition and/or by modifying geometrical parameters of the plasma reactor, such as distance between the shower dispenser and the substrate.[2] These changes modify the condensation processes of oxide particles in the gas phase. Thereby, porosity is controlled by the different size of particles and nuclei coming from the plasma. Deposition of porous SiO_2 thin films by accumulation of aggregates was also possible with our reactor setup by using $Si(CH_3)_3Cl$ as precursor and oxygen as plasma gas, with a working pressure over 0.5 Torr. Under these conditions, gas phase deposition processes were maximized and the film grew by the accumulation of powder particles. However, these films had very poor mechanical properties.

The sacrificial layer method relies on a different concept. A polymeric-organic film is plasma oxidized and removed simultaneously to the deposition of the inorganic SiO_2 layer.

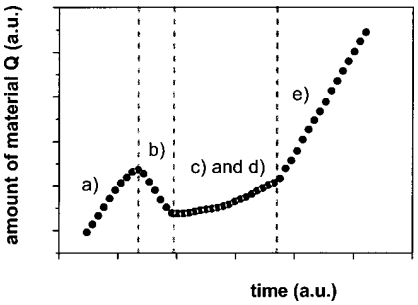

FIG. 8. Evolution of the amount of material Q deposited on a quartz oscillator and detected with a QCM during deposition of the sacrificial organic layer and posterior deposition of the SiO_2 thin film (see text).

Although a model of the SiO_2 deposition cannot be fully outlined at the present stage, we can consider several phenomena which, under our experimental conditions, are likely to control the final porosity. The first is the modification of the nucleation and initial growth steps of SiO_2 because of the presence of the organic layer. The fact that this organic film is formed by highly oxygenated carbonaceous chains seems critical to provide access pathways to the substrate surface to activated precursor molecules and other species of the plasma. A critical clue for the process is that the polymeric layer is easily removed by plasma oxidation under the ECR conditions utilized for SiO_2 deposition.[22] Under these conditions, the polymer etching rates are about ten times higher than the deposition rate of the SiO_2 layers. This means that deposition of the inorganic film mainly occurs when the polymeric layer has already been burned off. Figure 8 shows a plot of the amount of material Q deposited on the quartz oscillator during a deposition cycle of an organic layer followed by the SiO_2 material. Initially, during the initial deposition of the organic layer, Q increases (a). Then, during the initial stages of deposition of the SiO_2 (b), Q decreases, thus indicating that the removal of the organic layer is the predominant process. The zone where Q decreases is followed by the other with a smooth increase of Q (c) and (d) that ends up with a last region with a sharp increase of Q (e). The latter indicates a net deposition of the SiO_2 without interference by any other removal process. We assume that the intermediate zones (b)–(d), characterized first by a negative slope and then by a small positive slope, reflect a sequence of the experiment where etching of the organic layer and deposition of the inorganic oxide take place simultaneously. With respect to this behavior, it is important to stress the importance of using sacrificial organic layers which can be efficiently removed by plasma etching. Experiments carried out in our laboratory with other sacrificial layers which are burned out more slowly show the formation of sandwich structures where the organic layer is embedded within an oxide layer with less porosity than that of the porous thin films described in the previous sections.

Taking into account the results of Fig. 8 obtained during each cycle of deposition of the porous SiO_2 thin films, Fig. 9 shows a schematic description of a mechanism which is proposed to account for the evolution of the microstructure of

Seoul Semiconductor, Exhibit 2001
LGI v. SSC, IPR2019-01154

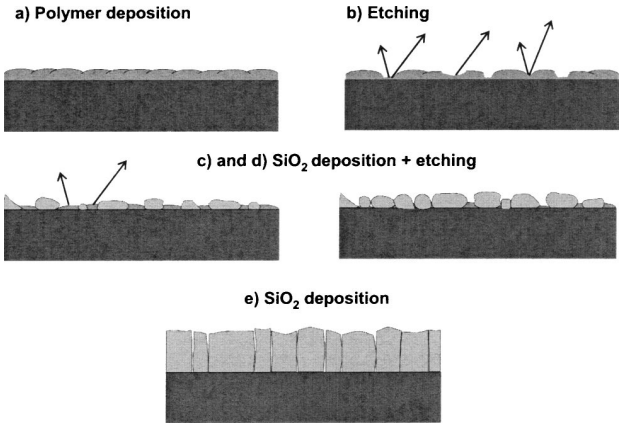

FIG. 9. Proposed scheme for the deposition process of a porous SiO_2 layer over a previously deposited sacrificial organic layer (see text).

these films. The SiO_2 deposition is initiated on a substrate fully covered by an organic layer (a). In the initial stages of SiO_2 deposition, fast removal of this sacrificial layer takes place (b). At the same time, SiO_2 starts to nucleate at certain sites of the substrate that are becoming free from the polymeric material (c) and (d). The columnar growth of the inorganic oxide (e) will be much influenced by the effectiveness of the removal of the organic material, so that the final microstructure will depend on a very delicate balance of different factors like shadowing, restriction of mobility of adatom species of silicon, release of gases (CO_2, H_2O) produced by oxidation of the organic film, etc. Depending on the relative importance of these factors and the characteristics of the initially formed nuclei (i.e., size, dispersion, etc.), growth of the silicon dioxide film occurs in different ways and leads to different microstructures.

IV. CONCLUSIONS

The presented results show that it is possible to control the microstructure of oxide thin films deposited by room temperature PECVD by using sacrificial polymeric organic layers. The method is very versatile and permits to tailor a large variety of pore microstructures as required for many applications, from optical films to gas diffusion membranes and supports. This method extends the synthesis of oxide films by PECVD to the preparation of porous films with a columnar porous structure perpendicular to the surface and enables the deposition of porous thin films on polymers and other substrate sensitive to high temperatures.

Preliminary studies have shown that other oxide materials besides SiO_2 can be deposited in the form of porous thin film following a similar procedure. This opens the possibility of preparing porous thin film structures of mixed and/or gradient compositions. This ability, together with the in-depth control of porosity which is another key feature of the method, could permit the tailoring synthesis of thin films where both composition and porosity can be simultaneously and independently controlled.

Since the preparation protocol is based on a PECVD procedure, the method is compatible with the silicon technology (e.g., as low-*k* materials).

ACKNOWLEDGMENTS

The authors thank C. Clerc from the Ion Accelerator ARAMIS (Orsay, France) for her assistance with the RBS measurements, J. Benítez from ICMSE (Sevilla, Spain) for the AFM images, and the financial support of the Spanish Ministerio de Ciencia y Tecnología (Project No. MAT2001-2820) and the EU (Project No. ENV4-CT97-0633 and the MULTIMETOX network).

[1]I. M. Thomas, Appl. Opt. **31**, 6145 (1992).
[2]H. Nagel, A. Metz, and R. Hezel, Sol. Energy Mater. Sol. Cells **65**, 71 (2001).
[3]G. Helsch, E. Rädlein, and G. H. Frishat, J. Non-Cryst. Solids **265**, 193 (2000).
[4]J. K. Hong, H. S. Yang, M. H. Jo, H. H. Park, and S. Y. Choi, Thin Solid Films **308–309**, 495 (1997).
[5]A. Jain, S. Rogojevic, S. Ponoth, N. Agarwal, I. Matthew, W. N. Gill, P. Persans, M. Tomozawa, J. L. Plawsky, and E. Simonyi, Thin Solid Films **398**, 513 (2001).
[6]J. K. Hong, H. R. Kim, and H. H. Park, Thin Solid Films **332**, 449 (1998).
[7]H. P. Hsieh, Catal. Rev. - Sci. Eng. **33**, 1 (1991).
[8]W. J. Koros and G. K. Fleming, J. Membr. Sci. **83**, 1 (1993).
[9]A. B. Shelekhin, S. Pien, and Y. H. Ma, J. Membr. Sci. **103**, 39 (1995).
[10]L. Cot, A. Ayral, J. Durand, C. Guizard, N. Hovnanian, A. Julbe, and A. Larbot, Solid State Sci. **2**, 313 (2000).
[11]A. Ohl and K. Schröder, Surf. Coat. Technol. **116–119**, 820 (1999).
[12]D. R. Lloyd, editor, *Material Science of Synthetic Membranes* (American Chemical Society, Washington, DC, 1985).
[13]P. Liu, S. H. Lee, C. Edwin Tracy, Y. Yan, and J. A. Turner, Adv. Mater. (Weinheim, Ger.) **14**, 27 (2002).
[14]P. D. Yang, D. Y. Zhao, D. I. Margolese, B. F. Chmelka, and G. D. Stucky, Nature (London) **396**, 152 (1998).
[15]P. D. Yang, D. Y. Zhao, D. I. Margolese, B. F. Chmelka, and G. D. Stucky, Chem. Mater. **11**, 2813 (1999).
[16]N. K. Raman, M. T. Anderson, and C. J. Brinker, Chem. Mater. **8**, 1682 (1996).
[17]I. Honma, H. S. Zhou, D. Kundu, and A. Endo, Adv. Mater. (Weinheim, Ger.) **20**, 1529 (2000).
[18]A. Grill, *Cold Plasma in Materials Fabrication* (Wiley-IEE Press, 1994).
[19]G. Lucovsky and D. V. Tsu, J. Vac. Sci. Technol. A **5**, 2231 (1987).
[20]D. Korzec, D. Theirich, F. Werner, K. Traub, and F. Engemann, Surf. Coat. Technol. **74–75**, 67 (1995).
[21]A. Barranco, F. Yubero, J. P. Espinós, A. R. González-Elipe, and J. Cotrino, *Procedure for the Preparation of Porous Thin Films of Inorganic Oxides* (ref. Spanish patent 200100911, 19th April 2001; PCT ES02/00192).
[22]A. Barranco, J. Cotrino, F. Yubero, and A. R. González-Elipe, J. Vac. Sci. Technol. A **21**, 1655 (2003).
[23]F. Werner, D. Korzec, and J. Engemann, Plasma Sources Sci. Technol. **3**, 473 (1994).
[24]A. Barranco, J. Cotrino, F. Yubero, J. P. Espinós, J. Benítez, C. Clerc, and A. R. González-Elipe, Thin Solid Films **401**, 150 (2001).
[25]J. Cotrino, A. Palmero, V. Rico, A. Barranco, J. P. Espinós, and A. R. González-Elipe, J. Vac. Sci. Technol. B **19**, 410 (2001).
[26]F. N. Dultsev, L. A. Nenasehva, and L. L. Vasilyeva, Thin Solid Films **315**, 72 (1998).
[27]M. R. Baklanov, L. L. Vasylyeva, T. A. Gavrilova, F. N. Dultsev, K. P. Mogilnikov, and A. Nenasheva, Thin Solid Films **171**, 43 (1989).
[28]S. Roualdes, A. Van der Lee, R. Berjoan, J. Sanchez, and J. Durand, AIChE J. **45**, 1566 (1999).
[29]S. F. Durrant, S. G. Castro, J. I. Cisneros, N. C. da Cruz, and M. A. Bica de Moraes, J. Vac. Sci. Technol. A **14**, 118 (1996).
[30]P. Lange, J. Appl. Phys. **66**, 201 (1989).
[31]R. M. Almeida and C. G. Pantano, J. Appl. Phys. **68**, 4225 (1990).

Seoul Semiconductor, Exhibit 2001
LGI v. SSC, IPR2019-01154

[32]L. Martinu and D. Poltras, J. Vac. Sci. Technol. A **18**, 2619 (2000).
[33]W. H. Southwell, J. Opt. Soc. Am. A **5**, 1558 (1988).
[34]W. A. Weyl and E. C. Marbone, *The Constitution of Glasses* (Wiley-Interscience, New York, 1964).
[35]S. J. Gregg and K. S. W. Sing, Adsorption, *Surface Area and Porosity*, 2nd ed. (Academic, New York, 1997), and references therein.
[36]M. Tsapatsis and G. R. Gavalas, AIChE J. **38**, 847 (1992).
[37]M. Tsapatsis and G. R. Gavalas, J. Membr. Sci. **87**, 281 (1994).
[38]M. Moaddeb and W. J. Koros, J. Membr. Sci. **125**, 143 (1997).
[39]M. Moaddeb and W. J. Koros, J. Membr. Sci. **136**, 273 (1997).
[40]E. J. Jakobs, Ph. D. thesis, The University of Texas at Austin, University Microfilms International Dissertation Services, Ann Harbor, 1996.

Seoul Semiconductor, Exhibit 2001
LGI v. SSC, IPR2019-01154

APPENDIX E

Available online at www.sciencedirect.com
SCIENCE DIRECT®
Thin Solid Films 442 (2003) 222–226
thin solid films
www.elsevier.com/locate/tsf

Antireflection treatment of low-emitting glazings for energy efficient windows with high visible transmittance

Elin Hammarberg*, Arne Roos

The Ångström Laboratory, Uppsala University, Box 534, S-751 21 Uppsala, Sweden

Abstract

The objective of this study is to increase the visible transmittance of a low-emittance (low-e) glazing as much as possible by antireflection treatment. This has been carried out by depositing thin porous films of silicon dioxide, SiO_2, on both sides of a commercial glazing with a pyrolytic low-e tin oxide-based coating. SiO_2 was chosen because its refractive index makes it suitable for antireflection treatment of both the uncoated glass side and the side of the tin oxide coating. The deposition of the antireflective films was performed with a dip-coating method, where the substrate was dipped in a sol–gel of silica. Two different silica sol–gels were used, one was manufactured in the laboratory and the other one was a commercial solution with a higher porosity. An increase of the integrated visible transmittance (T_{vis}) by 9.8% points up to 0.915 was achieved for a coating produced with the commercial solution. Calculations of U value, g value and T_{vis} for window configurations were also performed.
© 2003 Elsevier B.V. All rights reserved.

Keywords: Optical coatings; Optical properties; Dip coatings; Antireflection coatings

1. Introduction

The use of energy efficient windows is steadily increasing in Europe, although many new buildings are still equipped with uncoated standard windows. This is unfortunate since for every standard uncoated window fitted in new production, large amounts of energy will be wasted during the lifetime of this window. This fact is also pointed out in a report from GEPVP where it is claimed that 1.1 million gigajoules of energy would be saved every year if all single and double glazed uncoated windows in Europe were replaced by energy efficient coated windows [1]. In many European countries, coated low-e glazing is standard in new production and a key factor has been the introduction of new building regulations. In general it is true that the market for coated glazing products is steadily increasing [2,3].

One problem that could have led to the slow response of the market is the enormous choice of products. Among the vast number of different coated glazings on the market there are several with a fairly low luminous transmittance. These are often seen as dark or tinted, and a common misconception among the public is that all coated glazing products are tinted. In the hunt for low U-values, many combinations of glazings have been suggested and sometimes 'super windows' with triple panes and two low-e coatings are proposed. Sometimes such a combination leads to a light transmittance which is lower than what is desired.

Low-e coated products can be divided into two main categories: hard and soft coatings [4]. The hard coatings are based on tin oxide and are often also referred to as 'on-line' coatings due to the production process, which is in direct connection to the float line [5]. Soft coatings are usually based on a thin layer of silver surrounded by dielectric protective layers. Soft coatings are produced in a sputtering process, not necessarily at the same place as the float line. The materials used in the different coatings set limits on the optical properties. In general the soft silver-based coatings have higher infrared reflectance and lower solar transmittance than the hard tin oxide-based coatings. The impact of these coatings on the energy performance of the windows has been described in several papers [6–9].

While the oxide layers used for the protection of the silver in the soft coatings also act as antireflective layers, the tin oxide-based coatings have no antireflective layer. This leads to reflective losses and since tin oxide has a higher refractive index than glass, the

*Corresponding author.

0040-6090/03/$ - see front matter © 2003 Elsevier B.V. All rights reserved.
doi:10.1016/S0040-6090(03)00986-6

APPENDIX E

reflection losses tend to be higher than that for uncoated glass. In this paper we have used a dip coating technique developed for the antireflection treatment of solar collector covers [10–12] to reduce reflection losses of tin oxide-coated glass. It is shown that using existing products and known deposition techniques it is possible to design windows with very low *U*-values without sacrificing the light transmittance.

There are several glazing products with antireflective coatings available on the market today. The Amiran glass by Schott is a well-known example with very high light transmittance in the visible range. It is made by a dip coating technique similar to the one we have used in this project. Other manufacturers offer sputtered products and they are usually based on double (or more) layers including silicon and titanium oxides (high–low refractive index stacks). These products are generally optimised for the visible range and have a higher reflectance in the near infrared than the uncoated glass. In order to obtain a reduction of the reflection losses throughout the entire solar spectrum it is necessary to use a single layer of low (less than that of glass) refractive index. This study has been restricted to single layers partly because of the fact that thickness control is less crucial when only one layer is involved and partly because of the wider range of antireflection. In Ref. [8] we included the Amiran glass in our study of antireflective coatings in windows.

The type of coating used in this study was primarily developed for solar collector covers. It is similar to the coatings manufactured by Flabeg in Germany which was developed in co-operation with Fraunhofer Institute for Solar Energy Research in Freiburg [13]. Another coating manufactured for solar collectors is the etched glass by Sunarc in Denmark, which was evaluated after 7 years of outdoor exposure in Älvkarleby, Sweden [14]. These two coatings can be expected to perform in the same way as our coating studied here, although it is uncertain if the etching technique will work on the tin oxide surface. The intention of this work is, however, not to compare coatings from different sources, but to investigate what level of performance is possible to achieve when using antireflective coatings and to verify this by experiments. Important factors such as coating homogeneity, haze and colour rendering have not been evaluated in this study. The porous nature of the coating is a possible source of light scattering, often noted as haze, which can be a problem. The scattering is not investigated in detail, but the haze from the antireflective layer is not more pronounced than the haze from the hard tin oxide coating. In fact, we have noticed a slight decrease in light scattering from the tin oxide glass when coated with the antireflective dip coating. These results are, however, preliminary and are not presented in this study.

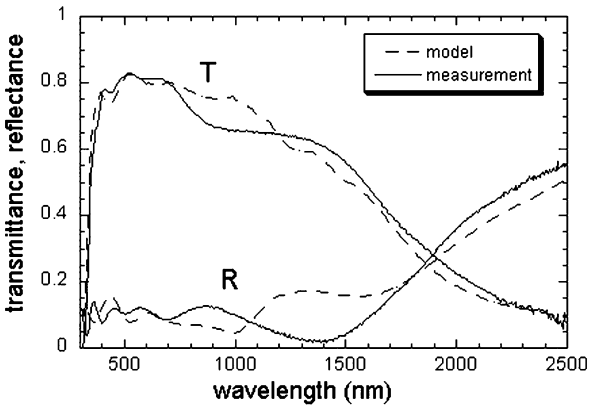

Fig. 1. Measured transmittance and reflectance of a low-e glazing together with modeled values for float glass with a 300-nm-thick layer of SnO_2:F with altered *n* and *k* values.

2. Modeling

The low-e glazing used in this study was a commercial glazing with a hard tin oxide-based pyrolytic coating [5]. A simplified optical model of the low-e glazing was developed to study the effect of the deposition of an antireflective coating on the sample. The exact composition of the low-e coating is not known, but it consists mainly of doped tin oxide, SnO_2:F. The model was built up from a substrate of 3-mm-thick float glass [15] coated by a 300-nm-thick layer of SnO_2:F. The *n* and *k* values of SnO_2:F experimentally acquired earlier [16] were modified to fit the measured *T* and *R* values for the low-e glazing. A comparison of the model and the measured spectra is shown in Fig. 1.

There are some differences between the model and the measurement, but the purpose here was not to determine the exact values of *n* and *k* of the low-e glazing, only to obtain values realistic enough to use for further calculations. Theoretical values of the visible transmittance for an AR coating with a varying refractive index placed on the glass side, the low-e side and both sides, respectively, on the model sample from Fig. 1 were then calculated. A plot of the calculated results is shown in Fig. 2, and a summary of the most important parameters is given in Table 1.

The T_{vis} maximum values in Table 1 should not be considered as a theoretical limit of what is achievable, since the model is only approximate. However, they should be rather realistic, since the visible transmittance of the model sample (0.814) is approximately the same as one of the commercial low-e glazing (0.817). Therefore, the maximum positions are also likely to be near the real ones. Regarding the refractive indices in Table 1, SiO_2 should be a good choice of material for the AR coating. Values of the solar factor, *g*, and the *U*-value

Seoul Semiconductor, Exhibit 2001
LGI v. SSC, IPR2019-01154

APPENDIX E

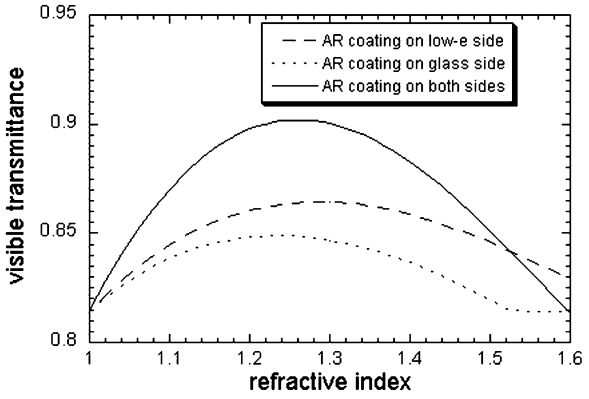

Fig. 2. Calculated T_{vis} values for an AR coating with a varying refractive index deposited on float glass with a low-e coating on one side.

have been calculated according to international standards [17–19].

3. Sample preparation

Silicon dioxide coatings were deposited on the low-e glazing by the use of a dip-coating method. The substrates were dipped in one of the two different silica sol–gels. One sol–gel was prepared in laboratory by mixing tetraethyl orthosilicate (TEOS), nitric acid, deionized water and propanol. The TEOS concentration was 7.5% per volume. Coatings manufactured using this sol–gel are referred to as coating 1. The other sol–gel was a commercial solution diluted with ethanol to a concentration of 10% per volume. Coatings manufactured using this sol–gel are referred to as coating 2. Apart from the low-e glazing, float glass was also coated with the same sol–gels to determine their refractive indices. The substrates were lowered into a container of the sol–gel, held for 1 min and then withdrawn at a constant rate. When coating only the low-e side of the substrate, the glass side was covered with tape, which was easily removed after the coating. All coated samples were cured at 300 °C for 10 min.

4. Results

4.1. Low-e glazing

The refractive indices of coating 1 and 2 were determined from measurements on coated float glass.

Table 1
The results of the calculations shown in Fig. 2

AR coating deposited at	T_{vis} maximum	Refractive index at maximum	Thickness at maximum (nm)
Glass side	0.849	1.23	113
Low-e side	0.864	1.29	103
Both sides	0.902	1.26	107

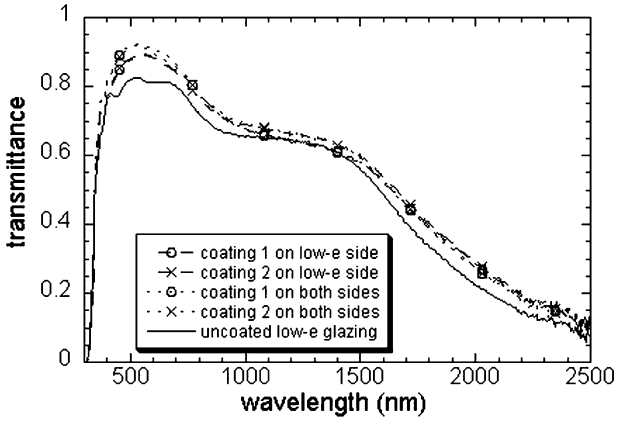

Fig. 3. Transmittance in the solar wavelength interval for the low-e glazing coated with coating 1 and 2, respectively.

For coating 1 the refractive index was 1.34 and for coating 2 it was 1.44 in the middle of the visible wavelength region. It should be noted that these values might not be exactly the same for the coatings deposited on the low-e side of the substrate. They should be rather similar though. A plot of the best results obtained when coating the low-e side and both sides of the low-e glazing with coating 1 and 2, respectively, is shown in Figs. 3 and 4. A summary of the results is given in Table 2.

As is seen in Fig. 3, the transmittance is increased in the whole solar wavelength region, and particularly in the visible region, see Fig. 4. As can be observed from Table 2, the best results originate from the case of coating 2 on both sides, for which the increase of the visible transmittance is 9.8% points and for the solar transmittance it is 6.3% points. It should be noted that the experimentally obtained maximum value 0.915 is

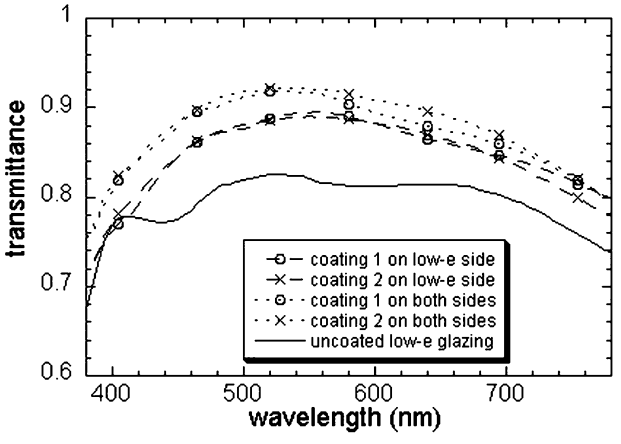

Fig. 4. Transmittance in the visible wavelength interval for the low-e glazing coated with coating 1 and 2, respectively.

Seoul Semiconductor, Exhibit 2001
LGI v. SSC, IPR2019-01154

APPENDIX E

Table 2
Summary of the results shown in Figs. 3 and 4

Coating	T peak	T_{vis}	T_{vis} increase	T_{sol}	T_{sol} increase
Coating 1, low-e side	0.8960	0.886	0.069	0.737	0.043
Coating 2, low-e side	0.890	0.884	0.067	0.740	0.046
Coating 1, both sides	0.919	0.908	0.091	0.750	0.056
Coating 2, both sides	0.922	0.915	0.098	0.757	0.063
Uncoated low-e	0.826	0.817	–	0.694	–

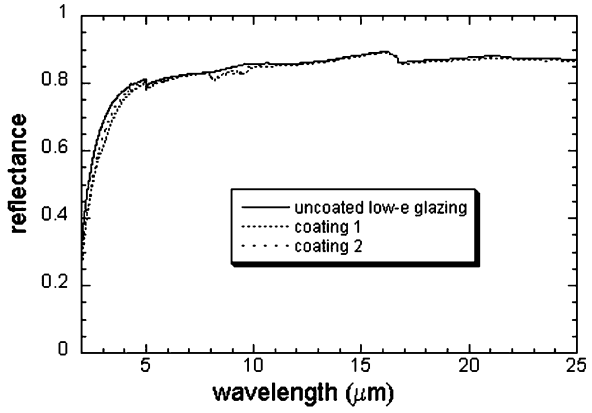

Fig. 5. Reflectance in the IR wavelength interval for a coated and an uncoated low-e glazing.

Table 3
The results for calculations of DGU and TGU window configurations

	Pane 1	Pane 2	Pane 3	T_{vis}	g	U
(a)	Float	Float		0.817	0.786	2.93
(b)	Float	Low-e		0.743	0.743	1.92
(c)	AR float	AR low-e		0.893	0.833	1.92
(d)	Float	Float	Float	0.746	0.713	1.95
(e)	Low-e	Float	Low-e	0.619	0.572	1.14
(f)	AR low-e	AR float	AR low-e	0.818	0.689	1.14

approximately 1% point higher than the theoretically calculated maximum value 0.902.

The ratio between the T_{vis} increase obtained when coating the low-e side and both sides was computed and the results for experiment and theory were compared. In experiment the quotient is 0.76 for coating 1 and 0.68 for coating 2. In theory (Fig. 2) the quotient 0.76 corresponds to a refractive index of 1.47 and the quotient 0.68 corresponds to $n=1.43$. These results are an indication that the values 1.34 and 1.44 mentioned above could be too low, but are themselves on the other hand only approximate.

It is very important that the low-emitting quality in the infrared is not affected by the AR treatment. The reflectance in the IR wavelength interval of the coated samples was, therefore, measured and the results are shown in Fig. 5. It is seen that the IR reflectance is hardly changed when the low-e glazing is coated. The emittance is thereby unchanged and the U-value of the coated glass is assumed to be the same as for the uncoated low-e glazing. The unevenness in the reflectance curve at 5 and 16.7 μm are caused by instrumental alternations of gratings.

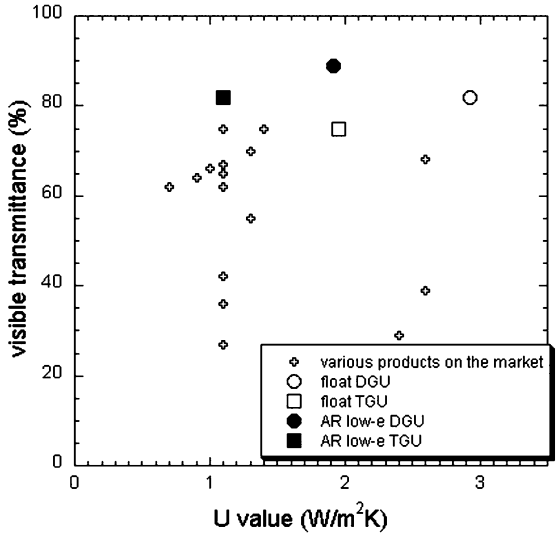

Fig. 6. Visible transmittance vs. U value for samples manufactured in this study and a number of products currently on the market.

4.2. Window configurations

To evaluate the effect of using AR-treated panes in a window, calculations were performed for some different configurations. Calculations of the g value, the U value and the visible transmittance were performed for three double glazing unit (DGU) and triple glazing unit (TGU) window configurations. The results are shown in Table 3 below. The calculations are based upon experimental data for single panes. AR float had a visible transmittance of 0.975 and a solar transmittance of 0.912. The visible transmittance as a function of the U value is shown for configurations a, c, d and f, together with other products on the market in Fig. 6.

It is seen in Table 3 and Fig. 6 that using an AR-treated low-e configuration instead of a standard DGU or TGU float glass configuration increases the g value and the T_{vis} value while decreasing the U value. It also

Seoul Semiconductor, Exhibit 2001
LGI v. SSC, IPR2019-01154

APPENDIX E

shows that it is even possible to construct a low-e TGU configuration with the same visible transmittance as a float glass DGU configuration.

5. Conclusions

In this work it has been seen that the transmittance of a low-e glazing can be largely increased if it is antireflection treated by depositing a thin film of silicon dioxide on both sides of the sample. SiO_2 gives an efficient AR treatment both to the glass side and to the low-e tin oxide side of the commercial low-e glazing. This is the reason why an increase of the visible transmittance as high as 10% could be achieved. It has also proved possible to construct a TGU window with AR-treated low-e and float glass panes with the same visible transmittance as a standard float glass DGU window. The AR-treated TGU window thereby greatly decreases the *U*-value while not decreasing the visibility. It is probable that an even larger increase of the visible transmittance could be achieved if the sol–gels used for the AR layers are optimized regarding the refractive index, which was not the case in this study.

Acknowledgments

This work has been sponsored by a grant from the Carl Trygger Foundation. The tin oxide-coated K-glass samples were provided by Pilkington Floatglass, Halmstad, Sweden.

References

[1] Low-e glass in buildings, Impact on the environment and on energy savings, Groupement Europeen des Producteurs de Verre Plat, 2000.
[2] E.J. Wegener, J. Non-Cryst. Solids 218 (1997) 7–11.
[3] A. Arnaud, J. Non-Cryst. Solids 218 (1997) 12–18.
[4] T.E. Johnson, Low-e Glazing Design Guide, Butterworth-Heinemann, 1991.
[5] R. Gordon, J. Non-Cryst. Solids 218 (1997) 81–91.
[6] P. Pfrommer, K.J. Lomas, C. Seale, Chr. Kupke, Solar Energy 54 (1995) 287–299.
[7] J. Karlsson, Windows—Optical Performance and Energy Efficiency, Doctoral Thesis, Uppsala University, Sweden, 2001 (ISBN 91-554-5147-0).
[8] J. Karlsson, B. Karlsson, A. Roos, Performance of antireflection glazings in windows, Proceedings, Glass Processing Days-2001, Tampere, Finland, June 18–21, 2001.
[9] C.G. Granqvist, et al., J. Non-Cryst. Solids 218 (1997) 273–279.
[10] A. Gombert, et al., Solar Energy 62 (3) (1998) 177–188.
[11] P. Nostell, A. Roos, B. Karlsson, Thin Solid Films 351 (1999) 170–175.
[12] P. Nostell, Preparation and optical characterisation of antireflection coatings and reflector materials for solar energy systems, Doctoral Thesis, Uppsala University, Sweden, 2000 (ISBN 91-554-4794-5).
[13] A. Gombert, et al., Solar Energy 62 (1998) 177–188.
[14] G.K. Chinyama, A. Roos, B. Karlsson, Solar Energy 50 (1993) 105–111.
[15] M. Rubin, Solar Energy Mater. 12 (1991) 275–288.
[16] A. Roos, Thin Solid Films 203 (1991) 41–48.
[17] International Standard, ISO 9845-1, Solar Energy—Reference Solar Spectral Irradiance at the Ground at Different Receiving Conditions—Part 1: Direct Normal and Hemispherical Solar Irradiance for Air Mass 1, vol. 5, 1992.
[18] European Standard, EN 673, Thermal Insulation of Glazing—Calculation Rules for Determining the Steady State 'U' Value (Thermal Transmittance) of Glazing, 1998.
[19] International Standard, ISO 9050, Glass in Building—Determination of Light Transmittance, Solar Direct Transmittance, Total Solar Energy Transmittance, Ultraviolet Transmittance and Related Glazing Factors, 1990.

Seoul Semiconductor, Exhibit 2001
LGI v. SSC, IPR2019-01154

APPENDIX F

H944 *Journal of The Electrochemical Society*, **154** (11) H944-H947 (2007)
0013-4651/2007/154(11)/H944/4/$20.00 © The Electrochemical Society

Enhancement of InGaN/GaN Flip-Chip ITO LEDs with Incline Sidewalls Coated with TiO_2/SiO_2 Omnidirectional Reflector

C. H. Chiu,[a] H. C. Kuo,[a,z] C. F. Lai,[a] H. W. Huang,[a] W. C. Wang,[a] T. C. Lu,[a] S. C. Wang,[a] and C. H. Lin[b]

[a]*Institute of Electro-optical Engineering, National Chiao Tung University, Hsinchu 300, Taiwan*
[b]*Epistar Corporation, ChuNan 350, Taiwan*

The light extraction enhancement of GaN-based flip-chip indium-tin oxide light-emitting diodes (FC ITO LEDs) with an inclined sidewall coated with TiO_2/SiO_2 omnidirectional reflectors (ODRs) is presented. At a driving current of 350 mA and a chip size of 1×1 mm, the light output power and the light extraction enhancement of the FC ITO LEDs coated TiO_2/SiO_2 ODRs with inclined sidewall reached 183 mW and 15% when compared with the results from the same device, FC ITO LEDs coated TiO_2/SiO_2 ODRs with vertical sidewall. Furthermore, by examining the radiation patterns of the FC ITO LEDs, the increased optical power within 150° cone contributed to the stronger enhancement around the vertical direction of an inclined sidewall ODR within blue regime. Our work offers promising potential for enhancing output powers of commercial light-emitting devices.
© 2007 The Electrochemical Society. [DOI: 10.1149/1.2775286] All rights reserved.

Manuscript submitted February 7, 2007; revised manuscript received July 2, 2007. Available electronically September 6, 2007.

GaN-based material is a direct wide bandgap semiconductor that has attracted considerable interest in applications for blue, green and ultraviolet light-emitting diodes (LEDs). The availability of higher brightness, high power and large area of GaN-based LEDs has enabled their applications in traffic signals, back-side lighting in liquid crystal display and backlight for various handheld devices.[1] Due to the large refractive index difference between GaN of 2.5 and air of 1.0, the total internal reflection is mainly responsible for the photon trapping. Emitting photons that strike the GaN-air interface at angles exceeding the critical angle θ_c are reflected back, the majority of which are guided laterally through the air-GaN-sapphire waveguide structure. Thus, the critical angle at which light generated in the InGaN–GaN active region can escape is approximately $[\theta_c = \sin^{-1}(n_{air}/n_{GaN})] \sim 23°$, which limits the external quantum efficiency of conventional GaN-based LEDs to only a few percent. However, there is a great need to improve the external quantum efficiency of GaN-based LEDs in order to further increase their light output power.

Several approaches have been proposed to improve the external quantum efficiency and the output power of packaged LEDs; light emitted downward toward the substrate must be reflected upward in order to contribute to usable light output[2-4] and the output light could be enhanced through the sample surface or the sidewall profile.[5-8] Chang et al. reported 10% output power enhancement from the InGaN–GaN multiple quantum well (MQW) LEDs by the introduction of the wavelike textured sidewalls.[5] Kao et al. reported the experiment results for enhancing light extraction efficiency from the GaN-based LEDs with ~23° undercut sidewalls.[6] Lin et al. reported the enhancement of light extraction efficiency using photoelectrochemical wet oxidation on the GaN-based LEDs with inclined undercut sidewalls.[8] All these methods have one thing in common, which is that photons generated within the LEDs experience multiple opportunities to find the escape cone. Bhat, Ludowise, and Steigerwald[9] proposed a dielectric distributed Bragg reflector (DBR) coated on the inclined mesa wall of a flip-chip LED to enhance the light output power. The dielectric DBR is selected to maximize the reflection of light to enhance light extraction of the flip-chip LED.

DBRs have many advantages, such as very low optical loss, high reflectance, and high mechanical robustness. A one-dimensional (1D) periodic dielectric structure possessing this characteristic is known as an omnidirectional one-dimensional photonic crystal (1D PhC). Total reflection of light with incidence angle onto a periodic structure can be realized with the existence of a complete photonic bandgap (CPBG) at the wavelengths of interest.[10] Since there is no allowed photon propagation state for wavelengths within the CPBG, an omnidirectional reflector (ODR) made from such 1D PhC can totally reflect the light with wavelengths within the CPBG at any incidence angle and polarization. Therefore, compared with a DBR mirror, a substantially higher reflectance can be achieved. In our previous work, we have demonstrated enhancement in the extracted light intensity for a GaN-based LED with p-side up and flip-chip configuration incorporated with an ODR composed of alternate layers of TiO_2 and SiO_2.[4,11] In this paper, we have designed and fabricated a flip-chip indium-tin oxide LED (FC ITO LED) coated TiO_2/SiO_2 ODR with inclined sidewalls.

Experimental

The schematic cross-sectional representations of the structures of InGaN/GaN vertical-injection LED coated ODRs we proposed are shown in Fig. 1a, with vertical sidewall, and Fig. 1b, with inclined sidewall. The GaN-based LED samples were grown by metallorganic chemical vapor deposition with a rotating-disk reactor (Emcore) on a *c*-axis sapphire (0001) substrate at the growth pressure of 200 mbar. The LED structure consists of a 50 nm thick GaN nucleation layer grown at 500°C, a 2 μm undoped GaN buffer, a 2 μm Si-doped GaN buffer layer grown at 1050°C, an unintentionally doped InGaN/GaN MQW active region grown at 770°C, a 50 nm thick Mg-doped p-AlGaN electron blocking layer grown at 1050°C, a 0.25 μm thick Mg-doped p-GaN contact layer grown at 1050°C and a Si-doped InGaN/GaN short period superlattice structure. The MQW active region consists of five periods of 3 nm/7 nm thick InGaN/GaN quantum well layers and barrier layers. After annealing to activate Mg in the p-type layers, the FC ITO LEDs coated TiO_2/SiO_2 ODR were fabricated using standard process with a mesa area of 1×1 mm, the same as in Ref. 4.

Figure 1a shows the schematic diagram of the FC ITO LED coated TiO_2/SiO_2 ODR with vertical sidewall. We partially etched the surfaces of the LED samples using Cl_2/Ar as the etching gas by inductive-coupled-plasma reactive ion etching (ICP-RIE) until the n-type GaN layers were exposed. A 300 nm thick ITO layer was subsequently evaporated onto the sample surface by electron beam (E-beam) evaporation for current spreading. The ITO layer had a high electrical conductivity (about $1.7 \times 10^1\ \Omega^{-1}\ cm^{-1}$) and a high transparency (>95% at 460 nm). Ti/Al/Ni/Au contacts were subsequently deposited onto the exposed n-type GaN layers to serve as the n-type electrodes. SiO_2 layers were then deposited over all wafers by plasma enhanced chemical vapor deposition. Photolithography and HF solution etching were subsequently performed to define

[z] E-mail: hckuo@faculty.nctu.edu.tw

Downloaded on 2019-09-16 to IP 143.215.34.165 address. Redistribution subject to ECS terms of use (see ecsdl.org/site/terms_use) unless CC License in place (see abstract).

Seoul Semiconductor, Exhibit 2001
LGI v. SSC, IPR2019-01154

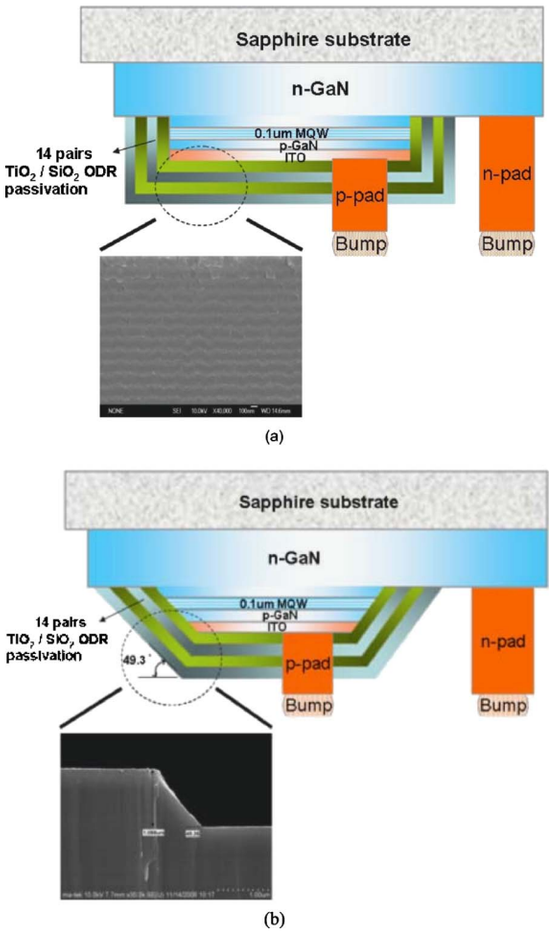

Figure 1. (Color online) Schematic diagram of the GaN-based FC ITO LEDs (a) containing the TiO_2/SiO_2 ODR, and (b) with ~50° inclined angle coated TiO_2/SiO_2 ODR. The inset shows the SEM picture of the ~50° inclined sidewall profile.

the P/N pad pattern for bump electroplating. The close-up scanning electron microscopy (SEM) image in Fig. 1a shows the step coverage of the SiO_2 films which was well controlled to cover the entire chips. Figure 1b depicts a schematic diagram of the FC ITO LED device coated TiO_2/SiO_2 ODR with an inclined sidewall. Instead of depositing TiO_2/SiO_2 ODR on the mesa structure directly, an additional etching process for FC ITO LEDs to form inclined sidewalls about 50° was carried out to mesa etching by using the ICP-RIE process. The inclined angle of the sidewall profile is defined as the angle between the horizontal line and sidewall. The inclined angle could be well controlled by using different ICP-RIE etching condition. The inset of Fig. 1b shows the SEM picture of inclined sidewalls profile of the FC ITO LED coated TiO_2/SiO_2 ODR with an inclined sidewall. It can be observed that the about 50° oblique inclined sidewall profile compared with initial etching mesa. $Au_{80}Sn_{20}$ solder was used for electrical and mechanical interconnection due to its very high reliability of good mechanical properties, good thermal conductivity, and low growth of intermetallic phase. Au_{80}/Sn_{20} (1600/400 nm) layers were then evaporated onto both FC ITO LED device coated TiO_2/SiO_2 ODR with vertical and inclined sidewall samples while P/N bumps were defined by the lift-off process. During the bonding process, chips were picked, orientated, and flipped by a die bonder system. The FC ITO LED was soldered onto an AlN submount. For comparison reasons, both FC ITO LED devices coated TiO_2/SiO_2 ODR with vertical and inclined sidewall were fabricated from exactly the same epitaxial wafer with the same chip size.

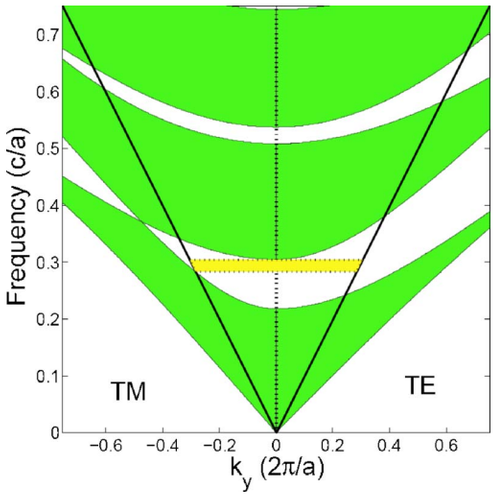

Figure 2. (Color online) Photonic band structure diagram of a 1D PC composed of TiO_2 and SiO_2 multilayers. Refractive indexes and layer thickness are assumed to be $n_1 = 2.52$, $d_1 = 56$ nm for TiO_2, and $n_2 = 1.48$, $d_2 = 77$ nm for SiO_2. The green and white regions distinguish between the allowed and forbidden photon states, respectively. The region with yellow area of the complete photonic bandgap (CPBG) represents an omnidirectional reflection region.

In this paper, the TiO_2/SiO_2 ODR structure is similar to Ref. 4. An ODR with 14 pairs of TiO_2/SiO_2 (as shown in inset of Fig. 1b for a SEM picture), was evaporated onto both samples by an E-beam evaporator at 150°C, and at an oxygen partial pressure of 2×10^{-4} Torr with Ar and O_2 as the ion source inlet gases. The film deposition rates of TiO_2 and SiO_2 were 0.4 and 0.8 nm/s, respectively. By the modal transmission-line method[12] to calculate the various thicknesses as shown in Fig. 2, we found the most optimal CPBG at frequencies between 0.282 c/a and 0.304 c/a, where c is the speed of light and a is the lattice constant. We chose the lattice constant $a = 133$ nm to give a CPBG centered at 465 nm. Thus we found that our TiO_2/SiO_2 ODR has a CPBG from 437 to 472 nm if the thickness of TiO_2 and SiO_2 layers were chosen as 56 and 77 nm, respectively. We observed that rather low transmission (<0.05%) can be achieved from 441 to 465 nm from the angle dependent

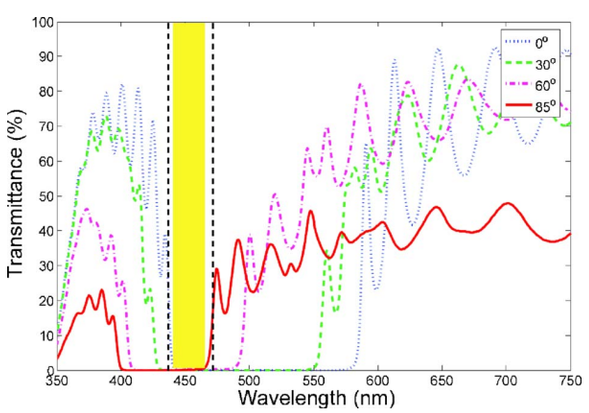

Figure 3. (Color online) Measurement transmittance results of the four transmittance curves with different incidence angles (e.g., 0°, 30°, 60°, 85°) for unpolarized light vs wavelength.

Downloaded on 2019-09-16 to IP 143.215.34.165 address. Redistribution subject to ECS terms of use (see ecsdl.org/site/terms_use) unless CC License in place (see abstract).

Seoul Semiconductor, Exhibit 2001
LGI v. SSC, IPR2019-01154

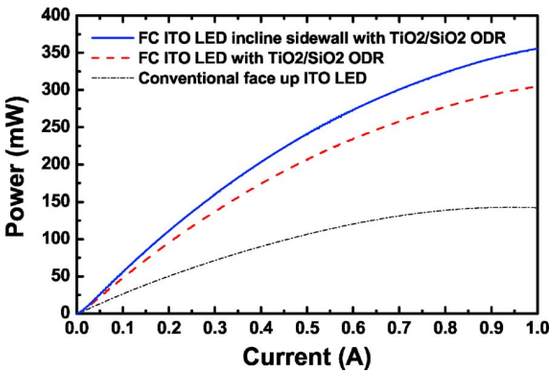

Figure 4. (Color online) EL intensity-current (*L-I*) characteristics of the FC ITO LEDs with an inclined sidewall coated TiO_2/SiO_2 ODR, FC ITO LEDs with TiO_2/SiO_2 ODR and conventional face up ITO LEDs, respectively.

transmission measurements. Figure 3 shows the measured transmittance at incidence angles of 0°, 30°, 60°, and 85° for unpolarized light as a function of the wavelength. We observed that rather high reflectance (>99.5%) can be achieved from 441 to 465 nm, and up to an incidence angle of 85° (e.g., the yellow region). This wavelength region falls in the CPBG shown in Fig. 3 and is expected from the photonic band diagram in Fig. 2.

Results and Discussion

We performed electroluminescence measurements by injecting a continuous current into our LEDs at room temperature. The light output was detected by a calibrated integrating sphere with Si photodiode on the package device. We found that the measured forward voltages under injection current 350 mA at room temperature for the FC ITO LED device coated TiO_2/SiO_2 ODR with vertical and inclined sidewall and the conventional face up ITO LED were all about 3.4 V. It was also found that the *I-V* curves were almost identical for the FC ITO LED coated TiO_2/SiO_2 ODR with vertical and inclined sidewall.

The intensity-current (*L-I*) characteristics of the three different types of LEDs were shown in Fig. 4. We clearly observed that the light output power of the FC ITO LED coated TiO_2/SiO_2 ODR with the inclined sidewall was larger than that with vertical sidewall under all driving currents. At an injection current of 350 mA, we found that the MQW emission peaks of those three different devices were all located at about 465 nm, and the light output power of the FC ITO LED coated TiO_2/SiO_2 ODR with vertical and inclined sidewall and the conventional face up ITO LED were approximately

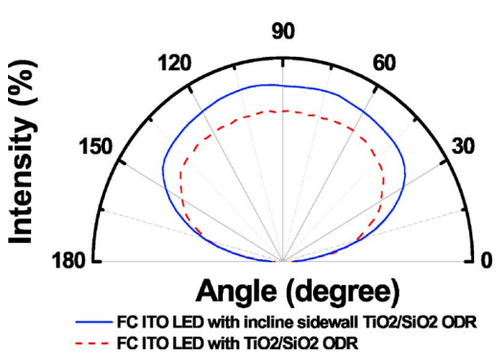

Figure 5. (Color online) Measurements of the far-field patterns distribution from the FC ITO LEDs with an inclined sidewall coated TiO_2/SiO_2 ODR and the FC ITO LEDs with TiO_2/SiO_2 ODR, respectively.

Table I. Parameters of structure layer in the simulated GaN-based FC ITO LEDs with TiO_2/SiO_2 ODR.

Layer	Sapphire	n-GaN	MQW	p-GaN	ITO	TiO_2	SiO_2
Thickness (μm)	100	2.0	0.1	0.25	0.2	0.056	0.077
Refractive index	1.63	2.5	2.3	2.5	2.0	2.52	1.48

183, 158, and 83 mW, respectively. In other words, the FC ITO LED coated TiO_2/SiO_2 ODR with inclined and vertical sidewall show the light output power enhancement by 122% and 92%, respectively, when compared to the conventional face up ITO LED. The FC ITO LED coated TiO_2/SiO_2 ODR with an inclined sidewall increased the light output power by a factor of 1.15 more than the device with vertical sidewall. It indicated that the FC ITO LED coated TiO_2/SiO_2 ODR with about 50° inclined sidewall had better light extraction efficiency than that with vertical sidewall.

We also measured the light output radiation patterns of the FC ITO LED coated TiO_2/SiO_2 ODR with vertical and inclined sidewalls at a driving current of 350 mA, as shown in Fig. 5. We mounted both structures on the header only and without epoxy pack-

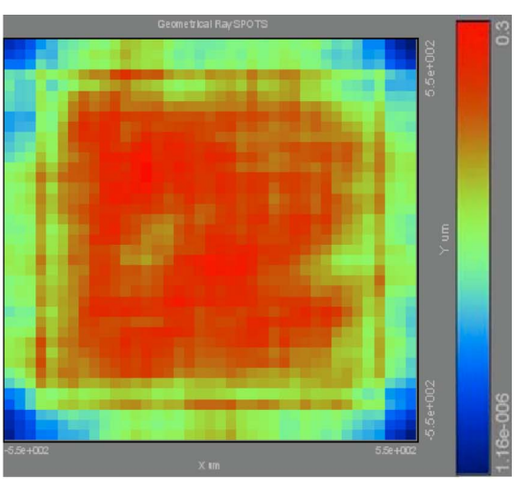

(a)

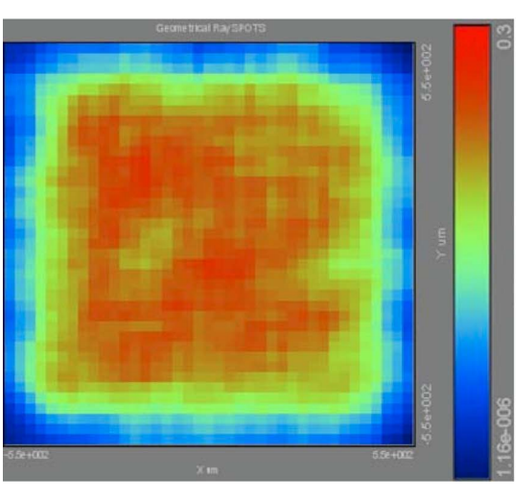

(b)

Figure 6. (Color online) Top-view ray tracing images of the (a) FC ITO LED with an inclined sidewall coated ODR and (b) FC ITO LED with ODR.

Downloaded on 2019-09-16 to IP 143.215.34.165 address. Redistribution subject to ECS terms of use (see ecsdl.org/site/terms_use) unless CC License in place (see abstract).

Seoul Semiconductor, Exhibit 2001
LGI v. SSC, IPR2019-01154

age. Then the far-field pattern was measured from 0° to 180° by the conventional goniometric radiometer measurement technique. It can be seen that the FC ITO TiO_2/SiO_2 ODR LED with inclined sidewall shows higher extraction efficiency with a view angle about 150° than the LED with vertical sidewall. This enhancement is attributed to the higher reflectance of TiO_2/SiO_2 ODR coated on inclined sidewall within the blue regime when compared to TiO_2/SiO_2 ODR coated on vertical sidewall.

We also simulated the light propagation and reflection using the ray tracing method provided by Advanced System Analysis program software (ASAP). For simplicity, we employed a three-dimensional model on both GaN-based FC ITO TiO_2/SiO_2 ODR LED with vertical and with about 50° inclined sidewall. In addition, the simulation structure neglected sidewalls roughness and the absorption coefficient. The relative thickness and refractive index of each structure layer of the simulated GaN-based FC ITO TiO_2/SiO_2 ODR LEDs are described in Table I. The top mesa area of both FC ITO LEDs was 1×1 mm. Figures 6a and b show the top-view ray tracing images of FC ITO TiO_2/SiO_2 ODR LED with inclined and vertical sidewall, respectively. The x and y axes correspond to the chip length, 1×1 mm, and the color represents the light intensity. The result also shows the light extraction efficiency can be greatly enhanced by the inclined sidewall. Such an enhancement could have a larger probability to be scattered from the inclined sidewall and, thus, achieve high brighter LEDs.

Conclusion

In conclusion, GaN-based FC ITO TiO_2/SiO_2 ODR LEDs with an inclined sidewall were designed and fabricated. At a driving current of 350 mA and a chip size of 1×1 mm, the light output power and the light extraction enhancement of FC ITO TiO_2/SiO_2 ODR LEDs with an inclined sidewall reaches 183 mW and an enhancement of 30% when compared to the same device without the inclined sidewall. Furthermore, stronger enhancement around the vertical direction and wider view angle as shown in the radiation patterns of the FC ITO TiO_2/SiO_2 ODR LED with inclined sidewall showed stronger optical power within 150° cone due to the higher reflectance and the inclined sidewall of the designed ODR within blue regime. Our work offers promising potential for enhancing output powers of commercial light emitting devices.

Acknowledgments

This work was supported by the National Science Council of the Republic of China (ROC) in Taiwan under contract no. NSC 94-2120-M009-007 and NSC 94-2752-E009-007-PAE.

National Chiao Tung University assisted in meeting the publication costs of this article.

References

1. M. Koike, N. Shibata, H. Kato, and Y. Takahashi, *IEEE J. Sel. Top. Quantum Electron.*, **8**, 271 (2002).
2. J. K. Kim, Th. Gessmann, H. Luo, and E. F. Schubert, *Appl. Phys. Lett.*, **84**, 4508 (2004).
3. S. J. Chang, C. S. Chang, Y. K. Su, C. T. Lee, W. S. Chen, C. F. Shen, Y. P. Hsu, S. C. Shei, and H. M. Lo, *IEEE Trans. Adv. Packag.*, **28**, 273 (2005).
4. C. H. Lin, C. F. Lai, T. S. Ko, H. W. Huang, H. C. Kuo, Y. Y. Hung, K. M. Leung, C. C. Yu, R. J. Tsai, C. K. Lee, T. C. Lu, and S. C. Wang, *IEEE Photon. Technol. Lett.*, **18**, 2050 (2006).
5. C. S. Chang, S. J. Chang, Y. K. Su, C. T. Lee, Y. C. Lin, W. C. Lai, S. C. Shei, J. C. Ke, and H. M. Lo, *IEEE Photon. Technol. Lett.*, **16**, 750 (2004).
6. C. C. Kao, H. C. Kuo, H. W. Huang, J. T. Chu, Y. C. Peng, Y. L. Hsieh, C. Y. Luo, C. C. Yu, C. F. Lin, and S. C. Wang, *IEEE Photon. Technol. Lett.*, **17**, 19 (2005).
7. C. F. Lin, Z. J. Yang, J. H. Zheng, and J. J. Dai, *IEEE Photon. Technol. Lett.*, **17**, 2038 (2005).
8. C. F. Lin, Z. J. Yang, B. H. Chin, J. H. Zheng, J. J. Dai, B. C. Shieh, and C. C. Chang, *J. Electrochem. Soc.*, **153**, G1020 (2006).
9. J. C. Bhat, M. J. Ludowise, and D. A. Steigerwald, U.S. Pat. 6,891,197B2 (2005).
10. J. Q. Xi, M. Ojha, J. L. Plawsky, W. N. Gill, J. K. Kim, and E. F. Schubert, *Appl. Phys. Lett.*, **87**, 031111 (2005).
11. C. H. Lin, J. Y. Tsai, C. C. Kao, H. C. Kuo, C. C. Yu, J. R. Lo, and K. M. Leung, *Jpn. J. Appl. Phys., Part 1*, **45**, 1591 (2006).
12. C. H. Lin, K. M. Leung, and T. Tamir, *J. Opt. Soc. Am. A*, **19**, 2005 (2002).

Downloaded on 2019-09-16 to IP 143.215.34.165 address. Redistribution subject to ECS terms of use (see ecsdl.org/site/terms_use) unless CC License in place (see abstract).

Seoul Semiconductor, Exhibit 2001
LGI v. SSC, IPR2019-01154

APPENDIX G

Applied Physics Letters

Enhanced light extraction in light-emitting diodes with photonic crystal structure selectively grown on p-GaN

Cite as: Appl. Phys. Lett. **96**, 181110 (2010); https://doi.org/10.1063/1.3427352
Submitted: 05 January 2010 . Accepted: 15 April 2010 . Published Online: 07 May 2010

Chu-Young Cho, Se-Eun Kang, Ki Seok Kim, Sang-Jun Lee, Yong-Seok Choi, Sang-Heon Han, Gun-Young Jung, and Seong-Ju Park

View Online Export Citation

ARTICLES YOU MAY BE INTERESTED IN

Origin of efficiency droop in GaN-based light-emitting diodes
Applied Physics Letters **91**, 183507 (2007); https://doi.org/10.1063/1.2800290

Enhanced light extraction from GaN-based green light-emitting diode with photonic crystal
Applied Physics Letters **91**, 181109 (2007); https://doi.org/10.1063/1.2804005

Enhanced light extraction from GaN-based light-emitting diodes with holographically generated two-dimensional photonic crystal patterns
Applied Physics Letters **87**, 203508 (2005); https://doi.org/10.1063/1.2132073

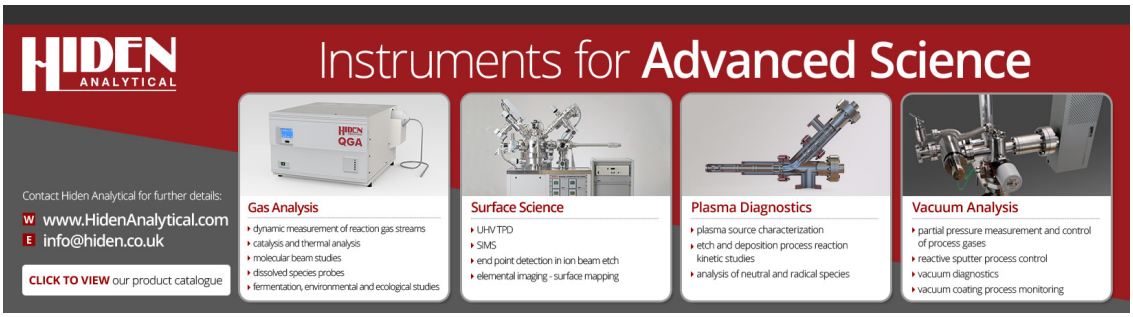

AIP Publishing

© 2010 American Institute of Physics.

Seoul Semiconductor, Exhibit 2001
LGI v. SSC, IPR2019-01154

APPLIED PHYSICS LETTERS **96**, 181110 (2010)

Enhanced light extraction in light-emitting diodes with photonic crystal structure selectively grown on *p*-GaN

Chu-Young Cho,[1] Se-Eun Kang,[1] Ki Seok Kim,[1] Sang-Jun Lee,[1] Yong-Seok Choi,[1] Sang-Heon Han,[1,3] Gun-Young Jung,[1] and Seong-Ju Park[1,2,a)]
[1]*Department of Materials Science and Engineering, Gwangju Institute of Science and Technology, Gwangju 500-712, Republic of Korea*
[2]*Department of Nanobio Materials and Electronics, Gwangju Institute of Science and Technology, Gwangju 500-712, Republic of Korea*
[3]*Samsung LED Co. Ltd., Suwon 443-743, Republic of Korea*

(Received 5 January 2010; accepted 15 April 2010; published online 7 May 2010)

We report on the properties of green light-emitting diodes (LEDs) with a photonic crystal (PC) structure on *p*-GaN. A PC structure was fabricated by the selective area epitaxy of *p*-GaN using SiO_2 nanopillars. The electrical characteristics of LEDs with PC were not degraded and the optical output power of green LEDs with PC was increased by 70% at 20 mA of injection current compared with that of conventional LEDs without PC. This enhancement of optical output power was attributed to the improvement in light extraction efficiency by the SiO_2/*p*-GaN PC layer on *p*-GaN. © *2010 American Institute of Physics*. [doi:10.1063/1.3427352]

Light-emitting diodes (LEDs) based on group III-nitride materials have been rapidly developed for various applications, such as full-color displays, automobile headlights, traffic lights, and solid-state lighting. However, for next-generation applications of high efficiency LEDs, further improvement of the light extraction efficiency ($\eta_{extraction}$) is required. In particular, since the green LEDs show much lower external quantum efficiency (η_{ext}) compared to blue LEDs, improvement of the $\eta_{extraction}$ in green LEDs is crucial.[1] The low $\eta_{extraction}$ of GaN-based LEDs is mainly due to the total internal reflection of light by the difference between the refractive indices of GaN (n=2.5) and air (n=1). The photons can only escape from LEDs to air within a critical angle of 23.6°, and the photons emitted outside the critical angle are reflected from the interface and are reabsorbed by the LEDs. Therefore, to enhance the $\eta_{extraction}$ several methods such as texturing of surface,[2,3] patterned sapphire substrate,[4,5] and photonic crystal (PC)[6–13] have been proposed. A PC is a periodic structure comprising two materials with different refractive indices. Multiple scattering of photons by lattices of periodically varying refractive indices acts to form a photonic band gap (PBG) in which propagation of certain wavelengths of the electromagnetic waves are prohibited, resulting in an enhanced light extraction in a vertical direction from LEDs.[6–8]

The PC structure for enhancement of $\eta_{extraction}$ in GaN-based LEDs has generally been formed directly in the *p*-GaN layer.[9–12] However, the incorporation of a PC structure in the *p*-GaN layer requires the use of a plasma etching process, resulting in plasma damage to the *p*-GaN layer. Many groups have reported that the electrical characteristics of LEDs with PC structures were degraded due to the etching damage to *p*-GaN.[9–12,14] To overcome the problem of plasma damage in *p*-GaN and electrical degradation in LEDs with a PC structure, we realized a PC structure on a *p*-GaN layer using a selective area epitaxy (SAE) method. In this paper, we report on the electrical and optical properties of green LEDs with a PC structure formed on *p*-GaN. The $\eta_{extraction}$ of LEDs with a PC structure on a *p*-GaN layer was significantly enhanced by the PC effect and showed no degradation of electrical characteristics by avoiding the use of the plasma etching process on *p*-GaN.

The green InGaN/GaN LEDs were grown on a *c*-plane (0001) sapphire by metalorganic chemical vapor deposition (MOCVD). After the growth of a 25 nm thick GaN nucleation layer at 550 °C, a 2 μm thick undoped GaN layer and a 2 μm thick *n*-GaN layer were grown at 1020 °C. Then, five periods of InGaN/GaN multiple quantum wells (MQWs) were grown at 730 °C, followed by the growth of a 150 nm thick *p*-GaN layer at 970 °C. A PC structure on *p*-GaN layer was realized by SAE of *p*-GaN using SiO_2 nanopillars. To fabricate the PC structure, a 100 nm thick SiO_2 layer was deposited as an SAE mask on *p*-GaN layer using plasma-enhanced chemical vapor deposition. Then, PC patterns with circular hole patterns were generated in a photoresist (PR) layer on the SiO_2 layer by employing two-beam laser holography. The PR was subsequently removed after deposition of 5 nm Cr mask to etch the SiO_2 pillar with circular cylinder shape. The SiO_2 layer with a Cr mask was etched by reactive ion etching using CH_4 gas to form the SiO_2 nanopillars on the *p*-GaN as shown in Fig. 1(a). The period (a), radius (r), and height (h) of the SiO_2 nanopillars are 320 ± 7, 100 ± 5, and 100 nm, respectively. After selective regrowth of *p*-GaN at 970 °C for 4 min, the *p*-GaN filled the surrounding region of SiO_2 nanopillars. The thickness of the regrown *p*-GaN layer is 100 nm and this is same as that of the SiO_2 nanopillars as shown in Fig. 1(b). As a result, a periodic PC structure of SiO_2 and *p*-GaN with different refractive indices is formed on the *p*-GaN layer. Then, thermal activation of *p*-GaN was performed at 800 °C for 5 min under ambient nitrogen by a rapid thermal annealing process. To fabricate the LEDs, the *p*-GaN layer was etched by an inductively coupled plasma (ICP) etching process using $Cl_2/CH_4/H_2/Ar$ gases until the *n*-GaN layer was exposed for *n*-type Ohmic contact formation. Next, the LEDs with a size of 300

a)Author to whom correspondence should be addressed. Electronic mail: sjpark@gist.ac.kr.

 © 2010 American Institute of Physics

Seoul Semiconductor, Exhibit 2001
LGI v. SSC, IPR2019-01154

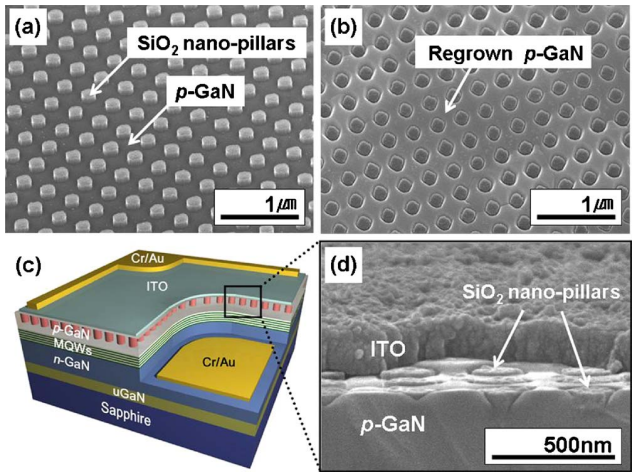

FIG. 1. (Color online) Tilted plan-view SEM images of (a) SiO_2 nanopillars on the *p*-GaN layer, (b) *p*-GaN regrown by SAE. (c) Schematic of green LEDs with a selectively grown PC structure. (d) Cross-sectional SEM image of a SiO_2/*p*-GaN PC structure on *p*-GaN.

$\times 300\ \mu m^2$ were fabricated using indium tin oxide (ITO) with a thickness of 150 nm as a transparent current spreading layer and Cr/Au as the *n*- and *p*-pad electrodes by e-beam evaporation. Figure 1(c) shows the schematic of a green LED with a selectively grown PC structure. Figure 1(d) is a cross-sectional scanning electron microscopy (SEM) image of a *p*-GaN layer, showing that the SiO_2 nanopillars were entirely surrounded by *p*-GaN.

In this study, the PC structure on a *p*-GaN layer was designed using a simulation program based on the preconditioned conjugate-gradient plane-wave expansion method.[6,7] Figure 2(a) shows the result of the simulation, which describes the normalized frequency $(\omega a/2\pi c = a/\lambda)$ as a function of the ratio (r/a) for a PC structure consisting of a square array of 100 nm thick SiO_2 nanopillars surrounded by *p*-GaN. This study is focused on transverse-electric (TE) mode bands that are characterized by light propagating in parallel to the slab of LED. The optimal period and radius of

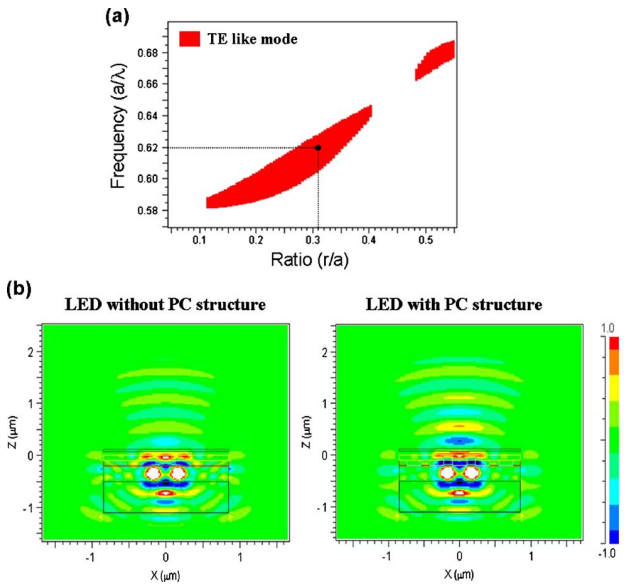

FIG. 2. (Color online) (a) The gap map for a PC structure with a square lattice array of SiO_2 nanopillars surrounded by *p*-GaN. (b) 3D-FDTD simulation results of light propagation in LEDs with and without a PC structure.

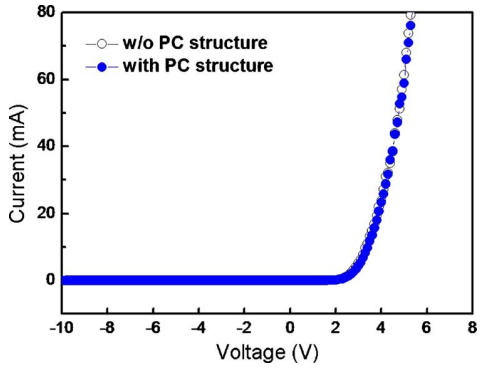

FIG. 3. (Color online) *I-V* characteristics of green LEDs with and without a PC structure.

SiO_2 nanopillar are estimated to be 323 and 100 nm, respectively. Details of the simulation method have been described elsewhere.[12,13] Moreover, we predict the $\eta_{extraction}$ and the propagation of light emitted from the MQWs via the PC structure using a three-dimensional finite difference time domain (3D-FDTD) simulation based on a genetic algorithm with periodic boundary condition introduced by a square array of the SiO_2 nanopillar structure. Figure 2(b) shows the results of the FDTD simulation of a green LED with and without a PC structure on *p*-GaN. Figure 2(b) clearly shows that the light emitted from the MQWs of the LED with a PC structure propagates more vertically, compared to the LED without a PC structure. This result is attributed to a PBG where photons with frequencies within the PBG are not allowed to propagate but coupled to escape into the air in a vertical direction.[6–13]

Figure 3 shows the current-voltage (*I-V*) characteristics of green LEDs with and without a PC structure. As shown in Fig. 3, the forward voltage of the LED with a PC structure is 3.8 V, which is same as that of LED without a PC structure. The series resistance of 24.3 Ω of LED with a PC structure is very close to 25.8 Ω of LED without a PC structure. The slight decrease in series resistance is attributed to the high quality regrown *p*-GaN. These results indicate that a PC structure selectively grown on a *p*-GaN layer does not cause the degradation of electrical properties. The plasma dry etching process has been reported to produce surface defects such as vacancies, impurities, and residuals, resulting in degradation of electrical properties of *p*-GaN and optical output power of LEDs because surface defects increase the junction leakage and nonradiative recombination.[14,15] However, the PC structure fabricated by SAE could effectively reduce the surface defects in *p*-GaN layer because the surface was epitaxially grown by MOCVD. Furthermore, the threading dislocations are also terminated when they encounter the SiO_2 nanopillars, resulting in a decrease in dislocation density of selectively grown *p*-GaN layer.[16,17] Therefore, the selectively grown *p*-GaN layer could contribute to the nondegradation of electrical properties of LEDs.

In order to investigate the optical properties of green LEDs with a PC structure, the electroluminescence (EL) was measured from the LEDs. Figure 4(a) shows the EL spectra of green LEDs with and without a PC structure at the injection currents of 20 and 100 mA. The EL emission wavelength is blueshifted from 528 nm at 20 mA to 521 nm at 100 mA with increasing injection current. The EL peak shift toward a higher energy side, with the increasing injection cur-

Seoul Semiconductor, Exhibit 2001
LGI v. SSC, IPR2019-01154

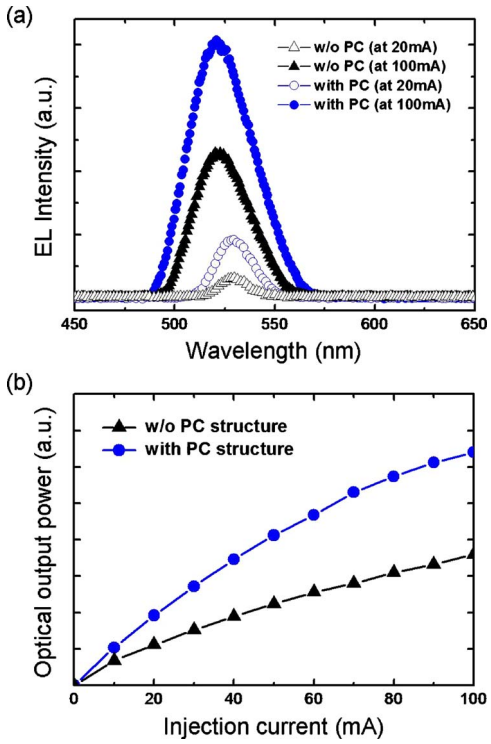

FIG. 4. (Color online) (a) Room temperature EL spectra of green LEDs with and without a PC structure, which were measured at an injection current of 20 and 100 mA. (b) Optical output power of green LEDs with and without a PC structure.

rent, is due to a screening effect of the polarization-induced electric field by carriers and to the band-filling effect of the localized energy states formed by potential fluctuation in MQWs.[18] As shown in Fig. 4(a), there are no peak shifts in the EL emission peaks of both LEDs at the same current. However, the EL intensities of green LEDs with a PC structure are much higher than those of LEDs without a PC structure. This result is attributed to the enhanced $\eta_{\text{extraction}}$ of a LED with a PC structure on the *p*-GaN layer. It is believed that the light from a laterally guided mode is redirected to a vertically radiated mode in LEDs.[6–13] Figure 4(b) shows the optical output power of green LEDs with and without a PC structure as a function of injection current. The optical output power of each LED was measured from the top side of LEDs using a 2 cm diameter Si photodiode connected to an optical power meter. The distance between the photodiode and the LEDs was 10 cm. As shown in Fig. 4(b), the optical output power of green LEDs with a PC structure is increased by 70% at 20 mA of injection current compared with that of conventional LEDs without a PC structure. This improvement of optical output power is a result of the increase in the $\eta_{\text{extraction}}$ due to the PC effect, which inhibits the emission of guided modes and redirects trapped light into the radiated modes.

In conclusion, we demonstrate the green LEDs with a PC structure formed on a *p*-GaN layer. The electrical characteristics of green LEDs with a PC structure are not degraded and the optical output power of LEDs with a PC is increased by 70% at 20 mA compared with that of conventional LEDs without a PC. The enhancement of optical output power is attributed to an increase in $\eta_{\text{extraction}}$ by a SiO_2/*p*-GaN PC layer on *p*-GaN.

This work was supported by World Class University (WCU) program through a grant provided by the Ministry of Education, Science and Technology (MEST) of Korea (Project No. R31-2008-000-10026-0) and the Ministry of Land, Transport, and Maritime Affairs (Grant No. 20090006) and the Air Force Office of Scientific Research (AFOSR) (Project No. AOARD09–4062).

[1]E. F. Schubert, *Light-Emitting Diodes* (Cambridge University Press, Cambridge, UK, 2003).
[2]C. Huh, K. S. Lee, E. J. Kang, and S. J. Park, J. Appl. Phys. **93**, 9383 (2003).
[3]T. Fujii, Y. Gao, R. Sharma, E. L. Hu, S. P. DenBaars, and S. Nakamura, Appl. Phys. Lett. **84**, 855 (2004).
[4]K. Tadatomo, H. Okagawa, Y. Ohuchi, T. Tsunekawa, Y. Imada, M. Kato, and T. Taguchi, Jpn. J. Appl. Phys., Part 2 **40**, L583 (2001).
[5]Y. J. Lee, J. M. Hwang, T. C. Hsu, M. H. Hsieh, M. J. Jou, B. J. Lee, T. C. Lu, H. C. Kuo, and S. C. Wang, IEEE Photon. Technol. Lett. **18**, 1152 (2006).
[6]S. Fan, P. R. Villeneuve, J. D. Joannopoulos, and E. F. Schubert, Phys. Rev. Lett. **78**, 3294 (1997).
[7]E. Yablonovitch, T. J. Gmitter, and R. Bhat, Phys. Rev. Lett. **61**, 2546 (1988).
[8]S. G. Johnson and J. D. Joannopoulos, *Photonic Crystal* (Kluwer Academic, Boston, 2002).
[9]T. N. Oder, K. H. Kim, J. Y. Lin, and H. X. Jiang, Appl. Phys. Lett. **84**, 466 (2004).
[10]J. Shakya, K. H. Kim, J. Y. Lin, and H. X. Jiang, Appl. Phys. Lett. **85**, 142 (2004).
[11]D. H. Kim, C. O. Cho, Y. G. Roh, H. Jeon, Y. S. Park, J. Cho, J. S. Im, C. Sone, Y. Park, W. J. Choi, and Q. H. Park, Appl. Phys. Lett. **87**, 203508 (2005).
[12]J. Y. Kim, M. K. Kwon, K. S. Lee, S. J. Park, S. H. Kim, and K. D. Lee, Appl. Phys. Lett. **91**, 181109 (2007).
[13]M. K. Kwon, J. Y. Kim, I. K. Park, K. S. Kim, G. Y. Jung, S. J. Park, J. W. Kim, and Y. C. Kim, Appl. Phys. Lett. **92**, 251110 (2008).
[14]X. A. Cao, S. J. Pearton, A. P. Zhang, G. T. Dang, F. Ren, R. J. Shul, L. Zhang, R. Hickman, and J. M. Van Hove, Appl. Phys. Lett. **75**, 2569 (1999).
[15]H. S. Yang, S. Y. Han, K. H. Baik, S. J. Pearton, and F. Ren, Appl. Phys. Lett. **86**, 102104 (2005).
[16]S. D. Hersee, X. Y. Sun, and X. Wang, Nano Lett. **6**, 1808 (2006).
[17]Y. S. Chen, W. Y. Shiao, T. Y. Tang, W. M. Chang, C. H. Liao, C. H. Lin, K. C. Shen, C. C. Yang, M. C. Hsu, J. H. Yeh, and T. C. Hsu, J. Appl. Phys. **106**, 023521 (2009).
[18]Y. D. Qi, H. Liang, D. Wang, Z. D. Lu, W. Tang, and K. M. Lau, Appl. Phys. Lett. **86**, 101903 (2005).

Seoul Semiconductor, Exhibit 2001
LGI v. SSC, IPR2019-01154

APPENDIX H

phys. stat. sol. (c) **4**, No. 1, 25–28 (2007) / **DOI** 10.1002/pssc.200673554

Fabrication and optical properties of blue LEDs with silica microsphere coating

K. Kusakabe[*, 1], **S. Funazaki**[1], **K. Okamoto**[1], **S. Nishizawa**[1], and **K. Ohkawa**[1, 2]

[1] Department of Applied Physics, Faculty of Science, Tokyo University of Science, 1-3 Kagurazaka, Shinjuku, Tokyo 162-8601, Japan
[2] Exploratory Research for Advanced Technology (ERATO), Japan Science and Technology Agency (JST), Japan

Received 16 May 2006, revised 17 July 2006, accepted 18 July 2006
Published online 11 January 2007

PACS 81.05.Ea, 81.15.Gh, 85.60.Jb

We report the enhancement of light extraction efficiency of InGaN-based blue light emitting diodes by using a surface light-scattering layer. A number of SiO_2 microspheres embedded into a ZrO_2 thin layer played a role of a light-scattering medium. Coating the light-scattering layer on device surface, the interference fringes of electroluminescence (EL) spectra were eliminated and the EL intensity around 440–450 nm was increased by a factor of 1.3.

© 2007 WILEY-VCH Verlag GmbH & Co. KGaA, Weinheim

1 Introduction

III-V nitride semiconductors are very attractive materials for optoelectronic applications [1]. The InGaN-based light emitting diodes (LEDs) are widely used for display and illumination fields. Today, for the production of single color of light, LEDs are more efficient than filtered incandescents by over ten times, and white LEDs are currently more than twice as efficient as their incandescent counterparts [2]. As they are solid state light sources, they should offer high-flux performance beyond that of fluorescent lamps. Therefore, it is considerably requested to increase the external quantum efficiency of InGaN-LEDs. The light extraction efficiency is a key factor of the external quantum efficiency of LEDs. There have been several reports to improve the light extraction efficiency, for example, a cone-shaped surface texture via laser lift-off [3], a microlens array and photonic crystal structure which are subjected sophisticated process techniques [4, 5]. Above those, however, make device fabrication further complicated. In this study, we report a simple method to increase the light extraction efficiency of LEDs through a surface light-scattering layer. The surface light-scattering layer was composed by SiO_2 microspheres embedded into a thin ZrO_2 layer.

2 Results and discussion

The InGaN-based LED wafers were grown on *c*-plane sapphire substrates by atmospheric metalorganic vapor-phase epitaxy [6–8]. The device structures were fabricated by means of conventional photolithograph and dry etching processes, then electrodes were deposited by electron beam evaporation. After those, the surface light-scattering layer was coated on the LED surface.

The light-scattering layer has two components of the flat ZrO_2 layer and SiO_2 microspheres, of which the refractive indices are n = 2.1 and n = 1.5 at 450 nm. The former acts to reduce a total internal reflec-

[*] Corresponding author: e-mail: kusakabe@rs.kagu.tus.ac.jp, Phone & Fax: +81-3-3260-4280

WILEY InterScience® DISCOVER SOMETHING GREAT

© 2007 WILEY-VCH Verlag GmbH & Co. KGaA, Weinheim

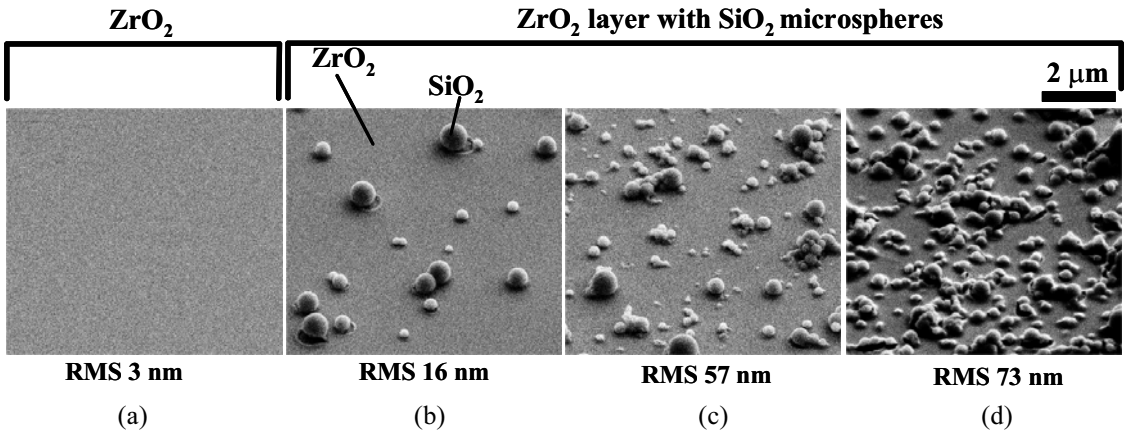

Fig. 1 SEM surface images showing the light-scattering layers. (a) The ZrO_2 layer without SiO_2 microspheres, (b)–(d) the ZrO_2 layer with SiO_2 microspheres for various surface roughness, where the RMS values were evaluated from a 200 μm line scan.

tion at the epilayer surface (n = 2.5), while the latter serves as a light-scattering center. Here, the ZrO_2 thin layer was made from a solvent precursor and deposited by spin coating and thermal annealing. The SiO_2 microspheres with diameters of 0.2–0.6 μm were introduced into the ZrO_2 solvent with 2.5–3.0 wt% concentrations. The density of microspheres or the surface roughness of light-scattering layer was controllable thorough the iteration of spin coating. Figure 1 shows scanning electron microscope (SEM) images of light-scattering layers for various surface roughness. The layer without SiO_2 microspheres appeared almost featureless and its roughness was 3 nm in RMS. On the other hand, the layers with SiO_2 microspheres changed surface roughness from 16 nm to 73 nm by the deposition procedure. It is expected that the scheme of light-scattering or light extraction varies with RMS values.

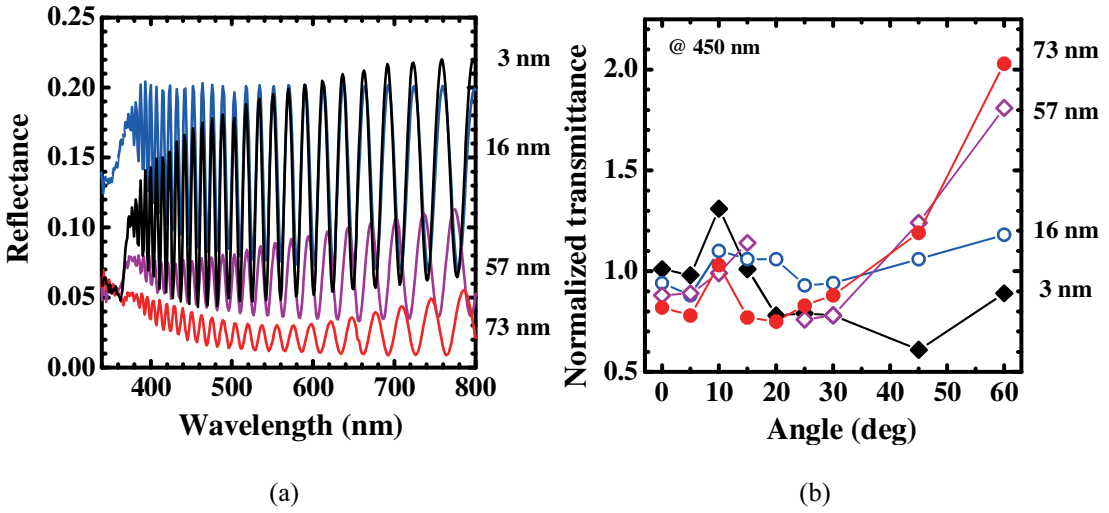

Fig. 2 (a) Reflectance spectra of the light-scattering layers on GaN. (b) Transmission intensities at 450 nm normalized by the transmittance of an uncoated sample. The right-side values indicate the corresponding surface roughness in RMS.

© 2007 WILEY-VCH Verlag GmbH & Co. KGaA, Weinheim

Seoul Semiconductor, Exhibit 2001
LGI v. SSC, IPR2019-01154

In order to characterize light scattering and extraction by the coating layer, reflectance spectra and transmission intensities were measured. Figure 2(a) shows the reflectance spectra of the surface scattering layers on GaN. It was found that interference amplitudes were reduced with increasing of surface roughness, due to an increment of the light-scattering magnitude. This result clearly indicates that the coating layer plays a role of the light-scattering medium. Figure 2(b) shows transmission intensities normalized by the transmittance of uncoated sample as a reference. A white light source was illuminated from backside normal. The transmission intensities were measured changing a detection angle from surface normal and monochromated at 450 nm. The normalized transmittances were an approximately unity at the narrow angle side, where the 23 deg was corresponding to the critical angle of GaN/air. On the contrary, the normalized transmittances were further increased for the large RMS sample at the wide angle side. This result points out that the coating layer improves the light extraction efficiency.

Next, we demonstrated availability of the light-scattering layer through the blue-LED performance. Electroluminescence (EL) spectra of LEDs with and without the surface light-scattering layer were obtained under a DC 20 mA operation. The EL spectra were detected at the 50 deg inclined from surface normal orientation. Figure 3 shows the EL spectra and current-voltage (I-V) characteristic of LEDs. The bare chip LED showed blue emission at a 440–450 nm range. The EL spectrum of bare LED had a single peak with weak fringes due to an interference effect. The surface coated LED indicated the increase of EL intensity and the elimination of interference fringes. The increment factor was 1.3.

The emission profile of LEDs was observed. Figure 4 shows the optical micrograph images showing the emission pattern of LEDs at 20 mA. The dark squares in photograph correspond to the n-electrode while the rectangular bars correspond to the p-electrode. The electrical probes contact the each electrode. The bare LED indicated that the bright area was placed only near the p-electrode. However, the coated LED possessed the wider bright area. This is due to the light propagation along the surface coating layer. Thus, an edge of the surface coating area indeed appeared bright. This phenomenon also contributes to the improvement of the light extraction efficiency.

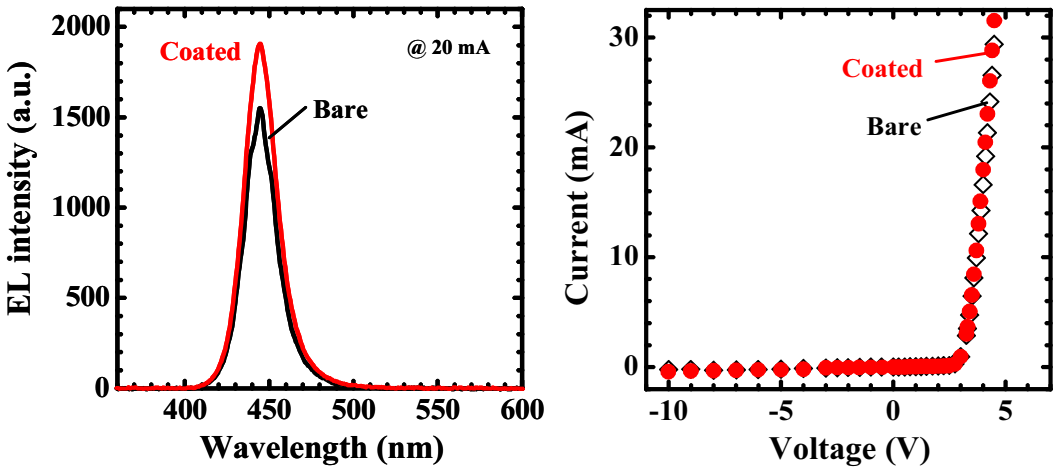

Fig. 3 (a) EL spectra of LEDs with or without the surface coating. (b) I-V characteristic of LEDs.

© 2007 WILEY-VCH Verlag GmbH & Co. KGaA, Weinheim

Seoul Semiconductor, Exhibit 2001
LGI v. SSC, IPR2019-01154

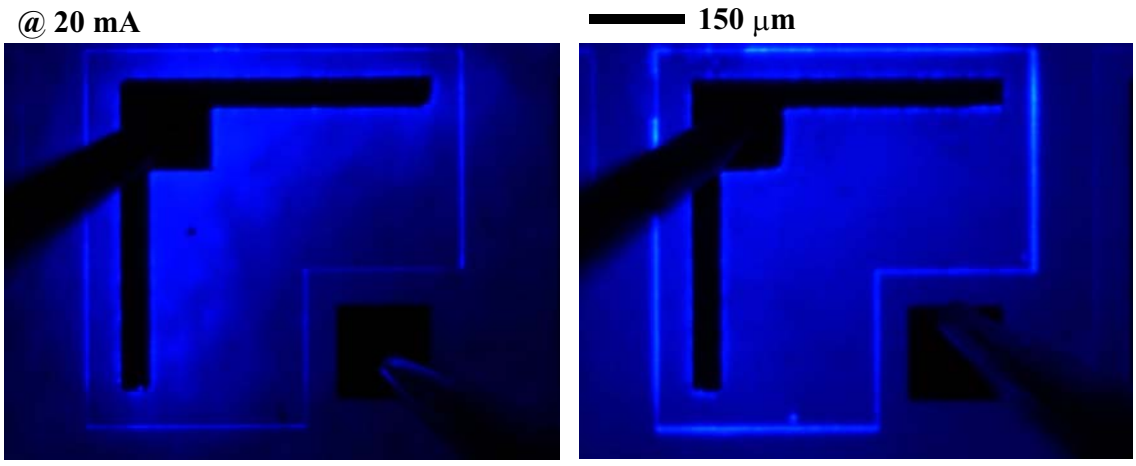

(a) Bare chip (b) Coated chip

Fig. 4 Optical micrograph images showing the emission pattern of LEDs.

3 Conclusion

We report the enhancement of light extraction efficiency of blue LEDs by coating the surface light-scattering layer. The SiO_2 microspheres embedded into the ZrO_2 layer act as the light-scattering medium. Coating the light-scattering layer on LEDs, the interference fringes of EL spectra were eliminated. The EL intensity around 440–450 nm was enhanced by a factor of 1.3.

Acknowledgements This work was partially supported by "Open Research Center" Project for Private Universities; matching fund subsidy from MEXT, 2002-2007.

References

[1] S. Nakamura and S. F. Chichibu (Eds.), Introduction to Nitride Semiconductor Blue Laser and Light Emitting Diodes (Taylor & Francis, London/New York, 2000).
[2] F. M. Steranka et al., phys. stat. sol. (a) **194**, 380 (2002).
[3] T. Fujii, Y. Gao, R. Sharma, E. L. Hu, S. P. DenBaars, and S. Nakamura, Appl. Phys. Lett. **84**, 855 (2004).
[4] H. W. Choi, C. Liu, E. Gu, G. McConnell, J. M. Girkin, I. M. Watson, and M. D. Dawson, Appl. Phys. Lett. **84**, 2253 (2004).
[5] K. Orita, S. Tamura, T. Takizawa, T. Ueda, M. Yuri, S. Takigawa, and D. Ueda, Jpn. J. Appl. Phys. **43**, 5809 (2004).
[6] K. Ohkawa, A. Hirako, and M. Yoshitani, phys. stat. sol. (a) **188**, 621 (2001).
[7] A. Hirako, M. Yoshitani, M. Nishibayashi, Y. Nishikawa, and K. Ohkawa, J. Cryst. Growth **237–239**, 931 (2002).
[8] A. Hirako and K. Ohkawa, phys. stat. sol. (a) **194**, 489 (2002).

© 2007 WILEY-VCH Verlag GmbH & Co. KGaA, Weinheim

Seoul Semiconductor, Exhibit 2001
LGI v. SSC, IPR2019-01154

APPENDIX I

Journal of Applied Physics

Stress in oxidized porous silicon layers

Cite as: Journal of Applied Physics **59**, 439 (1986); https://doi.org/10.1063/1.337036
Submitted: 16 July 1985 . Accepted: 25 September 1985 . Published Online: 04 June 1998

K. Barla, R. Herino, and G. Bomchil

View Online Export Citation

ARTICLES YOU MAY BE INTERESTED IN

Thermal oxidation of porous silicon: Study on structure
Applied Physics Letters **86**, 041501 (2005); https://doi.org/10.1063/1.1853519

The structural and luminescence properties of porous silicon
Journal of Applied Physics **82**, 909 (1997); https://doi.org/10.1063/1.366536

Porous silicon formation: A quantum wire effect
Applied Physics Letters **58**, 856 (1991); https://doi.org/10.1063/1.104512

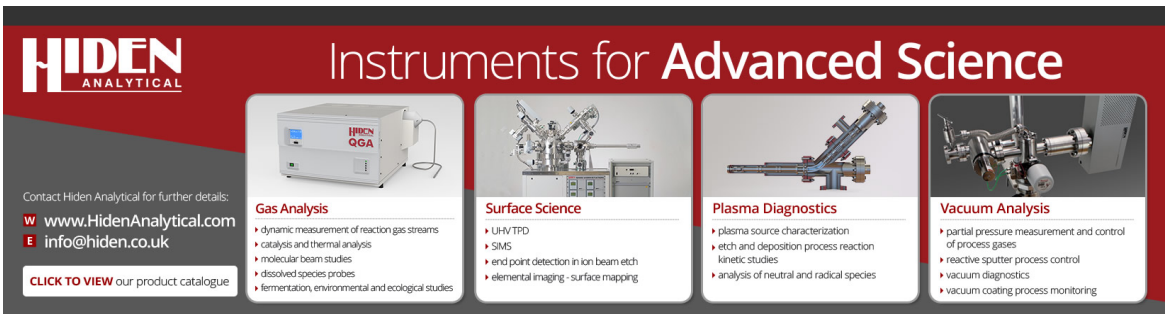

© 1986 American Institute of Physics.

Seoul Semiconductor, Exhibit 2001
LGI v. SSC, IPR2019-01154

Stress in oxidized porous silicon layers

K. Barla, R. Herino,[a] and G. Bomchil
Centre National d'Etudes des Télécommunications-CNS, Chemin du Vieux Chene-BP:98, 38243 Meylan Cedex, France

(Received 16 July 1985; accepted for publication 25 September 1985)

Stress was determined in oxidized porous silicon layers using x-ray diffraction to measure the substrate curvature. Stress is always compressive and its magnitude depends on oxide quality. The maximum value is reached when the oxide obtained from porous silicon is densified by a high-temperature process and is equivalent to standard thermal silicon dioxide. The stress magnitude decreases when oxide porosity increases. An increase in layer thickness is always observed when oxidation conditions lead to a porous oxide or when the initial porosity of the layer is lower than 56%, due to volumic expansion of silica relative to silicon, otherwise the thickness decreases.

INTRODUCTION

Different methods are investigated to obtain silicon-on-insulator (SOI) structures for applications in integrated circuit technology.[1] One of the promising techniques is based on the use of oxidized porous silicon. The different approaches[2–6] using porous silicon result in monocrystalline silicon islands on the top of a porous silicon layer that must be completely oxidized. Most of the papers which deal with porous silicon oxidation report wafer warpage induced by this process.[2] The origin of the wafer warpage is associated to the presence of a silicon dioxide layer over the silicon substrate. If this oxide layer were obtained only from bulk silicon, it is well known that due to the difference in thermal expansion coefficients between the silicon and the silicon dioxide and the volume expansion resulting from the transformation of Si into SiO_2 the oxide layer would be under compressive stress. In the case of porous silicon, the oxidation processes may result in an oxidized layer presenting different elastic properties than standard thermal dioxide. Even though the same phenomena of compressive stress exist, their magnitude may be quite different according to the quality of the oxides obtained form porous silicon.

The purpose of this work was to determine the strains induced in a sample by the oxidation of a porous layer. We will show that the thermal expansion difference between Si and SiO_2 always induces compressive stress in the layer whose magnitude decreases with increasing oxide porosity, while the volume expansion mainly affects the final thickness of the layer.

EXPERIMENT

Porous silicon layers were formed on 2-in. wafers of different resistivities: $10^{-2}\Omega$ cm (P^+) and 1 Ω cm (P). Different anodization conditions were used to obtain 2-μm-thick porous layers of different porosities, 51% for P^+ and 60% for P.

For both substrates, oxides were formed after a preoxidation step (300 °C, 1 h in dry O_2), either by a low-temperature oxidation (850 °C, 1 h in wet O_2), or by a low-temperature oxidation followed by a densification step (1090 °C, 1 h for P^+ and 15 min for P substrates in wet O_2).[7] Densified oxides present the same dissolution rate in buffered HF solutions than standard thermal oxides, while low-temperature oxides have a dissolution rate greater by a factor of 15.

Oxide volume expansion was determined by measuring the oxide thickness. This determination is complicated by the fact that during the porous layer oxidation, the bulk silicon at the bottom of the layer is also oxidized. In order to obtain the actual value of porous oxide expansion, it is necessary to take this oxide growth into account, and therefore to have a reference level in the layer. This is obtained by etching a strip in the middle of the porous layer (Fig. 1). After oxidation and localized etching in HF, the different steps are measured with a profiler; h_1 is the total thickness of the oxide obtained from porous silicon and oxidation of the substrate at the bottom of the porous layer. h_2 is the thickness of the oxide grown in the bare substrate. h_3 is the difference between the levels under the porous layer and the substrate after oxidation.

During oxidation, the silicon volume increases by a factor of 2.27. That is considering the Si substrate, only 56% of

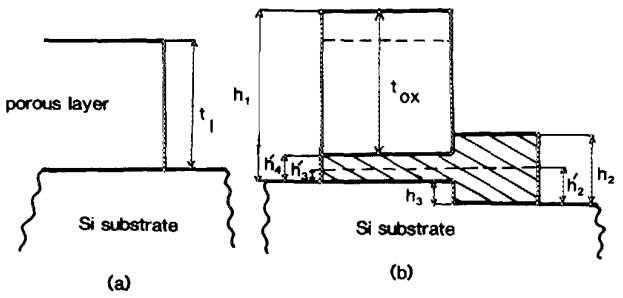

FIG. 1. Schematic drawing of the variation in thickness of a porous layer during oxidation process. (a) Before oxidation, (b) after oxidation, ▨ oxide grown in the Si substrate.

[a] Also at Université Scientifique et Médicale de Grenoble.

 0021-8979/86/020439-03$02.40 © 1986 American Institute of Physics

Seoul Semiconductor, Exhibit 2001
LGI v. SSC, IPR2019-01154

the oxide thickness is grown above the initial level of the substrate. So the initial level of the bare substrate is at $h_2' = 0.44\,h_2$ and the initial level under the porous level at $h_3' = h_2' - h_3$.

The thickness h_4' of the oxide grown in the substrate at the bottom of the porous layer during oxidation process by the rapid diffusion of oxidizing species through the porous structure is deduced from h_3' by the relation $h_3'/0.44$.

The actual value of the oxide thickness obtained from porous silicon layer is then

$$t_{ox} = (h_1 - h_3'/0.44) = h_1 - h_2 + h_3/0.44\,.$$

The variation in thickness Δt of the porous layer after oxidation is $\Delta t = t_1 - t_{ox}$.

The stress in the oxide layer is calculated after measurement of the wafer curvature. After etching the back oxide, curvature $(1/R)$ is determined by an x-ray technique[8] and the stress σ is obtained from the following expression[9]:

$$\sigma = \frac{1}{6R}\,\frac{E}{(1-\nu)\mathrm{Si}}\,\frac{t_s^2}{t_{ox}}, \tag{1}$$

where E is (Young's modulus) for silicon, ν its Poisson's ratio, and t_s and t_{ox} the thickness of the substrate and of the oxide, respectively.

RESULTS

A summary of the experimental results is presented in Table I. It is shown that after oxidation at low temperature, an expansion of the layer is always observed, positive step of 480 and 240 nm are obtained for P^+ and P samples, respectively. These values are much larger than those expected by taking into account the volume expansion due to the transformation of Si into SiO_2 and the initial porosity of the porous layer. This indicates that oxides formed at this temperature do not occupy the whole available volume and strongly suggests that they remain porous, as confirmed by the large etch rate in buffered HF solutions. The porosity of the porous silicon oxides can be obtained from the thickness measurements t_1 and t_{ox}. The actual silicon volume to be oxidized in a porous layer of porosity P_0 and of thickness t_1 is $V = t_1 S(1 - P_0)$, where S is the sample area. The resulting oxide volume is $V_{ox} = t_{ox} S(1 - P_{ox})$, where P_{ox} is the oxide porosity and t_{ox} its thickness. Knowing that $V_{ox} = 2.27\ V$, due to the transformation of the silicon into silica, it yields

$$P_{ox} = 1 - 2.27 t_1/t_{ox}(1 - P_0)\,. \tag{2}$$

From the experimental values of t_1, t_{ox}, and P_0, the calculated values of P_{ox} are 11% and 19% for P^+ and P substrates, respectively.

For oxides which have been densified at 1090 °C, results show that the final oxide thickness corresponds well to what is expected from the volume of silica, that is a slight expansion for the P^+ substrate and a shrinkage for P substrate. These results confirm that the resulting oxide is no more porous in agreement with the low etch rate in buffered HF.

The comparison of the oxide thicknesses obtained by oxidation at 850 °C, t_{ox} (850 °C), and after a step at 1090 °C, t_{ox} (1090 °C) is demonstrative of the oxide layer shrinkage by a densification process. The porosity of the low-temperature oxide can be obtained from the ratio of oxide thickness values t_{ox} at 1090 °C and 850 °C according to

$$P_{ox} = 1 - \frac{t_{ox}(1090\ ^\circ\mathrm{C})}{t_{ox}(850\ ^\circ\mathrm{C})}\,. \tag{3}$$

It leads to values of 12% and 19% for P^+ and P substrate, respectively, in good agreement with that calculated above by comparing t_{ox} (850 °C) and t_1.

In addition, the initial porosity P_0 of the porous layer can be obtained from Eq. (2), using the value of t_{ox} for the densified oxide where $P_{ox} = 0$. The results are in good agreement with porosity values of Table I determined by weight measurements.

STRESS DETERMINATION

As the wafer curvature measurement is performed at room temperature, the deduced stress is the sum of two terms, the intrinsic stress σ_i due to the volume expansion during the oxide growth and the thermal stress σ_{th} generated during the sample cooling due to the difference in thermal expansion between the silicon substrate and the oxide layer.[10] The total stress is then

$$\sigma_{ox} = \sigma_i + \sigma_{th}\,, \tag{4}$$

with

$$\sigma_{th} = (\alpha_{Si} - \alpha_{ox})(E_{ox}/1 - \nu_{ox})\Delta T\,. \tag{5}$$

α_{Si} and α_{ox} are the dilatation coefficients of silicon and silica, respectively, E_{ox} is the silica Young's modulus, and ν_{ox} the silica Poisson's ratio. Due to the viscoelastic behavior of silica when oxidation temperature is higher than 960 °C, there is no contribution of the intrinsic stress to the total stress value.[11] Furthermore, the thermal stress corresponding to the cooling from the oxidation temperature to about 960 °C is also relaxed by viscous flow of silica. Thus, the stress for oxides grown at high temperatures only involves the thermal stress generated from 960 °C to the measurement temperature. Taking $\alpha_{Si} = 4.5\times10^{-6}\ \mathrm{K}^{-1}$ and $\alpha_{ox} = 0.5\times10^{-6}\ \mathrm{K}^{-1}$,[12] and $E_{ox}/1 - \nu_{ox} = 0.8\times10^{11}\ \mathrm{N/m^2}$,[13] the corresponding value which can be calculated for σ is $2.9\times10^8\ \mathrm{N/m^2}$. This only gives an approximate value because the elastic constant of a thermal oxide and the tem-

TABLE I. Experimental characteristics of the porous silicon and oxidized porous silicon layers, where t_1 and t_{ox} are the porous silicon layer and oxide thickness, respectively, P_0 and P_{ox} the porosities of the porous silicon and of the corresponding oxide, respectively, T the oxidation temperature, V the etch rate in buffered HF solutions and σ the measured stress.

Type	t_1 (μm)	P (%)	T (°C)	V (μm/mn)	P_{ox} (%)	$t_{ox} - t_1$ (μm)	σ 10^{-8} (N/m²)
P^+ 10^{-2} Ω cm	1.95	51	850	1.2	12	0.48	1.5
	1.95	51	1090	0.08	0	0.20	2.9
P 1 Ω cm	2.05	60	850	1.4	19	0.24	0.8
	2.05	60	1090	0.08	0	−0.20	2.6

Seoul Semiconductor, Exhibit 2001
LGI v. SSC, IPR2019-01154

perature dependence of α_{Si} are not known accurately.[14] However, this value agrees quite well with the reported stress values.[15]

When oxidation of the porous silicon layer is performed at 850 °C, curvature measurements lead to stress values of 1.5×10^8 N/m^2 for P$^+$ and 0.8×10^8 N/m^2 for P samples. These values are much lower than that expected for standard thermal silicon dioxide. At this temperature, the corresponding calculated thermal stress would be about 2.5×10^8 N/m^2, but the contribution of the intrinsic stress is also very important, values as large as 7×10^8 N/m^2 being reported for oxides grown at temperature below 950 °C.[16] These low experimental stress values which are obtained with oxidized porous silicon result from the fact that the porosity alters the elastic properties of the oxides; that is when porosity increases, the oxide stiffness decreases.

The stress determined for oxides densified at 1090 °C agrees well with that expected for the stress of standard thermal oxide (see Table I). It is important to point out that this stress, which is determined for a nonporous oxide represents the maximum stress which can be generated in an oxide layer obtained from porous silicon. It is also interesting to notice that the same results are obtained for oxidized porous layers up to 8 μm thick. It seems there are no intrinsic effects due to the porous silicon on the magnitude and sign of the stress.

It is interesting, to relate this stress to the wafer warpage, which is defined by $x = r^2/2R$ where r is the wafer radius. Using relation (1), it yields

$$x = \frac{6\sigma}{E_{Si}/1-\nu_{Si}} \frac{t_{ox}}{t_s^2} r^2 . \quad (6)$$

As for standard 2-, 3-, and 4-in. wafers, the ratio r/t_s is quite constant, the warpage is directly proportional to $\sigma\times t_{ox}$. So, by taking $\sigma = 2.9\times10^8$ N/m^2, which corresponds to a good oxide, warpages of about 100 μm for a 2-μm-thick oxide layer, and about 400 μm for a 8-μm-thick layer are obtained.

CONCLUSION

We have shown that when oxidation is performed at low temperature, the oxide is porous and there is always a thickness increases whatever the initial porosity may be. After densification of these oxides, the final thickness relative to the initial thickness depends on the initial porosity of the material. It will be higher if the porosity is lower than 56%, otherwise it is lower. The stress in an oxide layer formed from porous silicon is mainly due to the thermal expansion difference between the oxide and the substrate, and is always compressive. Its magnitude depends on the elastic properties of the oxide which are related to its porosity. The maximal value is obtained after oxide densification.

For the SOI applications, the volume expansion may be an additional source of stress resulting in a plastical deformation of the silicon islands. The wafer warpage induced by the oxide layer increases with its thickness. When the thickness is about 2 μm, its influence on the wafer curvature can be balanced by the oxide grown on the back of the sample during thermal oxidation. When the thickness is as thick as 8 μm, like in FIPOS technology[2] an appropriate mean to decrease the sample deformation is to keep the oxide porous. The drawback of this method could be a very fast etching rate of the oxide during the following steps of the technological process.

[1] L. Jastrzebski, J. Cryst. Growth **70**, 253 (1984).
[2] K. Imai and H. Unno, IEEE Trans. Electron Devices **ED-31**, 297 (1984).
[3] R. P. Holmstrom and J. Y. Chi, Appl. Phys. Lett. **42**, 386 (1983).
[4] H. Takai and T. Itoh, J. Electron. Mater. **12**, 973 (1983); F. Arnaud d'Avitaya, K. Barla, R. Herino, and G. Bomchil, Electrochem. Soc. Meeting, Toronto, May 1985 (to be published).
[5] G. Bomchil, R. Herino, and K. Barla, J. Phys. (Paris) (to be published).
[6] K. Ansai, F. Otoi, M. Ohnishi, and H. Kitabayashi, IEDM Tech. Digest, 796 (1984).
[7] K. Barla, J. J. Yon, R. Herino, and G. Bomchil, Intern. Conf. Insulating Films on Semicond., Toulouse, France (1985) (unpublished).
[8] G. A. Rozgonyi, P. M. Petroff, and M. B. Panish, J. Cryst. Growth **27**, 106 (1974).
[9] F. K. Reinhart and R. A. Logan, J. Appl. Phys. **44**, 3171 (1973).
[10] A. K. Sinka, H. J. Levinstein, and T. E. Smith, J. Appl. Phys. **49**, 2423 (1978).
[11] E. P. Eernisse, Appl. Phys. Lett. **30**, 290 (1977).
[12] Y. Yoriume, J. Electrochem. Soc. **129**, 2081 (1982).
[13] R. J. Jaccodine and W. A. Schlegel, J. Appl. Phys. **37**, 2429 (1966).
[14] I. Blech and U. Cohen, J. Appl. Phys. **53**, 4202 (1982).
[15] O. B. Cavin and J. L. Cook, J. Appl. Phys. **41**, 5115 (1970).
[16] E. P. Eernisse, Appl. Phys. Lett. **35**, 8 (1979).

Seoul Semiconductor, Exhibit 2001
LGI v. SSC, IPR2019-01154

APPENDIX J

Available online at www.sciencedirect.com
SCIENCE DIRECT®
Thin Solid Films 425 (2003) 196–202
thin solid films
www.elsevier.com/locate/tsf

Optical investigation of silicon nitride thin films deposited by r.f. magnetron sputtering

Gang Xu*, Ping Jin, Masato Tazawa, Kazuki Yoshimura

National Institute of Advanced Industrial Science and Technology, 2266-98, Shidami, Moriyama-ku, Nagoya 463-8560, Japan

Received 6 November 2002; received in revised form 6 November 2002; accepted 16 November 2002

Abstract

We prepared SiN_x thin films by r.f. magnetron sputtering without intentional substrate heating with refractive index approximately 2.0. Several different deposition routines showed that sputtering pressure played the most dominant role in film oxygen incorporation, film packing density and resistance to oxidation. High sputtering pressure led to a porous structure of the film and post-depositional oxidation in the atmosphere. The film refractive index was directly dependent on the sputtering conditions indicating a correlation with film stoichiometry and microstructure, and could be looked as an indication of film stoichiometry if the film was highly packed and with low-level dopant or contamination.
© 2002 Elsevier Science B.V. All rights reserved.

Keywords: Silicon nitride; Sputtering; Optical properties; Amorphous materials

1. Introduction

Silicon nitride (Si_3N_4) films have attracted much interest for over two decades for their important applications in microelectronic and optoelectronic industry [1–5]. The remarkable properties of the films, such as extreme hardness, high thermal stability, chemical inertness and good insulating properties make them valuable materials used as oxidation masks, protection and passivation barrier layers, gate dielectrics, etch stop layer and interlevel insulators.

Silicon nitride thin films are also good optical materials and therefore have been widely applied in photovoltaic devices. The application mainly involves two aspects: as an antireflection (AR) coating or as one kind of barrier layer within the device. The former application takes advantage of the adjustability of the film refractive index. The SiN_x film refractive index can be continuously varied over a wide range by changing its stoichiometry (N/Si atomic ratio) and index-graded coatings with broadband antireflection effects are achievable [6–8]. For the latter application, stoichiometric or near-stoichiometric silicon nitride Si_3N_4(:H) films are often applied not only because of its passivation properties but also because of its wide range of transparency from the ultraviolet (~250 nm) to the infrared region (~9 μm) [9–11]. In some cases, the pertinent value of refractive index of SiN_x film approximately 2.0 also plays a role in optimizing the optical performance of the devices [12].

Silicon nitride films can be deposited by a variety of methods such as thermal chemical vapor deposition (CVD), thermal nitridation of silicon [13], plasma enhanced CVD [14], ion plating [15], ion beam deposition [16], pulsed laser ablation [17], reactive evaporation [18] and reactive sputtering [19–24]. Among these methods, reactive sputtering of a silicon target has been demonstrated to be one of the promising ways to produce the hydrogen-free SiN_x films at a low temperature, which are necessary for wide ranging advance applications. It is well known that the optical properties of the SiN_x film strongly depend on the sputtering conditions such as substrate temperature, N_2 partial pressure, and target power. Most of the previous works were concentrated on one aspect of these preparation parameters and few works have been performed concerning the effects of sputtering atmosphere (including the gas species and total pressure) on optical properties, composition and microstructure of the near-stoichiometric films.

*Corresponding author. Tel.: +81527367283; fax: +81527367282.
E-mail address: gang-xu@aist.go.jp (G. Xu).

0040-6090/03/$ - see front matter © 2002 Elsevier Science B.V. All rights reserved.
PII: S0040-6090(02)01089-1

APPENDIX J

Table 1
Deposition conditions and three routines for film growth

Target	Silicon (∅ 50 mm, 99.99%)
r.f. power	150 W
Substrates	Quartz, silicon, carbon slices & alumina ceramics
Substrate temperature	Without intentional heating
Base pressure	$\sim 4\times10^{-4}$ Pa
Routine I	Ar: 16 sccm; N_2: 1.5–10 sccm; total pressure: 0.2–0.24 Pa
Routine II	Ar: 16 sccm; N_2: 2.2 sccm; total pressure: 0.2–1.0 Pa by throttle
Routine III	Ar: 0 sccm; N_2: 8.0 sccm; total pressure: 0.5–1.5 Pa by throttle

In the present study, we prepared SiN_x films with refractive index approximately 2.0 under various different conditions of sputtering atmosphere with the purpose to obtain high quality near-stoichiometric films. The films were deposited by r.f. magnetron sputtering of a silicon target without intentional substrate heating. Three deposition routines were employed: changing N_2 flow rate while keeping Ar flow constant, changing the total pressure under the condition of a constant flow ratio of N_2/Ar and depositing films completely in N_2 ambient. The optical, microstructural and compositional properties of the near-stoichiometric films were characterized by transmission ultraviolet–visible (UV–Vis) spectroscopy, Fourier transform infrared (FTIR), scanning electronic microscopy (SEM), X-ray diffraction (XRD) and Rutherford backscattering spectroscopy (RBS).

2. Experimental techniques

2.1. Preparation of SiN_x films

All of the SiN_x films were prepared in a reactive r.f. magnetron sputtering system. The water-cooled target was a silicon disc (99.99% in purity), with a thickness of 5 mm and a diameter of 50 mm. Gases of high-purity Ar and N_2 (99.9995 and 99.999%, respectively) were admitted to the sputtering chamber via two separate mass flow controllers. The sample holder is approximately 12 cm distant to the target and was kept rotating throughout film growth. Fused quartz, silicon, carbon slices and polished alumina ceramics were used as the substrates for various measurements.

We here concentrate on the influence of atmosphere conditions, including the gas flow ratio of N_2/Ar and the total pressure on the film formation and properties. The r.f. power input was kept constant and the substrates were not heated intentionally. The SiN_x films were produced via three routines as listed in Table 1, together with some of the common deposition conditions.

2.2. Film characterization

The film optical properties were stressed in the present work. Optical transmission spectra of the films deposited on quartz substrates were measured with a double-beam spectrometer (Jasco-V570) in the 200–2000-nm wavelength range. The film refractive index $n(\lambda)$, extinction coefficient $k(\lambda)$, and film thickness d were calculated according to the transmission maxima and minima with the method described by Swanepoel [25]. For rather thin films ($d<100$ nm), these quantities were obtained with a thin-film measurement system (Filmetrics F20) by measuring reflectance of the samples deposited on silicon substrates. The optical energy bandgap E_g of film was deduced from the absorption spectra in UV–Vis range according to Tauc relation [26]. The IR transmission spectroscopy was used to assess the chemical bonding configurations and film oxidation. Measurements were performed on films deposited on Si substrates with a FTIR spectrometer (Jasco FTIR-620 V) in the wavenumber range of 4000–400 cm^{-1}.

Other properties of the near-stoichiometric films were also characterized by several means. XRD was used to identify the possible phases present in the films. SEM was used to investigate the film topography, and the stoichiometry of some of the films was characterized by RBS. The film packing density was evaluated according to the band of IR absorption located approximately 3350 cm^{-1}.

3. Results

3.1. Deposition of SiN_x films

Three series of samples were deposited along with the three routines listed in Table 1. The dependence of refractive index, n (at $\lambda=630$ nm), and optical bandgap, E_g, of the films on deposition conditions is shown in Fig. 1a–c, which respectively correspond to the three deposition routines. As shown, n and E_g vary with their deposition conditions, and some difference in their variation tendency can be seen.

For the first routine of changing N_2 flow rate, the film index and bandgap show a strong dependence on N_2 flow rate. Once the film index approaches approximately 2.0, further increase in N_2 flow has only a limited effect, behavior observed by other authors [16]. The rapid changing region is Si-rich while the relatively flat region is N-rich. The index of Si-rich film is sensitive to the Si/N atomic ratio and index-graded

Seoul Semiconductor, Exhibit 2001
LGI v. SSC, IPR2019-01154

APPENDIX J

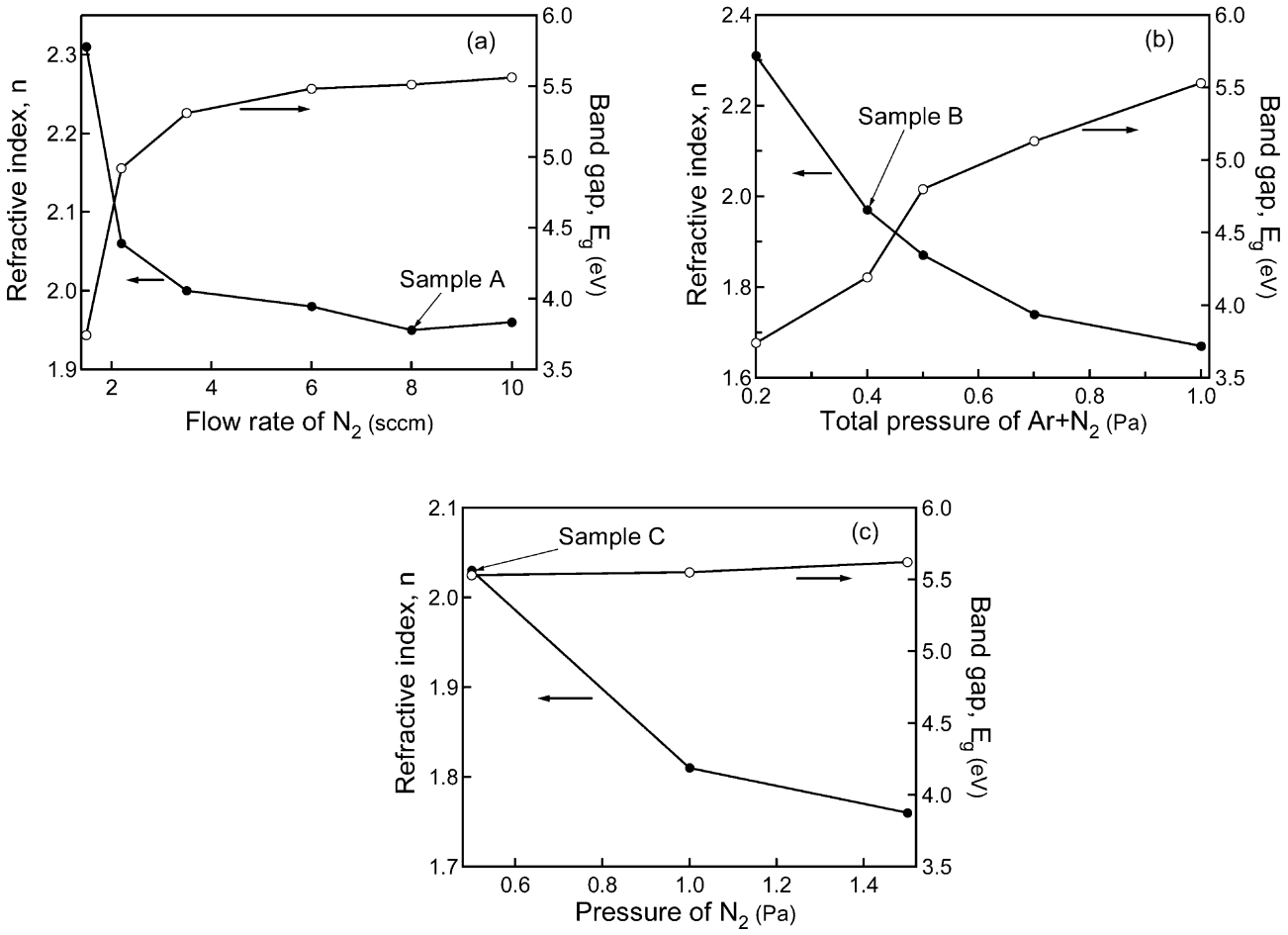

Fig. 1. Dependence of refractive index and optical bandgap of SiN_x film on different deposition routines: (a) changing N_2 flow rate while keeping Ar flow constant; (b) changing the total pressure under the condition of a constant flow ratio of N_2/Ar; and (c) depositing film completely in N_2 atmosphere. Samples A, B and C marked in each plot were selected for further investigation.

films can be obtained if one of the deposition conditions is continuously adjusted.

For Routines II and III, neither obvious Si-rich nor N-rich regions can be seen. Film refractive index decreases with increasing gas pressure, even after reaching the point $n=2.0$. As the matter of fact, a film with an index as low as 1.6 can be obtained if the total pressure, P_{total}, is sufficiently high, for example $P_{total}=$ 1.8 Pa for Routine II. We believe that this is mainly caused by the oxygen incorporation during film growth, as we will demonstrate by FTIR and RBS.

Each of the three deposition routines can lead to a near-stoichiometric film which has a refractive index approximately 2.0. We here temporarily call them 'near-stoichiometric' only because their refractive index is similar to that of the stoichiometric film. The validity of this description is discussed later.

In the following, we focus on the three so-called near-stoichiometric films of the three routines. These are indicated as samples A, B and C in Fig. 1, and their deposition conditions are listed in Table 2. The film deposition rate was calculated with the measured thickness and deposition time.

3.2. Optical properties

Fig. 2 shows the transmittance spectra of the three films deposited on quartz substrates, with transmittance of the bare substrate also included for comparison. Each sample exhibits a pronounced absorption edge at different wavelengths, which means different band gaps (E_g), and different absorption characteristics. The wavelength dispersions of refractive index $n(\lambda)$ and extinction coefficient $k(\lambda)$ of the films in the UV–Vis region shown in Fig. 3 show similar refractive index but significant difference in extinction coefficient. The optical parameters including the films thickness d of each sample are tabulated in Table 2 and listed along with their deposition conditions.

Seoul Semiconductor, Exhibit 2001
LGI v. SSC, IPR2019-01154

APPENDIX J

Table 2
Sputtering conditions and optical parameters of samples A, B and C

Sample	Gas flow (sccm)	Total pressure (Pa)	Dep. rate (nm/min)	n ($\lambda = 630$ nm)	k ($\lambda = 500$ nm)	E_g (eV)	d (nm)
A	Ar: 16.0 N_2: 8.0	0.2	1.83	1.95	5×10^{-4}	5.51	511
B	Ar: 16.0 N_2: 2.2	0.4	5.23	1.97	6.7×10^{-3}	4.19	942
C	N_2: 8.0	0.5	0.51	2.03	0	5.53	77

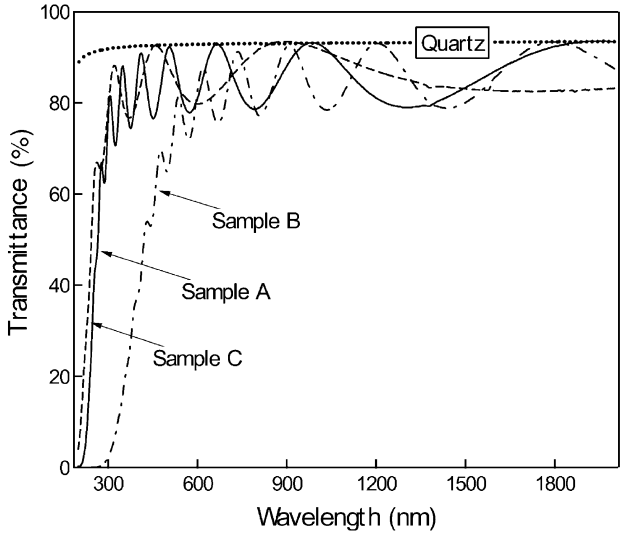

Fig. 2. Transmittance spectra of the selected three samples deposited on quartz substrates. The three samples were produced via different routines as marked in Fig. 1.

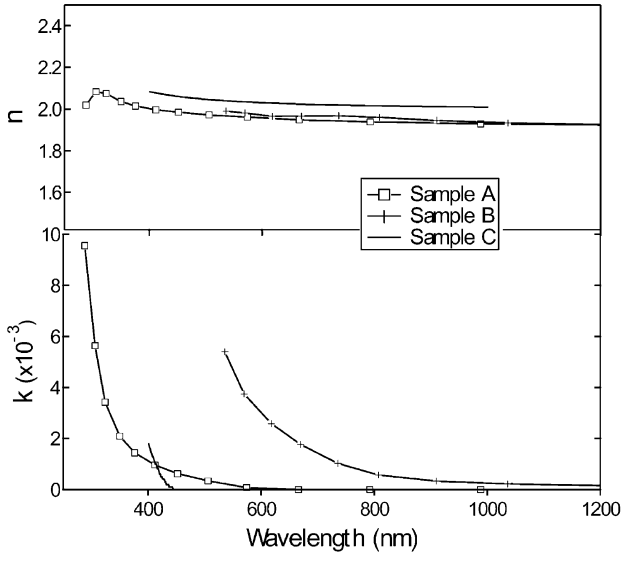

Fig. 3. Wavelength dispersion of refractive index, n, and extinction coefficient, k, for samples A, B and C.

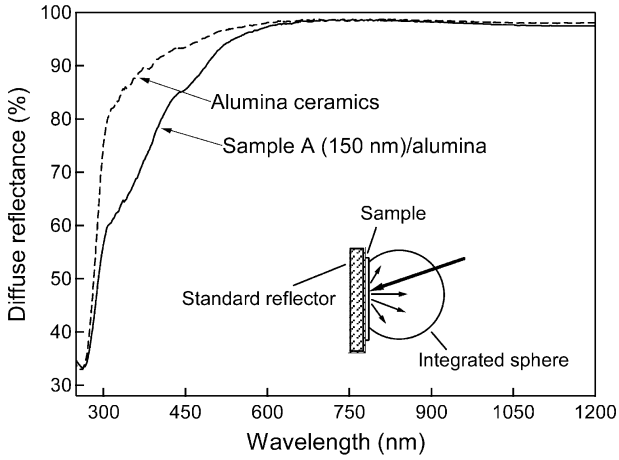

Fig. 4. Integrated reflectance spectrum for sample A (150-nm thick) deposited on alumina ceramics. The spectrum of the ceramics substrate is also present for comparison. Inset: measurement configuration.

Also, a film with thickness $d = 150$ nm was fabricated on a well-polished alumina ceramic substrate (roughness < 20 nm). The film was deposited under the same condition as that of sample A. Diffuse reflectance measurement was performed on this sample by a spectrometer equipped with an integrated sphere. Fig. 4 shows the result and the measuring configuration is illustrated by the inset. One can clearly see that the film has strong absorption in the wavelength region $\lambda < 600$ nm. It is interesting to note that the absorption of this sample on ceramics is much larger than on quartz, as shown in Fig. 5. This absorption enhancement effect, we believe, results from the bulk diffuse effect of the ceramic substrate, and we will discuss it later.

3.3. Chemical bonds and resistance to oxidation

FTIR was used to estimate the chemical bonding configuration for the three samples. The IR transmission spectra, measured in the range of 400–4000 cm^{-1} and corrected for the absorption of silicon substrate, are shown in Fig. 6. Samples A and C exhibit a strong absorption band centered at approximately 845 cm^{-1},

Seoul Semiconductor, Exhibit 2001
LGI v. SSC, IPR2019-01154

APPENDIX J

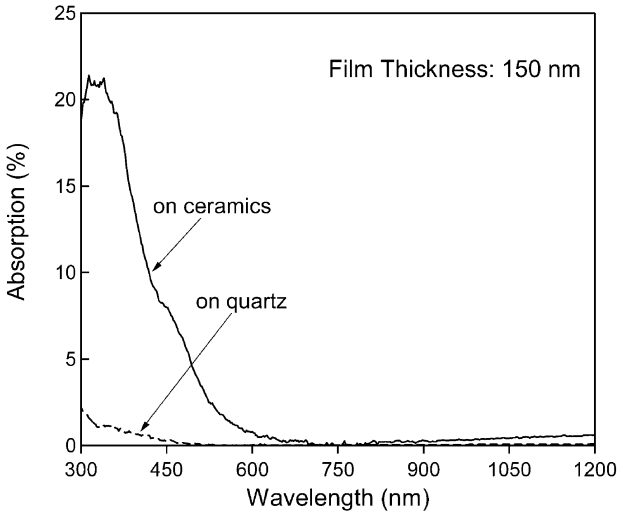

Fig. 5. Absorption spectra for sample A deposited on ceramics (solid curve) and on quartz (dashed curve). Film thickness is approximately 150 nm.

which corresponds to the Si–N asymmetric stretching vibration mode [27]. The broad shape is characteristic of an amorphous structure of the film. The additional small absorption band at approximately 480 cm^{-1} is due to the Si–N breathing mode [27]. For sample B the intense band shifts to a higher frequency of 904 cm^{-1}, which implies an increase in the bond polarity. It is normally assumed that the replacement of some nitrogen by oxygen in the SiN molecule is responsible for this shift.

In the high frequency region, the different periodicity is due to the film thickness. However, one band of absorption at $\sim$3350 cm^{-1} can be observed. For the experiments showed that this band does not always appear for all samples and the band becomes more apparent with films deposited at a higher total pressure, this band may be attributed to (1) N–H (1177 and 3340 cm^{-1}) [28], (2) SiO–H (944 and 2800–3700 cm^{-1}) [21,29] or (3) H–O (3620 and 3380 cm^{-1}) [28]. The probability for the first case can be excluded because our samples were grown in a hydrogen-free atmosphere. The second and third attributions are both H_2O-related and we believe that absorption of moisture in the film is the cause; however, the presence of water in the film is not yet understood. While some authors suggest the second attribution [18], we can not find direct confirmation. For example, the band at 944 cm^{-1} and the H-related band such as Si–H (2126–2152 cm^{-1}) were not present in our samples. Since this band is less intense in measurements at elevated temperature, we believe that the H–O band is mainly attributed to the H_2O molecules in the voids of film.

We found that samples with a higher total pressure during deposition show a worse stability, as evidenced

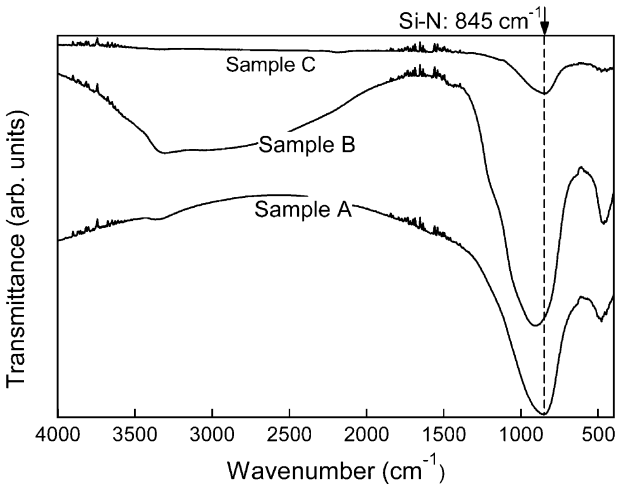

Fig. 6. Infrared transmittance spectra of the SiN_x films: samples A, B and C which were produced under different conditions.

by FTIR measurements shown in Fig. 7. The top three curves show the sample deposited via Routine I with a sputtering pressure of 0.2 Pa, whereas the bottom three curves represent the sample via Routine II at a higher pressure, 0.8 Pa. The change was compared in three cases: as-deposited, put in the air for 3 months and heated in the air at 300 °C for 4 h. The sample deposited

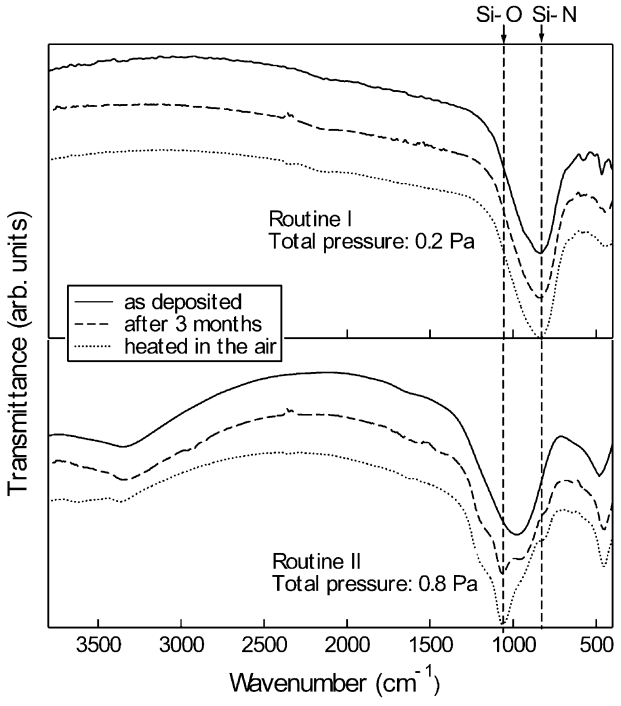

Fig. 7. FTIR investigation of two samples deposited at lower sputtering pressure, 0.2 Pa, and at a higher pressure, 0.8 Pa. Three cases are compared: as deposited (solid curve), after 3 months (dashed curve) and after heated at 300 °C for 4 h in the air (dotted curve).

Seoul Semiconductor, Exhibit 2001
LGI v. SSC, IPR2019-01154

APPENDIX J

at the lower pressure is very stable with no change in spectra. In contrast, the sample with higher pressure shows an oxidation process. The Si–N bonds in the film are unstable and gradually replaced by Si–O bonds (at 450 and 1060 cm^{-1}) [28].

3.4. Compositional and structural properties

The film packing density can be estimated by FTIR measurements according to the absorption of water vapor at approximately the wavenumber of 3350 cm^{-1}. This method has been applied by several authors to study oxide or fluoride films [30,31], but not for nitride films. Assuming that the voids in film all are full with water, the total volume of the void can be determined according to the amount of water. Measuring the transmittances T and T_0 of a film that contains and does not contain water, one can calculate the volume fraction P_w of water based on the relation

$$P_w = \frac{\ln(T_0/T)}{\alpha_w d}, \quad (1)$$

where α_w ($\approx 1.27\times10^4$ cm^{-1}) is the water absorption coefficient at approximately 3350 cm^{-1} and d is film thickness. Film packing density P_f which is the volume fraction not containing voids is given by

$$P_f = 1 - P_w = 1 - \frac{\ln(T_0/T)}{\alpha_w d}. \quad (2)$$

The value T_0 can be simply obtained by interpolating the transmittance curve.

RBS analysis was performed on the samples to examine elemental composition with samples A and C having an N/Si atomic ratio close to the stoichiometric value of 1.33. The amount of oxygen is associated with the total pressure of deposition with the content of oxygen in sample C approximately 4 times higher than in sample A. Further measurement shows that the oxygen content progressively increases if we use a higher total pressure even the film was deposited completely in nitrogen. For instance, the molecular formula becomes $SiN_{1.2}O_{0.41}$ if the N_2 pressure reaches 1.5 Pa. The oxygen incorporation in the films may come from the residual water vapor or oxygen during deposition and/or the post-depositional oxidation under atmospheric exposure after deposition [21].

XRD measurements show all the samples have an amorphous structure, consistent with observations with FTIR. The film surfaces were investigated by SEM, and no feature can be seen in a scanned area of 2.5×2.5 μm^2. All these properties are summarized in Table 3.

Table 3
Compositional and structural properties of samples A, B and C

Sample	Composition (by RBS)	Packing density (by FTIR)	Structure (by XRD)	Surface (by SEM)
A	$SiN_{1.33}O_{0.07}$	0.987	Amorphous	Featureless
B	–	0.912	Amorphous	Featureless
C	$SiN_{1.33}O_{0.27}$	0.979	Amorphous	Featureless

4. Discussion

The first topic we want to discuss is the film refractive index. The three samples which we have investigated in detail based on their refractive index are not certain to be stoichiometric. Sample B is believed to be Si-rich, though it possesses an index similar to that of the stoichiometric film. Unfortunately, the thickness ($d=$ 942 nm) did not permit RBS evaluation. However, sample B has a relatively low packing density as shown in Table 3. According to the effective medium approximation (EMA) theory [32], the refractive index of this sample should be a little large if we take the voids in the film out of consideration. The Bruggeman EMA gives

$$P_f\frac{n_s^2-n^2}{n_s^2+n^2} + (1-P_f)\frac{1-n^2}{1+n^2} = 0, \quad (3)$$

where n is the resulting refractive index of the porous film and n_s the index of the solid part of the film. For sample B with $n=1.97$ and $P_f=0.912$, $n_s\approx2.1$, which proves our hypothesis. This value is actually underestimated because of the underestimation in the film porosity; that is, the sample is thick so that the effective thickness of moisture penetrating in the film is actually smaller than the film thickness (Eq. (1)). The surplus of silicon in the film makes the sample more absorbing and narrower in optical band gap, as shown in Table 2. The other two samples, A and C, which have a packing density close to unity, are really near-stoichiometric. So, we say that refractive index of a SiN_x film can be looked at as an indication of film stoichiometry if the film is highly packed and with low-level dopant or contamination.

Among the three routines attempting to produce near-stoichiometric SiN_x films, Routine I seems best. With this method, the resulting film has a high packing density and high resistance to post-depositional oxidation. This is hence the most common way employed in various fabrication techniques. Routine II produces films with high porosity, which is a fundamental consequence of atomic self-shadowing in concert with the low adatom mobility. Routine III, which is completely in pure nitrogen atmosphere, only reflects the fact that high sputtering pressure leads to high oxygen incorporation during film fabrication. The deposition rates of these

Seoul Semiconductor, Exhibit 2001
LGI v. SSC, IPR2019-01154

APPENDIX J

three routines are substantially different. Deposition via Routine II shows the fastest rate whereas deposition via Routine III shows the slowest one. Obviously the deposition rate is related with the film microstructures or density. A high rate maybe means more void generation in the film.

Finally, we discuss the absorption of SiN_x films in a solar cell. From Fig. 5, films deposited on ceramics have a much stronger absorption than films on quartz. This absorption enhancement originates from the randomization of incident light within the film caused by diffuse reflectance of the ceramics, which is equal to thickening the film many times. This effect has been applied to silicon solar cells to enhance the absorption of silicon layers [33,34]. Unfortunately, absorption enhancement simultaneously takes place in the other so-called transparent layers in a cell, such as the AR coatings, transparent electrodes, and barrier layers, and might cause unexpected absorption loss. Although a transparent film with $k<10^{-4}$ is sufficient in ordinary optical application, this criterion for transparency seems not sufficient for solar cells because of the enhancement effect. As shown by Fig. 5, the absorption of the film on ceramics is approximately 10 times larger than that of the sample on quartz, which means the criterion for transparency should be at least one order higher in magnitude (rising from 10^{-4} to 10^{-5}). Sample A seems not fully meet this requirement in the range of solar radiation of interest (0.3–1.2 μm) though it has a high packing density and satisfactory deposition rate. This means more effort should be made to decrease its absorption. Note that the absorption enhancement originates from the bulk diffuse reflectance of the ceramics substrate; roughness of the ceramics surface plays only a negligible role.

5. Conclusions

We have deposited silicon nitride films by r.f. magnetron sputtering a silicon target via various routines with various film properties. The total pressure is an essential factor affecting film properties when the deposition temperature is low. High sputtering pressure leads to a porous structure of the film and post-oxidation easily takes place because of the absorption of moisture. Further, more oxygen may incorporate into the films during film growth. The film refractive index could be looked as an indication of film stoichiometry if the film was highly packed and with low-level dopant or contamination.

References

[1] M. Tamura, H. Sunami, Jpn. J. Appl. Phys. 11 (1972) L1097.
[2] M.J. Powell, J. Orton, Appl. Phys. Lett. 45 (1984) 171.
[3] Y. Manabe, T. Mitsuyu, J. Appl. Phys. 66 (1989) 2475.
[4] J. Ahn, K. Suzuki, Appl. Phys. Lett. 64 (1994) 3249.
[5] P.V. Bulkin, P.L. Swart, B.M. Lacquet, Thin Solid Films 241 (1994) 247.
[6] N. Shibata, Jpn. J. Appl. Phys. 27 (1988) 480.
[7] R. Kishore, S.N. Singh, B.K. Das, Renewable Energy 12 (1997) 131.
[8] S.H. Lee, I. Lee, J. Yi, Surf. Coat. Technol. 153 (2002) 67.
[9] M. Vetter, Thin Solid Films 337 (1999) 118.
[10] F. Duerinchx, J. Szlufcik, Sol. Energy Mater. Sol. Cells 72 (2002) 231.
[11] T. Jana, S. Mukhopadhyay, S. Ray, Sol. Energy Mater. Sol. Cells 71 (2002) 197.
[12] M. Tazawa, K. Yoshimura, K. Igarashi, S. Tanemura, in: J. Schmid, H.A. Ossenbrink, P. Helm, H. Ehmann, E.D. Dunlop (Eds.), Second World Conference and Exhibition on Photovoltaic Solar Energy Conversion, Vienna, Austria, July 6–10, 1998, p. 1732.
[13] H. Matsumura, Jpn J. Appl. Phys. 28 (1989) 2157.
[14] C.S. McCormick, C.E. Weber, J.R. Abelson, G.A. Davis, R.E. Weiss, V. Aebi, J. Vac. Sci. Technol. 15 (1997) 2770.
[15] Y. Murayama, T. Takao, Thin Solid Films 40 (1977) 309.
[16] M.F. Lambrinos, R. Valizadeh, J.S. Colligon, Appl. Opt. 35 (1996) 3620.
[17] I. Umezu, K. Kohno, T. Yamaguchi, A. Sugimura, J. Vac. Sci. Technol. A 20 (2002) 30.
[18] J.S. Yoon, C.V. Deshp, R.F. Bunshah, Thin Solid Films 220 (1992) 80.
[19] L.F. Cordes, Appl. Phys. Lett. 11 (1967) 383.
[20] Y. Hirohata, N. Shimamoto, T. Hino, T. Yamashima, K. Yabe, Thin Solid Films 253 (1994) 425.
[21] J.H. Kim, K.W. Chung, J. Appl. Phys. 83 (1998) 5831.
[22] S. Tan, T.E. Schlesinger, M. Migliuolo, Appl. Phys. Lett. 68 (1996) 2651.
[23] H.P. Löbl, M. Huppertz, Thin Solid Films 317 (1998) 153.
[24] M.S. Aida, A. Attaf, M.L. Benkhedir, Phil. Mag. B 73 (1996) 339.
[25] R. Swanepoel, J. Phys. E 16 (1983) 1213.
[26] J. Bauer, Phys. Status Solidi A 39 (1977) 411.
[27] G.N. Parsons, J.H. Souk, J. Batey, J. Appl. Phys. 70 (1991) 1553.
[28] V.T. Volkov, L.F. Satunkina, Thin Solid Films 247 (1994) 145.
[29] N. Banerji, J. Serra, P. Gonzalez, S. Chiussi, E. Parada, B. Leon, M. Perez-Amor, Thin Solid Films 317 (1998) 214.
[30] H.J. Kuehn, A. Duppare, W. Richter, A. Lehmann, U. Bergner, Thin Solid Films 201 (1992) 281.
[31] G. Atanassov, R. Thielsch, D. Popov, Thin Solid Films 233 (1993) 288.
[32] T.C. Choy, Effective Medium Theory, Clarendon, Oxford, 1999.
[33] E. Yablonovitch, G.D. Cody, IEEE Trans. Electron. Devices ED-29 (1982) 300.
[34] P. Sheng, IEEE Trans. Electron. Devices ED-31 (1984) 634.

Seoul Semiconductor, Exhibit 2001
LGI v. SSC, IPR2019-01154

APPENDIX K

PHYSICAL REVIEW B VOLUME 42, NUMBER 6 15 AUGUST 1990-II

Optical dielectric function and infrared absorption of hydrogenated amorphous silicon nitride films: Experimental results and effective-medium-approximation analysis

Z. Yin and F. W. Smith
Department of Physics, City College of the City University of New York, New York, New York 10031
(Received 27 December 1989)

The optical dielectric function ϵ (1.5–6.5 eV), ir absorption (400–4000 cm^{-1}), and film density have been measured for a series of hydrogenated amorphous silicon nitride (a-$Si_xN_yH_z$) films deposited at 400 °C via rf plasma-enhanced chemical vapor deposition for varying $[NH_3]/[SiH_4]$ ratios R. From a detailed analysis of the ir and density results, the concentrations of Si—N, N—H, Si—H, and Si—Si bonds and of Si, N, and H atoms have been obtained for the films studied. An effective-medium-approximation analysis of the measured ϵ based on the Si-centered tetrahedron model presented in the preceding paper has provided a more sensitive means of determining the concentration of Si—Si bonds in the films and has demonstrated that careful measurements of ϵ_1 and ϵ_2 can serve as a useful probe of the bonding in these alloys. Approximately 9×10^{20} Si—Si bonds/cm^3 have been found in N-rich films which are close in composition to silicon diimide, $Si(NH)_2$, and these Si—Si bonds have been found to have a significant influence on both the optical energy gap E_{opt} and the refractive index n of the films. New results obtained from the ir absorption measurements include the identification of (1) a shoulder near 1030 cm^{-1} on the main 880-cm^{-1} Si—N(s) band and (2) a weak absorption feature near 640 cm^{-1} which is not hydrogen related. It has been found that the N-rich diimidelike films prepared here have very low porosities and are thermally stable up to 700 °C, properties which will be important for their future applications.

I. INTRODUCTION

Silicon nitride films have been deposited via a variety of chemical-vapor-deposition (CVD) techniques, including plasma-enhanced CVD (PECVD), and have a wide range of applications in microelectronics as passivation layers, diffusion barriers, and insulators.[1] In addition, PECVD silicon nitride films have recently been used as gate dielectrics in applications requiring low deposition temperatures, such as hydrogenated amorphous silicon thin-film transistors.[2] These films are generally referred to as hydrogenated amorphous silicon nitride (a-$Si_xN_yH_z$) and have physical, electrical, and optical properties which are strongly dependent on the film composition, i.e., the [N]/[Si] ratio y/x and the hydrogen content z. Although the incorporation of considerable amounts of hydrogen (up to 30–40 at. %) can have a negative influence on certain film properties such as thermal stability,[3] it has been demonstrated recently[4] that N-rich films ($[N]/[Si] > \frac{4}{3}$) can be deposited with compositions approaching that of silicon diimide, a-$Si(NH)_2$, and that these films can serve as useful low-temperature dielectric layers.[5] In addition, such polymeric layers can be relatively stable thermally, apparently up to at least 600 °C.[6]

It is clearly important to establish as close a correlation as possible between the macroscopic properties of these a-$Si_xN_yH_z$ films and the film microstructure, i.e., the local atomic bonding configurations involving the Si, N, and H atoms. We report here on detailed measurements of infrared absorption, film density ρ, and optical dielectric function ϵ for several a-$Si_xN_yH_z$ films, focusing on films which are N-rich. The bond and atom concentrations obtained from the ir absorption and film density measurements are compared with those obtained from an effective-medium-approximation (EMA) analysis of the measured ϵ of the film. This EMA analysis is based on the microstructural model presented in paper I (Ref. 7) in which Si-centered tetrahedra are considered to be the fundamental structural units which determine the optical response of the films. This analysis has yielded results for the bond and atom concentrations which are consistent with those obtained from the ir absorption and film density measurements for the N-rich films, thus confirming the applicability of the microstructural model to the alloys studied.

It has also been possible to specifically address the issue of the existence of Si—Si bonds in the films studied. This is an important point since it has been suggested recently[8] that these bonds are potentially harmful defects in the a-$Si_xN_yH_z$ films used in device applications. The dependence of the concentration of Si—Si bonds on the deposition conditions and their effect on film properties will be discussed.

Details of the experimental procedure will be presented in Sec. II, followed by the results and analysis of the various measurements in Sec. III. The EMA analysis for ϵ will appear in Sec. IV, with discussion and conclusions following in Sec. V.

II. EXPERIMENT

The a-$Si_xN_yH_z$ films studied here were prepared via rf (13.56 MHz) plasma-enhanced CVD in a stainless-steel deposition system which has been described previously.[9]

 ©1990 The American Physical Society

Seoul Semiconductor, Exhibit 2001
LGI v. SSC, IPR2019-01154

Undiluted silane and ammonia were delivered via separate lines to the deposition chamber, with typical deposition parameters as follows (see Table I): substrate temperature $T_s = 400\,^{\circ}C$, discharge power of 0.43 W/cm^2, total pressures of 0.5 or 0.15 Torr, flow rates of 100 or 60 sccm (cubic centimeters per minute at STP) for NH_3 and variable flow rates for SiH_4 to obtain the desired ratios $R = [NH_3]/[SiH_4] = 10$, 20, or 40. The substrates, polished clear fused quartz for measurements of ϵ, intrinsic Si (polished both sides) for measurements of ir absorption and film composition, and Al foils for density measurements, were mounted on the powered electrode.

For the determination of the optical dielectric function $\epsilon = \epsilon_1 + i\epsilon_2$ of these a-$Si_xN_yH_z$ films, measurements of film transmittance and of the reflectance from the free surface of the film have been carried out from 1.5–6.5 eV using an Aviv 14DS uv-visible spectrophotometer. For these reflectance measurements, the calibration of an NBS standard mirror has been extended from 4.9 up to 6.7 eV using the known optical constants[10] of a polished Si wafer. Details of the analysis procedure for obtaining n and k, the real and imaginary parts of the index of refraction, and film thickness d have been given previously.[9] Values of the optical energy gap E_{opt} have been obtained from plots of $E\epsilon_2^{1/2}$ versus energy E, using the Tauc relation.[11]

Infrared measurements were carried out using a Digilab FTS-40 Fourier transform infrared spectrophotometer in the range from 400 to 4000 cm^{-1}, with a resolution of 8 cm^{-1}. Absorbances for the various absorption modes [N—H(stretching), Si—N(stretching), etc.] have been obtained from the measured film absorbance by subtracting a fitted baseline to account for interference effects in the film itself. The ir absorption of the $R = 40, P = 0.15$ Torr film has also been measured as a function of the annealing of the film up to 1000 °C. Film densities have been obtained from the masses of the films, determined by weighing the Al-foil substrates before and after deposition, and the film volumes, obtained from measurements of film area and the average thickness. Information concerning film composition has been obtained via depth profiling using a Perkin-Elmer PHI 600 scanning Auger microprobe. The depth profile of each film was obtained by sputtering using a 3-keV Ar^+-ion beam.

III. RESULTS AND ANALYSIS

a-$Si_xN_yH_z$ films have been prepared using $[NH_3]/[SiH_4]$ ratios R of 10, 20, and 40 at $P = 0.5$ Torr and $R = 40$ at 0.15 Torr. The deposition rates for these films are given in Table I where it can be seen that R_{dep} decreases from 320 to 200 Å/min as R increases from 10 to 40 at $P = 0.5$ Torr. R_{dep} then decreases further to 60 Å/min at $R = 40$ and $P = 0.15$ Torr. It is clear that the deposition rates are limited primarily by the availability of Si, i.e., by the flow rates of SiH_4 into the deposition chamber (see Table I). This result is reasonable, given the large excess of NH_3 relative to SiH_4 present during the depositions. Film compositions (x, y, and z) have been determined in two ways, the first using ir absorption and film density measurements and the second in addition using measurements of ϵ to obtain the concentration of Si—Si bonds. These analyses are presented below, in Secs. III B and IV, respectively.

The infrared absorption and film density results will now be presented, followed by the analysis for the bond and atom concentrations and the results for ϵ. The EMA analysis for ϵ based on the Si-centered tetrahedron model is presented in Sec. IV.

A. ir absorption and film density

The ir absorption spectra for the $R = 10$ and $R = 40$ films prepared at $T_s = 400\,^{\circ}C$ and $P = 0.5$ Torr are shown in Fig. 1 in the range from 400 to 4000 cm^{-1}. Note that interference effects in the films have already been removed from these spectra via the baseline correction procedure. Absorption bands for the N—H(stretching) mode have been observed near 3320 cm^{-1}, for Si—H(stretching) near 2180 cm^{-1}, for H—N—H(bending) near 1550 cm^{-1}, for N—H(bending) near 1180 cm^{-1}, for Si—N(stretching) near 880 cm^{-1}, and for Si—N(breathing) near 480 cm^{-1}. The weak features seen near 2320 cm^{-1} result from an incomplete subtraction of the absorption due to CO_2 in the spectrophotometer sample chamber. The film thicknesses d, peak wave numbers ν(peak), maximum absorption coefficients α(max), full widths at half maximum (FWHM), and normalized absorption band areas $\int \alpha d\nu$ for these bands are listed in Table II for the four alloy

TABLE I. Deposition parameters and properties of a-$Si_xN_yH_z$ films studied.

Sample	T_s (°C)	P (Torr)	R $[NH_3]/[SiH_4]$	R_{dep} (Å/min)	ρ[a] (g/cm^3)	n[b]	E_{opt}[c] (eV)
1	400	0.5	100/10=10	320	2.49	1.86	3.83
2	400	0.5	100/5=20	280	2.24	1.84	5.05
3	400	0.5	100/2.5=40	200	2.08	1.79	5.20
4	400	0.15	60/1.5=40	60	2.18	1.82	5.42

[a]Film density; typical uncertainty is ±0.1 g/cm^3.
[b]Index of refraction at 1.5 eV; typical uncertainty is ±0.02.
[c]Optical energy gap; typical uncertainty is ±0.1 eV.

Seoul Semiconductor, Exhibit 2001
LGI v. SSC, IPR2019-01154

APPENDIX K

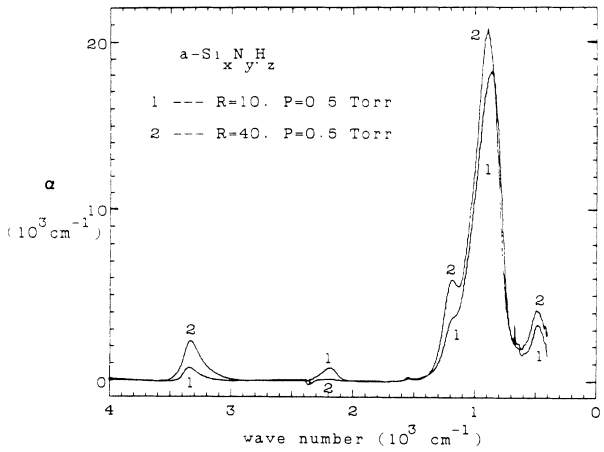

FIG. 1. Absorption coefficient α vs wave number for the $R=[NH_3]/[SiH_4]=10$ and 40 a-$Si_xN_yH_z$ films prepared at $T_s=400$ °C and $P=0.5$ Torr.

films studied, along with the results for absorption bands which have been identified as being present near 1030 and 640 cm^{-1} from deconvolutions of the main absorption band, an example of which is shown in Fig. 2 for the $R=40, P=0.5$ Torr film.

It is important to note here that, for a given alloy, measurable changes in the peak position and FWHM of the main Si—N(stretching) band have been observed for films of different thicknesses prepared under identical conditions. For example, the Si—N(stretching) peak positions are about 20 cm^{-1} higher for thicker films ($d=0.5-1.0$ μm) than for thinner films ($d=0.1-0.2$ μm). While the FWHM's of the thicker films are also greater by 20–40 cm^{-1} than the FWHM's for the thinner films, the normalized Si—N(stretching) absorption band areas have been found to be independent of film thickness, to within experimental error (±5%), for the films studied. Thus, the areas of the Si—N(stretching) bands can be used, in principle, to determine bond concentrations for these films (see Sec. III B below). It is clear, however, that correlations of parameters such as index of refraction n within the peak wave number of the Si—N(stretching) band are valid only when carried out for films of comparable thickness. The observed shifts in ν(peak) and α(max) with film thicknesses are due to changes in film reflectance[12] resulting from the strong absorption of the Si—N(stretching) mode.

The N—H(stretching) band near 3320 cm^{-1} is observed to be an asymmetric peak, with a tail extending on the low wave-number side down to about 2900 cm^{-1} (see Fig. 3). This asymmetry is likely to be due at least in part to hydrogen bonding[13] between the H atoms in the N—H bonds and lone-pair electrons on nearby N atoms, which is indicated by the notation N—H · · · N. Also, in the $R=40$ films with higher concentrations of hydrogen, evidence can be seen for increasing absorption due to the stretching modes of the $N\text{-}H_2$ unit between 3400 and 3500 cm^{-1}. In the same films, the H—N—H(bending)

TABLE II. Infrared-absorption results for a-$Si_xN_yH_z$ films.

		Si—N				N—H and Si—H (in parentheses)			
Sample	d (Å)	ν(peak)[a] (cm^{-1})	α(max)[b] (cm^{-1})	FWHM[c] (cm^{-1})	$\int \alpha d\nu$[d] (10^5 cm^{-2})	ν(peak)[a] (cm^{-1})	α(max)[b] (cm^{-1})	FWHM[c] (cm^{-1})	$\int \alpha d\nu$[d] (cm^{-2})
1	9800	877	18 300	223	43.50	3340	810	141	1.36×10^5
($R=10, P=0.5$)		1035	2860	103	3.13	1163	3520	206	7.72×10^5
		478	3150	175	5.85	1543	60	32	1.80×10^3
		631	838	63	0.55	(2184	750	139	11.03×10^4)
2	5930	877	20 200	197	42.35	3317	1860	177	3.89×10^5
($R=20, P=0.5$)		1034	3850	120	4.91	1178	4120	184	8.06×10^5
		487	3700	140	5.53	1547	160	38	6.49×10^3
		644	1230	76	0.99	(2182	310	153	4.93×10^4)
3	12 250	888	20 400	196	42.42	3336	2290	163	4.47×10^5
($R=40, P=0.5$)		1034	4750	130	6.56	1185	5540	178	10.48×10^5
		476	4060	183	7.92	1546	190	42	8.24×10^3
		656	1640	104	1.80				
4	2435	868	20 700	169	37.19	3325	2310	189	5.18×10^5
($R=40, P=0.15$)		1022	4310	125	5.73	1181	3620	158	6.10×10^5
		475	3790	178	7.16	1551	180	46	8.80×10^3
		661	1400	96	1.43				

[a]Peak wave number; typical uncertainty is ±5 cm^{-1}.
[b]Maximum absorption coefficient; typical uncertainty is ±4%.
[c]Full width at half maximum; typical uncertainty is ±5 cm^{-1}.
[d]Normalized absorption band area $\int \alpha d\nu$, where $\alpha=(2.303/d)A$ is the absorption coefficient; d is the film thickness and A the absorbance. Typical uncertainty is ±5%.

Seoul Semiconductor, Exhibit 2001
LGI v. SSC, IPR2019-01154

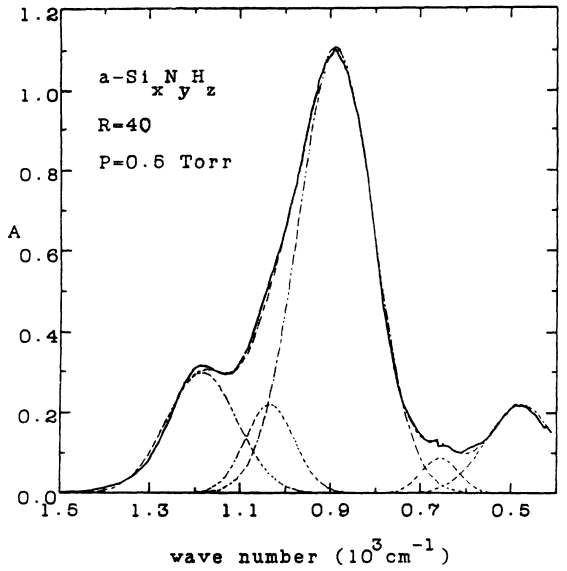

FIG. 2. Absorbance A vs wave number for the $R=40, P=0.5$ Torr film in the range from 1500 to 400 cm^{-1}. The solid curve is the experimental result, while the dashed curves are the individual fitted absorption bands and their sum (see text for discussion).

absorption band near 1550 cm^{-1} is also observed to be stronger. These results are consistent with those of previous studies.[4] Following the anneal of the $R=40, P=0.15$ Torr film at 700 °C, the absorption band at 1550 cm^{-1} was observed to increase, thus providing evidence for the conversion of N—H bonding units to N-H_2 units. This conversion is apparently one of the steps leading to the formation and subsequent evolution of NH_3 molecules from the annealed film.

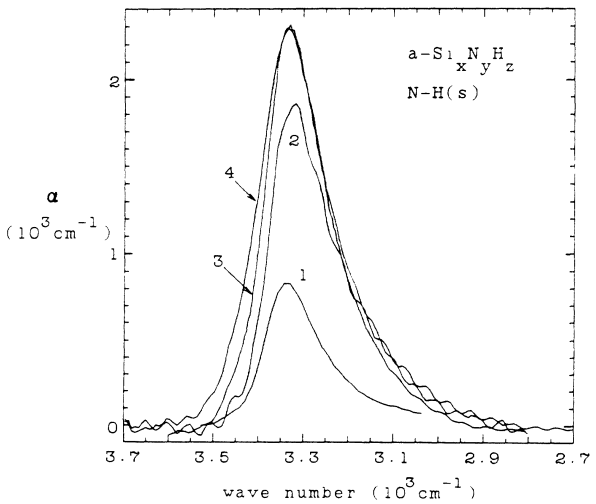

FIG. 3. Absorption coefficient α vs wave number in the N—H(stretching) region from 3700 to 2700 cm^{-1} for the four films studied. See Table I for the numbering of the curves.

Evidence for Si—H(stretching) absorption near 2180 cm^{-1} has been observed only in the films prepared with $R=10$ and $R=20$ (samples 1 and 2, respectively, in Table II). This absorption band appears to consist of two subbands near 2170 and 2250 cm^{-1}, which is consistent with Si—H(stretching) absorption arising from Si-HN_2Si and Si-HN_3 tetrahedra, respectively.[14]

In order to accurately determine the absorbances of the N—H(bending) band near 1180 cm^{-1} and the Si—N(stretching) band near 880 cm^{-1}, it has been necessary to carry out deconvolutions of the broad region of absorption extending from 400 to near 1500 cm^{-1}. For this purpose, five Gaussian absorption bands have been employed, centered near 1180, 1030, 880, 640, and 480 cm^{-1}. The deconvolution for the $R=40, P=0.5$ Torr film is shown in Fig. 2, and the results of this procedure for all the films studied are presented in Table II. There is only one absorption feature in this region which is clearly hydrogen related, namely, the N—H(bending) band near 1180 cm^{-1}. The absorption band centered near 1030 cm^{-1} is proposed to be a shoulder on the main Si—N(stretching) band near 880 cm^{-1}. The small absorption feature consistently observed in these films near 640 cm^{-1} would normally be assumed to be due to Si—H(rocking, wagging) modes.[15] This cannot be the complete explanation here since this feature has been observed in the $R=40$ films for which there is no evidence for absorption due to the Si—H(stretching) mode near 2180 cm^{-1}. In addition, annealing experiments on these films have shown that, as the hydrogen is driven out of the $R=40$ film via heating up to 1000 °C, no significant changes are observed to occur in the 640 cm^{-1} absorption. We propose instead that this absorption band is due to a vibration of the N—Si_3 bonding unit,[16] so that the existence of three absorption bands (near 880, 640, and 480 cm^{-1}) for this unit may be analogous to the observation of three absorption bands (near 1070, 800, and 450 cm^{-1}) for the Si—O—Si bonding unit in a-SiO_2 films.[17]

Film density ρ results are shown in Table I for the four alloys studied and it can be seen that ρ is a decreasing function of R, the $[NH_3]/[SiH_4]$ ratio. As will be seen later, increasing R results in a decrease of the Si atomic fraction x and an increase in the H atomic fraction z in these a-$Si_xN_yH_z$ films, so that, as expected, ρ decreases with increasing H content of the films.[18] There is a small increase observed in ρ for the $R=40, P=0.15$ Torr film, which may be related to the lower deposition rate measured for this film.[19]

B. Bond and atom concentrations

The concentrations of N—H, Si—H, and Si—N bonds in these alloys have been obtained from the normalized ir absorption band areas presented in Table II, using the expression

$$N(X-Y)=K(X-Y)\int \alpha(\nu)d\nu\ , \qquad (1)$$

where $N(X-Y)$ is the concentration of $X-Y$ bonds, $K(X-Y)$ is their ir absorption cross section, and the normalized area is given by the wave-number integral of

Seoul Semiconductor, Exhibit 2001
LGI v. SSC, IPR2019-01154

the absorption coefficient α over the band in question. The bands used for this purpose are the 3320-cm^{-1} N—H(stretching) band, the 2180-cm^{-1} Si—H(stretching) band, and the sum of the Si—N(stretching) bands near 880 and 1030 cm^{-1}. Values of $K(\text{N—H})=8.2\times10^{16}$ cm^{-1} and $K(\text{Si—H})=5.9\times10^{16}$ cm^{-1} have been obtained from the results of Lanford and Rand[20] [using $K=1/(2.303\sigma)$], while the results $K(\text{Si—N})=1.82\times10^{16}$ and 2.1×10^{16} cm^{-1} have been obtained, respectively, from measurements carried out here for the $R=40, P=0.5$ Torr and $R=40, P=0.15$ Torr films. To obtain these results for K(Si—N), it has been assumed that these two $R=40$ films contain no N—N bonds and that $N(\text{Si—Si}) \ll N(\text{Si—N})$. These are reasonable working assumptions as these films are N-rich ($y/x \sim 1.9$, see Table III) and contain from 36 to 39 at. % H. The densities of Si—N bonds in these two films were obtained in a self-consistent manner using the measured values for N(N—H) and N(Si—H) and the film density ρ, along with the relationships between bond and atom concentrations and ρ presented below [Eqs. (2)–(5)]. Once N(Si—N) was obtained, Eq. (1) was inverted to obtain the results for K(Si—N) quoted above from the measured normalized Si—N(stretching) band areas. Previous estimates[21] of K(Si—N) for films with lower [N]/[Si] ratios have yielded values in the range $(0.9-1.0)\times10^{16}$ cm^{-1}, lower by about a factor of 2 compared to the results obtained here. A more recent analysis[22] carried out for nearly stoichiometric films has obtained the result $K(\text{Si—N})=2.4\times10^{16}$ cm^{-1}, in better agreement with the values obtained here. It is not unreasonable to expect that K(Si—N) will depend on the [N]/[Si] ratio y/x and H content z of the films studied. An alternative approach to obtaining N(Si—N) and, hence, K(Si—N) using the values of N(Si—Si) obtained from the EMA analysis for ϵ will be presented in Sec. IV.

The results obtained here for the concentrations of N—H, Si—H, and Si—N bonds are presented in Table III. For the computation of the experimental uncertainties in the bond concentrations, the accuracies of the cross sections have been assumed to be ±5% for K(N—H) and K(Si—H) and ±10% for K(Si—N) for the two $R=40$ films. It should be pointed out that the reproducibility of the bond concentrations measured for films of different thicknesses prepared under the same conditions is much better than the estimated absolute accuracies quoted in Table I. It can be seen that N(N—H) and N(Si—N) are increasing functions of R and that both also increase slightly as P decreases from 0.5 to 0.15 Torr. In contrast, N(Si—H) is highest for $R=10$ (6.5×10^{21} cm^{-3}) and then decreases with R, falling to zero to within experimental error (less than about 2×10^{19} cm^{-3}) for the $R=40$ films.

In order to obtain the atom concentrations N(Si), N(N), and N(H) [along with the Si—Si bond concentration N(Si—Si)], the following expressions have been employed:

$$N(\text{Si})=[N(\text{Si—N})+N(\text{Si—H})]/4+N(\text{Si—Si})/2\ , \quad (2)$$

$$N(\text{N})=[N(\text{N—H})+N(\text{Si—N})]/3\ , \quad (3)$$

$$N(\text{H})=N(\text{N—H})+N(\text{Si—H})\ , \quad (4)$$

and

$$\rho=m_{\text{Si}}N(\text{Si})+m_{\text{N}}N(\text{N})+m_{\text{H}}N(\text{H})\ , \quad (5)$$

where the m_i are atomic masses. Note that it has been assumed here that there are no N—N or H—H bonds in the films. From the results for N(N—H), N(Si—H), N(Si—N), and ρ presented in Tables I and III, Eqs. (2)–(5) have been solved for the four unknowns, N(Si), N(N), N(H), and N(Si—Si), with the results also given in Table III. Values for the composition parameters x,y,z, and the [N]/[Si] ratios y/x for these a-$Si_xN_yH_z$ alloys are also given in Table III. Again, the reproducibility of the results obtained for the atom concentrations (and for x, y, and z) is much better than the estimated absolute uncertainties given in Table III. The estimated uncertainties in N(Si—Si) are large, $\pm0.9\times10^{22}$ cm^{-3}, primarily due to the indirect manner in which it has been determined. More reliable results for N(Si—Si) obtained from the EMA analysis for ϵ are given below (see Table IV).

It can be seen from the results presented in Table III that N(Si) is a decreasing function of $R=[NH_3]/[SiH_4]$, as expected, while both N(N) and N(H) increase with increasing R. From the [N]/[Si] ratio, it can be seen that the $R=20$ and the two $R=40$ films are N rich ($y/x > \frac{4}{3}$), with y/x in the range from 1.44 to 1.95. This last value is quite close to the [N]/[Si] ratio of silicon di-

TABLE III. Bond and atom concentrations for a-$Si_xN_yH_z$ films obtained from ir and density measurements.

Sample	Film composition[a] (a-$Si_xN_yH_z$)	y/x[b] [N]/[Si]	N(Si—N)[c] (10^{22} cm^{-3})	N(N—H)[c] (10^{22} cm^{-3})	N(Si—H)[c] (10^{22} cm^{-3})	N(Si—Si)[c] (10^{22} cm^{-3})	N(Si)[d] (10^{22} cm^{-3})	N(N)[d] (10^{22} cm^{-3})	N(H)[d] (10^{22} cm^{-3})
1	$Si_{0.42}N_{0.37}H_{0.21}$	0.88	8.49	1.12	0.65	2.76	3.66	3.20	1.77
2	$Si_{0.27}N_{0.39}H_{0.34}$	1.44	8.60	3.19	0.29	0.96	2.70	3.93	3.49
3	$Si_{0.22}N_{0.42}H_{0.36}$	1.91	8.90	3.66	less than 0.002	less than 0.7	2.23	4.19	3.66
4	$Si_{0.21}N_{0.41}H_{0.38}$	1.95	9.13	4.24	less than 0.008	less than 0.9	2.28	4.46	4.24

[a]Typical uncertainties are ±0.05 for x, ±0.04 for y, and ±0.03 for z.
[b][N]/[Si] ratio; typical uncertainty is ±15%.
[c]Bond concentrations; typical uncertainties are ±8% for N(N—H) and N(Si—H), ±10% for N(Si—N), and $\pm0.9\times10^{22}$ cm^{-3} for N(Si—Si).
[d]Atom concentrations; typical uncertainties are ±8% for N(N) and N(H) and $\pm0.5\times10^{22}$ cm^{-3} for N(Si).

Seoul Semiconductor, Exhibit 2001
LGI v. SSC, IPR2019-01154

TABLE IV. Results of EMA analysis for N(Si—Si) and derived values of composition (x,y,z), N(Si—N), and K(Si—N).

Sample	x	y	z	y/x	N(Si—Si) (10^{22} cm^{-3})	N(Si—N) (10^{22} cm^{-3})	K(Si—N) (10^{16} cm^{-1})
1 ($R=10, P=0.5$)	0.35	0.46	0.19	1.31	0.36	11.35	2.43
2 ($R=20, P=0.5$)	0.25	0.41	0.34	1.64	0.15	9.56	2.02
3 ($R=40, P=0.5$)	0.22	0.41	0.37	1.86	0.084	8.79	1.80
4 ($R=40, P=0.15$)	0.21	0.40	0.39	1.91	0.092	9.02	2.10

imide, $Si(NH)_2$. The results for N(Si—Si) are of interest as Si—Si bonds have been proposed to be potentially important defects in these films.[8] It can be seen that this analysis of the ir absorption and film density measurements suggests that there is a significant concentration of Si—Si bonds, 2.76×10^{22} cm^{-3}, in the $R=10$ film, which is equal to about $\frac{1}{3}$ of N(Si—N)$=8.49\times10^{22}$ cm^{-3} for the same film. N(Si—Si) falls to 0.96×10^{22} cm^{-3} for $R=20$ and then to less than $(0.7-0.9)\times10^{22}$ cm^{-3} for the $R=40$ films, values which are equivalent to zero to within the limits of the accuracy of these measurements and the analysis employed. It should be noted that the results obtained here indicate that the presence of Si—Si bonds in these films seems to be correlated with the presence of Si—H bonds (see Table III).

The scanning Auger microprobe (SAM) study has also shown that the [N]/[Si] ratio is an increasing function of R, a result which is consistent with the analysis presented here. A more detailed analysis of the SAM measurements has not been undertaken due to a lack of absolute sensitivity factors for N and Si in the films studied. It should be noted that no evidence for oxygen has been found in the as-deposited films from either the ir absorption studies or from the SAM results. In addition, no evidence has been found for the diffusion of either O_2 or H_2O into the films during the period of 17 months following their initial exposure to the atmosphere. This observation indicates that these films can be prepared with very low porosities.

C. Optical dielectric function ϵ

The measured real part ϵ_1 and imaginary part ϵ_2 of the optical dielectric function ϵ for the four films studied are shown in Fig. 4 as functions of photon energy E between 1.5 and about 6.5 eV. Also shown in Fig. 4 for comparison are the results of Philipp[23] for a CVD a-Si_3N_4 film which was essentially hydrogen free. The indices of refraction n at 1.5 eV and the optical energy gaps E_{opt} for the four films studied are given in Table I. It can be seen from $\epsilon_2(E)$ and E_{opt} that the optical-absorption edge shifts to higher energies with increasing R as stronger Si—N bonds replace weaker Si—Si bonds in the films (see Table III for the bond concentrations). This behavior has been observed previously.[24] The two N-rich films prepared here using $R=40$, and labeled 3 and 4 in Fig. 4, have absorption edges which are higher in energy than that of the CVD film studied by Philipp.[23] Note that ϵ_1 and ϵ_2 are observed to be essentially independent of pressure P for the two $R=40$ films. Also, n decreases with increasing R as the H content of the films increases and the film density falls. All four of the films studied here have values of n which are lower than that of the CVD film studied by Philipp, due to their lower densities resulting from the incorporation of hydrogen.

It has been observed here that thinner a-$Si_xN_yH_z$ films

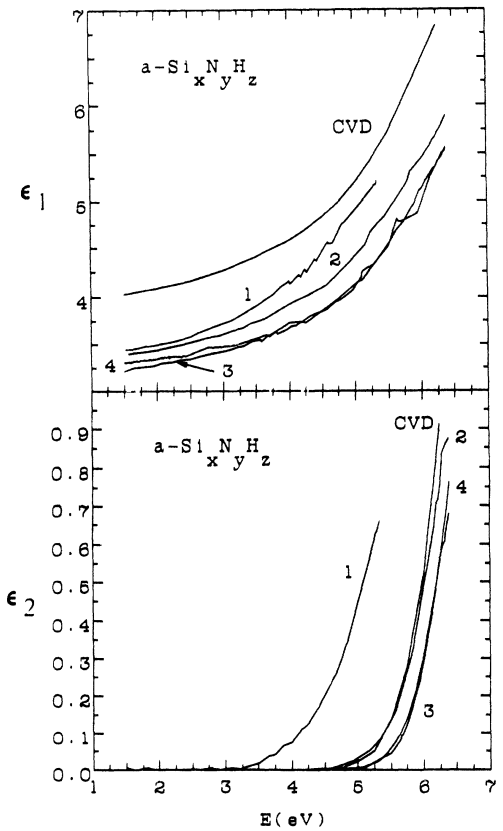

FIG. 4. Real part ϵ_1 and imaginary part ϵ_2 of the optical dielectric function vs energy E, as measured for the four films studied. Also shown are the experimental results of Philipp (Ref. 23) for a CVD a-Si_3N_4 film, labeled CVD. See Table I for the numbering of the other curves.

Seoul Semiconductor, Exhibit 2001
LGI v. SSC, IPR2019-01154

have higher values of n than thicker films prepared under the same conditions. We believe that this is due to the existence of enhanced concentrations of Si-centered tetrahedra containing Si—Si bonds near the film-substrate interfaces. Such tetrahedra would lead to higher n values and it is clear that this effect would be more important for thin films.

IV. EMA ANALYSIS OF THE OPTICAL DIELECTRIC FUNCTION

The measured optical dielectric function ϵ will now be used within the framework of the Bruggemann effective-medium approximation[25] (EMA) in order to obtain important additional information concerning the microstructure of the films studied. The microstructural model to be employed in the EMA analysis is based on Si-centered tetrahedra. This model has been presented in detail for these a-$Si_xN_yH_z$ alloys in paper I (Ref. 7) and has also been used previously in the analysis of the optical response of hydrogenated amorphous films based on carbon[26] (a-C:H), silicon[27] (a-Si:H), and silicon-based alloys[9,28] (a-Si_xC_{1-x}, a-Si_xO_{1-x}, and a-Si_xN_{1-x}).

The Bruggemann EMA is defined by the following two expressions:

$$\sum_i v_i \frac{\epsilon_i - \epsilon}{\epsilon_i + 2\epsilon} = 0 \tag{6}$$

and

$$\sum_i v_i = 1 \ , \tag{7}$$

where ϵ_i and v_i are the complex optical dielectric function and volume fraction, respectively, of the ith component and ϵ is the measured value for the film. We will also make use of the following relationship for the measured film density ρ:

$$\sum_i v_i \rho_i = \rho \ , \tag{8}$$

where ρ_i is the density of the ith component. The components to be used in the EMA analysis are the Si-centered tetrahedra and the ϵ_i and ρ_i determined for specific tetrahedra in the preceding paper (see Figs. 2–4 and Tables I–III of Ref. 7) will be used in Eqs. (6)–(8) along with the measured ϵ and ρ in order to determine the tetrahedron volume fractions v_i appropriate for the films under consideration. The goal of this EMA analysis is to obtain independent estimates for the bond and atom concentrations which can be compared with the results previously obtained from the analysis of ir absorption and film density measurements presented in Sec. III. It will be particularly interesting to attempt to confirm the results already obtained for N(Si—Si). It should be pointed out that an advantage of the EMA analysis is that information can be obtained concerning not only the concentrations of bonds and atoms, but also the manner in which the bonds and atoms are incorporated into the Si-centered tetrahedra.

Table IV presents the results of the EMA analysis for the N(Si—Si) bond concentrations of the four films studied. The analysis for each film has employed only those tetrahedra which are necessary to model the optical response and which are consistent with the film composition and density. The analysis and results for each alloy film will now be briefly discussed, beginning with the two N-rich films.

A. Sample 3 ($R = 40, P = 0.5$ Torr)

For this N-rich a-$Si_xN_yH_z$ film, the five Si-centered tetrahedra, Si-$N_{4-i}(NH)_i$, $i = 0$–4, provide the dominant contribution to the measured ϵ and ρ. With these five tetrahedra, however, it has not been possible to obtain a satisfactory fit to the measured ϵ_2 and so an additional tetrahedron containing a Si—Si bond has been included in the EMA analysis. The addition of the Si-Si$(NH)_3$ tetrahedron leads to a shift of the onset of ϵ_2, i.e., the absorption edge, to lower energies, in better agreement with experiment. The comparison between the measured and fitted ϵ for this alloy film is shown in Fig. 5(a) where it can be seen that satisfactory agreement has been obtained. The concentration N(Si—Si) of Si—Si bonds resulting from this analysis is 8.3×10^{20} cm^{-3}, which is in fact consistent with the upper limit of 7×10^{21} cm^{-3} previously obtained from the analysis of the ir absorption and film density measurements (Table III). The results of the EMA fit for the film composition, density, and N—H and Si—N bond concentrations for this film all agree with the results of the ir absorption and the film density analysis presented in Table III, to within experimental error.

B. Sample 4 ($R = 40, P = 0.15$ Torr)

The EMA analysis for this N-rich film has employed the same six Si-centered tetrahedra which were used for sample 3, see above, and the resulting fit to the measured ϵ has also been quite satisfactory. The value of N(Si—Si) obtained, 9.2×10^{20} cm^{-3}, is again consistent with the upper limit of 9×10^{21} cm^{-3} previously obtained.

C. Samples 1 ($R = 10, P = 0.5$ Torr) and 2 ($R = 20, P = 0.5$ Torr)

Evidence for the presence of Si—H bonds has been found in the ir absorption spectra of these two films and so additional tetrahedra containing Si—H bonds have been used in the EMA analysis. For the $R = 10$ film the following five tetrahedra have been employed: Si-$N_2(NH)_2$, Si-$HN_2(NH)$, Si-$HN(NH)_2$, Si-$SiN_2(NH)$, and Si-Si_2N_2. Although a reasonable fit to the measured ϵ can be obtained, the fitting procedure is not unique. One result which has been confirmed, however, is that a Si-centered tetrahedron containing two Si—Si bonds is required to obtain even a qualitative fit to the measured ϵ_2 for this alloy. The EMA analysis has yielded N(Si—Si) $= 3.6\times10^{21}$ cm^{-3} for this $R = 10$ film. A void component with a volume fraction of 0.06 has been used to obtain the fit for this alloy.

For the $R = 20$ film, the five Si-$N_i(NH)_{4-i}$, $i = 0$–4, tetrahedra along with two tetrahedra containing Si—Si

Seoul Semiconductor, Exhibit 2001
LGI v. SSC, IPR2019-01154

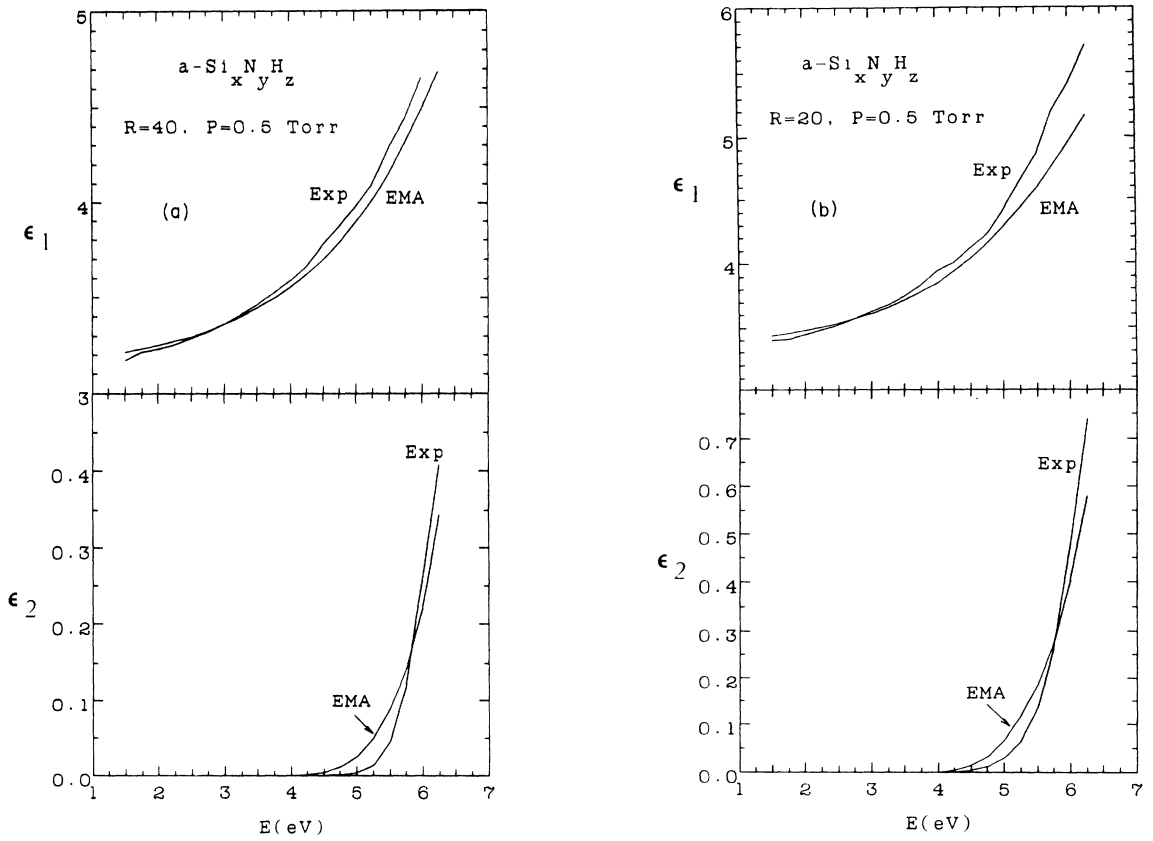

FIG. 5. Comparison between the measured and fitted optical dielectric functions $\epsilon=\epsilon_1+i\epsilon_2$ for the (a) $R=40$ and (b) $R=20$, $P=0.5$ Torr films. Exp, measured ϵ; EMA, fitted result of EMA analysis (see text).

bonds and two containing Si—H bonds have been employed in the EMA analysis. The results of this fit are shown in Fig. 5(b) and it can be seen that reasonable agreement has been obtained with experiment. For this alloy tetrahedra containing just one Si—Si bond are sufficient to obtain the fit shown and the EMA analysis has yielded N(Si—Si)$=1.5\times10^{21}$ cm^{-3}.

The results for N(Si—Si) for these last two alloy films obtained from this EMA analysis are systematically lower than those obtained from the analysis of the ir absorption and film density results by about a factor of 7 (see Table III). These lower values of N(Si—Si) are more reliable as the EMA analysis emphasizes the film absorption which is directly related to the presence of Si—Si bonds in the films. The analysis involving the ir absorption and film density measurements is, in principle, also capable of yielding reliable results, but unfortunately this analysis involves the use of ir absorption cross sections, particularly K(Si—N), whose determination is difficult to achieve with high accuracy.

The values of N(Si—Si) obtained here from the EMA analysis have been used in Eqs. (2)–(5), along with the measured values of N(Si—H) and N(N—H) (Table III) and of film density ρ (Table I), in order to determine more reliable values for N(Si—N) and the compositions (x,y,z) of the alloys studied. The results of this analysis are also presented in Table IV. The results obtained for the two $R=40$ films are in good agreement with these obtained via the previous analysis (see Table III). For the $R=10$ and 20 films, on the other hand, this analysis has yielded higher values for y and lower values for x than obtained previously. The resulting higher [N]/[Si] ratios y/x are in fact more consistent with the results of the SAM measurements.

Also given in Table IV are values for the ir absorption cross section K(Si—N) determined from the values of N(Si—N) given in Table IV and the measured normalized ir absorption band areas for Si—N(stretching) presented in Table II. These values are consistent with those derived in Sec. III B for the two $R=40$ films, while the value for $R=10$ is in good agreement with the results of a recent analysis[22] for nearly stoichiometric films.

V. DISCUSSION AND CONCLUSIONS

The microstructural model which appears to be appropriate for these a-$Si_xN_yH_z$ alloy films and which is consistent with the results obtained here is the one presented in paper I.[7] This model is essentially the random-bonding model (RBM) originally proposed by Philipp[23,29] in which Si-centered tetrahedra are the fundamental structural units which determine the optical

Seoul Semiconductor, Exhibit 2001
LGI v. SSC, IPR2019-01154

response of the films. The RBM, however, needs to be generalized for these alloys as the bonding is not actually completely random. Instead, there is strong evidence for chemical ordering in the sense that there is a preferential tendency for the formation of Si—N and N—H bonds in the N-rich alloys. This should not be surprising since in the two important stable compounds in the Si:N:H alloy system, i.e., Si_3N_4 and $Si(NH)_2$, each Si atom is bonded directly to four N atoms and, in addition, H is bonded to N.

Current applications of a-$Si_xN_yH_z$ alloys involve films which are typically deposited at low T_s (<400 °C), so that H is unavoidably incorporated. In order to be useful, these films should be thermally stable and also should be free of Si—Si bonds.[8] It is becoming clear that silicon diimide films a-$Si(NH)_2$ have the potential to satisfy both of these requirements. The results presented here indicate that films with compositions close to that of silicon diimide, i.e., with a [N]/[Si] ratio greater than 1.9 and with low concentrations of Si—Si bonds (less than 9×10^{20} cm^{-3}), can be deposited via PECVD at $T_s=400$ °C using $[NH_3]/[SiH_4]$ ratios equal to 40. It is important to stress that these films are not porous and are, in fact, quite stable with respect to exposure to O_2 and H_2O in the atmosphere, in contrast to some diimide-like films prepared at lower T_s.

It is clear that the high $R=[NH_3]/[SiH_4]$ ratios which are needed in the discharge in order to minimize N(Si—Si) are necessary due to the fact that SiH_4 is easier to dissociate[30] than NH_3. For lower values of R, the [N]/[Si] ratio falls below about 1.9 and there are no longer enough N atoms in the films to satisfy all of the bonds to the Si atoms, especially when it is recognized that N—H bonds are also formed. As a result, Si—Si and also Si—H bonds appear in the films. It has been observed here that the presence of Si—Si bonds in the films can actually be inferred from the presence of Si—H bonds, which can be detected directly via ir absorption. The bond concentration ratio $[N(\text{Si—Si})]/[N(\text{Si—H})]$ has been found to be close to $\frac{1}{2}$ for the $R=10$ and $R=20$ films. It will be important to determine if this correlation can also be found for a-$Si_xN_yH_z$ films prepared by other workers.

The results obtained here for N(Si—Si) have been determined in two separate ways, with the results of the EMA analysis (Table IV) considered to be more reliable than those obtained from the analysis of the ir absorption and film density measurements (Table III). For the $R=40$, N-rich films, however, the results of the two analyses are in fact consistent with each other.

It has been found to be difficult, if not impossible, to deposit a-$Si_xN_yH_z$ films in which the concentration of Si—Si bonds is less than about 1%, or 9×10^{20} cm^{-3}. This low concentration cannot be accurately inferred from ir absorption and film density measurements. It has been shown, however, that such a level can be detected from careful measurements of ϵ_2, the imaginary part of the optical dielectric function. Even at this low level, the optical properties of the N-rich films are influenced significantly by the presence of the Si—Si bonds. For example, the tetrahedron model presented in the preceding paper has predicted (see Fig. 8 of Ref. 7) that E_{opt} should approach about 6.2 eV and that n should be near 1.7 for diimidelike films with $y/x>1.9$. For the $R=40$ films studied here with y/x equal to about 1.9, however, it has been found that $E_{\text{opt}}=5.2$–5.4 eV and $n=1.79$–1.82. The EMA analysis employed here has shown that this difference is due to the presence of Si—Si bonds at the level previously mentioned (9×10^{20} cm^{-3}). In addition, it has been found that the EMA analysis which has been employed is capable of establishing the existence of Si atoms bonded to either one or two other Si atoms. More work will be required in order to make this analysis more quantitative.

ACKNOWLEDGMENTS

We wish to thank D. V. Tsu of North Carolina State University for his interest in this research and for many helpful discussions. We also wish to thank R. Sabatini of Brookhaven National Laboratory (Upton, NY) for carrying out the SAM measurements on these films. This research has been supported by the U.S. Department of Energy under Grant No. DE-FG02-87ER45317.

[1]For useful reviews, see C. E. Morosanu, Thin Solid Films **65**, 171 (1980); A. C. Adams, in *Proceedings of the Symposium on Reduced Temperature Processing for VLSI*, edited by R. Reif and S. R. Srinivasan (Electrochemical Society, Pennington, NJ, 1986), Vol. 86-5.

[2]K. D. Mackenzie, A. J. Snell, I. French, P. G. Lecomber, and W. E. Spear, Appl. Phys. A **31**, 87 (1983).

[3]H. J. Stein and H. A. R. Wegener, J. Electrochem. Soc. **124**, 908 (1977).

[4]D. V. Tsu, G. Lucovsky, and M. J. Mantini, Phys. Rev. B **33**, 7069 (1986); G. Lucovsky and D. V. Tsu, J. Vac. Sci. Technol. A **5**, 2231 (1987).

[5]D. Jousse, J. Kanicki, D. T. Krick, and P. M. Lenahan, Appl. Phys. Lett. **52**, 445 (1988).

[6]R. C. Budhani, S. Prakash, H. J. Doerr, and R. F. Bunshah, J. Vac. Sci. Technol. A **5**, 1644 (1987).

[7]Z. Yin and F. W. Smith, this issue, the preceding paper, Phys. Rev. B **42**, 3658 (1990).

[8]D. Jousse and J. Kanicki, Appl. Phys. Lett. **55**, 1112 (1989).

[9]K. Mui, D. K. Basa, F. W. Smith, and R. Corderman, Phys. Rev. B **35**, 8089 (1987).

[10]D. E. Aspnes and A. A. Studna, Phys. Rev. B **27**, 985 (1983); H. R. Philipp, J. Appl. Phys. **43**, 2836 (1972).

[11]J. Tauc, R. Grigorovici, and A. Vancu, Phys. Status Solidi **15**, 627 (1966).

[12]C. J. Mogab, J. Electrochem. Soc. **120**, 932 (1973); H. R. Philipp, J. Appl. Phys. **50**, 1053 (1979).

[13]M. Maeda and H. Nakamura, J. Appl. Phys. **58**, 484 (1985).

[14]G. Lucovsky, Solid State Commun. **29**, 571 (1979).

[15]M. Cardona, Phys. Status Solidi B **118**, 463 (1983).

[16]Y. N. Volgin, G. P. Dubrovskii, and Y. I. Ukhanov, Fiz. Tverd. Tela (Leningrad) **17**, 1671 (1975) [Sov. Phys.—Solid State **17**, 1089 (1975)].

[17]T. S. Ericksson and C. G. Granqvist, J. Appl. Phys. **60**, 2081

Seoul Semiconductor, Exhibit 2001
LGI v. SSC, IPR2019-01154

(1986).
[18]W. A. P. Claassen, W. G. J. N. Valkenburg, M. F. C. Willemsen, and W. M. v. d. Wijgert, J. Electrochem. Soc. **132**, 893 (1985).
[19]W. A. P. Claassen, W. G. J. N. Valkenburg, F. H. P. M. Habraken, and Y. Tamminga, J. Electrochem. Soc. **130**, 2419 (1983).
[20]W. A. Lanford and M. J. Rand, J. Appl. Phys. **49**, 2473 (1978).
[21]A. D. Yadav and M. C. Yoshi, Thin Solid Films **59**, 313 (1979); A. Chayahara, M. Ueda, T. Hamasaki, and Y. Osaka, Jpn. J. Appl. Phys. Pt. 1 **24**, 19 (1985); C. Chaussat, E. Bustarret, J. C. Bruyere, and R. Groleau, Physica B+C (Amsterdam) **129B**, 215 (1985); S. Hasegawa, M. Matuura, H. Anbutu, and Y. Kurata, Philos. Mag. B **56**, 633 (1987).
[22]E. Bustarret, M. Bensouda, M. C. Habrard, J. C. Bruyere, S. Poulin, and S. C. Gujrathi, Phys. Rev. B **38**, 8171 (1988).
[23]H. R. Philipp, J. Electrochem. Soc. **120**, 295 (1973).
[24]N. Ibaraki and H. Fritzsche, Phys. Rev. B **30**, 5791 (1984); B. Dunnett, D. J. Jones, and A. D. Stewart, Philos. Mag. B **53**, 159 (1986).
[25]D. A. G. Bruggemann, Ann. Phys. (Leipzig) [Folge 5] **24**, 636 (1935).
[26]F. W. Smith, J. Appl. Phys. **55**, 764 (1984).
[27]K. Mui and F. W. Smith, Phys. Rev. B **38**, 10 623 (1988).
[28]D. E. Aspnes and J. B. Theeten, J. Appl. Phys. **50**, 4928 (1979).
[29]H. R. Philipp, J. Phys. Chem. Solids **32**, 1935 (1971).
[30]S. V. Nguyen, J. Vac. Sci. Technol. B **4**, 1159 (1986).

Seoul Semiconductor, Exhibit 2001
LGI v. SSC, IPR2019-01154

APPENDIX L

PROCEEDINGS OF SPIE

SPIEDigitalLibrary.org/conference-proceedings-of-spie

The microstructure and LIDT of Nb2O5 and Ta2O5 optical coatings

G. Abromavicius, R. Buzelis, R. Drazdys, A. Melninkaitis, D. Miksys, et al.

G. Abromavicius, R. Buzelis, R. Drazdys, A. Melninkaitis, D. Miksys, V. Sirutkaitis, A. Skrebutenas, R. Juskenas, A. Selskis, "The microstructure and LIDT of Nb2O5 and Ta2O5 optical coatings," Proc. SPIE 6403, Laser-Induced Damage in Optical Materials: 2006, 640315 (15 January 2007); doi: 10.1117/12.696259

SPIE.

Event: Boulder Damage Symposium XXXVIII: Annual Symposium on Optical Materials for High Power Lasers, 2006, Boulder, Colorado, United States

Downloaded From: https://www.spiedigitallibrary.org/conference-proceedings-of-spie on 17 Sep 2019 Terms of Use: https://www.spiedigitallibrary.org/terms-of-use

The microstructure and LIDT of Nb_2O_5 and Ta_2O_5 optical coatings

G. Abromavicius[a], R. Buzelis[a], R. Drazdys[a], A. Melninkaitis[b], D. Miksys[b], V. Sirutkaitis[b], A. Skrebutenas[c], R. Juskenas[d], A. Selskis[d].

[a]Institute of Physics, Savanoriu pr. 231, LT-02300 Vilnius, Lithuania
[b]Laser Research Centre, Vilnius University, Sauletekio al. 10, LT-10222 Vilnius, Lithuania
[c]Optida Co., A.Gostauto g. 12, LT-01108 Vilnius, Lithuania
[d]Institute of Chemistry, Gostauto g. 9, LT-01108 Vilnius, Lithuania

ABSTRACT

High power laser systems are one of the most rapidly growing areas in the development of laser technology. This also leads towards higher requirements for environmental stability of optical components and their resistance to laser radiation. There are some reports showing that porous dielectric coatings are more resistant to intense laser radiation, however they have smaller environmental stability than denser coatings, which are more sensitive to laser radiation.

The influence of important technological parameters (deposition rate, substrate temperature, energy of ions) on optical and microstructural properties of high reflection dielectric coatings based on Nb_2O_5/SiO_2, and Ta_2O_5/SiO_2 in VIS spectral region is presented.

Furthermore the LIDT measurements using repetitive nanosecond laser pulses of Nb_2O_5/SiO_2 and Ta_2O_5/SiO_2 high reflecting optical coatings based on ISO 11254-2 standard are presented.

Keywords: optical damage, optical coatings, ion-assisted deposition, niobia, tantala, LIDT

1 INTRODUCTION

Almost in all of today's high-power laser applications, thin-film dielectric coatings are especially important. Optical losses, degradation of spectral characteristics in time and damage due to intensive laser radiation usually degrades the driving performance.

Improved stochiometry, increased environmental stability, smoother surfaces and densities of thin films approaching values of bulk materials are the main benefits of ion-assisted deposition (IAD) technology. However, the information about the influence of IAD on laser induced damage threshold (LIDT) is contradictory [1,2,3,4].

Niobium oxide has one of the highest refractive indices in the VIS-NIR regions, but the UV transparency is not as good as for tantalum oxide. Tantala exhibits low losses, high stability and is widely used as a high index material for manufacturing dielectric optical coatings.

The aim of this work was to investigate the influence of important technological parameters (deposition rate, substrate temperature, energy of ions) on optical properties of single niobia and tantala layers, radiation resistance and microstructure of high reflection dielectric coatings of Nb_2O_5/SiO_2 and Ta_2O_5/SiO_2, centered at 1064 nm wavelength.

Laser-Induced Damage in Optical Materials: 2006, edited by G. J. Exarhos, A. H. Guenther, K. L. Lewis, D. Ristau, M. J. Soileau, C. J. Stolz, Proc. of SPIE Vol. 6403, 640315, (2007) · 0277-786X/07/$15 · doi: 10.1117/12.696259

Downloaded From: https://www.spiedigitallibrary.org/conference-proceedings-of-spie on 17 Sep 2019
Terms of Use: https://www.spiedigitallibrary.org/terms-of-use

Seoul Semiconductor, Exhibit 2001
LGI v. SSC, IPR2019-01154

2 EXPERIMENTAL SETUP

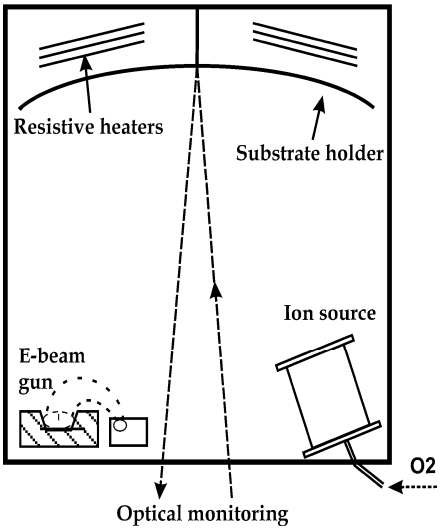

Fig. 1. Experimental setup.

Experiments were carried out using VU-2M coating plant (Fig. 1). The system was equipped with a high vacuum diffusion pump backed by rotary oil and rotary lobe pumps. The coating chamber was 70 cm in diameter and 70 cm in height with a spherical rotational substrate holder. Two 180° electron-beam sources and gridless end-Hall ion source for the substrate pre-cleaning and ion beam assisted deposition were installed in the chamber. Substrates can be heated to 300°C by resistive heaters during the coating deposition.

The coating process was controlled by optically monitoring reflection or transmission through the test glass pieces at the selected control wavelength. Optical monitoring was performed using a spectrophotometer with operating range from 250 m to 1500 nm. The main designed specifications of the ion beam source:

Ion energy: 80-120 eV

Beam current: 750 mA (Anode current is 4 A)

Ion beam current density: 5 mA/cm^2 (Central part at 150 mm distance)

3 RESULTS AND DISCUSSION

3.1 Optical properties of single Nb_2O_5 and Ta_2O_5 layers.

The first experiments were targeted to examine the optical properties of single layers deposited using different deposition rates, temperature and energy of ions bombarding the growing film. All deposition runs and their technological parameters are presented in Table 1. The same flow rate of oxygen gas was used for feeding the ion gun during all experiments. The mean energies of impinging ions were estimated using anode voltage Ua values and were from 70 to 130 eV. Precleaning of substrates with ion gun was the same for all processes.

Table 1. Deposition parameters for the single layer experiments

Run number	Material	Temperature (°C)	Deposition rate (Å/s)	Deposition pressure (Pa)	Anode voltage (V)	Anode current (A)	Thickness (nm)
1	Nb_2O_5	300	1	~1×10^{-2}	220	2	242
2		50*	1	~1×10^{-2}	220	2	248
3		300	4	~2×10^{-2}	220	2	259
4		50*	3	~1.5×10^{-2}	220	2	249
5		50*	3	~2×10^{-2}	190	0.9	266
6	Ta_2O_5	300	1	~1.5×10^{-2}	220	2	255
7		50*	1	~1.5×10^{-2}	220	2	269
8		300	2	~1.5×10^{-2}	220	2	255
9		50*	2	~1.5×10^{-2}	220	2	269
10		50*	3	~1.5×10^{-2}	190	0.9	271

*- deposition of the substrates without heating. However, during longer coating runs, ion gun cathode, cathodes of e-beam guns raises the temperature of substrates up to the ~ 50°C approximately.

Downloaded From: https://www.spiedigitallibrary.org/conference-proceedings-of-spie on 17 Sep 2019
Terms of Use: https://www.spiedigitallibrary.org/terms-of-use

Seoul Semiconductor, Exhibit 2001
LGI v. SSC, IPR2019-01154

Transmittance spectra in 230 – 2000 nm region were measured using Perkin Elmer Lambda 950 spectrophotometer. Optical parameters (refractive index and extinction) and physical thickness were evaluated using commercial software package OptiChar. OptiChar estimates optical properties of the target film by fitting model and measured spectrophotometric curve. All fitting procedures were done using homogeneous film models. Since only transmittance spectra was used for fitting procedure, the basic fitting steps were the following: 1) comparing measured transmittance curve and defining the spectral region, where extinction is present; 2) fitting the selected virtually "extinction-free" spectral region by adjusting dispersion of refractive index and physical thickness; 3) adding excluded "extinction-present" spectral range and manually adjusting *k* values trying to match the UV part of measured spectra where transmission of the film is cut off by extinction and to match amplitudes of measured transmittance maxima in UV and VIS region where the optical thickness of film is equal to half-wavelength; 4) fitting dispersion of refractive index and optical film thickness again, with manually introduced extinction.

All these steps were repeated many times, each time improving the match between the model and the measurements until the improvements after each iteration became negligible. Of course, possible inhomogeneity of the film and lack of reflectance spectra automatically introduces some errors to the final results, but as far as all the films were modeled using the same procedure, we believe that at least the results are relatively correct and are very close to real properties. In later discussion about extinction we also use extinction values at the cut-off of transmittance spectra (360 nm for niobia and 270 nm for tantala), where extinction is dominant.

Refractive indices and extinction coefficients of single niobia layers are shown in Fig 2.

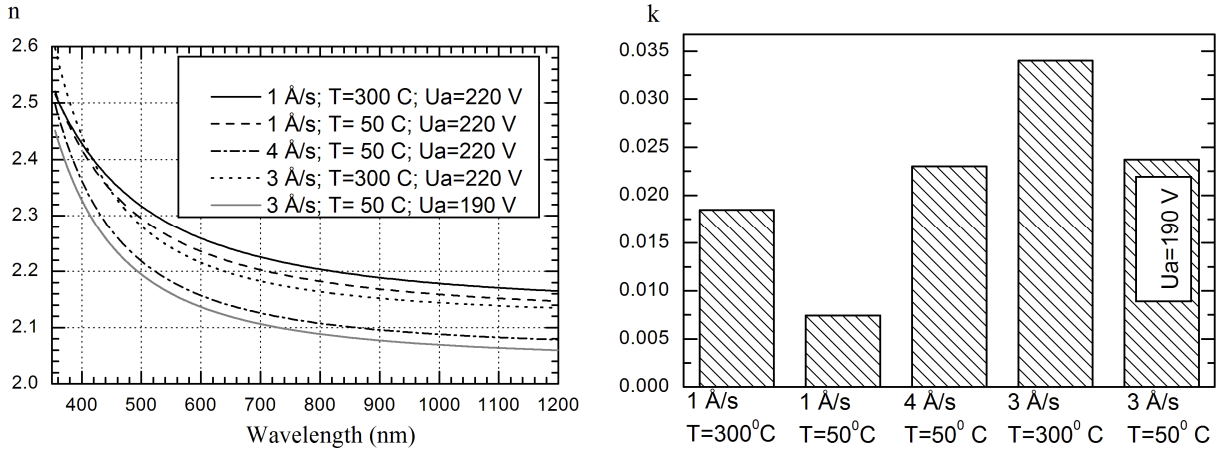

Fig. 2. Refractive indices (*n*) and extinction coefficients (*k* at 360 nm) of single niobia layers deposited using different substrate temperature, deposition rate and anode voltage.

The observed trend of refractive index curves reflects the energetic conditions during niobia layer formation. Larger substrate temperature and slow deposition rate increases migrating times of adatoms on the substrate surface[5]. Therefore more compact microstructure and dense niobia layer is formed which has higher refractive index. Fast deposition on unheated substrates leads to formation of porous layer structure, which exhibits smaller refractive index. Bombardment of forming layer with energetic oxygen ions also introduces additional energy input to niobia adatoms. The energy of bombarding ions is directly proportional to the anode voltage of ion beam gun, so smaller voltage leads to smaller ion energies.

The influence of all these processes is clearly seen in Fig. 2. The biggest refractive index was obtained depositing niobia at 1 Å/s deposition rate and heating the substrate to T = 300°C. The smallest refractive index resulted in deposition at 3 Å/s without heating the substrate and bombarding the film with less energetic oxygen ions.

However, a value of extinction coefficient at 360 nm seems also correlated with deposition parameters (Fig. 2). Usually smaller extinction level is more desirable, so slower deposition on unheated substrate is more favorable than other conditions. Dependence of extinction on deposition rate could be interpreted that slower deposition leads to better oxidation of niobia. Dependence of extinction on substrate temperature is not clear and needs additional investigations.

Downloaded From: https://www.spiedigitallibrary.org/conference-proceedings-of-spie on 17 Sep 2019
Terms of Use: https://www.spiedigitallibrary.org/terms-of-use

Seoul Semiconductor, Exhibit 2001
LGI v. SSC, IPR2019-01154

Similar trends in refractive index change were observed in the deposition of single tantala layers (Fig. 3.) – slow deposition on heated substrates led to the densest layer microstructure, having the largest refractive index. However, the situation in extinction level dependence on deposition rate was reverse than in niobia case. Fast deposition on unheated substrates resulted in lower extinction and using low anode voltage gave the smallest extinction. Slow deposition on heated substrates yielded the highest extinction levels.

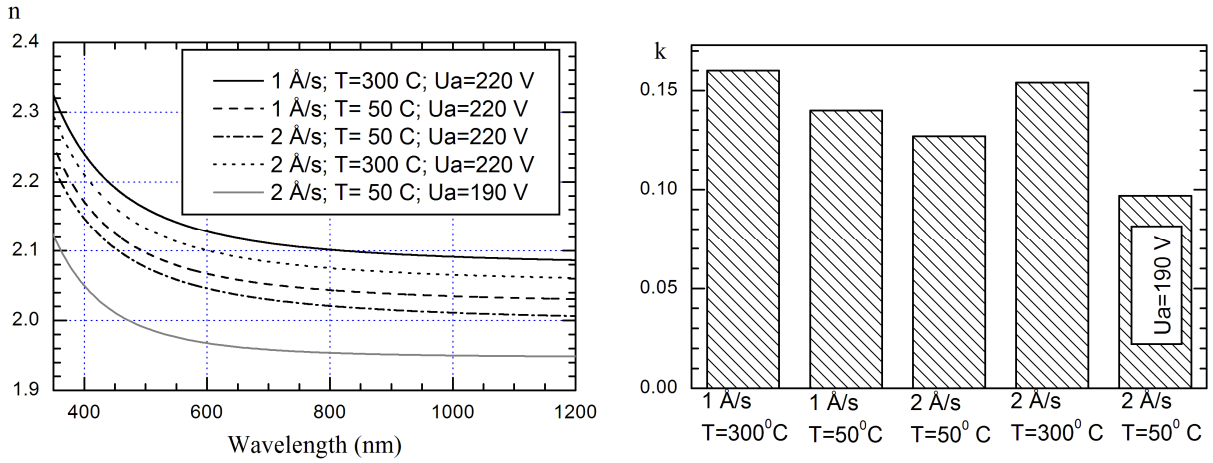

Fig. 3. Refractive indices and extinction coefficient (at 270 nm) of single tantala layers deposited using different substrate temperature, deposition rate and anode voltage.

This controversial situation could be the result of additional "external" extinction, introduced by possible contamination from tungsten cathode of ion source[6,7], which is proportional to its operating time and energy of oxygen ions. Since tantala is much more transparent in UV region than niobia, contamination of ion gun should be much more pronounced for tantala layers, especially in slower depositions, which take more time. However, confirmation of this phenomenon needs further investigations.

The microstructure of deposited niobia and tantala layers was investigated using difractometer D8 (Bruker AXS) equipped with primary beam monochromator for Cu radiation. X-ray diffraction patterns shown on Fig. 4.

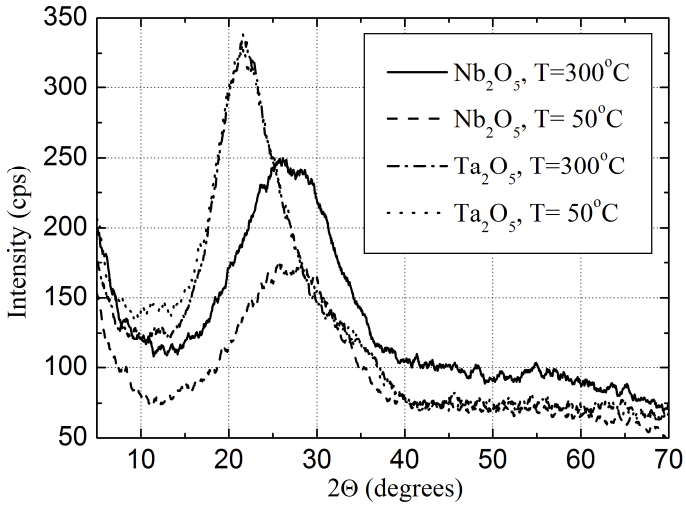

Fig. 4. X-ray diffraction patterns of single hafnia layers.

Niobia and tantala coatings demonstrated amorphous structure irrespectively of deposition parameters.

Downloaded From: https://www.spiedigitallibrary.org/conference-proceedings-of-spie on 17 Sep 2019
Terms of Use: https://www.spiedigitallibrary.org/terms-of-use

Seoul Semiconductor, Exhibit 2001
LGI v. SSC, IPR2019-01154

3.2 Optical properties of high reflecting coatings

Optical coatings usually consist of many layers. Niobia – silica, tantala – silica high reflection coatings consisting of 16 layers and centered at 1064nm were deposited on BK7 substrates using different deposition conditions In order to investigate optical, structural properties and resistance to laser radiantion.

Two substrates were deposited during each coating run. Deposition parameters are summarized in Table 2.

Table 2. Deposition parameters of high reflection coatings

Run number	High index material	Temperature (°C)	Deposition rate (Å/s)	Silica deposition rate (Å/s)	Deposition pressure (Pa)	Anode voltage (V)	Anode current (A)
1	Nb_2O_5	300	2	4	$\sim 1 \times 10^{-2}$	220	2
2		50*	2	4	$\sim 1 \times 10^{-2}$	220	2
3		50*	3	5	$\sim 2 \times 10^{-2}$	160	3
4	Ta_2O_5	300	3	5	$\sim 1 \times 10^{-2}$	220	2
5		50*	4	7	$\sim 1 \times 10^{-2}$	220	2
6		50*	3	4	$\sim 2 \times 10^{-2}$	160	2.6-2.8

* $T=50^0$ C means deposition of the substrates without heating. However, during longer coating runs, ion gun cathode, cathodes of e-beam guns raises the temperature of substrates up to the 50°C approximately.

Transmittance spectra of niobia-silica and tantala-silica dielectric mirrors are shown in Fig. 5. Mean refractive indices of niobia and tantala layers in these multilayer stacks were evaluated using transmittance spectra and commercial software package OptiRe. Again, deposition on heated to $T = 300$°C substrates gave the highest niobia index $n = 2.19$ at 1064 nm. This also led to slightly bigger spectral width of the mirror. Second and third coating runs showed average $n = 2.15$ and $n = 2.13$ of niobia layers, respectively.

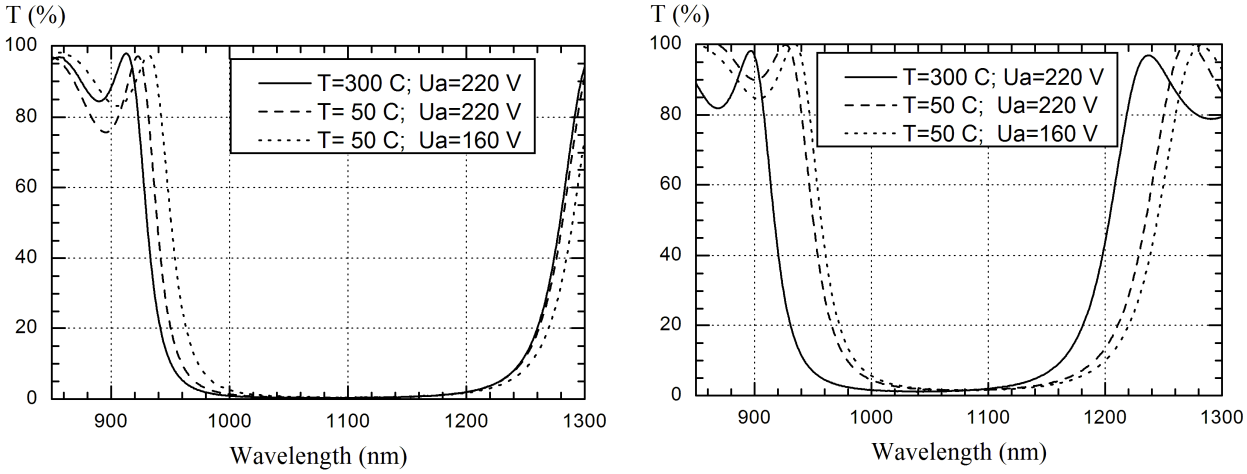

Fig. 5. Transmittance of high reflective niobia-silica (left) and tantala-silica (right) coatings using different substrate temperature and anode voltage.

Deposition on heated to $T = 300^0$ C substrates of tantala-silica mirror gave the highest average tantala index $n = 2.02$ at 1064 nm. This also led to slightly wider spectral width and higher reflectance of the mirror. Second and third coating runs showed average $n = 1.99$ of tantala layers.

All the coating runs were controlled in the same monitoring wavelength, however it is clearly seen, that depositions without heating and with smaller bombarding ion energies resulted in shifted spectra towards longer wavelengths. This spectral shift confirms, that these mirror coatings have less dense structure and are more porous, so accumulate more air and water vapor when exposed to the atmosphere.

Downloaded From: https://www.spiedigitallibrary.org/conference-proceedings-of-spie on 17 Sep 2019
Terms of Use: https://www.spiedigitallibrary.org/terms-of-use

3.3 LIDT of high reflection coatings

Laser induced damage threshold (LIDT) was experimentally measured according to the requirements of ISO 11254-2 standard[8]. For observations of LIDT behaviour the first harmonic of Nd:YAG laser radiation (λ = 1064 nm, τ = 3.4 ns) was used. All measurements were performed at 10 Hz pulse repetition rate (S on 1 test). Automated equipment and methodology for these measurements are presented in detail in the reference[3]. LIDT results are presented in Fig 6.

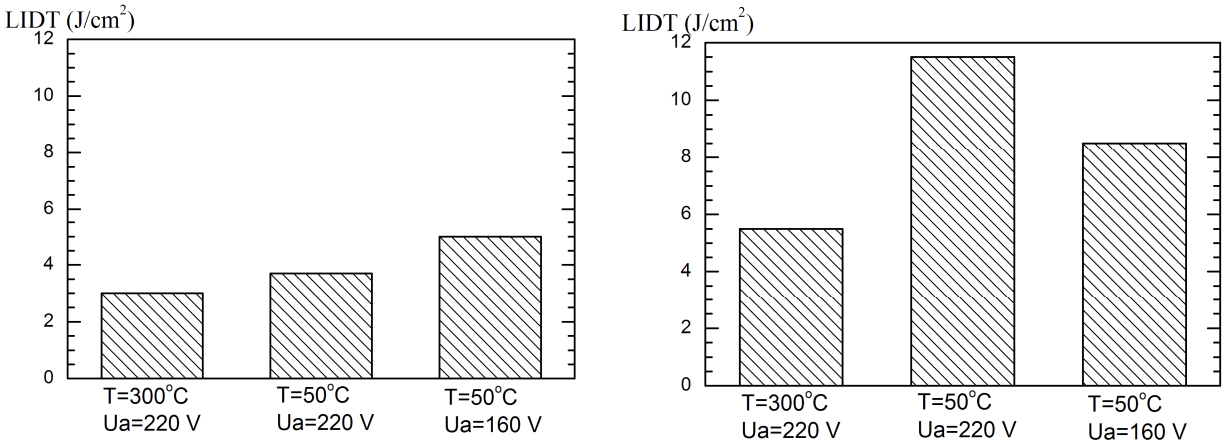

Fig. 6. LIDT of high reflective niobia-silica (left) and tantala-silica (right) coatings.

Most porous microstructure niobia-silica mirrors, deposited on unheated substrates using less energetic ions, demonstrated the highest LIDT of 5 J/cm^2. Tantala-silica mirror, deposited on unheated substrates, but using more energetic ions gave the best result of 11.5 J/cm^2 among tantala mirror runs. These results coincide with some investigations that show the increase of LIDT with decreasing the packing density of the coating. This behaviour was explained by possibly better heat dissipation in more porous film[9].

4 CONCLUSIONS

Investigation of influence of important technological parameters (deposition rate, substrate temperature, energy of ions) on optical properties of single niobia and tantala layers showed that the most densest layers with highest refractive indices resulted depositing at 1 Å/s rate on heated substrates to T = 300°C for both materials. However, these conditions also resulted to slightly higher extinction levels in the films, while deposition without heating, lowered down extinction. We identify two possible reasons for increased extinction – incomplete oxidation during faster deposition for niobia layers and possible contamination by ion source operation during longer depositions of tantala layers. However, more detailed investigations are needed to confirm these phenomena.

LIDT measurements of deposited high reflection dielectric coatings of Nb_2O_5/SiO_2 and Ta_2O_5/SiO_2, centered at 1064 nm wavelength revealed that more porous coatings, deposited on unheated substrates demonstrated the highest resistance to laser radiation, reaching 5 J/cm^2 for niobia and 11.5 J/cm^2 for tantala mirrors. Therefore tantalum oxide seems much better high refractive index material for preparing optical coatings for high power laser applications in VIS and IR spectral range.

XRD analysis of niobia and tantala coatings demonstrated amorphous structure irrespectively on used deposition parameters.

ACKNOWLEDGEMENTS

This research has been supported by Lithuanian State Science and Studies Foundation grant.

Downloaded From: https://www.spiedigitallibrary.org/conference-proceedings-of-spie on 17 Sep 2019
Terms of Use: https://www.spiedigitallibrary.org/terms-of-use

Seoul Semiconductor, Exhibit 2001
LGI v. SSC, IPR2019-01154

REFERENCES

1. P. Gu, J. Tang, "Laser-induced damage resistance of thin-film polarizers prepared by ion-assisted deposition". Opt. Lett. vol. 19, no. 2, p. 81-83 (2002).
2. J. H. Herringer, T. A. Caughey, “Ion assisted vs. non-ion assisted high laser damage resistant coatings on BBO”, Laser-Induced Damage in Optical Materials, Vol. 4932, p. 35-37, Proc. SPIE, 2003.
3. A. Melninkaitis, V. Sirutkaitis, T. Rakickas, R. Grigonis, D. Miksys, A. Skrebutenas, R. Buzelis, R. Drazdys, G. Abromavicius, R. Juskenas, A. Selskis, “Effect of deposition method and substrate surface quality on laser-induced damage threshold for repetitive 13-ns and 130-fs pulses”. Advanced Microlithography Technologies. Edited by W. Yangyuan, Y. Jun-en; P. J. Christopher, Vol. 5647, pp. 43-52, Proc. SPIE, 2005.
4. R. Thielsch, A. Gatto, J. Heber, N. Kaiser, “A comparative study of the UV optical and structural properties of SiO_2, Al_2O_3, and HfO_2 single layers deposited by reactive evaporation, ion-assisted deposition and plasma ion-assisted deposition”. Thin Solid Films, 410 p. 86–93 (2002).
5. P.W.Baumeister. Optical Coating Technology. (SPIE Press monograph). p. 3-17 (2004).
6. T. Jensen, J. Warren, R. Johnson, "Ion-Assisted Deposition of Moisture-Stable Hafnium Oxide Films for Ultraviolet Applications". Appl. Opt. 41, 3205-3210 (2002).
7. G. Abromavicius, R. Buzelis, R. Drazdys, R. Grigonis, A. Melninkaitis, D. Miksys, T. Rakickas, V. Sirutkaitis, A. Skrebutenas, R. Juskenas, A. Selskis. Influence of ion-assisted deposition on laser-induced damage threshold and microstructure of optical coatings. Laser-Induced Damage in Optical Materials: 2005. Proc. SPIE Vol. 5991, p. 436-442, 2006.
8. ISO 11254-2, Lasers and laser-related equipment. Determination of laser-induced damage threshold of optical surfaces. Part 2: S-on-1 test, 2001.
9. M. Alvisi, G. De Nunzio, M. Di Giulio, M. C. Ferrara, M. R. Perrone, L. Protopapa, L. Vasanelli, “Deposition of SiO_2 films with high laser damage thresholds by ion-assisted electron-beam evaporation”. Applied Optics, Vol. 38 (7) 1237-1243 (March 1999)

Downloaded From: https://www.spiedigitallibrary.org/conference-proceedings-of-spie on 17 Sep 2019
Terms of Use: https://www.spiedigitallibrary.org/terms-of-use

Seoul Semiconductor, Exhibit 2001
LGI v. SSC, IPR2019-01154

APPENDIX M

PROGRESS IN PHOTOVOLTAICS: RESEARCH AND APPLICATIONS
Prog. Photovolt: Res. Appl. **7**, 245–260 (1999)

Research

Optimised Antireflection Coatings for Planar Silicon Solar Cells using Remote PECVD Silicon Nitride and Porous Silicon Dioxide

Henning Nagel*, Armin G. Aberle and Rudolf Hezel
Institut für Solarenergieforschung Hameln/Emmerthal (ISFH), Am Ohrberg 1, D-31860 Emmerthal, Germany

Silicon nitride (SiN) films fabricated by remote plasma-enhanced chemical vapour deposition (RPECVD) have recently been shown to provide an excellent electronic passivation of silicon surfaces. This property, in combination with its large refractive index, makes RPECVD SiN an ideal candidate for a surface-passivating antireflection coating on silicon solar cells. A major problem of these films, however, is the fact that the extinction coefficient increases with increasing refractive index. Hence, a careful optimisation of RPECVD SiN based antireflection coatings on silicon solar cells must consider the light absorption within the films. Optimal optical performance of silicon solar cells in air is obtained if the RPECVD SiN films are combined with a medium with a refractive index below 1·46, such as porous SiO_2. In this study, the dispersion of the refractive indices and the extinction coefficients of RPECVD SiN, porous SiO_2, and several other relevant materials (MgF_2, TiO_x, ZnS, B270 crown glass, soda lime glass, ethylene vinyl acetate and resin as used in commercial photovoltaic modules) are experimentally determined. Based on these data, the short-circuit currents of planar silicon solar cells covered by RPECVD SiN and/or porous SiO_2 single- and multi-layer antireflection coatings are numerically maximised for glass-encapsulated as well as non-encapsulated operating conditions. The porous SiO_2/RPECVD SiN-based antireflection coatings optimised for these applications are shown to be universally suited for silicon solar cells, regardless of the internal blue or red response of the cells. Copyright © 1999 John Wiley & Sons, Ltd.

INTRODUCTION

Since the early days of photovoltaic (PV) energy conversion with silicon solar cells, the reduction of reflection losses by means of an antireflection (AR) coating fabricated on the cells has been common practice. With regard to the design of the AR coating, there are two fundamentally different applications of solar cells. The standard application is the encapsulation of the cells into a glass-covered PV module. In order to ensure the required long-term stability, a suitable encapsulant material

* Correspondence to: Henning Nagel, ISFH, Am Ohrberg 1, D-31860 Emmerthal, Germany. E-mail: h.nagel@isfh.de

CCC 1062–7995/99/040245–16$17·50
Copyright © 1999 John Wiley & Sons, Ltd.
Received 14 March 1998
Revised 19 November 1998

Seoul Semiconductor, Exhibit 2001
LGI v. SSC, IPR2019-01154

[ethylene vinyl acetate (EVA) or a resin] is used between the glass and the solar cells to prevent the penetration of humidity into the PV module. As the refractive index of the encapsulant is around 1·52 at the reference wavelength of 632·8 nm (i.e. the wavelength of a helium–neon laser) while the corresponding refractive index of silicon is 3·87, reflection losses can most easily be reduced by an AR coating with a refractive index between 1·52 and 3·87. In principle, a multi-layer AR coating gives the best optical performance. In practice, however, the AR coating generally consists only of a single layer (usually TiO_x). The reason is that all materials known to date with a large refractive index ($n > 2{\cdot}5$), as required for a multi-layer AR coating, absorb a significant amount of sunlight. The outer surface of the glass cover is not AR-coated as no durable low-cost coating has been identified in the past. Due to this problem, the air/glass interface of today's PV modules leads to a wavelength-independent reflection loss of 4%.

Besides the above-mentioned standard application, there are other applications (such as UV detectors or calibration measurements of high-efficiency laboratory cells) where solar cells are not encapsulated. In this case, the AR coating must be optimised against air ($n_{air} \approx 1{\cdot}0$). According to the well-known equation[1] $n = \sqrt{n_{air} n_{Si}}$, a single-layer AR coating on silicon should have a refractive index of about 1·97. Because of the missing glass plate/encapsulant, a single-layer AR coating is not sufficiently effective, so that a double-layer AR coating consisting of MgF_2 and ZnS (refractive index of 1·38 and 2·34 at 632·8 nm, respectively) is usually applied.

A very promising alternative to MgF_2 is porous SiO_2, which might be deposited cost-effectively onto large areas and which features a very low refractive index that can be varied between 1·10 and 1·46 via the porosity of the films.[2] Hence, this material is ideally suited to minimise the optical losses of glass-encapsulated as well as non-encapsulated silicon solar cells. In the first case, the porous SiO_2 is deposited onto the outer surface of the glass cover of the PV module, while in the latter case it is deposited as the final layer of the AR coating on the solar cell. However, it should be noted that additional progress has to be made concerning the scratch resistance of porous SiO_2 films, which is particularly important for outdoor applications.

In the past, there has been a trend towards ever increasing solar cell efficiencies. In the case of crystalline silicon, high efficiencies can only be achieved if, in addition to the reduction of reflection losses, the AR coating also minimises surface recombination losses ('surface passivation'). As the standard AR coatings TiO_x and ZnS provide negligible surface passivation, the surfaces of silicon solar cells are often passivated with a single layer of thermally grown SiO_2. However, its refractive index (1·46) is too small to act as an efficient single-layer AR coating on silicon solar cells. In order to circumvent this problem, a thin passivating SiO_2 film below an AR coating with higher refractive index has been used in the past.[1,3] This SiO_2 film is made as thin as possible to minimise its detrimental optical effect, but still thick enough to ensure a sufficient surface passivation.

Recently, silicon nitride (SiN) films fabricated by remote plasma-enhanced chemical vapour deposition (RPECVD) have been shown to provide an extremely low surface recombination velocity (SRV) on *p*-type silicon[4,5] and a very high degree of passivation on n^+-diffused silicon surfaces.[6] The refractive index of RPECVD SiN films is very high and can be varied over a wide range (1·85–2·62 at 632·8 nm in this work).[5] These unique properties make RPECVD SiN an ideal candidate for a surface-passivating AR coating on glass-encapsulated, as well as non-encapsulated, monofacial and bifacial silicon solar cells. A problem with RPECVD SiN films is the fact that low SRVs are only obtained for relatively large refractive indices (i.e. low optical bandgap). This results in a significant degree of optical absorption for wavelengths below 600 nm, and hence RPECVD SiN-based AR coatings have to be thoroughly optimised with regard to the above-mentioned applications (encapsulated and non-encapsulated cells). A key issue in such an optimisation is the consideration of the extinction coefficients of the films.

The potential of porous SiO_2 and remote-plasma SiN films with regard to the reduction of optical losses of silicon solar cells and modules has not yet been quantified. Therefore, this study presents an experimental determination of the dispersion of the refractive index n and the extinction coefficient k of porous SiO_2 and various RPECVD SiN films via a fit of reflection and transmission measurements. In order to compare the performance of the proposed porous SiO_2/RPECVD SiN-based single-layer, double-layer and triple-layer AR coatings with today's standard AR coatings, we also measure the

Copyright © 1999 John Wiley & Sons, Ltd.

Seoul Semiconductor, Exhibit 2001
LGI v. SSC, IPR2019-01154

spectral dependences of n and k of MgF_2, TiO_x, ZnS, B270 crown glass, soda lime glass, EVA and a resin as used in commercial photovoltaic modules. Owing to the absorption within the AR coating, the comparison is based on the resulting short-circuit current density J_{SC} of the solar cell instead of the reflection weighted with the solar photon flux. This approach has the additional advantage that differences in the internal quantum efficiencies of the solar cells can be considered.

The J_{SC} optimisations are performed for glass-encapsulated as well as non-encapsulated planar (i.e. non-textured) silicon solar cells covered by RPECVD SiN and/or porous SiO_2 antireflection coatings. The sunlight illuminates the solar cell perpendicularly, which is the standard test condition for solar cells and modules. The results are compared with the optimised short-circuit currents of planar silicon solar cells featuring a TiO_x or ZnS based antireflection coating.

EXPERIMENTAL DETAILS

The RPECVD SiN films are deposited as described in Ref. 7, using optimised parameters for very low SRVs. By increasing the NH_3/SiH_4 flow ratio from 10 to 45, the refractive index (measured at 632·8 nm) decreases from 2·62 to 1·85. Porous SiO_2 films are prepared by wet chemical deposition.[2] MgF_2 and ZnS are evaporated at room temperature in a high-vacuum chamber. TiO_x is reactively evaporated with an oxygen partial pressure of $3{\cdot}5 \times 10^{-5}$ mbar at a sample temperature of 220°C. Upon fabrication, the TiO_x films do not receive an additional thermal treatment. B270 crown glass specified as Superwhite® was obtained from Desag. The soda lime glass was supplied by Schott. EVA foil is inserted between two B270 glass plates and heated for 10 min at 90°C. In order to ensure an intimate contact between EVA and glass, the glass plates are pressed together during the thermal treatment. The investigated resin is used in commercial photovoltaic modules.

Reflection and transmission measurements covering the wavelength range 300–1150 nm are performed with a commercially available Bentham M300 monochromator, a halogen lamp, and a $BaSO_4$ coated integrating sphere. The transfer matrix method[8] is implemented on a personal computer to calculate (i) the wavelength-dependent reflection $R(\lambda)$ and transmission $T(\lambda)$ of a multi-layer stack consisting of an arbitrary order of coherent and incoherent layers (thickness < 1 μm or > 100 μm, respectively), and (ii) the absorption $A(\lambda)$ of individual layers within the multi-layer stack. Curve fitting is achieved by means of the Simplex downhill optimisation procedure.[9]

In a first step, the optical parameters $n(\lambda)$ and $k(\lambda)$ of the B270 Superwhite® crown glass and the soda lime glass are determined by curve fitting of the measured $R(\lambda)$ and $T(\lambda)$ data. In order to measure the optical parameters of the EVA and the resin (neither of which are self-supporting), these materials are embedded between two B270 glass plates. Using the previously measured optical properties of the B270 glass, $n(\lambda)$ and $k(\lambda)$ of EVA and the resin are then obtained from the measured $R(\lambda)$ and $T(\lambda)$ data of the stack air/glass/EVA(or resin)/glass/air. The required thicknesses of the B270 and soda lime glass plates, the EVA and the resin are measured with a micrometer screw.

In order to determine the optical properties of the thin-film materials, RPECVD SiN, porous SiO_2, MgF_2, TiO_x and ZnS, each of these films is deposited onto one surface of separate B270 glass plates. $n(\lambda)$ and $k(\lambda)$ of the films are then obtained from the measured $R(\lambda)$ and $T(\lambda)$ data of the stack air/film/glass/air. As this stack is not symmetrical in structure and furthermore absorption within the stack cannot be neglected, care must be taken that in the calculations and measurements the light illuminates the same surface of the stack. The required thicknesses of the individual films are determined with an ellipsometer at 632·8 nm.

MEASUREMENT OF REFRACTIVE INDICES AND EXTINCTION COEFFICIENTS

Figures 1–6 show the dispersion of the optical constants (refractive index and extinction coefficient) of the examined materials. A parameterisation of the measured data is given in the Appendix. B270 crown glass

Copyright © 1999 John Wiley & Sons, Ltd.

Seoul Semiconductor, Exhibit 2001
LGI v. SSC, IPR2019-01154

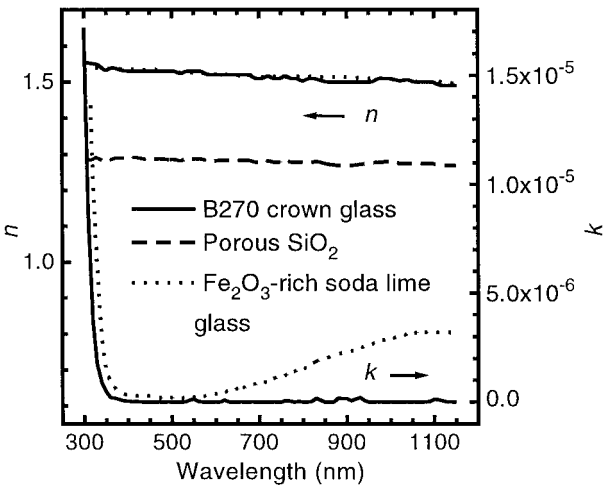

Figure 1. Measured dispersion of the refractive indices (left axis) of B270 crown glass, Fe_2O_3-rich soda lime glass and porous SiO_2, and of the extinction coefficients (right axis) of B270 crown glass and soda lime glass

and soda lime glass have a refractive index of about 1·52, which is virtually constant for wavelengths in the 300–1150 nm range (see Figure 1). The extinction coefficients of B270 crown glass and soda lime glass are very low ($<2 \times 10^{-5}$) for these wavelengths. However, $k(\lambda)$ of the soda lime glass increases for wavelengths above 600 nm. This is due to its higher Fe_2O_3 content, which is also the reason for its greenish appearance.[10] The refractive index of porous SiO_2 is approximately constant in the 300–1150 nm wavelength range and can be adjusted between 1·10 and 1·46 by appropriate changes of the process parameters. As a representative example, Figure 1 shows the $n(\lambda)$ dependence of a particular porous SiO_2 film fabricated in the course of this work. The very low refractive index of porous SiO_2 can be explained with the effective medium model[11]

$$n = V_{SiO_2} n_{SiO_2} + V_{air} n_{air}, \tag{1}$$

where V_{SiO_2} is the volume fraction of SiO_2 and V_{air} the volume fraction of the pores filled with air. The pores are small compared to the wavelengths, so that there is no scattering of light. The extinction coefficient of porous SiO_2 can be neglected in the considered wavelength range.

Figure 2 shows the measured wavelength dependence of the refractive indices of five different RPECVD SiN films fabricated for this work. Film 1 has a low silicon content and hence a low, slightly wavelength-dependent, refractive index around 1·85. With increasing silicon content in the film the refractive index increases and the wavelength dependence becomes more pronounced (films 2–5). For the film with the largest silicon concentration (film 5), the refractive index approaches 3·0 at wavelengths around 400 nm. An increasing silicon content leads to a decreasing bandgap and hence to an increasing absorption within the film. This can be seen in Figure 3, which shows the measured extinction coefficients of the five films of Figure 2. It should be noted that the optical behaviour of the remote PECVD SiN films investigated in the present work is similar to that reported in Refs 12 and 13 for SiN films fabricated by means of direct PECVD.

The measured refractive index of MgF_2 is 1·29 (Figure 4), which is about 0·09 lower than reported in the literature.[1] This is probably due to micropores in the examined evaporated MgF_2 film. As can be seen from Figure 5, the extinction coefficient of MgF_2 is very low in the wavelength range 300–1150 nm. Thus, MgF_2 is optically very similar to a porous SiO_2 film with the same refractive index. Also shown in Figures 4 and 5 are the dispersion of n and k of TiO_x and ZnS. They have quite high refractive indices ($n \approx 2{\cdot}3$ at 632·8 nm) and low extinction coefficients for wavelengths down to 400 nm. EVA and the examined resin have even lower extinction coefficients (Figure 6). However, as their thickness in typical photovoltaic modules is of the order of 1 mm (i.e. 10^4 times the thickness of the TiO_x or ZnS films), absorption becomes

Copyright © 1999 John Wiley & Sons, Ltd.

Seoul Semiconductor, Exhibit 2001
LGI v. SSC, IPR2019-01154

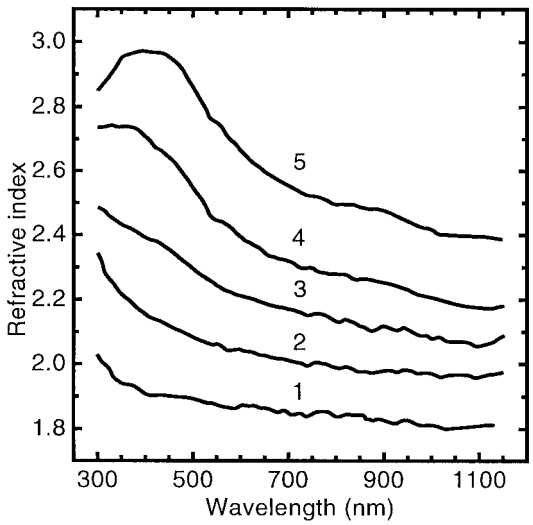

Figure 2. Measured dispersion of the refractive indices of five different RPECVD SiN films. Film 5 has the highest and film 1 the lowest silicon concentration

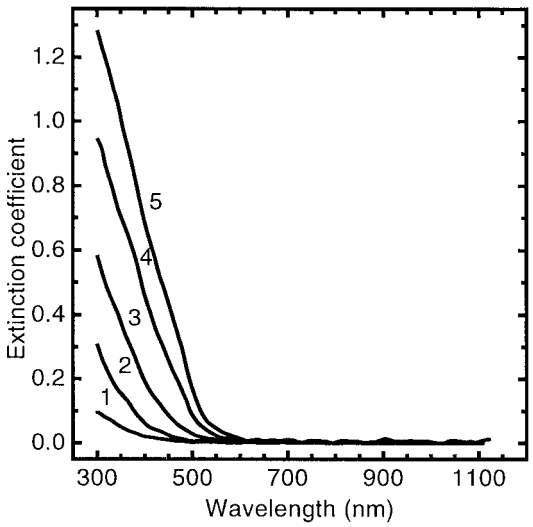

Figure 3. Measured dispersion of the extinction coefficients of the five RPECVD SiN films of Figure 2

important for short wavelengths. The refractive indices of EVA and the examined resin are virtually the same as those of the B270 crown glass.

OPTIMISATION OF ANTIREFLECTION COATINGS

Essentially the same software as described above is used to maximise the short-circuit current density J_{SC} of an illuminated antireflection-coated silicon solar cell. J_{SC} is given by

$$J_{SC} = q \int_0^\infty IQE(\lambda) \times F_{Ph}(\lambda) \times A(\lambda)\, d\lambda, \tag{2}$$

Copyright © 1999 John Wiley & Sons, Ltd.

Seoul Semiconductor, Exhibit 2001
LGI v. SSC, IPR2019-01154

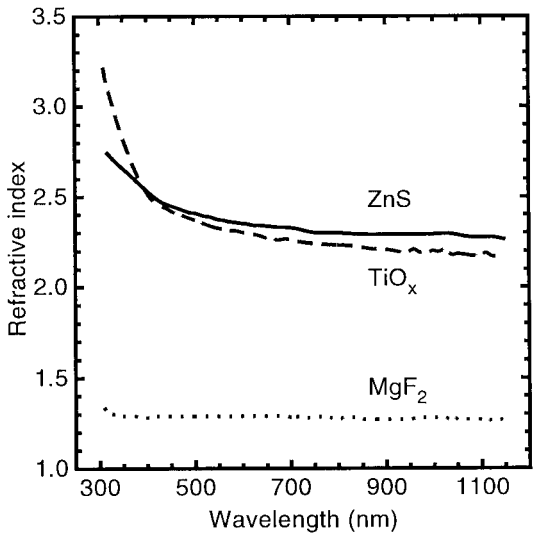

Figure 4. Measured dispersion of the refractive indices of MgF_2, TiO_x and ZnS

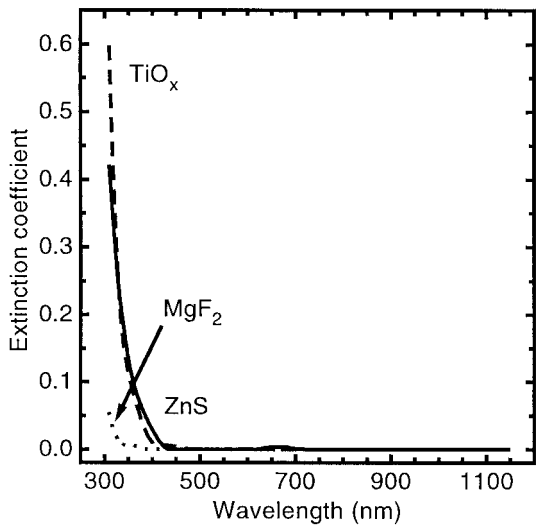

Figure 5. Measured dispersion of the extinction coefficients of MgF_2, TiO_x and ZnS

where q is the elementary charge, $IQE(\lambda)$ the internal quantum efficiency of the solar cell, $F_{Ph}(\lambda)$ the incident photon flux of the AM1·5G spectrum[14] normalised to a power density of 100 mW cm^{-2} and $A(\lambda)$ the calculated absorption within the silicon. The current densities associated with the reflected and transmitted photon fluxes are calculated from Equation (2) by replacing $A(\lambda)$ by $R(\lambda)$ or $T(\lambda)$, respectively. Shading due to the metal contact grid of actual solar cells is neglected throughout this work.

The internal quantum efficiencies used for the optimisation of AR coatings are calculated with the device simulation programme PC-1D.[15] Figure 7 summarises the calculated *IQE*s of all solar cells investigated in this work. The reference cell is representative for state-of-the-art experimental high-efficiency silicon solar cells. It is characterised by a moderately diffused emitter, a large bulk diffusion length and well passivated front and rear surfaces. The most important cell parameters are summarised in Table I. As can be seen from the triangles in Figure 7, the *IQE* of this cell is excellent for wavelengths between 300 and 1000 nm. The cell with the reduced red response is obtained by setting the back surface recombination

Copyright © 1999 John Wiley & Sons, Ltd.

Seoul Semiconductor, Exhibit 2001
LGI v. SSC, IPR2019-01154

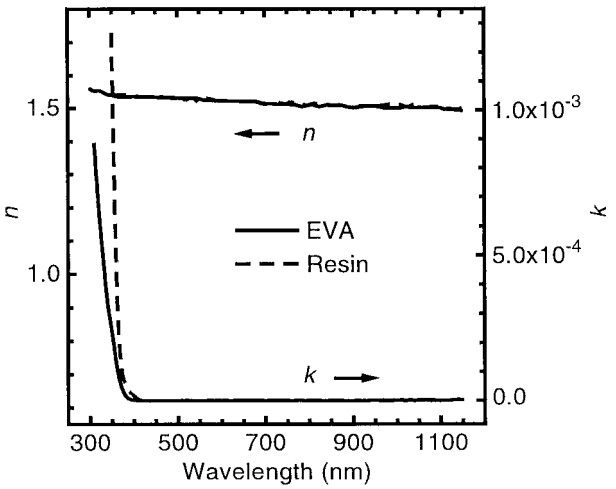

Figure 6. Measured dispersion of the refractive indices and extinction coefficients of EVA and resin as used in commercial PV modules

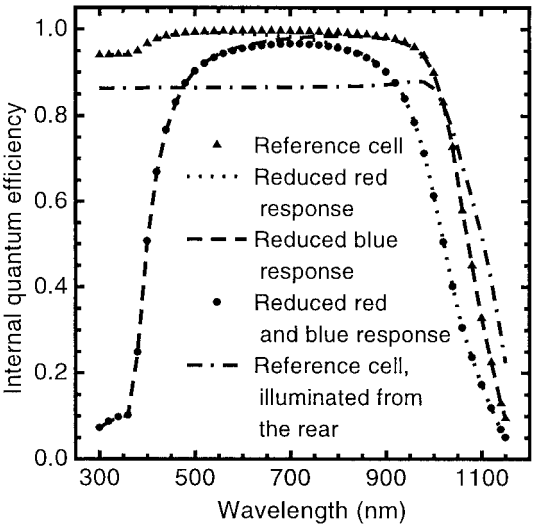

Figure 7. PC-1D calculations of the internal quantum efficiencies of silicon solar cells used for the optimisation of AR coatings ($T = 300$ K)

velocity parameter $S_{0.\mathrm{back}}$ to the thermal limit (10^7 cm s^{-1}). Correspondingly, the cell with the reduced blue response is obtained by setting the front SRV parameter $S_{0.\mathrm{front}}$ to 10^7 cm s^{-1}. In the case of the cell with reduced blue and red response, both SRV parameters are set to 10^7 cm s^{-1}. Also shown in Figure 7 is the IQE of the reference cell for the case of illumination from the rear. This IQE is used for the calculation of J_{SC} of the bifacial version of the reference cell.

According to Equation (2), the optimisation of the optical properties of a particular solar cell or photovoltaic module requires the calculation of the corresponding $A(\lambda)$ within the silicon wafer. This calculation is based on the measured wavelength-dependent refractive indices and extinction coefficients of each layer. As discussed above, the optical properties of RPECVD SiN and porous SiO_2 can be varied significantly by appropriate changes of the processing conditions. Hence, our J_{SC} optimisation also considers RPECVD SiN and porous SiO_2 films whose optical properties have not been measured. These

Copyright © 1999 John Wiley & Sons, Ltd.

Seoul Semiconductor, Exhibit 2001
LGI v. SSC, IPR2019-01154

Table I. Parameters used for the calculation of the *IQE* of the reference solar cell with the device simulation programme PC-1D

Parameter	Numerical value
Cell thickness	350 μm
Temperature	25°C
Diffusion length within the base	810 μm
Specific resistance of the base	1·5 Ωcm, *p*-type
Emitter peak doping	7×10^{19} cm^{-3}, *n*-type
Junction depth	0·4 μm, Erfc
⇒ Emitter sheet resistance	100 Ω/□
$S_{0.\mathrm{front}}$	15,000 cm/s
⇒ Saturation current density of the emitter	$1{\cdot}0 \times 10^{-13}$ A/cm^2
$S_{0.\mathrm{back}}$	60 cm/s
⇒ Saturation current density of the base	$1{\cdot}0 \times 10^{-13}$ A/cm^2

data are obtained by a linear interpolation of the corresponding measurements. The optical parameters of silicon are taken from the literature.[16]

Non-encapsulated monofacial cells

Figure 8 shows the calculated short-circuit current density J_{SC} of the non-encapsulated reference solar cell coated with single-layer (SL), double-layer (DL) and triple-layer (TL) antireflection coatings (ARCs) on the front surface with optimised refractive indices and thicknesses. For comparison, the J_{SC} of the bare cell (25·7 mA cm^{-2}) is included in the plot. The dashed line in Figure 8 is obtained for (hypothetical) AR coatings with negligible extinction coefficients and wavelength-independent refractive indices. It can be seen that an optimised SLARC improves J_{SC} from 25·7 to 36·4 mA cm^{-2}, while a DLARC gives an additional current boost of 2·3 mA cm^{-2}. Compared to a DLARC, a TLARC further improves J_{SC} by 0·6 mA cm^{-2} to 39·2 mA cm^{-2}. The solid line in Figure 8 is obtained for optimised AR coatings consisting of RPECVD SiN and/or porous SiO_2 films. For the calculation of the corresponding data, the measured wavelength dependence of the refractive indices and the extinction coefficients of both materials

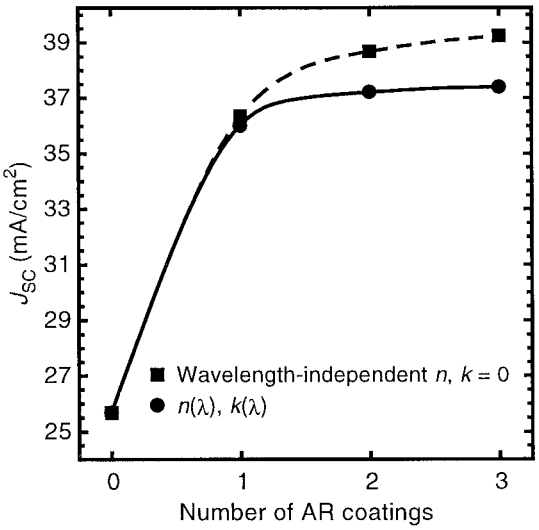

Figure 8. Calculated J_{SC} of non-encapsulated reference solar cells covered with optimised SLARCs, DLARCs and TLARCs. The squares show the (hypothetical) case of zero k and wavelength-independent n. The circles refer to actual AR coatings consisting of porous SiO_2 and RPECVD SiN. The interpolation lines are guides to the eye

Copyright © 1999 John Wiley & Sons, Ltd.

Seoul Semiconductor, Exhibit 2001
LGI v. SSC, IPR2019-01154

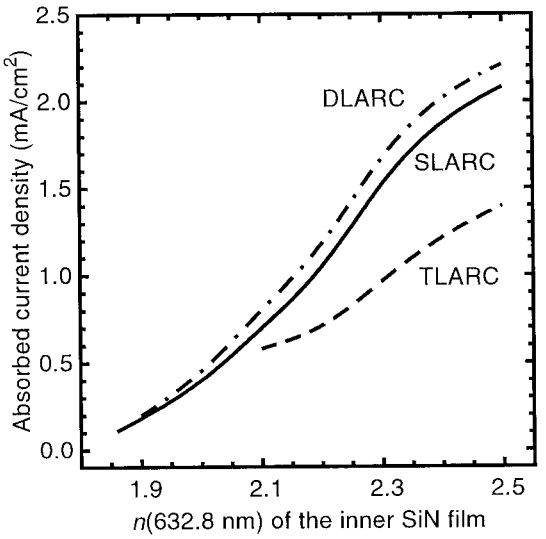

Figure 9. Calculated current density absorbed within optimised SLARCs, DLARCs and TLARCs on non-encapsulated reference solar cells as a function of the refractive index of the inner SiN film at 632·8 nm

are considered by the optimisation procedure. It can be seen that a RPECVD SiN single-layer AR coating provides about the same J_{SC} as a SLARC consisting of the hypothetical non-absorbing material described above. The implementation of a DLARC improves J_{SC} by about 1·2 mA cm^{-2}, which is well below the corresponding increase for the case of absorption-free AR coatings (2·3 mA cm^{-2}). Compared to the DLARC, an optimised TLARC does not further improve J_{SC}.

It should be noted that the reference solar cell (as well as any other monofacial cell simulated in this work) features an excellent back surface reflector consisting of a RPECVD SiN film with $n = 2{\cdot}40$ at 632·8 nm and a 5 μm thick Al film (the optical constants of A1 were taken from Ref. 17). This configuration reflects most of the infrared light that reaches the rear surface back into the cell, improving J_{SC}. For every optimised front-surface AR coating, the thickness of the rear SiN film is simultaneously optimised. However, due to the large thickness of 350 μm of the simulated solar cells, the thickness of the rear SiN film varies only slightly (100 ± 4 nm) for the different optimised front AR coatings.

As mentioned in the Introduction, the surface recombination velocity provided by RPECVD SiN decreases with increasing refractive index. It saturates for n(632·8 nm) $\geqslant 2{\cdot}0$ on the n^+-diffused emitters described in Table I[6] and for $n \geqslant 2{\cdot}4$ on 1·5-Ωcm p-type silicon.[5] The solid line in Figure 9 shows the J_{SC} loss of the reference cell due to absorption within the AR coating as a function of the 632·8-nm refractive index of a thickness-optimised single-layer RPECVD SiN film. The solid line in Figure 10 shows the corresponding J_{SC} loss due to reflection, while Figure 11 shows the combined impact on the J_{SC} of the cell. As can be seen from Figure 11, the J_{SC} of the single-layer AR coated reference solar cell is maximised by RPECVD SiN with a 632·8-nm refractive index of 1·86. This value is too low to ensure an optimum surface passivation. However, also shown in Figures 9–11 is the corresponding behaviour for the case of optimised double-layer AR coatings consisting of porous SiO_2 and RPECVD SiN. It can be seen that J_{SC} is maximal for a refractive index of the SiN film of about 2·1. Additionally, the behaviour of triple-layer AR coatings consisting of two RPECVD SiN films and one porous SiO_2 film is shown in Figures 9–11. As can be seen from Figure 11, a triple-layer AR coating allows the use of a RPECVD SiN film with very large refractive index (up to 2·5) on the silicon surface. This is very advantageous for the emitter properties of MIS inversion-layer cells[18] and the base properties of bifacial cells[19] where a large SiN refractive index is required for optimum surface passivation. On n^+-diffused emitters, however, the optimised DLARC with n(632·8 nm) = 2·10 of the SiN film is sufficient. The reference cell then yields a J_{SC} of 37·2 mA cm^{-2}. This value has to be compared with the ultimate J_{SC} limit of 39·6 mA cm^{-2} of the reference cell for the case of an *ideal* AR coating (i.e. $R = 0$ for all wavelengths, no absorption within the

Copyright © 1999 John Wiley & Sons, Ltd.

Seoul Semiconductor, Exhibit 2001
LGI v. SSC, IPR2019-01154

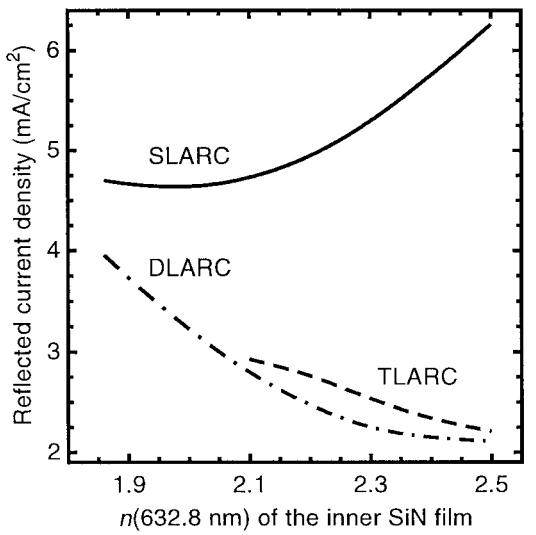

Figure 10. Calculated reflected current density of non-encapsulated reference solar cells covered with optimised SLARCs, DLARCs and TLARCs as a function of the refractive index of the inner SiN film at 632·8 nm

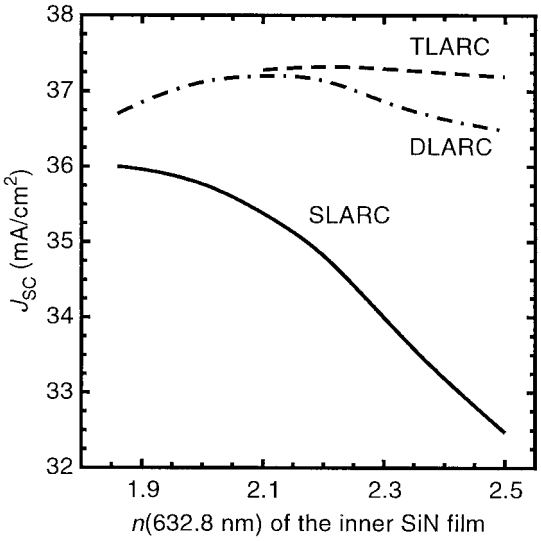

Figure 11. Calculated J_{SC} of non-encapsulated reference solar cells covered by optimised SLARCs, DLARCs and TLARCs as a function of the refractive index of the inner SiN film at 632·8 nm

AR coating). Note that the J_{SC} limit of the reference cell would shift to 40·9 mA cm^{-2} if a perfect light trapping could be assumed.

The thicknesses and the refractive indices of the optimised single-layer, double-layer and triple-layer AR coatings consisting of RPECVD SiN and/or porous SiO_2 are summarised in Table II ($SLARC_{opt}$, $DLARC_{opt}$ and $TLARC_{opt}$, respectively). Because of the positive impact on the surface passivation, the parameters of a TLARC with a fixed refractive index of 2·40 of the SiN film contacting the silicon is included in Table II ($TLARC_{2·4}$). This AR coating gives nearly the same J_{SC} as the optimised $TLARC_{opt}$. Note that the AR coatings $TLARC_{opt}$ and $TLARC_{2·4}$ deviate from the usual quarter-wavelength design. The two SiN layers of each TLARC are much thinner due to their absorption properties. Both SiN layers together have nearly the same optical thickness as the single SiN film in the optimised double-layer AR

Copyright © 1999 John Wiley & Sons, Ltd.

Seoul Semiconductor, Exhibit 2001
LGI v. SSC, IPR2019-01154

Table II. Optimised refractive indices n (measured at a wavelength of 632·8 nm) and thicknesses d of different AR coatings on the non-encapsulated reference solar cell. The refractive index of the SiN layer contacting the silicon solar cell of $TLARC_{2\cdot4}$ was fixed at 2·40 because of surface passivation reasons. Also shown are the parameters of the optically most efficient triple-layer AR coatings $TLARC_{TiO_x}$ and $TLARC_{ZnS}$ consisting of porous SiO_2/TiO_x(or ZnS)/20-nm RPECVD SiN

	n_1 at 632·8 nm	d_1 [nm]	n_2 at 632·8 nm	d_2 [nm]	n_3 at 632·8 nm	d_3 [nm]	J_{SC} [mA/cm^2]
$SLARC_{opt}$	1·86	82	—	—	—	—	36·0
$DLARC_{opt}$	1·30	103	2·10	66	—	—	37·2
$TLARC_{opt}$	1·29	100	1·86	25	2·20	50	37·4
$TLARC_{2\cdot4}$	1·29	104	2·02	47	2·40 (fixed)	27	37·2
$TLARC_{TiO_x}$	1·38	100	2·29	39	2·20	20 (fixed)	37·7
$TLARC_{ZnS}$	1·38	103	2·34	38	2·20	20 (fixed)	38·0

coating, i.e. the single SiN film in the optimised $DLARC_{opt}$ is replaced by two SiN films in the TLARCs. The physical thickness is not increased significantly either and thus the two SiN films of the TLARCs can possibly be deposited as cost-effectively as the single SiN film of the optimised $DLARC_{opt}$, for instance by using a computer controlled RPECVD system which automatically performs the required changes of the gas flow during the SiN deposition. It is also worthwhile to mention that there is no need to use films with refractive indices between 1·46 and 1·85 like silicon oxynitrides, even if they were implemented in the optimisation procedure assuming constant refractive indices and zero extinction coefficients.

As mentioned before, TiO_x and especially ZnS have relatively high refractive indices and moderate extinction coefficients for short wavelengths, but these films do not reduce the SRV at the silicon surface. Therefore, high cell efficiencies can only be obtained with TiO_x or ZnS AR coatings if a thin passivating film of thermally grown SiO_2 or RPECVD SiN (or another suitable material) is fabricated on the silicon surface prior to the deposition of the AR coating. The required minimum thickness for the surface-passivating RPECVD SiN film is around 20 nm.[5] For a fixed SiN thickness of 20 nm, the reference cell produces a J_{SC} of 38·0 mA cm^{-2} for an optimised porous SiO_2/ZnS/RPECVD SiN antireflection coating (see Table II). An optimised porous SiO_2/TiO_x/20-nm RPECVD SiN AR coating yields a J_{SC} of 37·7 mA cm^{-2}. This is slightly below the performance of the corresponding ZnS-based AR coating because of the higher refractive index of ZnS. If the 20 nm thick surface-passivating RPECVD SiN film is replaced by a 20 nm thick SiO_2 film, the short-circuit current densities of the cells with optimised ZnS- or TiO_x-based AR coatings decrease by 0·5 mA cm^{-2}, respectively. This is due to the lower refractive index of thermal SiO_2 compared to RPECVD SiN. If the surface recombination effect on the *IQE* is neglected, then optimised porous SiO_2/TiO_x or porous SiO_2/ZnS DLARCs without surface-passivating layer yield a 0·7 mA cm^{-2} higher J_{SC} than the corresponding AR coating with 20 nm SiO_2 films.

Additional AR coating optimisations based on RPECVD SiN and/or porous SiO_2 films were performed for the cell with reduced red response, the cell with reduced blue response and the cell with reduced red and blue response. As a remarkable result, the optimised single-layer, double-layer and triple-layer AR coatings were found to provide only a negligibly small performance advantage ($\Delta J_{SC} \leqslant 0{\cdot}08$ mA cm^{-2}) over the AR coatings optimised for the reference cell ($SLARC_{opt}$, $DLARC_{opt}$, $TLARC_{opt}$ and $TLARC_{2\cdot4}$ in Table II). Thus, the AR coatings listed in Table II are universally suited for silicon solar cells featuring internal quantum efficiencies between the reference cell and the cell with reduced red and blue response in Figure 7.

Non-encapsulated bifacial cells

Bifacial solar cells have the advantage of utilising light falling onto the back, but they cannot benefit from a back surface reflector. Under consideration of the different *IQE*s for front and back illumination (see Figure 7), we simultaneously optimised AR coatings consisting of RPECVD SiN and porous SiO_2 on the front and back of a bifacial version of the reference cell. Due to surface passivation reasons we chose a

Copyright © 1999 John Wiley & Sons, Ltd.

Seoul Semiconductor, Exhibit 2001
LGI v. SSC, IPR2019-01154

triple-layer AR coating on the non-diffused *p*-type back surface with $n(632{\cdot}8\text{ nm}) = 2{\cdot}40$ of the silicon-contacting SiN film, while a double-layer AR coating was assumed on the front surface. The calculated front-illuminated J_{SC} of the bifacial cell is about 0·6 mA cm^{-2} below the one of the corresponding monofacial cell featuring a back surface reflector. Again, J_{SC} decreases negligibly (for front as well as rear illumination) if the specially optimised DLARC on the front and the TLARC on the back are replaced by the optimised double-layer and triple-layer AR coatings of Table II ($DLARC_{opt}$ and $TLARC_{2{\cdot}4}$, respectively).

Glass-encapsulated monofacial cells

The standard encapsulants in today's photovoltaic modules are EVA or resin, as discussed in the Introduction. In order to demonstrate the optical performance of such a structure, we consider a PV module consisting of the following layer sequence: air, a 2 mm B270 glass plate, a 1 mm EVA layer, a RPECVD SiN film with variable thickness and refractive index, the reference solar cell, a RPECVD SiN film with $n(632{\cdot}8\text{ nm})$ fixed at 2·40 and a 5 μm Al layer. Using the above-mentioned J_{SC} optimisation procedure, the optimal refractive index of the front SiN film and the thicknesses of the front and the rear SiN films are determined. It is found that the optimised EVA module yields a J_{SC} of 34·1 mA cm^{-2}, see Table III. If a (hypothetical) encapsulant is assumed with wavelength-independent refractive index and zero extinction coefficient, the optimum J_{SC} of 35·0 mA cm^{-2} is obtained for a refractive index of 1·52 of the encapsulant. EVA modules with optimised TiO_x or ZnS AR coatings instead of RPECVD SiN yield a J_{SC} of 34·5 mA cm^{-2} or 34·8 mA cm^{-2}, respectively (Table III). J_{SC} reduces by 0·5 mA cm^{-2}, respectively, if a 20-nm thick surface-passivating SiO_2 layer is included.

The air/glass interface of the modules investigated above leads to a wavelength-independent reflection of about 4%. This is equivalent to a J_{SC} loss of about 1·5 mA cm^{-2} in the wavelength range 300–1150 nm. This loss can be reduced to 0·3 (0·1) mA cm^{-2} if an optimised single-layer (double-layer) AR coating consisting of porous SiO_2 is deposited onto the outer surface of the glass cover, see Table IV. These calculations show that it is very worthwhile to investigate if the porous SiO_2 films can be implemented into

Table III. Optimised refractive indices n and thicknesses d of RPECVD SiN, TiO_x and ZnS based ARCs, the latter two with and without surface-passivating SiO_2 layer. The AR-coated solar cell is encapsulated in a photovoltaic module with a 2 mm B270 glass cover and a 1-mm thick EVA layer

	n_1 at 632·8 nm	d_1 [nm]	n_2 at 632·8 nm	d_2 [nm]	J_{SC} [mA/cm^2]
$SLARC_{SiN}$	2·20	67	—	—	34·1
$SLARC_{TiO_x}$	2·29	64	—	—	34·5
$SLARC_{ZnS}$	2·34	63	—	—	34·8
$DLARC_{TiO_x/SiO_2}$	2·29	40	1·46	20 (fixed)	34·0
$DLARC_{ZnS/SiO_2}$	2·34	39	1·46	20 (fixed)	34·3

Table IV. Optimised refractive indices n and thicknesses d of single- and double-layer porous SiO_2 AR coatings on the outer surface of the 2 mm B270 glass cover of a photovoltaic module with 1-mm thick EVA layer

	n_1 at 632·8 nm	d_1 [nm]	n_2 at 632·8 nm	d_2 [nm]	Reflected J_{SC} [mA/cm^2]
Without ARC_{glass}	—	—	—	—	1·5
$SLARC_{glass}$	1·23	127	—	—	0·3
$DLARC_{glass}$	1·13	136	1·35	108	0·1

Copyright © 1999 John Wiley & Sons, Ltd.

Seoul Semiconductor, Exhibit 2001
LGI v. SSC, IPR2019-01154

actual photovoltaic modules. Promising results have already been achieved on glass-covered solar thermal collectors.[20] A novel PV module design exploiting this approach has recently been proposed by us.[21]

Simulations of EVA-encapsulated solar cells featuring reduced red and/or blue response show that, similar to the case of non-encapsulated solar cells, the AR coatings listed in Tables III and IV are universally suited for solar cells featuring internal quantum efficiencies between the reference cell and the cell with deteriorated red and blue response in Figure 7. This follows from the fact that the short-circuit current density decreases by less than 0·02 mA cm^{-2}. It is also worth mentioning that the performance of the EVA module is reduced by 1·3 mA cm^{-2} if the highly transparent B270 crown glass is replaced by a Fe_2O_3-rich soda lime glass. As can be seen from Figure 1, this is due to enhanced light absorption in the near infrared region.

CONCLUSIONS

In this work, numerical fitting of reflection and transmission measurements is used for the determination of the wavelength-dependent refractive indices and extinction coefficients of semitransparent films and substrates. $n(\lambda)$ and $k(\lambda)$ of important materials for silicon solar cell applications are determined, including RPECVD SiN (which is the most efficient low-temperature surface passivation known to date for crystalline silicon), porous SiO_2, MgF_2, TiO_x, ZnS, highly transparent crown glass, Fe_2O_3-rich soda lime glass, EVA and a resin as used in commercial photovoltaic modules. Based on these data, the short-circuit current densities of silicon solar cells covered by single- and multi-layer AR coatings are numerically maximised for glass-encapsulated as well as non-encapsulated operating conditions.

In the case of non-encapsulated silicon solar cells, the optimisation of AR coatings based on porous SiO_2 and RPECVD SiN shows that a double-layer AR coating already gives virtually optimal performance. The SiN film has a refractive index of 2·1, ensuring a good passivation of the n^+-diffused surface of n^+p silicon solar cells. In order to further increase J_{SC} without reducing the surface passivation quality of the AR coating, a porous SiO_2/TiO_x(or ZnS)/RPECVD SiN triple-layer AR coating is required. Compared to the n^+-diffused front surface of n^+p solar cells, the front surface of MIS inversion-layer cells and the non-diffused rear surface of bifacial cells are more sensitive to surface recombination losses. In these cases, the use of AR coatings with an excellent surface passivation is essential for high cell efficiencies. This can be achieved by RPECVD SiN films with very large refractive indices ($n \geqslant 2{\cdot}40$). Considering the strong absorption of short-wavelength light in these films, an optimised triple-layer AR coating consisting of porous SiO_2 and RPECVD SiN with $n(632{\cdot}8\text{ nm}) = 2{\cdot}40$ of the SiN film contacting the silicon is determined. As a remarkable result, all these optimised AR coatings are universally suited for non-encapsulated silicon solar cells, regardless of the internal quantum efficiency of the cells.

Solar cells encapsulated in today's photovoltaic modules have a reduced J_{SC} compared to the non-encapsulated case due to the high extinction coefficients at short wavelengths of embedding materials like EVA or resin and due to reflection at the air/glass interface. The latter can be effectively reduced by single- or double-layer porous SiO_2 AR coatings on the outer surface of the glass cover of the PV module. Furthermore, as in the non-encapsulated case, the calculations show that the optimised AR coatings on the solar cells are universally suited for encapsulated conditions, regardless of the internal quantum efficiency of the cells.

Acknowledgements

The authors wish to thank D. Pavic (then at ISFH) for the processing of the porous SiO_2 films and his introduction to the reflection and transmission measurement system. We are grateful to U. Schubert of the Fraunhofer Institute for Solar Energy Systems in Freiburg, Germany, for the preparation of the MgF_2, TiO_x and ZnS films and to H. Gochermann (Gochermann Solar Technology, Holm, Germany) for valuable discussions. The ISFH is supported by the state of Niedersachsen and is a member of the German FORSCHUNGSVERBUND SONNENENERGIE.

Copyright © 1999 John Wiley & Sons, Ltd.

Seoul Semiconductor, Exhibit 2001
LGI v. SSC, IPR2019-01154

APPENDIX

A parameterisation of the optical constants of the examined materials is given in order to make the measured data easily accessible. In the considered wavelength region from 300 to 1150 nm, the wavelength-dependent refractive index $n(\lambda)$ and extinction coefficient $k(\lambda)$ of RPECVD SiN, MgF_2, TiO_x and ZnS are well described by the dispersion relations of amorphous materials proposed by Forouhi and Bloomer:[22]

$$n(\lambda) = D + \frac{B_0 X + C_0}{X^2 - BX + C}, \tag{A1}$$

$$k(\lambda) = \frac{A(X - E)^2}{X^2 - BX + C}, \tag{A2}$$

with

$$B_0 = \frac{A}{Q}\left(-\frac{B^2}{2} + EB - E^2 + C\right),$$

$$C_0 = \frac{A}{Q}\left((E^2 + C)\frac{B}{2} - 2EC\right),$$

$$Q = \frac{1}{2}(4C - B^2)^{1/2},$$

and

$$X = \frac{1239{\cdot}85}{\lambda},$$

with λ in nm. The values of the five fitted parameters A–E are listed in Table V.

The wavelength-dependent refractive index of B270 crown glass, soda lime glass, EVA and the examined resin are nearly identical and can be described by the first-order polynom

$$n(\lambda) = 1{\cdot}56 - 5{\cdot}75 \times 10^{-5}\lambda,$$

with λ in nm.

Table V. Fitted parameters describing the dispersion relation of the refractive indices and extinction coefficients of five different RPECVD SiN films, MgF_2, TiO_x and ZnS according to Equations (A1) and (A2)

	A	B	C	D	E
RPECVD SiN #1	$9{\cdot}955 \times 10^{-2}$	11·30	37·92	1·649	1·295
RPECVD SiN #2	$7{\cdot}995 \times 10^{-2}$	9·655	25·12	1·743	1·112
RPECVD SiN #3	$2{\cdot}082 \times 10^{-1}$	8·001	18·76	1·766	1·334
RPECVD SiN #4	$4{\cdot}039 \times 10^{-1}$	7·460	17·20	1·618	1·206
RPECVD SiN #5	$4{\cdot}595 \times 10^{-1}$	6·894	14·54	1·728	1·168
MgF_2	$1{\cdot}461 \times 10^{-9}$	8·317	17·31	1·273	−1·203
TiO_x	$7{\cdot}059 \times 10^{-2}$	8·883	19·90	1·944	2·239
ZnS	$8{\cdot}395 \times 10^{-2}$	8·661	19·32	2·119	2·162

Copyright © 1999 John Wiley & Sons, Ltd.

Seoul Semiconductor, Exhibit 2001
LGI v. SSC, IPR2019-01154

Table VI. Fitted parameters describing the dispersion relation of the extinction coefficients of B270 crown glass, EVA and the examined resin according to Equation (A3)

	λ_C	W	A
B270 glass	249·1	56·70	$6{\cdot}07 \times 10^{-3}$
EVA	277·1	77·11	$1{\cdot}195 \times 10^{-1}$
Resin	296·8	43·41	1·378

The dispersion relation of the extinction coefficient of B270 crown glass, EVA and the resin is approximated by the Gaussian function

$$k(\lambda) = \frac{A}{W\sqrt{\pi/2}} \exp\left(-2\frac{(\lambda - \lambda_C)^2}{W^2}\right), \tag{A3}$$

with the fitted parameters λ_C, W, and A (see Table VI). $k(\lambda)$ of the soda lime glass has to be described with the sum of two Gaussian peaks

$$k(\lambda) = \frac{1{\cdot}36 \times 10^{-3}}{53{\cdot}37\sqrt{\pi/2}} \exp\left(-2\frac{(\lambda - 285{\cdot}5)^2}{2848}\right) + \frac{2{\cdot}03 \times 10^{-3}}{507{\cdot}1\sqrt{\pi/2}} \exp\left(-2\frac{(\lambda - 1106)^2}{2{\cdot}572 \times 10^5}\right),$$

where λ is in units of mm. Note that Equations (A1) and (A2) are not suited for the parameterisation of the optical constants of the latter materials, as their absorption properties are determined by small amounts of contaminants like Fe_2O_3 in soda lime glass and not by the fundamental absorption of amorphous materials.

REFERENCES

1. J. Zhao and M. A. Green, 'Optimized antireflection coatings for high-efficiency silicon solar cells', *IEEE Trans. Electron Devices*, **38**, 1925 (1991).
2. D. Pavic and M. Mack, 'Reflexionsmindernde Beschichtungen für die Solartechnik', *Proc. 7th Symposium Thermische Solarenergie*, Ostbayerisches Technologie Transfer Institut, Regensburg (in German) p. 256, 1997.
3. Z. Chen, P. Sana, J. Salami and A. Rohatgi, 'A novel and effective PECVD SiO_2/SiN antireflection coating for Si solar cells', *IEEE Trans. Electron Devices*, **40**, 1161 (1993).
4. T. Lauinger, J. Schmidt, A. G. Aberle and R. Hezel, 'Record low surface recombination velocities on 1 Ωcm *p*-silicon using remote plasma silicon nitride passivation', *Appl. Phys. Lett.*, **68**, 1232 (1996).
5. T. Lauinger, A. G. Aberle and R. Hezel, 'Comparison of direct and remote PECVD silicon nitride films for low-temperature surface passivation of *p*-type crystalline silicon', *Proc. 14th European Photovoltaic Solar Energy Conference*, p. 853, Stephens, Bedford, 1997.
6. B. Lenkeit, T. Lauinger, A. G. Aberle and R. Hezel, 'Comparison of remote versus direct PECVD silicon nitride passivation of phosphorus-diffused emitters of silicon solar cells', *Proc. 2nd World Conference on Photovoltaic Solar Energy Conversion*, (in press) Stephens, Bedford, 1998.
7. A. G. Aberle, T. Lauinger and R. Hezel, 'Remote PECVD silicon nitride — a key technology for the crystalline silicon PV industry of the 21st century?', *Proc. 14th European Photovoltaic Solar Energy Conference*, p. 684, Stephens, Bedford, 1997.
8. B. Harbecke, 'Coherent and incoherent reflection and transmission of multilayer structures', *Appl. Phys. B*, **39**, 165 (1986).
9. W. H. Press, B. P. Flannery, S. A. Teukolsky and W. T. Vetterling, *Numerical Recipes in C*, p. 305, Cambridge University Press, Cambridge, 1988.
10. J. A. Duffie and W. A. Beckman, *Solar Engineering of Thermal Processes*, p. 231, Wiley, New York, 1991.
11. Z. Knittl, *Optics of Thin Films*, p. 474, Wiley, London, 1976.

Copyright © 1999 John Wiley & Sons, Ltd.

Seoul Semiconductor, Exhibit 2001
LGI v. SSC, IPR2019-01154

12. R. Brendel, R. Ziegler and R. Hezel, 'A method for the measurement of thin film optical constants with a spectral photometer from 230 nm to 850 nm and its application to plasma silicon (oxy)nitride', *Thin Solid Films*, **200**, 219 (1991).
13. P. Doshi, G. E. Jellison and A. Rohatgi, 'Characterisation and optimisation of absorbing plasma-enhanced chemical vapour deposited antireflection coatings for silicon photovoltaics', *Applied Optics*, **36**, 7826 (1997).
14. M. A. Green and M. Keevers, 'Optical properties of intrinsic silicon at 300 K', *Progress in Photovoltaics*, **3**, 189 (1995).
15. P. A. Basore, 'PC-1D version 3: Improved speed and convergence', *Proc. 22nd IEEE Photovoltaic Specialists Conference*, p. 299, IEEE, New York, 1991.
16. M. A. Green, *Silicon Solar Cells*, Centre for Photovoltaic Devices and Systems, Sydney, p. 333, 1995.
17. E. D. Palik, *Handbook of Optical Constants of Solids*, p. 400, Academic Press, Boston, 1985.
18. M. Grauvogl, A. G. Aberle and R. Hezel, '17·1% efficient metal-insulator-semiconductor inversion layer silicon solar cells using truncated pyramids', *Appl. Phys. Lett.*, **69**, 1462 (1996).
19. A. Hübner, A. G. Aberle and R. Hezel, 'Novel cost-effective bifacial silicon solar cells with 19·4% front and 18·1% rear efficiency', *Appl. Phys. Lett.*, **70**, 1008 (1997).
20. A. Gombert and M. Rommel, 'Antireflexbeschichtungen für thermische Solarsysteme', *Proc. 7th Symposium Thermische Solarenergie*, Ostbayerisches Technologie Transfer Institut, Regensburg (in German) p. 251, 1997.
21. H. Nagel, A. Metz, A. A. Aberle and R. Hezel, 'Photovoltaic module with enhanced optical performance', *Proc. 2nd World Conference on Photovoltaic Solar Energy Conversion*, (in press) Stephens, Bedford, 1998.
22. A. R. Forouhi and I. Bloomer, 'Optical dispersion relations for amorphous semiconductors and amorphous dielectrics', *Physical Review B*, **34**, 7018 (1986).

Copyright © 1999 John Wiley & Sons, Ltd.

Seoul Semiconductor, Exhibit 2001
LGI v. SSC, IPR2019-01154

APPENDIX N

Thin Solid Films 519 (2010) 1325–1333

Contents lists available at ScienceDirect

Thin Solid Films

journal homepage: www.elsevier.com/locate/tsf

Optical and structural properties of silicon oxynitride deposited by plasma enhanced chemical vapor deposition

J. Dupuis [a,*], E. Fourmond [a], D. Ballutaud [b], N. Bererd [c,d], M. Lemiti [a]

[a] Institut des Nanotechnologies de Lyon, UMR 5270, INSA-Lyon, 7 avenue Jean Capelle, Bât. Blaise Pascal, 69621 Villeurbanne Cedex, France
[b] Groupe d'Etude de la Matière Condensée, UMR 8635, CNRS, 1 place Aristide Briand, 92195 Meudon Cedex, France
[c] Université de Lyon, Université Claude Bernard Lyon 1(UCBL), CNRS, Institut de Physique Nucléaire de Lyon, 4 rue Enrico Fermi, Bât Paul Dirac, 69622 Villeurbanne Cedex, France
[d] Institut Universitaire Technologique (IUT) A de Lyon; Département de chimie, UCBL; 43, boulevard du 11 novembre 1918; 69622 Villeurbanne cedex; France

ARTICLE INFO

Article history:
Received 2 July 2009
Received in revised form 17 September 2010
Accepted 20 September 2010
Available online 29 September 2010

Keywords:
SiON
XPS
FTIR
ERDA
Surface passivation
Solar cells

ABSTRACT

We present an overview of the properties of silicon oxynitride material (SiON) deposited by plasma enhanced chemical vapor deposition (PECVD) for photovoltaic applications. SiON films were deposited using silane (SiH_4), ammonia (NH_3) and nitrogen protoxide (N_2O) as precursor gases in a low frequency PECVD. Varying the gas flow mixture leads to a whole range of SiON layers starting from the silicon oxide to the silicon nitride with unique stoichiometries and properties. Thanks to spectroscopic ellipsometry measurements we have confirmed the suitability of SiON for antireflection coating layers due to the range of the refractive indexes attainable. SiON structure was analyzed by X-ray photo-electron spectroscopy. We have thus highlighted the critical role of oxygen behavior on the SiON network and the progressive replacement of nitrogen by oxygen atoms when the oxygen precursor increases. The type of chemical bonds present in SiON layers was also investigated by infrared spectroscopy. The SiON layers also contain a non-negligible amount of hydrogen which might be useful for passivation applications. The behavior of hydrogen content was thus analyzed by elastic recoil decay analysis and desorption characterization. A typical rapid thermal annealing was performed on the SiON samples in order to simulate the solar cells contact annealing and to investigate its impact on the dielectric film properties. It was found that hydrogen becomes weakly bonded to the films and strongly decreases in quantity with the annealing. The surface passivation effect is presented in the last part of this paper. The trend before and after a rapid thermal annealing showed opposite results which could be explained by the high porosity of the layers and the formation of Si–O bonds.

© 2010 Elsevier B.V. All rights reserved.

1. Introduction

Silicon nitride (SiN) and silicon oxynitride (SiON) are widely used in the microelectronic field as in Si-based large-scale integration circuit technology or in optoelectronic devices. In the photovoltaic field, the refractive index of the amorphous hydrogenated form of SiN (SiN_x:H) was found to be ideal as it causes very low absorption in the solar spectrum range and excellent passivation properties on the silicon surface and within the silicon bulk in the case of multi-crystalline material [1]. For that reason, in the previous decade, silicon nitride has become a standard to make the front antireflection coating of industrial solar cells. Plasma enhanced chemical vapor deposition process (PECVD) is currently one of the preferred deposition methods for the SiN films due to a lower thermal budget than the other CVD processes and a high amount of hydrogen in the layer.

At the present time, the SiON stays a suitable material for opto-electronic devices and integrated circuits such as waveguides or thin-film transistors [2–4]. But until recently, this material was not a serious candidate to compete with SiN for photovoltaic applications.

The situation might yet change. The amorphous hydrogenated form of the SiON dielectric (SiO_xN_y:H) presents some similar aspects to SiN: it can be deposited at low temperature by PECVD, it exhibits low absorbance and an adjustable refractive index below 1.5 and up to 3.0 [5,6] by changing the precursor gas flow ratio during the deposition process. Thus, these properties can be suitable for photo-voltaic industry especially for the antireflection multi-layers coatings by adjusting carefully the optical index and the thickness of the film [7]. Multi antireflection layers can increase the short circuit current more than two percent for cell under air which may be used for high efficiency or specific module technology [8]. With the use of SiON, multi antireflection layer can be performed in the same reactor at relatively low temperature (≤400 °C). The passivation effect of SiON is also under investigation to look for an alternative to the actual aluminium back surface field, which is responsible for high constraints on the back side of the thin silicon solar cells. From this point

* Corresponding author. Tel.: +33 681 108 156; fax: +33 478 604 763.
E-mail address: dupuis@apollonsolar.com (J. Dupuis).

0040-6090/$ – see front matter © 2010 Elsevier B.V. All rights reserved.
doi:10.1016/j.tsf.2010.09.036

of view, a layer of SiN can be used but its passivation effect could be limited due to its high positive fixed charge density [7]. On the other hand, stack structures consisting of SiN and/or silicon oxide layers (abbreviated SiO afterwards) are a promising way to optimize the rear surface passivation without the use of high temperature process [9–11]. Finally, the low SiON refractive index makes this layer suitable to act as a rear surface reflector for infrared photons which are less absorbed in the silicon.

Although a lot of studies have been done on the SiON material deposited by PECVD, the microelectronics and photovoltaics objectives are not completely similar. For that reason, the optimization of the SiON films will be different in both cases.

This work aims to study the optical, structural and electrical properties of SiON deposited by PECVD on silicon substrates for solar cells applications. Firstly, the optical properties of the layers deposited in our PECVD reactor will be presented. Secondly, we will investigate the structure of these layers by X-ray photo-electron spectroscopy, Fourier-transform infrared spectroscopy and elastic recoil decay analysis measurements with a special attention to the hydrogen content of our films. Finally, we will study the passivation properties using minority carrier lifetime measurements, in order to show whether the PECVD SiON is a suitable material for passivation purposes.

2. Experimental details

SiON layers were deposited with a mixture of ammonia (NH_3), pure silane (SiH_4) and nitrous oxide (N_2O) as precursor gases in a semi-industrial Low Frequency PECVD reactor (LF-PECVD). The reactor was developed by SEMCO-Engineering and presents a vertical configuration chamber (Fig. 1).

We chose to keep the silane gas flow constant at 25 sccm, while varying both NH_3 and N_2O gas flows in order to keep the total gas flow constant. Different SiON stoichiometries were obtained by varying the "Ox" ratio, defined as:

$$Ox = \frac{N_2O}{N_2O + NH_3}$$

The Ox ratio is also an indicator of the oxygen and nitrogen content of the SiON layers: Ox = 0.00 corresponds to a SiN layer deposition, whereas Ox = 1.00 gives a SiO layer. This ratio will be used in the following as the main indicator to identify our samples.

A total of five different SiON layers, including a SiN and a SiO samples, were elaborated on <100> float zone 2 in. p-type silicon wafers with both sides polished and a resistivity of 4–7 Ω cm. The gas flows parameters for each sample are summarized in Table 1.

Table 1
Gas precursors flow for the five samples used in this study.

Sample	SiH_4 flow (sccm)	NH_3 flow (sccm)	N_2O flow (sccm)
Ox = 0.00	25	775	0
Ox = 0.20	25	620	155
Ox = 0.58	25	323	452
Ox = 0.87	25	100	675
Ox = 1.00	25	0	775

A spectroscopic ellipsometer (Jobin Yvon UVISEL) was used to obtain the optical indexes of the SiON layers, using the Tauc–Lorentz model [12]. The composition and the structure of the SiON films were analyzed by XPS (X-ray Photo-electron Spectroscopy) and ERDA (Elastic Recoil Detection Analysis) characterizations. In both cases, the measurements were made deep enough in the layers to avoid carbon or oxygen outside contaminations.

The XPS measurements were carried out in a VG Esclalab 220iXL system, with a base pressure of $6.7 \cdot 10^{-8}$ Pa, and using an AlK source (1486.6 eV) X-ray monochromatized radiation. The energy measurements were made with a Thermo Electron hemispheric analyzer in transmission mode. The spectra were obtained with a detector using six channeltrons put in series. The pass electron energy was 20 eV with a 0.1 eV pitch. The spectra resolution is 0.3 eV. The samples surface were etched using an Ar beam of 3 keV with a current density of 4 μA/mm^2 applied during 1 min. The energy levels of XPS were calibrated with Au single crystal. The spectra were processed using the VG Eclipse Datasystem. The background contribution was included in the fitting process, using the Shirley method [13].

The ERDA characterizations were performed on the 4 MV Van de Graaff accelerator of the Nuclear Physic Institute of Lyon using 1.7 MeV kinetics energy alpha particles.

To study the hydrogen bonding environment we have used infrared transmission measurements. We have operated a Fourier-Transform infrared spectrometer (FTS60 A, Bio-Rad Inc.) associated with a Deuterated Triglycine Sulfate detector operating in the spectrum range of 1.6 to 20 μm to characterize the SiON samples.

The loss of hydrogen in the SiON layers due to thermal treatment has also been investigated in more details with Temperature Programmed Desorption (TPD) measurements. The characterization process consists to put the sample under vacuum and to apply a slow temperature ramp. The quantity of hydrogen that exodiffuses

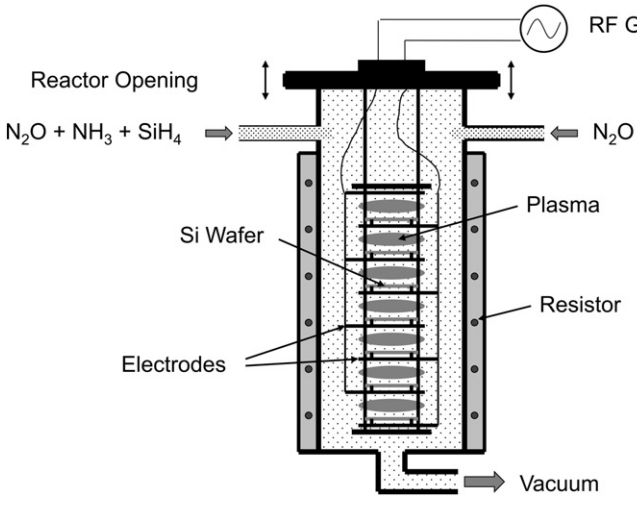

PECVD Parameters	
Number of Wafers	15 (150x150 mm²)
Frequency	440 kHz
Deposition Temperature	370 °C
Pressure	200 Pa
Power	0.26 W.cm^{-2}
Gas Total Flow	800 sccm

Fig. 1. Diagram of the LF-PECVD reactor. The table on the right summarizes the parameters for the deposition.

Seoul Semiconductor, Exhibit 2001
LGI v. SSC, IPR2019-01154

from the layer under such a treatment is then measured by mass spectrometry.

Finally, we have studied the surface passivation properties of our layers by measuring the minority carrier lifetime (MCL), using photoconductance decay measurements by a WCT-100 Photoconductance Tool from Sinton Consulting [14]. SiON layers of 70 nm have been deposited on both sides of float-zone polished 1–10 Ω cm silicon wafers, n-type and p-type (≤100≥ oriented). The high quality of the silicon wafer implies that the effective lifetime measured depends essentially on the surfaces recombination velocity, since the bulk minority carrier lifetime is superior to 3 ms in this case.

3. Optical properties

The refractive indexes and the thicknesses results are summarized in the Table 2. The refractive index incertitude is ±0.02 and the thickness is ±2%. The values are in agreement with the literature [15–18]. As previously discussed [6], the absorption coefficient k remains lower than 10^{-3} for wavelengths above 300 nm. For that reason, front solar cells applications as antireflection coatings are possible.

The increase of the Ox ratio, and consequently the N_2O flow, entails lower refractive indexes. According to Mattson et al. [16], the refractive index is controlled by the oxygen specific volume, in other words by the Si–O electron density bonds. The replacement of the nitrogen atoms by the oxygen atoms induces a slight increase of the bond angle of the Si–O–Si bridges, and results in a lesser Si–O electron density, which decreases the refractive index. The refractive index of the Ox = 1.00 layer is still above the value observed for SiO_2, since the layer has not the same stoechiometry and contains hydrogen, as it will be shown in the following.

4. Structural properties

Most of the XPS results has been already published in a previous study [6]. In this section, we will combine the XPS and the ERDA results to establish the complete stoichiometry of the dielectrics layers.

4.1. Atomic composition

The SiON chemical compositions are plotted on Fig. 2. The incertitude was taken to ±2% for the ERDA results, according to the approximate density of the layers, and to ±4% for XPS results because of some variations in the composition depending on the depth of the analysis within the layer.

The main change in the composition from Ox = 0 to Ox = 1 comes from the oxygen and the nitrogen contents. As expected, a higher N_2O flow during the process leads to an increase in the oxygen incorporation within the layer. Moreover the plot highlights the fact that the relative oxygen content is almost opposed to the nitrogen one, while silicon and hydrogen contents do not vary notably. This trend suggests a replacement of the nitrogen atoms by the oxygen atoms during the increase of the Ox ratio. This replacement is partly due to the higher oxygen precursor concentration during the deposition process, but also to a more thermodynamic stability of the Si–O bond (4.7 eV) compared to the Si–N bond (3.7 eV) [19]. This

Table 2
Summary of the refractive indexes and thicknesses of the five samples studied.

Sample	Refractive index at 633 nm	Thickness (nm)
Ox = 0.00	1.85	302
Ox = 0.20	1.77	225
Ox = 0.58	1.64	195
Ox = 0.87	1.57	159
Ox = 1.00	1.54	152

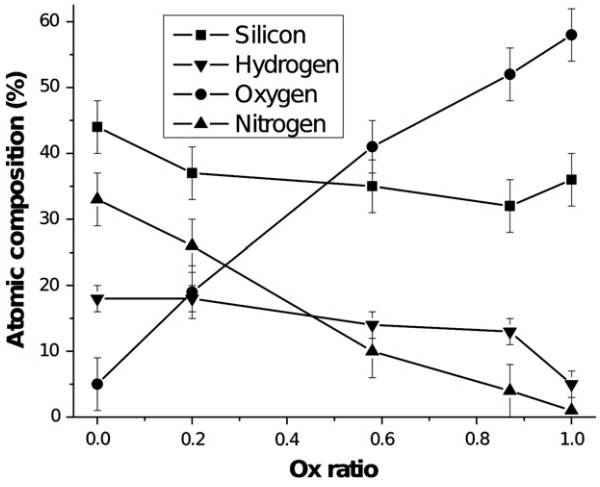

Fig. 2. Atomic composition of the five studied SiON samples. Lines are guide for the eye.

tendency has been previously observed for SiON layers deposited by PECVD with no ammonia in the precursor gases [15,20].

The amount of hydrogen within the layers is in accordance with other authors [15,18] and does not vary significantly between the samples (13%–18%), except for the SiO layer (4%). This notable drop of concentration can be explained by the low hydrogen content of the precursor's gases, since no ammonia is used in that case. Naskar noticed the same phenomenon for SiON samples based on N_2O and SiH_4 when the flow of SiH_4 becomes low [15].

4.2. XPS peak decomposition

The XPS analysis does not only give the atomic composition of a material but brings also information about the bonding environments within the layer.

Although our materials are amorphous, non-stoichiometric and contain a lot of hydrogen, a microscopic order is always observed within the layer. Two models are commonly used to describe this order: the random mixture model (RMM), and the random bounding model (RBM) [21]. Both models are based on the silicon-centered tetrahedrons with in-plane triply coordinated nitrogen as bonding structures. For the RMM, the bonding structure of the SiON consists of a random mixture of silicon, nitrogen and oxygen, where stable phases like Si_3N_4 and SiO_2 prevail. In the RBM, the structure is controlled statistically by the nearest nitrogen and oxygen atoms bonded randomly to the silicon tetrahedrons.

4.2.1. Silicon 2p electron configuration peaks

The 2p electron configuration of the silicon has been analyzed to investigate the degree of organization of the SiON matrix, and to study its change with the progressive replacement of nitrogen by oxygen atoms. The associated XPS peak is located near an electron binding energy of 100 eV. The peaks and the Gaussian fits for the five samples are presented on Fig. 3 and Table 3.

A shift occurs when the oxygen concentration increases in the layer. This shift is particularly obvious when the SiN film and the SiON films are compared. Usually, a shift in the electron binding energy can be attributed to a charge transfer caused by the atoms electronegativity [22]. The electronegativities of silicon, hydrogen, nitrogen and oxygen are respectively 1.74, 2.20, 3.07 and 3.50, considering the Allred and Rochow scale [23]. Thus, the Si–O and Si–N bonds have both a strong ionic behavior and consequently, the shift can be mainly attributed to the energy difference between these two bonds.

Every peak exhibits a nearly-Gaussian profile, independently of the stoichiometry. This tends to prove that the film structure is dominated by a single amorphous phase as suggested by the RBM. But

Seoul Semiconductor, Exhibit 2001
LGI v. SSC, IPR2019-01154

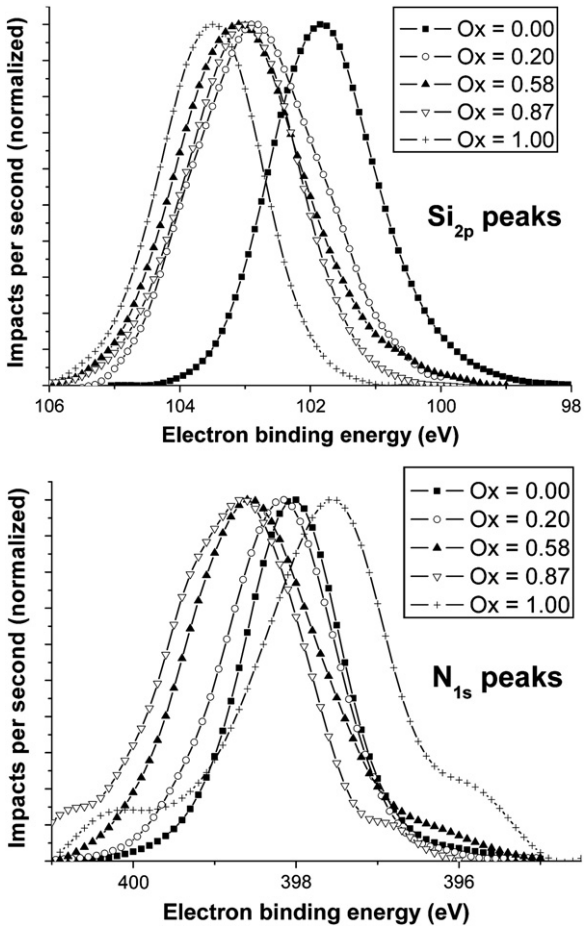

Fig. 3. Normalized XPS peaks of the silicon (for the 2p electron configuration) and the nitrogen (for the 1s electronic configuration) in the five SiON studied. The shoulders on the SiO N(1s) peak are due to the signal noise.

the change of the full width at half maximum (FWHM) between the samples reveals some dispersions on the bond frequencies, and thus points out structural disorders and different local bonding environments [24]. This indicates that the layer could contain some local specific environments within the matrix (like for instance the silicon nanocrystals for silicon-rich SiN as reported by [25]), or a more various bonding environment due to oxygen incorporation.

To analyze the cause of the shift and the FWHM variation, XPS peaks are decomposed according to the reference data from [7,21] and [22]. The Table 4 presents the results of the decomposition for the five samples. The uncertainties on the peak contributions are ±3%. Note that we did not choose to introduce hydrogen environment in the database because it would have involved too many possible chemical species with similar electron binding energy. The hydrogen will be analyzed further by the decomposition of the XPS nitrogen 1s peak configuration.

Table 3
Silicon 2p peaks position and FWHM results for a Gaussian fit of the five samples studied.

Sample	Position (eV)	FWHM (eV)
Ox = 0.00	101.9	1.92
Ox = 0.20	102.9	2.38
Ox = 0.58	103.1	2.25
Ox = 0.87	103.0	2.01
Ox = 1.00	103.5	1.82

Table 4
XPS Si2p peaks decomposition. The table gives the contribution of each species to the experimental peak with their relative FWHM. The energy position of the chemical species came from [7,21] and [22].

Sample	Peak contribution (%) (FWHM (eV))				
	Si_x–Si–N_y	Si–N_4	O_x–Si–N_y	Si–O_4	Peak energy position
Ox = 0.00	25 (1.57)	73 (1.41)	–	–	**Si_x-Si–N_y** : 101.0 eV
Ox = 0.20	6 (1.31)	32 (1.18)	27 (0.94)	39 (1.26)	**Si–N_4** : 102.0 eV
Ox = 0.58	3 (1.58)	12 (1.92)	43 (1.55)	42 (1.57)	**O_x–Si–N_y** : 102.8 eV
Ox = 0.87	–	6 (1.60)	56 (1.40)	38 (1.56)	**Si–O_4** : 103.6 eV
Ox = 1.00	–	–	8 (1.01)	89 (1.48)	

The decomposition of the SiN sample, presented in Fig. 4, is in accordance with previous work [7]. The layer is however richer in silicon than the reference silicon nitride Si_3N_4 (The N/Si ratio is 0.75 compared to 1.33). The silicon bonding environment thus reveals a high contribution of the Si–N_4 species (Si_3N_4) with a silicon-rich contribution.

Unsurprisingly, the bonding environment tends to become oxygen-rich while increasing the Ox ratio. This point is evident on the decomposition of the Si(2p) global peak, with the disappearance of the species based on nitrogen. More interesting is the high contribution of the Si–O_4 species related to SiO_2 right from the nitrogen-rich SiON (Ox = 0.20): nearly 40% of the peak decomposition is associated with Si–O_4 although the layer contains only 20% of oxygen (Fig. 2). Besides, as suggested by the high FWHM, the bonding environment is more varied and four contributions are needed to decompose correctly the richer nitrogen SiON films (Ox = 0.20 and 0.58) as shown in the Fig. 4. The contribution of the Si–O_4 species does not vary for the three intermediate SiON: the decrease of the Si–N_4 is counter-balanced by the increase of the O_x–Si–N_y species.

The strong change in the matrix with the incorporation of oxygen is probably due to its high reactivity with the silicon. As it was already mentioned, this reaction is thermodynamically preferred to any others. This may explain the high contribution of the oxygen-based environment despite the relatively low oxygen content (near 20% on Fig. 2). The disappearance of the nitrogen environment when Ox increases is slow and follows the decrease of the atomic nitrogen contribution in the film (Fig. 2), as Table 4 and Fig. 4 tend to prove.

4.2.2. Nitrogen 1s electron configuration peaks

Contrary to silicon, N–O bonds are not thermodynamically privileged compared to N–H or N–Si (2.1 eV against 4.0 and 3.7 eV respectively [7,19]). Thus, to analyze the hydrogen content through the study of the nitrogen peak N(1s) is easier than with the Si(2p) peak.

Unfortunately, the nitrogen composition varies significantly with the Ox ratio and the decomposition becomes harder for the nitrogen-poor films. Thus, we have chosen to focus on the general trend of the peaks.

As for the silicon, the nitrogen peaks seem to be Gaussian (Fig. 3). The nitrogen environment is probably also dominated by a single amorphous phase. A shift of the N(1s) peak to higher binding energy and a variation of the FWHM are also visible (Table 5). The larger FWHM obtained when the Ox ratio increases is probably caused by some more various chemical environments with the oxygen complex. The reason of the shift could be a consequence of the oxygen content increase. However, since N–O bonding is non-thermodynamically privileged, hydrogen atoms may also play a role due to their electronegativity. This hypothesis is strengthened by the behavior observed on the SiO sample: a strong shift of the N(1s) peak occurs to lower energy for this layer although oxygen was present in high concentration. But contrary to the oxygen, the hydrogen concentration fall steeply between the SiON (Ox = 0.87) and the SiO sample. Thus, the disappearance of the hydrogen could explain the shift of

Seoul Semiconductor, Exhibit 2001
LGI v. SSC, IPR2019-01154

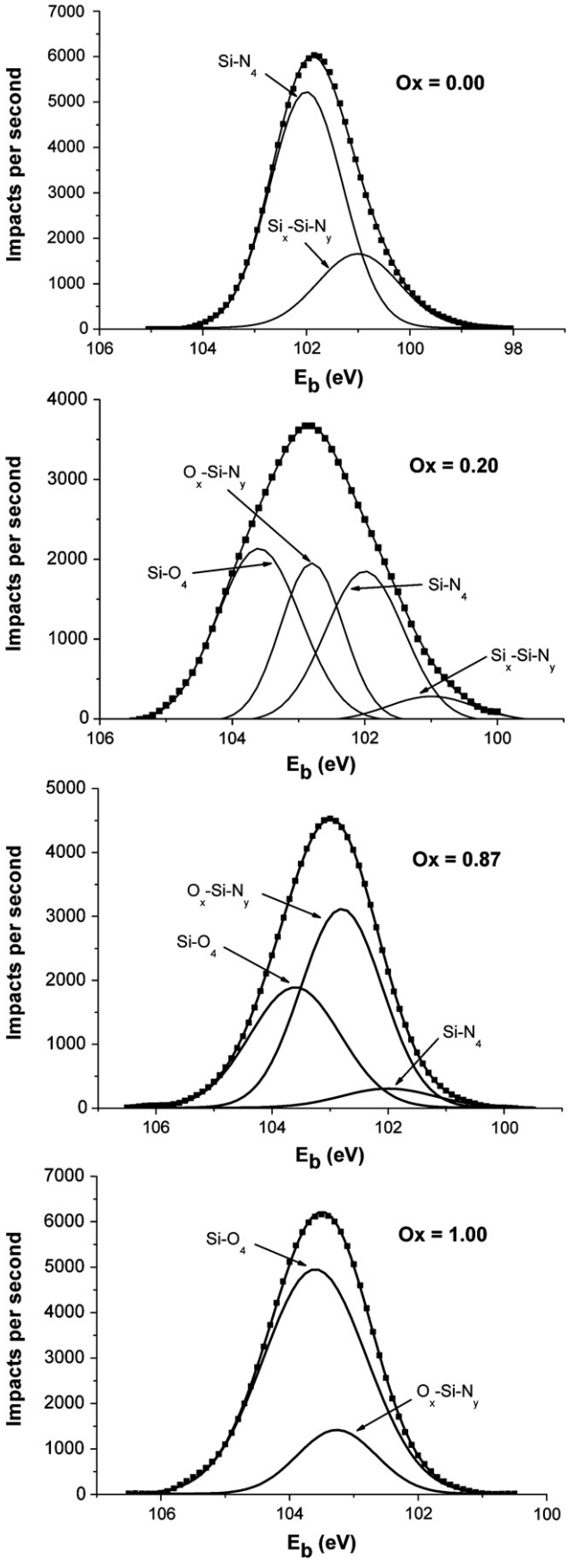

Fig. 4. XPS silicon 2p peak of four SiN films.

Table 5
Nitrogen 1s peaks position and FWHM results for a Gaussian fit of the five samples studied.

Sample	Position (eV)	FWHM (eV)
Ox = 0.00	398.0	1.23
Ox = 0.20	398.2	1.40
Ox = 0.58	398.5	1.66
Ox = 0.87	398.8	1.69
Ox = 1.00	397.6	1.30

the N(1s) peak. Note that the FWHM reduction for the Ox = 1.00 sample suggests a more uniform bonding environment, but the signal of the nitrogen peak was too noisy to analyse the N(1s) peak unambiguously. The decomposition of the N(1s) peaks confirms that the evolution of the matrix is driven by a progressive replacement of the nitrogen atoms by the oxygen atoms. Moreover, the hydrogen is probably localised preferentially near the nitrogen atoms, as suggested by the shift of the N(1s) peaks.

4.3. Infrared spectroscopy measurements

In the photovoltaic field, the hydrogen content of the film is very important for the passivation point of view [26]. It is thus necessary to investigate in more details how the hydrogen is bonded within the films, and how it reacts when the layers are annealed during the metallic front contacts formation at the end of the standard solar cell fabrication process.

One set of the samples was annealed in a lamp furnace under pure air atmosphere at 800 °C during few seconds. The annealing profile is shown in Fig. 5, and is equivalent to the standard annealing process for the contact formation. The Fourier-transform infrared (FTIR) spectra obtained with these samples are shown in Fig. 6. We will describe the most important regions and confront them to the XPS results. A more detailed analysis of the FTIR spectra has been already published in [6].

The predominant band between 800 cm^{-1} and 1200 cm^{-1} is mainly caused by the Si–N and the Si–O groups in the stretching mode [20,28]. The peaks localised at 1180 cm^{-1} and 3350 cm^{-1} correspond to N–H bending and stretching vibration respectively [29]. At 2200 cm^{-1} stands the Si—H stretching mode and lastly, the small peak at 3500 cm^{-1} can be identified as the H–O–H stretching vibration [17]. Note that the 2000–4000 cm^{-1} spectral region was magnified five times for appreciation.

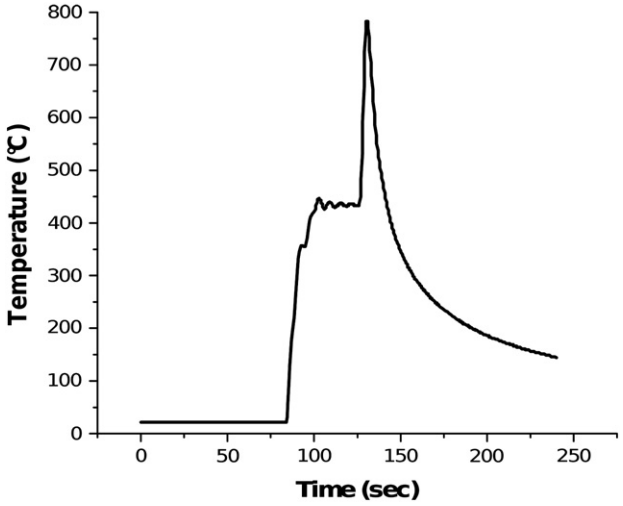

Fig. 5. Temperature profile of the rapid thermal annealing step.

Seoul Semiconductor, Exhibit 2001
LGI v. SSC, IPR2019-01154

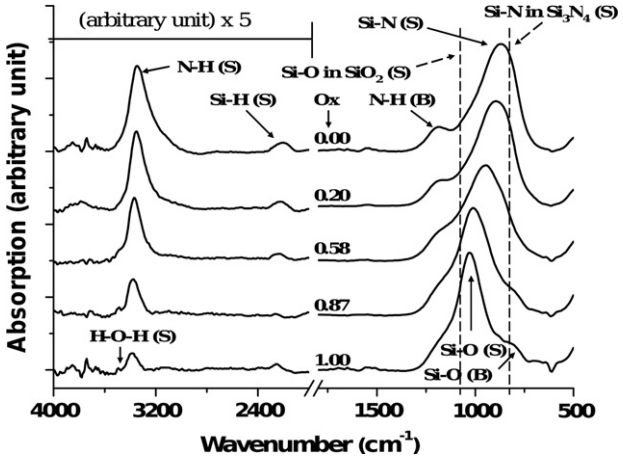

Fig. 6. Thickness normalized FTIR spectra of the as-deposited SiON layers in function of the Ox ratio indicated above each spectrum. The dotted lines indicate the position of the Si–N stretching vibration mode in Si_3N_4 (830 cm^{-1}) and the Si–O stretching vibration mode in thermal SiO_2 (1070 cm^{-1}), respectively [27].

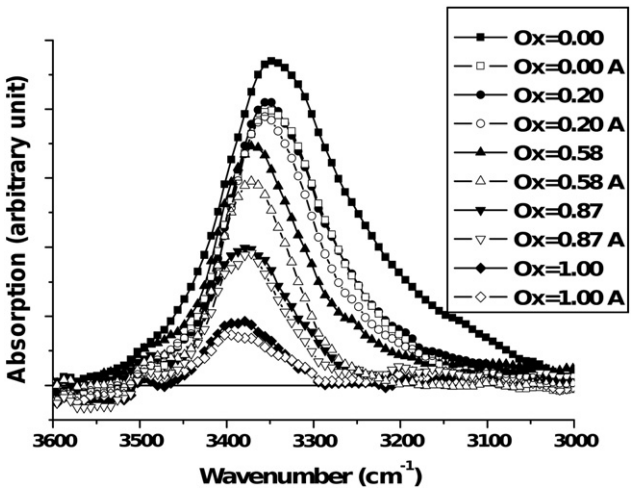

Fig. 7. Zoom on the normalized FTIR N–H stretching bond spectrum. The solid and dotted lines stand for respectively un-annealed and annealed samples.

Going from the SiN to the SiO films, the main peak moves from the Si–N stretching mode to the Si–O stretching and rocking modes as expected from the previous XPS analysis: the oxygen atoms take progressively the place of the nitrogen atoms and the oxygen reacts in priority with the silicon. This is confirmed by the decrease of the Si–N, N–H and Si–H related peaks. The presence of water is also detected through the H–O–H bond and the presence of absorption peaks in the 1400–1800 cm^{-1} range, despite a complete atmosphere purge in the FTIR chamber. The presence of water in SiON films has also been reported by Yeh and Lee [30] for oxygen-rich samples deposited at 250 °C. The authors have suggested that the water presence was related to the decrease of the incoming rate of SiH_n radicals towards the surface during the deposition. This would allow the hydrogen atoms in the plasma to remove the O–H bonded to silicon more easily, and to form water. Nevertheless, the quantity of water remains extremely weak in our layers. Note that no water-related peak is visible for the annealed films, which confirms its formation during the layer deposition.

The hydrogen is mainly bonded to the silicon and the nitrogen for the nitrogen-rich SiON, and to the nitrogen for the oxygen-rich SiON. Going from SiN to SiO, the Si–H and N–H bonds quantity decreases slowly, until the almost disappearance of both contributions in the spectra, probably due to the formation of preferential Si–O bonds.

No noticeable change is observed in the FTIR spectrum after annealing. The N–H stretching modes decrease in intensity (Fig. 7), and the Si–H stretching mode remains only slightly visible for the SiN and the nitrogen-rich SiON films. A shift of the Si–O stretching mode to a higher wavenumber is also visible (Fig. 8).

Despite its rapidity, the annealing step reached 800 °C and was efficient enough to break a significant amount of the weakest bonds in the SiON films. The FTIR spectra highlight clearly a loss in bonded hydrogen within the layers after the annealing. We would have expected a higher decrease of the Si–H bonds due to its relative weak energy compared to the others (3.3 eV against 4.0 and 3.7 eV for N–H and Si–N bonds [7][17]). In practice, some authors have observed a higher breaking rate for the N–H bonds than for the Si–H, caused by the so-called cross-linking effect [31]. It is a synergy effect between the Si–H and N–H bonds which leads to the reaction:

$$Si{-}H + N{-}H \rightarrow Si{-}N + H_2$$

This effect is not always effective and depends on the layer formation conditions. In our case, the lost of N–H and Si–H bonds after annealing are both significant. The cross-linking effect seems to play a major role for the nitrogen-rich SiON since more Si–N bonds are present after the annealing (Fig. 8). In the oxygen-rich films, this effect is not visible since the Si–O bonds formation is preferred and leads to a slight shift of the Si–O stretching mode after annealing. Note that the annealing seems to affect also the Si–N bonds in oxygen-rich SiON as the steep fall of the peak may suggest.

The bonded hydrogen seems to decrease evenly with the Ox ratio, although the ERDA analysis points out only a slight decrease for atomic hydrogen, followed by a strong drop for the SiO sample. This may indicate the existence of other forms of hydrogen bonds.

4.4. Hydrogen characterisation

To investigate more precisely the various form of hydrogen in our SiON films, ERDA, Raman and TPD measurements were used. Both ERDA and Raman characterizations were performed on as-deposited and annealed samples.

Fig. 9 displays the atomic hydrogen content for our SiON films determined by ERDA before and after annealing. The data before annealing is the same than the one presented on the Fig. 2. As assumed by the FTIR results, the annealing treatment decreases the hydrogen concentration, but not uniformly. Thus, another source of

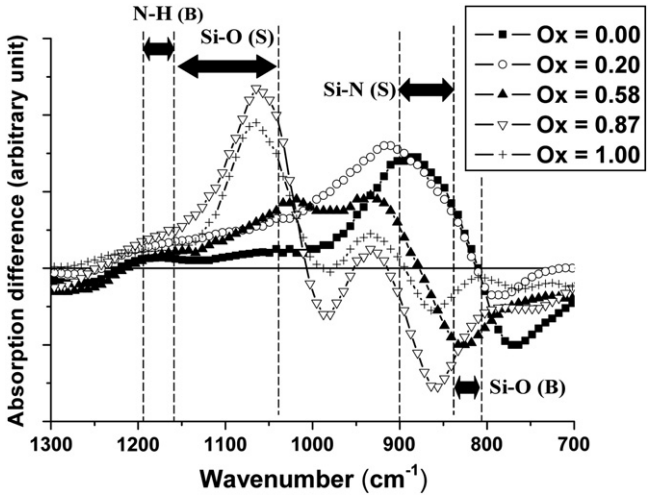

Fig. 8. Subtraction of the annealed samples FTIR spectra with the un-annealed ones.

Seoul Semiconductor, Exhibit 2001
LGI v. SSC, IPR2019-01154

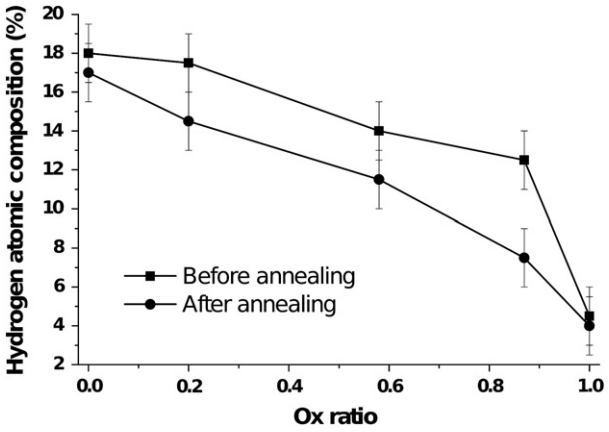

Fig. 9. Evolution of the hydrogen atomic composition with the Ox ration determined by ERDA before and after annealing. Lines are guide for the eye.

hydrogen should exist in the films. Trapped water could be a possible element but as shown in the FTIR section, the quantity seems to be too small to explain the whole change in the hydrogen content in the ERDA results. Moreover, this explanation could not work with nitrogen-rich SiON films since no water is detected. Another hypothesis is the presence of the dihydrogen molecules trapped in the SiON matrix.

4.4.1. Raman analysis

The Raman spectra on the Fig. 10 show the contribution of the H_2 molecule (near 4120 cm^{-1}) [32] for the four nitrogen-richest films. We note that the spectra after annealing (not presented) show no evidence of dihydrogen molecules in any sample.

Although the Raman peak proves the presence of trapped dihydrogen molecules, the signal remains too weak to bring a significant contribution to the total content of hydrogen within the layer. This is confirmed by the weak variation of the hydrogen content for the SiN layer (Fig. 9) despite a clear loss of dihydrogen molecules with the annealing observed on Raman spectra.

The presence of trapped dihydrogen molecules in the nitrogen-rich SiON films could be possible within denser films than the oxygen-rich layers, which could probably not keep the H_2 molecules efficiently [30].

4.4.2. Hydrogen desorption

The temperature ramp used for TPD measurements is linear, with a rate of 20 °C/min. This process is thus really different from the rapid thermal annealing profile used for solar cell contact firing.

The desorption profiles shown on Fig. 11 are quite different, depending on the type of SiON films. The strong signals observed at temperature higher than 750 °C are due to the destruction of the films. The SiN film begins to release hydrogen near 450 °C, whereas it starts at lower temperatures for the others samples. The desorption profile is also weaker for the SiO film according to its low hydrogen content.

The most important point is the desorption threshold temperature localized near 200 °C for most of the SiON films, whereas all the films depositions are performed at 370 °C (Fig. 1). This may be explained by the rapid cooling rate of the samples at the end of the deposition process: the samples are extracted from the PECVD reactor in the ambient air when they are still hot. Thus, a rapid cooling could occur and may freeze the SiON network suddenly. Consequently, a strong disorder might exist in the network, so that a moderate temperature increase would allow the release of a part of the hydrogen trapped in the films. For the SiN film, the higher density of the layer (2.6 versus 2.3 for the SiO layer) could refrain the hydrogen exodiffusion at low temperature. In all cases, a portion of the hydrogen is weakly linked to the SiON films. The FTIR spectra have shown the presence of covalent hydrogen bonds like N–H and Si–H, which are strong enough to be broken only above 400 °C, as suggested by the previous results for the SiN sample [7] [33]. The presence of dihydrogen and water in some SiON samples is thus demonstrated, but despite being good candidates to exodiffuse at low temperature, their quantities remain too small to be significant.

Another possibility to explain the low temperature exodiffusion of hydrogen may be the presence of hydrogen in the form of polar bond. This type of bond is essentially electrostatic, and is generally present in solution with high electronegative atoms; its energy is clearly inferior to a covalent bond [34]. The best example for these hydrogen bonds is the water where most of the individual molecules are linked to their neighbors, due to the polarity of the H_2O molecule. The presence of a similar type of bond is possible in the SiON samples because the layers are rich in nitrogen and oxygen, both atoms with high electronegativity. During the annealing time shown on Fig. 5, the plateau at 450 °C during 25 s can lead to the release of this weak-bonded hydrogen for the SiON samples. But the SiN and SiO samples are only weakly affected by this plateau because most of the hydrogen is strongly bonded (SiN), or it is in small quantity (SiO). The decrease in H content is thus more important for SiON samples (Fig. 9), and

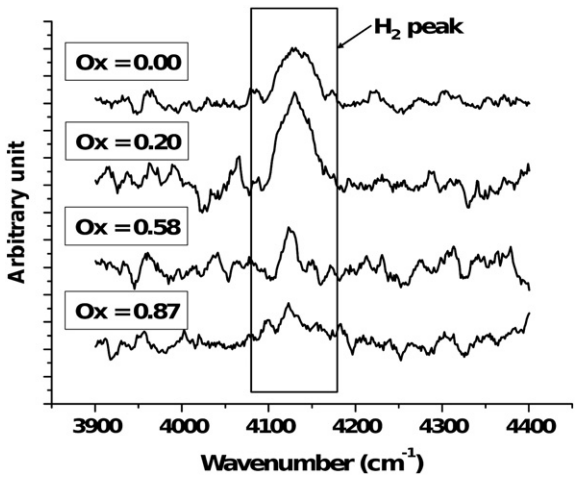

Fig. 10. Raman H_2 peak before annealing the SiON films.

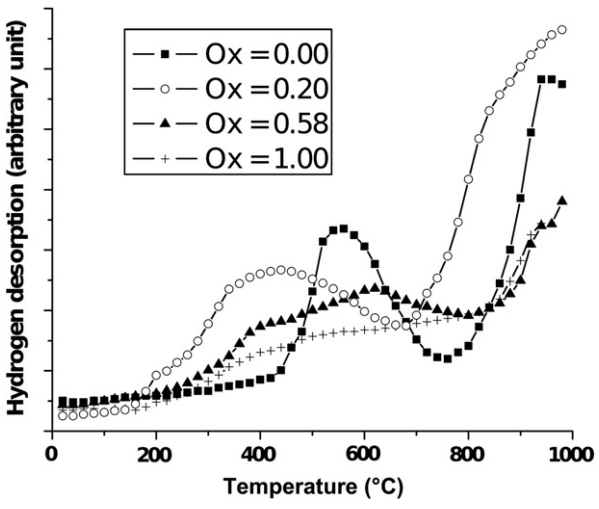

Fig. 11. Hydrogen desorption profiles of the SiON films.

Seoul Semiconductor, Exhibit 2001
LGI v. SSC, IPR2019-01154

the release of hydrogen starts at lower temperature (Fig. 11). The TPD profiles differences between these three intermediate SiON samples could be attributed to their respective structural networks (see Section 4.2) which might enhance the exodiffusion of the hydrogen. Finally, if a part of the hydrogen is effectively bonded to high electronegative atoms, the oxygen concentration can probably play a major role on the quantity of weak-linked hydrogen.

5. Surface passivation properties

The investigation about the hydrogen gives information about its quantity and its chemical configuration within the layers. These parameters are known to be strongly related to the properties of the surface passivation layers. For example, in a silicon nitride study, Mäckel and Lüdemann [35] have considered the Si–H bonds concentration as a good indicator for the passivation quality of the layer. Surface passivation results obtained from previous work on our silicon nitride layers are detailed in [7,33].

The evolution of the minority carriers lifetime (MCL) is presented in Fig. 12. For clarity, only the results for n-type silicon are plotted, but the trend for p-type is exactly similar, with slightly lower values due to the higher capture cross-section of electron in p-type silicon [36].

Before annealing the passivation effect decreases slowly from SiN to SiO. The MCL is one order of magnitude lower for the SiO than for the SiN sample. We have mentioned that the Si–H bond density might be considered as an indicator of the passivation quality [14]. In our case the hydrogen could be linked to the P_b centers ($Si_3{\equiv}Si\cdot$), which are reported to be the dominating defect in un-passivated SiO layer [37], and which can be well passivated by the hydrogen [38]. In this point of view, the decrease of the MCL seems to be well correlated with the decrease of the Si–H stretching mode observed with the FTIR analysis. As we have already reported elsewhere [6], we can also expect a lower fixed charges density in SiON than in the SiN layer, due to the reduction of the K^+ centers concentration [1], i.e. the $N_3{\equiv}Si^+$ defect, which follows the decrease of the nitrogen content. This would also induce a reduction of the surface passivation when Ox increases. Nevertheless, additional charges might be brought by the P_{ox} and similar centers ($O_3{\equiv}Si\cdot$, $O_2N{\equiv}Si\cdot$and $ON_2{\equiv}Si$ defects) [1]. Although their charging states are not necessarily positives, it is known that the P_{ox} centers bring mainly a positive contribution in the silicon thermal oxide fixed charge density.

After annealing, the results of the passivation change deeply: the nitrogen-rich samples exhibit poor MCL and the situation is opposite for the oxygen-rich SiON. The passivation effect does not change much for the SiN film and stays quite efficient (MCL near 100 µs). In our previous study, the strong MCL decrease for the nitrogen-rich SiON was suspected to be caused by a lower density of the layer [6]. The strong hydrogen desorption at low temperature (Fig. 11) partly confirms this point. Despite the formation of Si–N bonds with the annealing (Fig. 8), the passivation is affected by the loss of the weakly bonded hydrogen.

For the richer oxygen films, the passivation slowly increases and becomes even similar to that of the SiN layer with SiO. In these layers, the presence of a higher oxygen concentration seems to help in the creation of Si–O bonds as suggested by Fig. 8. Moreover, the exodiffusion of hydrogen from the SiO layer is clearly weaker than for the other layers. These two tendencies may explain the better passivation effect obtained with the oxygen-rich layers: the loss of hydrogen is counter-balanced by the formation of Si–O bonds, which passivate the surface. Besides, since the exodiffusion of hydrogen from the layer is slower in that case, it might also participate in the passivation improvement by decreasing the P_b centers concentration and the other defects at the SiON/Si interface.

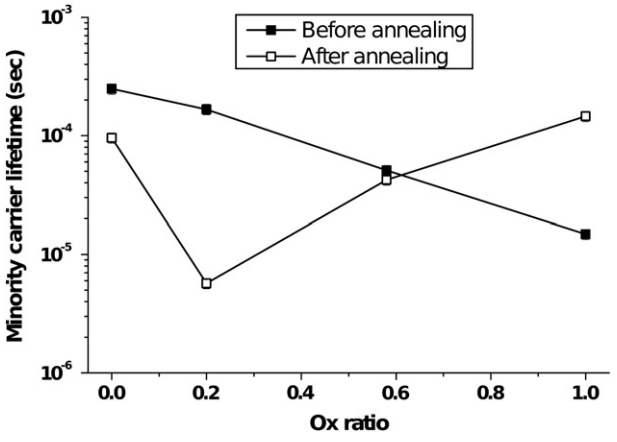

Fig. 12. Evolution of minority carrier lifetime for different SiN and SiON layers according to the Ox ratio and for an excess carrier concentration of $7 \cdot 10^{14}$ cm^{-3}. The incertitude is near 10%.

6. Conclusion

We have contributed in the chemical and structural description of the silicon oxynitride layers deposited by plasma enhanced CVD. These films have numerous advantages for photovoltaic applications. Their adjustable refractive index makes them suitable for multi-layers antireflection coating, in combination with a silicon nitride layer.

The ERDA and XPS characterizations have underlined the strong influence of the oxygen on the SiON network: the favourable formation of the Si–O bonds disturbs strongly the SiON matrix and a part of the hydrogen becomes weakly bonded to the layer. Thus, a rapid thermal annealing has a strong impact on the hydrogen content of the layer and may degrade the passivation properties of the films.

The differences between FTIR and ERDA measurements for the bonded hydrogen and the total hydrogen content suggest the presence of other forms of hydrogen within the SiON layers. Although dihydrogen and water have been detected in the samples, their quantities are not significant to explain the differences between the ERDA and FTIR results. Thus, it is possible that the hydrogen is linked within the layer by another type of weak chemical bonds, such as polar bonds.

Although the hydrogen does not contribute to the passivation as much as in the SiN layer due to its strong exodiffusion, the formation of Si–O bonds for the oxygen-rich films leads to a similar surface passivation. Consequently, in addition to antireflection coatings, the PECVD SiO layer becomes a good candidate for the surface passivation of solar cells. It is already widely studied in combination with SiN on the rear side of thin solar cells.

Acknowledgments

The authors want to thanks the Nanolyon platform staff for its technical contribution, and the National Research Agency (ANR) with the French Agency for Environment and Energy Management (ADEME) for their financial contributions through the national projects PHARE, REDUCOP and INFIME.

References

[1] A.G. Aberle, Sol. Energy Mater. Sol. Cells 65 (2001) 239.
[2] Y. Wang, X. Cheng, Z. Lin, C. Zhang, F. Zhang, Vacuum 72 (2004) 345.
[3] K. Wörhoff, A. Driessen, P.V. Lambeck, L.T.H. Hilderink, P.W.C. Linders, Th.J.A. Popma, Sens. Actuators, A 74 (1999) 9.
[4] B. Semmache, M. Lemiti, C. Chanelière, C. Dubois, A. Sibai, B. Canut, A. Laugier, Thin Solid Films 296 (1997) 32.
[5] A. del Prado, E. San Andrés, F.L. Martínez, I. Mártil, G. González-Díaz, W. Bohne, J. Röhrich, B. Selle, M. Fernández, Vacuum 67 (2002) 507.
[6] J. Dupuis, E. Fourmond, J.-F. Lelièvre, D. Ballutaud, M. Lemiti, Thin Solid Films 516 (2008) 6954.

Seoul Semiconductor, Exhibit 2001
LGI v. SSC, IPR2019-01154

APPENDIX B

[7] J.F. Lelièvre, PhD Thesis, Institut des Nanotechnologies de Lyon, INSA de Lyon, France, 2007.
[8] R. Einhaus, K. Bamberg, R. de Franclieu, H. Lauvray, R. Monna (Eds.), 20th European Photovoltaic Solar Energy Conferences, Barcelona, Spain, June 6–10, 2000, p. 1993.
[9] J. Dupuis, E. Fourmond, O. Nichiporuk, F. Gibaja, M. Lemiti (Eds.), 23rd European Photovoltaic Solar Energy Conference, Valencia, Spain, September 1–5, 2008, p. 1633.
[10] M. Hofmann, S. Kambor, C. Schmidt, D. Grambole, J. Rentsch, S. Glunz, R. Preu (Eds.), 22nd European Photovoltaic Solar Energy Conference, Milan, Italy, September 3–7, 2007, p. 1030.
[11] B. Rémiat, P. Saint-Cast, F. Souche, N. Enjalbert, R. Monna (Eds.), 22nd European Photovoltaic Solar Energy Conference, Milan, Italy, September 3–7, 2007, p. 1755.
[12] G.E. Jellison Jr., F.A. Modine, Appl. Phys. Lett. 69 (1996) 371.
[13] D.A. Shirley, Phys. Rev. B: Condens. Matter Mater. Phys. 5 (1972) 4709.
[14] R. Sinton, A. Cuevas, Appl. Phys. Lett. 69 (1996) 2510.
[15] S. Naskar, PhD Thesis, Case Western Reserve University, Cleveland, United States, 2006.
[16] K.E. Mattsson, J. Appl. Phys. 77 (1995) 6616.
[17] F. Ay, A. Aydinli, Opt. Mater. 26 (2004) 33.
[18] M. Józwik, P. Delobelle, C. Gorecki, A. Sabac, L. Nieradko, C. Meunier, F. Munnik, Thin Solid Films 468 (2004) 84.
[19] B.deB. Darwent, National Standard Reference Data Series, National Bureau of Standards, No. 31, Washington, DC, , 1970.
[20] M.I. Alayo, I. Pereyra, W.L. Scopel, M.C.A. Fantini, Thin Solid Films 402 (2002) 154.
[21] P. Cova, S. Poulin, O. Grenier, R.A. Masut, J. Appl. Phys. 97 (2005) 073518.
[22] R. Saoudi, G. Hollinger, A. Straboni, J. Phys. III 4 (1994) 881 (in french).
[23] A.L. Allred, E.G. Rochow, J. Inorg. Nucl. Chem. 5 (1958) 264.
[24] D.V. Tsu, G. Lucovsky, M.J. Mantini, S.S. Chao, J. Vac. Sci. Technol., A 5 (1987) (1998).
[25] J.-F. Lelièvre, H. Rodriguez, E. Fourmond, S. Quoizola, J. De la Torre, A. Sibai, G. Bremond, P.-J. Ribeyron, J.-C. Loretz, D. Araujo, M. Lemiti, Phys. Status Solidi B 4 (2007) 1401.
[26] B.L. Sopori, X. Deng, J.P. Benner, Sol. Energy Mater. Sol. Cells 41 (42) (1996) 159.
[27] S. Dreer, P. Wilhartitz, Pure Appl. Chem. 76 (2004) 1161.
[28] I.V. Afanasyev-Charkin, L.G. Jacobsohn, R.D. Averitt, M. Nastasi, J. Vac. Sci. Technol., A 22 (2004) 2342.
[29] E. Bustarret, M. Bensouda, M.C. Habrard, J.C. Bruyère, Phys. Rev. B: Condens. Matter Mater. Phys. 38 (1988) 8171.
[30] J. Yeh, S. Lee, J. Appl. Phys. 79 (1996) 656.
[31] C.M.M. Denisse, K.Z. Troost, F.H.P.M. Habraken, W.F. van der Weg, J. Appl. Phys. 60 (1986) 2543.
[32] H.F.W. Dekkers, G. Beaucarne, M. Hiller, H. Charifi, A. Slaoui, Appl. Phys. Lett. 89 (2006) 211914.
[33] J.-F. Lelièvre, E. Fourmond, A. Kaminski, O. Palais, D. Ballutaud, M. Lemiti, Sol. Energy Mater. Sol. Cells 354 (2009) 4341.
[34] T.W. Martin, Z.S. Derewenda, Nat. Struct. Biol. 6 (1999) 403.
[35] H. Mäckel, R. Lüdemann, J. Appl. Phys. 92 (2002) 2602.
[36] R.B.M. Girisch, R.P. Mertens, R.F. De Keersmaecker, IEEE Trans. Electron Devices 35 (1988) 203.
[37] G. Agostinelli, P. Choulat, Y. Ma, Guy Beaucarne (Eds.), 17th NREL Workshop on Crystalline Silicon Technology, Vail, Colorado, USA, August 5–8, 2007.
[38] A. Stesmans, J. Appl. Phys. 88 (2000) 489.

Seoul Semiconductor, Exhibit 2001
LGI v. SSC, IPR2019-01154

APPENDIX O

A NEW PROCESS OF OXIDE GROWTH ON SILICON

UTPAL K. CHAKRABARTI AND V. JOSHI

(Department of Electrical Engineering, Indian Institute of Science, Bangalore 12)

Received on May 17, 1975 and in revised form on September 27, 1975

ABSTRACT

A new technique of growing silicon dioxide film is described. The film is obtained from a organosilane derivative. The film is evaluated for bond-strain, porosity, etc., by infrared spectroscopy, P-etch, density and refractive index measurements. Though the as-deposited film lacks desirable properties, a very good film can be obtained by densification of the deposited film.

Key words: SiO_2 deposition, organosilane derivative.

INTRODUCTION

High temperature (900° C–1200° C) oxidation of silicon can produce very pure and stable silicon-dioxide films. But high temperature thermal oxidation process suffers from the disadvantage of junction movement and junction degradation [1]; also this process cannot be used for deposition of silicon dioxide on other substrates.

The films of SiO_2 have also been produced by decomposition of ethyl-silanes such as tetraethoxy silane [2] or oxidation of silane [3] but these films suffer from the disadvantages of high porosity, high etch rates and a high load of carbon contamination and less stability towards moisture.

In this article we will describe a new technique of growing oxide and evaluate its physical and chemical properties.

EXPERIMENTAL PROCEDURE

(*a*) *Oxide Deposition*

The oxide film is deposited from a organo-silane compound (acyloxy-silane). The compound is dissolved in a suitable organic solvent (*e.g.*, acetone) and is applied on the wafer which is mounted on a 'Spinner'. The centrifugal forces distribute the liquid evenly and the excess material is thrown off at the substrate edges. The compound reacts in the air and produces SiO_2 layer almost instantaneously.

Seoul Semiconductor, Exhibit 2001
LGI v. SSC, IPR2019-01154

Silicon wafers of *n*- and *p*-types of different resistivities and two types of crystal orientation (⟨100⟩ and ⟨111⟩) are used as substrates. No change was found in the deposited film properties (described latter). The surface finish of the substrates is a very important factor. On badly prepared surfaces discontinuous films are produced. All descriptions that will follow are regarding to optical-polish-finished surfaces. The cleaning of the substrates is also an important factor. If the surface is not properly degreased no films could be grown. The wafers are cleaned by the method described in [4].

The thickness of the film is dependent on the spinner speed; with higher speed the thickness reduces as shown in Fig. 1. In general, uniform thicknesses of the film is obtained for spinner speed greater than 3000 rpm. In the 1000–2000 rpm range, two regions of films are obtained as shown in Fig. 1 inset. The region A covered almost all of the wafer but region B, which is at the edges of the wafer is of higher thickness. The reason of this is that due to surface tension the liquid film is thicker at the edges which gives rise to thicker oxide.

(*b*) *Evaluation*

The deposited oxide is evaluated by infrared spectroscopy, *p*-etch and refractive index measurement. Some meachanical properties are also evaluated.

Infrared spectroscopy.—The half widths and position of bands near 1090 cm.$^{-1}$ and 805 cm.$^{-1}$ in the infrared spectra of SiO_2 is greatly influenced by the bonding character, stoichiometry, density and porosity of the films. All infrared spectra is taken on double beam Carl Zeis instrument. In all cases, a bare silicon wafer of the same thickness is placed in the reference beam to eliminate lattice absorption of silicon.

Figure 2 shows the spectra of as-deposited film. The main bands are 450 cm^{-1}, 805 cm^{-1} and 1070 cm^{-1}. The weak band at 935 cm^{-1} is attributed to silanol group. The film is subjected to densification at 800° C for 15 min in steam and purified dry nitrogen atmosphere. The spectra are shown in Fig. 3. The Si–O stretching band shifts to higher frequency and the half-widths are reduced. By comparing the figures in Table I we conclude that steam densification is more efficient. Also the band at 935 cm^{-1} is removed. To test the moisture stability, the film after densification, is boiled in water for one hour but there is no significant water pick-up which could be detected by infrared spectroscopy.

J 57978

Seoul Semiconductor, Exhibit 2001
LGI v. SSC, IPR2019-01154

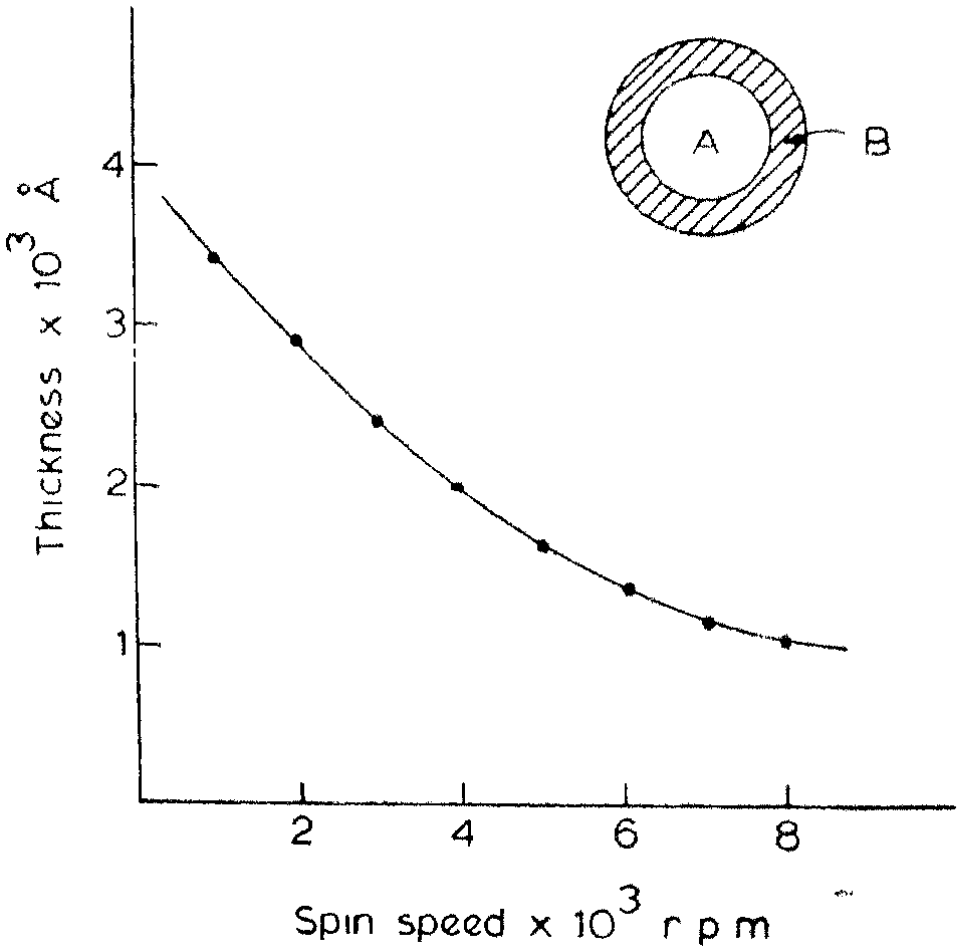

FIG. 1. Oxide thickness *vs.* speed of the spinner. Inset shows two regions of oxide layer for speeds <3,000 rpm.

P-etch technique.—A very commonly used etchant is P-etch [5] in which the etch rate is highly dependent upon density, bondstrain and porosity and the etch rate is a good indication of the film quality.

The P-etch rate of as deposited film is very high but can be reduced drastically by the heat treatments. The various values are given in Table II from which we conclude the steam densification is the best.

Thickness, Refractive index and density.—The as deposited film is porous and can be densified by heat treatments as described earlier. After the densification there is a marked change in thickness, refractive index and density. The various values are shown in Table III.

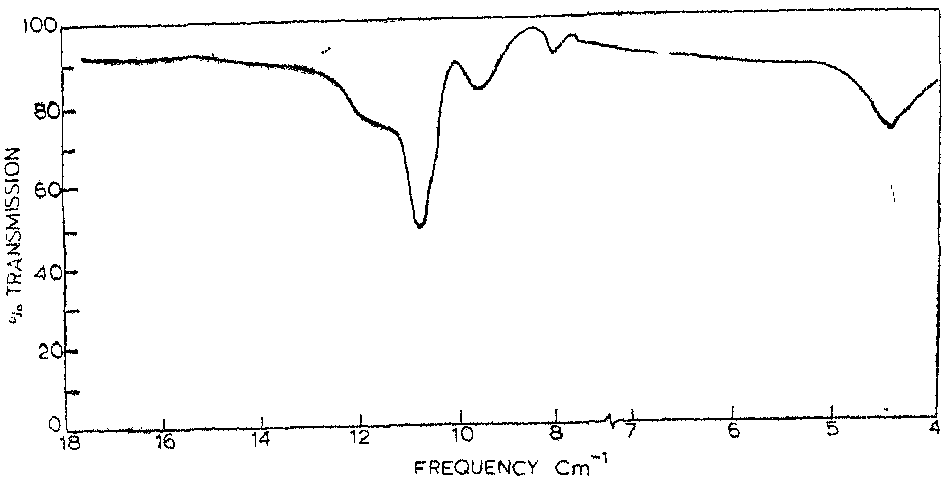

FIG. 2. The I.R. spectra of as-deposited film. The bands are at lower frequency and band widths are more.

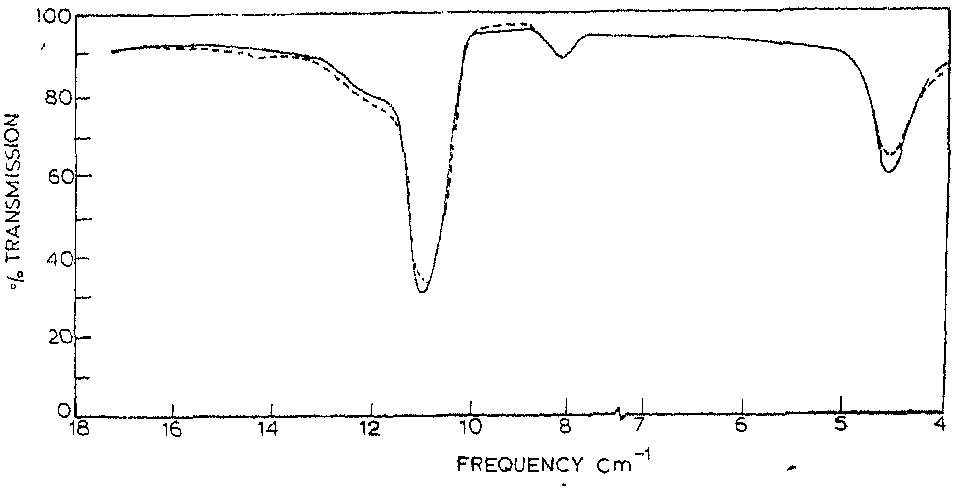

FIG. 3. The I.R. spectra after densification; continuous line ———, densification in steam for 15 min at 800° C. dotted line ..... densification in dry N_2 for 15 min at 800° C. The Si–O stretching has shifted to higher frequency and band widths are less.

Mechanical property.—The oxide film was found to have good mechanical properties. Sharply defined scratch marks can be made without the formation of any crack. Indentation tests were also carried out on the oxide film. A sharp diamond point (136° apex angle, square based pyramid) was pressed against the film and successively weights are added and the point was viewed through a microscope. The weight for which the film develops

TABLE I

Deposition and densification treatment	Band position cm^{-1}	Half-width cm^{-1}
As-deposited film	1070	90
Densified in dry N_2 for 15 min. at 800° C	1080	86·5
Densified in steam for 15 min. at 800° C	1090	83·4

TABLE II

Deposition and densification treatment	P-etch rate Å/sec
As-deposited	Very high
Densified at 350° C in air for 15 min.	15
Densified at 800° C in dry N_2 for 15 min.	3
Densified at 800° C in steam for 15 min.	2·5

TABLE III

Densification treatment for 15 min.	Thickness Å	refractive index	Density g/c.c.
As-deposited	1049	1·430	2·01
In air at 350° C	920	1·432	2·05
Dry N_2 at 800° C	875	1·451	2·12
Steam at 800° C	975	1·459	2·2

fracture gives a quantitative measure of mechanical strength. For as—deposited film, the required weight is 120 gms whereas for stem densified film the required weight it is 155 gm. In Fig. 4 a photomicrograph of the fracture is shown.

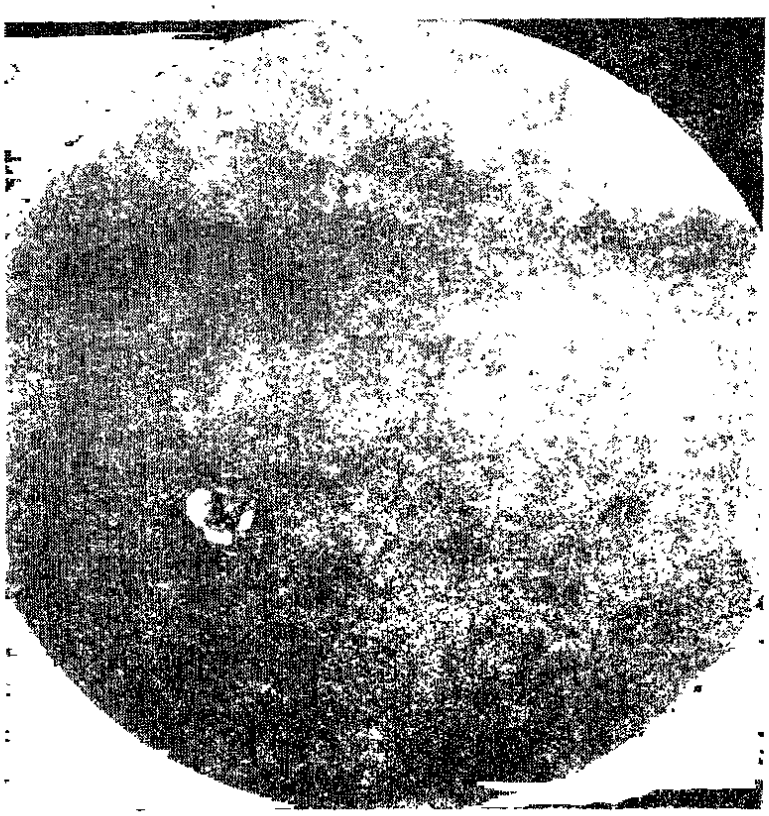

Fig. 4. Photomicrograph of the fracture which shows hair-like lines. Magnification, × 400.

Discussion and Conclusion

A new technique for oxide deposition is described in this paper. The most attractive aspect of this process is that the film is deposited at temperatures as low as room temperature. The apparatus required for depositing a uniform layer is also simple.

The properties of the film are evaluated by the combination of different techniques, *e.g.*, infrared spectroscopy, P-etch rate, refractive index, etc. From the infra-red spectrum of the as-deposited film Fig. 2 it is concluded that the film consists only of SiO_2 because the absorption peaks due to other oxides of silicon (*e.g.*, SiO and Si_2O_2) are absent. By comparing the

infrared spectra of as-deposited film and heat annealed films Fig. 3 it is observed that after heat treatments the absorption peaks are shifted to higher frequencies and bandwidths are reduced. The reason behind this is that the extent of polymerization in the oxide film is increasing and more covalent bonds are produced [6]. The fact that the density of annealed films are higher also supports that higher degree of polymerization is obtained in heat treated films.

From P-etch rate, refractive index and density data it is concluded that the as-deposited film is porous. Porosity of deposited films is a common characteristics and the lower the temerature of deposition, the greater is the porosity. The etch rate is high because the points for chemical attack is more. This porous nature of the film can be removed by densification treatments described earlier and the etching properrty is improved. In some photolithographic processes, sometimes it may however be, desirable to have a layer with high-etch rate [7].

Steam densification is found to be more efficient than other processes. In this process a thin layer of thermal oxide (≈ 100 Å) is produced. But this thin layer cannot account for all the improvements as it can be seen that there is a very little differences between the properties of purified dry nitrogen densified and steam densified films.

Mechanical properties are helpful in evaluating the adhesion of the film to the substrate. It is found that after heat treatment the adhesions is very strong so that when scratches are made there is no peel off along the scratch edges.

ACKNOWLEDGEMENT

One of the authors (UKC) acknowledges the financial assistance of the Department of Atomic Energy, Government of India.

REFERENCES

[1] Barson, F., Armstrong, W. J. and Mutter, W. E. Degradation of planar junctions during reoxidation. *Journal of Electrochemical Society*, 1964, **3**, 1263–1266.

[2] Klerer, J. .. A method for the deposition of SiO_2 at low temperatures, *Journal of Electrochemical Society*, 1961, **108**, 1070–1071.

[3] Goldsmith, N. and Kern, W. The deposition of vitreous silicon dioxide films from silane *RCA Review*, 1967, **28**, 153–165.

Seoul Semiconductor, Exhibit 2001
LGI v. SSC, IPR2019-01154

[4] Kern, W. and Puotinen, D. A. Cleaning solutions based on hydrogen peroxide for use in silicon semiconductor technology. *RCA Review*, 1970, **31**, 187–206.

[5] Pliskin, W. A. and Gnall, R. P. Evidence for oxidation growth at the oxide-silicon interface from controlled etch studies. *Journal of Electrochemical Society*, 1964, **3**, 872–874.

[6] Kolesova, V. A. .. Infrared absorption spectra of the silicates containing aluminium and of certain crystalline aluminates. *Optics and Spectroscopy*, 1959, **6**, 20–24.

[7] Raju, T. A. .. Department of Electrical Communication Engineering, I.I.Sc., Bangalore. Private communication.

Calendar of events: Conferences/Symposia at the Indian Institute of Science Campus

Sl. No.	Name of the School	Period	Sponsoring Department of the Institute
1.	50th Symposium of Biochemical Society	9–10 January 1976	Biochemistry
2.	QIP—"Design and Performance Estimation of Heat Exchangers"	1–14 February 1976	Mechanical Engineering
3.	" Design and Technology of Digital Equipment "	9–21 February 1976	Electrical Communicatic Engineering
4.	" Dynamics and Control of Industrial Organisers "	12–25 February 1976	Chemical Engineering
5.	QIP— "Public Water Supply Systems "	16–29 February 1976	Chemical Engineering
6.	QIP—" Dynamics of Engineering Systems "	1–15 March 1976	School of Automation and Mechanical Engineering
7.	QIP—"Limit State Design of Concrete Structures"	8–20 March 1976	Chemical Engineering
8.	"Applications of Computers for Load Despatch"	17-23 March 1976	School of Automatio and Aeronautical Engineering
9.	"An Intensive Course on Active and Digital Filters"	19 April to 2 May 1976	Metallurgy
10.	"Recent Developments in Physical Metallurgy— Techniques"	6–12 May 1976	Metallurgy
11.	QIP- "Insulation Problems in High Voltage Engineering"	9–23 May 1976	High Voltage Engineering
12.	"Particle Size Analysis and Separation"	14–29 May 1976	Metallurgy
13.	"Refresher Course Short Term Institute"	14 June to 13 July 1976	Microbiology apd Cel Biology Laborator
14.	"Advanced Institute on Reaction Mechanisms All India, University and College Teachers"	16 June to 13 July 1976	Organic Chemistry
15.	"Advanced Summer Institute in Theoretical Plasma Physics"	June–July 1976	Physics

On the basis of the information received by the Editorial Office on 30th December 1975

5618/75. Published by T. K. S. Iyengar. Executive Editor, Indian Institute of Science, Bangalore-560012 and Printed at the Bangalore Press, Bangalore-560018.

Seoul Semiconductor, Exhibit 2001
LGI v. SSC, IPR2019-01154

APPENDIX P

ELSEVIER

Thin Solid Films 386 (2001) 111–116

thin solid films

www.elsevier.com/locate/tsf

Effect of nitrogen plasma conditions on electrical properties of silicon oxynitrided thin films for flash memory applications

Akihiro Ikeda[a,*], M. Abd Elnaby[b], Reiji Hattori[a], Yukinori Kuroki[a]

[a] *Graduate School of Information Science and Electrical Engineering, Kyushu University, Kyushu, Japan*
[b] *Department of Electronics and Communications, Tanta University, Tanta, Egypt*

Received 23 June 2000; received in revised form 5 November 2000; accepted 8 November 2000

Abstract

Thin silicon oxynitride films were deposited on Si(100) substrates using nitrogen plasma at various exposure times, followed by thermal oxidation in dry O_2 without the use of toxic or global warming gases. Secondary ion mass spectroscopy measurements confirmed that nitrogen is confined to the immediate vicinity of the surface. The damage induced in the thin silicon oxynitride film after exposure to nitrogen plasma for between 10 and 60 s was estimated from an analysis of capacitance–voltage and current–voltage measurements. Generation of different densities of positive oxide charge was observed. Correlation between the local bonding structures in the oxynitride films and the electrically active defective states at the oxynitride/Si interface are also discussed. It is proposed that improved electrical characteristics such as positive charge trapping, interface state density, leakage current, and stress immunity of thin silicon oxynitride films, can be obtained by using an optimal plasma exposure time of approximately 30 s. The preliminary results obtained in this study indicate that these oxynitride films can be considered as potential candidates for ultra-thin gate oxide flash memory applications. © 2001 Elsevier Science B.V. All rights reserved.

Keywords: Nitrides; Plasma processing and deposition; Secondary ion mass spectroscopy; Electrical properties and measurements

1. Introduction

The deposition of silicon oxynitride (SiON) film is a promising technology for realizing reliable gate insulators for electrically-erasable non-volatile memory (Flash memory). It is known that the accumulation of incorporated nitrogen (N) atoms at the SiO_2/Si interface can improve hot carrier resistance [1], and the use of Si oxynitride can also suppress boron penetration from a p^+ poly–Si gate to Si. The characteristics of the metal-oxide semiconductor (MOS) structure, which incorporates a boron-diffused SiO_2 film, become unstable due to carrier trapping [2]. Silicon oxynitride also has a higher dielectric constant than alternative films, an hence a larger capacitance for given geometric parameters. Thus, nitrided oxides are attracting a great deal of attention for device applications that include not only flash memory, but also standard MOS logic circuits.

The high temperature annealing of SiO_2 in N_2O or NH_3 ambient at $\sim$1000°C is the conventional method of oxynitridation. However, both N_2O and NH_3 are toxic gases. Furthermore, N_2O is a potential global warming substance and the regulation of N_2O emission to the atmosphere is an international issue. Therefore, the development of novel deposition methods that do not involve the use of N_2O or NH_3 is needed for the future 'clean' ultra-large-scale integrated circuit (ULSI) processes.

The deposition of oxynitride layers on Si using nitrogen radicals or ions has been investigated for fabricating oxynitride films at low temperature [3,4]. We have investigated the fabrication of silicon oxynitride by

* Corresponding author. Tel.: +81-926-6423979; fax: +81-926-423975.
E-mail address: ikeda@ed.kyushu-u.ac.jp (A. Ikeda).

0040-6090/01/$ - see front matter © 2001 Elsevier Science B.V. All rights reserved.
PII: S0040-6090(00)01888-5

Seoul Semiconductor, Exhibit 2001
LGI v. SSC, IPR2019-01154

exposing Si to nitrogen plasma, followed by thermal oxidation in dry O_2 at high temperature (1050°C). It is possible that the distribution of nitrogen atoms in such plasma-deposited oxynitride films is different from that conventional thermally-grown layers. Therefore, in this report we present the characteristics of samples produced by our process, as determined by measuring the nitrogen concentration profile in our samples by secondary ion mass spectroscopy (SIMS). In particular, this study was concerned with investigating the effects of plasma exposure time on nitrogen concentrations, which is one of the most important parameters for determining the oxynitride quality and electrical properties of thin oxynitride films produced in this way. In previous studies we have demonstrated that the reliability of oxynitride films is improved with only light nitridation (shorter exposure time) [5]. Hence, the combination of ion damage and nitridation effects associated with nitrogen plasma exposure may result in an optimum exposure time for plasma nitridation. Flat-band voltage shifts and interface trap densities in the Si band gap as a function of plasma exposure time were estimated from an analysis of capacitance-voltage (C–V) characteristics.

2. Experimental procedure

P-type (100) CZ Si wafers with a surface resistivity of 3–5 Ω cm were used for the MOS capacitors. The Si wafers were cleaned with SC1 ($NH_4OH/H_2O_2/H_2O$ = 1:5:4) RCA cleaner at 60°C for 10 min, and then dipped in buffered hydrogen fluoride (BHF, NH_4F/HF) water to remove the native oxide. After drying with nitrogen gas, the wafers were immediately transferred into the load-lock chamber attached to the plasma apparatus for nitridation.

Inductively coupled plasma (ICP) was used for the generation of the nitrogen plasma. A single turn loop antenna was set around the quartz discharge tube. A clean process without metal contamination is necessary for gate oxide processes. In ICP system that we used, which was designed in our laboratory, the discharge chamber was formed from a quartz tube, similar to furnace oxidation equipment. Therefore, metal contamination from chamber wall sputtering was negligible and clean nitrogen plasma was produced. The base pressure in the discharge chamber was 5×10^{-4} Pa, and discharge pressure was 0.6 Pa. The gas flow rate in the nitrogen plasma was 40 cm^3/min. The wafer temperature during plasma exposure was maintained at room temperature, as monitored by a thermocouple attached to the wafer holder. Plasma exposure times were varied in the range 10–60 s in order to evaluate the effect of plasma exposure on the electrical stress immunity of the oxynitride films for light nitridation. For SIMS measurements, the plasma exposure times were set to 1 min and 3 min, representing light and heavy nitridation conditions, respectively. The plasma parameters measured by Langmuir probe are listed in Table 1. After N plasma exposure, the wafers were oxidized in a dry O_2 atmosphere at 1050°C. MOS capacitors with a gate area of 1.225×10^{-3} cm^2 were formed by photolithography and wet etching of Al deposited on the wafer by DC magnetron sputtering.

A schematic of the fabrication procedure is shown in Fig. 1. The thickness of silicon nitride layer formed by the N plasma was 4.8 nm, as determined by ellipsometry, for heavy nitridation with 3 min plasma exposure. The thicknesses of silicon nitride layers produced by light nitridation were between 0.8 nm to 3.6 nm for plasma exposure of 10–60 s. The thickness of the oxynitride layer after subsequent thermal oxidation for heavy nitridation was 5.6 nm, and that for the light nitridation samples was 5.0 ± 0.3 nm. The thicknesses of the oxynitride layers were measured by ellipsometry using a single-layer model. The thickness of the Al electrode was 300 nm, as determined using a step surface profiler.

The nitrogen depth profiles of the samples were investigated by SIMS. The capacitance-voltage (C–V) characteristics were evaluated under high frequency conditions(1 MHz) and quasi-static conditions using HP4284A and HP4140B, respectively. The current-voltage (I–V) characteristics were determined using HP4156A. The shift in flat-band voltage V_{FB} was calculated as a function of plasma exposure time in order to investigate the charge trapping in oxynitride films associated with nitrogen plasma exposure. Additionally, interface state density profiles in the Si band gap were analyzed.

3. Results and discussions

3.1. Secondary ion mass spectroscopy measurements

SIMS depth profiles recorded for a heavy nitrided and light nitrided sample are shown in Fig. 2a,b, re-

Table 1
Nitrogen plasma parameters as measured by Langmuir probe

	Discharge power (kW)	Electron energy (eV)	Electron density (cm^{-3})	Incident ion energy (eV)
Heavy nitridation	2.0	2.6	1.3×10^{11}	20.2
Light nitridation	0.5	1.7	4.3×10^{10}	13.6

Seoul Semiconductor, Exhibit 2001
LGI v. SSC, IPR2019-01154

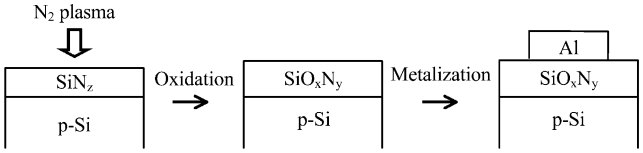

Fig. 1. Schematic of sample fabrication procedure.

spectively. The depth resolution of the SIMS measurements was ~3 nm. It can be observed that nitrogen is not uniformly distributed throughout the samples, rather, it accumulates in a thin layer localized near the oxide surface in lightly nitrided samples. Elements in plasma-deposited layers usually have homogeneous distributions, however, such homogeneity is not observed in this case. This may be attributable to the redistribution of nitrogen atoms in the film during the thermal oxidation process that follows plasma nitridation. Moreover, heavy nitridation processes produce a broader nitrogen distribution with a lesser peak than for lightly nitrided samples.

The accumulated nitrogen concentration near the oxynitride film surface is approximately 10^{21} atoms/cm^3, whereas the oxygen concentration increases towards the SiON/Si interface. At the surface, the nitrogen, oxygen and silicon profiles appear to decrease. This is a typical and unavoidable error in SIMS measurement. X-Ray photoelectron spectroscopy (XPS) measurements of a typical sample [5] revealed a peak in the N1s spectra at 397.5 eV binding energy, indicating that 3Si≡N bonds were formed in the oxynitride films. However, the formed film does not act as a perfect barrier layer for thermal oxidation, although the thermal oxidation rate was observed to decrease with increasing nitridation of the Si surface [5].

In ULSI applications, boron penetration from p^+ poly–Si gates through gate oxide is a serious problem, and nitrogen atoms accumulate at the SiON/Si interface if conventional N_2O or NH_3 thermal deposition of silicon oxynitride are used [6,7]. Therefore, the conventional deposition of silicon oxynitride prevents boron penetration through the Si substrate, whereas it can not prevent penetration into the SiO_2 [8]. The nitrogen profile must have a peak at the oxide surface. Therefore, our silicon oxynitride process is effective in preventing boron penetration from the p^+ poly − Si gate to MOS devices. Moreover, as shown in Fig. 2b, the nitrogen concentration at the interface in our films is approximately 3×10^{20} atoms/cm^3. This value is significantly higher than those for conventional thermal oxidation techniques [6], and results in an improvement of the interface properties at the SiON/Si interface.

3.2. C–V characteristics

The high frequency C–V characteristics of 5 nm oxynitride films prepared at different nitrogen plasma exposure times are shown in Fig. 3, as measured at 1 MHz. The estimated flat band voltage (V_{FB}) is shown in Fig. 4 as a function of plasma exposure time. For plasma exposure times shorter than 20 s, the negative C–V shift increases with exposure time. However, after the initial increase during the first 20 s, V_{FB} decreases with a minimum negative shift at a plasma exposure time of 30 s. The flat band voltage then increases for plasma exposure times of 40–60 s. This behavior is called the 'turn around' effect [9,10].

Physically, the behavior of V_{FB} with respect to plasma conditions is associated with the nature of plasma-

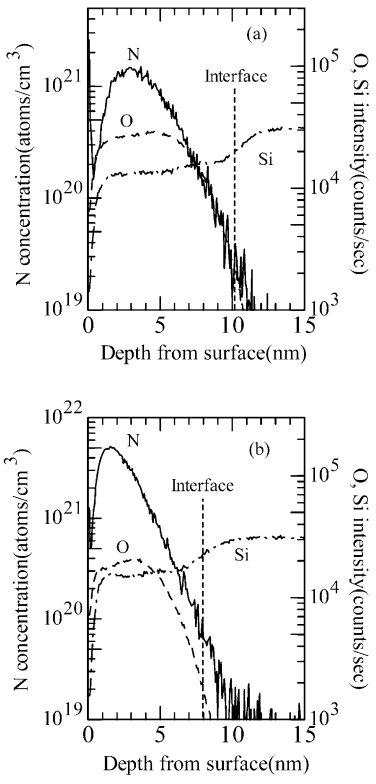

Fig. 2. SIMS depth profiles for typical oxynitride thin films; N, O and Si distribution profiles in (a) heavy and (b) light nitrided films.

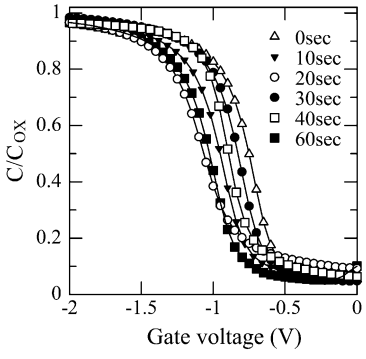

Fig. 3. 1 MHz C–V characteristics for films with different nitrogen plasma exposure times.

Seoul Semiconductor, Exhibit 2001
LGI v. SSC, IPR2019-01154

APPENDIX P

induced defects in the Si-oxynitride structures and the change in such defects with varying plasma conditions including exposure time. These findings may be explained by a combination of the effects of ion damage and nitridation annealing. It can be suggested that for short plasma exposure times (<30 s), the damage resulting from ion bombardment and the generation of defects such as strained or broken Si–O bonds near the Si surface, dominate during the initial stages of growth. Consequently, positive charges related to oxygen atom vacancies, E' centers, are generated. After plasma processing time of approximately 30 s, the surface layer of the Si substrate is fully nitrided. The number of broken Si–O bonds and positive charge trapping are both reduced by the formation of Si–N bonds. At longer plasma exposure times (>30 s), Si–N bond formation is limited to a shallow region within a few nanometers of the substrate surface where nitrogen atoms act as a diffusion barrier to nitrogen atoms from the nitrogen plasma to the SiON/Si interface. Hence, ion damage occurs in the Si substrate and positive charge increases. Consequently, a negative V_{FB} shift is observed at longer plasma exposure times, as shown in Fig. 4.

3.3. Interface trap density

The interface trap density D_{it} was determined by the conventional low frequency C–V measurement method [11], and low frequency C–V measurements were made using the quasi-static technique. The capacitance of the MOS capacitor was determined by measuring the displacement current in response to a linear gate voltage ramp. The measured capacitance includes parasitic capacitance caused by interface traps. The parasitic capacitance causes the measured MOS capacitance to be higher than the ideal MOS capacitance without interface traps. Therefore, the distribution of interface trap density can be obtained from the difference between measured and ideal capacitances as a function of Si surface potential.

The variation of D_{it} with plasma exposure time is shown in Fig. 5. Similar to the results of C–V characteristics mentioned in the previous sections, D_{it} exhibits a maximum after 10 s or 20 s exposure. Therefore, we believe that the mechanism responsible for

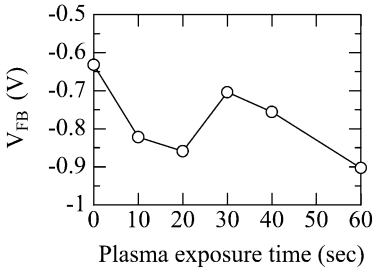

Fig. 4. V_{FB} as a function of nitrogen plasma exposure time.

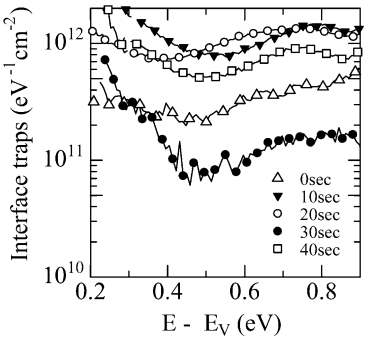

Fig. 5. D_{it} profiles in Si band gap as a function of nitrogen plasma exposure time.

this D_{it} behavior for plasma exposure may be the same as that for the C–V characteristics. It is well known that E' centers (origins of positive charge) exist near the SiON/Si interface, and act as donor-type slow interface states [12]. Moreover, the generation of high density positive oxide charge, even during the first 15 s of nitrogen plasma exposure, has been reported [13]. A D_{it} peak at approximately 0.75 eV is observed in Fig. 5 for samples with 10, 20 and 40 s of plasma exposure. This peak, which occurs above the mid-gap of Si (0.56 eV), is known to be an acceptor-type fast interface state ($3Si{\equiv}Si{-}O^-$), and is also caused by ion damage [14]. However, at longer plasma exposure times (>30 s), the nitrogen concentration in the oxynitride film increases and the mechanical stress changes, resulting in the formation of excess charge traps at the interface. As the Si substrate reacts with the nitrogen, the energy of the SiON/Si system is reduced by the formation of bonds between Si and N. The presence of strain at the SiON/Si interface, however, partially offsets the gain in energy due to bond formation. This strain energy cost can be reduced if defects that relieve the strain locally are formed during the nitridation process [15].

Therefore, we suggest that the optimum plasma exposure time for producing highly reliable oxynitride films is 30 s. It should be noted that the D_{it} of approximately 7×10^{10} eV^{-1} cm^{-2} obtained after 30 s exposure time using our technique is lower than that reported by other research groups for similar oxides prepared using other techniques [16]. Therefore, it can be suggested that optimal results are achieved when there is an optimal level of nitrogen at the interface, the realization of which depends on the technique used to introduce the nitrogen. However, higher nitrogen concentrations may result in levels that exceed optimal conditions [17].

3.4. I–V characteristics

The dependence of leakage current on plasma exposure time is presented in Fig. 6. Leakage current is

Seoul Semiconductor, Exhibit 2001
LGI v. SSC, IPR2019-01154

reduced to approximately 10^{-9} A/cm^2 at 30 s exposure. This is in accordance with the findings of the C–V measurements and the detected lower interface trap density. These results indicate that the positive oxide charge accounts for the majority of the relatively high leakage current. When the density of the oxide charges is high enough, the trapping process is very efficient. This also confirms the expected sensitivity of leakage current to the induced charges, and implies that the increase of leakage current is directly proportional to the degree of plasma induced damage. Higher leakage currents associated with lower exposure times of <30 s support the conclusion that the first 20 s of plasma exposure is critical to the plasma damage creation process.

At 30 s exposure, and due to the contribution of the existence of an optimum level of nitrogen at the interface, the leakage current is reduced. However, with increasing exposure time, >30 s, the samples are damaged more severely by plasma exposure. The oxynitride film is weakened, yet not completely destroyed. Higher leakage currents observed in all samples in the high gate field region (>-8 MV/cm), may be associated with different tunneling mechanisms associated with the high field region [18]. Therefore, in general, the results derived from the I–V and C–V measurements are consistent and agree with the widely accepted concept of breakdown as a result of hole trapping in oxide [19].

3.5. Stress immunity

The changes in C–V characteristics after plasma exposure are shown in Fig. 7 for a typical sample without nitrogen plasma exposure and a sample subjected to 30 s exposure. The C–V curve for the untreated sample exhibits significant distortion under stress. It is likely that the lower stress immunity, which may be due to distortion of the band structure of the thermally-grown oxynitride film, is dependent on plasma exposure time. The improved C–V characteristics after

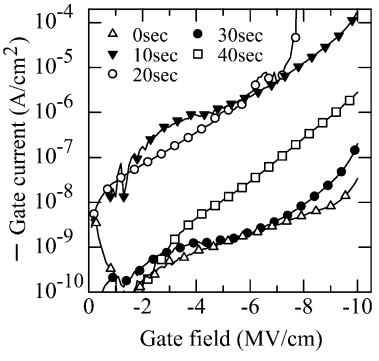

Fig. 6. I–V characteristics for various nitrogen plasma exposure times.

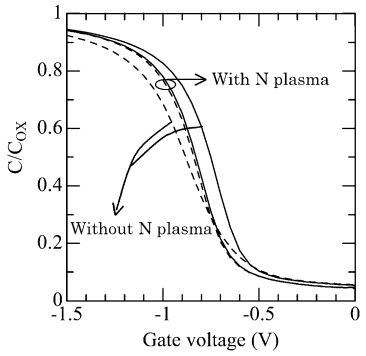

Fig. 7. 1 MHz C–V curves before and after electrical stress; dashed lines, measured curves after five cycles of sweep from 0 to -10 MV/cm.

30 s plasma exposure can be explained in terms of a strain reduction as nitrogen is incorporated in the film near the interface region. It can be concluded that nitrogen plasma exposure for 30 s can also improve the stress immunity of oxynitrides grown by this method. Lu et al. [20] attributed such a reduction to the formation of Si_3N_4, which functions as a buffer layer and consequently reduces the stress caused by high Si lattice mismatch between the bulk Si and subsequent oxide layers.

4. Conclusion

The experimental results show that plasma exposure time strongly influences the electrical properties of oxynitride films. Electrically stable SiON/Si interfaces with low defect-charge densities of the order of 7×10^{10} eV^{-1} cm^{-2} and high breakdown strength can be obtained after 30 s of plasma exposure. However, longer exposure time exceeding 30 s may result in degraded oxynitride properties, such as increased trap density and low breakdown strength. There is evidence that the excess leakage current is directly proportional to positive oxide charge. The preliminary results obtained in this study indicate that these nitrided films can be considered as potential candidates for ultrathin gates and dynamic random access memory (DRAM) insulators for very large scale integration devices.

References

[1] T. Hori, H. Iwasaki, IEEE Electron. Device Lett. 10 (1989) 64.
[2] T. Itoh, T. Nakamura, H. Ishikawa, IEEE Trans. Electron. Device 29 (1982) 498.
[3] Y. Okamoto, S. Kimura, F. Oka, S. Tsuchiya, H. Ikoma, J. Appl. Phys. 83 (1998) 7685.
[4] T.D.M. Salgado, F.C. Stedile, C. Krug, I.J.R. Baumvol, C. Radtke, Nucl. Instrum. Methods Phys. Res. B 148 (1–4) (1999) 252.
[5] A. Ikeda, M. Abd Elnaby, T. Fujimura, R. Hattori, Y. Kuroki, in: N. Mastorakis (Ed.), Advances in Physics, Electronics and Signal Processing Applications, Electrical and Computer Engi-

Seoul Semiconductor, Exhibit 2001
LGI v. SSC, IPR2019-01154

APPENDIX P

neering International Reference Book SeriesWorld Scientific and Engineering Society Press, Athens, 2000, p. 178.
[6] A. Uchiyama, H. Fukuda, T. Hayashi, T. Iwabuchi, S. Ohno, Proceedings of IEEE Int. Electron. Devices Meeting (1990) 425.
[7] T. Arakawa, R. Matsumoto, A. Kita, Jpn. J. Appl. Phys. 35 (1996) 1491.
[8] D. Kapila, S. Hattangady, M. Douglas, R. Kraft, M. Gribelyuk, J. Electrochim. Soc. 146 (1999) 1111.
[9] A. Paskaleva, E. Atanassova, Solid State Electron. 42 (1998) 777.
[10] G.J. Dunn, J. Appl. Phys. 65 (1989) 4879.
[11] M. Kuhn, Solid State Electron. 13 (1970) 873.
[12] C.T. Sah, Solid State Electron. 33 (1990) 147.
[13] Y. Ma, G. Lucovsky, J. Vac. Sci. Technol. B 12 (1994) 2504.
[14] M.V. Fischetti, J. Appl. Phys. 52 (1984) 575.
[15] R.P. Vasquez, A. Madhukar, Appl. Phys. Lett. 47 (1985) 998.
[16] D. Landheer, Y. Tao, D.X. Xu, G.I. Sproule, J. Appl. Phys. 78 (1995) 1818.
[17] K.S. Krisch, C.G. Sodini, J. Appl. Phys. 76 (1994) 2284.
[18] S. Manzini, F. Volonte, J. Appl. Phys. 58 (1985) 4300.
[19] S. Holland, C. Hu, J. Electrochem. Soc. 133 (1986) 1705.
[20] Z.H. Lu, R.J. Hussey, M.J. Graham, R. Gao, S.P. Tay, J. Vac. Sci. Technol. B 14 (1996) 2882.

Seoul Semiconductor, Exhibit 2001
LGI v. SSC, IPR2019-01154

APPENDIX Q

US006797650B1

(12) **United States Patent**
Wang et al.

(10) **Patent No.: US 6,797,650 B1**
(45) **Date of Patent: Sep. 28, 2004**

(54) **FLASH MEMORY DEVICES WITH OXYNITRIDE DIELECTRIC AS THE CHARGE STORAGE MEDIA**

(75) Inventors: **Zhigang Wang**, Santa Clara, CA (US); **Nian Yang**, San Jose, CA (US); **John Jianshi Wang**, San Jose, CA (US); **Jiang Li**, San Jose, CA (US)

(73) Assignee: **Advanced Micro Devices, Inc.**, Sunnyvale, CA (US)

(*) Notice: Subject to any disclaimer, the term of this patent is extended or adjusted under 35 U.S.C. 154(b) by 0 days.

(21) Appl. No.: **10/342,032**

(22) Filed: **Jan. 14, 2003**

(51) **Int. Cl.**[7] **H01L 21/31**
(52) **U.S. Cl.** **438/786**; 438/769
(58) **Field of Search** 438/769, 786

(56) **References Cited**

U.S. PATENT DOCUMENTS

4,725,560	A	*	2/1988	Abernathey et al.	438/394
4,871,689	A	*	10/1989	Bergami et al.	438/427
5,455,204	A		10/1995	Dobuzinsky et al.	
5,455,453	A	*	10/1995	Harada et al.	257/675
5,656,837	A		8/1997	Lancaster et al.	
5,768,192	A		6/1998	Eitan	
5,789,776	A		8/1998	Lancaster et al.	
6,171,947	B1	*	1/2001	Pangrle et al.	438/624
6,440,797	B1	*	8/2002	Wu et al.	438/261
6,445,030	B1		9/2002	Wu et al.	
6,465,303	B1		10/2002	Ramsbey et al.	
6,465,306	B1		10/2002	Ramsbey et al.	
2002/0019085	A1	*	2/2002	Chen et al.	438/197

* cited by examiner

Primary Examiner—Allan R. Wilson
(74) *Attorney, Agent, or Firm*—Eschweiler & Associates, LLC

(57) **ABSTRACT**

One aspect of the invention relates to flash memory device that stores charge in a substantially stoichiometric silicon oxynitride dielectric. A stoichiometric silicon oxynitride dielectric can be represented by the formula $(Si_3N_4)_x(SiO_2)_{(1-x)}$, where x is from 0–1. A substantially stoichiometric silicon oxynitride dielectric has relatively few atoms that do not fit into the foregoing formula. The flash memory devices of the present invention have fewer defects and lower leakage than comparable SONOS-type flash memory devices. Another aspect of the invention relates to assessing the stoichiometry by FTIR, refractive index measurement, or a combination of the two.

22 Claims, 4 Drawing Sheets

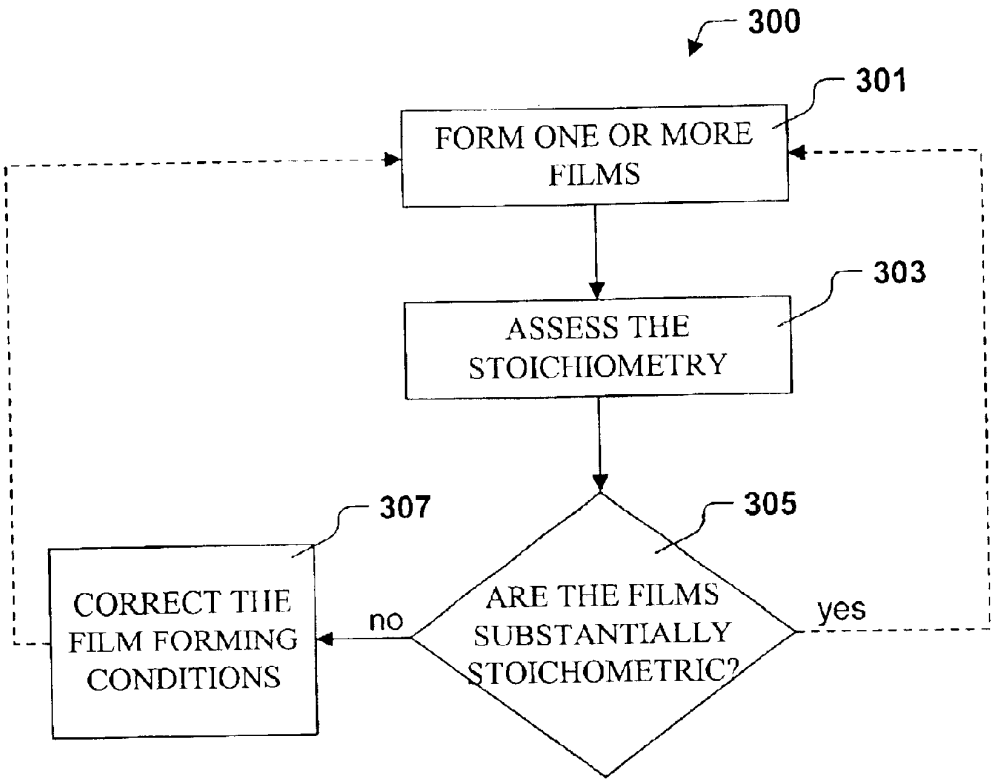

Seoul Semiconductor, Exhibit 2001
LGI v. SSC, IPR2019-01154

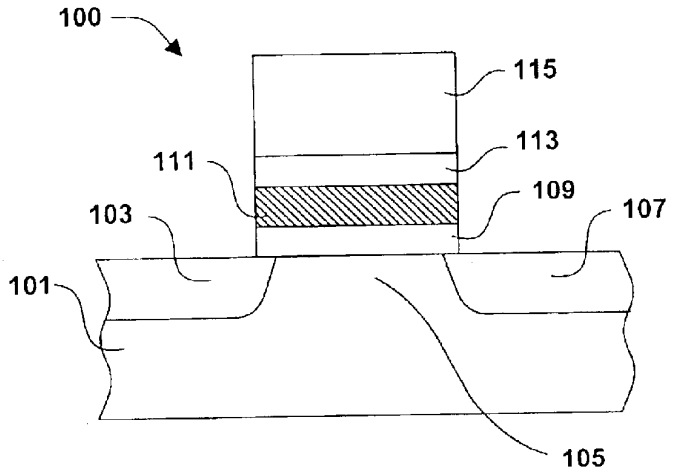

FIGURE 1

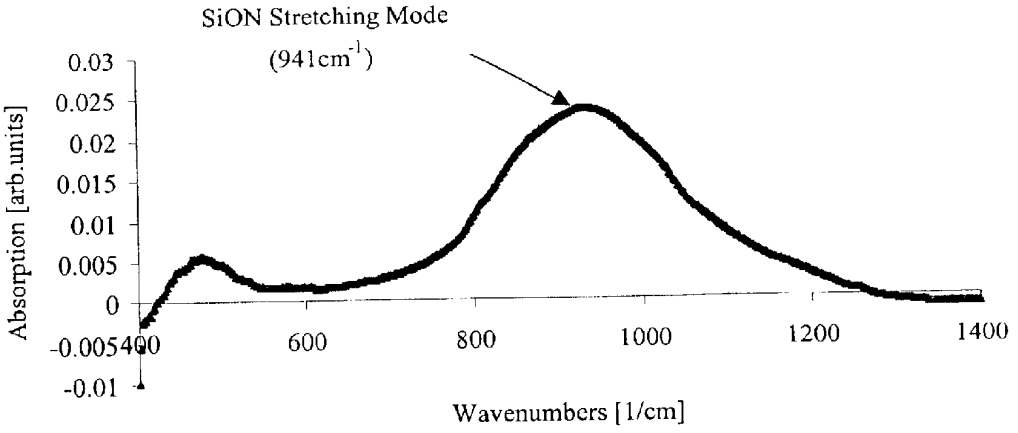

FIGURE 2

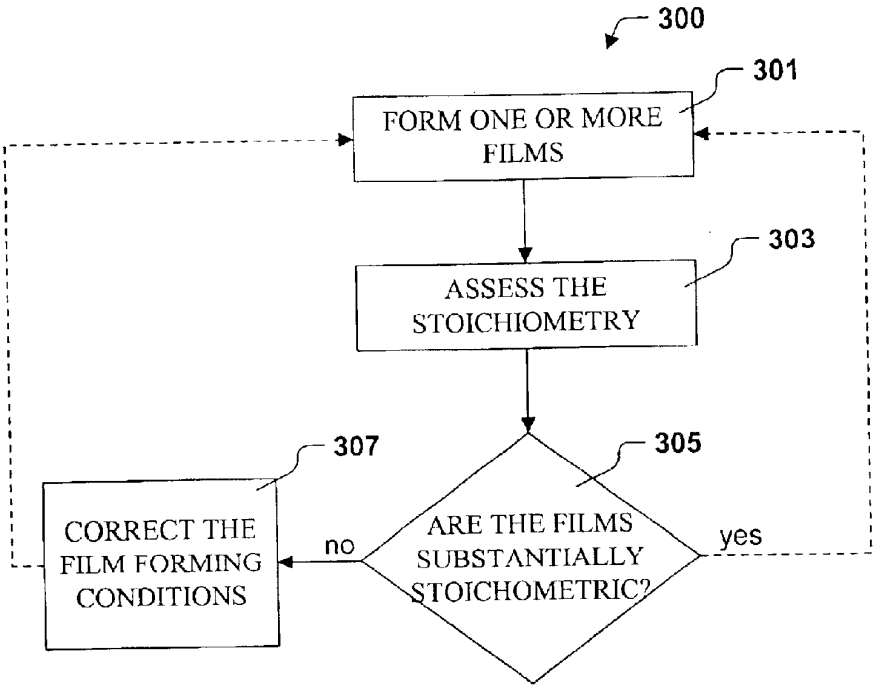

FIGURE 3

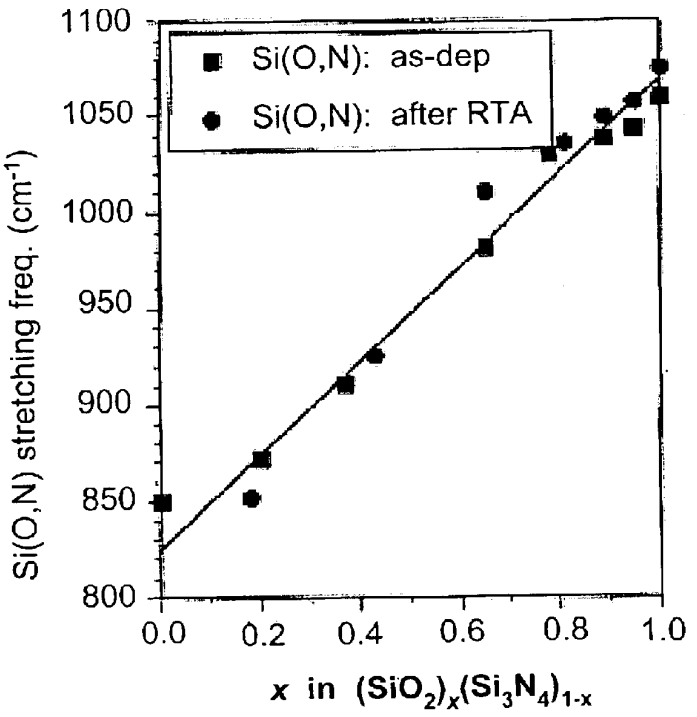

FIGURE 4

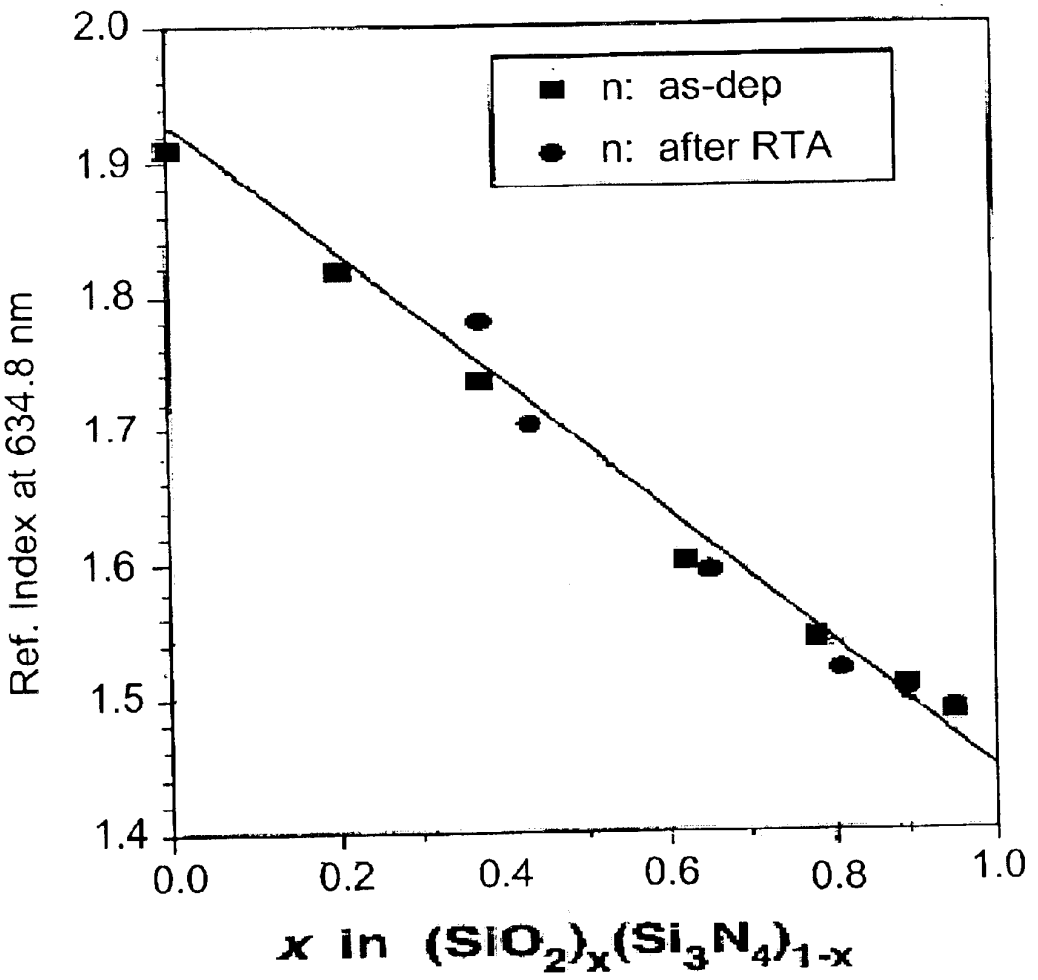
n: as-dep
n: after RTA
Ref. Index at 634.8 nm
2.0
1.9
1.8
1.7
1.6
1.5
1.4
0.0
0.2
0.4
0.6
0.8
1.0
x in $(SiO_2)_x(Si_3N_4)_{1-x}$

FIGURE 5

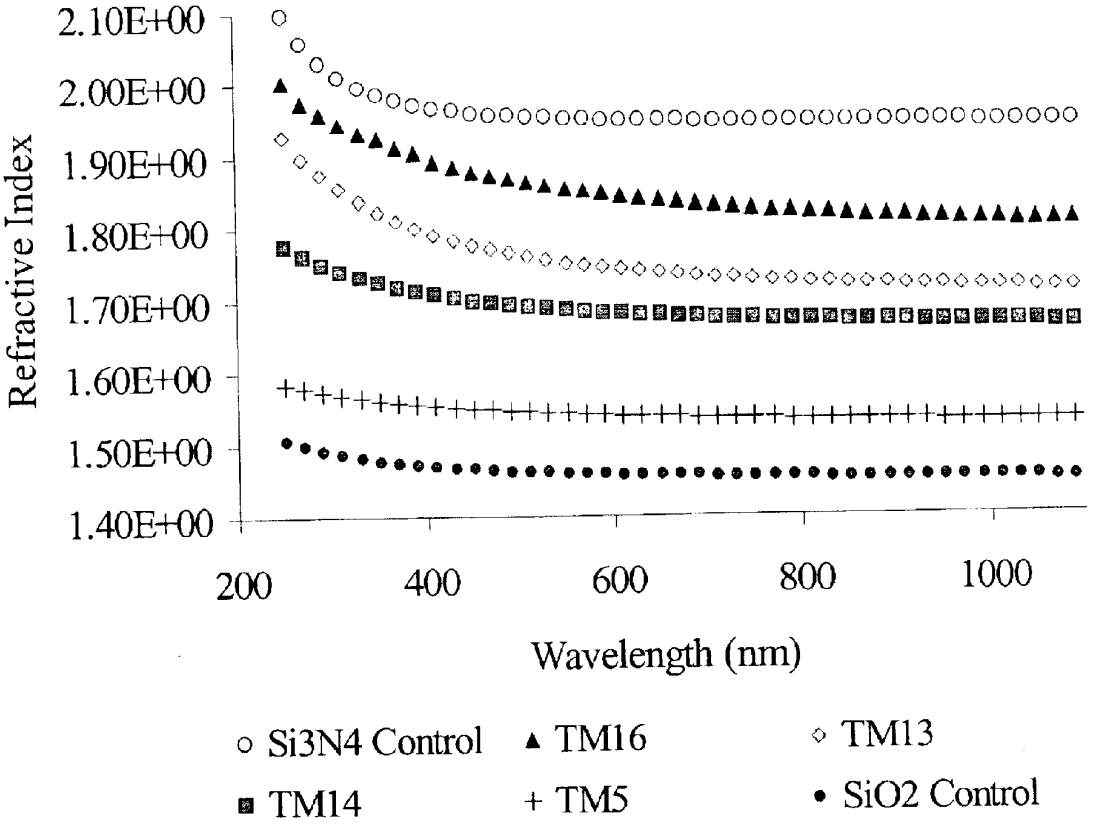
2.10E+00
2.00E+00
1.90E+00
1.80E+00
1.70E+00
1.60E+00
1.50E+00
1.40E+00
Refractive Index
200
400
600
800
1000
Wavelength (nm)
Si3N4 Control
TM16
TM13
TM14
TM5
SiO2 Control

FIGURE 6

FLASH MEMORY DEVICES WITH OXYNITRIDE DIELECTRIC AS THE CHARGE STORAGE MEDIA

TECHNICAL FIELD OF THE INVENTION

The present invention relates generally to semiconductor devices and more particularly to flash memory.

BACKGROUND OF THE INVENTION

There has long been a demand for small, portable personal devices. These devices include cellular phones, personal computing equipment, and personal sound systems, which are sought in continuously smaller sizes and with continuously lower power requirements. At the same time that smaller and more portable devices are sought, computational power and on-chip memory requirements are increasing. In light of these requirements, there has been a long-felt need for computational devices that have substantial memory and logic functions integrated within individual semiconductor chips. Preferably, the memory is configured such that if power is interrupted, as when a battery fails, the contents of the memory are retained. Memory that retains its content without a continuous supply of power is called non-volatile memory. Non-volatile memory types include, for example, electrically erasable, programmable read only memory (EEPPROM) and flash EEPROM. The term "flash" refers to the ability of the memory to be erased in blocks. Flash memory devices store electrical charge, representing data, in transistors having either a floating gate or a charge-trapping dielectric.

Conventional flash memory uses a floating gate. A floating gate memory cell characteristically includes a vertical stack of a tunnel oxide, a first polysilicon layer (the floating gate), an ONO tri-layer (silicon oxide, silicon nitride, silicon oxide) interlevel dielectric, and a second polysilicon layer (control gate) over the interlevel dielectric. Thus, the conductive floating gate is sandwiched between two dielectrics.

A floating gate memory cell can be programmed by inducing hot electron injection from a portion of the substrate, such as the channel near a drain region, to the floating gate. Typically, a source region and a bulk portion of the substrate are grounded while a relatively high positive voltage is applied to the control gate. A moderate positive voltage is applied to the drain region causing electrons to flow from source to drain. Near the drain, "hot" (high energy) electrons form and are attracted into the floating gate by the electric field from the control gate. After sufficient negative charge accumulates in the floating gate, the floating gate raises the threshold voltage of the memory cell and inhibits current flow through the channel region during subsequent "read" operations. The magnitude of the current when read voltages are applied to the gates is used to determine whether or not a flash memory cell is programmed.

The act of discharging a flash memory cell is called the erase function. For a floating gate memory cell, the erase function is typically carried out by inducing Fowler-Nordheim tunneling between the floating gate and the source region of the transistor (source erase or negative gate erase) or between the floating gate and the substrate (channel erase). A source erase operation is induced by applying a high positive voltage to the source region and a 0 V to the control gate and the substrate while floating the drain region.

An alternative to floating gate flash memory is SONOS-type flash memory. SONOS-type flash memory cells are

constructed with a charge trapping dielectric layer, typically a silicon nitride layer, separated from the channel by a tunnel oxide, typically silicon dioxide. A control gate layer is formed over the charge trapping layer, and is optionally separated from the charge trapping layer by another dielectric layer, also typically silicon dioxide. The charge trapping layer holds charge, which represents data. Electrical charge is trapped within the layer locally near whichever side of the transistor is used as a drain in programming the cell. By reading in the opposite direction of programming, the presence or absence of charge at either side can be separately detected, whereby two bits of data can be stored per cell. Thus, a SONOS-type cell can be described as a two-transistor cell, or two-bit per cell architecture. If multi-level is used, then four or more bits per cell can be stored.

Storing two or more bits per cell provides a way of achieving high memory density.

Both bits of a SONOS-type memory cell are programmed in a conventional manner, such as hot electron programming. The right bit can be programmed by applying programming voltages to the gate and the drain while the source is grounded or at a lower voltage. Hot electrons are accelerated sufficiently so that they are injected into a region of the charge trapping dielectric layer near the drain. To read the device in the opposite direction from which it is written, voltages are applied to the gate and the source while the drain is grounded or at a lower voltage. The left bit is similarly programmed and read by swapping the functionality of source and drain terminals. Programming and reading one of the bits generally leaves the other bit with its information intact.

Reading in the reverse direction is most effective when relatively low gate voltages are used. A benefit of utilizing relatively low gate voltages in combination with reading in the reverse direction is that a relatively small trapped charge region, which affects the potential in the channel only beneath that region, is sufficient to significantly alter the potential drop needed for current to flow through the channel. Less charge needs to be stored, which permits much shorter programming times.

SONOS-type memory devices offer additional advantages as well. In particular, the erase mechanism of the memory cell is greatly enhanced. Both bits of the memory cell can be erased by applying suitable erase voltages to the gate and the drain for the right bit and to the gate and the source for the left bit. Another advantage is that SONOS-type memory cells undergo less wear from cycling and thus have greater longevity.

A potential disadvantage of SONOS-type memory is the length of time over which SONOS-type memory holds charge without power. In a typical SONOS-type memory cell, charge is gradually lost, most likely through pinhole defects in the silicon nitride film. There is an unsatisfied need for flash memory that has high density and can hold charge over more extended periods of time without power.

SUMMARY OF THE INVENTION

The following presents a simplified summary of the invention in order to provide a basic understanding of some of its aspects. This summary is not an extensive overview of the invention and is intended neither to identify key or critical elements of the invention nor to delineate its scope. The primary purpose of this summary is to present some concepts of the invention in a simplified form as a prelude to the more detailed description that is presented later.

One aspect of the invention relates to flash memory devices that store charge in a substantially stoichiometric

silicon oxynitride dielectric. A stoichiometric silicon oxynitride dielectric can be represented by the formula $(Si_3N_4)x(SiO_2)_{(1-x)}$, where x is from 0–1. A substantially stoichiometric silicon oxynitride dielectric has relatively few atoms that do not fit into the foregoing formula. The flash memory devices of the present invention have fewer defects and lower leakage than comparable SONOS-type flash memory devices.

Another aspect of the invention relates to a process of forming a substantially stoichiometric silicon oxynitride layer for a flash memory device. The process involves assessing the stoichiometry and adjusting process conditions as needed to improve stoichiometry. In one embodiment, the stoichiometry is assessed from an FTIR spectrum. In another embodiment, the stoichiometry is assessed by measuring the refractive index at two or more wavelengths.

Other advantages and novel features of the invention will become apparent from the following detailed description of the invention and the accompanying drawings. The detailed description of the invention and drawings provide exemplary embodiments of the invention. These exemplary embodiments are indicative of but a few of the various ways in which the principles of the invention can be employed.

BRIEF DESCRIPTION OF THE DRAWINGS

FIG. **1** is a schematic illustration of SONOS-type memory cell.

FIG. **2** is an FTIR spectrum of a silicone oxynitride film.

FIG. **3** is a flow chart of a process according to one aspect of the present invention.

FIG. **4** is a plot of the Si—(O,N) stretching peak position as a function of the silicon nitride mole fraction in a silicon oxynitride film.

FIG. **5** is a plot of the relationship between refractive index at 634.8 nm and mole fraction silicon nitride in a silicon oxynitride film.

FIG. **6** is a plot of refractive index versus wavelength for silicon oxynitride films of varying composition.

DETAILED DESCRIPTION OF THE INVENTION

The present invention will now be described with reference to the drawings. FIG. **1** is a schematic illustration of SONOS-type memory cell **100** according to one aspect of the present invention. Memory cell **100** includes a substrate **101**, in which is formed a first source/drain region **103**, a channel region **105**, and a second source/drain region **107**. Over the substrate are formed a tunnel oxide **109**, a silicon oxynitride charge trapping dielectric **111**, an optional interlevel dielectric **113**, and a control gate **115**.

The substrate **101** comprises a semiconductor, typically silicon. Other examples of semiconductors include GaAs and InP. In addition to a semiconductor, the substrate may include various elements therein and/or layers thereon. These can include metal layers, barrier layers, dielectric layers, device structures, silicon gates, word lines, source regions, drain regions, bit lines, conductive lines, and conductive vias.

The first and second source/drain regions, **103** and **107**, and the channel region **105**, are generally formed by ion implantation of dopants into the substrate **101**. The channel can be doped either p-type or n-type, but is typically p-type. The source/drain regions **103** and **107** are doped to an opposite conductivity type.

The tunnel oxide **109** is formed over the channel region. The thickness of the tunnel oxide depends in part on the size of the memory cells being formed, the thickness being less when smaller memory cells are desired. In one embodiment, the tunnel oxide is about 30 Angstroms to about 150 Angstroms thick. In another embodiment, the tunnel oxide is about 80 Angstroms to about 120 Angstroms thick. In a further embodiment, the tunnel oxide is about 100 Angstroms thick.

The term tunnel oxide has a functional definition according to its role as an insulating layer between the channel and the charge trapping dielectric. Generally a tunnel oxide is an oxide and is formed by oxidizing a silicon semiconductor surface. In general, however, the tunnel oxide can be any suitable insulating layer, including for example, a silicon rich silicon dioxide, an oxygen rich silicon dioxide, or a high-k dielectric.

Generally, the silicon oxynitride charge trapping dielectric **111** is sandwiched between the tunnel oxide **109** and an interlevel dielectric layer **113**. However, the interlevel dielectric layer **113** is optional. Where the interlevel dielectric layer **113** is provided, it is generally a CVD deposited silicon dioxide or similar layer and can have a thickness comparable to that of the tunnel oxide layer **109**.

The control gate **115** is generally a polysilicon layer and may also form part of a word line. The control gate is typically several thousand Angstroms thick. The silicon oxynitride charge trapping dielectric **113** can be of any suitable thickness. A somewhat thicker silicon oxynitride film may be required to achieve the same performance as a pure silicon nitride film. In one embodiment, the silicon oxynitride is about 75 Angstroms to about 300 Angstroms thick. In another embodiment, the silicon oxynitride is about 100 Angstroms to about 225 Angstroms thick. In a further embodiment, the silicon oxynitride is about 110 Angstroms to about 150 Angstroms thick.

The silicon oxynitride charge trapping dielectric **113** can contain any suitable silicon oxide to silicon nitride ratio. In one embodiment, the dielectric layer **113** is from about 20 to about 95% silicon nitride on a mole basis. In another embodiment it is from about 40 to about 90% silicon nitride. In a further embodiment, it is from about 60 to about 80% silicon nitride. It has been appreciated by the inventors of the present invention that the silicon oxynitride dielectric **113** has fewer intrinsic defects then a pure silicon nitride dielectric, and is expected to hold charge for longer periods of time, thereby improving device reliability.

The silicon oxynitride charge trapping dielectric **113** can be further characterized as being a substantially stoichiometric combination of silicon oxide and silicon nitride. A substantially stoichiometric combination has a ratio of atoms substantially in accordance with the formula $(Si_3N_4)_x(SiO_2)_{(1-x)}$, where x is from 0–1.

Silicon oxynitride films formed without measuring the stoichiometry of films and correcting process conditions accordingly are generally not stoichiometric. It has been appreciated by the inventors of the present invention that a silicon oxynitride film that is substantially stoichiometric advantageously has fewer defects than a silicon oxynitride film that is not and holds charge longer.

A substantially stoichiometric silicon oxynitride film can be represented by the formula $\zeta_y((Si_3N_4)_x(SiO_2)_{(1-x)})_{1-y}$, where y is minimized and ζ represents all atoms that cannot be fit to the formula $(Si_3N_4)_x(SiO_2)_{(1-x)}$. In one embodiment, y is about 0.3 or less. In another embodiment, y is about 0.1 or less. In a further embodiment, y is about 0.05 or less.

According to another aspect of the invention, the substantially stoichiometric silicon oxynitride film is characterized

by a low ratio of Si—H and N—H bonds to Si—O and Si—N bonds. FIG. **2** provides a the FTIR (Fourier transform infra-red) spectrum of a silicon oxynitride film. The relatively large peak around 900 results from Si—O and Si—N bonds. The relatively small peak around 450 results from Si—H bonds. If there were a significant number of N—H bonds, there would be another peak around 1300. Without process control, there is generally a moderate sized peak either at 450 (Si—H) or 1300 (N—H).

The ratio of the areas under the Si—H and the N—H peaks to the area under the Si—(O,N) peak can be used to approximate the ratio of Si—H and N—H bonds to Si—O and Si—N bonds. In one embodiment, this ratio is about 1:15 or less. In another embodiment, it is about 1:40 or less. In a further embodiment, it is about 1:100 or less.

FIG. **3** illustrates a process **300** according to a further aspect of the invention for obtaining a substantially stoichiometric silicon oxynitride film. Process **300** can be a development process, used to find conditions that are applied to many batches without change, or a type of process control, used to continuously modify conditions from batch to batch. Although the method **300** is illustrated and described hereinafter as a series of acts or events, it will be appreciated that the present invention is not limited by the illustrated ordering of such acts or events. For example, some acts may occur in different orders and/or concurrently with other acts or events apart from those illustrated and/or described herein, in accordance with the invention. In addition, not all illustrated steps may be required to implement a methodology in accordance with the present invention. Furthermore, the method according to the present invention may be implemented in association with the apparatus and systems illustrated and described herein as well as in association with other apparatus or systems not illustrated.

Process **301** includes forming a film (or series of films), act **301**, assessing the stoichiometry obtained, act **303**, determining whether the films are substantially stoichiometric, act **305**, and selectively correcting process conditions as needed with act **307**.

While not strictly required, process **300** can, and generally does, incorporate actions for obtaining a film with a desirable silicon oxide to silicon nitride ratio. In particular, when the stoichiometry of the film is assessed with act **303**, the oxide to nitride ratio is generally also assessed. The film forming conditions are corrected in act **307**, as necessary, to achieve a desired silicon oxide to silicon nitride ratio as well as to achieve a substantially stoichiometric film.

One method of assessing the silicon oxide to silicon nitride ratio is FTIR. FIG. **4** is a plot of the Si—(O,N) stretching peak position as a function of the silicon nitride mole fraction in a silicon oxynitride coating. There is a substantially linear relationship between the mole fraction and the peak position.

Another method of assessing the silicon oxide to silicon nitride ratio is a refractive index analysis. FIG. **5** shows the relationship between the refractive index of a silicon oxynitride film at 634.8 nm and mole fraction silicon nitride. The refractive index varies with mole fraction and this relationship is also substantially linear.

The stoichiometry of the film can be assessed by any suitable method. One option uses FTIR and looks at the size of peaks corresponding to hydrogen bonds. A peak around 450 cm^{-1} reflect the presence of Si—H bonds. A peak around 1300 cm^{-1} reflects the presence of N—H bonds. Another method is to use two methods to assess the silicon oxide to silicon nitride ratio. If both methods are calibrated using stoichiometric films, a disparity between the two assessments is indicative of a non-stoichiometric film. The two methods can be, for example, FTIR and refractive index measurement, or the refractive index measured at two different wavelengths. A related third method looks at the shape of the refractive index versus wavelength curve. For a substantially stoichiometric film, the refractive index has little dependence on wavelength. For films that are not substantially stoichiometric, the refractive index generally shows a sharp rise as wavelengths approach **200** as illustrated by the curves labeled Si_3N_4, TM**16**, and TM**13** in FIG. **6**.

The stoichiometry is used to selectively modify silicon oxynitride film forming conditions with acts **305** and **307**. The conditions apply to a process of forming films used in act **301**. Any suitable process can be used. An exemplary process is remote plasma deposition.

Remote plasma deposition involves flowing gases through a chamber containing the substrate(s) on which the film is to be deposited. In one part of the chamber, the gases are ionized. Ionized gas convects and diffuses to substrate surfaces on which the ionized gas deposit to form the film.

Generally, three source gases are used to deposit a silicon oxynitride film: A silicon source gas, an oxygen source gas, and a nitrogen source gas. The silicon source gas contains a silicon compound, such as SiH_4. Additional examples of silicon compounds include halosilanes and silanes, such as SiF_4, $SiCl_4$, $SiCl_3H$, $SiCl_2H_2$, $SiClH_3$, alkyl silanes, siloxanes, silanols, and silazanes. The oxygen source gas contains an oxygen compound, such as O_2, O_3, N_2O, NO, or NO_2. The nitrogen source gas contains a nitrogen compound such as N_2 or NH_3.

As a rule, oxygen compounds deposit preferentially over nitrogen compounds. To achieve a balance between the deposition rates, the oxygen concentration in the gas is kept low. The concentrations are controlled through the feed gas flow rates (and to a lesser extent, the exhaust gas flow rate). Due to the high reaction rate of oxygen compounds and the limited precision of flow control devices, the oxygen compound is generally diluted in the feed. In a preferred embodiment, the silicon source gas is SiH_4, the oxygen source gas is 1% N_2O in N_2, and the nitrogen source gas is N_2. As an example, these gases can be provided in a ratio of 1:10:10. Other process conditions for this example are 300 mTorr pressure, 300° C. temperature, and 300 Watts of power to ionize the gases. Due to variations among deposition chambers and substrates, some adjustment of these conditions may be required.

The flow rate ratio between the nitrogen source gas and the oxygen source gas can be adjusted as needed to achieve a desired silicon nitride to silicon oxide ratio. Increasing the flow rate of the nitrogen source gas relative to the oxygen source gas increases the silicon nitride fraction. Decreased the flow rate of the nitrogen source gas relative to the oxygen source gas decreases the silicon nitride fraction.

The stoichiometry of the film is improved by adjusting the ratio of the silicon source gas to the other gases. For example, when an FTIR spectrum shows a significant peak near 450, reducing the silicon source gas flow rate will reduce the size of the peak in further samples. When an FTIR spectrum shows a significant peak near 1300, increasing the silicon source gas flow rate will reduce the size of the peak and improve the stoichiometry.

Although the invention has been shown and described with respect to certain embodiments, alterations and modifications providing equivalent structures and acts are likely

to occur to those of ordinary skill in the art upon the reading and understanding this specification and the associated drawings. Such alterations and modifications are intended to fall within the scope of the present invention, unless expressly stated to the contrary, Components described in functional terms have structure and involve acts, unless otherwise indicated, corresponding to any of the devices and methods known to those of ordinary skill in the art to perform those functions, even though not equivalent to any of the structures and acts that perform those function in the exemplary embodiments of the invention. In addition, while a particular feature of the invention may have been disclosed with respect to only one of several embodiments, such feature may be combined with one or more other features of the other embodiments as may be desired or advantageous for a given or particular application.

What is claimed is:

1. A method of manufacturing flash memory devices having a silicon oxynitride charge trapping dielectric, comprising:

forming a first silicon oxynitride coating using a first set of processing conditions, wherein the first silicon oxynitride coating is represented by the formula $\zeta_y((Si_3N_4)_x(SiO_2)_{(1-x)})_{1-y}$ wherein ζ represents all atoms that cannot be fit into the formula $(Si_3N_4)_x(SiO_2)_{(1-x)}$;

assessing a stoichiometry of the silicon oxynitride by determining a first value of y in the formula $\zeta_y((Si_3N_4)_x(SiO_2)_{(1-x)})_{1-y}$;

selectively adjusting the first set of processing conditions to provide a second set of processing conditions that are directed towards obtaining a more stoichiometric silicon oxynitride having a value of y in the formula $\zeta_y((Si_3N_4)_x(SiO_2)_{(1-x)})_{1-y}$ that is lower than the first value of y; and

forming a second silicon oxynitride coating using the second set of processing conditions.

2. The method of claim **1**, wherein selectively adjusting the first set of processing conditions to provide a second set of processing conditions comprises developing a process for manufacturing a silicon oxynitride coating in flash memory devices to obtain a more stoichiometric silicon oxynitride using the second set of processing conditions.

3. The method of claim **1**, wherein forming a second silicon oxynitride coating using the second set of processing conditions comprises controlling a process for manufacturing the second silicon oxynitride coating in flash memory devices using the second set of processing conditions.

4. The method of claim **1**, wherein assessing the stoichiometry of the silicon oxynitride comprises determining a silicon oxide to silicon nitride ratio of the first silicon oxynitride using FTIR.

5. The method of claim **4**, wherein the first silicon oxynitride contains hydrogen and the process conditions are selectively adjusted to provide less hydrogen in the second silicon oxynitride.

6. The method of claim **1**, wherein assessing the stoichiometry of the silicon oxynitride comprises measuring a refractive index of the first silicon oxynitride at two or more wavelengths.

7. The method of claim **6**, wherein the first silicon oxynitride contains hydrogen and the process conditions are selectively adjusted to provide less hydrogen in the second silicon oxynitride.

8. The method of claim **1**, further comprising assessing the ratio between silicon oxide and silicon nitride in the first silicon oxynitride.

9. The method of claim **8**, wherein the second set of processing conditions are further directed towards obtaining a silicon oxynitride having a silicon oxide to silicon nitride ratio closer to a predetermined silicon oxide to silicon nitride ratio than the first silicon oxynitride.

10. The method of claim **1**, wherein assessing the stoichiometry of the silicon oxynitride comprises:

assessing a first silicon oxide to silicon nitride ratio of the silicon oxynitride using an FTIR technique; and

assessing a second silicon oxide to silicon nitride ratio of the silicon oxynitride using a refractive index technique;

wherein selectively adjusting the first set of processing conditions to provide a second set of processing conditions comprises adjusting the first set of processing conditions if a disparity exists between the first and second ratios.

11. A method of manufacturing a flash memory device, comprising:

forming a silicon oxynitride film over a semiconductor substrate using remote plasma deposition, wherein the silicon oxynitride film serves as a charge trapping dielectric;

forming a gate over the silicon oxynitride film; and

forming source/drain regions in the semiconductor substrate and defining a channel therebetween, wherein the channel resides under the silicon oxynitride film and the gate,

wherein the silicon oxynitride charge trapping dielectric has silicon-oxygen, silicon-nitrogen, and silicon-hydrogen bonds, and wherein a ratio of silicon-hydrogen bonds to combined silicon-oxygen and silicon-nitrogen bonds is 1:15 or less.

12. The method of claim **11**, wherein the ratio is 1:50 or less.

13. The method of claim **11**, wherein the ratio is 1:100 or less.

14. A method of manufacturing a flash memory device, comprising:

forming a silicon oxynitride film over a semiconductor substrate, wherein the silicon oxynitride film serves as a charge trapping dielectric;

forming a gate over the silicon oxynitride film; and

forming source/drain regions in the semiconductor substrate and defining a channel therebetween, wherein the channel resides under the silicon oxynitride film and the gate,

wherein the silicon oxynitride charge trapping dielectric has a silicon nitride content of about 20% or more and about 95% or less on a mole basis.

15. The method of claim **14**, wherein the silicon oxynitride charge trapping dielectric has a silicon nitride content of about 40% or more and about 90% or less on a mole basis.

16. The method of claim **14**, wherein the silicon oxynitride charge trapping dielectric has a silicon nitride content of about 60% or more and about 80% or less on a mole basis.

17. A method of manufacturing a flash memory device, comprising:

forming a silicon oxynitride film over a semiconductor substrate, wherein the silicon oxynitride film serves as a charge trapping dielectric;

forming a gate over the silicon oxynitride film; and

forming source/drain regions in the semiconductor substrate and defining a channel therebetween, wherein the channel resides under the silicon oxynitride film and the gate,

wherein the silicon oxynitride charge trapping dielectric is represented by the formula $\zeta_y((Si_3N_4)_x(SiO_2)_{(1-x)})_{1-y}$, wherein ζ represents all atoms that cannot be fit to the formula $(Si_3N_4)_x(SiO_2)_{(1-x)}$, and wherein y is about 0.3 or less.

18. The method of claim **17**, wherein y is about 0.1 or less.

19. The method of claim **17**, wherein y is about 0.05 or less.

20. A method of manufacturing a flash memory device, comprising:

forming a silicon oxynitride film over a semiconductor substrate, wherein the silicon oxynitride film serves as a charge trapping dielectric;

forming a gate over the silicon oxynitride film; and

forming source/drain regions in the semiconductor substrate and defining a channel therebetween, wherein the channel resides under the silicon oxynitride film and the gate,

wherein the silicon oxynitride charge trapping dielectric has a ratio of Si—H and N—H bonds to Si—O and Si—N bonds of about 1:15 or less.

21. The method of claim **20**, wherein the ratio of Si—H and N—H bonds to Si—O and Si—N bonds in the silicon oxynitride charge trapping dielectric is about 1:40 or less.

22. The method of claim **20**, wherein the ratio of Si—H and N—H bonds to Si—O and Si—N bonds in the silicon oxynitride charge trapping dielectric is about 1:100 or less.

* * * * *

APPENDIX R

ıced

Network access provided by: Georgia Institute of Technology

Issue 28, 2012

Previous Next

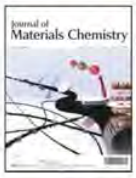

From the journal:
Journal of Materials Chemistry

Highly porous TiO_2 films for dye sensitized solar cells

Antonio Tricoli,*[a] Anna S. Wallerand[a] and Marco Righettoni[a]

Author affiliations

Abstract

Highly porous nanoparticle films were investigated as alternative working electrode morphology for the synthesis of dye sensitized solar cells (DSSCs). These films were rapidly assembled by flame synthesis and direct aerosol deposition of TiO_2 nanoparticles with high specific surface area. Structural–functional analysis of their properties revealed that the film porosity is a key parameter greatly determining the resulting energy conversion efficiency (η). In fact, aerosol deposition at low substrate temperatures (~100 °C) led to very high porosity (ε = 98%) and weak film cohesion. These films were easily resuspended upon immersion in the dye and/or electrolyte solutions resulting in very poor performances (η = 0.08%). In contrast, allowing for partial nanoparticle sintering by deposition at moderate temperatures (~400 °C) decreased the film porosity from 98 to 95% leading to higher mechanical stability and partially preserving the large surface required for dye adsorption. As a result, these films had drastically higher current density (12.2 mA cm^{-2}) and overall performances (η = 5%) representing an 8 times improvement with respect to the best reported for similar highly porous morphologies. Remarkably, their conversion efficiency

decreased only slightly with increasing film thickness reaching 4.6% at 128 μm. This unique attribute suggests that high film porosity may inhibit recombination losses enabling utilization of thick films with enhanced light absorption properties.

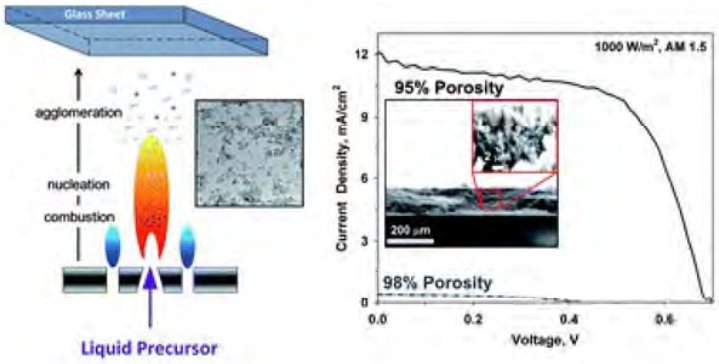

1. Introduction

Dye sensitized solar cells (DSSCs) are a promising technology for renewable energy harvesting that offer some advantages over heterojunction-based devices.[1,2] A key strength of DSSCs is the separation of electron generation and transport processes in two distinct materials.[2] This allows utilization of an optimized dye for photon absorption and of a wide bandgap semiconductor for electron–hole separation and collection.[1] The costs for the fabrication of such devices could reach a fraction of Si-based ones[3] as the semiconductor film is usually made of inexpensive TiO_2 nanoparticles that are already produced in large scale such as by flame synthesis.[4] These unique features have triggered considerable academic and industrial interest in DSSC technology resulting in the rapid development of sophisticated dyes[5,6] and semiconductor film morphologies.[7] However, the maximum solar energy conversion efficiency (~10.4%) of available DSSCs is still considerably below that of Si- (25%) or GaAs-based (26.1%) devices limiting their commercialization.[8]

Optimal engineering of the TiO_2 film morphology is mandatory for assembly of efficient DSSCs.[7] Best results have been achieved so far with inhomogeneous films made of transparent (d = 23 nm), scattering (d = 50 nm) and mixed (d = 23, 50 nm) TiO_2 nanoparticle layers.[7] Utilization of scattering nanoparticles was found to be a viable method to increase the optical film thickness[7,9] and thus to compensate for the poor light absorption of most

dyes in the red domain.[5] In contrast, attempts to increase light absorption by merely increasing the film thickness resulted in lower conversion efficiencies as, above an optimal thickness, electron–hole recombination losses are dominant.[7,10] For wet-made TiO_2nanoparticle films, an optimal thickness of 5–20 μm and porosity of 50–65% corresponding to a film mass density of 1–4 mg cm^{-2} have been reported.[11] Such sophisticated films, however, seem to suffer from fundamental limitations as scattering particles offer less surface for dyeadsorption and decrease incident photon to current efficiency (IPCE) at lower wavelengths (<650 nm).[7] In fact, further optimization of multi-layer film morphologies has not yet led to significant improvements of DSSC performances.[8,12]

To overcome these limitations several alternative morphologies (Table 1) have been proposed for the assembly of DSSC working electrodes including mesoporous,[8,13] granular nanoparticle[14] and nanowire films.[15] The latter have demonstrated to considerably reduce recombination losses owing to better electron transport properties but resulted in small energy conversion efficiencies[15] (1.5%) due to the small surface available for dye absorption.[15] Mesoporous TiO_2 films have demonstrated[13,16] very high open circuit voltage (V_{OC}) and fill factors (FFs) but relatively low current density and thus limited conversion efficiency (1.1–4.63%).[16] This was attributed to the rapid leveling off of efficiency gains with increasing film thickness[16] that may arise from the very small pore size and thus poor electrolyte ion exchange rates. In contrast, granular films made of transparent nanoparticles have very high porosity (≫65%) and offer high surface area for dyeadsorption.[14] These films have been successfully assembled by aerosol deposition of flame-made TiO_2nanoparticles and bear the potential to maximize light absorption by increasing drastically film roughness and thus dye loading.[14,17] However, first attempts to utilize such porous nanoparticle films as DSSC working electrodes have led to efficiencies below 1%.[14] Higher efficiencies were obtained only by sintering the nanoparticles into large columnar structures and thus drastically reducing porosity and surface area available for dyeadsorption.[18] These results are particularly surprising as high film porosities should enhance electrolyte ion exchange rates within the semiconductor film minimizing recombination losses and thus boosting conversion efficiencies.[10] Considering that highly porous nanoparticle films suffer from low mechanical stability,[19–21] optimization of their structural properties still bears the potential to improve considerably the resulting DSSC performance.

Table 1 Performances of alternative (DSSC) working electrode morphologies at 1 sun illumination[a]

Film morphology	Thickness δ (μm)	V_{OC} (V)	J_{SC} (mA cm^{-2})	FF (–)	Efficiency η (%)	Ref.
Porous granular TiO_2 NP	3.5	0.78	2.54	0.43	0.63	17
ZnO nanowires	18–24	0.71	5.85	0.38	1.5	15
Randomly oriented TiO_2 NP	18	0.79	~4.5	—	2.74	13
Mesoporous TiO_2	1	0.799	7	0.72	4.04	13
P25 NP	—	0.76	5.04	—	2.7	38
Highly porous TiO_2 NP	38	0.68	12.2	0.59	5.03	This work

a NP: nanoparticles.

Among several methods for the synthesis of highly porous nanoparticle films, flame spray pyrolysis of nanoparticles and direct deposition of the resulting aerosol have demonstrated potential for the assembly of gas sensors,[22,23] functional coatings[24] and phosphor screens.[25] The high production rate of spray flames results in highly concentrated aerosols granting short film assembly time[19,24] and low production costs.[4] Furthermore, deposition at low substrate temperatures (100–200 °C) leads to very high film porosities[19,26] (98%) granting high accessibility of the nanoparticles surface.[27] This enhances overall reaction rates resulting, for example, in highly sensitive metal-oxide gas sensors.[27] However,

increasing the mechanical stability of such films is mandatory for further handling.[19] This is also very challenging as high substrate temperatures (≫200 °C) can lead to multi-crystalline, gas tight domains and drastic drops in film porosity as observed for SnO_2[28] and TiO_2[18]nanoparticles.

Here, highly porous nanoparticle films have been investigated as alternative morphology for the assembly of DSSCs. First, crystalline TiO_2nanoparticles with high specific surface area have been produced by flame synthesis. Films were self-assembled by direct aerosol deposition of these TiO_2nanoparticles on TCO substrates. The evolution of the film morphology was investigated as a function of the deposition conditions. Optimization of the films' mechanical stability was conducted to allow their utilization in liquid solutions while preserving high porosity and specific surface area for dyeadsorption. Upon functionalization of the TiO_2 surface with a standard dye (N719) and cell assembly, the DSSC performance was investigated with respect to key film structural properties such as phase composition, thickness and porosity. The feasibility of utilizing highly porous nanoparticle films as DSSC working electrodes was critically assessed focusing on the strengths of these morphologies and proposing new strategies to minimize their deficit in mechanical stability.

2. Results and discussion

2.1 Film assembly, morphology and stability

Fig. 1 shows exemplary TEM images of TiO_2nanoparticles filter-collected from the flame-made aerosol at 50 cm height above the burner (HAB). The visible particle size (Fig. 1a) was considerably below 50 nm in agreement with their Sauter diameter (d_{BET} = 15 nm). There was no evidence of the formation of larger particles (≥50 nm) that may act as light scattering centers. The composition of these nanoparticles was further investigated by FTIR analysis indicating the absence of carbon-related species. This confirms optimal combustion of the liquid precursor solution[29] in line with previous reports[24,30] on spray flame synthesis of TiO_2nanoparticles. At higher magnification (Fig. 1b), the particle size was polydisperse ranging from less than 5 nm to slightly above 20 nm. This is in agreement with the size distribution reported[31] for flame-made SnO_2nanoparticles produced with similar

conditions. Some broad sintering necks (Fig. 1b) were visible between large and very small particles. In contrast, large particles were mainly connected by open necks leading to the high specific surface area (SSA = 90 m^2 g^{-1}) of the as-prepared particles. As a result, these TiO_2nanoparticles were comparable to that previously utilized (d = 25 nm) for the synthesis of transparent nanoparticle layers[7] offering even higher surface for dyeadsorption.

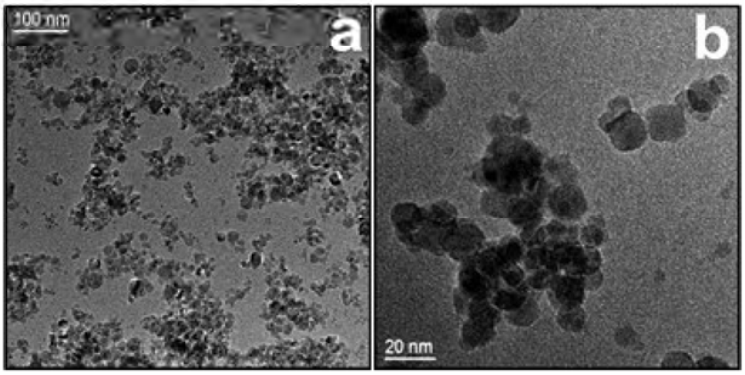

Fig. 1 TEM images of TiO_2nanoparticles made by liquid-fed spray flame synthesis and filter-collected from the hot aerosol. These nanoparticles were polydisperse (a) with size ranging (b) from 3 to 25 nm.

This flame-made TiO_2 aerosol was orthogonally impinged on cooled TCO substrates leading to the rapid (2–10 min) self-assembly of highly porous films as previously reported for SnO_2,[32] Eu:Y_2O_3 (ref. 25) and TiO_2 (ref. 24 and 30) nanoparticles. The height above the burner (HAB) plays a major role in determining the properties of flame-made aerosols and thus on the resulting deposition dynamics and film morphology.[33] Here, a minimal HAB of 10 cm was necessary to avoid damage of the TCO substrates due to too high thermal stress. The deposited films' mass density (m_d) increased linearly (Fig. 2) with increasing deposition time at all HAB indicating a constant nanoparticle deposition rate. Increasing the substrate HAB from 10 to 20 cm (Fig. 2) decreased the resulting film growth rate from 3.9 to 0.6 mg cm^{-2} min and the substrate surface temperature from *ca.* 400 to 100 °C. This is attributed to the high air entrainment of such open flames[33,34] that drastically decreases aerosol concentration and temperature with increasing HAB. At 10 cm HAB (Fig. 2, triangles), aerosol deposition led to the rapid synthesis of very thick nanoparticle films with specific mass density (m_d) comparable to that (~2 to 4 mg cm^{-2}) utilized for the assembly

of highly efficient DSSCs.[11] These constant deposition rates are in agreement with the nanoparticle deposition mechanisms from hot flames that have been suggested recently.[33]

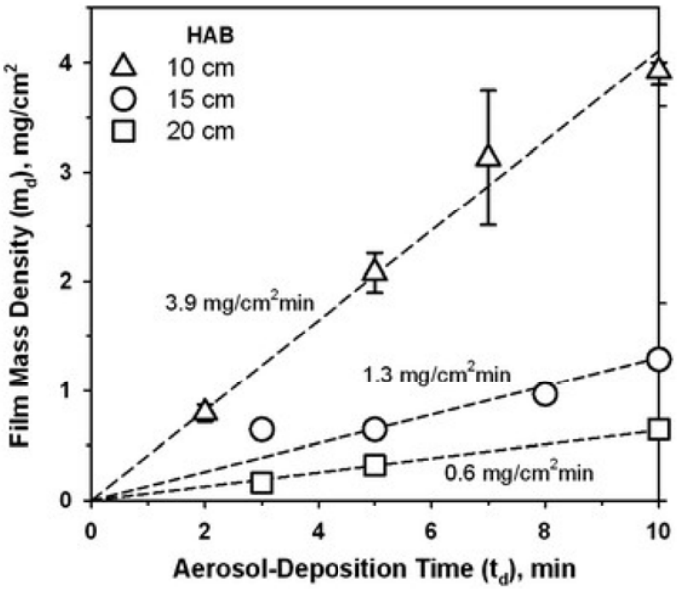

Fig. 2 Deposited TiO_2 film mass density (m_d) as a function of the aerosol-deposition time (t_d) at several heights above the burner (HAB). Increasing the HAB from 10 (triangles) to 20 cm (squares) decreased the film growth rate and substrate surface temperature from 3.9 to 0.6 mg cm^{-2} min and 400 to 100 °C, respectively.

Aerosol deposition at 10 cm HAB resulted in TiO_2 films with a relatively homogeneous surface (Fig. 3a) and internal structure (Fig. 3d) as previously observed for SnO_2nanoparticle deposition at 20 cm HAB.[19] This excludes the direct deposition of liquid precursor droplets that would result in the formation of a rougher surface as reported for flame-assisted spray pyrolysis (FASP).[35] At higher magnification (Fig. 3b), a very porous surface morphology was visible (Fig. 3c) that consisted of fine nanoparticles (≪100 nm) agglomerated in larger macrostructures. Analysis of the film cross-sections (Fig. 3d, inset) indicated a branch-like growth throughout the whole film thickness. This morphology (Fig. 3b–d) is considerably different from that previously reported[19,24,26] for aerosol deposition of flame-made metal-oxidenanoparticles at 20 cm HAB. There the film surface was made of an intricate net of loose nanoparticle bridges extending over large surface pores that resulted in an average film porosity (ε, eqn (1)) of 98%.[19,26] This is in line with the results, obtained here (not

shown), for TiO_2 deposition at 20 cm HAB that led also to 98% film porosity. In contrast, deposition at 10 cm HAB resulted in more compact macrostructures (Fig. 3b and c) with an average film porosity of 95% indicating considerable sintering of the nanoparticles during deposition. This film porosity (95%), however, is still extremely high with respect to that usually obtained by wet synthesis of DSSC TiO_2 films (50–65%)[11] and has considerable consequences on their thickness and morphology. For example, here, a TiO_2 film with a mass density of 2.4 mg cm^{-2} (Fig. 3d) had a thickness (δ) of *ca.* 110 μm while standard wet-synthesis methods[11] would have led to only 13–18.6 μm.

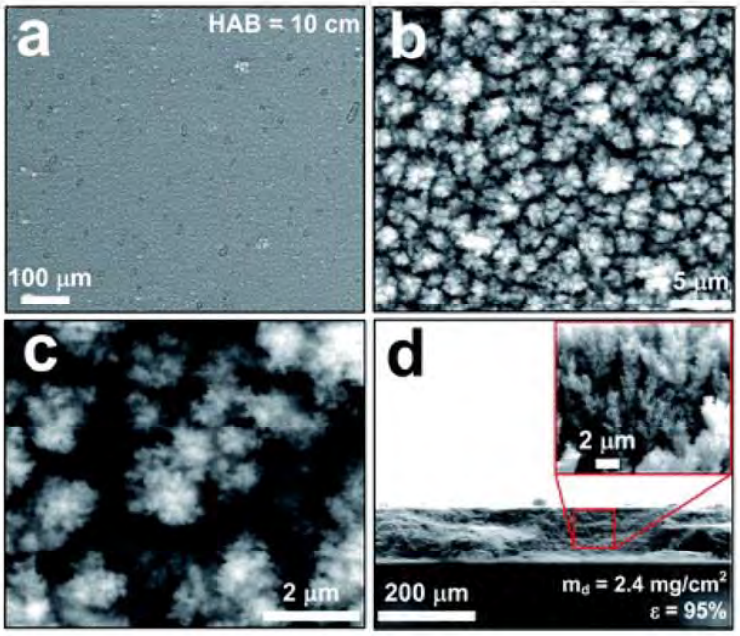

Fig. 3 SEM images of an exemplary TiO_2nanoparticle film aerosol-deposited at 10 cm HAB. The film surface is homogeneous (a) and highly porous (b). The surface pore size is in the range of 2 μm similarly to that observed for deposition at 20 cm HAB. However, this morphology (b and c) is considerably more compact resulting in a porosity (ε) of 95% (d) against the 98% obtained by deposition at 20 cm HAB. Cross-sectional SEM images of the film (d, inset) suggest branch-like self-assembly of the TiO_2nanoparticles in a homogeneous and highly porous film structure.

To assess the mechanical stability of these aerosol-deposited films (ε = 95–98%) for utilization as DSSC working electrodes, they were immersed in a liquid solution (similar to the dye one) and, upon drying, the residual film mass on the substrate was measured. Films

having 98% porosity disintegrated completely during immersion in the liquid solution and *ca.* 0% residual film mass was measured independently of the film thickness. This is in good agreement with the poor mechanical stability of flame-made SnO_2 nanoparticle films aerosol-deposited on Si-wafer at 20 cm HAB.[19] In contrast, here, films having 95% porosity and 40 μm thickness had on average 80% residual film mass. This confirms that deposition at 10 cm HAB leads to more robust film morphologies. However, it also suggests that some restructuring of the film morphology still finds place upon immersion in the liquid solution and thus it is expected that further reduction of the porosity (<95%) is required to fully stabilize such loose nanoparticle films.

The stabilization dynamics of the TiO_2 films deposited at 10 cm HAB was investigated further by analysis of their crystal composition as a function of the film thickness. The filter-collected TiO_2 particles (Fig. 1) had 86 and 14 wt% anatase and rutile content (Fig. 4), respectively. This is in good agreement with the crystal structure reported for TiO_2 nanoparticles flame-made with similar process conditions.[30] The nanoparticle films deposited at 10 cm HAB had always smaller anatase contents (Fig. 4) than the filter-collected TiO_2 particles. In particular, the film anatase content (Fig. 4) decreased from 81 to 57 wt% with increasing film thickness from 44 to 206 μm. This is attributed to the relatively high temperature (~400 °C) of the substrate surface during deposition at 10 cm HAB that facilitated the transformation from anatase to the thermodynamic more favorable rutile phase. In contrast, the anatase content of the films deposited at 20 cm HAB (not shown) was identical to that of the filter-collected nanoparticles (Fig. 4) as the substrate temperature (~100 °C) was too low to induce measurable phase transformation in the short (≤10 min) deposition times utilized.

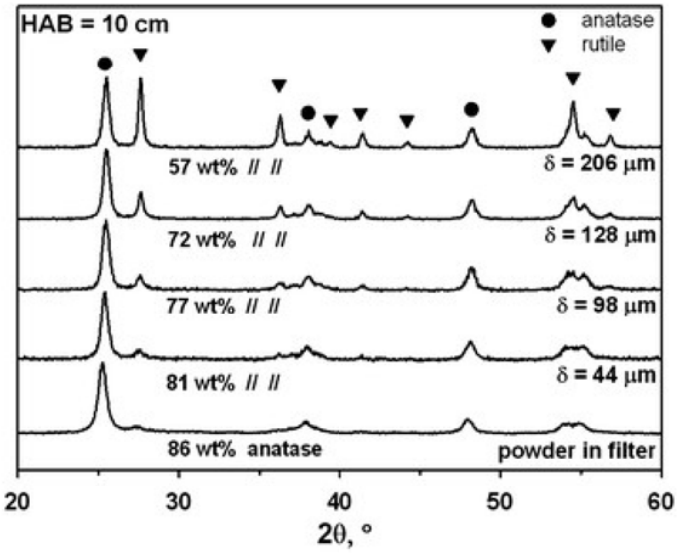

Fig. 4 XRD patterns of the filter-collected TiO_2 powders and aerosol deposited TiO_2 films at 10 cm HAB as a function of the film thickness (δ). The as-prepared flame-made TiO_2nanoparticles were constituted by 86 wt% anatase (triangles), the most favorable phase for DSSCs, and by 14 wt% rutile (circles). The anatase content decreased with increasing film thickness due to the relatively high (~400 °C) substrate surface temperature during deposition.

This phase transformation from anatase to rutile played a major role in the resulting film morphology and stability. The anatase (Fig. 5, triangles) and rutile (circles) crystal sizes of the filter-collected TiO_2 powder were 18 and 8 nm, respectively. For the films, the anatase (Fig. 5, triangles) crystal size increased only moderately from 23 to 27 nm with their thickness increasing from 44 to 206 μm while the rutile crystal size (Fig. 5, circles) increased drastically from 14 to 42 nm. This suggests that during nanoparticle deposition the film undergoes two restructuring stages. The first stage up to 44 μm thickness, where surface diffusion was the main force driving particle sintering. This led rapidly to the achievement of a nearly stable anatase crystal size of 23 nm (Fig. 5, triangles) and is in line with the small variation in crystal composition (Fig. 4). During the second stage, the phase transformation from anatase to rutile was predominant and alimented the drastic growth of the rutile crystal size (Fig. 5, circles). This phase transformation is particularly a negative side effect of the higher substrate temperatures necessary to stabilize such loose nanoparticle films. In fact, it reduced the amount of the best DSSC-performing anatase phase[36] and increased

the rutile crystal size (Fig. 5, circles) possibly increasing back scattering of incident photons. Furthermore, while the initial sintering stage (Fig. 5) increased considerably the film mechanical stability (80% residual mass) with respect to that (0% residual mass) of the TiO_2 films deposited at 20 cm HAB, the second stage did not lead to further improvements. As a result, further studies on aerosol deposition of flame-made TiO_2nanoparticles for assembly of DSSC working electrodes should focus also on the inhibition of the anatase–rutile phase transformation.

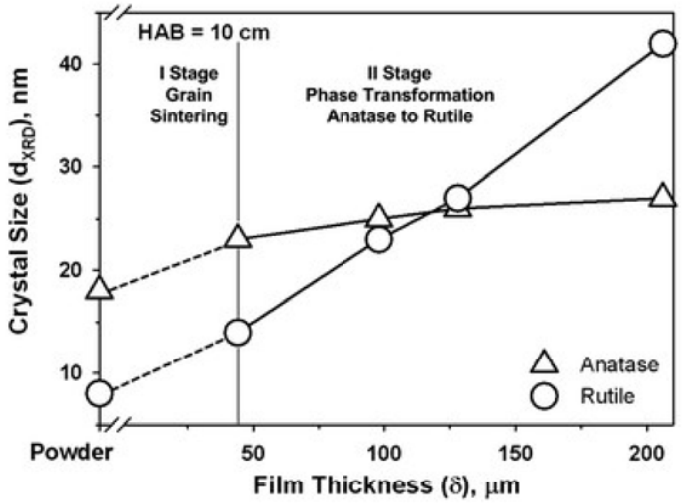

Fig. 5 Anatase (triangles) and rutile (circles) crystal size of the filter-collected TiO_2nanoparticles and of the aerosol-deposited films at 10 cm HAB as a function of their thickness (δ). The restructuring of the film composition during deposition is characterized by two stages. The first stage up to *ca.* 44 μm thickness controlled by grain boundary sintering, where the anatase crystal size (triangles) nearly reaches an asymptotic value of 23 nm. A second (δ > 44 μm) controlled by the anatase–rutile phase transformation where the rutile crystal size (circles) drastically increases above that of anatase (triangles).

2.2 DSSC performance

The N719 dye saturation adsorption capacity (8.5×10^{-7} mol m^{-2}) of these as-prepared TiO_2 particles was comparable to that reported (6.9×10^{-7} mol m^{-2}) for small (d_{BET} = 15 nm) wet-made nanoparticles with other Ru-based dyes.[37] Upon sensitization with N719, the TiO_2 films were sealed to Pt-coated counter electrodes and filled with a liquid electrolyte. The performance (Fig. 6) of these cells (at AM 1.5, 1000 W m^{-2}) was strongly

dependent on the TiO_2 film morphology. Deposition at 20 cm HAB led to solar energy conversion efficiencies (eqn (2)) always below 0.1%. Fig. 6 shows the *I–V* plot of a TiO_2 film deposited for 10 min at 20 cm HAB (broken line). This cell had a short-circuit current density (J_{SC}) and an open circuit voltage (V_{OC}) of only 0.41 mA cm^{-2} and 0.42 V, respectively, resulting in a conversion efficiency of 0.08%. This poor performance is in good agreement with the low conversion efficiencies (≤0.6%) previously reported[14,17] for granular (flame-made) TiO_2nanoparticle films (Table 1) and was attributed to their low mechanical stability. More in detail, the V_{OC} (0.42 V) of these films was very low in comparison to that usually obtained (~0.7 V) which corresponds to the difference between the (quasi)Fermi level of TiO_2 and the redox potential of the electrolyte.[11] This suggests the formation of cracks throughout the TiO_2 film that result in the direct contact of the oxidised electrolyte with the TCO surface and thus low V_{OC}.

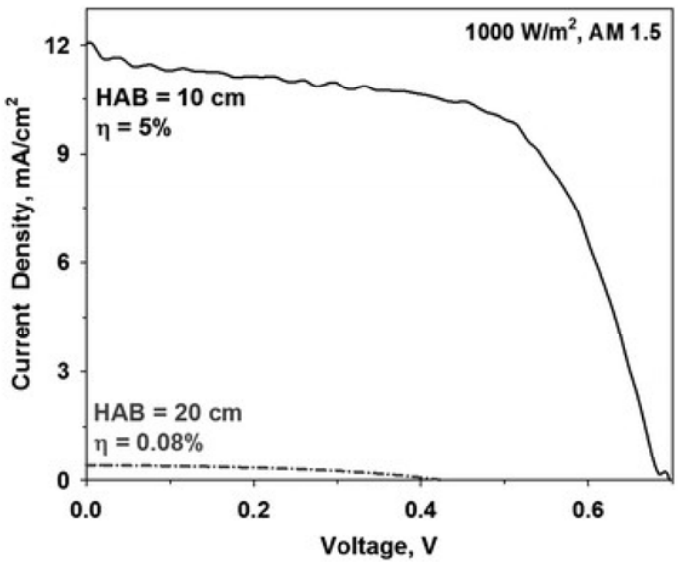

Fig. 6 *I–V* plots of DSSCs made of TiO_2nanoparticle films deposited at 10 (continuous line) and 20 cm (broken line) HAB. The film deposited at 20 cm HAB had very poor performance in line with the low mechanical stability observed at 98% porosity. In contrast, the film deposited at 10 cm HAB reached high V_{OC} and relatively high J_{SC} resulting in an efficiency of 5%.

Aerosol deposition at 10 cm HAB led to significant enhancement of the solar energy conversion efficiencies in line with the higher mechanical stability of these films. Fig. 6

shows the *I*–*V* plots of an exemplary TiO_2 film (ε = 95%) with a thickness of 38 μm under artificial sun light illumination. This film reached a V_{OC} and J_{SC} of 0.68 V and 12.2 mA cm^{-2}, respectively, resulting in a conversion efficiency of 5.03%. This is an 8 times enhancement with respect to the maximum efficiency previously reported[14,18] for granular TiO_2nanoparticle films (Table 1) aerosol-deposited upon flame synthesis. The V_{OC} (0.68 V) obtained here indicates that sufficient stabilization of the TiO_2 film was reached to exploit nearly the full potential of the utilized electrolyte–semiconductor couple. However, further improvements of the film phase composition (higher anatase content) are necessary to achieve (Table 1) the very high V_{OC} (0.78–0.799 V)[13,16,17] reported for granular and mesoporous TiO_2 films. The fill factor (eqn (3)) of these TiO_2 films deposited at HAB = 10 cm (Table 1) was (0.59) considerably higher than that (0.43) reported for granular films but still lower than the best reported (0.72) for mesoporous ones. This FF (0.59) is also smaller than that (~0.7) commonly achieved[11] by TiO_2-based DSSCs. This is attributed to the only partial stability (80% residual mass) of the TiO_2 films deposited at 10 cm HAB that led to some reorganization of the films morphology upon immersion in the dye solution. This suggests that although considerable stabilization was obtained higher conversion efficiencies can be achieved by further optimization of the film morphology.

The J_{SC} of these (10 cm HAB) films (12.2 mA cm^{-2}) was remarkably higher (Table 1) than that reported for other alternative (Table 1) working electrode morphologies. In particular, mesoporous TiO_2 films (Table 1) reached a maximum J_{SC} of 7 mA cm^{-2} and randomly oriented TiO_2nanoparticle produced only 4.5 mA cm^{-2}.[13] Recently, films made of standard P25 nanoparticles (Table 1), sensitized with the same dye (N719), resulted in a J_{SC} of 5.04 mA cm^{-2} and a conversion efficiency of 2.7%.[38] Here, the high J_{SC} obtained (12.2 mA cm^{-2}) is comparable to that (14.5 mA cm^{-2}) achieved[12] by more sophisticated multi-layer (transparent/scattering) film morphologies. This demonstrates that highly porous nanoparticle films, such as those produced here, are able to achieve considerable light absorption even without utilization of light scattering nanoparticles. This is attributed to the very high surface area (Fig. 3) of these transparent nanoparticle films that results in high dye loading and thus electron–hole generation. As a result, the low J_{SC} (2.54 mA cm^{-2}) previously reported[17] (Table 1) for porous granular nanoparticle films as well as their low FF cannot be attributed to their high porosity and may result from insufficient mechanical stabilization. Reference cells made by wet-deposition of the same flame-made

TiO_2 nanoparticles led to less homogeneous morphologies characterized by deep cracks and with a thickness of 35 ± 10 mm. Their efficiency varied from 3.6 to 5.7%. This indicates that aerosol deposition leads, even for much thicker films (>100 mm) and relatively fragile morphologies, already to performance comparable to standard wet-deposition methods.[39] However, it should be stressed out that the overall performance of these films is not yet very high as standard multi-layer DSSCs have already reached certified efficiencies of *ca.* 11%[40] and thus further optimization is necessary to reach competitive performances.

The performance of the TiO_2 films aerosol-deposited at 10 cm HAB was further investigated (Fig. 7) as a function of their thickness. Their conversion efficiency (Fig. 7a, triangles) increased from 4.5 to 5% with increasing thickness from 21 to 38 μm mainly due to an increase in J_{SC} (Fig. 7a, circles) from 11.8 to 12.2 mA cm^{-2}. This is in line with the higher surface available for dyeadsorption with increasing film thickness. Simultaneously, the FF (Fig. 7b, diamonds) of these films increased from 0.52 to 0.59 suggesting an improvement of their morphology. This is in agreement with the observed (Fig. 5) initial mechanical stabilization of the TiO_2 films during the first stage of growth and with the relatively high anatase content (Fig. 4) preserved up to a film thickness of 44 μm. However, these positive effects were countered by a drop in the V_{OC} (Fig. 7b, squares) from 0.71 to 0.68 V suggesting a localized rutile increase at the TiO_2 film–TCO interface.

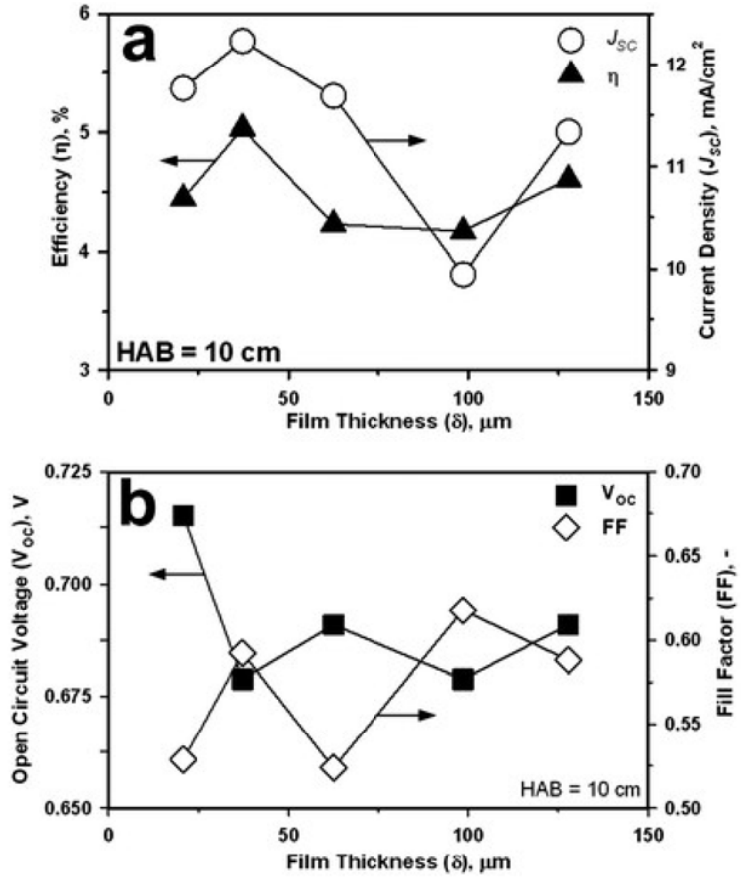

Fig. 7 (a) Efficiency (triangles) and J_{SC} (circles) of TiO_2 nanoparticle films deposited at 10 cm HAB as a function of their thickness (δ) under 1 sun illumination (1.5 AM, 1000 W m^{-2}). A maximum efficiency (triangles) was found at 44 μm thickness in agreement with the highest J_{SC} (circles). (b) The V_{OC} (squares) decreased with increasing thickness while the fill factor (FF, diamonds) was nearly constant.

Increasing further the TiO_2 film thickness from 38 to 128 μm (Fig. 7a, triangles) decreased the conversion efficiency to 4.6% mainly due to a 7.3% drop in J_{SC} (Fig. 7a, circles). This was attributed to the rapidly increasing rutile content (Fig. 4) and crystal size (Fig. 5, circles) measured with increasing film thickness in the second stage of film stabilization. In fact, these sintered multi-crystalline rutile structures may act as light scattering centers[9] decreasing light absorption and thus electron generation as observed[12] in films made of a single layer of large scattering TiO_2 nanoparticles. Nevertheless, these results show, for the first time, that highly porous films of nanoparticles (95%) can sustain nearly initial efficiencies at least up to a thickness of 128 μm. This is quite remarkable as usually the

conversion efficiency of TiO_2 working electrodes with standard porosity (ε = 50–65%) decreases rapidly already above a film thickness of *ca.* 5–20 μm.[11] The J_{SC} of mixed nanoparticle films (23, 50 nm), for example, decreased by *ca.* 14% with increasing film thickness from 17 to 31 μm.[7] This is commonly attributed to lower electrolyte ion exchange rates in thick films that result in slower neutralization of photogenerated holes in the working electrode and thus to higher recombination losses.[7,10] Here, the stability of the conversion efficiency and J_{SC} up to 128 μm film thickness suggests that highly porous film morphologies may inhibit recombination losses by enhancing electrolyte ion exchange rates. As a result, highly porous films of transparent TiO_2nanoparticles bear the potential to provide considerable enhancements of the solar energy conversion efficiency of state-of-the-art DSSCs. However, the limited number of necking points in highly porous films could also inhibit electron transport as observed for porous films ($\varepsilon \approx 74\%$) of inverse anatase opals[39] and thus further investigation of the properties of such morphologies is required.

3. Conclusions

Highly porous films of transparent TiO_2nanoparticles were investigated as alternative morphology for assembly of DSSC working electrodes. First insights into the structural–functional relationships of these films were presented highlighting strengths and deficits of these loose morphologies. Highly porous films were rapidly (2–10 min) self-assembled by direct aerosol deposition of flame-made nanoparticles. Enhancement of the film mechanical stability was achieved by reduction of their porosity from 98 to 95% allowing their utilization in liquid environments. The film stabilization dynamics was further investigated suggesting two restructuring stages of the film morphology. The first stage controlled by grain boundaries sintering and the second stage driven by a rapid phase transformation from anatase to rutile. Mechanical stabilization occurred mainly during the first stage while during the second stage the amount of the most favorable anatase phase was drastically reduced and the rutile crystal size was remarkably increased.

Nanoparticle films having 95% porosity had drastically higher solar energy conversion efficiency (η = 5%) than those with 98% (η = 0.08%) and achieved an 8 times improvement with respect to the best performance (η = 0.6%) previously reported for porous, granular films of flame-made TiO_2nanoparticles. This was attributed to the remarkable J_{SC} (12.2 mA

cm^{-2}) obtained by these highly porous films that was significantly higher than those reported (≤7 mA cm^{-2}) for some other novel working electrode morphologies. Relatively high conversion efficiencies (4.6%) were preserved up to a film thickness of 128 μm suggesting that recombination losses may be inhibited in such morphologies. These results suggest that highly porous films are a promising alternative design for the synthesis of advanced DSSCs. Further optimization of their mechanical stability and phase composition is expected to lead to considerable improvements in solar energy conversion efficiencies. Furthermore, TiO_2 film fabrication by direct aerosol deposition of flame-made nanoparticles has shown to be a rapid (min) synthesis route that combines the strengths of a scalable nanoparticle source with the benefit of a single-step film assembly process.

4. Experimental

4.1 Nanoparticle film synthesis and characterization

Titanium oxide[24,30]nanoparticle aerosols were synthesized by flame spray pyrolysis as previously described in detail.[41] The TiO_2 precursor solution was prepared as follows: titanium(IV) isopropoxide (TTIP, Aldrich, purity > 97%) was diluted in xylene (Fluka, purity > 98.5%) and toluene (Sigma-Aldrich, purity > 99.7%), respectively, with a total metal (Ti) atom concentration of 0.5 mol l^{-1}. This solution was supplied at a rate of 5 ml min^{-1} through the LSF nozzle and dispersed to a fine spray with 5 l min^{-1} oxygen (pressure drop 1.5 bar). This spray was ignited by a supporting ring-shaped premixed methane–oxygen flame (CH_4 = 1.2 l min^{-1}, O_2 = 3.2 l min^{-1}). Additional 5 l min^{-1} sheath oxygen were supplied from an annulus surrounding the spray flame to assure excess oxidant flow. The TiO_2nanoparticles were collected on water cooled glass-fiber filters placed at 50 cm height above the burner (HAB) and characterized by transmission electron microscopy (TEM) with a Hitachi H600 microscope, operated at 100 kV.

Nanoparticle films were aerosol-deposited on soda lime glass substrates coated on one side with a F-doped SnO_2 (FTO) layer (TCO22-15, Solaronix AG) of 1.5 cm × 1.5 cm that were placed on a water cooled holder at a constant (10–20 cm) HAB. This resulted in a high nanoparticle flux toward the substrate surface and rapid growth of a very porous film. Prior to DSSC assembly, the TiO_2 films deposited at 20 cm HAB were further stabilized during 30

s by a previously reported *in situ* annealing step.[19] During deposition, the substrate holder and surface temperatures were measured by an n-type thermocouple and IR-sensor, respectively.

The film specific mass (m_d) and bulk thickness (BT) were computed by gravimetric measurement of the deposited film mass on the F-SnO_2 or on Ti substrates over the coated substrate surface and from the content-weighted density of TiO_2 anatase and rutile. The film visible thickness (δ) and morphology were characterized by SEM analysis with a LEO 1530 Gemini (Zeiss/LEO, Oberkochen) and a Tecnai F30 microscope (FEI (Eindhoven); field emission cathode, operated at 300 kV). The average film porosity (ε) was computed as follows:[19,26]

$$\varepsilon(\%) = \left(1 - \frac{\mathrm{BT}}{\delta}\right) \cdot 100 \qquad (1)$$

X-ray diffraction (XRD) patterns of the films and filter-collected nanoparticles were obtained by a Bruker, AXS D8 Advance diffractometer operated at 40 kV, 40 mA at 2θ (Cu Kα) = 15–75°, step = 0.03° and scan speed = 0.6° min^{-1}. The crystal size (d_{XRD}) was determined using the Rietveld fundamental parameter method with the structural parameters of TiO_2 anatase[42] and rutile.[43] The nanoparticle specific surface area (SSA) was measured by BET analysis using a Micromeritics Tristar 3000. The BET equivalent diameter (d_{BET}) was calculated using the density of TiO_2 anatase (3.84 g cm^{-3}) and rutile (4.26 g cm^{-3}) for the given XRD composition. The films' mechanical stability was characterized by immersion in an ethanol bath for 10 s and measurement of the mass loss due to film disintegration and re-suspension of the nanoparticles. The FTIR analysis was performed with a Bruker, Vector 22 operated with a resolution of 2 cm^{-1} between 4500 and 500 cm^{-1} and averaging 128 scan. Previous to each measurement the *in situ* heating cell (Harrick) was kept at 400 °C for 2 h while flushed with 25 ml min^{-1} synthetic air (Pan Gas 5.0). The (dye) saturation adsorption capacity of these flame-made TiO_2nanoparticles was computed by measuring the optical thickness of a 1.5×10^{-4} mol l^{-1} N719 dye–ethanol solution at λ = 534 nm (extinction coefficient, $\varepsilon = 1.47 \times 10^4$ l mol^{-1} cm)[44] before and after (1 h) impregnation of the TiO_2nanoparticles.

4.2 DSSC assembly and characterization

Before assembly of the solar cells, the TiO_2 films were first heated up to 450 °C in order to remove adsorbed H_2O and impurities. This short heating step did not change the crystal properties of the TiO_2 films in line with previous sintering studies[45] of such flame-made TiO_2nanoparticles. Upon cooling to 60 °C, they were sensitized by 1 h immersion in a solution containing Ruthenizer 535-bis TBA (N719 dye, Solaronix AG) with a concentration of 2×10^{-3} mol l^{-1} in ethanol (Fluka, purity > 99.8%). After sensitization, the solution residuals were washed away by immersion in an ethanol bath for 10 s. The counter electrodes were prepared by doctor-blading of a commercially available Pt-paste (Plastisol T/SP, Solaronix) on the FTO substrates (TCO22-15, Solaronix AG). The working and counter electrodes were sealed together by thermal application of a commercially available foil (Meltonix 1170-100, Solaronix AG) on the working electrode margins leading to a working electrode area of 6 mm × 6 mm. The electrolyte was prepared by addition of 0.6 M *tert*-butyl ammonium iodide (Aldrich), 0.1 M LiI (Aldrich, purity > 98%), 0.1 M I_2 (Aldrich, purity > 98%), 0.5 M *tert*-butylpyridine (Aldrich, purity > 98%) to acetonitrile (Aldrich, purity > 99%).[46] The electrolyte was let into the cell by a small (0.5 mm in diameter) opening previously drilled in the counter electrode. Thereafter this opening was closed by application of a sealing foil and a thin borosilicate glass sheet (1.5 mm) (613-0121, VWR international) on the backside of the counter electrode. To improve the conductivity, the external surface of the FTO substrates was coated with a colloidal silver paste (#05063-AB, SPI supplies) and air dried for 30 min.

The DSSC performance was evaluated along the film porosity and thickness. Current–voltage (*I*– *V*) plots were obtained both in the dark and under one sun illumination (AM 1.5, P_{source} = 1000 W m^{-2}) as supplied by a solar simulator (Solarsim 150, Solaronix AG) calibrated with a standard reference cell (ESTI Sensor, ES 1034, European Solar Test Installation) before each measurement session. The cells solar energy conversion efficiency (η) was computed by:[11,47,48]

$$\eta(\%) = \frac{J_{sc} \cdot V_{oc} \cdot FF}{P_{source}} \cdot 100 \qquad (2)$$

where J_{SC} is the short-circuit current density, V_{OC} is the open circuit voltage and FF is the fill factor. The fill factor was computed by:

$$FF = \frac{V_{max} \cdot J_{max}}{V_{OC} \cdot J_{SC}} \quad (3)$$

where V_{max} and J_{max} are the voltage and current density, respectively, at maximum power output density (P_{max}).

Acknowledgements

The authors kindly acknowledge the assistance of Prof. A. Tiwari and Mr S. Seyrling at EMPA Zurich and Dr M. Scott at Solaronix AG for their help with the photovoltaic characterization, K. Piran and J. Knijnenburg for their help with the TiO_2 film deposition and Dr F. Krumeich at EMEZ for the TEM and SEM characterizations. The authors are grateful to Prof. S. E. Pratsinis for fruitful discussions. Financial support was provided by the Swiss National Science Foundation, grant 200021_130582/1 and European Research Council.

References

1. B. O'Regan and M. Gratzel , *Nature*, 1991, **353** , 737 CrossRef CAS .
2. M. Gratzel *Nature*, 2003, **421** , 586 CrossRef .
3. R. Knödler , J. Sopka , F. Harbach and H. W. Grünling , *Sol. Energy Mater. Sol. Cells*, 1993, **30** , 277 CrossRef .
4. S. E. Pratsinis *Prog. Energy Combust. Sci.*, 1998, **24** , 197 CrossRef CAS .
5. M. K. Nazeeruddin , A. Kay , I. Rodicio , R. Humphrybaker , E. Muller , P. Liska , N. Vlachopoulos and M. Gratzel , *J. Am. Chem. Soc.*, 1993, **115** , 6382 CrossRef CAS .
6. M. K. Nazeeruddin , P. Pechy and M. Gratzel , *Chem. Commun.*, 1997, 1705 RSC .
7. Z. S. Wang , H. Kawauchi , T. Kashima and H. Arakawa , *Coord. Chem. Rev.*, 2004, **248** , 1381 CrossRef CAS .
8. M. A. Green , K. Emery , Y. Hishikawa and W. Warta , *Progr. Photovolt.: Res. Appl.*, 2010, **18** , 144 CrossRef CAS .

9. J. Ferber and J. Luther , *Sol. Energy Mater. Sol. Cells*, 1998, **54** , 265 CrossRef CAS .
10. J. Ferber , R. Stangl and J. Luther , *Sol. Energy Mater. Sol. Cells*, 1998, **53** , 29 CrossRef CAS .
11. M. Gratzel *J. Photochem. Photobiol., C*, 2003, **4** , 145 CrossRef CAS .
12. Z. Zhipan , S. Ito , B. O'Regan , K. Daibin , S. M. Zakeeruddin , P. Liska , R. Charvet , P. Comte , M. K. Nazeeruddin , P. Pechy , R. Humphry-Baker , T. Koyanagi , T. Mizuno and M. Gratzel , *Z. Phys. Chem.*, 2007, **221** , 319 CrossRef .
13. M. Zukalova , A. Zukal , L. Kavan , M. K. Nazeeruddin , P. Liska and M. Gratzel , *Nano Lett.*, 2005, **5** , 1789 CrossRef CAS .
14. E. Thimsen and P. Biswas , *AIChE J.*, 2007, **53** , 1727 CrossRef CAS .
15. M. Law , L. E. Greene , J. C. Johnson , R. Saykally and P. D. Yang , *Nat. Mater.*, 2005, **4** , 455 CrossRef CAS .
16. M. Zukalova , J. Prochazka , A. Zukal , J. H. Yum and L. Kavan , *Inorg. Chim. Acta*, 2008, **361** , 656 CrossRef CAS .
17. E. Thimsen , N. Rastgar and P. Biswas , *Sol. Hydr. Nanotechnol. II*, 2007, **6650** , G6500 Search PubMed .
18. E. Thimsen , N. Rastgar and P. Biswas , *J. Phys. Chem. C*, 2008, **112** , 4134 CrossRef CAS .
19. A. Tricoli , M. Graf , F. Mayer , S. Kühne , A. Hierlemann and S. E. Pratsinis , *Adv. Mater.*, 2008, **20** , 3005 CrossRef CAS .
20. A. Tricoli and S. E. Pratsinis , *Int. J. Nanomanuf.*, 2010, **6** , 125 CrossRef CAS .
21. B. E. Russ and J. B. Talbot , *J. Adhes.*, 1999, **68** , 257 CrossRef .
22. A. Tricoli and S. E. Pratsinis , *Nat. Nanotechnol.*, 2010, **5** , 54 CrossRef CAS .
23. M. Righettoni , A. Tricoli and S. E. Pratsinis , *Anal. Chem.*, 2010, **82** , 3581 CrossRef CAS .
24. A. Tricoli , M. Righettoni and S. E. Pratsinis , *Langmuir*, 2009, **25** , 12578 CrossRef CAS .
25. R. Kubrin , A. Tricoli , A. Camenzind , S. E. Pratsinis and W. Bauhofer , *Nanotechnology*, 2010, **21** , 225603 CrossRef .
26. L. Mädler , A. Roessler , S. E. Pratsinis , T. Sahm , A. Gurlo , N. Barsan and U. Weimar , *Sens. Actuators, B*, 2006, **114** , 283 CrossRef .

27. A. Tricoli , M. Righettoni and A. Teleki , *Angew. Chem., Int. Ed.*, 2010, **49** , 7632 CrossRef CAS .
28. Y. Liu , E. Koep and M. L. Liu , *Chem. Mater.*, 2005, **17** , 3997 CrossRef CAS .
29. R. Jossen , S. E. Pratsinis , W. J. Stark and L. Madler , *J. Am. Ceram. Soc.*, 2005, **88** , 1388 CrossRef CAS .
30. A. Tricoli , M. Righettoni and S. E. Pratsinis , *Nanotechnology*, 2009, **20** , 315502 CrossRef .
31. H. Keskinen , A. Tricoli , M. Marjamäki , J. M. Mäkelä and S. E. Pratsinis , *J. Appl. Phys.*, 2009, **106** , 084316 CrossRef .
32. L. Mädler , A. A. Lall and S. K. Friedlander , *Nanotechnology*, 2006, **17** , 4783 CrossRef .
33. A. Tricoli and T. D. Elmøe , *AIChE J.*, 2012, 10.1002/aic.13739 Search PubMed .
34. M. C. Heine , L. Madler , R. Jossen and S. E. Pratsinis , *Combust. Flame*, 2006, **144** , 809 CrossRef CAS .
35. R. Kubrin and W. Bauhofer , *J. Lumin.*, 2009, **129** , 1060 CrossRef CAS .
36. N. G. Park , J. Van de Lagemaat and A. J. Frank , *J. Phys. Chem. B*, 2000, **104** , 8989 CrossRef CAS .
37. M. K. Nazeeruddin , P. Pechy , T. Renouard , S. M. Zakeeruddin , R. Humphry-Baker , P. Comte , P. Liska , L. Cevey , E. Costa , V. Shklover , L. Spiccia , G. B. Deacon , C. A. Bignozzi and M. Gratzel , *J. Am. Chem. Soc.*, 2001, **123** , 1613 CrossRef CAS .
38. S. Sun , L. Gao and Y. Liu , *Appl. Phys. Lett.*, 2010, **96** , 083113 CrossRef .
39. L. Kavan , M. Zukalova , M. Kalbac and M. Graetzel , *J. Electrochem. Soc.*, 2004, **151** , A1301 CrossRef CAS .
40. M. A. Green , K. Emery , Y. Hishikawa and W. Warta , *Progr. Photovolt.: Res. Appl.*, 2010, **18** , 346 CrossRef .
41. L. Mädler , H. K. Kammler , R. Mueller and S. E. Pratsinis , *J. Aerosol Sci.*, 2002, **33** , 369 CrossRef .
42. I. Djerdj and A. M. Tonejc , *J. Alloys Compd.*, 2006, **413** , 159 CrossRef CAS .
43. X. Bokhimi , A. Morales and F. Pedraza , *J. Solid State Chem.*, 2002, **169** , 176 CrossRef CAS .

44. M. K. Nazeeruddin , S. M. Zakeeruddin , R. Humphry-Baker , M. Jirousek , P. Liska , N. Vlachopoulos , V. Shklover , C. H. Fischer and M. Gratzel , *Inorg. Chem.*, 1999, **38** , 6298 CrossRef CAS .
45. A. Teleki , R. Wengeler , L. Wengeler , H. Nirschl and S. E. Pratsinis , *Powder Technol.*, 2008, **181** , 292 CrossRef CAS .
46. J. M. Kroon , N. J. Bakker , H. J. P. Smit , P. Liska , K. R. Thampi , P. Wang , S. M. Zakeeruddin , M. Gratzel , A. Hinsch , S. Hore , U. Wurfel , R. Sastrawan , J. R. Durrant , E. Palomares , H. Pettersson , T. Gruszecki , J. Walter , K. Skupien and G. E. Tulloch , *Progr. Photovolt.: Res. Appl.*, 2007, **15** , 1 CrossRef CAS .
47. M. A. Green , K. Emery , D. L. King , Y. Hishikawa and W. Warta , *Progr. Photovolt.: Res. Appl.*, 2006, **14** , 455 CrossRef .
48. A. Hagfeldt and M. Gratzel , *Acc. Chem. Res.*, 2000, **33** , 269 CrossRef CAS .

This journal is © The Royal Society of Chemistry 2012

About | Cited by | Related

Download this article
PDF format

Article HTML

Publication details

The article was received on 17 Nov 2011, accepted on 11 May 2012 and first published on 13 Jun 2012

Article type: Paper

DOI: 10.1039/C2JM15953H

Citation: *J. Mater. Chem.*, 2012, **22**, 14254-14261

BibTex

Request permissions

Search articles by author

- Antonio Tricoli
- Anna S. Wallerand
- Marco Righettoni

Spotlight

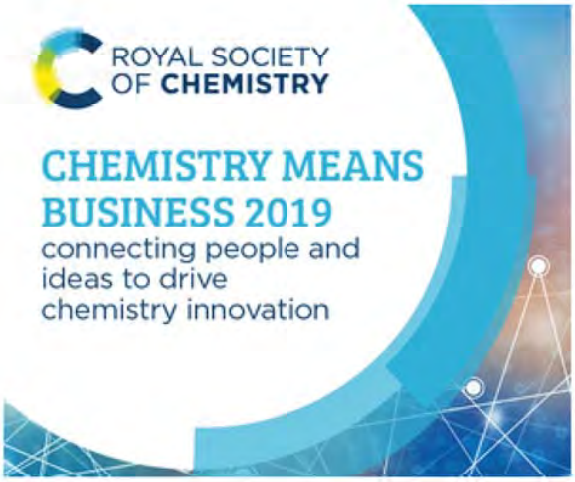

Advertisements

Journals, books & databases

Home
About us
Membership & professional community

APPENDIX R

Campaigning & outreach
Journals, books & databases
Resources & tools
News & events
Locations & contacts
Careers
Awards & funding
Advertise
Help & legal
Privacy policy
Terms & conditions

© Royal Society of Chemistry 2019
Registered charity number: 207890

APPENDIX S

APPENDIX S

PRODUCER® BLACK DIAMOND® PECVD

Applied Producer Black Diamond 3 extends Applied's leadership in nano-porous low-k (/glossary#k-value) dielectric (/glossary#dielectric) technology to enable the scaling of advanced interconnects (/glossary#interconnect) to 28nm and below.

Russ Perry explains the evolution of low-k films and the benefits of the newest member of the Black Diamond family of dielectrics.

The Black Diamond II nano-porous low-k film is the industry standard for the 45/32nm copper/low-k interconnects, with a k-value (/news/media-resources/technical-glossary#k-VALUE) of approximately 2.5. Its predecessor, Black Diamond (k~3.0), is the industry-standard for the 90/65nm nodes. Creating nano-porous low-k film is a two-step process consisting of PECVD deposition of an organosilicate glass "backbone" and a thermally labile (/news/media-resources/technical-glossary#LABILE) organic phase, followed by an ultraviolet (UV) cure that removes the labile phase—thereby inducing porosity—and restructures and strengthens the remaining silicon-oxide matrix to form the final nano-porous film. Small average pore size and tight pore size distribution eliminate the need for pore sealing.

The next-generation Black Diamond 3 film extends this industry-leading technology to ultra-low-k (ULK) film (k~2.2) for scaling to 22nm and below and improving device speed. It also imparts the mechanical strength (hardness and elasticity) required by emerging advanced packaging schemes. The film exhibits excellent moisture resistance, stable k-value after etch and photoresist (/glossary#photoresist) removal, and superior mechanical strength.

EXTENDING COPPER

INTERCONNECT

Volume 11, Issue 1, 2013

Read More (http://www.appliedmaterials.com/files/nanochip-journals/NanochipTechJournal_Vol11Issue1_2013_Security.pdf#page=7)

OPTIMIZING NANO-POROUS

DIELECTRICS

Volume 9, Issue 2, 2011

Read More (http://www.appliedmaterials.com/files/nanochip-journals/nanochiptechjournal_vol9_issue2_july2011.pdf)

TECHNICAL DOCUMENTS

Black Diamond 3 Technical Briefing (http://www.appliedmaterials.com/files/Black_Diamond_3_web.pdf) (700.2kB)

Nanocure 3 Technical Briefing (http://www.appliedmaterials.com/files/Nanocure_3_web.pdf) (699.1kB)

Black Diamond 3 Key Messages (http://www.appliedmaterials.com/files/BD3-Nanocure3-key-messages.pdf) (102.0kB)

Structural Evolution of Nano-Porous Ultra-Low-k Dielectrics under Broadband UV Curing (http://www.appliedmaterials.com/files/AMC2007_P513.pdf) (87.9kB)

Porous Low-k Dielectrics Using Ultraviolet Curing (http://www.appliedmaterials.com/files/ADemos_etal_PorousLow-kDielectricsUsingUltravioletCuring_SST_0905.pdf) (189.7kB)

SEMICONDUCTOR NEWS

07.09.19 Applied Materials Enables Emerging Memories for... (/company/news/press-releases/2019/07/applied-materials-enables-emerging-memories-for-the-internet-of-things-and-cloud-computing)

07.01.19 Applied Materials to Acquire Kokusai Electric (/company/news/press-releases/2019/07/applied-materials-to-acquire-kokusai-electric)

Cookie Policy (http://www.appliedmaterials.com/cookies)
Accept

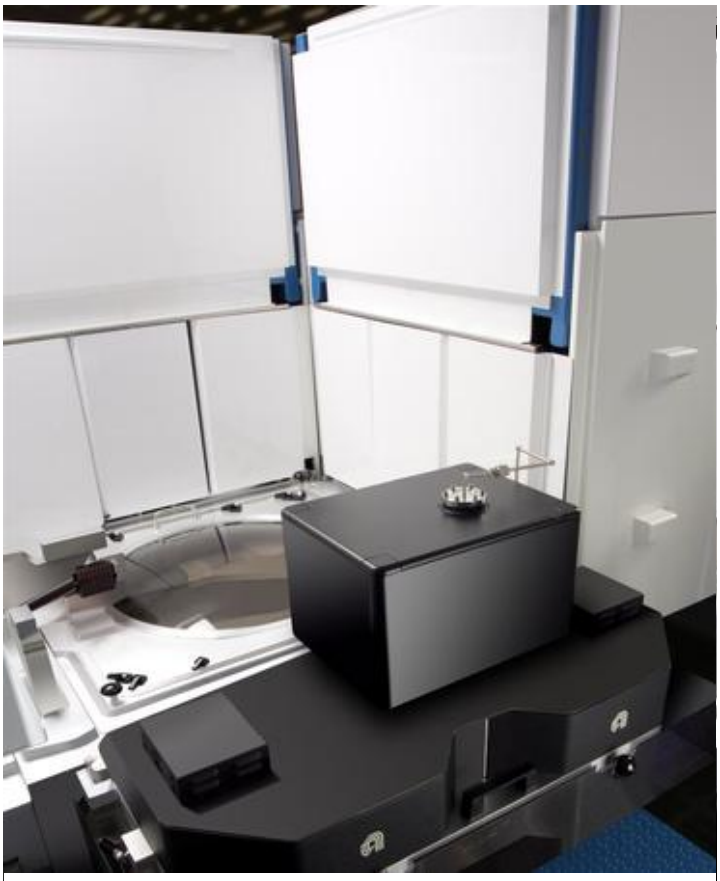

The Black Diamond 3 film is deposited using the production-proven, high-throughput Producer GT platform.

The Producer Black Diamond 3 system is designed to work with the Applied Producer Nanocure™ 3 (/technologies/library/producer-nanocure-3-uv-cure) UV curing system. The Nanocure 3 system employs a high-intensity UV source to stabilize and densify the Black Diamond 3 film to provide optimum mechanical and optical properties.

This two-step deposition and cure process provides up to twice the mechanical strength of Applied's successful second generation Black Diamond film – reducing device variability and boosting chip yield.

SEMICONDUCTOR BLOG

09.12.19 Themes of an AI Summer: VC Perspectives (http://origin-blog.appliedmaterials.com/themes-ai-summer-vc-perspectives)

08.21.19 The AI Paradox (http://origin-blog.appliedmaterials.com/ai-paradox)

07.31.19 Exploring the Future of Memory at Flash Memory... (http://origin-blog.appliedmaterials.com/flash-memory-summit)

Seoul Semiconductor, Exhibit 2001
LGI v. SSC, IPR2019-01154

Product Library (/products)

Contact Sales (/company/contact/global-services-and-sales)

(/company/corporate-responsibility)

Investor Relations (/company/investor-relations)

News & Events (/company/news)

Sitemap (/sitemap) | Terms of Use (/terms-of-use) | Privacy (/privacy) | Cookies (/cookies) © 2019 Applied Materials, Inc. All Rights Reserved.

Cookie Policy (http://www.appliedmaterials.com/cookies)

Accept

Seoul Semiconductor, Exhibit 2001
LGI v. SSC, IPR2019-01154